Wind Energy Systems Centre for Doctoral Training

Department of Electronic & Electrical Engineering

University of Strathclyde, Glasgow, Scotland

Wind Turbine Blade Leading Edge Erosion: An investigation of rain droplet and hailstone impact induced damage mechanisms

---

Mark Hugh Keegan

Submitted in fulfilment of the requirements for

the degree of Doctor of Philosophy

2014

This thesis is the result of the author's original research. It has been composed by the author and has not been previously submitted for examination which has led to the award of a degree.'

Signed: Date:

Abstract

Leading edge erosion of modern wind turbine blades is a growing and developing issue within the wind industry, effecting blade performance and efficiency. Little is known, researched or published on the phenomenon and there are currently no apparent full-proof material solutions for the issue. The research presented here looks to develop a fuller understanding of the issue of leading edge erosion, through first reviewing the literature (both within and outwith wind energy) on the topic to put the issues in context, and then subsequently further exploring and investigating the key damage mechanisms associated rain droplet and hailstone impact on the blade leading edge; identified as two of the most erosive types of environmental exposure. Both numerical (finite element) and experimental methods are employed to identify the key damage mechanisms associated with each form of impact in the different possible blade material coating and substrate systems. It is found that for rain exposure, surface degradation and erosion is a real risk for classical gelcoat coating systems. Whereas, for newer flexible and more erosive resistant materials, interface damage and debonding from the substrate is the most likely form of damage creation. Hailstone impact is found to pose a heightened erosive threat in comparison to rain, based on individual impact damage creation; although it is recognised that hailstorms are far more infrequent than rain showers in most regions. However, it is predicted that for extreme hailstones of sufficient mass, significant substrate composite damage could also be created through impact on the leading edge. Future work and further research development aimed at further understanding the issues of blade leading edge erosion are also identified and discussed.

Acknowledgements

I would firstly like to give thanks to both my academic advisors David Nash and Margaret Stack for their guidance, support and encouragement throughout my PhD studies. David has been a mentor as much as an advisor and has presented me with the support and opportunity to develop and grow my expertise in numerous other projects throughout my time as a PhD student. He was also responsible (a very long time ago now) for providing me with the opportunity to study in Japan for a semester, an experience which I treasure to this day and will never forget. Margaret has contributed a significant amount of support and input into my research, encouraging and shaping my efforts in publishing the findings of my work. Her drive and scrutiny has helped to get the best out of me and my research.

I would also like to thank the EPSRC for providing the funding for the research, through the Wind Energy Systems Centre for Doctoral Training. I would also like to thank Bill Leithead and David Infield for their vision and drive in establishing and running the centre, as well as the centre administrator Drew Smith for his support and company over the years. I also extend thanks to the rest of my fellow CDT students who made my time as a PhD student so enjoyable; perhaps more enjoyable than it should have been!

For their support to my research I would like to thank Chris Cameron for his fantastic work in creating the experimental apparatus required and his support thereafter, and also Irina Cortizo for helping to explore the available modelling options further.

I was also fortunate enough to have fantastic input and support from industry throughout my research, principally: John Bingham, Kirsten Dyer, Ewen Morrison, Michael Drachmann Haag and Christian Claus.

I would like to thank my long suffering family: my mother Christine, father John and sister Amy for their long standing support and love. I wouldn't be who I am today without them.

Last, but by no means least, I would like to thank my wife Sarah-Louise for all her love and support throughout the years, her belief in my abilities to finish the work, and for finding the time to marry me in my final year.

Contents

1. Introduction 1
   1.1 Wind Energy Deployment & Growth 1
   1.2 Environmental Exposure of Wind Turbine Blades 4
   1.3 Purpose of Current Research Project 5
2. Literature Review 8
   2.1 History of Wind Turbine Technology 8
   2.2 Wind Turbine Size and Performance 9
   2.3 Blade Design 11
      2.3.1 Historical Blade Design 13
      2.3.2 Modern Blade Design 13
   2.4 Blade Material Technology 14
      2.4.1 Engineering Material Selection 14
      2.4.2 Fibre Reinforced Polymer Composites 15
      2.4.3 Composite Material System Designs 17
      2.4.4 Wind Turbine Blade Composites 21
      2.4.5 Blade Surface Coatings 27
   2.5 Manufacturing 30
      2.5.1 Material Handling and Application 30
      2.5.2 Manufacturing Process 31
      2.5.3 Effect of Manufacturing Flaws on Impact Performance 34
   2.6 Summary 35
3. Blade Leading Edge Erosion 37
   3.1 Significance in Industry 37
      3.1.1 Documented Cases of Leading Edge Damage 37
      3.1.2 Leading Edge Protection Material Solutions and Developments 39
      3.1.3 The Role of Polyurethane Based Materials for Leading Edge Protection 45
      3.1.2 Effects of Leading Edge Erosion on Wind Turbine Performance 46
      3.1.3 Repair and Maintenance 49
   3.2 Rain Erosion 52
      3.2.1 Exposure 52
      3.2.2 Rain droplets as a projectile 54
      3.2.3 Liquid impact phenomena 57
      3.2.4 Rain droplet impingement induced damage 61
      3.2.5 Experimental rain erosion evaluation 66
   3.3 Hailstone Impact & Erosion 70
      3.3.1 Exposure 70
      3.3.2 Hailstones characteristics & material properties 71

3.3.3 Hailstones as an impact projectile 74
3.3.4 Experimental Hailstone Impact Evaluation 77
3.4 Other Environmental Influences 78
3.4.1 Ultraviolet light 79
3.4.2 Sea spray 79
3.4.3 Sand, dust and other particulate matter 79
3.5 Impact Performance of Polymer Matrix Composites 81
3.6 Summary of Threat 83
4. Rain Droplet and Hailstone Impact Numerical Modelling Techniques 85
4.1 Modelling Approaches & Software 85
4.1.1 Computer System Used 86
4.1.2 LS-DYNA Terminology 86
4.1.3 Explicit Dynamics 87
4.1.4 Classical Lagrangian Finite Element Method 88
4.1.5 Eulerian 89
4.1.6 Smooth Particle Hydrodynamics 90
4.2 Modelling Rain Droplet Impact 90
4.2.1 Previous Work in Literature 91
4.2.2 Selection of Modelling Approaches 95
4.3 Modelling Hailstone Impact 96
4.3.1 Previous Work in Literature 96
4.3.2 Selection of Modelling Approaches 116
4.4 Software Selection 117
4.5 Modelling Target Materials - LS-DYNA Approach 117
4.5.1 Element Type 118
4.5.2 Polymers 118
4.5.3 Composites 123
5. Projectile Modelling Method: Assessment and Selection 135
5.1 Rain Droplet 135
5.1.1 Assessment Model Configuration 135
5.1.2 Eulerian Approach 136
5.1.3 Smooth Particle Hydrodynamics Approach 138
5.1.4 Results 140
5.1.5 Evaluation of Methods 159
5.2 Hailstone 167
5.2.1 Carney Model-SPH Validation Model Setup 167
5.2.2 SPH Sensitivity Study for Ice 176
5.3 Characterisation of Wind Turbine Blade Properties for Numerical Analysis 178

5.3.1 Blade Target Configuration 178
5.3.2 Structural Stress States 181
6. Rain Impact Modelling 183
6.1 Rain droplet impact induced damage of a gelcoat 184
6.1.1 Gelcoat material properties 184
6.1.2 Model set up 187
6.1.3 Results & Discussion 191
6.2 Rain droplet impact induced erosion of a gelcoat material 210
6.2.1 Model Setup 210
6.2.2 Results and Discussion 212
6.3 Rain droplet impact induced damage of a gelcoat on a composite substrate 216
6.3.1 Model Setup 216
6.3.2 Results & Discussion 220
6.4 Rain droplet impact performance of flexible coatings 223
6.4.1 Model Setup 224
6.4.2 Results & Discussion 226
6.5 Protection provided by flexible tapes and the risk of debonding 237
6.5.1 Model Setup 238
6.5.2 Results and Discussion 242
6.6 Discussion 249
6.6.1 Rain droplet impact induced damage of the gelcoat 249
6.6.2 Rain droplet impact induced erosion of the gelcoat material 251
6.6.3 Rain droplet impact induced damage of a gelcoat on a composite substrate 251
6.6.4 Rain droplet impact performance of flexible coatings 251
6.6.5 Protection provided by protective tapes and the risk of debonding 252
7. Hailstone Impact Modelling 253
7.1 Theoretical Wind Turbine Blade Coating Hailstone Impact Response 254
7.1.1 Model Setup 255
7.1.2 Results and Discussion 257
7.2 Theoretical Blade Skin Hailstone Impact Response 271
7.2.1 Model Setup 272
7.2.2 Results & Discussion 277
7.3 Experimental Blade Sample Impact Simulation 294
7.3.1 Model Setup 294
7.4 Hailstone Impact Modelling Discussion 300
8. Experimental Hailstone Impact Analysis 302
8.1 Rig Design & Build 302
8.2 Hailstone Impact Rig Commissioning & Calibration 307

8.3 Wind Turbine Blade Composite Impact Verification Experiments 310
8.3.1 Aims & Objectives 310
8.3.2 Target Sample Configuration &Manufacturing 311
8.3.3 Projectile Manufacturing and Sourcing 314
8.3.4 Experimental Procedure 315
8.3.5 Results & Discussion 317
8.4 Experimental-Numerical Ceramic Validation 326
8.4.1 Batch A Results Comparison 326
8.4.2 Batch B Results Comparison 331
8.4.3 Numerical Validation Discussion 337
9. Discussion 338
9.1 Impact and Research Findings 338
9.1.1 Rain Impact 338
9.1.2 Hailstone Impact 340
9.2 Modelling Challenges and Barriers 341
10. Further Work and Future Developments 344
10.1 Rain 344
10.2 Hailstone 345
10.3 Further Flexible Coating Impact Analyses 346
10.4 Other Damage Influencing Factors 347
10.5 Probability Analyses 347
10.6 Related Studies 348
11. Conclusion 349
12. References 352
Appendix I – Sensitivity study: Hailstone SPH node total 1
Appendix II – Sensitivity study: Gelcoat target mesh sensitivity 2
Appendix III – Sensitivity Study: W4600 target mesh sensitivity 3
Appendix IV – Sensitivity Study: Hailstone Impact, Gelcoat Target Mesh Sensitivity 4

1. Introduction

Through increasing political, social and economic pressure and the requirements for sustainable energy sources, the global demand for installed wind capacity has gone through an unprecedented increase over the last decade. Driven by carbon emission reduction commitments, in Europe namely the European Commission 2020 targets [1], wind energy has played the most prominent role in the efforts of decarbonising global energy supply.

1.1 Wind Energy Deployment & Growth

Since 2002, the global cumulative installed wind capacity has grown from 6.1GW in 1996 to a current total of 282.43GW as of 2012 [2], as shown in Figure 1-1.

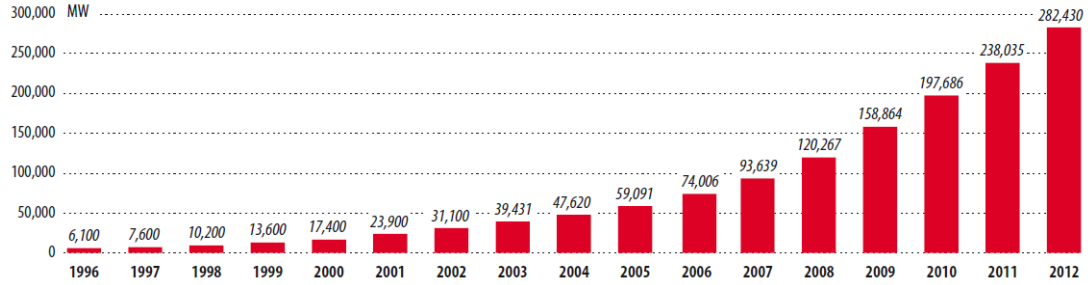

Figure 1-1. Global cumulative installed wind capacity. Source: **[2]**

From Figure 1-1 the rapid growth of installed wind capacity over the past decade is clearly illustrated. In the year 2012 alone, a global total of 44.7GW of wind energy capacity was installed, with China and the U.S.A. both accounting for 13GW each of this total number [2]. Figure 1-2 shows in greater detail the share of the global cumulative installed capacity amongst the 10 most active countries with regards to installed wind energy capacity.

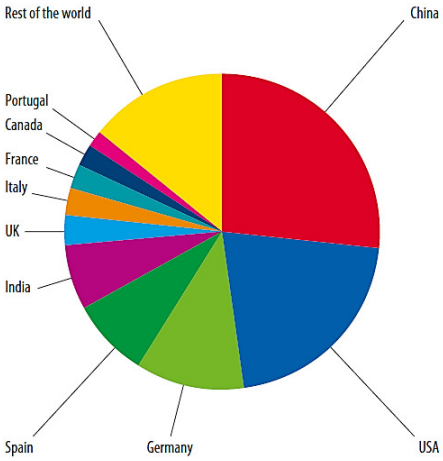

Country	MW	% SHARE
PR China**	75,564	26.8
USA	60,007	21.2
Germany	31,332	11.1
Spain	22,796	8.1
India	18,421	6.5
UK	8,445	3.0
Italy	8,144	2.9
France**	7,196	2.5
Canada	6,200	2.2
Portugal	4,525	1.6
Rest of the world	39,853	14.1
Total TOP 10	**242,630**	**85.9**
World Total	**282,482**	**100.0**

Figure 1-2. Top 10 cumulative installed wind capacity, globally. Source: [2]

This again highlights the prominent role of both China and the USA with regards to their cumulative installed wind capacity, but also shows that, collectively, EU countries also account for a significant portion of the global cumulative installed wind capacity.

In the year 2000 the total capacity of installed wind within the EU stood at 12.9GW, this total grew rapidly over the next decade to a total of 106GW by the year 2012; with 10% of this total comprising of offshore capacity [3]. The European Wind Energy Association (EWEA) [4] has also targeted further growth to a total of 230GW by the year 2020, with 40GW of this target comprising of offshore installations. Figure 1-3 looks specifically at the global cumulative installation of offshore wind capacity in the years 2011 & 2012 [2].

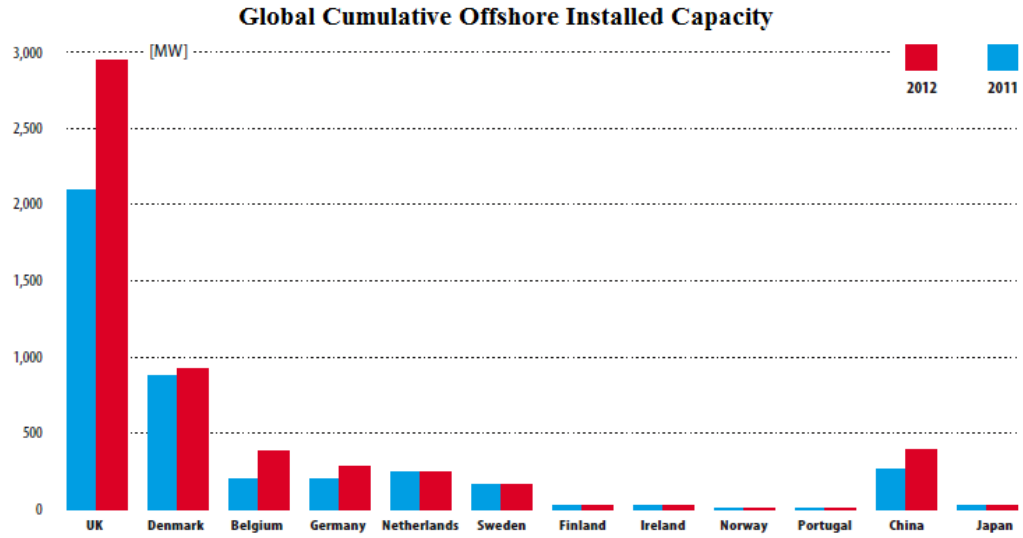

Offshore (MW)	Total 2011	New 2012	Total 2012
UK	2,093.6	854.2	2,947.9
Denmark	874.3	46.8	921.1
Belgium	195.0	184.5	379.5
Germany	200.3	80.0	280.3
Netherlands	246.8	0.0	246.8
Sweden	163.7	0.0	163.7
Finland	26.3	0.0	26.3
Ireland	25.2	0.0	25.2
Norway	2.3	0.0	2.3
Portugal	2.0	0.0	2.0
PR China	262.6	127.0	389.6
Japan	25.2	0.1	25.3
Total	**4,117.3**	**1,292.6**	**5,410.0**

Figure 1-3. Global cumulative offshore installed capacity. Source: **[2]**

From this it is clear that with regard specifically to offshore installed wind capacity, the UK has a significant share of the global total. The prominence of the UK in this regard can be attributed to several factors:

1. Perhaps most obviously, the UK is an island nation and therefore is completely surrounded by (potentially utilisable) bodies of water.

2. These bodies of water, such as the North Sea, are relatively shallow (typically under 100m) [5], meaning that the fixed installation of wind turbines on the sea bed has proven technically (and in a wider sense commercially) viable.
3. The wind resource in the offshore areas surrounding the UK (and in particular the North Sea) is also high [6], making many sites more commercially viable with regards to (what can be costly) offshore installations.

Further to this 2947MW cumulative offshore installed capacity in the UK, by the year 2020, the Crown Estate [7] aims to host a total wind capacity of 25GW in its offshore sites [8] (either operational or under construction). The current total onshore installed wind capacity in the UK stands at over 6000MW, there exists some ambiguity with regards to the potential further development of onshore installations in the UK, however a possible total between approximately 10-20GW has been reported [9].

The rapid growth in the deployment of installed wind energy capacity has presented numerous and varied challenges for governments, grid operators, turbine manufacturers and supporting industries and organisations; bringing about rapid developments and growth in what was a relatively young industry. With these challenges, numerous new technologies, industries and areas of research and development (both in technical and non-technical aspects) have emerged; alongside the growth and strengthening of pre-existing aspects.

As well as an unprecedented growth in the installed capacity of wind energy globally, the scale of wind turbine technology has also increased dramatically over the last decade. The significant up-scaling of wind turbine technology has been the source of many of the technological and engineering challenges. One of the biggest challenges has been brought about by the requirement for longer wind turbine blades, in order to increase the maximum potential energy capture for a given wind turbine. Such developments have required extensive research and development in the areas of material technology, structural design and manufacturing, culminating in the creation of highly advanced and bespoke wind turbine blade designs capable of performing to the high standards required by manufacturers.

This acceleration in development means that a blade length in excess of 50 metres is not only now feasible but also common in utility scale designs (as discussed in Section 2.2). In addition to this extreme in length, such blades will also commonly exhibit maximum blade tip speeds in excess of $70 m \cdot s^{-1}$ presenting new challenges with regards to erosion and damage to the blade leading edge in these regions, brought about through exposure to a potentially hostile operating environment.

1.2 Environmental Exposure of Wind Turbine Blades

The operational environmental conditions to which any given wind turbine is exposed to during its service life may vary significantly between continents, from country to country, from site to site and for some locations within a wind farm itself. Given the restrictions imposed through many planning processes with respect to siting wind farms at an agreeable distance from built-up or residential areas, many onshore wind farms are located in remote and exposed locations where the environmental conditions could be described as hostile; however, such locations may also be advantageous with regards to wind resource. Offshore wind farms are inherently completely exposed to the elements and hostilities of the offshore environment, but again may benefit from a strong wind resource. Some of the most prominent and likely environmental factors to which an onshore and offshore wind turbine blade may be exposed to throughout its service life are:

- **Extreme gusts & turbulence -** Particularly on exposed and/or hilly terrain where the turbine is fully exposed to strong winds and the turbulent effects induced by the topology of the surrounding landscape and foliage/forestry.
- **Sunlight -** All wind farm locations will be exposed to sunlight during their service life; however this will differ in both duration and intensity between sites.
- **Temperature extremes -** Some locations may experience extremes in temperatures and may also be subject to large swings in temperatures on an hourly, daily and/or seasonal basis.
- **Rain –** Almost all wind farm sites will be exposed to some degree of rainfall, again this will vary in frequency and intensity between sites.
- **Hailstones –** Some locations may experience hailstorm events, again differing in both frequency and intensity.
- **Icing –** In colder climates, icing on the blades can routinely occur [10].
- **Dust, dirt, sand & other particulates –** Many locations will be exposed to general dust, dirt and particulate matter. In arid, desert and/or coastal locations, sand impingement may also be another factor. Most onshore sites will also play host to varied wildlife which may include insects, birds or bats, all of which may come into contact with the blades
- **Sea spray & salt crystals/deposits –** In the offshore environment, spray whipped up from the water surface may come into contact with blade surface. Additionally, salt crystals carried in the wind may also be deposited on the blade surface.

This list is obviously not exclusive or exhaustive but represents perhaps the most common environmental factors at both on and offshore locations. As stated the frequency and intensity of each variable may differ significantly between sites (and in some cases turbines). However, it is clear that for any given wind turbine, exposure to a wide and varied range of environmental variables may be possible. Additionally, most blades will likely commonly be exposed to a combination of these variables acting together (i.e. strong winds and hailstones in storm conditions) to create uniquely hostile conditions. The significance of these potentially hostile conditions is made starker when considering the 20+ year proposed service life of many blade/turbine designs, during which the blade will be exposed to such conditions. In addition, during this time, inspection and maintenance (scheduled or otherwise) has to be kept a minimum in order to reduce costs and limit turbine down time. Therefore, a great deal of confidence in the performance of the blade materials with respect to environmental resilience is required in order to fulfil these requirements.

1.3 Purpose of Current Research Project

It is clear then that the increased magnitude of both typical blade lengths and blade tip speeds, coupled with a commonly hostile operating environment, present unique and challenging issues with regard to both the proper operation of wind turbines and the performance of the blades themselves.

Very little has been published or understood with regards to the wear and impact resistance of blade tip leading edge material technologies (paints, coatings etc.) and the erosive and impact damaging effects imposed by airborne particulates such as rain droplets or hailstones. Even less is known about the mechanisms through which leading edge damage is induced through rain and hailstone impact and the effects this damage may have on the material integrity of the blade leading edge in a wider sense.

In light of such shortcomings in knowledge and understanding on the issues discussed, the following research topic was initially proposed as a result of industrial consultation and interaction:

*"*Investigate the effects of erosion on the leading edge of wind turbine blades in the offshore *environment"*

The effect of rain and hailstone induced erosion and impact damage was the primary concern. In addition, although the conditions offshore were potentially more hostile, any research work undertaken may also be applicable to the onshore environment, and

consequently the effects onshore were not discounted from the final research programme. It was also believed that in order to investigate the effects of damage induced through rain and hailstone impact, a stronger understanding of the impact phenomena and the potential damage mechanisms was required. Numerical modelling and simulation work could aid in this endeavour; supplemented by a suitable experimental verification programme. Subsequently the research work proposed can be summarised as:-

"Investigate the* effects of rain and hailstone erosion and impact damage on the leading edge of wind turbine blades, and establish a robust understanding of the respective impact *phenomena and the damage mechanisms induced."

The key research objectives were identified as follows:-

1. **Literature Review –** A wide spanning literature review was identified as an essential early research activity, looking to review the issue of leading edge damage, ranging from the fundamental physics involved to documented cases and proposed solutions. This would entail developing an understanding of such things as: blade design, blade materials, wind turbine operation, the nature of rain and hailstone weather events and the phenomena of rain and hailstone impact. Through understanding these fundamental aspects and additionally reviewing the occurrence of real life leading edge damage and their effects on turbine performance, the real significance of leading edge damage could then be put into context. Such an endeavour was considered essential as it would both represent a first in the area of research, as well as set the agenda for further work.
2. **Establishment of Appropriate Impact Modelling Techniques –** It was established early on, that in order to better understand the respective impact phenomena and the associated blade material response, numerical simulations of both rain droplet and hailstone impact should be carried out. It was thought that such modelling efforts could provide detailed and useful insight into the impact phenomena and shed light on the potential damage mechanisms. Therefore, as well as conducting a wide spanning review of the issue of blade leading edge damage, a more asserted and refined review of the potential numerical impact modelling techniques would also be required. Such a review would then allow for the establishment of appropriate impact modelling approaches for both rain and hailstone impact. This process would also assist in creating a working familiarity with such techniques and develop the skills required to implement them correctly; using the respective software.

3. **Rain and Hailstone Numerical Impact Studies –** The establishment of appropriate modelling techniques would subsequently grant the freedom to begin impact studies addressing the impact of rain droplets and hailstones on typical wind turbine blade materials and leading edge profiles. The aim of such work would be to investigate forces and pressure exerted by such impact bodies, and the stresses, strains and importantly the damage created through such impact in the blade materials.
4. **Experimental Impact Studies –** Experimental investigations of both rain and hailstone impact on blade samples - through appropriate techniques and approaches - were targeted to both validate the numerical modelling findings and compliment and further the develop the understanding of such findings.

These four core activities would therefore bring about a greater level of understanding required with regards to leading edge impact and erosion damage on wind turbine blades. In addition, such a body of work could act as the foundation for a wider research programme in this field.

2. Literature Review

2.1 History of Wind Turbine Technology

Wind mills have been historically used for agricultural purposes for several thousand years [11], however for most of the early 20th century they were used only in a limited capacity for electricity generation; for purposes such as charging batteries for power in remote dwellings (away from grid access).

The prevalence and abundance of fossil fuel resources, coupled with an absence in carbon emission concerns, meant that there were no strong economic or societal drivers for the research and development of wind turbine electrical generation throughout much of the 20th century. However, there are several examples of pioneering wind turbine development from individual institutions and individuals - as reviewed by Burton et al. [11] - such as the 1250kW Smith-Putnam wind turbine [12] constructed in the USA in 1941.

The significant rise in oil prices in 1973 resulted in a heightened interest in exploring and developing the techniques and technologies associated with extracting power from the wind [11]; often heavily backed with funding from governments. In the USA a series of prototype turbine designs were created, starting with the 38m diameter 100kW Mod-0 in 1975 and ending with the 97.5m diameter 2.5MW Mod-5B in 1987 [11]. Several other governments also conducted their own programmes to research and develop their own wind turbine technologies. Such efforts and their outcomes provided a more robust and enhanced understanding of the science of extracting power from the wind; with respect to both understanding the resource and the required technologies and devices. However, there still remained a certain level of ambiguity and difference of opinion between different bodies as to which type of wind turbine architecture and design was the most effective, both in an economic and technological sense. Additionally, the challenges associated with running a large unmanned mega-watt turbine prototypes in hostile operating environments were often underestimated, and as such, many of these early prototypes experienced failure and proved unreliable.

However, at the same time as these developments in large multi-megawatt concepts and designs, private companies (heavily supported by the state) were also developing much smaller designs (approximately 100kW) for commercial sale. Such designs were employed extensively in the 1980's in California, where strong financial incentives existed for the installation of wind energy [11]. Over time the 'Danish' concept of wind turbine design became the most prominent and established; a simple horizontal axis, three bladed, stall

regulated wind turbine architecture. This maturing of wind energy technology in the 1980's did not however result in significant global uptake of the technology in the decade which followed; however some countries, such as Denmark, did install significant amounts of wind capacity. It took until about the turn of the century for a renewed and stronger government interest in wind energy to re-emerge, as a result of global concerns regarding carbon emission and climate change (discussed previously). This renewed interest has brought about dramatic changes in the state of the art wind turbine technology, both in regards to the scale and the performance of the turbines; as discussed in the following section.

2.2 Wind Turbine Size and Performance

The desire for increased energy capture for a given wind turbine has resulted in the requirement for an increase in the swept area of the blade. The power output for a given wind turbine is given by:

$$P = \frac{1}{2} C_P \rho A U^3 \tag{2.1}$$

where P, is the power output, C_P is the power coefficient, ρ is the density of the medium (air in this case), A is the swept area of the rotor and U is the incoming wind speed. The power coefficient is a characteristic of the given wind turbine design and represents the fraction of the total power in the incoming wind captured by the turbine and has a maximum theoretical 'Betz' limit value of 0.593 [11]. Therefore, besides improving the power coefficient, the only other method of increasing the potential energy capture of a given turbine (at a given location) is to increase the rotor swept area. However, this assumption does not consider the cost considerations associated with constructing large scale rotor, and therefore the optimum design size in relation to cost effectiveness is often a matter of debate. For example, those in favour of large designs claim that the economics of scale apply to wind turbine design, however this can be countered by the fact that although the power output scales with the square of the diameter, the mass of the rotor (and therefore cost) scales as the cube of the diameter [11]. There is of course a trade-off which will apply to specific wind turbine designs and this may differ greatly between designs.

Irrespective of this debate, the rotor diameters of commercial scale wind turbines have grown dramatically since the 1980's. Figure 2-1 shows the trend in blade length growth (and rated power) for utility scale wind turbines over nearly three decades.

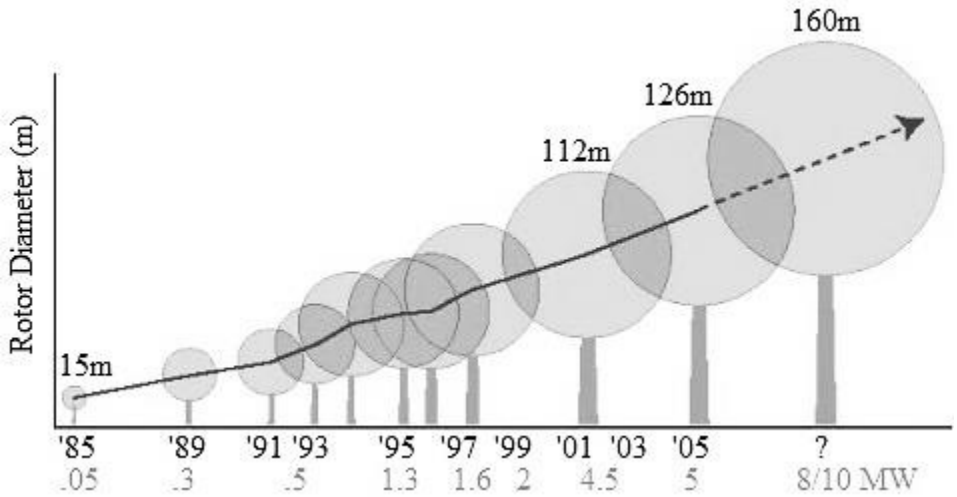

Figure 2-1. Blade length and rated power trends for wind turbines. Source: **[13]**

This increase in blade length coupled with the operational strategy of modern turbine designs has resulted in an increase in the blade tip speeds exhibited by many designs. Figure 2-2 plots the maximum blade tip speed against the associated rotor diameter for numerous utility scale turbines from various manufacturers; taken from a range of manufacturer literature.

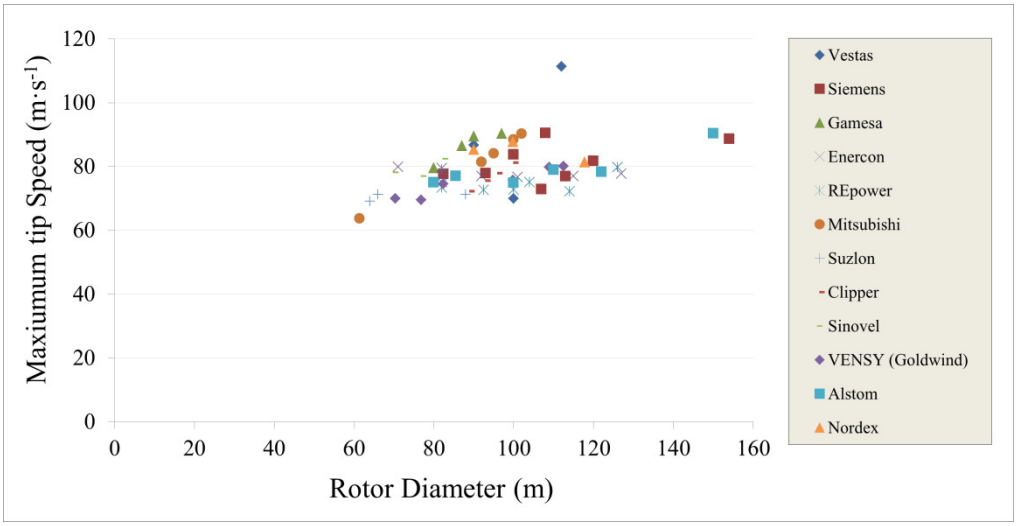

Figure 2-2. Blade tip speed vs. rotor diameter for various utility scale wind turbine models. Data sourced from manufacturer literature

As shown, tip speeds in excess of 80m·s^{-1} are now commonplace for large wind turbine designs. If operating at such tip speeds during a rain shower or hailstorm, the potential for high speed impact from rain droplets and hailstones on the blade leading edge becomes apparent. Additionally, when considering the impact of rain droplets and (more so) hailstones on the leading edge, the incoming freefalling velocity can further heighten the potential impact velocities on the blade leading edge. From reviewing the data there is an

apparent trend in increasing tip speed with increasing rotor diameter; however the tip speed is heavily dependent on turbine operational strategy and control. It should also be noted that these tip speeds only represent the maximum possible values for the given design. During their operational lifetimes, the turbines may only operate at these speeds for a limited (but significant) amount of time.

Indeed, it is important to note not only the magnitude of the tip speeds exhibited by the blades, but also the total amount of operational hours the blade will complete in its lifetime. A typical wind turbine may be expected to operate continuously for approximately 15 years over its service life (this is, of course, site and design sensitive), the significance of this duration is highlighted further when considering that most modern automobiles may only ever operate continuously for around 9 months during their service life [14]. During these years of continual operation, the materials of the blade are not only exposed to varied environmental factors, but are also subject to constant fatigue loading as part of their standard mode of operation. Furthermore, during this period, the frequency of maintenance and access to the blade has to be kept to minimum in order to reduce the production and financial losses associated with turbine down time.

It is clear then that most wind turbine blades may be considered as high-performance components in engineering terms, with respect to both the operational loads imparted on them and the environmental conditions within which they are typically placed. Tip speeds around and in excess of $80 m \cdot s^{-1}$ are now common in many turbine design, couple this with an operational duration of 15 years continuously over a turbines service life, and the wear and erosion challenges posed to the leading edge (especially at the tips) becomes significant. Therefore the design of wind turbine blades and the material technologies utilised within them have been the subject of intense research and development as discussed in the following section.

2.3 Blade Design

As a consequence of the desire to extract as much power as economically viable from the wind resource for a given site, modern turbines can feature extremely large blades; in some cases in excess of 70m long. These extreme lengths present a significant and complex challenge with regards to the design and characteristics of modern blades. In reality, blade designers have to make many trade-offs in their designs in order to meet the many criteria of the desired blade performance. Some of the key areas of interest and focus in the design of modern blades relate to the following:

- **Blade Aerodynamics –** The blades must of course meet the aerodynamic performance requirements as set by the designer. This discipline requires the specification of parameters such as: aerofoil type, chord, twist and thickness, all of which typically vary along the length of the blade. In stall regulated designs it is essential that the required aerodynamic stall is exhibited by the blade when necessary.
- **Structural Performance -** Sound structural performance is vital to the success of any blade. This criterion relates to both the instantaneous and long term performance of the blade, such as the blade response to extreme loads or fatigue loading respectively. Additionally, many modern blade designs implement a smart blade concept, whereby the aerodynamic performance of the blade is optimised to work in synergy with blade deflections. Therefore in such designs, the deflection characteristics of the blade need to be well understood and alterable.
- **Blade Materials –** The materials employed in the design of a blade are obviously central to performance. The selection of appropriate materials in many cases may be considered as an integral part of the structural design process; however material selection can affect many of the other key areas of design as well, such as the dynamics and the environmental robustness.
- **Blade Dynamics –** The blade dynamics are of great importance to the performance of modern blades. The dynamic response and behaviour of the blade needs to be well understood and designed, in order to avoid undesirable blade loads and vibration modes, which can have consequences throughout the turbine drive train.
- **Noise Generation** – The noise generated by wind turbine blades can in many cases be extremely important, such as when the turbines are sited near residences and other built up areas. Given that the aerodynamic noise created by a blade can be approximately proportional to the fifth power of the tip speed [11], noise considerations can significantly influence the design of some wind turbines.
- **Environmental Robustness –** The environmental robustness of any blade has to be well considered and designed, given the many types of potential environmental exposure.
- **Manufacturing & Cost –** Ultimately, any conceived or established blade design has to be possible to build, furthermore, it must be possible to manufacture the blade within certain time (and cost) requirements.

These are only a few of the most prominent design variables, considerations and areas of focus in the context of wind turbine blade design. From reviewing these factors, it is clear that many (if not all) of them are inter-dependant and there will most likely be complex relations between a number of the factors. To put these factors and their influence into context the following sections look at the history of blade design and the typical designs now implemented in modern commercial scale wind turbines

2.3.1 Historical Blade Design

Many of the earliest wind turbine prototypes featured blades made of metals and alloys, such as the Putnam-Smith turbine (detailed earlier) which featured steel spars and a stainless steel skin; much like the topology of typical aircraft wings. NASA prototype turbines, such as the 'Mod-0', initially feature blades made from aerospace grade aluminium, however structural issues were quick to arise from the use of these materials [15]; owing to their poor performance with respect to the fatigue, exacerbated by issues such as tower shadow. In light of this, many subsequent prototype turbines utilised glass fibre and wood composite materials in the blade structure, which were found to provide better performance.

Although many of the early large-scale prototypes initially performed to requirements, most ended in some form of failure after a short period time (within a year); mostly attributed to targeting too large a step in both size and technology over a short time-scale [16]. It was the smaller scale commercial designs (<100kW) created in the 1980 (principally in Denmark), which better stood the test of time, and which acted as a foundation for further research and development as the market grew. These designs featured composite material blades using fibreglass and balsa wood composites [16] which proved to be a reliable and robust material choice.

2.3.2 Modern Blade Design

It is clear from a review of the history of blade designs, that blades are components which have received extensive research and development, and consequently they are components which are ever evolving and changing, both with respect to design and material choice; due to higher demands for improved performance & better outputs

Although blade designs can vary widely between manufacturers (and models), the blade cross-section illustrated in Figure 2-3 shows a construction that may be described as typical in many current modern blade design.

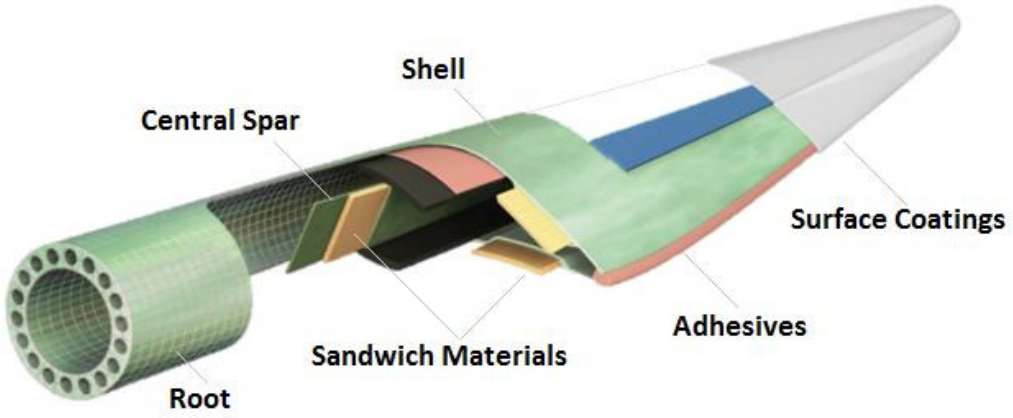

Figure 2-3. Typical blade cross section and materials. Original Image Source: **[17]**

The design features a thick sectioned root which acts as the connection point of the blade to the hub; the thick section is required due to the large bending moments to which it will be subjected. In order to provide stiffness in bending, most blade designs will incorporate some form of strong central spar member along the length of the blade. The exact details of such spars can vary greatly between different blade designs but are most commonly either box or I-Beam sections. The shell of the blade, which forms its aerodynamic profile, is usually rigidly attached to this central spar along the length of the blade. Surface coating and finishes are also applied to the blade shell to protect the composite substrate; as will be discussed. As stated, this design is by no means standard, and designs between manufacturers and models can vary widely, however most blades incorporate these basic design characteristics.

2.4 Blade Material Technology

2.4.1 Engineering Material Selection

Wind turbine designers and blade manufacturers recognise the need for blades to possess a high specific strength and stiffness in order to span the large distances required and deliver sufficient strength and stiffness without generating large root bending moments that would be associated with heavier materials. The specific strength and specific stiffness of a selection of engineering material classes are displayed in Figure 2-4, including metals and alloys, ceramics, composites, wood, polymers, foams and rubbers.

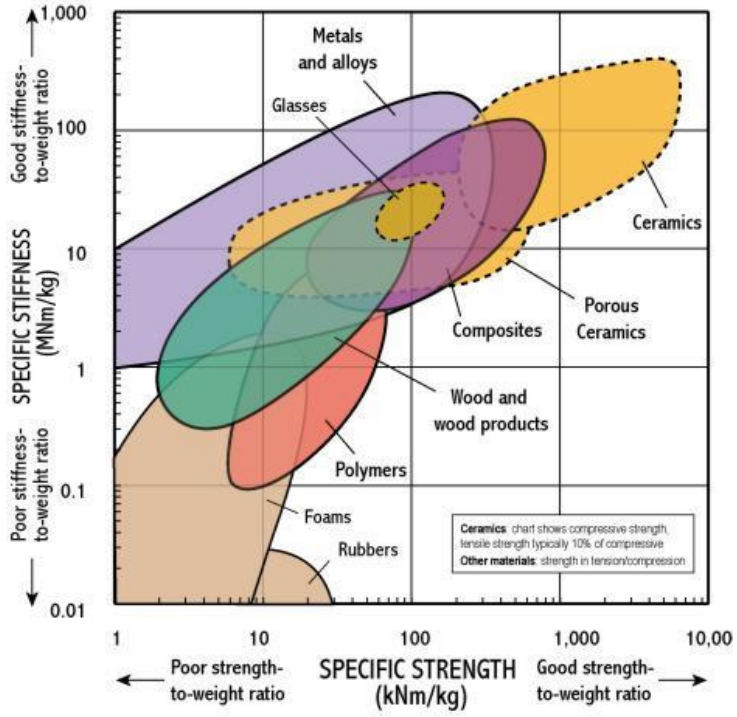

Figure 2-4. Specific stiffness and strength of various engineering material classes. Source: **[18]**

From Figure 2-4 it is clear that composite materials such as carbon and glass fibre reinforced plastics (CFRP and GFRP respectively) offer desirable specific strength and stiffness properties when compared to most metals and alloys. Such composite materials are only outperformed in this respect by more expensive and brittle ceramic materials; which are unsuitable for such large structures.

These merits have been at the heart of the decision by almost all large blade manufacturers to feature both GFRP and CFRP composite material technologies as the main structural material technology in their blades.

2.4.2 Fibre Reinforced Polymer Composites

The fundamental principle of fibre reinforced polymer composites is to combine extremely stiff and strong fibrous materials with a more ductile polymer matrix, to create a new material with engineering properties superior to that of the individual constituents. Figure 2-5 shows a typified representation of the stress-strain behaviour of the typical composite constituents (a fibre and matrix resin) and the resulting behaviour of a composite material created upon their combination (fibre reinforced plastic composite, FRP).

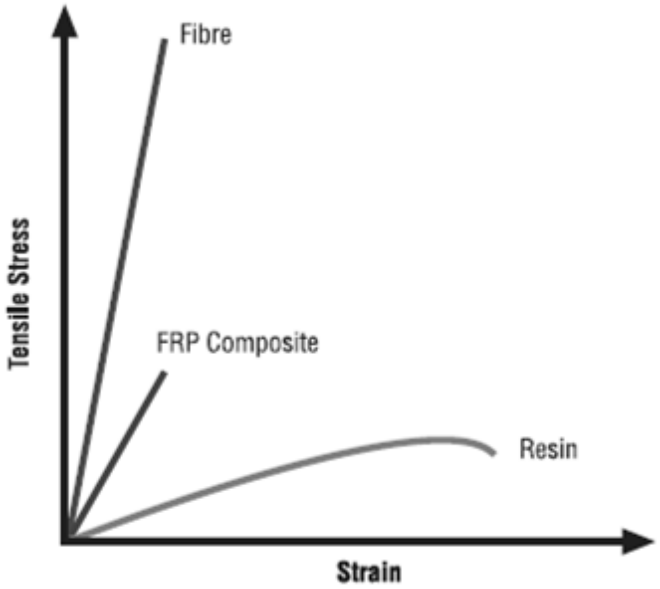

Figure 2-5. Stress-strain behaviour of a typified composite material and its constituent components. Source: **[19]**

As shown in Figure 2-5, although the reinforcing fibre constituent possesses a very favourable tensile strength it also exhibits very high stiffness (indicated by the steep slope) which, although perhaps desirable in theory, would make it an impractical engineering material for structures; given its brittleness and failure under low strain. Additionally, the strength and stiffness of a reinforcing fibre is strongly directionally dependant along the length of the fibre and off-centre loading will almost certainly result in breakage. Conversely, the resin material exhibits a more ductile stress-strain response, allowing for high levels of strain (deformation) in any direction, however offering limited tensile strength. Through embedding the fibres in the matrix material, a class of composite material is created, with the fibre reinforcement contributing high strength and stiffness and the matrix material offering a degree of flexibility and also acting as a bonding mode of load transfer between the fibres and throughout the material. Therefore, it is possible to create a material which, through adopting the beneficial properties of each constituent, possesses heightened mechanical and engineering properties and exhibits the high specific strength and stiffness values discussed (and illustrated in Figure 2-4).

The generalised rule of mixtures can provide insight into the probable mechanical properties of a given composite material, based on the properties, orientation and mixture of its constituents, as shown in Equation 2.2 [20].

$$E_{comp} = \eta_L \eta_o E_f V_f + E_m V_m \qquad (2.2)$$

where f and m subscripts refer to the reinforcing fibre and matrix respectively, E is the material property of interest, η_L and η_o are constants to incorporate the influence of both fibre length and orientation respectively and V is the volume fraction of the respective constituent.

It is clear then that through careful selection of the constituent materials and the method by which they are combined, that the material properties of FRP systems can be selected, adopted and fine tuned in order to perform in a specified way. This flexibility allows for a great deal of creativity and innovation in the application of composite materials in engineering structures, and as such the technology lends itself well to the needs of wind turbine blade designers and manufacturers.

2.4.3 Composite Material System Designs

The methods by which reinforcing fibres and polymer matrix materials are combined to create composite systems, with respect to factors such as fibre-to-matrix volume ratio or the orientation and distribution of the fibres, are almost unlimited. This freedom allows for creation and implementation of unique material system configurations, designed to meet the requirements of the component; or in this case the blade [21] [22].

2.4.3.1 Randomly orientated fibre composites

One of the simplest ways to create a fibre reinforced plastic composite is to impregnate the desired polymer matrix with randomly orientated reinforcing fibres. This form of random distribution in a bulk matrix form creates a quasi-isotropic composite material, with improved material properties over the original matrix polymer. The fibres may be chopped to ashort length and then embedded or left in longer strands. One of the most common techniques is to chop the fibres into lengths and then distribute them randomly in a thin layer of the polymer matrix to create what is known as a Chopped Strand Mat (CSM). Such materials exhibit heightened strength and stiffness in the plane of the sheet and therefore enhanced performance. However, due to the matted nature of the fibres within the polymer (i.e. laid out in the in-plane direction), the composite will exhibit much reduced performance in the out-of-plane direction; where the matrix will dominate the loading behaviour.

2.4.3.2 Unidirectional Plies

Although randomly orientated fibre composites offer advantageous with regards to enhancing the mechanical properties of polymer materials, due to the randomly orientated nature of the reinforcement, the high strength characteristics of the reinforcement are not fully utilised; as the strength and stiffness is exhibited along the fibre length. As such, if

higher performance and strength is required of a composite material component, a more measured implementation of fibre reinforcement is required.

The simplest way to achieve this is to create a composite which features a bias in the orientation of the reinforcing fibres, therefore creating a composite which exhibits high strength and stiffness when loaded on the axis of fibre orientation. Such composites are commonly referred to as unidirectional composite; a schematic diagram of the configuration for such a composite is shown in Figure 2-6.

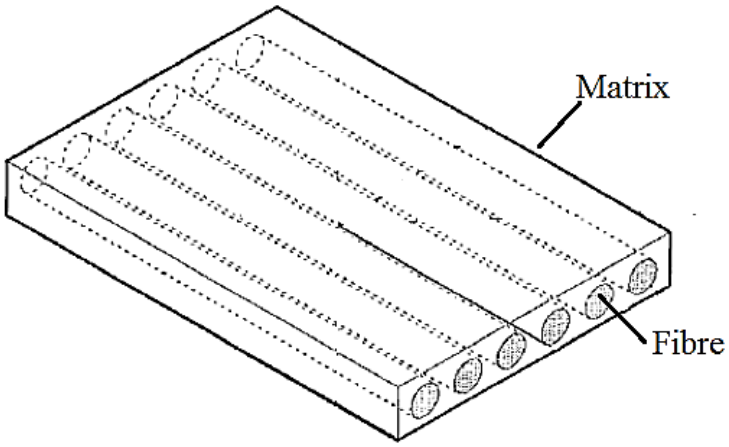

Figure 2-6. Unidirectional fibre composite ply. Source: **[23]**

The schematic features continuous strands of reinforcing fibre embedded in a polymer matrix resin; however it is also possible to implement discontinuous lengths of fibre uniformly orientated. The ratio of fibre-to-resin content in the composite can be varied to suit the design needs and is central to the mechanical properties of the composite.

However, although such technologies provide excellent mechanical properties in the fibre direction, they are inherent directionally sensitive to loading and provide a fraction of the strength when loaded off-axis. Figure 2-7 plots calculated load to failure for a unidirectional graphite-epoxy ply loaded with varying fibre orientation from 0˚ to 90˚; in-plane and transverse respectively.

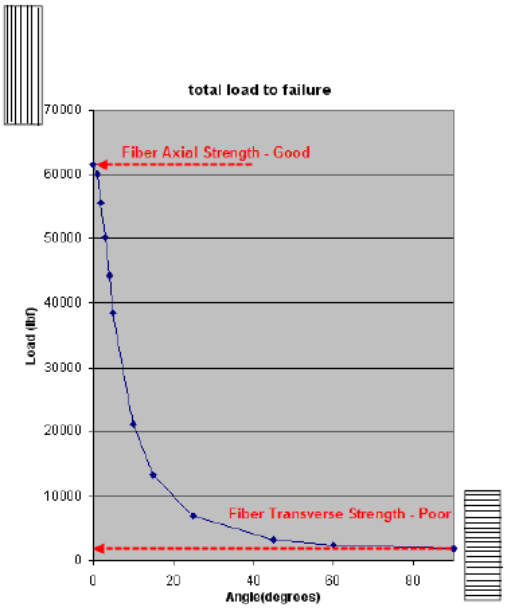

Figure 2-7. Variation of load to failure with changing fibre orientation, source: **[23]**

As can be seen when loaded in the transverse direction the strength of the composite is extremely poor as this is approximately equivalent to loading the matrix material alone, with the fibres forming micro-voids in the loading direction. It can also be seen that a slight variance from loading at 0˚ can result in a drastic reduction in the load bearing capacity of the material.

There are very few engineering applications that would result in exclusively unidirectional loading and as such unidirectional plies are often employed in a more sophisticated and considered manner, forming plies in larger multiple-ply laminate structures, shown in Figure 2-8.

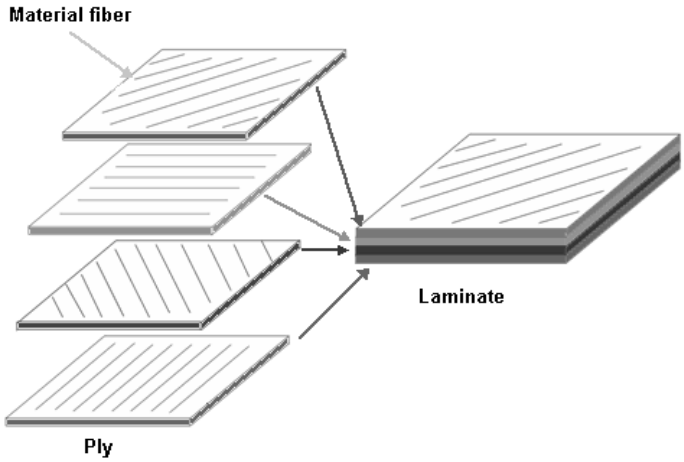

Figure 2-8. Multi-ply layup. Source: **[24]**

Such configurations make it possible to then tailor the load bearing response of the material to meet the specific needs of the structure concerned. Through introducing multiple orientations the sensitivity of the material to load direction as highlighted in Figure 2-7 can be lessened. As a result of this flexibility in design, such composite material configurations have been widely implemented in numerous engineering applications.

However such configurations also presents a unique set of engineering challenges in relation to how the component can be manufactured (as will be discussed) and how the strength of the interlaminar bond between the plies will perform in operation; as delaminations between plies are highly undesirable.

2.4.3.3 Fabric Weaves

An alternative to unidirectional composites are composites that feature fibre reinforcement in more than one distinct direction, forming either a biaxial or triaxial composite. This can be achieved through layering the fibres one onto another in alternating directions and embedding them together in the polymer matrix, creating a system similar to that shown in Figure 2-8 but as one piece. Alternatively a fabric weave of reinforcing material can be created, again with multiple fibre directions, and embedded in the matrix polymer. Figure 2-9 shows an example of a dry biaxial glass fibre weave.

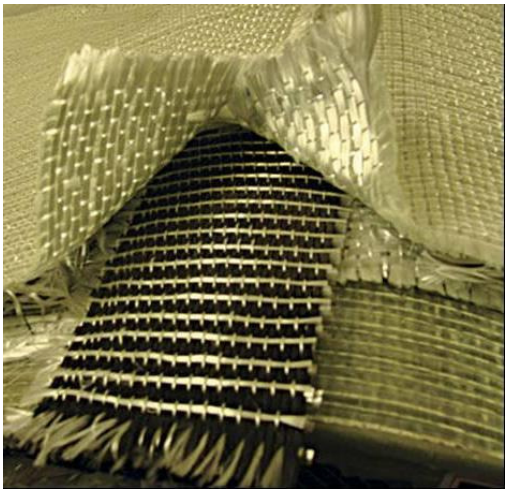

Figure 2-9. Dry **g**lass fibre biaxial weave, source: **[25]**

The configuration of the fibre weave can be altered to requirements; however a simple biaxial or triaxial weave is most commonly employed. As with the laminate systems previously discussed, the incorporation of multiple fibre orientations greatly reduces the directional load sensitivity of the material. As such, this type of composite technology is well

suited to components which undergo complex loading and which also require very high strength; such as the central spar or the blade root.

2.4.3.4 Sandwich

For some structural components the use of the composite technologies described may provide insufficient cross sectional thickness, particularly in areas susceptible to buckling under compression. In such cases, thickening sandwich materials may be incorporated into the material system. Such materials are typically extremely light and therefore help to maintain the lightweight nature of the material whilst adding thickness to the section.

Figure 2-10 shows a typical sandwich construction which features a honeycomb core with face sheets adhered to it. These face sheets may consist of a composite layup of some description, featuring the technologies discussed. The sandwich material featured in Figure 2-10 is honeycomb structured (therefore lightweight), however in wind turbine blade applications lightweight solid core materials such balsa wood or polymer foams are commonly employed [26].

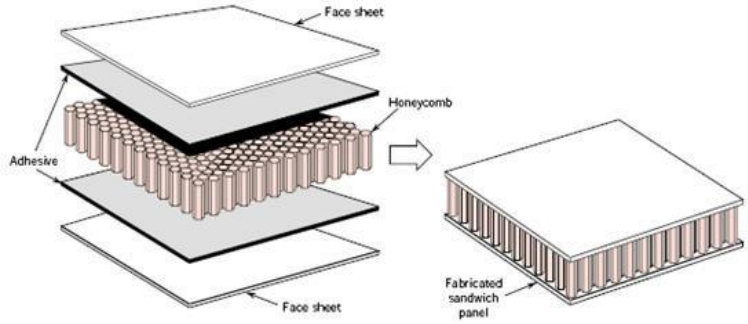

Figure 2-10. Typical sandwich composite configuration with honeycomb core. Source: **[27]**

As illustrated in Figure 2-3, and summarised by Thomsen [28], sandwich materials are utilised in many areas of a blade design, such as the spar or trailing edge of the blade shell, where thick sections are required to reduce the susceptibility of the design to buckling loads. The extent of the use of sandwich materials varies between designs to suit requirements and in particularly large blade design they may feature more prominently to add much needed thickness to the blade cross-section.

2.4.4 Wind Turbine Blade Composites

The technologies and composite material system designs discussed represent the basic technologies available and utilised by blade designers. However, it important not only to select the correct type of composite system for implementation in a wind turbine blade, but also to select the optimum constituent materials which form such systems. The pros and cons

of the potential constituent material are discussed in the following sections, as well as the basis for selection for the most commonly employed materials.

2.4.4.1 Matrix Materials

In a wind turbine blade context when reference is made to either glass or carbon fibre reinforced plastic composites (GFRP and CFRP respectively), it is most commonly referring to composites which employ a thermosetting polymer matrix; most commonly epoxy or polyester resins. Thermosetting polymers have gained prominence as a result of both their tough material properties and ease of manufacture.

Thermoplastic resins offer an alternative to thermosets but are currently very limited in their application in wind turbine components, however research and development is still on-going [29] (as discussed later in Section 2.4.4.1).

Gurit [30] are prominent manufacturers of composite material technologies across numerous industries, however they also manufacture an array of wind turbine blade material solutions. They helpfully disseminate and publish a considerable amount of information on their products relating to their characteristics and performance and how they are processed. [19]. They examined the tensile strength and modulus of three commonly employed polymer matrix materials in many industries: polyester, vinylester and epoxy. Figure 2-11 compares the values obtained for each resin; using two different curing approaches (7 days at 20˚C and 5 hours at 80˚C)

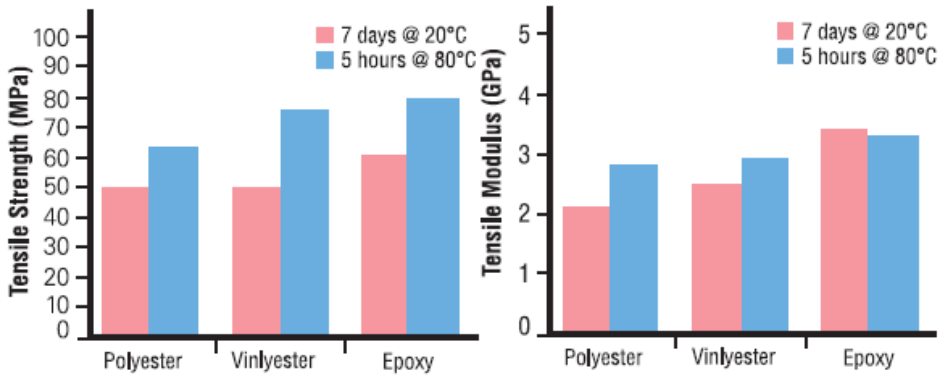

Figure 2-11. Comparison of Tensile Strength and Modulus of matrix resins, source: **[19]**

From Figure 2-11 it is clear that the epoxy resin tested offers the highest strength and stiffness of the three resin systems tested. The importance of employing the correct curing process is also made apparent from the varying levels of strength and stiffness for each given material.

The high strength and stiffness of epoxy resin coupled with some manufacturing benefits make it a popular choice for implementation in wind turbine blades for manufacturers such as Siemens [31], Enercon [32] and Gamesa [33]. However, polyester based composites are also utilised by some manufacturers such as LM Wind Power [34].

Although the implementation of thermosetting composites can deliver numerous benefits in wind turbine blade design (relating to strength, stiffness etc.) there are some drawbacks also associated with their use, such as:

- **Poor impact performance and damage tolerance** – Thermosetting composites are typically stiffer and stronger than thermoplastic composites [35], which is beneficial in respect to structural load bearing. However, this high stiffness results in some undesirable effects when the material is subjected to impact. Instead of absorbing the impact through allowable surface deformation, brittle thermosets may instead absorb the impact energy through micro-cracking damage and subsurface damage such as delaminations or laminate cracking [36]. This type of damage manifestation is very difficult to monitor as it requires thorough and detail inspection of the blade surface and sub-surface.
- **Non-Recyclable** – Thermosetting polymers cannot be melted down and re-used after initial curing, therefore limiting the potential after service life usefulness. Most thermosetting composites can only be shredded to act as filler or partial reinforcement in other composites [37].
- **Limited Shelf Life** – Thermosetting resins require refrigeration to prevent premature curing during storage and typically only have a shelf life of around 6 months [38].

When considering the durability of the blade leading edge, the shortcomings of thermosetting composites in relation to impact and damage tolerance are of significant consideration. To combat this impact vulnerability many manufacturers implement the use of surface coating technologies, typically consisting of more impact resistive materials, to protect the thermosetting composite substrate (discussed at length later in Section 2.4.5).

As detailed, one proposed competitor or possible replacement for thermosetting composites comes in the form of thermoplastic composites. Some of the many cited advantages of thermoplastic matrix composite materials over their thermosetting counterparts are [39]:

- Thermoplastic polymers can be re-melted without loss of material properties and thus can be readily recycled.
- This ability to melt and re-set without loss of properties delivers numerous possible manufacturing and repairing advantages, such as being able to heat weld components together or repairs onto existing components.
- Thermoplastic composites have superior impact properties and damage tolerance when compared to thermosetting composites.
- Unlimited shelf life and no requirement for cold storage (as with thermosets) [40].

However there are also some key - and currently prohibitive - disadvantages of thermoplastic composites, such as lower static strength and stiffness properties and the requirement of higher processing temperatures. Part of the strength problem relates the fact that the bond created between the thermoplastic matrix and the fibre is only mechanical (i.e. mechanical and frictional gripping) [41] whereas thermoset composites create a chemical bond between the matrix and reinforcement.

However, there has been previous research aimed at creating utility scale thermoplastic composite wind turbine blades, most prominently the GreenBlade project [42].

2.4.4.2 Reinforcing Fibre Materials

As the main source of mechanical strength and stiffness of the composite material, selecting the appropriate reinforcing fibre material is critical to the performance of any composite material.

Again Gurit [19] give insight into the key factors affecting the contribution of a reinforcing fibre to the performance of a composite, identifying them as follows:

1. The mechanical properties of the fibre
2. The nature of the interface between the fibre and the matrix
3. The Fibre Volume Fraction (the volume of fibre in the composite as a fraction of the total composite volume)
4. The orientation of the fibres.

Gurit [19] also give the mechanical properties of various reinforcing fibre technologies as shown in Table 2-1, detailing the same properties for other typical engineering materials as a means of comparison.

Table 2-1. Mechanical properties of various reinforcing fibres and other engineering metals, source: **[19]**

Material Type (MPa)	Tensile Str. (GPa)	Tensile Modulus (g/cc)	Typical Density Modulus	Specific
Carbon HS	3500	160 - 270	1.8	90 - 150
Carbon IM	5300	270 - 325	1.8	150 - 180
Carbon HM	3500	325 - 440	1.8	180 - 240
Carbon UHM	2000	440+	2.0	200+
Aramid LM	3600	60	1.45	40
Aramid HM	3100	120	1.45	80
Aramid UHM	3400	180	1.47	120
Glass - E glass	2400	69	2.5	27
Glass - S2 glass	3450	86	2.5	34
Glass - quartz	3700	69	2.2	31
Aluminium Alloy (7020)	400	1069	2.7	26
Titanium	950	110	4.5	24
Mild Steel (55 Grade)	450	205	7.8	26
Stainless Steel (A5-80)	800	196	7.8	25
HS Steel (17/4 H900)	1241	197	7.8	25

From Table 2-1 it can be seen that the carbon, aramid and glass fibres exhibit very high tensile stress values in comparison to other engineering metals; carbon fibres display some of the highest tensile strength and modulus values. Figure 2-12 displays the stress-strain behaviour of different laminates with the various fibre reinforcements shown; in both tension and compression [19].

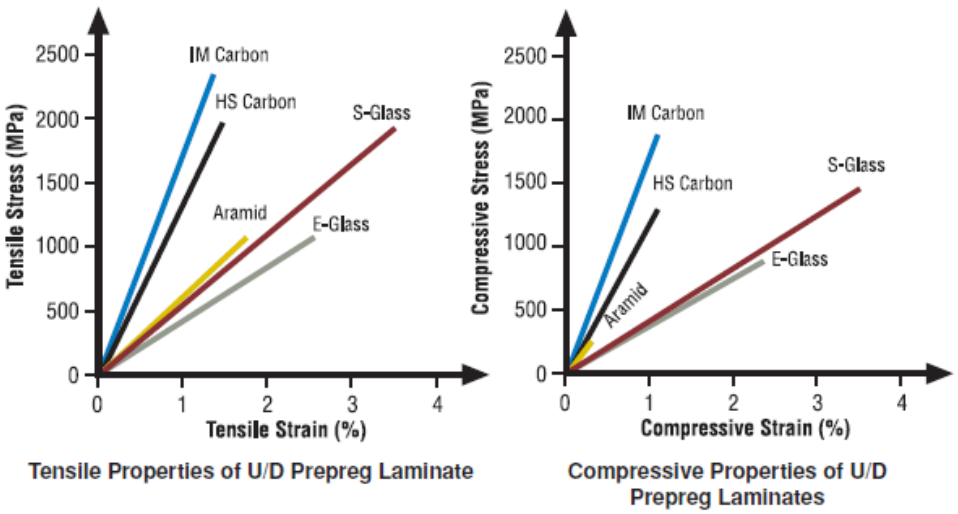

Figure 2-12. Stress-strain properties of numerous varied fibre laminates in tension and compression, source: **[19]**

It is clear from these plots that the heightened strength and stiffness of the carbon fibres translates into a strong and stiff laminate composite. However, the strength and stiffness characteristics of the composite are not the sole performance parameter under consideration. For example, E-Glass -although weaker in relation to tensile strength - provides improved laminate impact performance owing to its lower stiffness (tensile modulus) and thus greater ductility, as shown in Figure 2-13.

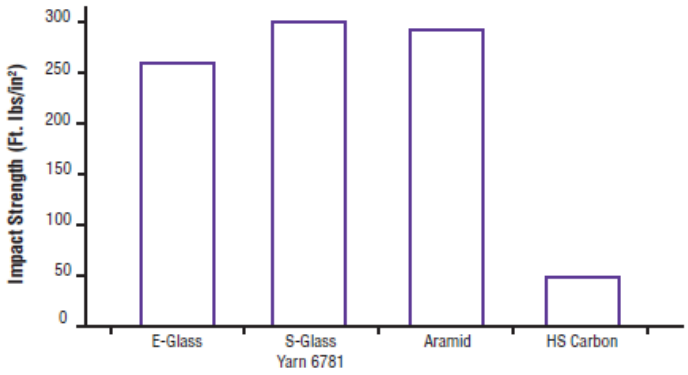

Figure 2-13 - Impact Strength Perormance of thin laminate with varied fibres, source: **[19]**

Here it can be seen that glass fibres and Aramid far outperform carbon in respect to impact. As such, hybrid glass/carbon reinforcements are sometimes employed in thin laminates to bring about improved impact performance where necessary. With respect to the impact of the leading edge of a wind turbine blade, it is apparent that glass reinforcement may provide improved impact performance over a carbon fibre reinforced equivalent.

Economic considerations are also a critical factor in engineering material selection and as Figure 2-14 shows, there is a significant potential for cost saving through implementing glass fibre in components; in place of carbon and aramid.

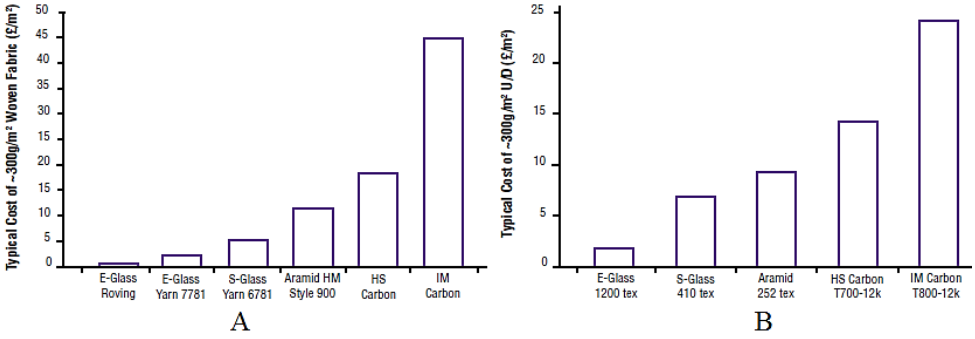

Figure 2-14. Cost comparison of: A) woven fibre, B) unidirectional fibre, source: **[19]**

It is also important to note that when selecting composite systems and their constituents, there is never an optimum selection for all designs and different manufacturers will select different materials which will meet their individual requirements for their own unique design. For instance, as stated (in Section 2.4.4.1), Enercon [32] and Siemens [31] both make use of their own versions of glass fibre reinforced epoxy in their largest models, whereas Vestas have developed an economically viable method of creating a wood/carbon fibre reinforced epoxy blade system [43] and Gamesa have also utilised both carbon and glass fibre reinforced epoxy composites in their blades [44]; not only will the material choices vary between manufacturers but also in some cases between model designs.

2.4.5 Blade Surface Coatings

2.4.5.1 Requirements

As the interface between the wind turbine blade and the given operational environment, surface coating material systems play a crucial role in the environmental protection - and therefore successful performance - of the blade. The performance critical roles of the blade surface coating technologies are:

1. **Light/UV Protection** – The exterior surfaces of the wind turbine blade will be exposed to light and therefore ultraviolet (UV) radiation on a day to day basis. If the surface coating on the blade material is not UV stable then damage can be done to the coating through shrinkage, cracking and blistering [45]. Damage to the surface coating could then lead to loss of coverage of the composite substrate, resulting in the degradation of the composite surface through both UV and other environmental exposure. It has been found that UV exposure can degrade the mechanical properties of Carbon fibre reinforced epoxy, with the transverse tensile strength of the matrix suffering up to a 29% reduction after only 1000 hours of cyclic UV exposure and condensation [46].
2. **Moisture Protection** – The effects of moisture ingress on composite materials can cause significant problems through both adding significant mass to the material and through degrading the mechanical properties of the composite. For instance, Gurit [19] states that a thin polyester laminate may retain only 65% of its interlaminar shear strength following immersion in water for a one year period. Therefore it is critical that the surface coatings employed protect the composite substrate below from any atmospheric moisture.
3. **Substrate Impact Protection** – Perhaps most prudent to the purpose of this research work, the surface coating must be able to withstand significant impact energies

imparted by rain, hail and sea-spray impact and the wear and erosive effects of these impact events over the lifetime of the turbine. If the coating is not robust enough (i.e. damage is inflicted on the coating through material removal) then the system will also fall short on the previous two performance criterion thus endangering the structural integrity of the blade. Furthermore, some designs may additionally task the coating system with not only being robust enough to endure such exposure but also to provide additional impact protection for the composite substrate surface.

These are of course only a core selection of the key performance requirements of the coating systems, and as discussed these will vary widely depending on circumstances. For instance, in colder climates anti-icing and de-icing may also be a critical factor in the performance to the coating system, whereas extreme heat tolerance may be more applicable in warmer climates.

2.4.5.2 Coatings

As is often the case with design and material selection in a commercial context, the exact choices made by individual wind turbine blade manufacturers are often difficult to ascertain as a result of commercial sensitivity. However, it is suggested that there are two general surface coating systems that are commonly employed, either:

- **Gelcoat –** An epoxy or polyester based coating that can be applied in mould during the manufacturing process if using polyester or painted on if using epoxy [47].
- **Polyurethane/Flexible Coating–** Polyurethane based surface coatings can be applied to the surface through spraying [47].

In addition to these coating technologies, painted coatings are also commonly employed to provide additional protections and performance; for instance to protect from UV radiation.

Thermosetting polymer based gelcoat technologies have seen the most widespread use in wind turbine blade designs, partly as a result of their proven track record in marine applications; such as their application as coatings for boat hulls. Their ease of incorporation into the blade manufacturing process has also proven an advantage, simplifying and reducing the cost of applying a coating system.

However, many manufacturers, operators and repair & maintenance firms have found that such gelcoat protection systems may not necessarily exhibit their desired or expected durability.

Consequently, there has been a widespread re-examination of these typical blade coating systems within the wind industry, with many manufacturers opting to explore alternative flexible coating systems, such a polyurethane based technologies. The benefits of employing (poly)urethane coatings are given as: high impact resistance, shape memory as a result of high elasticity, resistant to gouging and abrasion and more [48] [49]. Enercon state in their wind turbine product brochure that they employ a two component polyurethane coating system [50], as do LM Wind when describing their ProBlade surface coating [51] and 3M when describing their leading edge protection systems [52]. However many other manufacturers do not openly specify the material utilised in their surface coatings. Indeed, there exists a significant amount of ambiguity in the terminology associated with the technologies and as such they are often bracketed under the common name of a gelcoat. Additionally, many coating systems such as the polyurethane based materials are also commonly referred to as paints

The impact performance of both of these material technologies is the subject of extensive investigation in the work of this research and will be explored and discussed at length in later sections. However, for the avoidance of any further doubt or ambiguity, from now onwards, the following coating terminology system shall be adhered to:

1. **Gelcoat** – Refers to classical thermosetting polymer resin based coating technologies (most typically epoxy or polyester base).
2. **Flexible Coating** – Refers to the new and emerging highly flexible coating systems, most commonly polyurethane based technologies; such as those manufactured by 3M [52], described previously. These are (most typically) applied as an integrated coating component during blade manufacturing.
3. **Tapes –** Refers to commercially available highly flexible tape products (also primarily polyurethane based), designed to be incorporated post blade manufacture or applied to the blade when needed; to mitigate or prevent further surface degradation.

2.4.5.3 Leading Edge Tapes

In locations where the threat of leading edge erosion is considered likely, or where significant and problematic leading edge erosion has been observed, the additional application of leading edge tapes is commonly implemented. 3M is one of the most prominent providers of such tapes [53], and claim that the tapes exhibit advantageous impact, abrasion and wear properties, illustrated by the tested samples shown in Figure 2-15.

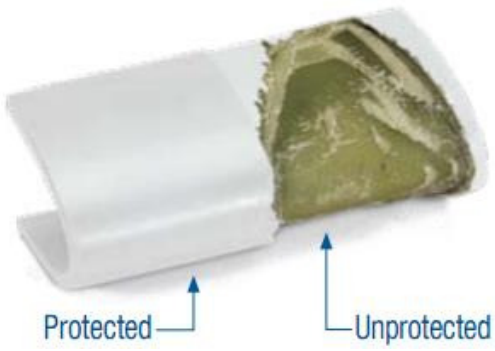

Figure 2-15. Unprotected and leading edge tape protected sample tested in rainfall of one inch per hour at 500mph at the Rain Erosion Test Facility, University of Dayton. Source: **[54]**

Figure 2-15 compares the damage created on an unprotected bare blade and a blade protected by a Wind Protection Tape, through accelerated rain erosion testing at 500mph in a one inch per hour simulated rain field, at the Rain Erosion Test Facility at the University of Dayton, USA [55]. As shown the protected sample remains undamaged even after this rigorous accelerated rain erosion process, whereas the unprotected sample shows extensive signs of significant material erosion, stripping away the upper layers of the composite substrate. The performance of such protective coating systems are reviewed in heightened detail in later sections.

2.5 Manufacturing

2.5.1 Material Handling and Application

Composite material systems can vary vastly in their design and makeup and consequently the manner in which composites are created and the form in which they are then handled during subsequent component manufacture can also vary widely.

For example, a blade manufacturer may desire a large degree of composite material design freedom and therefore may wish to create the component through combining the raw and separate constituent materials during the manufacturing process. In such cases the reinforcing fibre components may be sourced in dry roving and placed in the component mould. The fibres are then infused with the specified polymer resin matrix material in situ and cured in the mould. Such an approach enables the designer and manufacturer to specify the exact fibre content and orientation in the composite created, as well as providing the freedom to create a matrix component - through a bespoke chemical component mixing and curing procedure - with specified characteristics. However this approach also requires both a sound understanding of the structural requirements of the component, and a strong level of

manufacturing expertise in order to create a finished component free of flaws; such as areas of dry (or un-wetted) fibre.

Alternatively, many manufacturers prefer to source their composite materials in a pre-combined format [56]. Many material manufacturers offer pre-impregnated – or prepreg – composite materials, whereby the reinforcing fibres are pre-impregnated in the desired matrix resin which has not yet been fully cured. Such products are commonly supplied as rolls of material which can be conveniently stored and which lend themselves well to certain manufacturing processes. Prepregs also offer heightened confidence with respect to obtaining an even distribution of the matrix resin throughout the fibres, as the fibres are pre-impregnated. However, due to the uncured nature of the product the prepreg material has to be stored in a controlled environment, typically at -18˚C [56], in order to prevent premature curing before manufacture.

2.5.2 Manufacturing Process

As a consequence of the variations in blade design between product models and manufacturers there are numerous manufacturing methods employed to create the blade component and therefore it is difficult to categorise the manufacturing process with any specific example. However as alluded to in the previous discussion about material handling, the two most prominent approaches to manufacturing blades are through prepreg application or a resin infusion process, as summarised comprehensively by Brøndsted et al. [56] and discussed in the following sections. Although these processes vary between manufacturers and designs, as a result of the nature of thermosetting based composite materials, all large blade manufacturing process require the application of heat and pressure to effectively create a strong finished composite component.

2.5.2.1 Prepreg Manufacturing

As discussed previously, reinforcing fibres can be sourced from material manufacturers pre-impregnated in a matrix material of choice; most commonly on rolls. These prepreg sheets can then be layered on top of one another to create a desired laminate, before being subjected to heat and pressure to melt the resin and cure the final composite laminate. In order to better understand how this process works in reality, it is useful to consider an example of the use of prepreg materials in a blade manufacturing context. Wind turbine blade manufacturer Gamesa, detail their manufacturing process on their company website [44] and some of the process steps are illustrated in Figure 2-16.

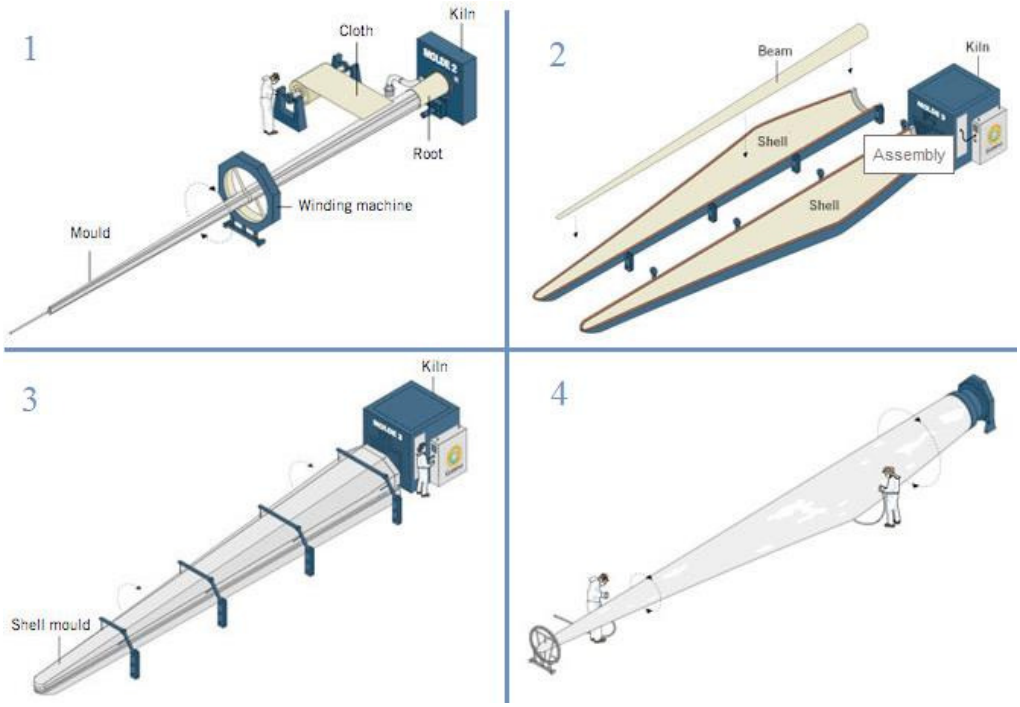

Figure 2-16. Gamesa blade manufacturing process. Source: **[44]**

Both glass/epoxy and carbon/epoxy prepreg clothes are applied (from rolls) to a rotating mould to first create the box beam spar geometry, as shown in image 1 of Figure 2-16. After the application of the prepreg material a curing process is then conducted to consolidate the spar (or beam). The two outer shells of the blade geometry are then created by first applying paint to the mould (to act as the surface coating) and then placing glass fibre epoxy prepregs in the mould which are then cured. Gamesa do not specify how pressure is applied to the mould during the curing process, however the most common method is to cover the composite material in a polymer sheet, secured at the edges of the mould, forming an air tight seal over the composite material. A vacuum is then created in the air gap causing the atmospheric pressure to push down on the polymer sheet and subsequently on the composite assembly, helping to consolidate the laminate assembly [56]. Following the creation and curing of the blade shells, the beam and two blade halves are assembles to form the final blade structure. This assembly is heated once more to form the whole blade structure (image 3 of Figure 2-16). The constructed blade is then removed from the mould and transferred to a finishing area where the trailing and leading edges are finished and the whole blade is subjected to a final inspection.

Brøndsted et al. [56] state that this approach of utilising prepreg material allows for easier control and obtainability of constant material (and therefore blade) properties. It also allows for the creation of blades with higher fibre content, therefore resulting in a lighter blade with

higher specific strength and stiffness. Such a process also offers a very clean method of manufacturing, negating the necessity for extensive ventilation; therefore creating a better working environment.

However some level of care is also obviously required to prevent the occurrence of flaws in the structure when utilising prepreg materials. By the very nature of a prepreg layup, the final strength and integrity of the structure created relies heavily upon the quality of the bond created between the layers. For instance a poorly cured bond between plies may prove weak and could result in delamination between the plies occurring, resulting in the degradation of the structural integrity of the blade created. In addition, air gaps between the plies as a result of poor compression during curing or creasing/crimping of the prepreg material in the mould may also result in a poor bond and thus reduced performance. Consequently, the manufacturing process has to be both well understood and considered, in order to avoid such issues and continuous improvement methods must be employed and encouraged to address and subsequently eradicate issues as and when they arrive.

2.5.2.2 Infusion Based Manufacturing

An alternative to utilising prepreg materials is to employ a resin infusion process, whereby the specified reinforcing fibre materials are laid out dry in the blade mould and sealed off to form an airtight package (similarly to the process detailed for prepreg material). The matrix resin material is then introduced into the package in liquid form, consequently wetting-out the fibres. The whole assembly can then be cured to create the desired composite component. The nature in which this process is carried out can differ greatly between manufacturer and the description given merely gives a general overview of the typical process.

Again it is useful to consider the real manufacturing process employed by some manufacturers to gain a better understanding of how the approach is adopted. For instance, Siemens have created their own unique manufacturing process which they call IntegralBlade® [57]. This process lays out glass fibre between a fixed closed outer mould and an expandable inner mould and then uses a vacuum infusion process to inject epoxy resin into the mould to comingle with the fibres. Upon completion of curing, the inner expandable mould is collapsed and removed, thus resulting in a seamless one piece outer shell (as opposed to two fused shell components).

One of the biggest challenges presented by the process of resin infusion is to ensure that the fibres are sufficiently wetted by the resin system. Areas of dry fibres in the material are

highly undesirable,. Brøndsted et al. [56] detail some of the key areas of developments focussed on addressing the issue of fibre wetting, as follows:

- Fibre sizing with increased wettability, to ensure sufficient wetting without the need to manipulate the fibre roving
- Special fibre fabric architectures that control the flow of the infused resin
- Low viscosity resins (at room or moderate temperature) which enhance wettability
- Resins which do not release volatile gases when place in a vacuum
- Accessories which help control the resin flow patterns over large areas and through thick laminates (special sandwich core etc.)
- Specialised design of moulds with respect to resin inlet and outlet, which prevent trapped air in the mould and subsequently dry fibres
- Sensors for monitoring the developing resin flow front
- Computational tools to predict resin flow behaviour and optimise the flow pattern for a given mould.

There are also many other challenges with regards to a resin infusion approach, such as the correct handling approach for fibres (to minimise surface damage/ breakage of the fibre) and correct mixing and curing of the resin matrix.

2.5.3 Effect of Manufacturing Flaws on Impact Performance

Cairns et al. [58] review some of the common issues relating to potential manufacturing flaws in wind turbine composite materials, citing some of the following examples:

- Porosity
- Debonding
- Delaminations
- Improper fibre/matrix distribution
- Fibre misalignment
- Improper fibre/resin ratio
- Bonding defects
- Foreign inclusions
- Incompletely cured matrix
- Matrix cracking

Many of these defects and flaws in blade production may compromise not only the structural integrity of the blade, but also the performance and response of the blade to surface impact

events such as rain and hailstone impact. Such defects and their effects are discussed sections that follow.

2.5.3.1 Improper Curing

As discussed previously in Section 2.4.4.1 and shown in Figure 2-11 the curing time for resins can play a strong role in the final strength and stiffness of the component. Therefore it is apparent that improper curing, as a result of insufficient cure time or incorrect cure temperature, can greatly affect the properties of both the blade surface coating technologies and the composite substrate.

If employing a thermosetting polymer such as epoxy on polyester as a gelcoat surface coating, then proper curing of the gelcoat is essential in order to provide a surface coating with optimum material properties. Any reduction in the strength or modulus of the gelcoat will greatly affect its impact performance and wear characteristics and may result in the eventual degradation of the gelcoat; through processes described in later chapters.

With respect to the impact of fibre reinforced composites in the direction normal to the fibres (i.e. matrix dominated) the strength and stiffness of the polymer matrix plays a significant role in the composites response and robustness. Therefore any reduction in the strength of the matrix may significantly weaken the composite in relation to impact response; this will also be discussed later.

2.5.3.2 Air Gaps in Laminate

Any air gaps (or delaminations) between the layers of a laminate, or the composite substrate and surface coating as a result of either improper application of prepreg layers or insufficient fibre resin wetting may also have a detrimental effect on the impact response and performance of the blade materials. Air gaps constitute a weakness or weak point in the contact between the layers of a composite/surface coating system. Such weaknesses may act as a seeding point for the initiation and propagation of delamination between material layers, exacerbated through impact from rain and hailstone.

2.6 Summary

It is clear that as an engineering component, wind turbine blades are complex and difficult to accurately characterise or standardise, owing to their variable design requirements and the diversity of their potential material configuration. The constant and pressing demand for larger blade sizes has brought about significant changes and progress in the areas of blade design, material science and manufacturing processes. However, of relevance to the current

research programme, are the effects of these ever evolving and advancing design requirements in the context of leading edge erosion issues. It has been shown that with increasing blade length, increased maximum blade tip speeds are also generated, up to values around and in excess of $80 m \cdot s^{-1}$. These speeds, coupled with the significantly lengthy required service life, may create extremely hostile and/or damaging operating conditions for the materials at the leading edged of the blade tip. Such operating conditions may stretch or overcome the wear performance of the blade materials, therefore bringing about the onset of leading edge erosion.

3. Blade Leading Edge Erosion

There is very little published information on leading edge erosion and impact damage of wind turbine blades; other than the contributions of the research described in this work [59] [60] [61]. However there are a handful of documented cases and discussions on the topic (discussed throughout this chapter), including test results from rain erosion tests performed by blade manufacturers. In this chapter, these cases are firstly reviewed in order to contextualise the issue of leading edge erosion and impact damage of wind turbine leading edge materials. The wind turbine performance altering effects of such leading edge damage are then reviewed along with the related maintenance and repair challenges. The threats posed specifically by rain and hailstone impact on the leading edge are then evaluated by establishing the projectile characteristics of each and analytically determining the energies, pressures and forces imparted by such impact phenomena. The significance of these impact conditions with respect to the response of typical wind turbine blade materials are also examined.

3.1 Significance in Industry

3.1.1 Documented Cases of Leading Edge Damage

Detailed and thoroughly documented examples of leading edge erosion on wind turbine blades are sparsely available in the publicly available literature. However, the occurrence of leading edge erosion is stated as a challenge and an issue for manufacturers and operators in many articles in industrial magazines and periodicals. Wood [62] states that some operators have found that leading edge erosion can become an issue after only two years of turbine operation; much sooner than expected time span (10+ years). This early onset of energy capture altering leading edge erosion has prompted some manufacturers to begin to address the issue in the design stage by exploring new protective coating options. Wood [62] also draws on the experiences of operators, manufacturers and inspection & repair companies to emphasize the need for effective inspection & maintenance to ensure satisfactory performance of the blade throughout its service life. In the early years of the North American wind industry, Rempel [63] stated there was an expectation that once blades were in operation, routine inspection and maintenance would not be necessary. As the industry matured, it became clear that the issue of leading edge erosion was significant and that maintenance would be essential if the blades were to reach their expected design life. Rempel [63] explained that careful handling of the blade during manufacture, transport and installation is also essential to avoid small tears or scratches which may act as a seeding point for further wear and erosion. She also states that leading edge erosion on an

unprotected blade may occur after only three years, with the tip being most susceptible to wear, but with erosion also exhibited on the more inboard portions of the blade.

The issue of leading edge erosion is cited by a selection of service & repair companies [62] [63] [64] [65]and although these sources and the previous two articles discussed [62] [63] are based mostly on first-hand experience and anecdotal accounts, these references to the issue and the supporting images given, such as that in Figure 3-1, emphasize the real dangers posed by erosion to the leading edge.

Figure 3-1. Example of leading edge erosion. Source: [63]

A significant issue with these sources is that they seldom give any real detail on the cause or mechanisms of damage. They therefore do not shed a great deal of light on the main causes of leading edge erosion, nor the manner in which the process evolves and progresses.

Dalili et al. [10] investigated a wide range of surface engineering issues in relation to the performance of wind turbine blades, focussing primarily however, on the problems presented by icing in Nordic climates. She states that particle or droplet laden winds can erode the leading edge of the wind turbine blade and for some aerofoils this may lead to a reduction in the aerodynamic efficiency of the blade. Methods of improving blade erosion resistance are also discussed, highlighting the proposed benefits of applying elastomeric materials to the leading edge (i.e. leading edge tapes), but also stating that tapes must be replaced frequently as they become worn down. Innovations in materials and design, with a view to improving erosion resistance are also discussed, making reference to the development of large thermoplastic based composite blade designs which would in theory provide superior impact and erosive resistance [29]. The development of adding nano-sized reinforcement to

elastomers to create a new nanocomposite material for leading edge application is also detailed. In a similar field of nano research, Karmouch and Ross [66] propose a method of embedding silica nanoparticles in an epoxy paint to act as a hydrophobic barrier on wind turbine blade surfaces. They have found that this simple method creates a water repellent surface, forcing water to run off. There is little discussion however with regard to how these surfaces would perform with regards to erosion.

Sayer et al. [67] detailed an investigation of the material properties of an 11.6m length DEBRA-25 wind turbine blade (100kw rating), after having completed almost 20 years of operation. They note that although the blade still exhibited good mechanical properties, there was significant evidence of rain erosion effects exhibited at the blade tips. The tip speed of the DEBRA-25 is stated as being 65.4m·s^{-1} [68], which is comparatively low compared to that of modern, larger scale turbines, as shown in Figure 2-2. The region of operation in southern Germany is also a relatively dry climate compared to many other regions in Europe [69] (as will be shown Figure 3-13). Given this comparatively low tip speed and dry climate, it is interesting to note that the issue of rain erosion at the blade tips was still significant.

Although cases of blade leading edge erosion are rarely well documented (or reported), as a result of the increased recognition of the issue, many manufacturers, operators and maintenance & repair companies are now actively monitoring and documenting the occurrence of such damage on blades. For instance, the service company Global Energy Service (GES) [70] are developing a database to record damage type and frequency on a portfolio of over 1000 blades in operation [71], recording defects such as erosion, spalling, cracks, lightning damage etc. Such a database may prove invaluable to interested stakeholders in quantifying not only the risks posed by leading edge erosion, but also numerous other potential forms of damage. Similarly, made known through industrial interaction [72], the blade manufacturer LM Wind Power is also developing a similar database, to identify any correlation between leading edge erosion and the local meteorological conditions.

3.1.2 Leading Edge Protection Material Solutions and Developments

As part of an effort to tackle and prevent leading edge erosion, blade manufacturers are researching and developing new material systems for their blade leading edges. Haag [51] detailed the development process behind the creation of a new advanced coating technology for LM Wind blades, named ProBlade™, in a presentation at the European Wind Energy Conference, 2013. The technology, developed in partnership with their suppliers, comprises of a “highly flexible 2-component solvent free UV-resistant polyurethane based paint” and

was developed to improve the erosion performance of blades with Polyester based substrates. It offers minimum aerodynamic influence and less noise generation than tape. Haag [51] showed the extent of the damage created on the leading edge of a blade sample, protected only by a typical Polyester gelcoat, after being subjected to simulated rain at 30-35mm·h^{-1} (varying along the sample length) at an impact velocity ranging from 123-157m·s^{-1} for 60 minutes. The testing was conducted through use of swirling arm rain erosion apparatus (discussed later in Section 3.2.5), resulting in the variation in test parameters along the sample length, performed by Polytech [73].

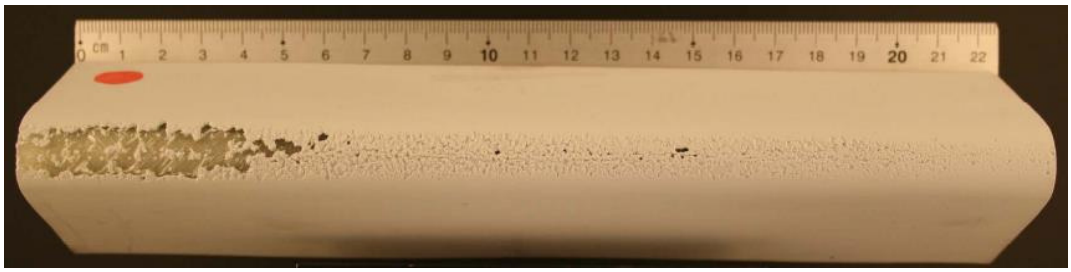

Figure 3-2. Blade sample with polyester gelcoat, tested at 123-157m·s^{-1}, in a 30-35mm·$^{-1}$ simulated rain field for 60 minutes. Source: [51]

The sample shown in Figure 3-2, exhibits a significant amount of leading edge erosion of the Polyester gelcoat, consequently exposing the composite substrate. Although brought about through an accelerated process, the damage created highlights the potentially harmful effects of rain induced leading edge erosion on wind turbine blades. It is also interesting to note that erosion occurs along the whole length of the blade sample, even moderately so in the lower velocity inboard section; where the test velocity is 123m·s^{-1}. The effectiveness of the developed ProBlade™ technology is compared to that of a leading edge tape, as shown in Figure 3-3.

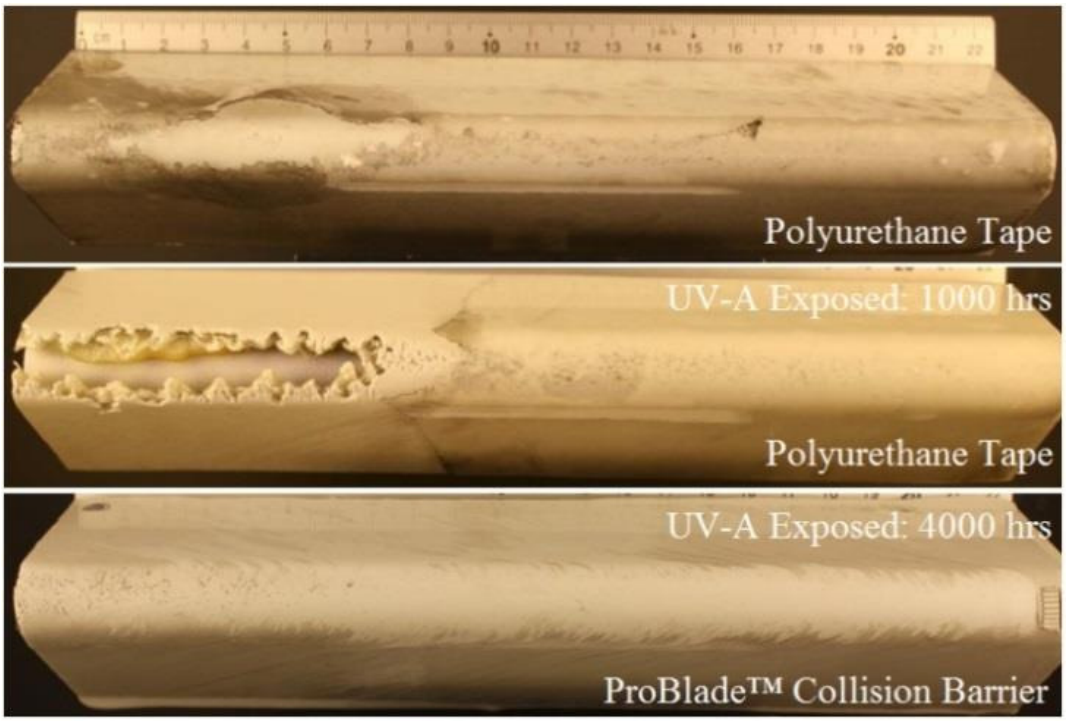

Figure 3-3. Samples tested under liquid droplet impact at 123-50m·s^{-1} in 30-35mm·h^{-1} simulated rain field for 6 hours. Top-to-bottom: polyurethane tape protection – no UV-A exposure, polyurethane tape - 1000hrs of UV-A exposure and ProBlade™ Collision Barrier protection with 4000hrs of UV-A exposure. Source: [51]

As shown in Figure 3-3, after 6 hours of rain erosion testing at 150m·s^{-1} with a rain rate of 30mm·h^{-1}, the ProBlade™ coating system successfully resisted any significant erosion effects. In the absence of any UV-A exposure, the polyurethane tape also successfully provided sacrificial protection to the leading edge, however the degradation of the tape would result in the requirement for replacement. It would appear that the ProBlade™ coating delivers further advantages with regards to UV-A exposure when compared to a standard polyurethane tape, as from inspecting the middle sample, it is clear that the introduction of UV-A exposure to the polyurethane tape protected sample resulted in significant leading edge degradation. Whereas, even with 4 times the exposure duration the ProBlade™ system shows very little evidence of significant erosion.

As well as manufacturing leading edge tapes [74], 3M have also developed a coating technology for wind turbine applications, named W4600 [53]; designed to protect against leading edge erosion. Powell [75] showed the effects that leading edge erosion can have over several years of operation, as shown in Figure 3-4.

Figure 3-4. Examples of leading edge erosion in the field across a range of years in service. Source: **[75]**

As shown, after only one year in service, leading edge erosion may become an issue, with evidence of significant leading erosion exhibited after ten years in service. As part of their product development and analysis, 3M also conducted rain erosion testing of samples with and without their coating technologies [75]. Figure 3-5 shows the results of their rain erosion testing, featuring samples protected by both leading edge tape and an early prototype surface coating [53], comparing them against the results of competitive coating technologies. The testing was conducted at the Rain Erosion Test Facility at the University of Dayton [76], at an impact velocity of 134m·s^{-1}.

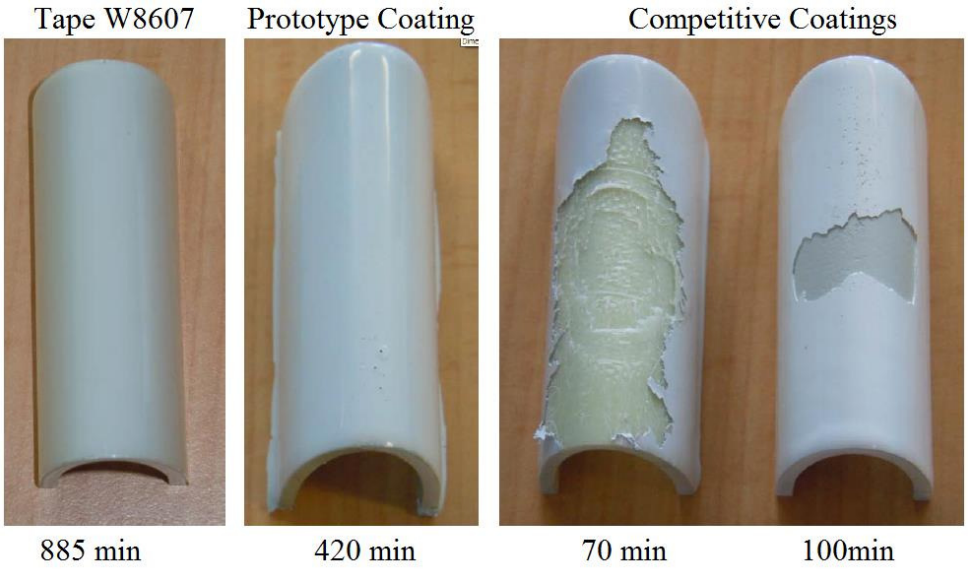

Figure 3-5. 3M results from rain erosion testing at 134m·s^{-1}, for samples protected by: leading edge tape, a prototype surface coating and competitor coatings. Source: **[75]**

As shown, the protective technologies were deemed successful in preventing leading edge erosion, when compared to competitor technologies. Significant leading edge erosion can be observed on the samples protected by competitive coatings, highlighting the potentially extreme damaging effects of rain erosion on blades with sub-standard protection. The further damaging effects of rain erosion with respect to eroding the composite substrate (following the removal of the coating) are also visible, with numerous layers of the composite substrate stripped away in one of the samples with a 'competitive coating'. Again it is notable that although no current generation blade design is likely to be subjected to an impact velocity of 134m·s^{-1}, some may experience impact velocities in excess of 100m·s^{-1} (Figure 2-2) and therefore over a longer period similar damage may be seen on actual wind turbine blades.

Claus [77] (also of 3M), presented further information on the rain erosion performance of 3M W8607 Wind Tapes and W4600 Coating [52] through comparing their rain erosion properties to other competitor coatings and typical wind turbine blade coatings and gelcoats. Figure 3-6 shows the results from rain erosion testing of a variety of wind turbine blade coatings, including the 3M technologies, conducted using the Polytech [73] facility. The samples were tested at 150m·s^{-1}, with a droplet size of 1-2mm and rain rate of 25-35mm·h^{-1}, over several hours. Figure 3-6 plots the total eroded surface area on the samples throughout the test duration.

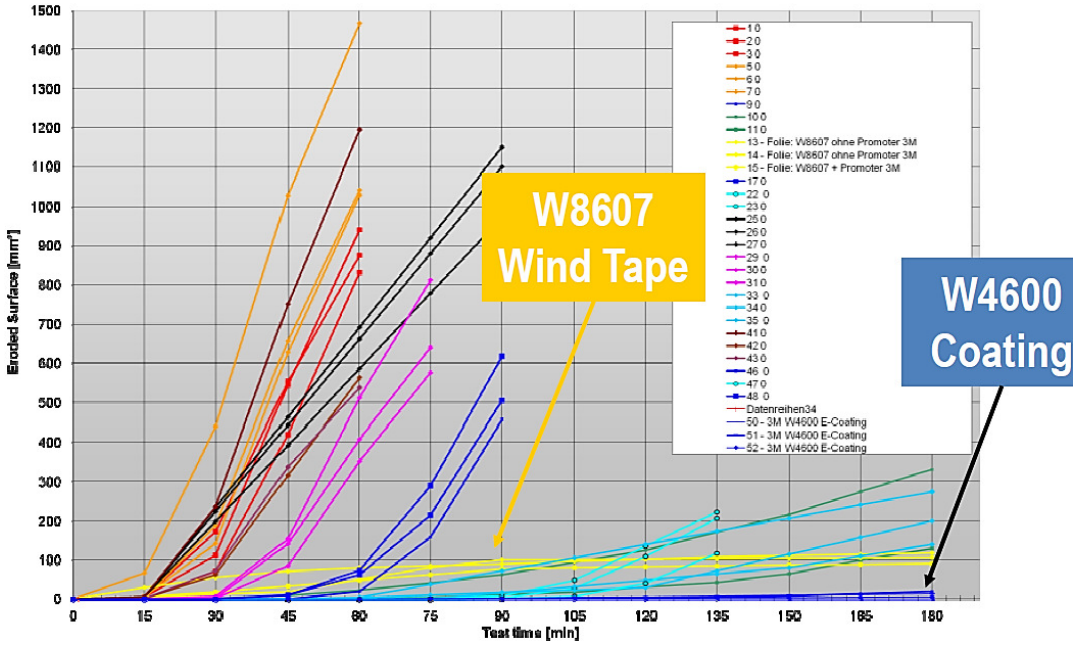

Figure 3-6. Rain erosion test results for various wind turbine blade coating technologies, testing conducted by Polytech **[73]**, on behalf of 3M. Samples were tested at 150m·s^{-1} with a droplet size of 1-2mm and rain rate of 25-35mm·h^{-1}. Both 3M products, W8607 and W4600 are highlighted. Source: **[77]**.

The polyurethane based 3M products, W8607 and W4600, displayed significantly improved rain erosion performance over other typical coating technologies; with the W4600 coating system exhibiting almost no significant erosion.

The use of highly deformable polyurethane based coatings seems to provide enhanced rain erosion performance for wind turbine blade leading edges. However, Claus [77] also makes clear the degrading effects of UV exposure on the properties of the coating materials. Figure 3-7 shows the time to rain erosion material breakthrough for the W4600 surface coating, with and without UV exposure ageing.

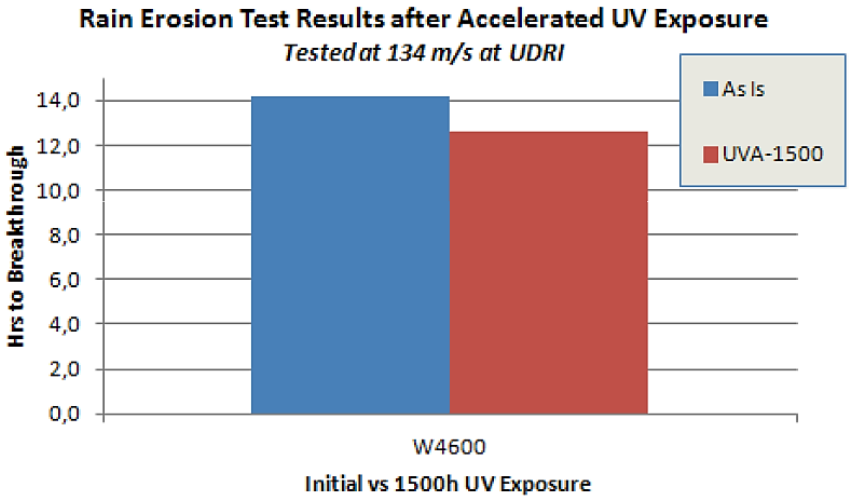

Figure 3-7. Time to material breakthrough from rain erosion testing for W4600 surface coating, with and without 1500 hours equivalent UV exposure. Source: **[77]**

From Figure 3-7, the accelerating effects of UV exposure on the rain erosion process for the W4600 coating material is evident, resulting in an appreciable decrease in the time required for erosion breakthrough.

Although the test results shown herein are not examples of erosion occurring on operational wind turbines, they do show the significant leading edge damage brought about through only water droplet impact. Showing that over the lifetime of a blade, a gelcoat alone may not guarantee protection from leading edge erosion. The results also highlight the effectiveness of applying highly elastic materials such as polyurethane to the leading edge, in order to absorb the impact energy imposed by rain droplet impact. The importance of considering the damaging effects of multiple environmental factors acting together, such as rain and UV exposure, is also highlighted.

It is possible also to examine and compare the literature for examples of leading edge erosion studies in the context of aviation applications, and the solution derived therein. Weigel [78]

discussed the importance of utilising an effective leading edge erosion protection system on helicopter rotor devices as well as describing the creation of a new advanced protection system. In order to select an appropriate leading edge protection material, the study evaluates the protection characteristics of a wide range of materials in relation to parameters such as rain and sand erosion resistance (using the Rain Erosion Test Facility at the University of Dayton Research Institute [76]) as well as performance under hydrolysis, impact, UV exposure and salt fog exposure. Weigel [78] identifies that elastomeric materials, such as polyurethanes, can provide superior resistance to solid particle erosion (such as sand) in comparison to metals, and are only outperformed with regards to rain erosion by metals; as a result of poorer polyurethane performance at direct impact angles. Gohardani [79] provided an in-depth review of erosion aspects in aviation applications, addressing both the fundamental physics of liquid and solid particulate impact as well as the techniques – both experimental and numerical – developed to better understand the phenomena of erosion. He finds that the phenomena of erosion and the efforts to analytically model and understand it using classical approaches can prove complex and highly specialised, and recognises that the introduction of high performance composite materials (as also utilised in wind turbine blades) may further complicate such analytical efforts in future. Gohardani [79] therefore highlights the requirements for both experimental and numerical analysis of the issue in future applications, whilst also recognising the added complexity of numerically modelling the response of advanced composite materials. The complexity of such modelling is further emphasised by Gohardani [79] by identifying the requirements in some cases to model on the microscopic, mesoscopic and macroscopic scales when considering composite materials.

3.1.3 The Role of Polyurethane Based Materials for Leading Edge Protection

From reviewing and discussing the current state of the art and next generation leading edge coating material technologies, there is a clear trend towards adopting or developing highly flexible, (most commonly) polyurethane based materials.

The successful implementation of such material systems in aviation applications gives credence to their proposed application to leading edges of wind turbine blades, in order to prevent erosion. However, given their limited application at the time of this research and the uncertainty and degrading influence associated with UV exposure, it is clear that although such coating can provide enhanced erosion protection (in comparison to standard gelcoats) they cannot yet be considered a full-proof solution to the issue of wind turbine blade leading edge erosion.

3.1.2 Effects of Leading Edge Erosion on Wind Turbine Performance

In order to understand the significance of leading edge erosion on wind turbine blades, it is important to consider the effects that such erosion will have on the performance and lifetime performance of the blade.

It is apparent that one of the most important characteristics of a wind turbine blade is its aerodynamic performance. If leading edge erosion does occur, then it may pose a threat to this aerodynamic performance as a result of roughening the blade surface. For instance, Dalili [10] states that debris from insects on the blade alone can result in a 50% reduction in the power output of turbines; this would prove a critical blow to the profitability of any wind turbine. However, through careful aerofoil selection, blade design and operational strategy selection, the sensitivity of blades to surface roughness/contamination can be significantly reduced [80]. Sareen et al. [81] found that leading edge erosion on a wind turbine aerofoil can produce significant aerodynamic performance degradation. In the study, DU 96-W-180 aerofoils with varying severity and types of leading edge erosion were tested to evaluate the effects of the erosion on performance, finding that such effects resulted in a large increase in the drag of the aerofoil and an earlier onset of stall (i.e. at lower angles of attack). The results from the study showed an increase in drag of 6-500% due to varying levels of leading edge erosion (light-to-heavy). Further analysis predicted that an 80% increase in drag could lead to approximately a 5% reduction in annual energy production. Additionally, in related research, Chinmay [82] also found that implementing leading edge tapes on such aerofoils resulted in a drag increase ranging from 5-15% - depending on placement and area size - and although this may not result in a measurable difference in annual energy production, research would be required to determine the optimum method of application to minimise any detrimental aerodynamic effects [82].

To evaluate the benefits of their leading edge protection products, 3M investigated the effect that leading edge erosion can have on the power output of a wind turbine [75] [83] working in conjunction with Sareen et al. [81]. It should be noted that there is a degree of cross-over between the results discussed previously from Sareen et al. [81] and the results shown by 3M in Figure 3-8.

This shows the calculate Annual Energy Production (AEP) over a period of 5 years, for turbines employing the 3 following leading edge protection configurations:

1. Protected by 3M wind protection tape
2. Unprotected and assuming moderate leading edge erosion

3. Unprotected and assuming worst case erosion.

The value of AEP was calculated by taking into account the aerodynamic effects (evaluated experimentally) of the specific level of erosion (on lift and drag) and the effect this has on energy production; assuming a 1.5MW rated turbine and a capacity factor of 30%.

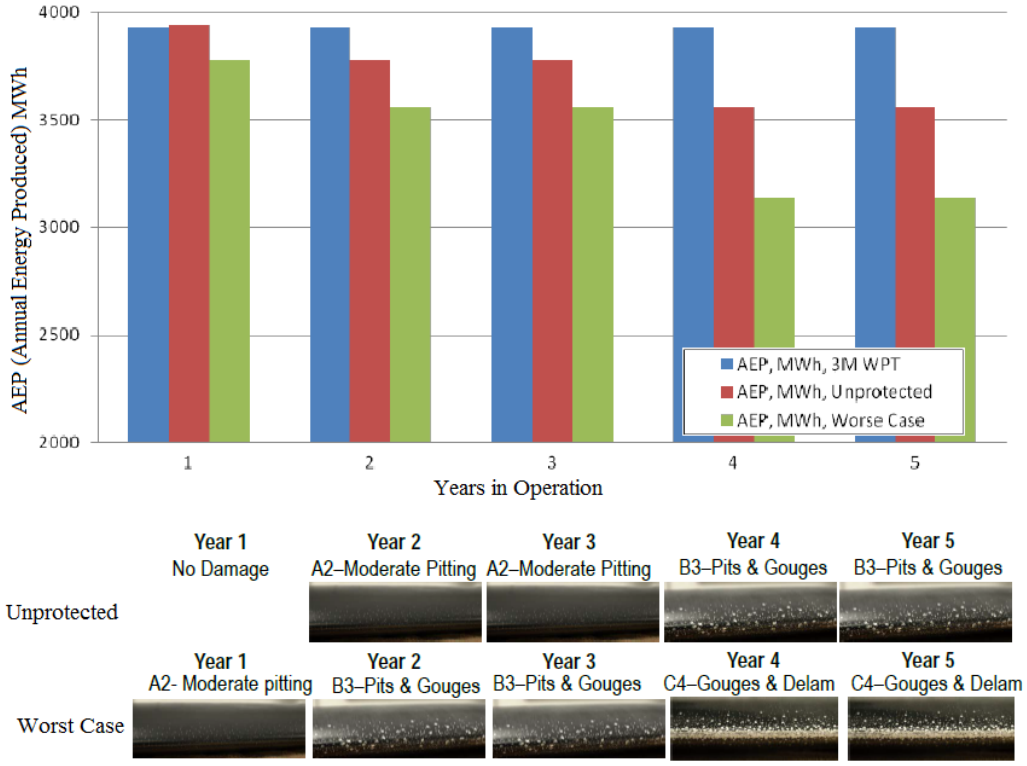

Figure 3-8. Calculated effects of varying levels of leading edge erosion on the Annual Energy Production of a 1.5MW wind turbine. Source: **[75]**

From this, it is clear that even moderate levels of leading edge erosion can have a potentially significant effect on the energy output of a wind turbine, with even only moderate pitting resulting in substantial losses. Such findings further highlight the real need for developers, manufactures and operators to develop and establish a more thorough understanding of the issue of leading edge erosion; in order to prevent any potential reductions in both energy capture and consequently profitability.

LM Wind Power also examined the effects of leading edge roughness and erosion on the power performance of an installed wind turbine. Figure 3-9 shows the effects of such roughness on the power curve of the operational wind turbine and shows the improvements brought about through repairing and restoring the leading edge.

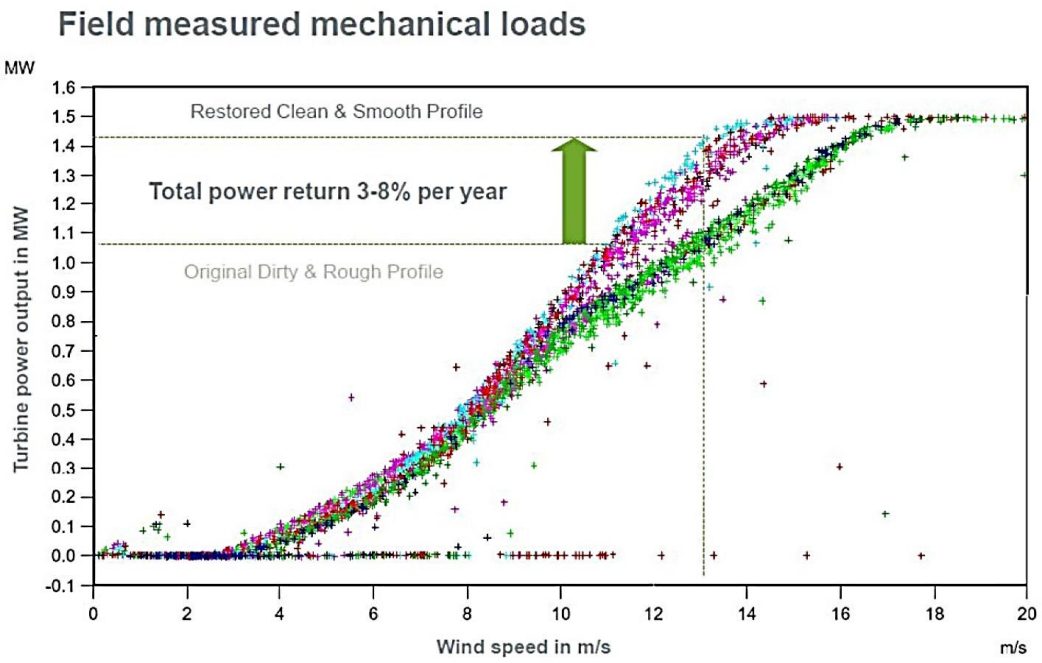

Figure 3-9. Effects of leading edge roughness on the power curve of a turbine. Image courtesy of LM Wind Power. Source: **[84]**

The exact source of the data is not fully apparent (with respect to site, model etc.), but is most likely from a turbine with either the LM34.0 or LM37.3 LM Wind Power blades. As shown, the presence of erosion or surface roughness on the leading edge may result in a decrease in the rated power of a turbine of up to 8% for this given turbine at this location; as shown by the green and dark blue data sets. Such a significant decrease in rated power would have a dramatic effect on both turbine energy output and the subsequent profitability of the installation; again highlighting the need for an enhanced understanding of the issue and the need for new solutions.

Additionally, it is possible to examine studies into the effects of erosion on the performance helicopter rotors to draw lessons applicable to wind turbine blades. Calvert et al. [85] utilised a Computational Fluid Dynamics approach (CFD) to study the effects of typical surface deformation (from the impact of sand erosion) on the aerodynamic profile of a NACA 63-414 aerofoil. It was found that the introduction of surface deformation resulted in detrimental effects on the aerodynamic performance of the profile, such as an earlier onset of stall (and therefore reduction in maximum lift), an increase in drag and a reduction in thrust. However, it must be noted that the study considered surface deformation of the upper and lower surfaces of the profile; not the leading edge.

Reductions in aerodynamic and power efficiency are not the only concerns with regards to leading edge erosion, as the material integrity of the blade is also an important consideration. As briefly discussed previously, the exposure of the composite substrate to moisture and UV light could have seriously detrimental effects on its material properties and performance.

The potential effects of UV exposure on the performance of the coating systems was shown in Figure 3-3, however the composite substrate is also based on polymer materials and therefore it is also susceptible to the influence of UV exposure. Shokrieh & Bayat [86] showed that through accelerated UV exposure, polyester resin exhibited a decrease of 15% in average failure strain, a decrease of 30% in ultimate strength and an 18% decrease in tensile modulus. When looking at a glass fibre reinforced polyester unidirectional composite under the same exposure, it was found that the shear modulus of the composite decreased by about 20% as a result of such exposure. Kumar et al. [87] showed that UV exposure of a carbon reinforced epoxy composite resulted in the reduction of matrix dominated properties, namely a 29% reduction in transverse tensile strength. These studies show the effects that UV exposure can have on the material properties of the polymer materials and composites, with large reductions in material strength exhibited; predominantly in the transverse (or impact) direction (i.e. the directions in which the fibres do not bear load).

The exposure of the composite substrate to water could also pose significant threats to the performance of the blade. Primarily, the removal of any surface coating will mean that the substrate itself will be exposed to further erosion; as previously exhibited in Figure 3-5. This would have obvious structural implications for the blade, and in the result of through-thickness erosion could result in water and particulate ingress to the internal blade structure. Generally speaking, epoxy resins exhibit good resistance to water degradation, whereas Polyester and Vinylester are more prone to water degradation. A report from the materials manufacturer Gurit [30] states that a thin polyester laminate may retain only 65% of its interlaminar shear strength following immersion in water for a one year period, whereas, an epoxy laminate may retain around 90%. This effect however, is heavily dependent on the chemical nature of the matrix materials employed, but highlights the possible sensitivities of the substrate to such exposure.

3.1.3 Repair and Maintenance

The occurrence of damage on the leading edge presents not only issues associated to power production losses and blade material property degradation, but also a range of challenges in relation to the subsequent repair of such damage and associated preventative maintenance. By nature of their design, the tips of wind turbine blades are extremely difficult to access in

situ, particularly so in the offshore environment where wave and weather conditions dictate access windows. However, the costly and risky nature of blade removal and re-installation means that this approach is seldom adopted for the purposes of blade repair, and as such, the blade must be inspected and repaired in situ.

Some of the most common blade access methods employed, involve using rope access technicians, cherry-pickers (for low height onshore blades) and custom descending modules; as illustrated in Figure 3-10.

Figure 3-10. Blade access techniques. Source: **[88]**

Each access method will provide different advantages and challenges with respect to the effective maintenance and repair of the wind turbine blade. For instance, a qualified rope technician can quickly access the area of interest and make assessments of the blade condition, usually in relatively wide window of weather conditions. However, making repairs whilst suspended from ropes obviously presents a unique set of challenges and may not guarantee and acceptable level of quality. Conversely, the other methods will take longer to set out and most likely result in higher costs, but will subsequently provide a more suitable working environment with respect to making repairs and inspecting the blade.

Blade access methods are only one factor in the proper management of blade maintenance and repair; access windows - dictated by factors such as wave and weather conditions - also impose many restrictions. In the offshore environment, these factors will greatly influence the accessibility and ease of repair of the blade. Further to this, with respect to performing repairs to the blade, many repair material product manufacturers (of fillers, patches etc.) can only guarantee the performance of such materials when applied in very specific environmental conditions, as set out by relevant standards. For instance, many repair companies work to the repair standard set by Germanischer Lloyd [89] which states that repairs to composite materials should be executed in conditions between 16-25˚C and a maximum relative humidity of 70% [90]; in order to guarantee effective curing/drying.

Obviously these conditions will be rare in the offshore environment and in some locations the onshore environment also, but repairs made outwith these conditions are less likely to be as robust and in some commercial agreements will not be covered by any form of guarantee; however new materials and techniques are constantly being developed to enable repairs to be made outwith these conditions [84]. In colder climates, these standards for repairs [90] present a significant challenge with respect to making repairs all year round. As such, novel repair techniques have to be devised to create controlled environmental conditions at the blade surface during repair. One example of this is to effectively create a fully enclosed access module which completely surrounds and envelops the area of the blade concerned, as shown in Figure 3-11. This shows a rig created by Bladefence [91] which allows for climate control conditions within the module, to dictate the air temperature and the relative humidity.

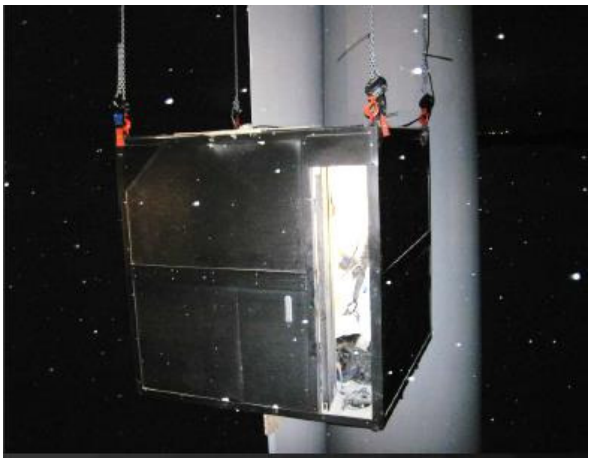

Figure 3-11. Climate controlled blade access module. Source: **[84]**

Given appropriate access and environmental conditions, the subsequent repair of leading edge damage is most commonly achieved through the simple application of putty materials which are applied to the damage area, smoothed over, and then cured to create a new flat and smooth surface finished to the effected blade area [84]. If applying tapes for preventative efforts, then the relevant tape product will be applied following the product manufacturer guidance.

The challenges and issues discussed in relation to maintenance and repair are only a small snapshot of the overall challenge. However, they serve to highlight the extremely challenging and diverse nature of repair and maintenance requirements with respect to wind turbine blades. Naturally, many of the techniques and challenges discussed will also have an associated cost, either directly or indirectly, and this further emphasises the threat to both the performance and profitability of a wind turbine, posed by blade leading edge erosion.

3.2 Rain Erosion

There is a need to look at a better understanding of the nature and threat posed by the phenomenon of rain droplet impact on the surface of wind turbine blades, approaching the issue from first principles. The probability and conditions for rain droplet impact on wind turbine blades are first considered, followed by an investigation of the physics of water droplet impact on solid surfaces and the potential damage modes induced by such impact. The nature of liquid droplet impingement erosion is then further explored along with the current rain erosion experimental techniques and associate testing standards.

3.2.1 Exposure

As with all environmental factors, for any given wind turbine, the frequency and severity of rain exposure will vary widely. However, if considering European locations, most sites will be exposed to some level of annual rainfall, and for most it will likely occur more frequently than other forms of precipitation.

Looking specifically at the UK, Figure 3-12 shows a map of the average annual rainfall for the period running from 1981-2010.

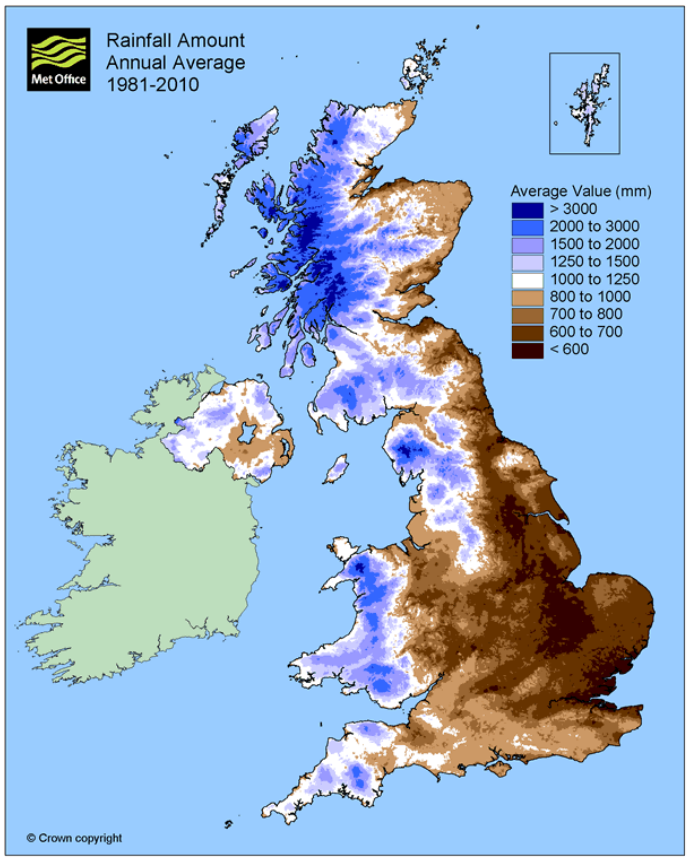

Figure 3-12. Map of the annual average total rainfall in the UK for the period 1981-2010. Source: **[92]**

From Figure 3-12 it is clear that in the UK the expected average annual rainfall varies vastly between different regions. Some areas in the southeast may see less than 600mm of rainfall over a year, whereas in the northwest, totals of up to and greater than 3000mm have been observed. Given that the Polyester gelcoat protected sample tested and shown in Figure 3-2 was subjected to an approximate rainfall total of 30-35mm·h^{-1} over 60 minutes, it is clear that a rainfall amount of 3000mm may be considered significant with regards to rain induced leading edge erosion over the lifetime of the blade. Using information such as that shown in Figure 3-12 may then be considered useful when assessing the threat posed by rain erosion for a given site.

It is possible also to examine a wider geographical scale, encompassing most of Europe, as shown in Figure 3-13.

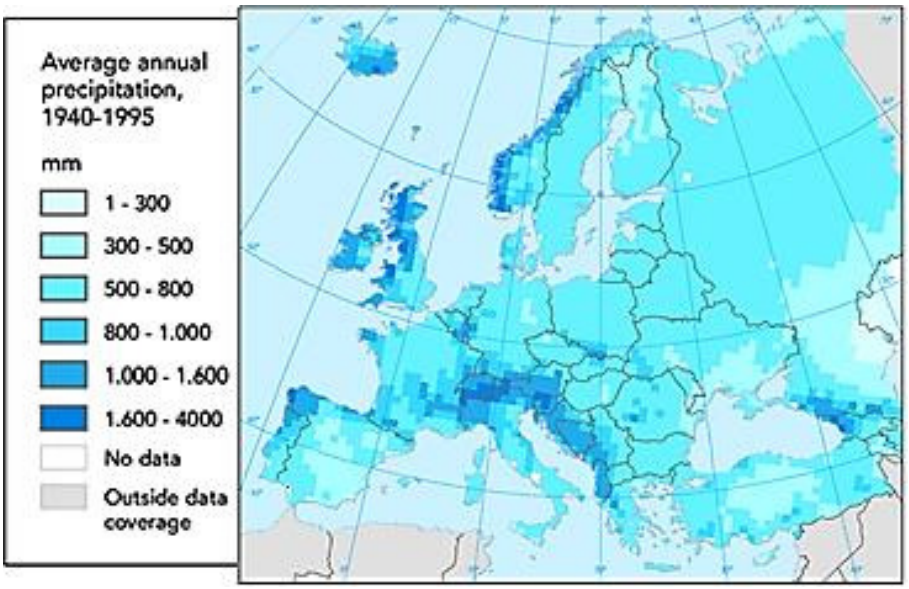

Figure 3-13. European average annual precipitation for the period of 1940-1995. Original image source: **[69]**

Looking at the precipitation levels in Europe, it is clear that in some mainland areas such as central Spain, Sweden and many eastern European countries, the threat posed by rain induced leading edge erosion may be minimal to none; as a consequence of very little rainfall. However, in Alpine regions and coastal regions, the level of rainfall may be considered significant enough, such that the issue of rain induced leading edge erosion may need to be investigated and designed against. As with the map of the UK, where significant rain fall is observed in the westerly regions, this further highlights the necessity in understanding the potential range of meteorological conditions at any proposed wind turbine site.

3.2.2 Rain droplets as a projectile

To understand the nature of rain induced leading edge erosion, the physical nature of rain droplets and their characteristics as a projectile should first be considered. Of importance to these characteristics are: the size and topology of typical rain droplets, the freefalling behaviour of water droplets and the likely impact conditions at the blade surface.

The diameter of a given raindrop varies with respect to the climatic conditions under which they are formed and the conditions of transport in the air. However, typical raindrop diameters are commonly cited as ranging from 0.5mm to 5mm [93]. At and above this maximum diameter of approximately 5mm, the droplet geometry may become unstable and fragment [94]. Kubilay et al. [95] produced a plot for the probability density for rain droplet diameters, as shown in Figure 3-14, using the equations derived by Best [96].

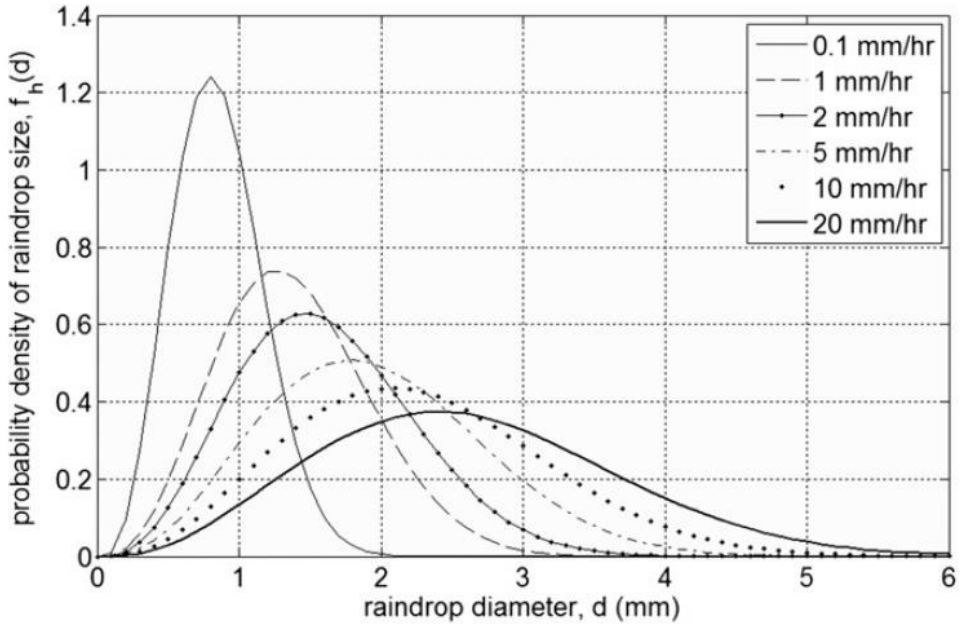

Figure 3-14. Probability density of rain droplet size. Image source: **[95]**. Using equations from: **[96]**

From the probability density plot it is clear that for mild to moderate rain rates, rain droplet diameters ranging from 0.5-3mm are most common; it is only during more extreme rain rates that droplet diameters in excess of 3mm are exhibited.

The terminal velocity of any given falling rain drop will be heavily influenced by the climatic conditions and therefore is difficult to typify. However, Gunn & Kinzer [97] conducted a measurement campaign to ascertain the terminal free fall velocity of varying water droplet sizes through stagnant air. The results of their findings are shown in Figure 3-15.

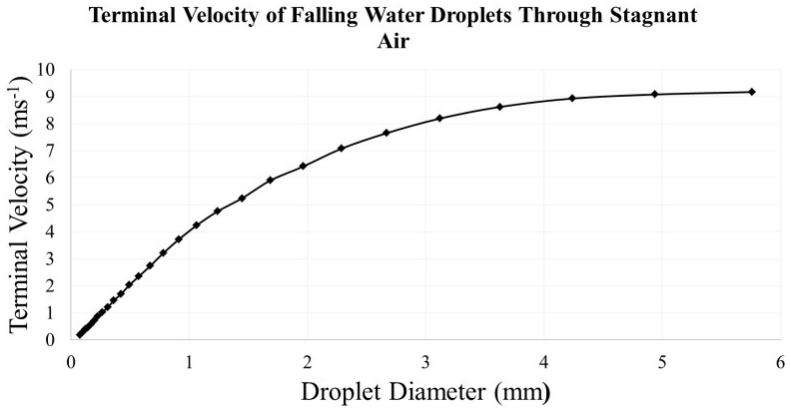

Figure 3-15. Free fall terminal velocity of water droplets through stagnant air for a range of stable droplet diameters. Data source: **[97]**

From Figure 3-15, it can be seen that the maximum free falling terminal velocity levels out at around 9m·s^{-1} for diameters in excess of about 3.5mm.

In the context of wind turbine blade leading edge erosion, the freefalling terminal velocity of the rain droplet plays only a minor role in the potential magnitude of the impact velocity when compared to the blade tip speeds. It is possible through a process of simple velocity vector calculations to establish an approximate value of potential impact velocity between incoming raindrops and the blade, at a given rotor position, θ, whereby in the upright position the blade is at $\theta = 0$ and pointing downwards is at $\theta = 180$; and assuming clockwise rotation. The blade tangential tip speed, V_{tip}, can be broken into its horizontal and vertical in-plane components, V_x and V_y respectively, as described in Equation 3.1 and Equation 3.2.

$$V_x = V_{tip} \cos\theta \tag{3.1}$$

$$V_y = -V_{tip} \sin\theta \tag{3.2}$$

Taking a rain droplet of terminal velocity, V_{term}, fully entrained in a completely horizontal free stream wind with velocity, U_∞, (i.e. assuming that the droplet is also travelling at this speed horizontally) it is possible to perform velocity vector analysis to ascertain the impact velocity magnitude, V_{impact}, at a given blade position, as shown in Equation 3.3.

$$V_{impact} = \sqrt{(V_{term} + V_y)^2 + {V_x}^2 + {U_\infty}^2} \tag{3.3}$$

It is possible then to calculate the impact velocity through a full rotor sweep ($\theta = 0 \rightarrow 360$), for a given set of rain conditions and turbine operating parameters. For example, taking a

rain droplet with a terminal velocity of $8m \cdot s^{-1}$, fully entrained in a horizontal $20m \cdot s^{-1}$ wind, striking a blade with a $90m \cdot s^{-1}$ tangential tip speed, it is possible to calculate the potential impact velocity magnitude for a full rotor sweep. Plotting these calculated potential impact velocity values against their respective rotor position gives the plot shown in Figure 3-16; which also shows the tip speed with a dotted line.

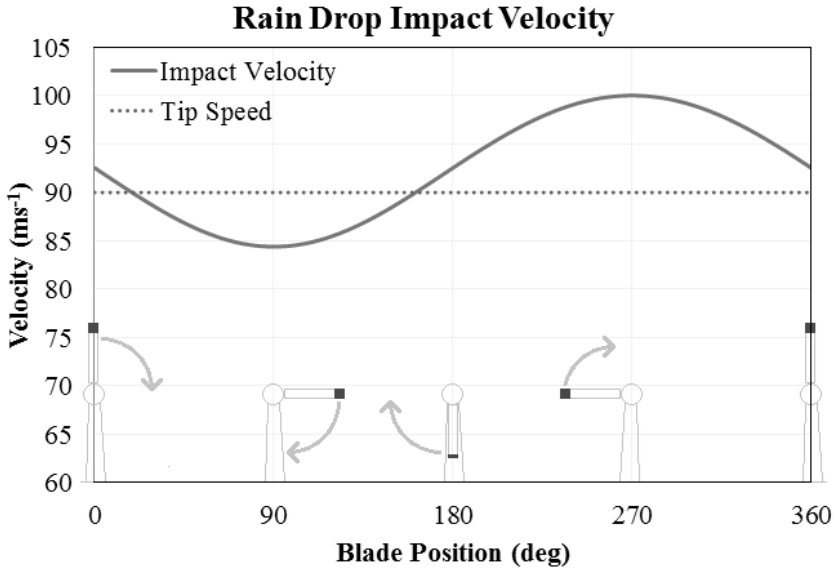

Figure 3-16. Rain droplet impact velocity at the blade tip, at positions through a full rotor sweep. Rain drop terminal velocity of $8m \cdot s^{-1}$, fully entrained in a $20m \cdot s^{-1}$ horizontal wind, striking a blade tip with a $90m \cdot s^{-1}$ tip speed. The tip speed has also been plotted for reference.

The values shown in Figure 3-16 are derived from a fairly rudimentary approach that makes the following assumptions:

- **Full droplet entrainment –** As stated previously, the droplet is assumed to possess a horizontal velocity component equal to that of the prevailing wind speed. In reality this may not be likely and would in fact the exact freefalling nature would be difficult to ascertain or typify, however it forms an appropriately conservative approach with regards to considering the worst case scenario.
- **No aerodynamic considerations –** Wind turbine induced aerodynamic effects such as induction and boundary layer effects are not considered. As such, the approach assumes that these effects do not greatly alter the impact velocity. It may be that induction effect may reduce or increase the incoming droplet velocity or that an aerodynamic boundary layer over the blade surface may act as a barrier or cushion to rain droplet impact.

- **Impact angles not considered** – The impact angle between the incoming droplets and the blade surface are not considered in this approach and as such it only informs on the potential magnitude of impact velocities.

Irrespective of these assumptions and simplifications this approach does well to both highlight the potential magnitude of impact velocity values and to act as an aid to understanding the nature of impact on the blade. For instance, it illustrates that even when the blade is rotating in a downward direction (1-179˚ position), as a result of the significant tip speed, the impact velocity between the rain and blade does not drop below 80m·s^{-1}; therefore the terminal velocity of the rain acts only to slightly lessen the impact velocity. Conversely, when looking at the impact velocity at the rotor position of 270˚, where the blade and rain drop trajectories are exactly opposed to one another, the additive effects of the terminal velocity to the blade tip velocity can be observed as the peak in the impact velocity. It can be seen then that for a turbine with a tip speed of 90m·s^{-1}, impact velocities of nearly 100m·s^{-1} may still be possible as a result of the nature of impact at a rotor position of $\theta = 270°$.

3.2.3 Liquid impact phenomena

The previous section contextualised and quantified the range of possible impact conditions with respect to rain droplet impact on the leading edge of a wind turbine blade. However, it is also important to understand what the magnitudes of these impact velocities mean in the context of liquid droplet impact on a solid surface.

Gohardani [79] detailed the nature of liquid droplet impact on a flat solid surface, as shown in Figure 3-17.

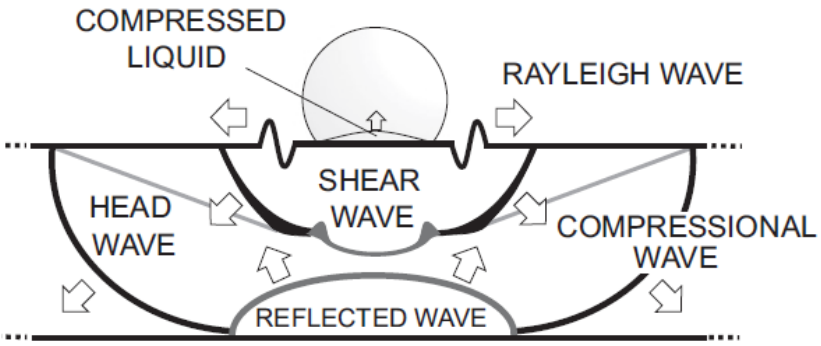

Figure 3-17. Liquid droplet-solid surface impact interaction, showing shockwave behaviour in both the droplet and target. Source: adapted from **[79]**

Figure 3-17 shows that upon impact an initial compressional wave is created in the solid target body, which is then propagated outwards from the initial locus of impact. Shortly after

the formation of these compressional waves, as the droplet/surface contact area increases, shear waves are also created in the target; which also propagate through the material, away from the impact zone. The interaction of these waves can be complex and will depend upon impact conditions and material properties. A Rayleigh wave created on (and confined to) the target surface is also generated and propagate away from the impact area. The creation of a compressed liquid wave front in the droplet itself is also illustrated, travelling upwards through the droplet body. This compressed liquid wave front behaviour is crucial to understanding the nature of the impact phenomenon, as after a short duration of impact, the wave front spreads towards and past the contact periphery between the droplet and the surface. After this point, lateral jetting (or 'splashing') of the droplet across the surface commences.

To predict the pressure exerted on the surface by the liquid droplet during the initial phases of contact (until the onset of lateral jetting), the waterhammer equation has historically been employed [98]. The waterhammer equation is shown in Equation 3.4, where P is the waterhammer pressure created during impact, ρ_0 is the undisturbed density of the fluid (water in this case), c_0 is the speed of sound in the undisturbed liquid and V_0 is the impact velocity.

$$P = \rho_0 \, c_0 \, V_0 \tag{3.4}$$

This simple equation was first developed to calculate the waterhammer pressure present in piping systems and is therefore based on the following assumptions:

1. The impact is a one dimensional event
2. The target surface is perfectly rigid
3. The water density remains constant during the impact event
4. The speed of sound remains constant during the impact event.

Although these are quite restrictive assumptions, the expression can still be used as a good indicator of the magnitudes of impact pressure that may be expected for a given impact event. Dear & Field [99] proposed a modified waterhammer equation, which takes into consideration not only the propagation of pressure through the liquid during impact, but also the target body; as shown in Equation 3.5, where P is the modified waterhammer pressure imparted during impact, V is the impact velocity, ρ is density, c is the speed of sound, and the subscripts l and s refer to the liquid and solid bodies respectively.

$$P = \frac{V\rho_l c_l \rho_s c_s}{\rho_l c_l + \rho_s c_s} \tag{3.5}$$

The expressions shown can be useful in approximating the impact pressure exerted, however they only predict the pressures created during the initial phases of contact. They do not apply to conditions after the onset of droplet lateral jetting across the target surface.

Indeed, the transition to and onset of lateral jetting in no way signifies the end of significant or noteworthy impact mechanisms in water droplet impact. Instead, the spreading behaviour acts to greatly accelerate the velocity of the water in the lateral direction across the given target surface. Bartolo et al. [100] showed that when water droplets gently impact a hydrophobic surface, the resulting lateral jet can exhibit a velocity up to 40 times the original impact speed. The additional significant impact mechanism imposed by this high velocity droplet spreading behaviour is the creation of extremely high pressures at the droplet spreading wave front. Heymann [98] found analytically that the pressure generated at this wave front can exceed the original waterhammer pressure by a factor of 3; imposed locally at the wave front. Subsequent experimental investigations by Field et al. [101] verified these findings. Li et al. [102] also observed through a numerical volume of fluid method that the highest pressure is generated at the expanding wave front, at the time of transition to lateral jetting.

The creation of these pressure spikes sweeping outwards across the target surface are suspected to have a significant influence on the damage created through first damaging the material and then subsequently jet washing and furthering eroding the surface.

An instantaneous approximation of the impact force imparted through liquid droplet impact has also been proposed in previous studies [103] [104], as shown in Equation 3.6, where F is the impact force, m and d are the mass and diameter of the droplet respectively and V, the impact velocity.

$$F = \frac{mV^2}{d} \tag{3.6}$$

The force exerted will obviously vary over the duration of the impact event; however this expression again serves as a good tool to approximate the magnitude of impact forces imparted.

It is interesting therefore to examine what these expressions can reveal about the potential magnitudes of the pressures and forces exerted on a blade surface through rain droplet

impact. Assuming a water density of 1000kgm^{-3} and a speed of sound in water of 1500m·s^{-1} [105] for the waterhammer equation (Equation 3.4) and a droplet diameter of 2mm for the instantaneous force equation (Equation 3.6), both expressions can be calculated and plotted against a range of potential impact velocities, as shown in Figure 3-18.

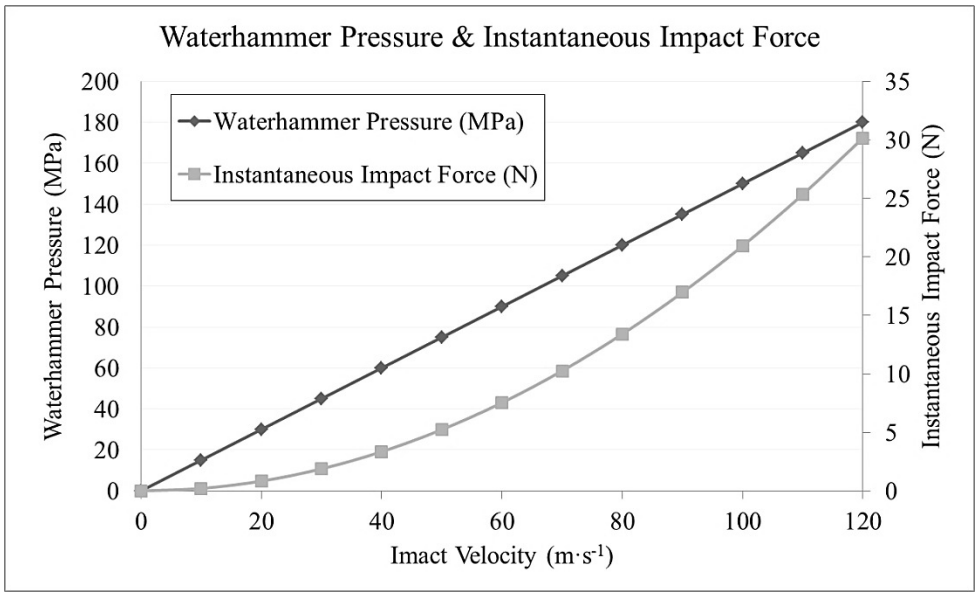

Figure 3-18. Waterhammer pressure and instantaneous impact force from a 2mm diameter liquid droplet impact over a range of potential impact velocities.

As shown in Figure 3-18, the potential impact pressures created through rain droplet impact can be considered significant in the context of leading edge impact. At a common tip speed of around 80m·s^{-1} (Figure 2-2) pressures of up to 120MPa could be imparted on the blade surface through rain droplet impact.

The impact energy is also an important consideration with regards to impact studies and for rain droplet impact it is simply equated to the kinetic energy of the impacting droplet (Equation 3.7).

$$KE = \frac{1}{2}mV^2 \tag{3.7}$$

where KE is the impact energy, m is the droplet mass and V is the impact velocity. Plotting the kinetic energy given by this equation for a range of droplet diameter across the potential range of impact velocities, gives the values shown in Figure 3-19.

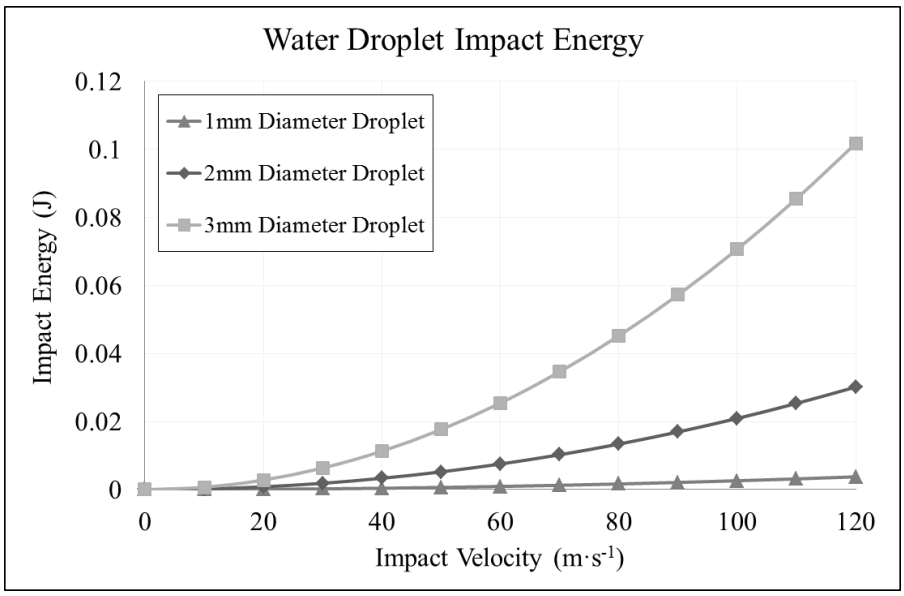

Figure 3-19. Water Droplet impact energy for a range of droplet diameters at various impact velocities, assuming a water density of 1000kg·m^{-3}.

As shown, the droplet diameter plays a significant role in the impact energy associated to a given rain drop. The squaring effect of the impact velocity also has a strong influence on the impact energy. The energies shown may not be deemed significant in many engineering disciplines, however, given the significant duration of the exposure of the blades to these conditions and factoring in the other hostile environmental conditions, the energies take on greater significance.

3.2.4 Rain droplet impingement induced damage

The potential magnitudes of forces and pressures exerted by rain droplet impact on the leading edge of wind turbine blades are significant. It is prudent therefore to also examine the potential mechanisms by which damage can be created in solid targets through liquid droplet impingement.

Exposure to liquid droplet impact is common to many engineering applications and as such, although there is limited research in the context of wind turbine blades, the phenomenon has been the centre of many previous research studies in other industries; namely aviation, which Gohardani [79] reviewed in depth. As discussed previously, these studies can be reviewed and examined to ascertain their relevance to the work of this research (i.e. in a wind turbine blade context), and therefore provide further information and insight into liquid droplet impingement induced damage.

The way in which damage is created on a surface due to liquid droplet impact depends on both the nature of the impact (impact velocity and inclination) and the target material. Figure

3-20 shows the typical damage formation caused by repeated liquid impact on a ductile target material.

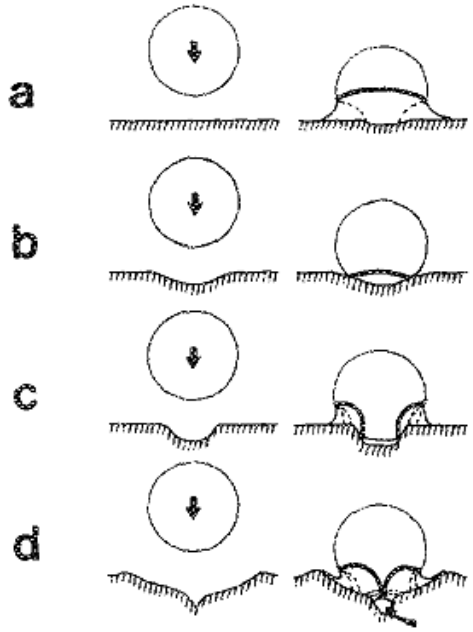

Figure 3-20. Ductile surface exposed to repetitive droplet impact, showing the formation of damage, source: **[106]**.

From, the initial impact events begin to create small indented craters on the surface and this is subsequently deepened through further exposure to impact. This topological change then begins to influence the shock wave behaviour in the impacting droplet and consequently the loading pattern exerted on the surface; with the lateral jetting process playing a critical role in the evolution of the damage. In turn this results in stress concentrations in the material, worsening the damage process and removing material. Although any damage in a component is typically undesirable, there are some applications in which this high level of deformation in response to impact may be desirable. For instance if the given component requires frequent examination and damage assessment, it may be possible (as a result of the high levels of deformation) to visually identify damage with the naked eye; negating the need for more complex inspection apparatus such as ultrasound scanners. This in turn makes it simpler to catalogue and monitor damage of the surface and allows for proactive mitigation. With stiffer brittle materials, as discussed in the following, this simple method of inspection may not be suitable, as such materials typically respond to impact with little observable deformation; instead manifesting damage through microscopic cracking and other mechanisms.

Adler and Hooker [107] investigated the rain erosion characteristics of brittle glass material through experimental means, classifying the rain erosion process in such brittle materials through the schematic shown in Figure 3-21.

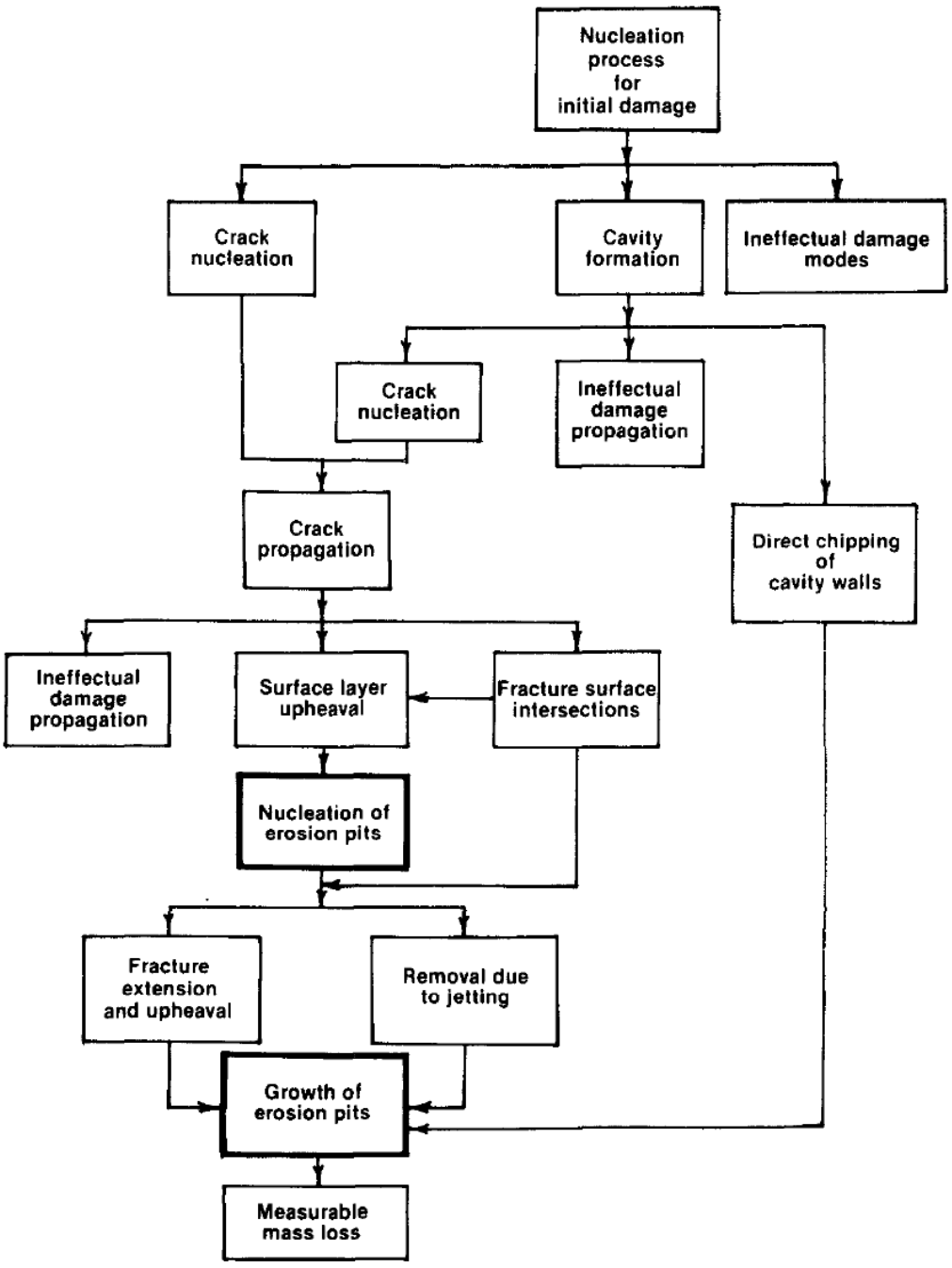

Figure 3-21. Schematic of damage modes due to rain erosion. Source: **[107]**.

From this schematic it can be seen that the mechanism of rain erosion in brittle materials differ to that of ductile materials. Brittle materials fail through the creation of cracking on the surface or through cavitation created; as opposed to high levels of deformation with ductile

materials Figure 3-20. The occurrence of cracking and cavitation acts as a nucleation point for further damage and material degradation.

Gorham et al [108] conducted experimental water jet impact testing on a range of polymers and polymer based composites to evaluate the effects of rain droplet impact induced damage erosion; citing that water jet tests provide good agreement with comparative water droplet impact tests. Figure 3-22 shows the result of water jet impact testing of a MY778 epoxy at 550m·s^{-1} and 860m·s^{-1} in A and B respectively.

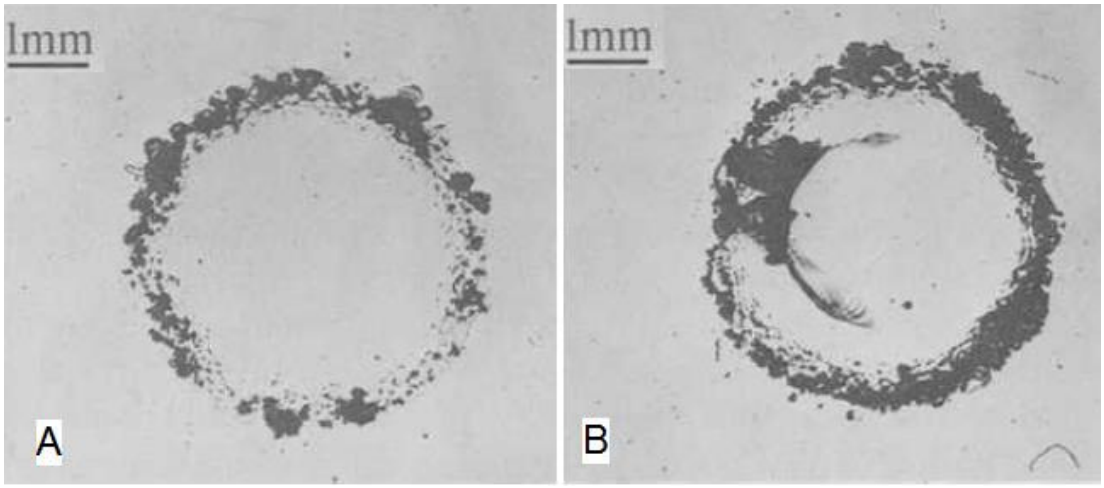

Figure 3-22. Surface damage created during a water jet test on a MY778 epoxy impacted at A – 550m·s^{-1} and B – 860m·s^{-1}. Source: **[108]**.

Although the impact velocities tested by Gorham et al. [108] far exceed those under consideration in this research, it is interesting to note the nature of the damage created on the surface of the epoxy as a result of liquid impact. The spreading behaviour and subsequent high pressure creation (as discussed previously in Section 3.2.3) appears to greatly the influence the nature in which damage on the surface is created, forming a ring-like area of damage around the impact centre. It further highlights the complexities associated with liquid on surface impact and the nature in which damage is manifested as a result.

Gohardani [79] states that in aviation studies a parameter often utilised for evaluating the erosion performance of materials under liquid impingement is the damage threshold velocity (DTV). This value is simply the lowest impact velocity at which damage in the target material is observed. The exact classification of such damage is not established, with some defining it as a loss of optical transmission or mass and others basing it on the occurrence of fracture [79]. Evans et al. [109] defined a theoretical expression for the DTV given by

$$V_{DT} \approx c_w 1.41 \left(\frac{K_{IC}^2 c_R}{\rho_w^2 c_w^2 d_w} \right)^{1/3} \quad (3.8)$$

where, V_{DT} is the DTV, K_{IC}^2 is the fracture toughness of the target material, c_R is the Rayleigh wave velocity of the target material, $\rho_w$and c_w are the density of the water and compressional wave speed in the water respectively and d_w is the droplet diameter. Gohardani [79] describes that the Rayleigh wave is created (and confined) on the target surface and is responsible for approximately 2/3 of the impact energy. The Rayleigh wave velocity in a solid is given by [110]

$$c_R = \left(\frac{0.862 + 1.14\nu}{1 + \nu} \right) \left(\frac{E}{2(1+\nu)\rho} \right)^{1/2} \quad (3.9)$$

where c_R is the Rayleigh wave velocity, ν is the Poisson's ratio of the material and E is the material Young's modulus.

Using both these equations, it is possible to evaluate an approximate DTV for a typical wind turbine blade epoxy based coating. The material properties of typical epoxy gel coat technologies vary vastly between products and manufacturers, however assuming a typical Young's modulus of 3.2GPa, a Poisson's ratio of 0.38 and a density of 1150kgm^{-3}, Equation 3.9 gives a Rayleigh wave speed of approximately 942m·s^{-1}. This value can then be used in Equation 3.8 to derive the theoretical approximate for the DTV, for a range of rain droplet diameters; assuming a water density of 1000kgm^{-3} and a compressional wave speed in water of 1490m·s^{-1}. However, the fracture toughness properties of epoxy material systems can vary widely from low values of 0.5 to higher values of 1.5MPa.m$^{1/2}$ [111]. Therefore, the values of DTV across a range of rain drop diameters can be calculated using 3 different fracture toughness values of 0.5, 1 & 1.5 MPa.m$^{1/2}$. The DTV values obtained across a range of potential rain drop diameters (and for the three toughness values) are shown in Figure 3-23.

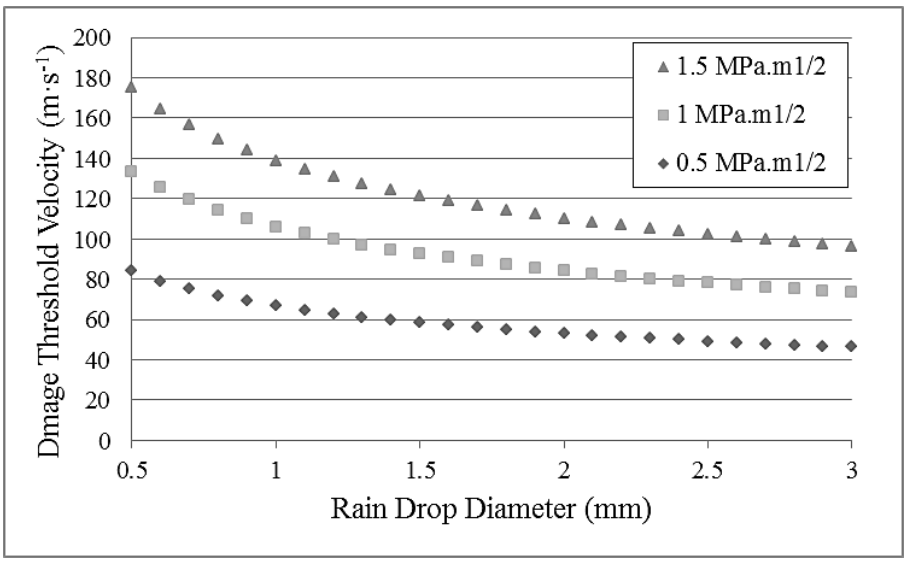

Figure 3-23. Damage Threshold Velocity for rain droplet impact on an epoxy target across a range of droplet diameters and for different epoxy fracture toughness values

This plot highlights the importance of employing a surface coating technology with heightened fracture toughness. For low values of fracture toughness, the DTV value could potentially be as low as $50 m \cdot s^{-1}$ for larger droplet sizes. However, it is also to possible to observe that even for tougher values, the DTV value can still be lower than $100 m \cdot s^{-1}$ for large droplet sizes. This approach assumes normal impact angles and therefore represents the worst case scenario for liquid droplet impact, but it is prudent to note that the ranges of DTV values are not far removed or significantly higher than some of the tip speed values discussed previously. Additionally, the DTV value predicts the minimum required impact energy to induce instantaneous damage; therefore impact velocities slightly below the DTV values may still induce damage over a longer period or after repeated impact.

3.2.5 Experimental rain erosion evaluation

In the absence of suitable rain erosion testing standards within the wind sector, the industry has instead looked to the aerospace sector where rain erosion testing techniques have been well developed and established [25]; in light of the need for rain resistive airframe and helicopter rotor components. The established industry standard for rain erosion is 'ASTM G73 – 10 Standard Test Method for Liquid Impingement Erosion Using Rotating Apparatus' [112], which is utilised to evaluate the erosion resistance of materials. Most testing approaches utilise a swirling arm type apparatus, whereby a sample is attached to the end of a rotating arm mounted on a motor. The sample is then rotated through a simulated rain field of a given intensity over a period of several hours, therefore exposing the sample to an accelerated life cycle process.

One of the longest serving and most established facilities is the Rain Erosion Test Facility, hosted at the University of Dayton Research Institute (UDRI), Ohio [55], which has been in operation on both an academic and commercial basis for 35 years and claims to be the national and international standard for testing the rain erosion resistance of aerospace materials. The testing apparatus and associated support equipment are shown in Figure 3-24.

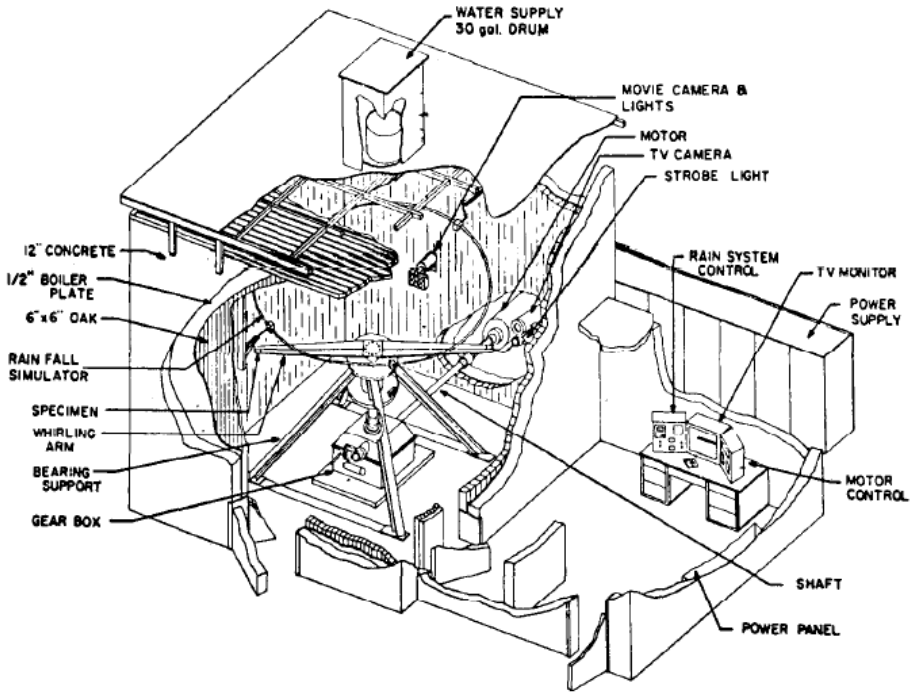

Figure 3-24.UDRI Rain Erosion Test Facility. Source: **[113]**

The facility features a 2.5m diameter rotating arm upon which the test samples are mounted on the tips, the arm is driven by a 400hp motor through a gear box which can deliver a maximum tip speed of 400m·s^{-1} (excessive for the purpose of this study) [113]. The rain fall is simulated via an aluminium pipe annulus mounted above the swept path of the rotating arm and fitted with 96 equally spaced hypodermic needles calibrated to deliver a rainfall rate of 25.4mm·h^{-1}, with a droplet diameter in the range of 1.5-2mm. This type of testing utilising a swirling arm apparatus is commonly referred to as a 'Helicopter Test'. The facility also utilises high speed photography equipment to record the impact events on the sample surface. Although the facility has historically been most commonly utilised to rate the erosion resistance of aerospace materials and components, the rain erosion testing described by Powell [75] and shown in Figure 3-5 were carried out using this facility.

A similar facility is also currently under development at the Composites Research Centre at the University of Limerick [114], named the Whirling Arm Rain Erosion Rig (WARER) as detailed by Tobin et al [115] [116], and shown in Figure 3-25.

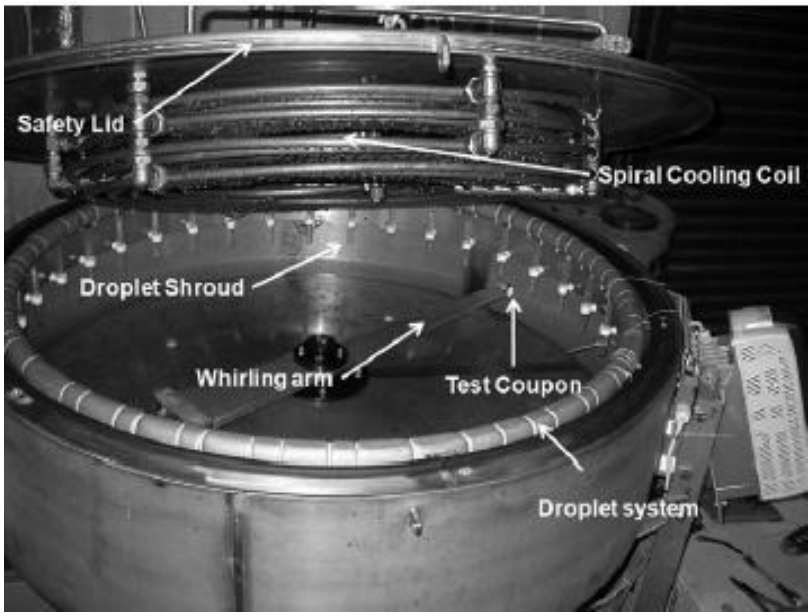

Figure 3-25. Rain erosion test apparatus, university of limerick, source: **[115]**

This apparatus works on a similar principle to that of the UDRI facility, using a spinning 600mm diameter arm sample mount passing through a series of spray heads with a rain fall rate of 25.4mm·h^{-1} and an impact speed of up to 129m·s^{-1}.

The testing conducted by Haag [51] and Powell [75], as previously discussed, also utilised this swirling arm technique to evaluate the performance of different blade material configurations and a new material technology. However, these tests were conducted using the apparatus hosted by Polytech [73], currently one of the only independent blade coating test companies, adopting the ASTM standard discussed and a swirling arm apparatus.

An alternative to the Helicopter style testing is to instead utilise a high velocity water jet, targeted at the intended target, whilst interrupting the flow using a rotating disc with a hole to create a more pulse-like (or droplet-like) impact event. Such an apparatus, named the Pulsating Jet Erosion Test (or PJET) is hosted by EADS [117] as shown schematically in Figure 3-26.

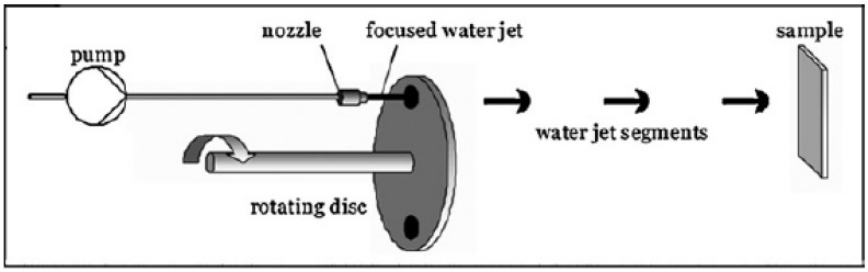

Figure 3-26. PJET rain erosion methodology. Source: **[116]**

In round robin testing trials conducted by Tobin et al. [116], this jet impact testing method was found to provide results agreeable with those obtained from the more popular helicopter tests.

The ASTM G73-10 standard [112] and associated testing techniques discussed can prove helpful in rating the rain erosion resistance of materials and characterising the damage created. However the ASTM standard has been adopted by the wind industry as a 'best fit' for rain erosion testing and requirements, and as such there are many elements of the standard which are not well fitted to wind turbine applications, and areas of interest to the industry which are not covered. From reviewing the documented rain erosion test results (discussed previously) shown by both LM Wind Power [51] (Figure 3-3) and 3M [77] [75], the effects that UV exposure can have on worsening or accelerating leading edge erosion were made clear. Therefore, it would seem appropriate that such effects should be incorporated into any wind turbine blade rain erosion testing standard (as LM Wind Power and 3M do), resulting in a more robust and more importantly representative rain erosion testing procedure. In light of such shortfalls and the need for more bespoke and appropriate standards, there is currently an ISO standard committee ISO/TC 35/SC 9/WG 32 [118] working on the development of appropriate coating testing standards for wind turbine (and tidal stream) blade materials. The scope of the committee is wide and far reaching, however the primary focus is to develop standards for representative rain erosion testing and secondarily to address hailstone impact and erosion and other factors (such as icing, lightning strike, dirt retention etc.).

3.3 Hailstone Impact & Erosion

There is a serious threat to the performance of a wind turbine system posed by the phenomenon of hailstone impact on the leading edge surface of the blade. The probability and conditions for hailstone impact on wind turbine blades are first discussed, followed by an investigation of the basic physics of hail impact on solid surfaces and the potential damage modes induced by such impact. An overview of the various experimental approaches of assessing hailstone impact is also presented.

3.3.1 Exposure

Wind turbine blade exposure to hailstone impact is a very site specific issue (even more so than rain). As with the rain fall maps shown previously (Figure 3-12) it is also possible to use climatic maps to examine the likelihood of hailstorm events across the UK, through the use of the map shown in Figure 3-27.

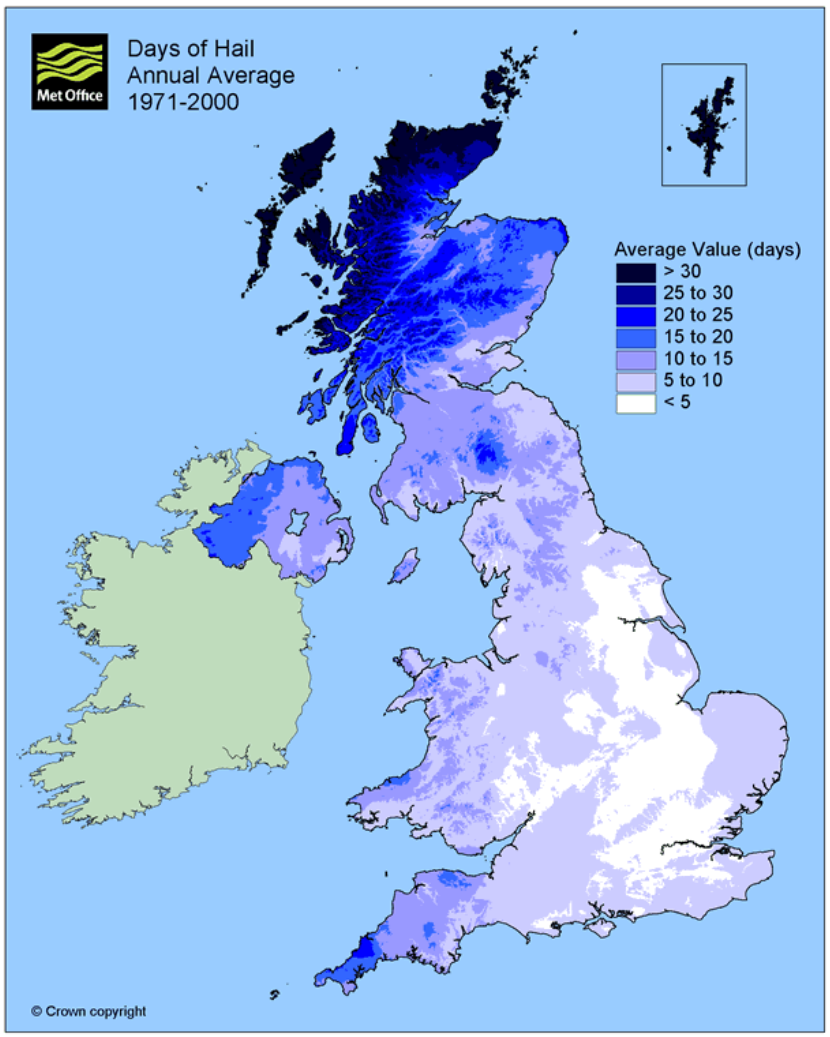

Figure 3-27. Days of hail, annual average from 1971-2000. Source: **[92]**

The map plots the annual average total days with hail events in the UK, using data covering the period of 1971-2000. However, the definition of a 'Day of Hail' is not explicitly stated, therefore it must be assumed to represent even the shortest duration of hailstorm events. From the map it is clear that even within the relatively small geographical area of UK, there is a wide variability in the frequency of days with hail. In south eastern and central regions of England and around the Greater London area, the occurrence of hailstorms are somewhat rare; occurring on less than 10 days over an annual period. It could therefore be said that in these regions, the threat posed by hailstone impact damage to the blade leading edge may be minimal. However, there still may be a threat posed by freak hailstorm events, as the maps say nothing of the magnitude or the intensity of the hailstorm events when and if they do occur. It is clear though that in north eastern regions, specifically in Scotland, the frequency of hailstorm events is much higher, with some areas in the Highlands and Western Isles experiencing more than 30 days with hail in a year. In these regions, it may indeed be critical to consider the effects of hail impact and erosion on the blade leading edge. Outside the UK, the same degree of variability in the frequency of hailstorm events can also be observed. For example, reviewing data from the Irish Meteorological Service [119] it can be seen that in some locations such as Malin Head in the North of Ireland there may be up to 48 days with hail events in a year (averaged over 30 years), whereas in other sites such as Roches Point, in the South of the country, Cork, the total average only comes to 8 days with hail in a year. Again, this highlights the necessity for a thorough understanding of the typical meteorological conditions for any proposed (or operational) site.

3.3.2 Hailstones characteristics & material properties

Convention states that a hailstone has a diameter of at least 5mm [120], whereas smaller particles are referred to as ice pellets or snow pellets. Hailstones are formed in cumulonimbus clouds (thunder clouds), especially those with a strong updraft, large liquid content, large vertical height and large cloud-drop sizes [121]. In these thunderclouds, drops of water rise up through the cloud and begin to freeze, upon reaching/accumulating a certain mass the ice particle will descend through the cloud. Some of these ice particles are then again caught in the updraft and acquire an additional layer of ice and this process of updraft and downfall can recur several times for any given initial particle. Through each cycle the particle will acquire an additional layer of ice until the thundercloud can no longer support its weight and it falls to earth as hail. It is this cyclic layering process that gives hail its onion like formation, as shown by the cross section of a large hailstone in Figure 3-28.

Figure 3-28. Cross section of a large hailstone, showing the onion-like layered formation. Source: **[122]**

The average size of hailstones is dependent on site location and established average values are difficult to accurately ascertain. The only certain way to establish the likely average size of hail at any given site would be through measurement on location. In the UK, some of the largest ever recorded hailstone sizes are in the range of 60-90mm [123], however these are considered freak events. The density of hail ice can vary widely between locations and storms. Field et al. [124] state that for hail sizes smaller than 20mm in diameter, densities can range widely from 50 to 890kgm^{-3}, but for larger sizes higher densities in the range of 810 to 915kgm^{-3} are observed. For the purposes of hail threat standardisation (for aerospace applications), they establish that it is reasonable to assume a worst case density of 917kgm^{-3} (solid ice) for hailstones.

Ice is a complex and highly variable material with regards to its material characteristics and properties and as such is widely considered as a class of material rather a single type. It has 13 different crystal structures, two amorphous states and its engineering properties are dependant and influenced by numerous other variables. As hailstones form under ambient conditions they form as polycrystalline ice '1h', known as ordinary or terrestrial ice [125]**.** Almost all ice in the natural environment forms as ordinary ice [126], therefore it is the only type considered in the research discussed and is therefore hereafter simply referred to as ice.

Schulson [127] states that ice may exhibit two types of inelastic behaviour when loaded under compression. When loaded at low strain rates ice behaves in a ductile manner, however with increasing strain rate it begins to behave in a more brittle manner, as indicated by Figure 3-29.

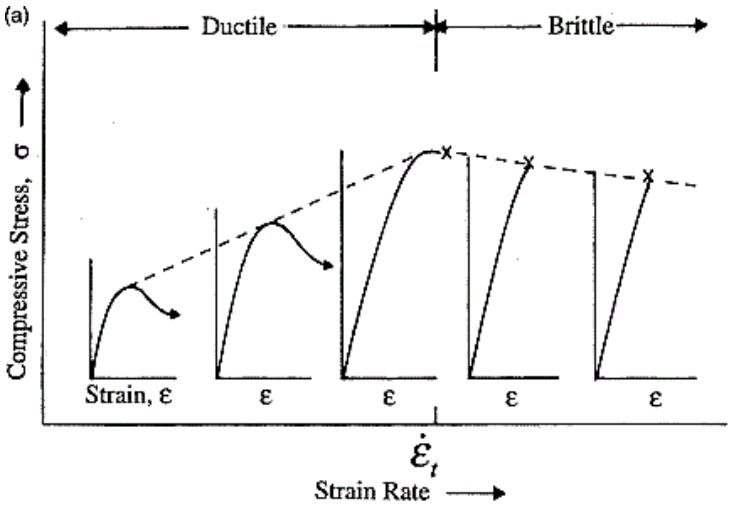

Figure 3-29. Schematic diagram showing the ductile to brittle transition in the behaviour of ice under increasing strain rates, whereby ε_t marks the theoretical point of transition. Source: **[127]**

From Figure 3-29 it can be seen that as the strain rate increases the ices material begins to behave in a more brittle manner with a more linear stress-strain curve and decrease in plastic deformation. The transition from ductile to brittle behaviour is reported to occur at a strain rate of the order of $10^{-3}s^{-1}$, under uniaxial compression (at -10˚C). This phenomenon is shown by Schulson [127] in Figure 3-30 which shows the relationship between the compressive failure stress and strain rate using data from various studies.

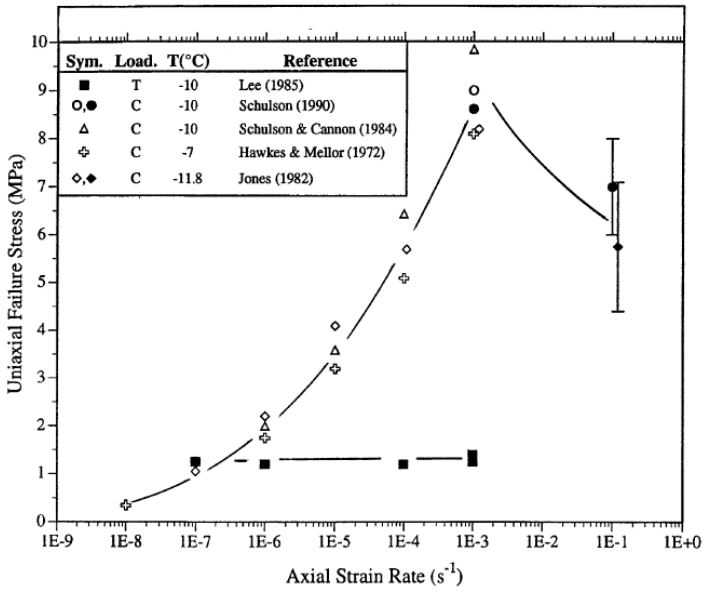

Figure 3-30. Relationship between compressive failure stress and strain rate, source: **[127]**.

The peak in the curve marks the ductile-to-brittle transition of the material. The plot shows good cross-study agreement on the compressive strength of ice and displays the strengthening effect of increased strain rates.

Carney et al. [128] summarized that polycrystalline and single crystal ice exhibit strain rate sensitivity from $10^{-8}s^{-1}$ to $10^{-2}s^{-1}$ and that single crystal ice has also been shown to be rate sensitive in the range of approximately 10^{0} to $10^{3}s^{-1}$. This strain sensitivity of single crystal ice at high strain rates was established through plotting data from tests conducted by Shazly et al. [129] and fitting it to a trend using a static strength of 14.8MPa, as shown in figure 24 [128].

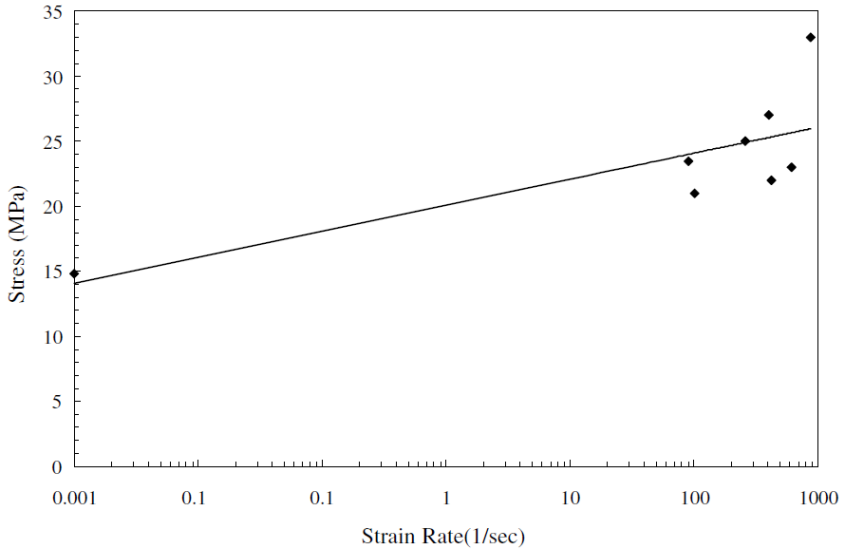

Figure 3-31. Strain rate sensitivity of single crystal ice under compression. Source: **[128]**

The variability of the material properties of ice highlight the challenges in confidently predicting the forces and stress imparted on the blade from a potential hailstone strike. The strain sensitive nature of ice makes it impractical to establish an analytical approximation (through Hertzian contact theory [130] or otherwise) of the predicted impact force from hailstones.

However, for the purposes of numerically modelling hailstone impact (as discussed later in Section 5.2.1) it should be acceptable to establish an approximation of the likely hailstone ice material properties. As although it is important to both understand and aim to replicate an accurate representation of hail ice behaviour during impact, the key area of interest from modelling results is the material response of the blade target.

3.3.3 Hailstones as an impact projectile

In the context of impact considerations, the large diameters of hailstones (specifically in comparison to rain drop impact) play an important factor in two ways. Firstly, with an increase in diameter there is an increase in the hailstones mass and therefore an increase in its impact energy, as described by Equation 3.7. Additionally, with increased diameter the

terminal velocity also increases according to the relationship shown in Equation 3.10, where V_t is the terminal velocity, g is the gravitational acceleration, C is the drag coefficient (0.5 for a sphere), ρ_{air} is the air density and A_h is the cross sectional area of the hail stone in the direction of travel [131].

$$V_t = \sqrt{\frac{2m_h g}{C\rho_{air}A_h}} \tag{3.10}$$

This equation is derived from balancing the gravitational forces pulling on the falling body with the aerodynamic drag forces acting to slow the fall. Although not applicable to all hailstone impact events, it acts as a useful guide to the range of possible terminal velocities. Using this equation, assuming a density of 900kg·m^{-3} for the hailstone (this value varies widely, as will be discussed) and 1.29kg·m^{-3} for air, and assuming a perfectly spherical hailstone shape and thus a drag coefficient of 0.5, it is possible to plot the theoretical terminal velocity for a range of hailstone diameters, as shown in Figure 3-32.

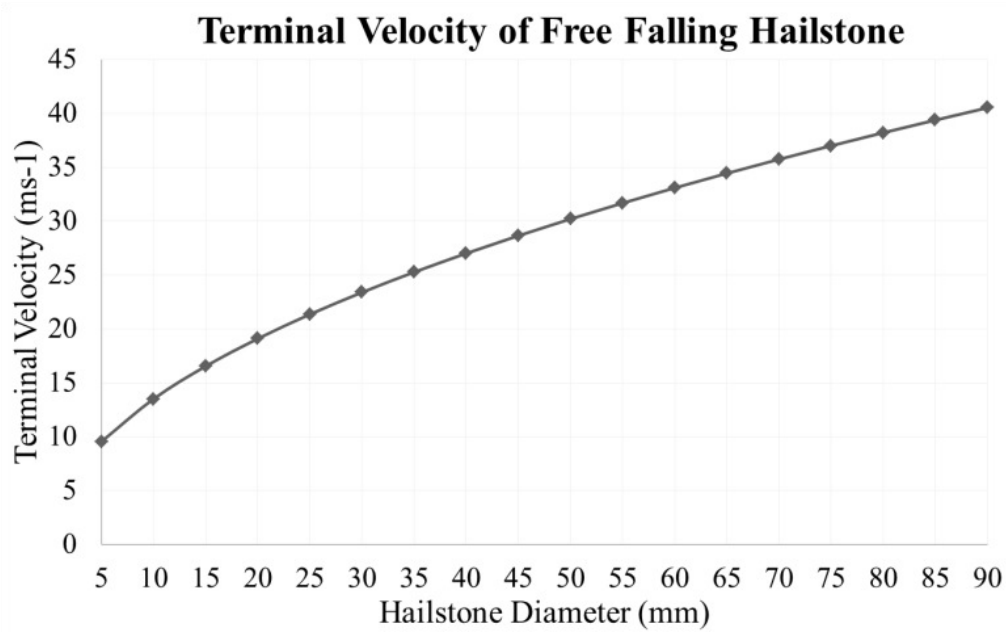

Figure 3-32. Terminal velocity of free falling hailstone of varying diameter, according to Equation 3.10. Assuming: Ice density of 900kgm^{-3}, air density of 1.29kgm^{-3} and a drag coefficient of 0.5.

Figure 3-32 shows the effects of the increased diameter and mass of the hailstones – in comparison to rain – on their theoretical terminal velocity. Adopting the same vector analysis as previously implemented to evaluate the impact velocity of rain drops on a wind turbine blade (Figure 3-16); it is also possible to evaluate the possible maximum hailstone-blade impact velocity. Figure 3-33 shows the maximum calculated impact velocity of both a

15mm and 30mm diameter hailstone, impacting a blade tip with a tip speed of 90m·s^{-1}, in a 20m·s^{-1} wind field. The previous results obtained for rain drops in these conditions are also shown for comparison; as is the constant tip speed for reference.

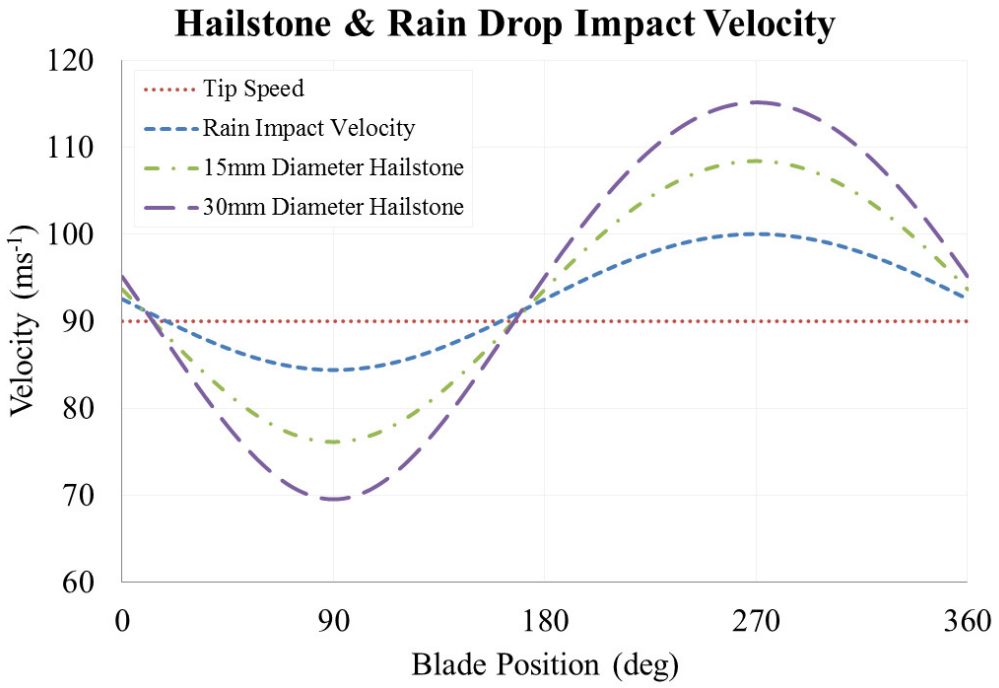

Figure 3-33. Hailstone impact velocity for a 15mm and 30mm diameter hailstone, fully entrained in a 20m·s^{-1} horizontal wind, striking a blade tip with a 90m·s^{-1} tip speed. The tip speed has also been plotted for reference, as has the impact velocity for the rain droplet shown previously in Figure 3-16.

It is clear from Figure 3-33 that as expected, the increased terminal velocity of hailstones (compared to rain droplet) results in higher maximum impact velocities during the upswing phase of blade rotation (180-360˚); and a reduction in the minimum impact speed.

As with rain impact, it is again useful to quantify the potential ranges of impact energies associated with hailstone impact. For example a hailstone ice density of 850kgm^{-3}, it is possible to calculate (using Equation 3.7) the impact energy for a range of diameters, across a range of potential impact velocities, as shown in Figure 3-34. From this, it is apparent just how important the diameter (and therefore the mass) of the hailstone is in determining the potential impact energy that it may impart during impact.

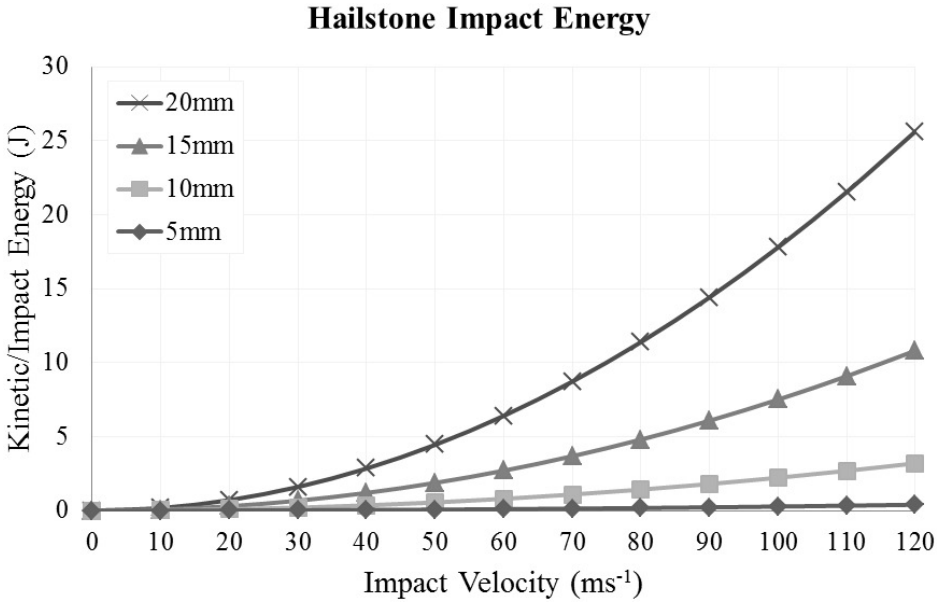

Figure 3-34. Hailstone impact energy for a set of hailstone diameters (5, 10, 15, 20mm) across a range of impact velocities, determined using Equation 3.7.

It is also clear, through comparison to the impact energy values for rain drop impact shown in Figure 3-19, that the potential impact energies associated with hail impact are far greater than that of rain impact.

3.3.4 Experimental Hailstone Impact Evaluation

Given the threats posed by hailstone impact in aerospace applications, there have been extensive efforts from many organisations and research projects [128] [132] with regards to experimentally replicating the phenomenon. Given the difficulties associated with the manufacture and subsequent handling of ice based projectiles, most experimental apparatus are developed for the purpose of investigating single (i.e. low frequency) impact events. This configuration has mostly met the needs of aerospace research, as hailstone and ice impact events occur only in very particular time windows, such as the ascent/descent stage of aircraft, or the lift off process for space rockets. As such, high frequency hailstone/ice impact has been of reduced significance, evident by the lack of development of apparatus in the literature.

Most commonly, such single impact event experimental rigs function through a compressed gas powered cannon mechanism. For instance, Kim et al. [133] [132] utilised the hail impact rig design shown schematically in Figure 3-35, as part of a combined numerical-experimental studies investigating hailstone impact induced damage in composite materials.

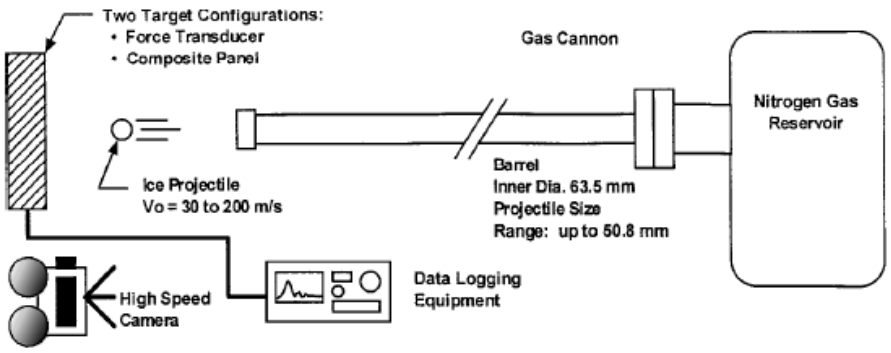

Figure 3-35. Schematic of a hailstone impact rig, as develop by Kim et al. Source: **[133]**

As shown the basic set up consists of a compressed gas reservoir attached to a long barrel, through which the ice projectile is fired, through releasing the gas from the reservoir. The schematic also shows the inclusion of data logging equipment, as well as photographic imaging apparatus. Carney et al. [128] (in a similar study) utilised a similar experimental rig, opting however to create vacuum conditions around the impact event, to produce a more controllable impact event with clearer data output. The work of both studies will be explored in further detail in later sections; however it is clear that historically the most popular approach to experimentally replicating hailstone impact has been through the use of such gas fired cannon systems.

With respect to the experimental investigation of repetitive hailstone impact, there is very little published research or work on such an endeavour. As noted previously, there are obvious challenges with respect to manufacturing, handling and firing bulk quantities of hailstones at a target. A compromise may be to use a substitute projectile with similar impact properties to hailstones, such as small polymer beads or wooden/ceramic balls. Through such an approach a similar impact rig to the swirling arm apparatus used in rain erosion studies (discussed previously) could be set up with a hopper feed configuration for the substitute projectiles. However as stated, there is little published research in this field and substantial work would be required to explore such an option.

3.4 Other Environmental Influences

Although the focus of the research presented here focusses primarily on the mechanisms of damage induced through rain and hailstone impact on the leading edge of the blade, there are of course numerous other types of environmental variables to which a blade will typically be exposed to during its operational lifetime. Although some of these variables may pose a limited threat in isolation with respect to damaging the blade leading edge, their influence may enhance or accelerate the potential damage caused by other factors such a rain and

hailstone impact. Some of the other key environmental variables are discussed in the following sections and their threat to the leading edge summarised.

3.4.1 Ultraviolet light

As shown previously (Figure 3-3 and Figure 3-7), the effects of UV exposure can act to dramatically alter and degrade the erosion performance of blade coating materials. The importance of including such UV exposure effects in the development of industrial testing standards have been noted and reasoned previously. With respect to the long term performance of coating materials, out with the direct impact mechanisms, UV exposure poses the biggest ongoing threat to the material integrity of the blade surface. However, as the aim of this research is to establish the base damage mechanisms associated with rain droplet and hailstone impact, the effects and finer details of UV exposure have not been more fully explored.

3.4.2 Sea spray

For offshore wind turbines the issue of impact on the blade from spray whipped up from the sea surface may present a threat to the leading edge of the blades. The nature of sea spray impact on the blade will most likely be very similar to that of rain with respect to the forces and pressures exerted and the development of individual impact events. However in some situations, larger volumes of sea spray water may impact the blade instantaneously. Another consideration with regards to particulate impact on the blade, when considering sea spray, relates to the transport of sea salt crystals in the sea spray. Airborne sea salt crystals can be an issue in many offshore applications, leading primarily to accumulation on components, which is cited as an issue from many sources [134] [135] [136]. Therefore, salt crystals – through accumulation on the blade leading edge – may lead to degradation in the aerodynamic performance of the blade; rather than any erosive effect and possibly lead to corrosive damage also. However, to date, there has been little research on this topic. Additionally, with sea water containing 3-3.5% NaCl typically [137], corrosion may be a significant issue for any metallic constituents.

3.4.3 Sand, dust and other particulate matter

In warm and arid climates, sand and dust may be a common type of airborne particulate and therefore may pose leading edge erosion problems, whereas in wetter, greener habitats the problem may be non-existent. Likewise, at near shore locations, the issue of sand erosion may be a considerable threat.

Finite element modelling techniques can be employed to better understand the nature and potential effects of sand and dust impingement on a blade leading edge. Numerous studies have looked at modelling solid particulate impact and erosion on solid target bodies across a variety of research fields and using both commercial and purpose made models [138] [139] [140] [141] [142]. As with rain and hail modelling, these approaches could be utilised as both a design and evaluation tool for the blade leading edge.

Experimental approaches to evaluating the effect of sand erosion can also be adopted through use of simple sand blasting techniques. However as with rain erosion testing, this approach will only act to inform on the potential resulting damage modes and the erosive resistance of certain materials, but will reveal little about individual impact development; this may be explained by the numerical approaches discussed.

3.5 Impact Performance of Polymer Matrix Composites

Damage through erosion and surface degradation is not the sole possible form of leading edge damage on wind turbine blades. Given sufficient impact energy and material conditions, damage to the composite substrate may also be possible; certainly so if the coating technologies are partially or wholly eroded. Given sufficient impact energy, composite materials can exhibit damage in a number of ways, some of the most common being:

1. Fibre-Matrix debonding
2. Matrix material cracking
3. Fibre breakage
4. Delaminations

Prayogo et al. [143] investigated the fatigue damage effects of repeated raindrop collisions on CSM glass fibre reinforced epoxy composite laminates. Using 4mm diameter nylon beads to represent raindrops, the samples were subjected to repeated impact and systematically inspected for signs of damage. Through this approach it was possible to establish the number of impact events required for the onset of material damage in the composite laminates, as shown in Figure 3-36.

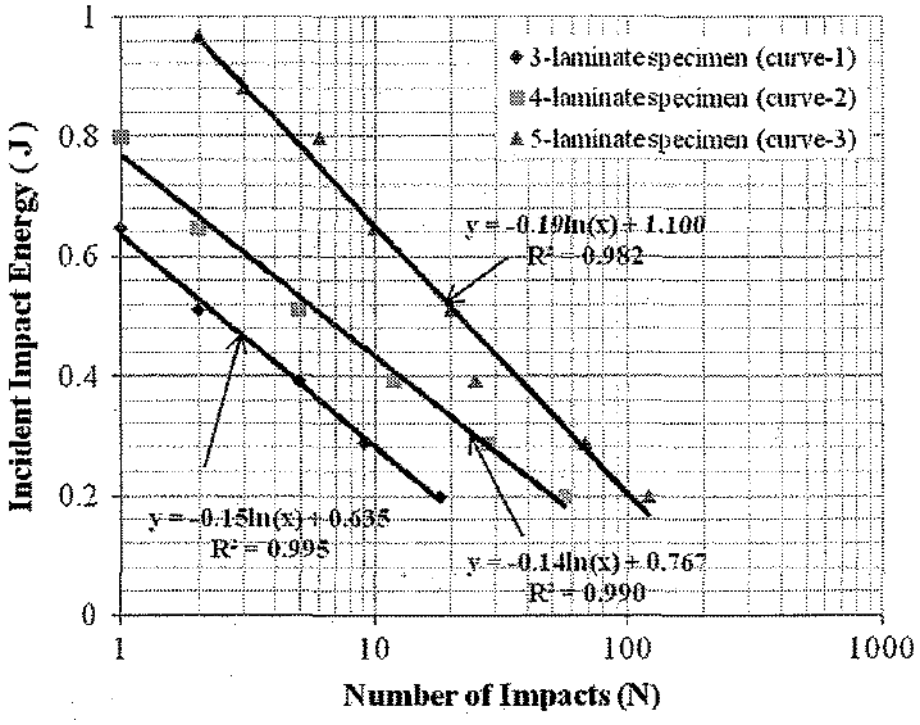

Figure 3-36. Impact fatigue damage in chopped strand mat glass fibre/epoxy composite laminates of varying ply numbers. Showing the number of impact events at specified impact energies required for the onset of material damage. Source: **[143]**

The work states that for each sample, internal damage was the first to take place in the form of interface debonding between the polymer matrix material and reinforcing fibre. The damage then progressed to the surfaces in the form of star cracking on the rear of the samples and ring cracking on the front face of the samples, leading eventually to delamination of the plies. Debonding between the fibre and matrix is attributed to tensile stress waves during impact and microvoid nucleation, growth and coalescence is attributed to the occurrence of delamination; in which shear stress is deemed to play a significant role [143]. It is prudent to note that the impact energies considered in Figure 3-36 are well within the range of the hailstone impact energies detailed in Figure 3-34 and although the samples considered by Prayogo et al. [143] were unprotected bare laminates of CSM - which are typically weaker than that of unidirectional or weaved reinforced composites - it highlights the threat posed by such impact energies.

The damage mechanisms described are not mutually exclusive and are only a few of the possible types of damage. It may be the case that a combination of many failure mechanisms may manifest as a result of either single or repetitive hailstone impact. Damage induced through impact has been shown to reduce both the static compressive [144] and tensile [145] strength of composite materials. However, impact damage may not only affect the static structural properties of the composite substrate, but may also greatly degrade the load bearing fatigue properties of the material. Many studies have shown that transverse impact can markedly reduce the fatigue life properties of glass fibre reinforced composite materials in a load bearing capacity [145] [146]. Yuanjian & Isaac [145] studied the tension-tension fatigue behaviour of glass fibre reinforced polyester composite laminates after being subjected to low velocity transverse impact at varying levels of energy. The study found that the ply orientations of the laminate strongly influenced the post impact tensile properties. For example, the tensile and fatigue properties of a $[\pm 45^{\circ}]_4$ laminate were seriously impaired at relatively low impact energy levels, whereas for a $[0/90^{\circ}]_{2s}$ laminate, the tensile properties (and consequently the fatigue life) only began to degrade above a critical impact energy. Figure 3-37 shows the post-impact fatigue life of the $[\pm 45^{\circ}]_4$ laminate samples, for varying levels of impact energy. It shows that for impact energies of 1.4J, very little effect on the fatigue properties were observed (compared to 0J). However at higher impact energies the effects on the fatigue performance are substantial.

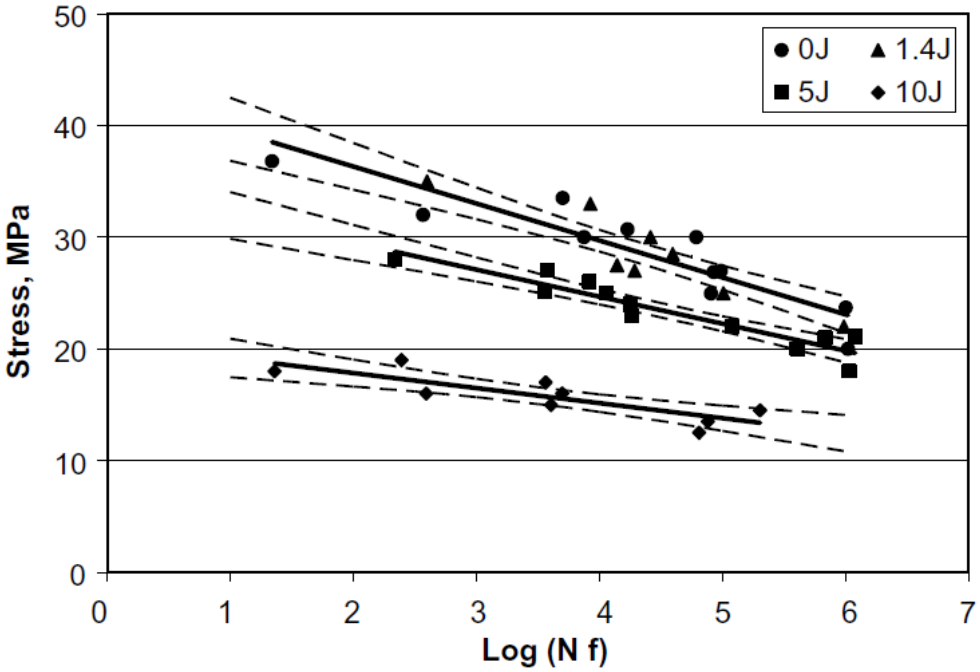

Figure 3-37. S-N fatigue data for a glass fibre reinforced polyester laminate of $[\pm 45^{\circ}]_4$ configuration, following impact at 0, 1.4, 5 & 10J. Source: [69]

It is important to note that the impact energies considered by Yuanjian & Isaac [145] are not out-with the proposed range of potential impact energies imparted by hailstone impact, as shown in Figure 3-34. Such reductions in the fatigue strength of wind turbine blade composites would prove very damaging to the material and lifetime performance of the blade; made worse by the very fact that blades undergo almost constant cyclic loading.

3.6 Summary of Threat

It is clear from reviewing the documented cases of leading edge erosion, the damage created through rain erosion testing and the impact energies imparted by rain and hailstone impact, that rain droplet and hailstone exposure may pose a significant threat to the material integrity of a given wind turbine blade leading edge.

The erosion damage created through rain exposure, as shown in Figure 3-2, Figure 3-3 and Figure 3-5, highlight the potential surface wearing effects of rain impact on the leading edge. These images also make clear the importance of utilising effective and robust surface coating technologies as a means of protecting the leading edge. Although the impact energies associated with rain droplet impact may not pose a significant risk with regards to immediate or short term sub-surface damage such as delaminations or composite failure (matrix cracking, fibre breakage etc.), the mid-to-long term surface damaging effects such as erosion or material plasticity may be significant.

The increased potential violence of hailstone impact presents numerous challenges with respect to maintaining the material integrity of the blade leading edge. As with rain impact, hailstone impact may pose an erosive risk to the leading edge by both wearing down and breaking down the surface coating materials. Additionally, it would seem that as a result of the impact energies associated with hailstone impact, significant sub-surface damage may also be induced through hailstone impact. This may take the form of delaminations, composite damage and resultantly a reduction in both the static and fatigue strength of the material (as shown by Figure 3-36 and Figure 3-37).

The potential damage discussed has been proposed based on the experimental evidence reviewed, documented cases and from considering the impact energies imparted and the likely material response from such impact events. However, in order to get a clearer idea of the characteristics of rain and hailstone impact on the leading edge and the potential damage mechanisms induced, more information is needed. Experimental techniques can provide useful information with regards to the impact resistive properties of a given material/component; however they offer limited insight into the fundamental nature of such impact events and the response of the material. Additionally, such experimental methods can prove both costly and time consuming, limiting the flexibility and creativity of the designer or manufacturer to explore the components impact response or propose new material systems and layup designs. It was from this understanding the proposition to conduct numerical modelling of such impact events was devised. It was intended that numerical modelling/simulation would deliver additional insight, and in turn provide a quicker, inexpensive and flexible means by which to understand the impact response of blade components.

4. Rain Droplet and Hailstone Impact Numerical Modelling Techniques

Numerically modelling rain droplet and hailstone impact on the leading edge of a wind turbine blade presents numerous challenges. Both rain droplets and hailstones are not classical or typical engineering components and neither have straightforward or easily characterisable material properties. Upon impact, both types of projectile are susceptible to rapid and large geometric deformation and material failures; as well as internal shock effects. Additionally, the blade component target is made entirely of neat polymer resins and polymer composite technologies, which also present numerous modelling challenges. Polymer resin materials can be difficult to classify with classic engineering material properties and can exhibit unique post-yield behaviour. The anisotropic material characteristics of composite materials are also a challenge to accurately represent and are an area of on-going and developing research in engineering, as is the interlaminar behaviour between composite plies.

The aim is to resolve and overcome these impact modelling challenges, through reviewing and discussing a selection of proposed methods in the literature; before they are tested and assessed later.

4.1 Modelling Approaches & Software

Numerical modelling of impact events can be carried out in many ways depending on requirements, for simple rigid body impact it may be possible to develop semi-analytical codes to determine impact forces and stresses created, similarly to the work of that of Heymann [98]. However, with increasing impact condition and material complexity such custom made numerical approaches become more impractical and more arduous to develop effectively. In such cases, it may then be more productive to employ commercially available finite element modelling software. These software packages boast the advantages of having been built upon years (or in some cases decades) of continuous work, research and development. As such, they already possess proven tools and solutions with regards to modelling complex impact scenarios.

Therefore, it was decided that the modelling would be undertaken using commercially available finite element software, ANSYS [147], which features numerous modelling tools. As the impact events considered were designated high velocity, transient and non-linear, an explicit dynamics approach, utilising explicit time integration, would be employed.

The version of ANSYS available (13), offers three solver environments capable of carrying out such explicit dynamic analyses:

1. **Explicit Dynamics STR(uctural)** [148] – This approach uses the ANSYS Autodyn solver, but using a fully embedded approach whereby the solver is fully integrated into the ANSYS Workbench Environment [149]. The Workbench Environment offers a wide range of pre and post processing tools, as well as the ability to integrate the model inputs and output into other analyses.
2. **ANSYS Autodyn** [150] – As well as utilising the Autodyn solver as an embedded tool in the workbench environment, the separate Autodyn solver and its pre/post-processing suite could also be utilised.
3. **ANSYS LS-DYNA** [151] – The ANSYS software suite also features the LS-DYNA solver [152], which can either be utilise as an integrated component within the Workbench Environment or on a standalone solver basis. If utilised as a standalone solver, the pre and post processing software tool, LS-PrePost [153] can be utilised for model creation and result analysis.

The tools discussed were all identified as potentially suitable for modelling the impact events concerned. However, in order to select the most appropriate tool and moreover to implement them as effectively as possible, a thorough literature review of previous modelling studies, which utilise these tools, was required.

4.1.1 Computer System Used

For all modelling discussed, a Dell Precision M4600 laptop with an Intel Core i7-2720QM CPU @ 2.20GHz and 12GB of installed RAM was used for all processes in the setup, running and post-processing.

4.1.2 LS-DYNA Terminology

For the purpose of clarity throughout the discussion to follow, it is useful to clarify some of the terminology used to describe the setup of LS-DYNA models and the way in which models are created. LS-DYNA input files take the form of a 'keyword' file which comprises of a range of various input 'cards', which each individually described/define a particular characteristic of the model created. For instance, one important card class is the '*CONTROL' card, which can be used to control certain model parameters throughout simulations such as the timestep used (*CONTROL_TIMESTEP) or the contact modelling (*CONTROL_CONTACT). However, there are numerous classes of cards available for LS-DYNA keywords, which can describe the model make up in relation to inputs such as

materials, element types, contact, damping and so on. Therefore, where and asterisk is placed in front of a word when describing the model setup, this is an indication that and input card is being referred to.

The LS-PrePost software used to created LS-DYNA models (and post-process results) is merely a graphical user interface based keyword compiler, used to create a keyword comprising of all the necessary input cards.

4.1.3 Explicit Dynamics

The LS-DYNA explicit dynamics approach is similar in many ways to classical implicit finite element approaches, whereby the structural bodies concerned are discretised into elements, collectively representing the whole body. However, the approach utilises an explicit (rather than iterative) method to solve the standard equations of motion (Equation 4.1).

$$ma^n + cv^n + kd^n = f^n \tag{4.1}$$

Where n is the given time step, and the premise of the solving process is to determine the displacement d^{n+1}, at time t^{n+1} [154]. Jensen [154] describes that conceptually the difference between Explicit and Implicit dynamic solutions can be written as:

$$\text{Explicit: } d^{n+1} = f(d^n, v^n, a^n, d^{n-1}, v^{n-1}, \dots) \tag{4.2}$$

where all these terms are known at this time state ‘n’ and therefore can be solved directly. Whereas, for an implicit approach the solution depends on unknown nodal velocities and accelerations at state ‘n+1’:

$$\text{Implicit: } d^{n+1} = f(v^{n+1}, a^{n+1}, d^n, v^2, \dots) \tag{4.3}$$

Jensen [154] also summarises the explicit dynamics solution process with the flow chart shown in Figure 4-1.

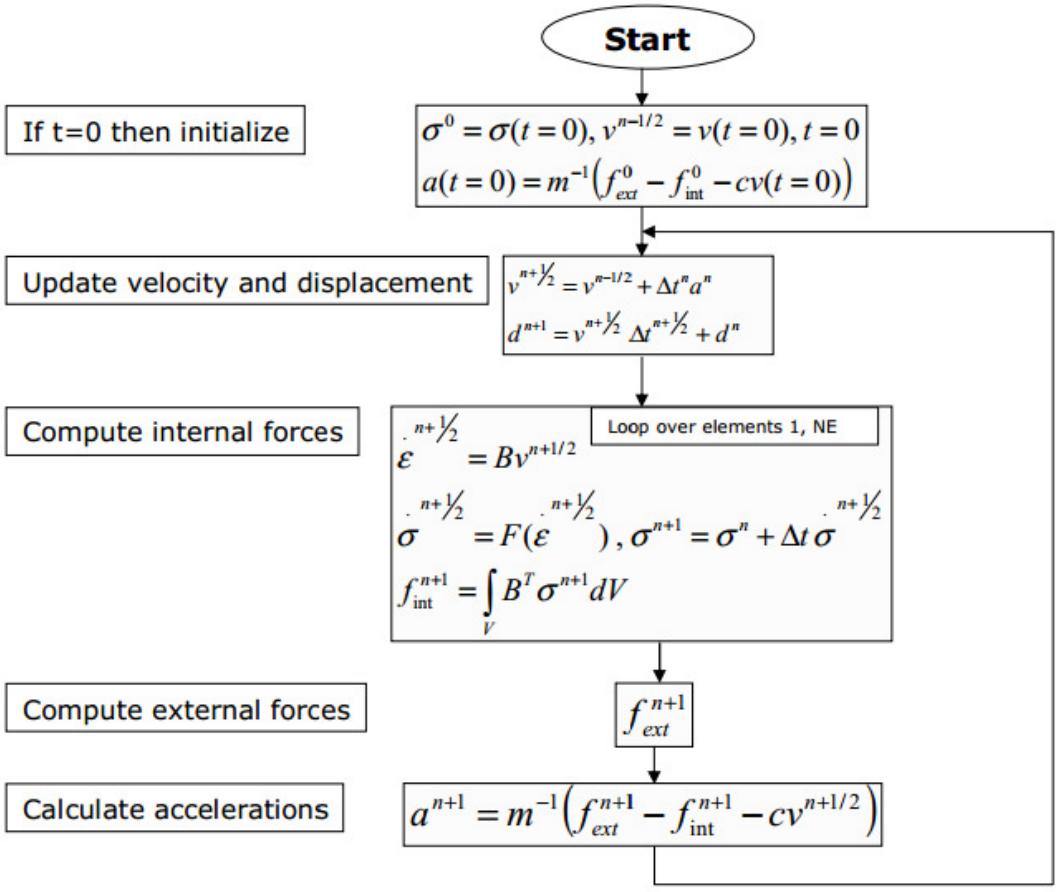

Figure 4-1. LS-DYNA Explicit solution procedure flow chart. Source: **[154]**

As shown, the velocities and displacements are calculated for n+1, based on these values the internal and external forces can then be calculated, subsequently the accelerations can then be determined. These acceleration values can then be fed back into the equations for the next time step; therefore initiating the next series of calculations.

This flow chart represents the basic work flow of an explicit dynamic simulation within LS-DYNA; however additions and alterations to this process may also be incorporated for different simulation types. Additionally, the method by which a simulation body (projectile, target, structure etc.) is discretised and represented can also vary, as discussed in the following sections.

4.1.4 Classical Lagrangian Finite Element Method

The classical approach to discretising bodies of interest in finite element analyses is to represent the body with a number of smaller elements, defined by a number of nodes. The interactions and relations defined between these adjoining nodes (and elements) are what constitute the material behaviour of the structure as a whole.

Elements can take many shapes and forms and can be represented by varying numbers of nodes. The two most common forms of elements utilised are hexahedral and tetrahedral (Figure 4-2); for three dimensional simulations.

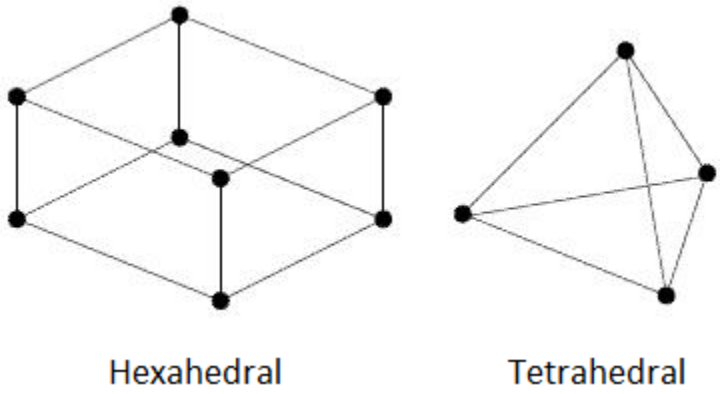

Figure 4-2. Common element types in LS-DYNA, Hexahedral and Tetrahedral. Source: **[155]**

This form of geometry discretisation is well practised and thoroughly establish in both implicit and explicit simulation work. However, where a body is likely to experience extreme levels of deformation during a simulation, the effectiveness and efficiency of this approach can be limited; as a result of element skewing and shape deterioration. High levels of deformation can consequently results in the skewing and stretching of typical hexahedral and tetrahedral elements. Such skewing can drastically reduce the accuracy of the modelling and additionally significantly increase the required computational power and time [156]. In light of these drawbacks and limitations, alternative methods of discretising and representing high deformation bodies in simulations have been developed.

4.1.5 Eulerian

Eulerian modelling approaches originate from computational fluid dynamic methods of modelling multiphase and liquid-solid interactions; however it has also seen increasing use in structural impact simulations; through coupling it with classical finite element methods. Unlike classic Lagrangian meshing methods whereby a mesh is attributed to the geometry of a body, an Eulerian meshing approach applies a mesh to a specified domain; within which the body of interest will be present (either stationary or moving). The body within the domain is therefore not represented by a fixed mesh applied to its geometry, rather the body adopts the nodes within the domain as it moves or deforms within it. This means that when the body moves and deforms, the mesh which represents the geometry can be altered either by changing to different nodes or altering the shape of the domain mesh. Different approaches to the method can make use of either or both of these techniques, however the

resulting benefit is that the mesh representing the body does not undergo excessive stretching or skewing; therefore avoiding the drawback associated with these effects.

The Eulerian method will be discussed further when describing the application of the method to model rain droplet impact.

4.1.6 Smooth Particle Hydrodynamics

The SPH method is a meshless approach to representing bodies in finite element analyses. The technique was originally developed for the purpose of modelling impact events in astrophysical studies [157] and has seen extensive use in fluid flow problems. However, the method is also gaining recognition with respect to its application to solid body impact mechanics [158].

The central difference between SPH methods and classical approaches is the absence of any grid or mesh. Instead the body of interest in represented by a collection of nodes (or particles) through which the governing equations are resolved [159]. As these particles form the basis of the computational framework a new approach to modelling calculation methods are required and implemented, as detailed at length by Hallquist [159] and Lacome [157]. Each particle is assigned part of the mass of the whole body and represents an interpolation point for the material properties and characteristic during modelling. The particles are not directly connected; rather they are the basis of an interpolatory scheme which uses a kernel function to determine the material behaviour [156].

The implementation and practise of utilising an SPH method are discussed in later sections in relation to the impact modelling work of this research.

4.2 Modelling Rain Droplet Impact

Exposure of components to high velocity water droplet impact has been a historical and on-going concern in aviation applications and studies. This has led to the establishment of rain erosion testing facilities, such as the Rain Erosion Test Facility previously discussed and illustrated in Figure 3-24, in order to evaluate the damage risk posed by rain impact on exposed components and the respective components resistance to such erosion. However, with the increased availability and continuing advances in computational technology, techniques to model the impact of water projectiles began development in such industries. As such, the techniques developed and established can be reviewed and assessed in order to select or develop an appropriate water droplet impact modelling method within the context of impact on the leading edge of a wind turbine blade.

It is important to first review the developments and established methods with regards to modelling liquid impingement on solid surfaces, and reviews their strengths, weaknesses and applicability to the context of the current work. Subsequently, the most suitable approaches are then selected and their applicability detailed.

4.2.1 Previous Work in Literature

Previous research has been conducted with respect to investigating the nature of liquid impact on rigid surfaces through use of computational fluid dynamics (CFD) techniques [102] [160]; using Eulerian methods as previously described. These approaches can reveal the compressible response of the droplet during impact and the forces and pressure exerted on the target surface.

Li et al. [102] utilised a two phase Eulerian-Eulerian approach to model a two dimensional high velocity single water droplet impact on a rigid surface. Figure 4-3 shows the impact progression of a 4mm diameter droplet impacting a rigid target at $500 m \cdot s^{-1}$, showing contours of pressure to illustrate the compressible response within the droplet.

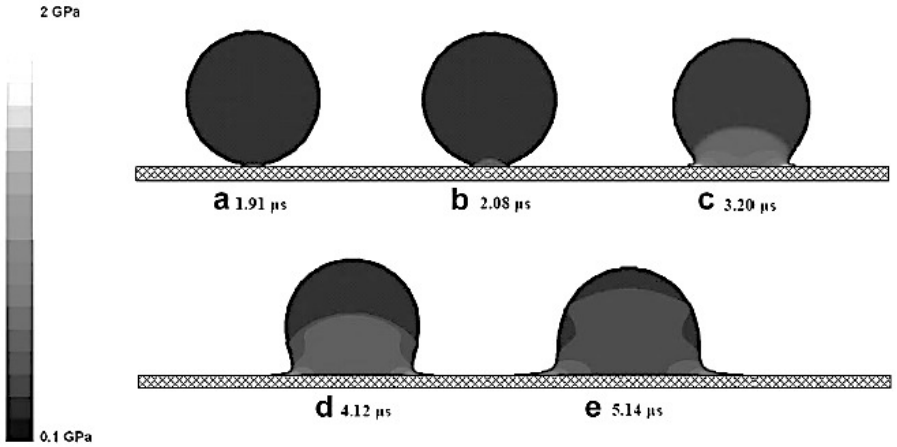

Figure 4-3. 2D Impact of a 4mm diameter water droplet at $500 m \cdot s^{-1}$ on a rigid surface, showing contours of pressure during impact. Source: **[102]**

As shown, the modelling accurately predicts the shockwave response of the droplet during impact, capturing the initial pressure shockwave and the subsequent lateral jetting upon the shockwave reaching the contact area periphery. Li et al. [102] then show that the pressure exerted in the modelling compare well to an analytical expression given by Heymann [98], which is a 2D approximation of the waterhammer equation (Equation 3.4). Although the approach agrees well with 2D analytical expression, Li et al. [102] recognise that liquid impact is inherently a three dimensional issue and as such any numerical approach should aim to adopt a three dimensional approach.

As stated, computational fluid dynamic approaches can provide useful insight into the impact response of the droplet, however in order to predict the impact response of the target, such approaches need to be coupled with a finite element modelling method.

Alternatively, a method which utilises a finite element method to model both the target geometry and the water droplet may be employed. Adler [161] conducted some of the earliest work concerned with the three dimensional modelling of rain droplet impact on a solid target, utilising a wholly finite element modelling approach. Utilising the DYNA3D solver [162] (the predecessor to LS-DYNA) Adler modelled both the water droplet and the target geometries with finite elements to model impact contact between them. The study details a number of preliminary uses of the approach and the results it can provide, such as that shown in Figure 4-4, which shows the pressure distribution in a 2mm diameter water droplet impacting a zinc sulphide target at 305ms^{-s}.

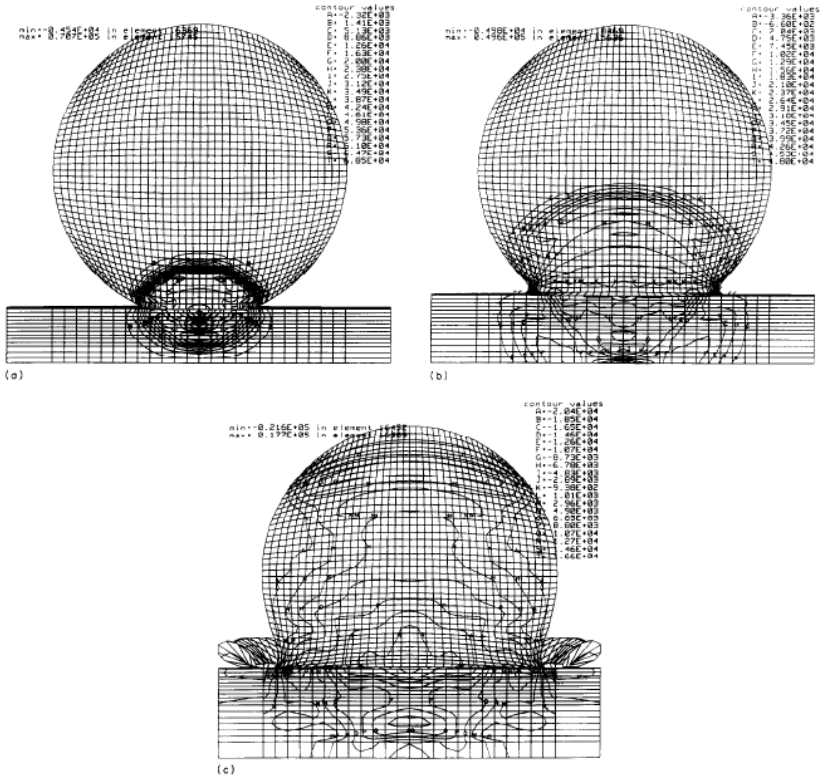

Figure 4-4. 2mm diameter water droplet striking zinc sulphide target at 305ms[1], time: (a) 0.2µs, (b) 0.5µs, (c) 1.1µs. Source: **[161]**

As shown, the modelling approach captures the shockwave propagation behaviour through the water droplet and target geometry, as well as the droplet spreading and lateral jetting phenomena. However, it is also possible to observe the significant deformation and stretching of the finite elements of the droplet geometry in the areas of lateral jetting.

Although Adler [161] states that the simulations remain stable until this point, further spreading may result in instability, a loss of accuracy and an increase in computational time.

However the benefit of such a finite element approach is that the stress evolution in the targeted solid can also be determined, as shown by Adler [161] in a plot of tensile radial stress in the zinc sulphide material during impact, as shown in Figure 4-5.

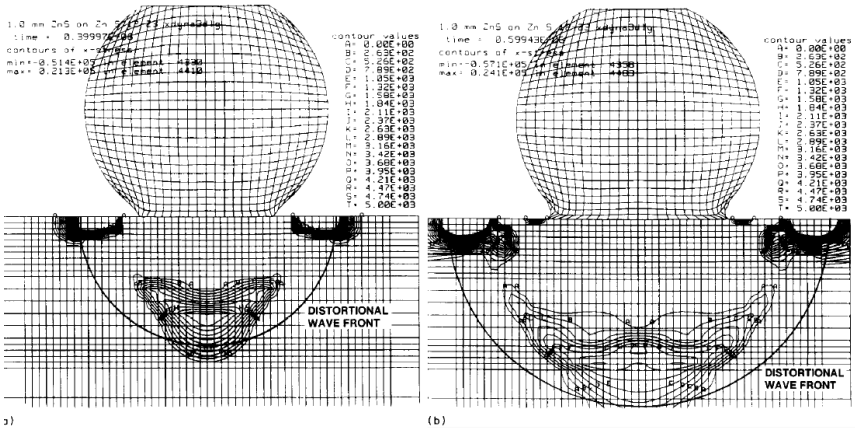

Figure 4-5. Tensile radial stress in zinc sulphide when impacted by 2mm diameter water drop at 305m·s^{-1}, (a) 0.4µs, (b) 0.6µs. Source: **[161]**

The plot shows the propagation of stress downwards through the target material as a wave front as well as lateral stress wave near the surface, which agrees well with the theoretical impact behaviour as described by Gohardani [79] and shown previously in Figure 3-17. Additionally, the formation of high stress at the contact periphery is observable in Figure 4-5(b), again a phenomenon commonly associated with water droplet impact [98].

Adler [161] described the usefulness the modelling approach with regards to obtaining information on the impact response and robustness of the target material without the need for extensive testing; given the condition that the computational costs (presently much reduced in comparison to the time of publication) are suitably low.

As stated, a classical Lagrangian based finite element approach offers good insight into the impact response of the target material but may encounter issues with regards to the large deformation of the water droplet. As such (and as previously alluded to), a combined Eulerian-Lagrangian approach may offer an approach to capture the detailed response of both the water droplet and the target body; whereby the droplet is modelled with an Eulerian mesh approach and the target with a Lagrangian approach.

Salman and Yıldırım [163] implemented an Arbitrary Eulerian Lagrangian (ALE) method to model the impact of water jets on silica float glass plates (modelled with a Lagrangian

approach) using LS-DYNA software. The approach models the behaviour of water using the material model *MAT_NULL and equation of state *EOS_GRUNEISEN. Figure 4-6 shows the impact of a 2mm diameter water jet impacting the target at 150m·s^{-1}, showing signs of damage in the 1mm thickness plate.

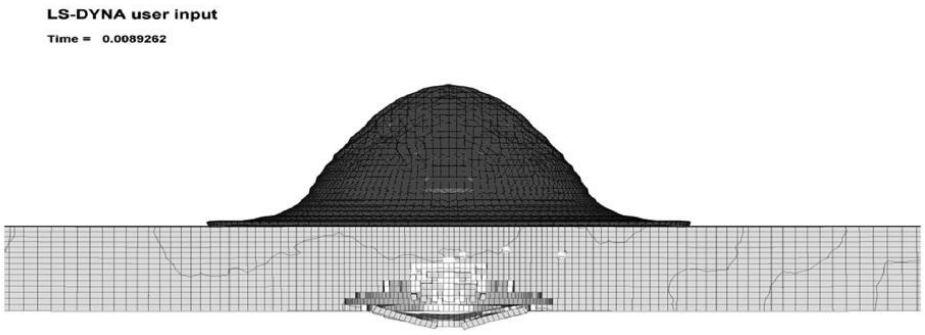

Figure 4-6. 2mm diameter water jet impact at 150m·s^{-1} on a 2mm silica float glass plate target. Water jet modelled with Arbitrary Eulerian Lagrangian technique. Source: **[163]**

As shown, the ALE method captures the fluid nature and spreading behaviour of the impacting water geometry and effectively couples the interaction between the water and the target material. The study compares the numerically determined pressure exerted during the water jet impact simulation to the values predicted by the waterhammer Equation 3.4. He finds that although the initial peak in impact pressures for impact velocities of 250 & 150m·s^{-1} are both approximately 1.6 the magnitude of the waterhammer value, the values of pressure quickly reduce and remain at the waterhammer value for a duration longer than that of the peak value.

The work detailed by Salman and Yıldırım [163] uses a similar approach to that implemented by the author in previous work [59], whereby an Eulerian approach was utilised to model water droplet impact on a polymer target.

An alternative to employing an Eulerian approach for the water geometry may be to employ a smooth particle hydrodynamics approach. There has been extensive use of SPH methods in the literature with respect to modelling the landing and crash dynamics of structures into bodies of water [164] [165] [166]. Many of these studies (using LS-DYNA) compare the use of SPH meshless methods to that of Eulerian method, validating the results against experimental results, mostly finding that the results are comparable and that the suitability of the approaches depends upon their specific application. SPH approaches are commonly less computationally expensive to implement than Eulerian methods, however there is limited

published research on the use of SPH methods with respect to the modelling of rain droplet impact on solid target surfaces.

4.2.2 Selection of Modelling Approaches

From reviewing the previous water droplet/jet impact modelling techniques, there are a number of potential approaches to modelling such phenomena. However, through assessing techniques discussed, the apparent advantages of both the Eulerian and Smooth Particle Hydrodynamic approaches have been made clear. Both approaches can model the large deformations associated with the droplet geometry during impact, due to the unique meshing methodologies. Implementing these methodologies within a finite element analysis allows for the transfer of the momentum loading of the droplet into the target material, therefore providing information on the impact response of the target material.

For this reason it was decided that, for the purposes of this research, both methodologies would be employed and trialled in order to assess the usefulness and applicability of both approaches for the purposes of modelling impact on the leading edge.

4.3 Modelling Hailstone Impact

4.3.1 Previous Work in Literature

Although little research with respect to hailstone impact on wind turbine components has been published (other than the authors work [60]), the threat posed by ice and hailstone impact on aerospace components has resulted in considerable development and research [156] [167] [128] [133] on the specific issue of modelling ice impact. Additionally, in the context of these applications the target material is often composite materials (similar to that of wind), therefore it is possible to review these studies and draw lessons and insight from them. The following sections review some of the most prominent proposed modelling approaches and models.

4.3.1.1 Study 1 - Kim & Kedward

Kim & Kedward [133] published one of the earliest studies aiming to implement a numerical method to simulated hail ice impacts on a composite structure. The paper features the details of their numerical model and uses experimental results to validate the model outcomes. The modelling work was carried out using the DYNA3D® finite element code which was the precursor to current LS-DYNA® code [162].

The work represents the ice material through use of an in-built DYNA3D material model named 'Mat 13 Elastic-Plastic with Failure' which in LS-DYNA is now named *MAT_ISOTROPIC_ELASTIC_FAILURE or numbered as *MAT_13 [168]. The following material properties (Table 4-1) were assigned for the material model, based on values found in literature and through tuning of the model in light of experimental comparison (as will be discussed):

Table 4-1. *MAT_13 Elastic-Plastic with Failure input values. Source: [16]

Property	Value
Density (kg·m^{-3})	846
Elastic Shear Modulus (GPa)	3.46
Yield Strength (MPa)	10.3
Hardening modulus (GPa)	6.89
Bulk Modulus (GPa)	8.99
Plastic failure strain (%)	0.35
Tensile Failure Pressure (MPa)	-4

This material model was employed as it allowed for hardening plastic behaviour as exhibited in their experimental results through micro-crack evolution just prior to changing to a crushed powder/fluid-like state. The values for shear and bulk modulus were obtained from

literature [169] [170] [171], however the values for hardening modulus, plastic failure strain and failure pressure were parametrically determined through the comparison of numerical and experimental data. The value for density was an average of the directly recorded density from the manufactured hailstones used in testing.

The material model was designed to perform in such a way that when the plastic failure strain value is reached, all shear stress components in the hailstone are relaxed to zero. Additionally, upon reaching the tensile failure pressure value the material is then capable only of carrying hydrostatic load; therefore behaving like a fluid. They acknowledge that the material model is a simplification of real ice, as it does not take into account strain rate strengthening nor the nonlinear pressure-volume characteristics of ice.

In order to validate and tune the numerical model for the hail ice, a regime of hail impact experiments were conducted using a gas powered cannon to fire manufactured hail ice spheres at a semi-rigid force measurement transducer system (FMT) to record the force and duration of different impact scenarios. This semi-rigid behaviour is of importance when trying to replicate the tests numerically, as the target will react with oscillations, therefore the impact forces are not strictly instantaneous. The experiments were carried out using two hail configurations, a monolithic ice sphere and a layered ice sphere construction; in an attempt to replicate the layered characteristics of a hailstone. Figure 4-7 shows a 42.7mm diameter layered hailstone 182µs after impacting the FMT at 73.5m·s^{-1}.

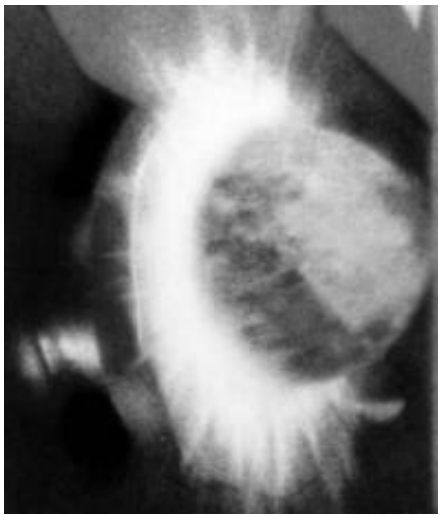

Figure 4-7. 42.7mm diameter layered hailstone at 73.5m·s^{-1} 182µs after impact with FMT. Source: **[133]**

The modelling work utilised a wholly Lagrangian mesh approach for both the hailstone and the target. The impact conditions featured in Figure 4-7 were replicated by the developed model, and the simulated impact event is shown by the deformation plot in Figure 4-8.

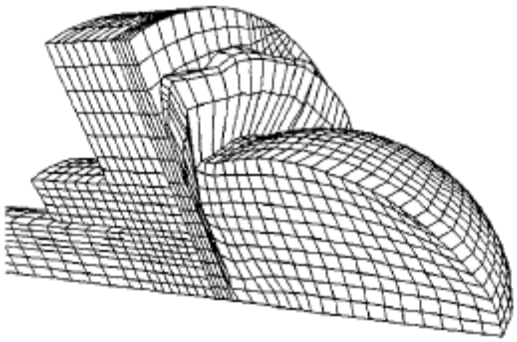

Figure 4-8. 42.7mm diameter hailstone at 73.5m·s^{-1} 182μs after impact with FMT. Source: **[133]**

From Figure 4-8 it can be said that at model is successful in portraying the spatial and temporal aspects of the impact event, capturing the squashing and powdering phenomena of the hailstone contact area. However, it is also possible to observe the stretching of the Lagrangian mesh attributed to the hailstone as a result of its large geometric deformation during impact. This stretching behaviour is undesirable as it both increases computational time and reduces the model accuracy. The experimental and numerical results were compared across a range of impact velocities and the material inputs tuned to create agreement between the two. With the model tuned and the experimental work conducted, the results obtained through both methods are compared in order to validate the numerical work. Figure 4-9 compares the numerical and experimental results for the peak force created against the projectiles kinetic energy.

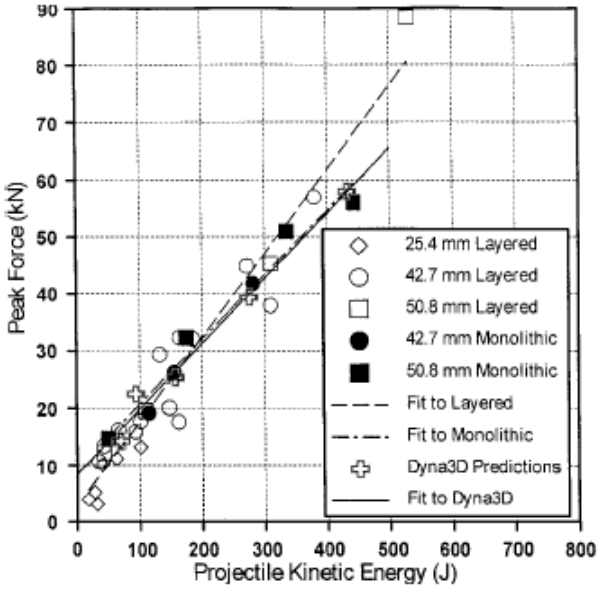

Figure 4-9. Numerical and Experimental Comparison. Source: **[133]**

The reference to monolithic and layered hailstones describes the nature by which the hailstone was manufactured. In an effort to replicate the onion-like layered characteristic of

hailstones, some of the samples were created through creating horizontal layers of ice in the mould (i.e. freezing a layer, then adding an extra layer of water and allowing that to freeze); the monolithic samples were simply create from one fully-filled mould.

For the given test and ice material conditions, it can be said that good agreement was achieved between the numerical and experimental work, however it is prudent to note that a level of material property tuning was required to achieve this. It can also be seen that the results obtained for both the monolithic and layered samples show no apparent signs of difference, perhaps indicating that a layered construction (horizontally in this case) makes little difference to the impact forces imparted

4.3.1.2 Study 2 - Anghileri et al.

Anghileri et al. [156] conducted a study to investigate the merits of three different hail modelling approaches using:

1. A Lagrangian based meshing process, as utilised by Kim & Kedward [133]
2. An Eulerian modelling approach or Arbitrary Eulerian Lagrangian (ALE)
3. A Smooth Particle Hydrodynamics approach (SPH)

The study used the LS-DYNA code and relied heavily on the work of Kim & Kedward [133] in that for both the Lagrangian and Eulerian approaches the same constitutive material model (*MAT_13) and the same material properties (Table 4-1) were implemented. However, as the *MAT_13 material model was not developed for the SPH approach a different material modelling approach was required and was subsequently developed. It instead utilised the material model entitled *MAT_ELASTIC_PLASTIC_HYDRO or *MAT_10 with material property values based on those quoted in Table 4-1 but modified to match experimental result obtained in other studies [172] [173]. The material properties used for *MAT_10 are shown in Table 4-2. *MAT_10 also requires an equation of state (EOS), so a Polynomial EOS for water was used [174].

Table 4-2. *MAT_10 material properties for ice. Source: **[156]**

Property	Value
Density ($kg \cdot m^{-3}$)	846
Elastic Shear Modulus (GPa)	3.46
Yield Strength (MPa)	10.3
Hardening modulus (GPa)	6.89
Tensile Failure Pressure (MPa)	-4

The study utilised the three approaches to simulate experimental work carried out by the British Royal Aircraft Establishment [175], which considered the impact of a 25.4mm

diameter hailstone against a plate of 2014-T4 aluminium alloy, at an initial impact velocity of 192m·s^{-1}. The plate was a square panel with a thickness of 0.91mm and 305mm side-edge, with the edges at the boundaries fixed with rivets so as to create a free square target surface with 200mm side-edge, as shown in Figure 4-10.

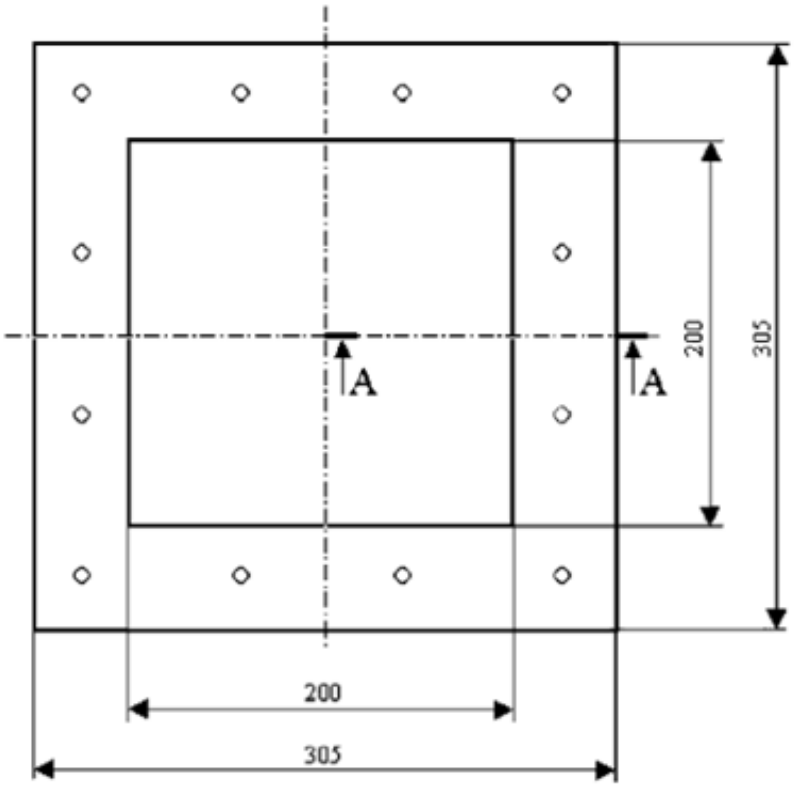

Figure 4-10. Experimental test plate. Source: **[156]**

The plastic strain in the plate was observed after impact along the section plane labelled A-A, shown in Figure 4-10, this was used as the reference with which to compare the numerical results.

Figure 4-11 shows the results of the numerical simulation at 150μs into the impact event and compares the numerically obtained values of maximum deflection in the plate to the experimentally stated values.

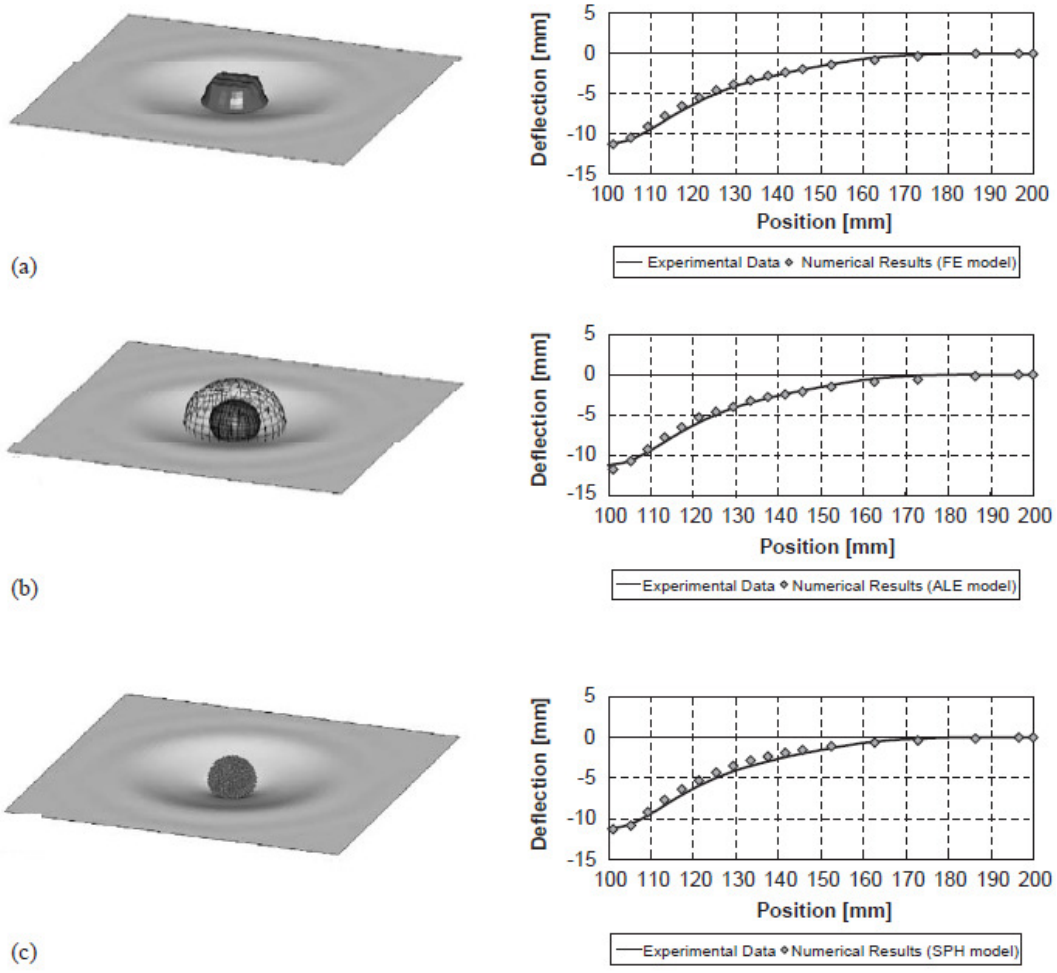

Figure 4-11. Hail impact at t=150μs and numerical-experimental comparison. (a) Lagrangian; (b) ALE; (c) SPH. Source: **[156]**

From the images and plots, it can be seen that agreement between the numerical and experimental approaches was obtained, with respect to the displacement on the plate. However, the paper states that the experimental displacement was taken from the measurement of plastic strain after the impact event but it does not clearly state at which point in the simulation the value of displacement was taken from; e.g. at 150μs into the simulation or after the completion of the impact event. Regardless of this ambiguity, the magnitude of the modelled displacement is clearly comparable to that of the experimental work and the three modelling approaches produce consistent and comparable results. They state that of the three approaches adopted, the SPH method produced the most qualitatively agreeable results with regards to capturing the behaviour of the ice hail material during impact. The SPH also required the least amount of computational time to complete the analysis when compared to the other two methods. The work then goes on to use the three

methods to simulate hail impact on a jet engine intake and again finds the SPH approach to be the most useful and computationally efficient.

The work is useful in the context of exploring the different meshing/modelling approaches available for modelling hailstone impact and in coming to the conclusion that the SPH approach is comparably the best method of hailstone impact modelling. However, with respect to the constitutive material model used for the ice/hail, the approaches adopted still require tuning to match the experimental work and makes the same fundamental assumptions and simplifications as those in the Kim & Kedward work [133]. These assumptions and tuning requirements are practical and acceptable when considering a specific type of impact event where the conditions are known or predictable (such as impact speed/angle and hailstone characteristics). However this approach does not represent a universally applicable modelling approach which truly considers the governing properties and mechanical behaviour of ice.

4.3.1.3 Study 3 - Tippmann

Tippmann [176] presented the latest revision – with previous revisions and alterations proposed by Kuene [177] and Park [178] - of the model presented by Kim & Kedward [133]. In this he discusses the developments and then compares numerical results of impact modelling with a comprehensive series of experimental studies.

The modelling work uses the Abaqus/Explicit finite element solver and improves on the previous work [133] through the addition of strain rate dependant material parameters. The ice is represented in Abaqus as a simple elastic-plastic material with failure criterion based on tensile hydrostatic pressure. The plastic yield stress features the strain rate dependency using dynamic compressive strain data reported in literature. The elastic and mass properties are shown in Table 4-3.

Table 4-3. Elastic and mass properties used by Tippmann. Source: **[176]**

Property	Value
Density ($kg \cdot m^{-3}$)	900
Young's Modulus (GPa)	9.38
Poisson's Ratio	0.33
Tensile Failure Pressure (kPa)	517
Yield Stress (MPa)	5.2
Rate Dependant Yield Stress	Tabular

The value of 900kgm^{-3} for the density was considered representative of the hailstones used in the experimental work. The elastic properties were taken from the values published by

Petrenko and Whitworth [179] and those subsequently used in the previous revisions [177] [178] of the model.

The improvement on the previous Abaqus model [178] is stated as the inclusion of a strain rate dependant yield strength value. In the previous models, the value for yield strength had to be tuned between 17 to 55MPa, depending on the size and velocity of the hailstone considered. The introduction of this strain rate sensitivity feature meant that different regions within the hail stone could possess different values of yield strength based on the local strain rate of the individual elements. The yield stress for the study is based on the compressive strength versus strain relationship. Once the plastic strain increases above the elastic limit, the stress remains constant at the specific yield stress at which it began to yield. The tensile failure pressure shown in Table 4-3 was found through a parametric study.

Figure 4-12 shows previous experimental data cited for the relationship between the compressive yield stress and strain rate for ice.

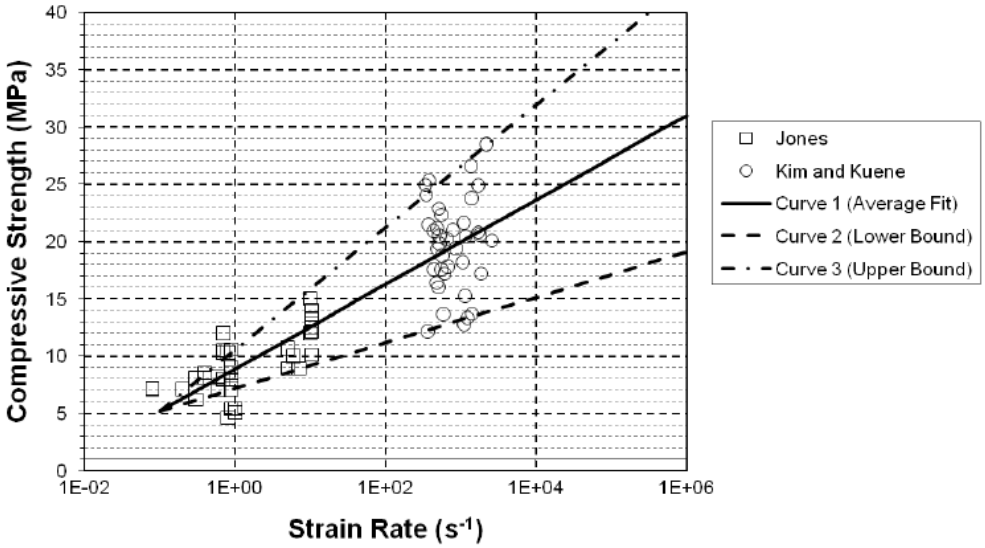

Figure 4-12. Experimental data for Compressive Strength against Strain Rate for ice material. Source: **[176]**

Three trend lines are fitted to the data to bind the upper and lower limits for the compressive strength over the range of strain rates and to also show the average value of compressive strength. Table 4-4 shows the calculated stress ratio required to scale the nominal yield strength (Table 4-3) across the range of strain rates considered, based on the average fitted trend in Figure 4-12.

Table 4-4. Tabular data for Stress Ratio and Strain Rate. Source: **[176]**

Stress Ratio	Strain Rate (s^{-1})
1	0
1.01	0.1
1.495577759	0.5
1.709011483	1
2.204589242	5
2.418022966	10
2.913600725	50
3.127034449	100
3.622612208	500
3.836045932	1000
4.331623691	5000
4.545057415	10000
5.040635174	50000
5.254068897	100000
5.749646657	500000
5.96308038	1000000

The modelling work utilises an all Lagrangian approach to simulate hailstone impact on a flat plate and uses previous experimental work by Kim et al. [132], several other contributors at Purdue University and new additional tests (conducted in a similar manner as per Kim & Kedward [133]) as a basis for numerical-experimental comparison and validation. The wealth of experimental data meant that a wide range of impact energies could be examined through the modelling work to understand the flexibility and performance of the model. Figure 4-13 shows the impact peak force against the kinetic energy of the hailstone for the experimental data, labelled DS1 (Kim et al. [132]) and DS2 (Tippmann [176]), and the Lower, Average and Upper Yield Stress/Strain Rate relationship trends.

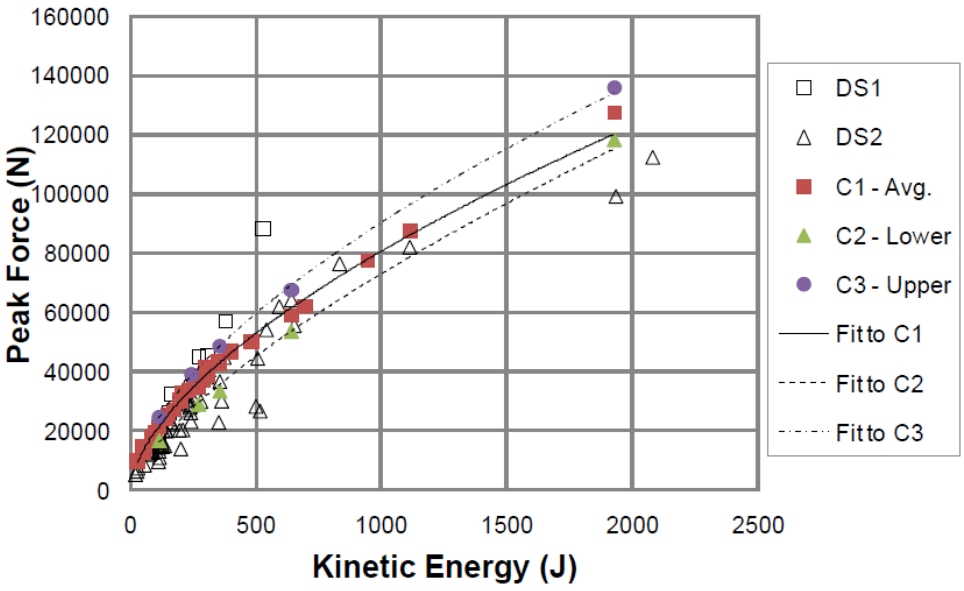

Figure 4-13. Peak Force v Kinetic Energy for numerical and experimental work. Source: **[176]**

It can be seen that good agreement has been achieved between the numerical and experimental work with regards to the quantitative value for peak force across a wide range of impact energies. Figure 4-14 gives a more detailed view of the values and trends at impact energies lower than 400J.

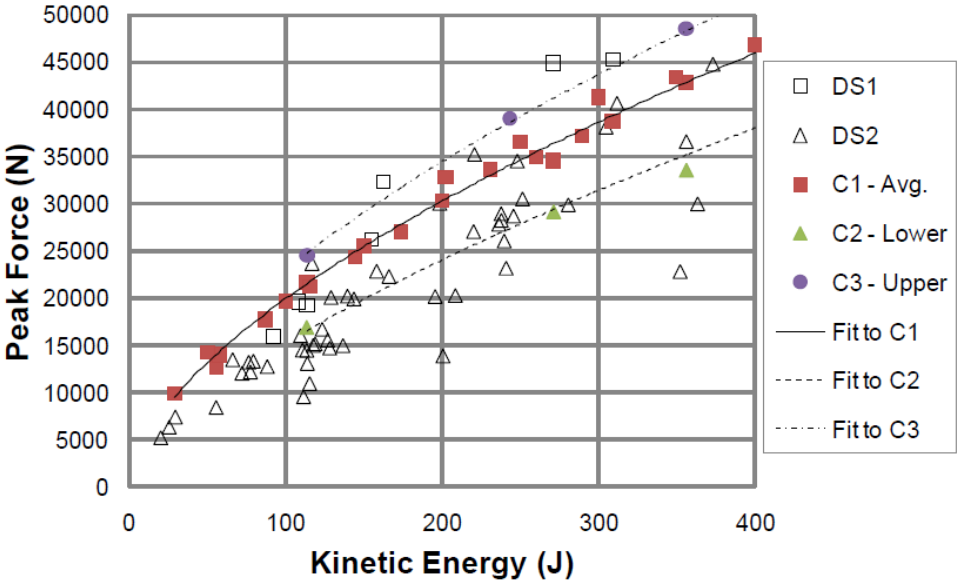

Figure 4-14. Peak Force v Kinetic Energy for numerical and experimental work below 400J, source: **[176]**

Zooming in on this region show the values for the experimental work more clearly and although there is a degree of scatter in the experimental data, it can be said that overall through the lower to upper bound trends that numerical-experimental quantitative agreement was achieved.

Through high speed photographic imaging, it was possible for the study to examine the qualitative aspect of the experimental impact events. Figure 4-15 shows the impact progression of a 50.8mm diameter manufactured hailstone impacting the target at 60.6m·s^{-1} (114J) it also displays the associated impact force time history with the markers relating to the image times.

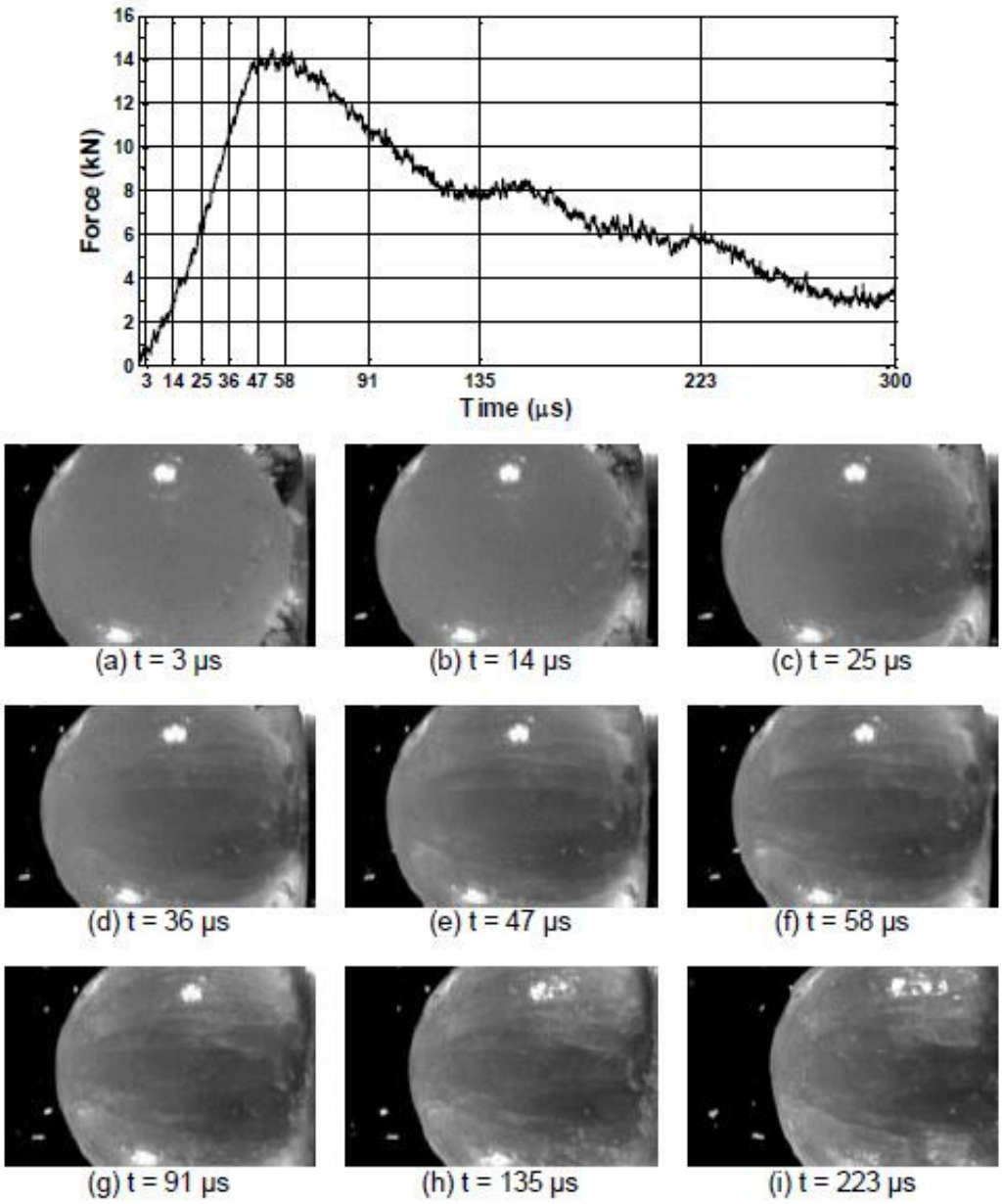

Figure 4-15. 50.8mm diameter manufactured hailstone with impact velocity of 60.6m·s^{-1} (114J). Source: **[176]**

In this, he discusses how upon the onset of impact longitudinal cracks develop in the ice, starting near the impact contact area and spreading back through the ice, terminating just before the rear surface. Additional intermediate cracks then form in between the initial cracks, after which the hailstone begins to lose its spherical shape. After 58µs the value of impact force begins to decrease, corresponding to the onset of transverse cracking and thus the transformation from a single homogenous projectile to a fragmented collection of ice sections. This region therefore marks the transition from an elastic-structural impact interaction to a simpler momentum impingement on the target from the fragmented ice.

Figure 4-16 shows the simulation of the same impact conditions as displayed in Figure 4-15 and displays the deformation of a cylindrically patterned view of a quarter-symmetric simulation. The associated force history is also shown, again with markers corresponding to the imaged.

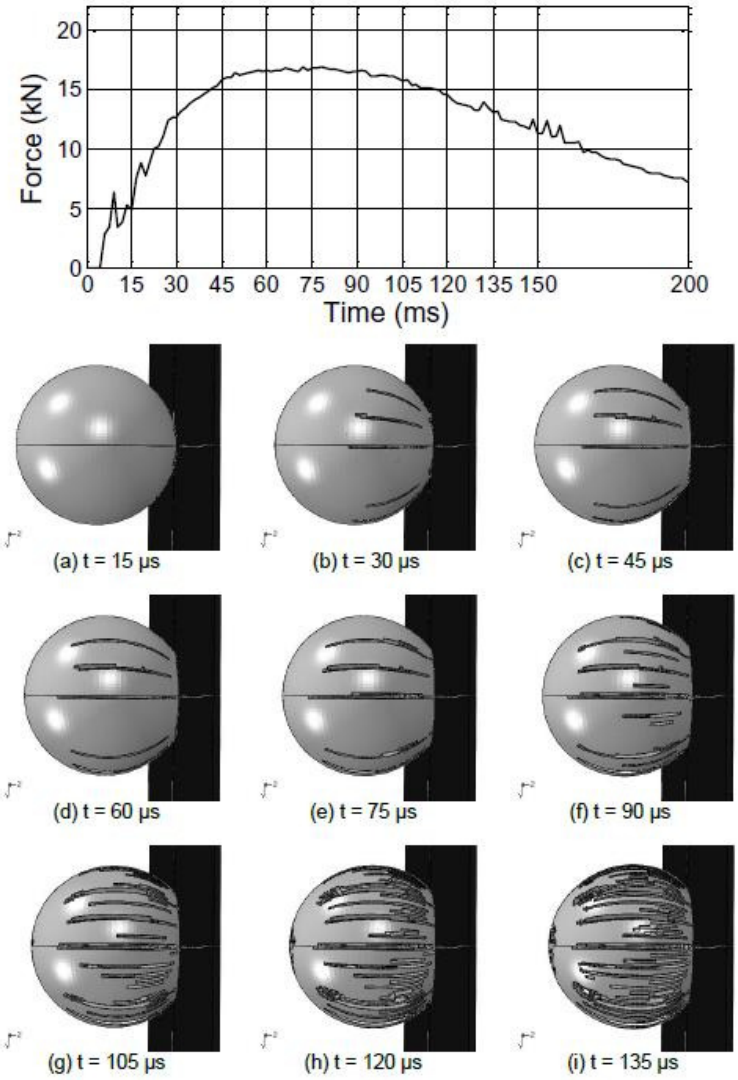

Figure 4-16. Simulated impact of 50.8mm diameter manufactured hailstone with impact velocity of 60.6m·s^{-1} (114J). Source: **[176]**

Failed elements in the model are removed from visual display in order to show the cracking and failure behaviour, this was achieved by setting the software to only show elements with a non-zero shear stress component therefore omitting failed elements that had exceeded the cut-off pressure. However, it is important to note that although they are removed from view, they are not removed from the actual model; therefore preserving the overall momentum of the model. Therefore, from Figure 4-15 and Figure 4-16 can be said that the model developed captures the experimentally observed cracking phenomenon; featured in Figure

4-15. The initial onset and spread of longitudinal cracking can be observed, followed by additional intermediate crack formation. He concludes that although this onset of cracking in the early stage of the impact (up until the peak force) is well captured, however the model does not fully capture the transverse cracking and break down of the hailstone in the lateral stages of impact. Furthermore, the model is therefore better suited for predicting early time-scale events but not the later splashing/powder developments.

4.3.1.4 Juntikka & Olssen

Juntikka & Olssen [180] presented the results from a joint numerical/experimental ice ball impact study on composite targets. The work employed both an experimental gas gun cannon and an SPH based modelling approach to investigate the ice ball impact of composite materials; with varying ice ball diameters.

The modelling work was performed using LS-DYNA and utilised an SPH approach to model the ice ball. Through numerical simulations, the material properties of the ice were calibrated, which then allowed for the subsequent composite impact analyses. Through this approach, a damage velocity threshold curve for the range of ice balls diameters tested and simulated was establish (for the given composite material system); obtaining agreement between the numerical and experimental results.

Figure 4-17 shows the simulated pressure wave behaviour in a 48mm diameter hailstone, as modelled through an SPH based approach by Juntikka & Olssen [180], whilst impacting a composite plate.

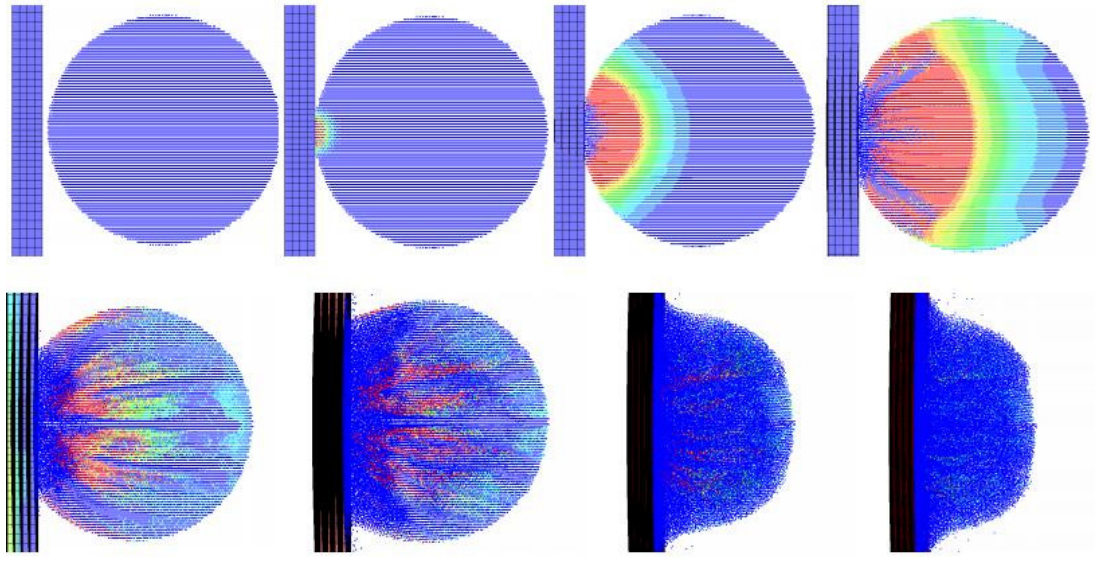

Figure 4-17. Pressure wave distribution in a simulated 48mm diameter hailstone, impacting a composite plate target. Modelled using an SPH based approach. Source: **[180]** (velocity and fringe scale not detailed).

Figure 4-17 shows the pressure wave and ice material failure behaviour obtained through the SPH based modelling approach employed by Juntikka & Olssen [180], giving a strong agreement with the results detailed by Tippmann [176]. A high pressure shockwave is shown to travel through the hailstone body, radially away from the initial impact site, resulting in subsequent failure and relaxation of the material. On the surface of the ice ball, claw like material failure distributions can be observed; as also shown by Tippmann in (Figure 4-16).

4.3.1.5 Carney et al.

Carney et al. [128] is considered to have developed a comprehensive material model for ice impact analysis; due to its considerations of the fundamental material behaviour of ice under impact loading. As such, this model is reviewed and the fundamental relationships that define the model.

As part of the return-to-flight requirements for the Space Shuttle Mission on July 26, 2005, modelling of high velocity ice impact was required as part of the safety calculations. Therefore a research programme began at the NASA Glenn Research Centre to tackle the issue of ice impact, as documented in a paper by Carney et al. [128]. The work identified that ice is not a common structural material and therefore commercial finite element programs do not have any appropriate material models. Therefore, in the absence of such appropriate models, work was carried out to develop a phenomenological model with failure based on experimental ballistic tests.

Carney et al. [128] acknowledge the work and contribution of the paper by Kim & Kedward [133] but recognises the need to develop a model which takes into consideration the rate sensitive nature of ice. As with other hail modelling work, the model was developed for use within the LS-DYNA software package, however, unlike previous studies an Eulerian mesh/modelling approach was adopted; as opposed to Lagrangian. The material model developed is now available for use in the commercial version of LS-DYNA and is named *MAT_PLASTICITY_COMPRESSION_TENSION_EOS.

As the modelling was to be utilised for safety calculations which are naturally conservative, the ice model detailed was developed to represent strong ice with repeatable material properties. However, the model can be used for weaker ice types by using an appropriate value for compressive strength.

A temperature of -10˚C is a common value at which material properties are determined for ice and therefore this is the temperature at which the model bases its values upon. The

Carney model also assumes a constant temperature during impact due to the high velocity nature of the impact events considered.

The Carney model uses tabular data and interpolation between specific points - instead of analytical functions - to define the dependency of the flow stress on the strain rate and pressure. This approach removes the time consuming step of fitting the experimental data to the analytical expressions (as practiced in earlier ice models) and eliminates the error between the measured response and the analytical relations. Carney et al. [128] presents the modelling approach giving in-depth detail on the processes and mechanisms of the material model. As such, it is possible to review the inner workings of the material model as detailed in the following.

To identify the tabular functions, a caret (â) will be placed over them.

Following yield, the flow stress of the material model has a product form,

$$\bar{\sigma} = \hat{s}(|\boldsymbol{D}|, P) \cdot \hat{\sigma}_f(\bar{\epsilon}^P) \tag{4.4}$$

where, ŝ, is a scaling function, and $\hat{\sigma}_f$, is the plasticity function which is a tabular function dependant on plastic strain, $\bar{\epsilon}^P$. This scaling function is composed of two tabular functions of the strain rate, $|\boldsymbol{D}|$, at a specified pressure, P. The scaling function is evaluated through interpolation between them based on the pressure,

$$\hat{s}(|\boldsymbol{D}|, P) = f \cdot \hat{c}_C(|\boldsymbol{D}|) + (1 - f) \cdot \hat{c}_T(|\boldsymbol{D}|) \tag{4.5}$$

where,

$$f = \min\left(1, \max\left(0, \frac{P - P_T}{P_C - P_T}\right)\right) \tag{4.6}$$

where subscripts T and C represent tension and compression respectively and $\hat{c}_C$ and $\hat{c}_T$ represent tabular functions of the values of strain at the constant pressure P_C and P_T, respectively.

Two different norms for the strain rate are evaluated in the model; the first is based on the deviatoric component of the deformation rate, **D'**,

$$|\boldsymbol{D}| = \sqrt{\frac{2}{3}\boldsymbol{D}' : \boldsymbol{D}} \tag{4.7}$$

The second is the Euclidian norm of **D**,

$$|\boldsymbol{D}| = \sqrt{D : D} \tag{4.8}$$

Carney et al. [128] state that the pressure is evaluated using the following tabulated equation of state with compaction,

$$P_{EOS} = \hat{C}(\epsilon_V) + \gamma \hat{T}(\epsilon_V)E \tag{4.9}$$

$$\epsilon_V = \ln(\frac{V}{V_0}) \tag{4.10}$$

where V_0 is the reference specific volume, E is the internal energy per reference volume, ϵ_V is the volumetric strain, $\hat{C}$ and $\hat{T}$ are tabular functions and γ is the Gruneisen coefficient; set to zero. Unloading and reloading occurs linearly with the bulk modulus at the peak volumetric strain. The pressure in tension is limited in magnitude by a pressure cut-off,

$$P = \max(P_{EOS,} P_{cut-off}) \tag{4.11}$$

where,

$$P_{cut-off} = \hat{s} P^0_{cut-off} \tag{4.12}$$

and $P^0_{cut-off}$ is the static pressure cut-off, which are evaluated both in tension (P_T) and compression (P_C). $P_{cut-off}$ is set to zero once the material has failed. Although the scaling function, ŝ, is a function of the current pressure, P, it is calculated using P_{EOS}. The paper states that although the pressures in the ice under consideration were below the shock pressure where a nonlinear response would be expected and the ice/water is volumetrically elastic, the introduction of the compaction feature of the equation of state allowed the matching of the numerical and experimental results. The feature is stated to minimise pressure oscillations which were observed in the damaged ice when using a linearly elastic equation of state; a feature not exhibited in ballistic testing. Figure 4-18 shows the heuristically developed $P - \epsilon_V$ relationship as described by the equation of state (Equation 4.9).

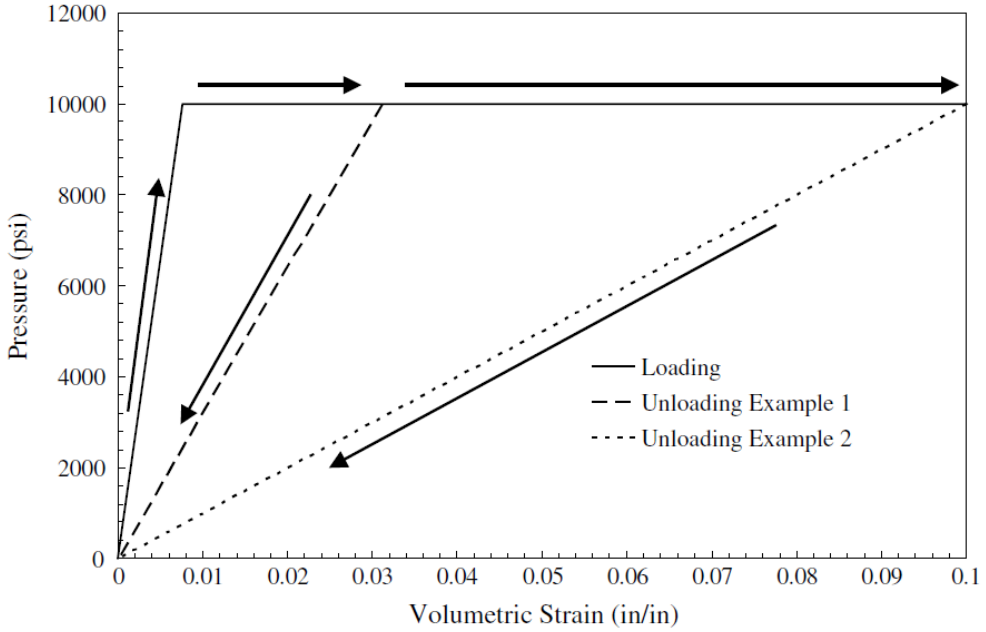

Figure 4-18. Equation of state with loading and unloading. Source: **[128]**

Two failure models are implemented in the material model. The final stress is given by

$$\boldsymbol{\sigma} = d^e \cdot d^P \cdot (\boldsymbol{\sigma}' - P\boldsymbol{I}) \tag{4.13}$$

where d^e and d^P are the damage variable associated to the plastic strain and pressure failure respectively. The plastic strain failure criterion is given as

$$d^e = \begin{cases} 0, & if\ \bar{\epsilon}^P > \bar{\epsilon}^P_{fail} \\ 1, & otherwise \end{cases} \tag{4.14}$$

The pressure failure criterion is given by

$$d^P = \begin{cases} 0, & if\ P > P_{cut-off}\ or\ P < P^T_{fail} \\ 1, & otherwise \end{cases} \tag{4.15}$$

The pressure cut-off terms, elastic properties and other model parameters utilised by Carney et al. [128] are cited in

Table 4-5. The compressive strain rate behaviour of the model is shown in tabulated form in Table 4-6 and the variables for the equation of state discussed are given in Table 4-7. The parameters listed in these three tables are all obtainable through direct material testing and represent the only required inputs for the Carney ice material model. The model assumes that the tensile strength strain rate sensitivity is constant and the plasticity function is assumed to have linear hardening with different initial values for compression and tension. However, Carney et al. [128] acknowledge that strain rate sensitivity in tension could be included given the appropriate experimentally obtained data.

Table 4-5. Carney Model material properties for strong ice at -10˚C. Source: **[128]**

Property	Value
Density (kg·m^{-3})	897.6
Young's Modulus (GPa)	9.31
Poisson's Ratio	0.33
Initial compressive flow stress, $\hat{\sigma}_f^C$ (MPa)	172.4
Initial tensile flow stress, $\hat{\sigma}_f^T$ (MPa)	17.24
Plastic Tangent Modulus, h (MPa)	6.89
Pressure cut-off in compression, P_C (MPa)	Single Crystal - 4.93
	Polycrystal - 3.0
Pressure cut-off in tension, P_T (MPa)	0.433

Table 4-6. Compressive strength strain rate sensitivity of ice. Source: **[128]**

Strain Rate (s^{-1})	Stress Scale Factor
1	1
10	1.2566
100	1.5132
200	1.59044
300	1.63562
400	1.66768
500	1.69255
600	1.71287
700	1.73005
800	1.74493
900	1.75805
1000	1.76979
1100	1.78042
1500	1.81498
10000	2.02639

Table 4-7. Equation of state loading parameters. Source: [128]

ln Volumetric Strain	Pressure		Bulk Modulus (psi)/Stated	
	(psi)	(MPa)	(psi)	Stated
0	0	0	1.3 x 10^6	8.96 GPa
-7.69 x 10^{-3}	10^4	68.9	1.3 x 10^6	8.96 GPa
-3.13 x 10^{-2}	10^4	68.9	3.2 x 10^5	2.2 GPa
-10	10^4	68.9	1.0 x 10^3	6.89 MPa

Carney et al. [128] also details two additional features added to the developing model which were excluded from the final safety calculations due to an absence of data with which to calibrate them. However, they state that given such data and calibration, the features would further improve the model accuracy.

Carney et al. [128] gives a detailed explanation of his methodology. This level of descriptive detail is absent in most other papers, but the clarity and transparency it presents is very helpful when it comes to implementing such a model.

The ice material model was implemented using an Eulerian approach in LS-DYNA and was used to simulate a series of experimental tests conducted with the use of a gas fired gun and a vacuum test chamber. The tests looked at the impact of cylindrical ice projectiles (single and poly-crystal) with a diameter of 17.46mm and length of 42.16mm, against a circular steel target plate with a 63.5mm diameter and 19.05mm thickness (Figure 4-20). The impact velocity was varied between 91.44, 152.4 and 231.36m·s^{-1} and the impact angle between 0 and 45˚.

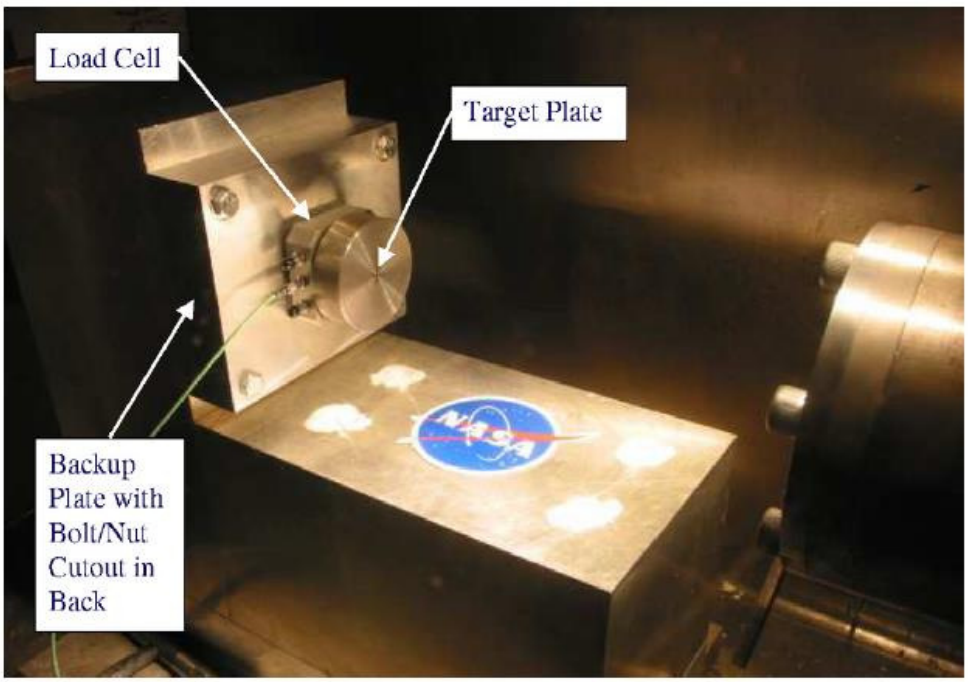

Figure 4-19. Target plate and load cell. Source: **[128]**

As the target structure was not mathematically rigid (i.e. the load cell and backup structure have some degree of movement during impact) a modal survey was conducted on the test rig apparatus, so that it could be confidently replicated in the LS-DYNA environment. The results of the modal survey are depicted in Figure 4-20.

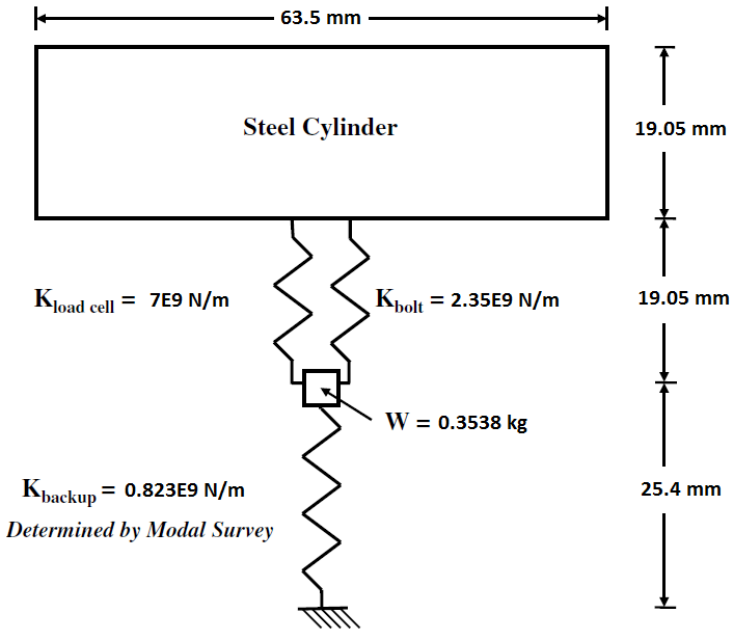

Figure 4-20. Results from modal survey of target apparatus (units converted to SI). Source: **[128]**

The results from simulating a 152.4m·s^{-1} impact at normal orientation are shown in the force time history plot shown in Figure 4-21.

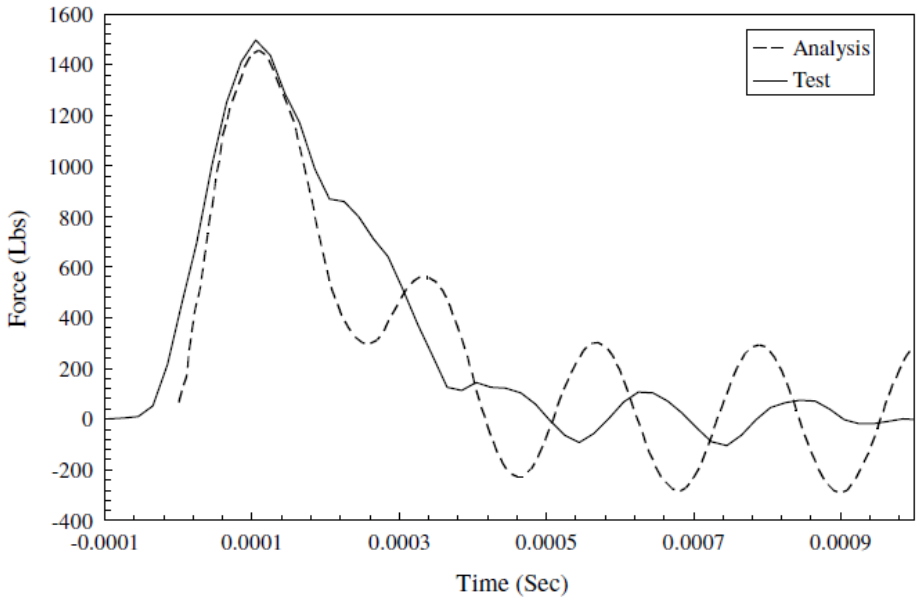

Figure 4-21. Force time history of impact at 152.4 m·s^{-1} for experimental and analytical results, normal impact. Source: **[128]**

It can be seen that good agreement was achieved between the experimental and numerical results and this is also the case for the other variations on speed and impact angle. However, it is recognised that the attenuation due to the inertia of the target plate made the matching of the test and numerical data somewhat easier and that the actual bodily contact force between

the two objects consists of a short and sharp force pulse. It is then said that although this contact behaviour is difficult to capture through experimental means, future experimental efforts will be conducted to try and capture such a force history. A calculated force history of pure contact loading is then also shown, as depicted in Figure 4-22.

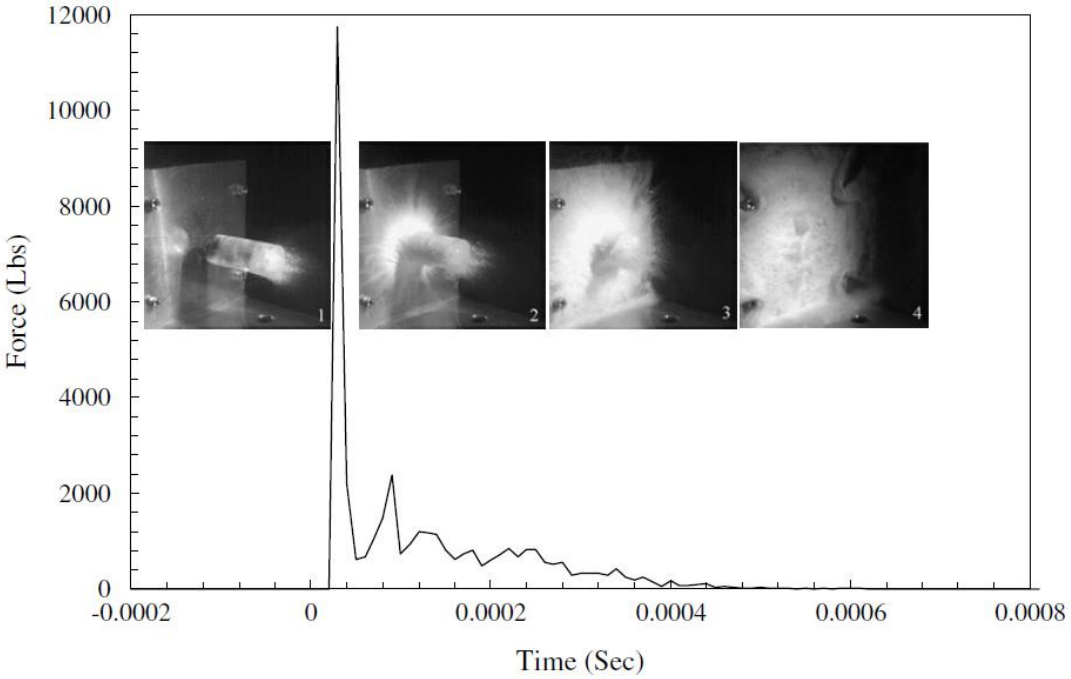

Figure 4-22. Calculated contact force at 152.4m/s. Source: **[128]**

From Figure 4-22 it is possible to observe the suggested sharp force pulse that acts between the immediate contact faces. Due to the energy from impact being transferred over such a short duration the resultant force acting on the surface is just under double that experienced by the load cell (Figure 4-21). This spiking phenomenon is apparent when also looking at the photographic images of the impact; however it is still lacking in experimental validation; an objective stipulated by Carney et al [128].

4.3.2 Selection of Modelling Approaches

From reviewing previous various attempts to model ice impact, it was clear that the model proposed by Carney et al. [128] represented the most developed and comprehensive approach.

Furthermore, from the review, it was apparent that for the purposes of modelling ice impact, the most common software choice is the LS-DYNA solver and that the most suitable meshing methods for ice projectiles are either an Eulerian approach or a SPH approach; owing to their capability to effectively model large strains and deformation.

For these reasons, it was decided that for the purposes of modelling hailstone impact on the leading edge of a wind turbine blade, the LS-DYNA solver would be employed to implement the Carney ice model. However, as a result of the benefits offered by the SPH approach, as detailed by Anghileri et al. [156], the Carney model would be implemented using the SPH approach. Such an approach would firstly require validation against the results already obtained by Carney et al. [128] (such as that shown in Figure 4-21) through replicating their modelling/experimental process.

4.4 Software Selection

From reviewing the literature on modelling techniques for both rain and hailstone impact and assessing their suitability, many potential solvers have been identified and detailed. It is clear that the most commonly employed solver with respect to modelling high velocity soft body impact is LS-DYNA [162]. For this reason, LS-DYNA (ANSYS 13 version) would be used for the modelling section of this work, using it in standalone solver mode rather than in the embedded version in the ANSYS Workbench environment. It was found that using it in a standalone capacity and using its purpose made pre/post-processor (LS-PrePost [153]) provided clarity with regards to the final make-up of the simulations and allowed for the full utilisation of all the simulation tools available to LS-DYNA.

However, for initial rain droplet impact modelling using an Eulerian approach, the ANSYS Explicit Dynamics environment was also used.

4.5 Modelling Target Materials - LS-DYNA Approach

There are many potentially viable methods for numerically modelling the impact of rain droplet and hailstone projectiles, identifying the LS-DYNA software package as the most suitable tool for modelling such impact events. However it is also important to consider the manner in which the material behaviour and response of the target materials is modelled within LS-DYNA. Wind turbine blade leading edge components, such as highly elastic polymer coatings, gel coats and fibre reinforced plastics, have complex physical responses and can be difficult to model accurately, however in order to gain accurate and reliable insight into the response of leading edge materials under impact, it is imperative that they are modelled as effectively as possible, with respect to their physical responses.

As such, it is important to review and evaluate the material models available to LS-DYNA in the context of modelling the behaviour of such blade materials.

4.5.1 Element Type

LS-DYNA is capable of modelling solid materials using an array of available element types, such as: shells, thick-shells, solid bricks, beams and SPH nodes. In the context of modelling thin composite materials, the most prominent and commonly used element types are shell, thick-shells and solids.

In analyses featuring large scale composite components or structures, shell elements or thick-shell elements may be most suitable, as the structural response of the structure as a whole may be of interest, and therefore the through thickness behaviour in the material is not of concern. However, in the context of examining the impact response of thin composite based target materials, such as a blade leading edge, the through thickness response of the material is of great interest and therefore shell elements, which model the material on a two dimensional plane, may not be suitable.

In order to capture the through thickness material behaviour of a given target structure, a three dimensional approach to modelling the target is required. Therefore, it is most suitable to model the targets using 3D solid brick elements, of which there are many types and configurations within LS-DYNA [181]. Many of the material models within LS-DYNA for both polymers and composite materials are compatible with solid type elements, and as such, these elements were identified as most suitable for the modelling work of this research.

4.5.2 Polymers

Effectively modelling the impact response of polymer based materials in a finite element environment presents many challenges; some of the most important of these are that many engineering polymers can exhibit:

1. Highly unique stress-strain behaviour as well as irregular or complex post-yield plastic behaviour.
2. Significant strain rate sensitivity.
3. Varying strength between loading in compression or tension (for a given polymer)

Any given polymer material may exhibit all these traits (and other complexities) or perhaps only a few. The importance of such characteristics will, of course, depend upon the nature of the finite element analysis required and it may be suitable in some situations to make simplifying assumptions. For instance, if a steady strain rate is predicted in the analysis then the effects of strain rate sensitivity may be ignored; assuming that the stress-strain behaviour at such a constant strain rate is well understood. Additionally, if the compressive and tensile behaviour of the material are comparatively similar or the analysis features primarily one

type of loading (compression/tension), then it may be suitable to assume and assign identical compressive/tensile behaviour.

However, it is clear that if such assumptions cannot be made for a given polymer, the constitutive material model for modelling the polymer in LS-DYNA will have to feature capabilities to:

1. Model complex post-yield plasticity behaviour through either the input of suitable material properties or experimental tabular data.
2. Incorporate the effects of the strain rate sensitivity of a given polymer
3. Model compression and tension loading behaviour differently

The LS-DYNA keyword manual [168] details and describes all the available constitutive material models within LS-DYNA and additionally defines which material models are suitable for modelling plastics. Table 4-8 details a list of available LS-DYNA material models designated in the LS-DYNA keyword manual as suitable for modelling plastics. The table details the required inputs to describe the plasticity behaviour of the material and consequently the nature in which the respective models represent the plasticity behaviour of the material. The designation 'ETAN' means that the model requires only a simple post-yield tangent modulus to represent post-yield loading, therefore the post-yield loading is modelled as a linear relationship, whereas 'Tabular' indicates that the post-yield stress-plastic strain behaviour can be input in tabular form; allowing for higher complexity (as will be discussed). The 'Parameter' designation indicates that experimentally or analytically derived material parameters or characteristics are required for input. The other columns indicate - with a Y(es) or N(o) - if the respective material mode can incorporate strain rate effects or failure and if the model handles compression loading differently to tension.

Table 4-8. Available materials within LS-DYNA designated as suitable for modelling the material behaviour of plastics. Detailing the available features associated with each material model, whereby Y & N indicate yes and no respectively. Source: **[168]**

Material Number	Material Model Number and Description	Plasticity Behaviour	Strain Rate Effects	Failure Criteria	Seperate Tension/Compression Behaviour
3	Plastic Kinematic	ETAN	Y	Y	N
24	Piecewise Linear Plasticity	ETAN/Tabular	Y	Y	N
81	Plasticity with Damage	ETAN/Tabular	Y	Y	N
89	Plasticity Polymer	Tabular	Y	N	Y
101	GE Plastic Strain Rate	Tabular	Y	Y	Y
106	Elastic Viscoplastic Thermal	Tabular	Y	N	N
112	Finite Elastic Strain Plasticity	ETAN/Tabular	Y	N	N
114	Layered Linear Plasticity	ETAN/Tabular	Y	Y	N
123	Modified Piecewise Linear Plasticity	ETAN/Tabular	Y	Y	N
124	Plasticity Compression Tension	Tabular	Y	Y	Y
141	Rate Sensitive Polymer	Parameters	Y	N	N
153	Damage 3	Tabular	Y	Y	N
168	Polymer	Parameters	N	N	Y
187	Semi-Analytical Model for Polymers - 1	Tabular	Y	Y	N
224	Tabulated Johnson Cook	Tabular/Parameters	Y	Y	Y
238	Piecewise linear plasticity (PERT)	ETAN/Tabular	Y	Y	N

As noted, there are numerous available material models for plastics in LS-DYNA, all of which feature varying capabilities. Most of the material models offer the option of including strain rate effects and material failure criteria, however far fewer are capable of modelling separate compression and tension behaviour. These variations in capabilities mean that some material models will be suitable for certain materials and perhaps not others, as discussed in the following.

The material models which make use of the ‘ETAN’ input option present a simplified means of modelling the stress-strain relationship of a material. For example, if the stress-strain behaviour of a given material is known and exhibits relatively simple elastic-plastic behaviour, such as that shown in Figure 4-23, then it may be possible to approximate this behaviour through simply inputting the Young’s (pre-yield slope) modulus, yield stress and a tangent modulus (ETAN – post-yield slope) value.

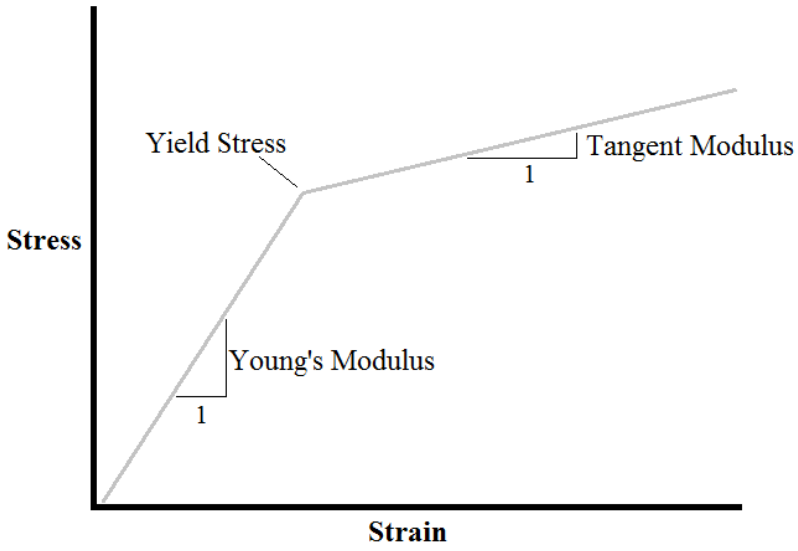

Figure 4-23. Elastic-Plastic material response

Although the perfectly linear elastic-plastic behaviour shown in Figure 4-23 may be rare, many stress-strain curves for materials can be approximated by two slopes to represent the elastic and plastic behaviour (Young's and tangent modulus respectively), therefore this approach may be applicable in many studies.

However, many engineering polymers exhibit far more complex post-yield behaviour which cannot be fully characterised by a simple tangent modulus. For example, polyurethanes such as that featured in protective coatings typically exhibit stress-strain behaviour as typified in Figure 4-24 (as indicated from manufacturer data [182] [77]).

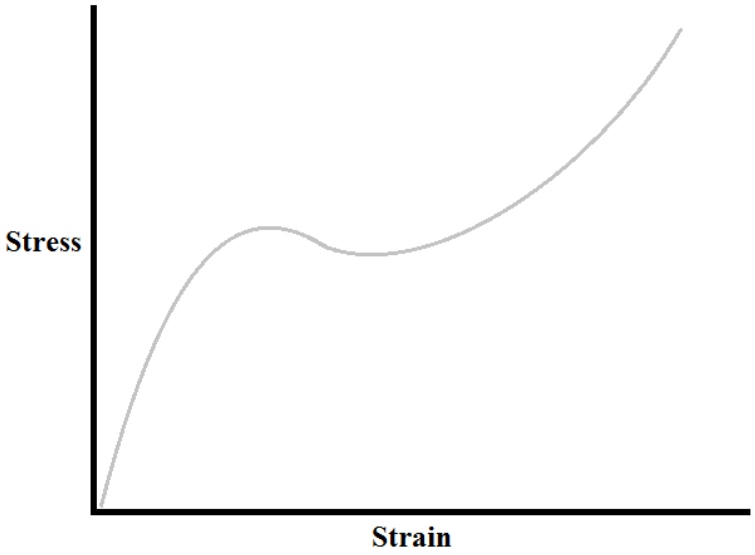

Figure 4-24. Typical complex high deformation plasticity as exhibited in some polymer materials such as polyurethanes.

The exact behaviour of the material is of course dependant on the properties of the material however complex plastic behaviour such as this may not be adequately approximated by two slopes. As such, when dealing with such materials it is more appropriate to adopt a material model which allows for the input of tabular data relating to the plastic behaviour of the material. Through this method such complex post-yield behaviour may be more accurately modelled.

Although within LS-DYNA there are numerous material models which can be utilised to model the material behaviour of plastics, very few of the models provide the capability to model compressive and tensile behaviour differently. The ability to do so was considered important owing to the nature of the impact simulations proposed, whereby the target materials will be subject to strong compressive forces from impact and then subsequently shear and tensile stresses through dissipation of the impact energy. Additionally, many of the target materials considered in the analyses of this study, such as epoxy resin, can exhibit higher strength under compression than tension. This higher compressive strength may be central to the real response and performance of the material when under impact and therefore should not be ignored in analyses, or assumed to be equal to a (potentially lower) tensile strength value.

Table 4-8 shows that material model *MAT_PLASTICITY_COMPRESSION_TENSION can model tensile and compressive behaviour differently, as well as incorporate strain rate effects, failure and complex plastic behaviour (through tabular input). It would seem that this material would therefore be robust enough to model most plastic materials, given that the appropriate material properties and data are available. The material model developed by Carney et al. [128] for the purposes of modelling ice impact, *MAT_PLASTICITY_COMPRESSION_TENSION_EOS, is based upon similar principles to that of *MAT_PLASTICITY_COMPRESSION_TENSION. The material model models elastic-plastic behaviour through the definition of a unique and separate yield stress versus plastic strain curve for both compression and tension [168]. Failure of the material can be modelled based upon a plastic strain failure value or a minimum time step and strain rate effects are modelled using a Cowper-Symonds strain rate model [181] or by entering two load curves which scale the stress values in compression or tension based on strain rates.

It is clear, then, that there are numerous material modelling options within LS-DYNA for the purposes of modelling polymer based materials and as such a number of these material models may be suitable for the modelling work of this research.

4.5.3 Composites

Modelling the impact response of composite material technologies in a finite element environment presents a significant challenge. The anisotropic material behaviour of composite material technologies (and many of those employed in wind turbine blades) requires careful and considered implementation in finite element analysis. Additionally the interlaminate interaction and response between plies in a composite laminate also has to be carefully modelled in order to accurately capture the material response of the composite.

Helpfully, the LS-DYNA simulation environment has been used extensively in numerous previous studies [167] [133] [180] [183] regarding the impact response of composite materials/laminates. As such, a great deal of development with regards to composite material models has been performed, resulting in the availability of a wide range of potential composite material modelling techniques and tools.

The following review describes the most suitable methods for the purposes of the present work with regard to modelling both the material behaviour and the interlaminate behaviour in laminate constructions.

4.5.3.1 Composite Material Behaviour

Composite materials can be manufactured in many forms and to numerous configurations for any given application. As such, effectively modelling any given composite material configuration in a finite element analysis can present many unique challenges. Central to the effective modelling of any composite material is a strong understanding of the behaviour of the composite technology concerned. LS-DYNA has numerous material models for the purpose of modelling composite material technologies; however each model will possess specific tools and features which, while appropriate for some technologies, may not be suitable for all application. Therefore, an evaluation of the appropriate material models within LS-DYNA for the purpose of modelling wind turbine blade composites; such as chopped strand mat materials and unidirectional/weaved reinforced materials is presented

Most chopped strand mat (CSM) material technologies are manufactured as thin sheets (stored on a roll) and are employed in blade applications as a thin layer in a larger laminate. Due to the randomly orientated nature of the reinforcing fibre, and assuming it is uniformly distributed, most thin CSM sheets can be assumed to exhibit isotropic material behaviour in the plane of the sheet. However, the material properties in the normal direction may differ significantly and as such, in the context of normal impact simulations, care must be taken if assuming that the properties are isotropic. As such, it may be more suitable to model CSM

materials with a standard composite material model in LS-DYNA, whereby the longitudinal and transverse properties are identical and the properties specified in the normal direction are lower. Deb et al. [184] employed such a method to investigate the effectiveness of a CSM based GFRP tube under axial impact loading (relating to automotive safety structures) using LS-DYNA and the material model *MAT_ENHANCED_COMPOSITE_DAMAGE. Deb et al. [184] validated the numerical modelling with experimental results, obtaining good correlation. The simulations featured primarily loading in the in-plane direction along the axis of the CSM based tubes, and therefore the normal plane behaviour of the material was not of primary concern. The material model is also designed only for shell elements [168] and therefore would not be suitable for the work of this study. However, Deb et al. [184] validated the approach of modelling such CSM materials as a quasi-isotropic material and therefore adopting such a technique with more suitable composite material models (for solid elements) should provide satisfactory modelling performance.

LS-DYNA supports a large number of constitutive material models for composites. However, many of the models are designed to be utilised with specific element types such as shells, and therefore may not be applicable to all element types. As such, all available solid element compatible composite material models in LS-DYNA, as documented in the LS-DYNA keyword manual [168] are reviewed. Table 4-9 lists all such compatible material models and details some of their key features.

Table 4-9. Table showing material models for composite materials within LS-DYNA which are compatible with solid elements. Showing features of the model, indicated by a Y(es) or N(o). Source: **[168]**

No.	Material Model Name	Strain Rate	Failure	Damage	Unique Compression/Tension
22	Composite Damage	N	Y	N	Y
59	Compolisite Failure Solid Model	N	Y	N	Y
161	Composite MSC (Additional License Required)	Y	Y	Y	Y
162	Composite DMG MSC (Additional License Requirment)	Y	Y	Y	Y
221	Orthotropic Simplified Damage	N	Y	Y	Y

Table 4-9 indicates whether the models incorporate strain rate, failure and/or damage effects and whether the model handles tension differently to compression. As shown, all the possible models incorporate a failure mechanism, whereby upon reaching a certain criteria such as a certain load or strain the material fails and the elements are eroded. Each model also models compression effects in the material differently to tension, which is an essential characteristic for impact modelling. Material models 161 & 162 can additionally model both strain rate effect and damage (i.e. progressive damage accumulation leading to failure), indicating that it may be the most advanced and developed model. However, these two models require the use of an additional license from the creators and as such were not available for the work of

this research. Therefore, the three material models numbered 22, 59 and 221 are the only applicable models and there is little from first inspection to differentiate between the models; besides the damage modelling capabilities possessed by material 221. To better understand the nature of each model and their capabilities, each one is examined and discussed as follows.

Material 22

Material 22 (*MAT_COMPOSITE_DAMAGE) is an orthotropic material model with an option for brittle failure (detailed previously in Table 4-9). The model requires the input of longitudinal, transverse and normal material properties (in both compression and tension) and can predict the three following failure mechanisms in the material [168]:

1. Tensile matrix mode
2. Compressive matrix mode
3. Tensile fibre mode

The failure option is based on the work of Chang and Chang [185], as detailed in the LS-DYNA keyword manual [168]. There are five material parameters used in the three failure criteria discussed, these are:

1. Longitudinal tensile strength, S_1
2. Transverse tensile strength, S_2
3. Shear strength, S_{12}
4. Transverse compressive strength, C_2
5. Nonlinear shear stress parameter, α

The first four parameters are obtained from strength measurement of the material, whereas α is defined by material shear stress-strain measurements (typically ranging between 0-0.5 [168]). The stress-strain behaviour of the material is given by the following terms [159] (Equations 4.16, 4.17 & 4.18).

$$\varepsilon_1 = \frac{1}{E_1}(\sigma_1 - \upsilon_1\sigma_2) \tag{4.16}$$

$$\varepsilon_2 = \frac{1}{E_2}(\sigma_2 - \upsilon_2\sigma_1) \tag{4.17}$$

$$2\varepsilon_{12} = \frac{1}{G_{12}}\tau_{12} + \alpha\tau_{12}^3 \tag{4.18}$$

where ε, σ and E are the strain, stress and Young's Modulus of the material, in the longitudinal, transverse and shear planes; denoted by subscript 1, 2 and 12 respectively. The terms G and τ are the shear modulus and shear stress respectively, which can be utilised (if known) to determine the nonlinear shear stress parameter, α.

Each of the three failure modes described are augmented by a fibre matrix shearing term as shown in Equation 4.19 [159].

$$\bar{\tau} = \frac{\frac{\tau_{12}^3}{2G_{12}} + \frac{3}{4}\alpha\tau_{12}^4}{\frac{S_{12}^2}{2G_{12}} + \frac{3}{4}\alpha S_{12}^4} \tag{4.19}$$

Failure through matrix cracking is defined by the term shown in Equation 4.20.

$$F_{matrix} = \left(\frac{\sigma_2}{S_2}\right)^2 + \bar{\tau} \tag{4.20}$$

where failure is assumed where $F_{matrix} > 1$, at which the material constants E_2, G_{12}, υ_1 and υ_2 are set to zero.

The compressive matrix failure criterion is defined by Equation 4.21.

$$F_{comp} = \left(\frac{\sigma_2}{2S_{12}}\right)^2 + \left[\left(\frac{C_2}{2S_{12}}\right)^2 - 1\right]\frac{\sigma_2}{C_2} + \bar{\tau} \tag{4.21}$$

Again, failure is assumed to occur whenever $F_{comp} > 1$, at which the material constants E_2, υ_1 and υ_2 are set to zero.

The final failure mode, due to tensile fibre breakage, is defined by Equation 4.22.

$$F_{fiber} = \left(\frac{\sigma_1}{S_1}\right)^2 + \bar{\tau} \tag{4.22}$$

Once more, failure occur when $F_{fiber} > 1$, when the constants E_1, E_2, G_{12}, υ_1 and υ_2 are set to zero.

The ability to model and capture such failure mechanisms adds great value to the usefulness of the material model, adding extra insight into the impact response of the material; however material 22 does not offer the capability to model gradual damage accumulation (leading to eventual failure/breakage), instead, it only models instant and complete failure upon reaching a certain threshold.

The model also does not incorporate strain rate effects in the material, this may be a disadvantage for some studies, however in order to make use of strain rate tools such as those available in MAT 161 & 162, a wealth of material data is required. In the absence of such data these features may be excess to requirements of the work.

Griškevičius et al. [186] utilised material 22 to study the impact absorption characteristics of a safety important honeycomb core sandwich structure; utilising it to model the facesheets of the structure (and material 3 *MAT_PLASTIC_KINEMATIC for the honeycomb structure). The study validates the modelling work in LS-DYNA with experimental data, and the subsequently carries out parameter studies using the validated numerical approach.

Kumrungsie et al. [187] also utilised material 22 to model the response of a aramid fibre reinforced epoxy 5mm thick plate to ballistic impact; exploring the effects of utilising bi-directional fibre reinforcement in place of unidirectional reinforcement. Utilising such a numerical approach allowed for the in-depth analysis of stress propagation and failure within the composite system.

It is clear then that for the appropriate impact studies, where progressive damage or strain rate effects are of little importance, that material 22 is a very capable material model for composite material modelling.

Material 59

Material 59 or *MAT_COMPOSITE_FAILURE_SOLID_MODEL (detailed previously in Table 4-9) can simulate the three-dimensional behaviour of orthotropic composite materials and predict the onset of the following three major failure modes [188]:

1. Tensile failure
2. Transverse shear failure
3. Compressive failure

These failure modes are invoked through the prediction of four independent failure parameters, which all contribute to the ultimate failure of a composite system. Cheng and Hallquist [188] describe the model in detail, stating that the constitutive model is based on orthotropic material, as defined by the relations shown below in Equation 4.23.

$$\begin{bmatrix} \frac{1}{E_a} & -\frac{\upsilon_{ab}}{E_b} & -\frac{\upsilon_{ac}}{E_c} & 0. & 0. & 0. \\ -\frac{\upsilon_{ba}}{E_a} & \frac{1}{E_b} & -\frac{\upsilon_{bc}}{E_c} & 0. & 0. & 0. \\ -\frac{\upsilon_{ca}}{E_a} & -\frac{\upsilon_{cb}}{E_b} & \frac{1}{E_c} & 0. & 0. & 0. \\ 0. & 0. & 0. & \frac{1}{G_{bc}} & 0. & 0. \\ 0. & 0. & 0. & 0. & \frac{1}{G_{ca}} & 0. \\ 0. & 0. & 0. & 0. & 0. & \frac{1}{G_{ab}} \end{bmatrix} \begin{Bmatrix} \sigma_{aa} \\ \sigma_{bb} \\ \sigma_{cc} \\ \sigma_{bc} \\ \sigma_{ca} \\ \sigma_{ab} \end{Bmatrix} = \begin{Bmatrix} \varepsilon_{aa} \\ \varepsilon_{bb} \\ \varepsilon_{cc} \\ \gamma_{bc} \\ \gamma_{ca} \\ \gamma_{ab} \end{Bmatrix} \tag{4.23}$$

where the subscripts a, b and c refer to the longitudinal, transverse and normal material directions respectively, and once again E, υ and σ are the Young's modulus, Poisson's ratio and stress properties respectively. The terms ε and γ refer to the plane strain and shear strain properties of the material.

Tensile failure in the longitudinal ('a') direction occurs when the following criterion is met:

$$\left(\frac{\sigma_{aa}}{X_t}\right)^2 + \left(\frac{\sigma_{ab}}{S_{ab}}\right)^2 + \left(\frac{\sigma_{ac}}{S_{ac}}\right)^2 \geq 1 \tag{4.24}$$

where X_t is the longitudinal tensile strength and S_{ab} and S_{ac} are the shear strength values in the 'ab' and 'ac' respectively.

When failure occurs the following terms are set to zero: E_a, all υ terms, all G values, σ_{aa}, σ_{bc}, σ_{ca} and σ_{ab}.

Tensile failure in the transverse material direction is based on an identical failure criterion, with the alteration of appropriate terms based on the material direction and resulting in the zeroing of appropriate terms, as discussed in full by Cheng and Hallquist [188].

Longitudinal through thickness shear failure ('ac' plane) is invoked upon reaching the following criteria:

$$\left(\frac{\sigma_{aa}}{X_t}\right)^2 + \left(\frac{\sigma_{ac}}{S_{ac}}\right)^2 \geq 1 \tag{4.25}$$

where the first term is considered only when $\sigma_{aa} > 0$. Again, upon occurrence of this failure mode the following terms are set to zero: E_a, all υ terms, all G values, σ_{aa}, σ_{bc}, σ_{ca} and σ_{ab}.

Transverse through thickness failure is again determined by the same criteria described in Equation 4.25, with the alteration of appropriate terms based on the material direction [188].

Longitudinal compressive failure is invoked upon meeting the following criteria:

$$\left(\frac{\sigma_{aa}}{X_c}\right)^2 \geq 1 \tag{4.26}$$

where X_c is the longitudinal compressive strength; and $\sigma_{aa} < 0$. Again, when considering longitudinal compressive failure, the same parameters as detailed for the previous two failure mechanisms are again set to zero.

Transverse compressive failure occurs when the following condition is met:

$$\left(\frac{\sigma_{bb}}{S_{ab}+S_{bc}}\right)^2 + \left[\left(\frac{Y_c}{S_{ab}+S_{bc}}\right)^2 - 1\right]\frac{\sigma_b}{|Y_c|} + \left(\frac{\sigma_{ab}}{S_{ab}}\right)^2 + \left(\frac{\sigma_{bc}}{S_{bc}}\right)^2 \geq 1 \tag{4.27}$$

where Y_c is the transverse compressive strength of the material, and $\sigma_{bb} < 0$.

Through thickness compressive failure occurs when the following is met:

$$\left(\frac{\sigma_{cc}}{S_{ac}+S_{bc}}\right)^2 + \left[\left(\frac{Z_c}{S_{ac}+S_{bc}}\right)^2 - 1\right]\frac{\sigma_{cc}}{|Z_c|} + \left(\frac{\sigma_{ac}}{S_{ac}}\right)^2 + \left(\frac{\sigma_{bc}}{S_{bc}}\right)^2 \geq 1 \tag{4.28}$$

where Z_c is the normal compressive strength of the material, and $\sigma_{cc} < 0$.

Material 59 has been utilised in many studies to investigate the impact dynamics of composite material systems. Menna et al. [183] utilised the material model to simulate the low-velocity impact of glass fabric reinforced epoxy laminates, implementing a solid element method of modelling the composite plies. Through comparison to experimental results, the study found that the simulations provided good agreement with respect to the force-displacement curve during loading as well as the irreversibly absorbed impact energy. The work also found that although the total modelled delamination was generally greater than that exhibited in experimentation, the nature of the delaminations were similar and that the difference may be attributed to interlaminar strengths assigned to the simulation which were assumed to be independent of the relative fibre orientations of each ply.

Nguyen et al. [189] utilised material 59, with shell elements (for computational resource requirements), to investigate and optimise the performance of a Kevlar 29 laminate under ballistic impact. The optimisation process was performed using the LS-OPT [190] software, which is a ‘standalone design optimisation and probabilistic analysis package’ which is

design to interface with LS-DYNA. The study looked to optimise the energy absorption characteristics of the plate and limit the plate displacement.

Peng et al. [191] implemented material 59 to study the effects of patchwork repairs to aerospace carbon fibre reinforced composites on the tensile performance of the repaired material. The study uses experimental date to validate the modelling work, finding good agreement between the two.

Material 59 was also utilised by LeBlanc and Shukla [192] to study the underwater shock loading behaviour of an E-Glass/Epoxy composite material panel, utilising experimental data for the purposes of validation. A high level of correlation was obtained between the numerical and experimental findings, and the material model exhibited accurate damage behaviour.

Material 221

Material 221 is an orthotropic material with an optional simplified damage and failure for composite systems [168]. The material model is only compatible with three-dimensional solid elements and its elastic behaviour is the same as that described for material 22. The model uses nine defined damage variables, applicable to E_a, E_b, E_c (both in compression and tension) and G_{ab}, G_{bc} and G_{ca}. Nine additional failure criteria are available based on strain levels and when failure occurs the affected elements are deleted.

The unique feature of this material model is its capability to model damage in the material, through altering the Young's modulus or shear modulus behaviour of the material on the specific material axis.

In spite of these attractive features, there is, as yet, very little supporting official documentation on the material model and sparse examples of its use in the technical literature. For these reasons, at the current time of this research the material model was deemed not yet suitable for implementation. However, it would seem that from their extensive use and validation in the literature both materials 22 and 59 are suitable for modelling the impact response of wind turbine blade composites; based on three-dimensional solid elements.

4.5.3.2 Interlaminate Composite Behaviour

Effectively modelling the constitutive material behaviour of composite materials is only part of the challenge when considering the numerical modelling of composite materials and structures within a finite element environment. Critical also to this endeavour is the accurate

modelling and representation of interlaminate material behaviour, i.e. how the individual composite plies interact with one another and how loads are transferred between them. Further to capturing the interaction and load transfer between plies, it is also of great interest in impact studies to effectively model failure of the connection between plies, and subsequently, delaminations in the structure. The following discussion on delamination modelling refers heavily to the work and documentation created by the LS-DYNA Aerospace Working Group [193].

Delamination occurs as a result of material failure between composite plies due to normal and shear stresses within the laminate. Laminate bonding and delamination between plies can be modelled in LS-DYNA using either an appropriate contact algorithm or cohesive zone elements [193].

Bonding between composite plies can be modelled using a contact algorithm such as *CONTACT_AUTOMATIC_SURFACE_TO_SURFACE_TIEBREAK [181], whereby the plies are bonded together through 'tying' adjacent nodes between the solid elements representing each ply. However, implementing this tiebreak based contact option also allows for the modelling of damage or failure of these ties, subsequently resulting in a breaking of the bonds and therefore delamination. This delamination modelling capability can be achieved through implementing the options 7, 9 or 11 within the contact algorithm. These options use a fracture mechanics based separation law, and as such can require extensive fracture toughness material data; which may not always be available. In such cases, an additional option number 6 may be used, which models failure based on a specified normal or shear stress. This can serve as a crude approximation for delamination, in the absence of the required fracture toughness data [193].

Cohesive zone elements can also be used to define the interlaminate behaviour of composites. These are 8-node solid elements which possess the material properties of the respective cohesive material employed, and act as a linking element between adjacent plies. However, if the bonding layer within the composite is sufficiently thin (as it is in many designs) there is no need for the mass of the bonding layer to be included; and therefore it is common practise to instead use a tied contact option instead [193].

The elastic/linear softening (bilinear) constitutive behaviour of the tie break contact algorithm with options 7, 9, & 11, is illustrated in Figure 4-25.

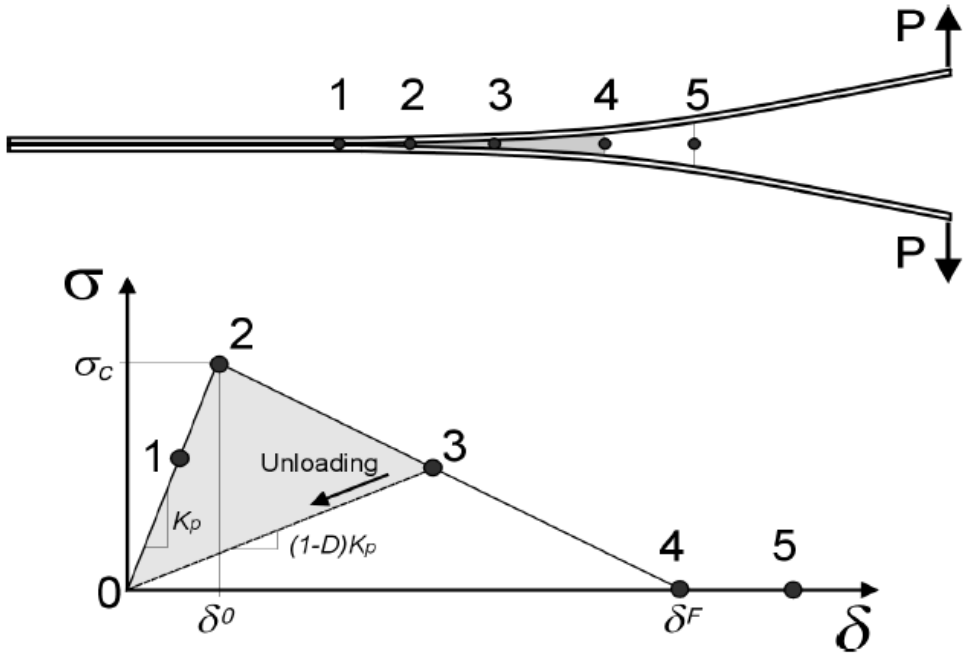

Figure 4-25. Bilinear constitutive model for delamination between composite plies (in tension, Mode I). The top image shows the delamination of two plies, whilst the bottom image shows the corresponding stress-strain behaviour at each point. Source: **[193]**

Figure 4-25 shows a graph of the stress-strain behaviour of the contact definition (tiebreak - options 7, 9 & 12), showing key points of the contact behaviour (1-5). The top image shows the varying corresponding delamination behaviour at each of the key points identified on the stress-strain graph; for two plies undergoing delamination in tension (Mode I). Loading at Point 1 represents elastic loading of the contact tie, which at unloading would follow the same elastic line back towards zero. Point 2 represents the initiation of damage in the contact, after this point all additional loading result in material softening and damage growth. For example, if loaded to Point 3 and then unloaded it is assumed that the contact (or material) will unload on a straight line back to zero; meaning that the shaded area represents energy irreversibly dissipated as damage in the bond. Therefore, the total area under the triangle (0, 2, 4) represents the energy required to delaminate the plies (at a given node), also known as the fracture energy [193]. Studies have shown that although the fracture energy of the bond has to be accurate, the initial stiffness and peak stress value do not need to be accurate [193], therefore an arbitrary stiffness value can be assigned and the peak stress adjusted accordingly (to maintain correct fracture toughness).

Although Figure 4-25 and the accompanying description detail the tensile loading behaviour of the constitutive law for bonding between plies, most applications require three-

dimensional modelling of interlaminate behaviour. Therefore, the normal (Mode I) and tangential (Mode II) displacements need to be 'mixed' for three-dimensional analysis [193].

There are three relative displacements between any two plies: δ_1, δ_2 and δ_3. The two tangential displacements can be combined into one shear displacement term [193]:

$$\delta_{II} = \sqrt{{\delta_1}^2 + {\delta_2}^2} \tag{4.29}$$

and Mode I is defined by normal displacement:

$$\delta_I = \delta_3 \tag{4.30}$$

The total mixed mode relative displacement can then be defined as:

$$\delta_m = \sqrt{{\delta_I}^2 + {\delta_{II}}^2} \tag{4.31}$$

and the mode 'mixity' can be given by:

$$\beta = \frac{\delta_{II}}{\delta_I} \tag{4.32}$$

The behaviour of a given bond under such mixed mode loading is illustrated in Figure 4-26 [193].

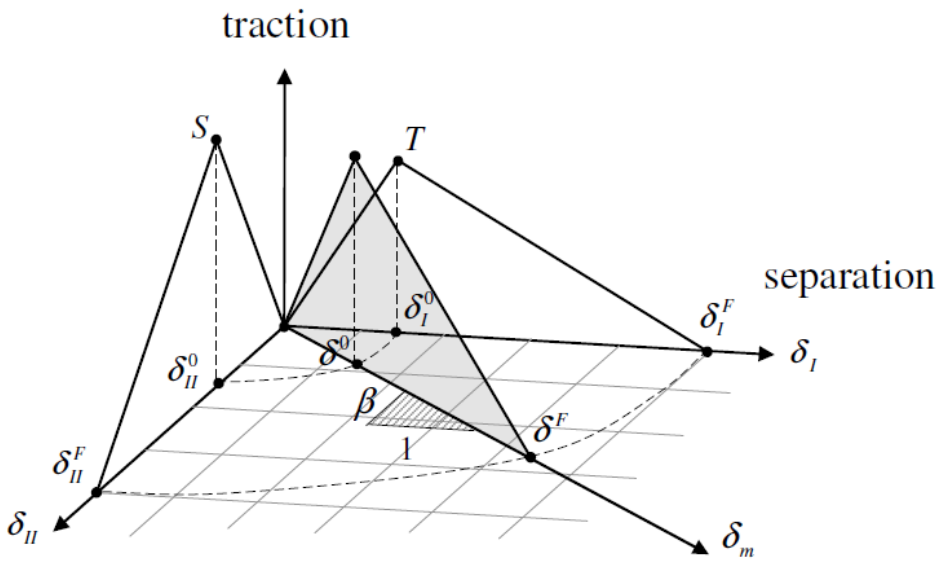

Figure 4-26. Mixed mode loading behaviour of a composite interlaminate bond as modelled through tiebreak contact in LS-DYNA, showing Traction-Displacement behaviour. S and T represent maximum tractions in shear and tension respectively.

As shown, through the simple terms and relationships discussed the mixed mode loading of the interlaminate bond can be effectively represented within LS-DYNA.

From reviewing the various methods and approaches to modelling the interlaminate bonds of composites within LS-DYNA, it is clear that the software is capable of modelling complex interlaminate composite behaviour. To ensure accuracy, it is desirable to possess the required fracture toughness material properties; however in their absence, option 6 within the tiebreak based contact algorithms may be employed as an approximate for delamination modelling.

4.5.3.3 Summary of LS-DYNA target modelling capabilities

From reviewing the literature and software documentation on the topics of modelling both polymers and composite materials within LS-DYNA it is clear that LS-DYNA can be considered a powerful tool for both.

The flexibility and adaptability of the polymer based constitutive material models mean, that with the appropriate material properties and data, most polymer materials can be effectively modelled within LS-DYNA. Additionally, the range of options with respect to modelling both the constitutive material behaviour and interlaminate response of composite systems is also a key strength.

The material models selected for the range of modelling campaigns of the research to be presented, are detailed and discussed in the relevant sections later.

5. Projectile Modelling Method: Assessment and Selection

It is clear that there are many viable methods for numerically modelling the impact of water and ice based projectiles, each with particular strengths and weaknesses. The following sections discuss the assessment process conducted for both rain drop and hailstone impact modelling techniques and establishes the most suitable methods; which were then adopted in wind turbine blade material impact analyses. Additionally, the establishment of a characteristic wind turbine blade leading edge layup/material configuration, for use in subsequent blade impact analyses is detailed; through drawing on examples in the literature and industrial consultation.

5.1 Rain Droplet

Through reviewing the literature on the topic of numerically modelling water droplet impact, Eulerian and Smooth Particle Hydrodynamic approaches were identified as potential modelling methods. Consequently it was decided that both methods would be utilised in a simple single droplet impact simulation in order to both validate the individual approaches and assess their strengths, weaknesses and applicability to subsequent blade impact analyses. The objectives of the simulations were to evaluate the forces and pressure generated and imparted by the droplet during impact as well as the internal shock response of the droplet. Therefore the material response of the target during impact was not of interest and the target could therefore be considered as rigid.

The basic configuration of the model and the implementation of each method are discussed in the following sections before reviewing the results and assessing and selecting the appropriate model.

5.1.1 Assessment Model Configuration

For the purposes of the assessment model a large droplet diameter of 3mm was selected, impacting a flat rigid target at a direct normal impact angle, as shown in Figure 5-1. Although early modelling work was conducted on a two dimensional basis, all subsequent work, and the analyses discussed from here onwards, were conducted on a fully three dimensional basis.

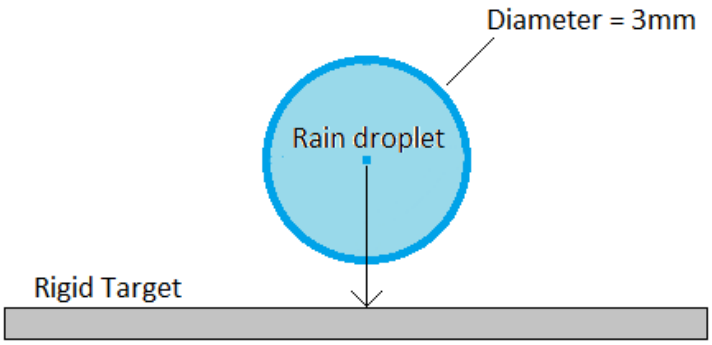

Figure 5-1. Schematic of model configuration, 3mm diameter water droplet impacting rigid target.

It was decided that an impact velocity range of 40-110m·s^{-1} would be simulated in order to cover the most likely impact velocities associated with impact on the blade leading edge, as well as to provide a wide span of results for analysis. The key model outputs from the analyses would be the impact force and impact pressure, which would then in turn be compared to the analytical equivalents from some of the equations previously described. Additionally the qualitative aspects of the impact simulations were also of interest, most notably the simulated droplet spreading phenomenon and the internal droplet shockwave behaviour.

Due to the high velocity nature of the impact events considered, the influences of droplet surface tension and contact friction were considered insignificant (as indicated by Adler [161]) and therefore were not included.

5.1.2 Eulerian Approach

During initial modelling work the ANSYS Explicit Dynamics STR [148] environment was utilised for the Eulerian modelling method.

5.1.2.1 Geometry Creation

The process of creating the 3D geometry was performed in the ANSYS Workbench, Design Modeller tool [194]. A base face 10mm square was first created, from which a 0.1mm extrusion was created to form the target plate. The raindrop geometry was created through sketching a half-circle geometry which was then revolved around its principle axis to create a sphere.

The plate geometry was then defined as a solid element and the droplet defined as a fluid before importing the geometry into the Explicit Dynamics [148] tool box.

5.1.2.2 Material Assignment & Body Interactions

As the target was to be set as a rigid body, the material assignment was completely arbitrary so was set as the default ANSYS material 'Structural Steel'.

The water droplet was assigned an in-built ANSYS material model 'WATER', modelled by a 'shock equation of state (EOS) linear', using the values given in Table 5-1.

Table 5-1. Water material properties (in-built ANSYS material 'WATER')

Property	Value
Density	998 $kg \cdot m^{-3}$
Shock EOS Linear	
Gruneisen Coefficient	0
C1	1647 $m \cdot s^{-1}$
S1	1.921
Parameter Quadratic S2	0

The droplet geometry was defined as an Eulerian body and the target geometry as Lagrangian which would subsequently affect the meshing process. The contact interaction between the two bodies was set as frictionless.

5.1.2.3 Meshing

A coarse hexahedral based mesh was applied to the rigid target plate geometry using the automated meshing tools within ANSYS, a fine mesh was not necessary due to the geometries rigid classification. Applying this mesh also created an arbitrary mesh for the droplet geometry; this process merely defines the shape of the droplet body within the applied Euler domain.

An Eulerian domain was created to incorporate only the space in which the Eulerian bodies (the droplet) would occupy, as shown in Figure 5-2.

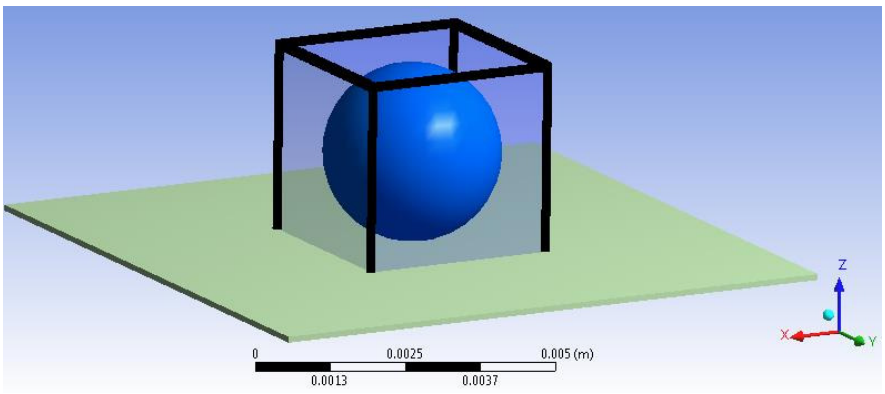

Figure 5-2. Droplet and plate geometry, showing the created Euler domain (black wire frame box) enclosing the droplet geometry

Care was required in taking account of the spreading of the droplet on the surface, as being a designated Eulerian body, the water droplet could only be modelled within this Eulerian domain. Therefore a restrictive sized domain would result in the flow being stopped at the domain boundary. In order to establish a suitable cell count (mesh) within the Euler domain, a sensitivity study was conducted to assess the effects of increased cell count on the output of the simulation, covering a range from 500 thousand to 1200 thousand cells; discussed further in the results section.

5.1.2.4 Boundary and Initial Conditions

As a rigid body, the target plate was automatically fully restrained and therefore the application of boundary conditions was not required. The required initial impact velocity was then applied to the droplet geometry. The simulation run time was varied for each impact simulation to take into account the differing impact durations (as a result of varying impact velocity).

The model was then set to output the pressure generated within the droplet during impact as well as the forced imparted on the target place by the droplet.

5.1.3 Smooth Particle Hydrodynamics Approach

LS-DYNA software [162] was utilised to implement an SPH approach to modelling rain drop impact. Both the pre and post processing work was performed using LS-PrePost [153] which is designed specifically for these tasks.

5.1.3.1 Geometry Creation

Although LS-PrePost has many geometry creation tools, it also allows for the direct creation of finite element bodies, whereby the geometry of the body is specified at the same as the element properties. As such, the target body was created in LS-PrePost utilising the 'Shape Mesher' tool (again 10x10x0.1mm), featuring a coarse uniform hexahedral mesh.

The droplet body was created through use of the SPH generation tool, by selecting a sphere geometry (many other pre-set shape types are available), entering a radius of 1.5mm and a material density value of 998kgm^{-3}. In order to fill the defined geometry with SPH nodes, a total node count within the geometry along the x, y and z axes required designation. As with the Eulerian analyses, a sensitivity study was conducted to establish the effects of SPH node total on the outputs of the model. The node total was varied across a range of 14k (14 thousand) to 113k nodes; also discussed in the results section.

Both the meshed target and nodes representing the water drop are shown in Figure 5-3, where it is possible to identify the individual constituent SPH nodes which make up the whole droplet geometry.

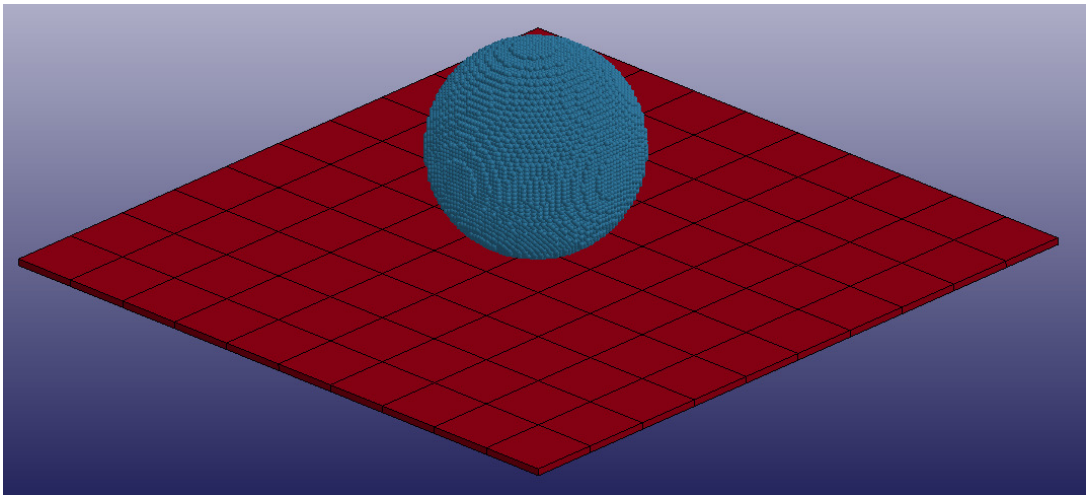

Figure 5-3. Meshed target geometry and SPH nodes representing water droplet

5.1.3.2 Material Assignment & Body Interactions

The material properties of the target were completely arbitrary and defined using the material model *MAT_RIGID, the water droplet was assigned the same material properties as used in the Eulerian analysis (Table 5-1). This was achieved through assigning them the material model *MAT_NULL and a Gruneisen equation of state *EOS_GRUNEISEN and entering the appropriate property values. The target body was assigned the section *SECTION_SOLID and the water droplet *SECTION_SPH

The interaction between the droplet and the target was defined by *CONTACT_AUTOMATIC_NODES_TO_SURFACE which assumes a frictionless sliding contact interface between the two bodies. As a result of the high number of SPH nodes featured in the simulation the frequency of contact checking was set to occur in every time step, in order to avoid unwanted undetected contact between the two bodies, which can result in artificial penetration of the SPH nodes through the solid elements. Due to the significant difference in stiffness of the two interacting bodies, the 'SOFT 1' option within the contact algorithm was activated, which improves the contact modelling between such bodies. From preliminary modelling efforts, it became apparent that as a result of these greatly differing stiffness levels and the nature by which contact is modelled within LS-DYNA, the results obtained from the simulations (such as force and pressure time history plots) displayed a high level of oscillatory behaviour. Consequently, it was decided that an additional sensitivity study should be conducted in order to evaluate the benefits of including

heightened damping in the contact algorithm, with the objective of smoothing out such oscillations and variance. The results of this contact damping sensitivity study are also discussed in the results section.

5.1.3.3 Boundary & Initial Conditions

The target geometry was fully restrained by fixing the nodes of the target body and the initial velocity was applied to the all the SPH nodes using the keyword *INITIAL_VELOCITY_NODE.

The simulation termination time was altered depending on the required impact duration. The time step reduction factor was set at 0.2 in order to maintain a small time step and reduce instabilities or contact errors.

A binary plot output time step of 0.1μs in order to provide a detailed visual output of the impact progression and to calculate a detailed pressure time history. The 'RCFORC' output option was invoked to record the impact force during the simulation.

5.1.4 Results

Result sets were populated for both approaches across the range of velocities stated. Some of the results are detailed and reviewed in the following sections in order to independently evaluate each method and assess the applicability of each approach with regard to modelling rain drop impact. Factors of consideration to this assessment are the force and pressures modelled during impact and the nature in which the two bodies interact and how this compares to the theory and observed reality of water droplet impact.

5.1.4.1 Eulerian

Eulerian Domain Resolution Sensitivity Study

Before a full set of analyses could be conducted across the range of proposed impact velocities, a sensitivity study was conducted to examine the effects of varying Euler domain cell totals on the outputs provided by the simulation. To do this, the simulations were run with cell totals of 500k, 600k, 800k, 1000k and 1200k and the force and pressure time histories for each plotted and compared, and the impact velocity set for these simulations was $100 m \cdot s^{-1}$. The impact force time history for all the analyses are shown for comparison in Figure 5-4.

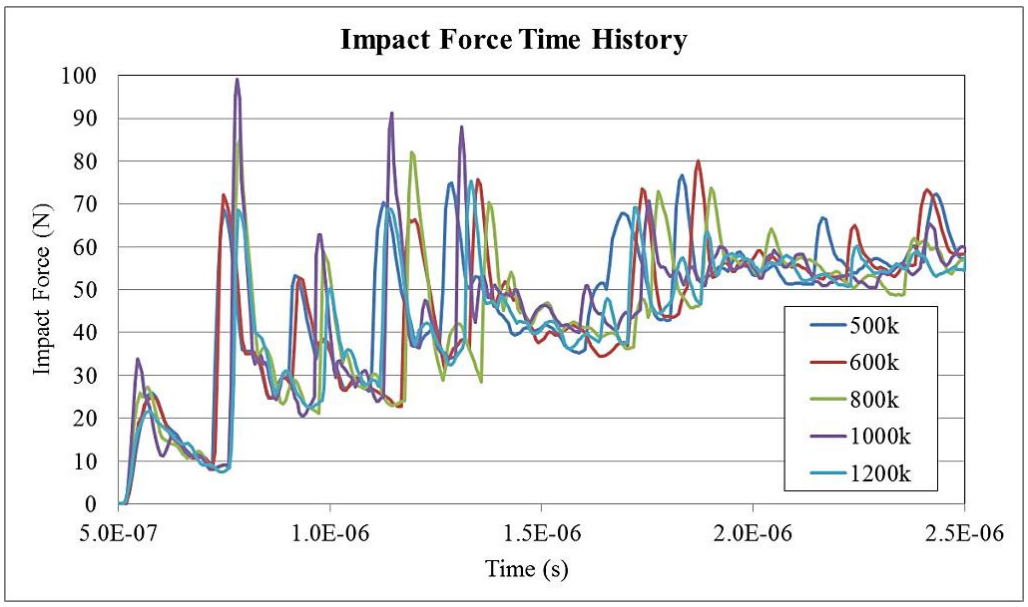

Figure 5-4. Impact force time history for Eulerian impact simulation using varying cell totals in Eulerian domain (100m·s^{-1} impact velocity).

Figure 5-4 shows varying (or increasing) the Eulerian domain cell count total had very little effect on the impact force imparted by the droplet on the target during the simulation. Therefore it would seem that increasing the cell total in an effort to increase accuracy with respect to impact force, has little benefit and results in no change. The effect of varying cell count on the pressure created in the droplet (and imparted on the surface) during impact is also shown in Figure 5-5. The plot shows the maximum value of pressure within the droplet geometry throughout the impact event.

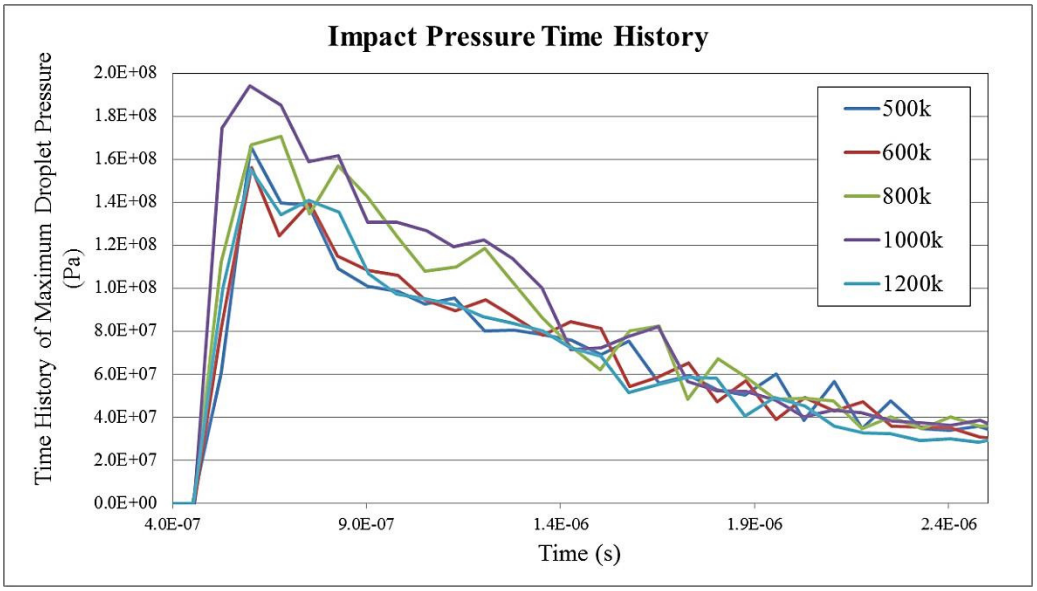

Figure 5-5. Impact maximum pressure time history for Eulerian impact simulation using varying cell totals in Eulerian domain (100m·s^{-1} impact velocity).

The pressure history results show that varying the Eulerian domain cell total has little significant effect on the impact pressure create during the simulation. From reviewing both plots it was decided that a cell total of 800 thousand would provide adequate accuracy at a reasonable computational cost. Subsequently all further simulations carried out for the validation assessment (across the range of impact velocities simulated) were conducted using this amount of cells, the results of which are discussed in the following.

Impact Results

All Eulerian based models created, ran successfully until the specified simulation end time. Solve times for the simulations ranged from around 40-60 minutes for a single impact event, depending on impact velocity and other parallel tasks being run on the machine.

One of the most basic and fundamental methods by which to preliminarily evaluate results from finite element analyses is to evaluate the temporal and spatial aspects captured by the simulation; and compare these to the expected real conditions. In the case of modelling water droplet impact, the droplet spreading behaviour is one of the key aspects which the model must fundamentally first capture before the qualitative results can be given any credence.

Figure 5-6 shows the droplet spreading behaviour (in profile) as predicted by the Eulerian modelling method.

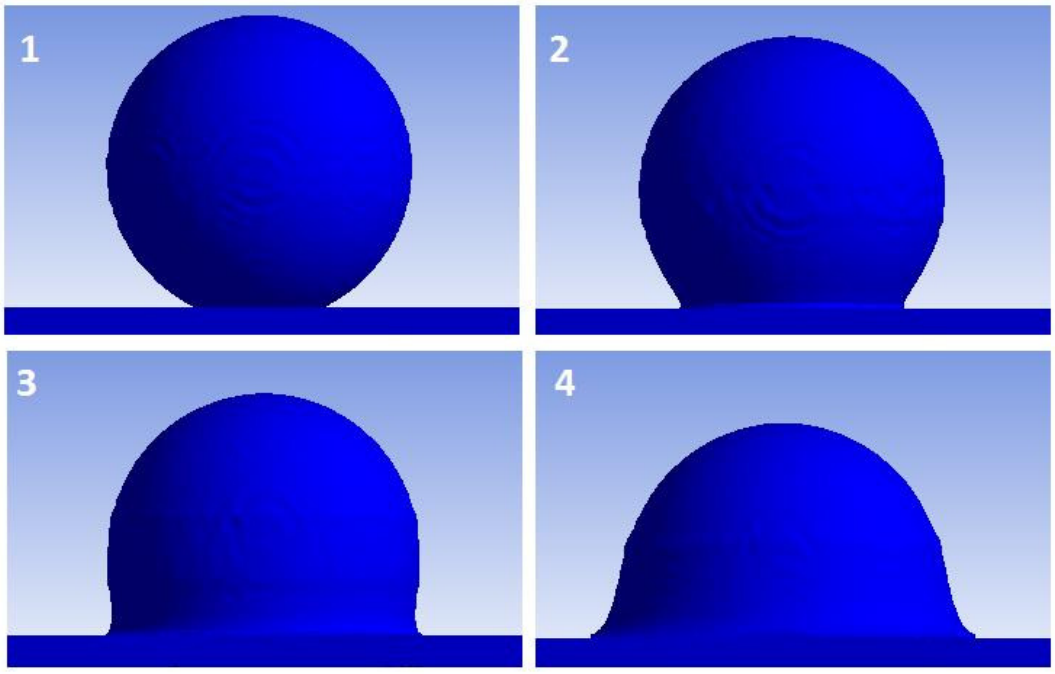

Figure 5-6. Water droplet spreading behaviour during impact as modelled with the Eulerian approach (shown in profile)

Here, it can be seen that the Eulerian method successfully models the droplet impact, spreading and subsequent lateral jetting. The issue of mesh stretching is not applicable due to the adaptive domain meshing method of the Eulerian approach, and therefore the droplet spreading behaviour and large geometric deformations are capably handled. Therefore, the Eulerian modelling approach captures the spatial and temporal aspects of water droplet impact on a flat solid surface well.

From each simulation (across the velocity range simulated) it was possible to extract and plot the forces imparted on the target geometry during impact. For example, Figure 5-7 shows the impact force time history of a 3mm diameter droplet impacting at 100m·s^{-1}.

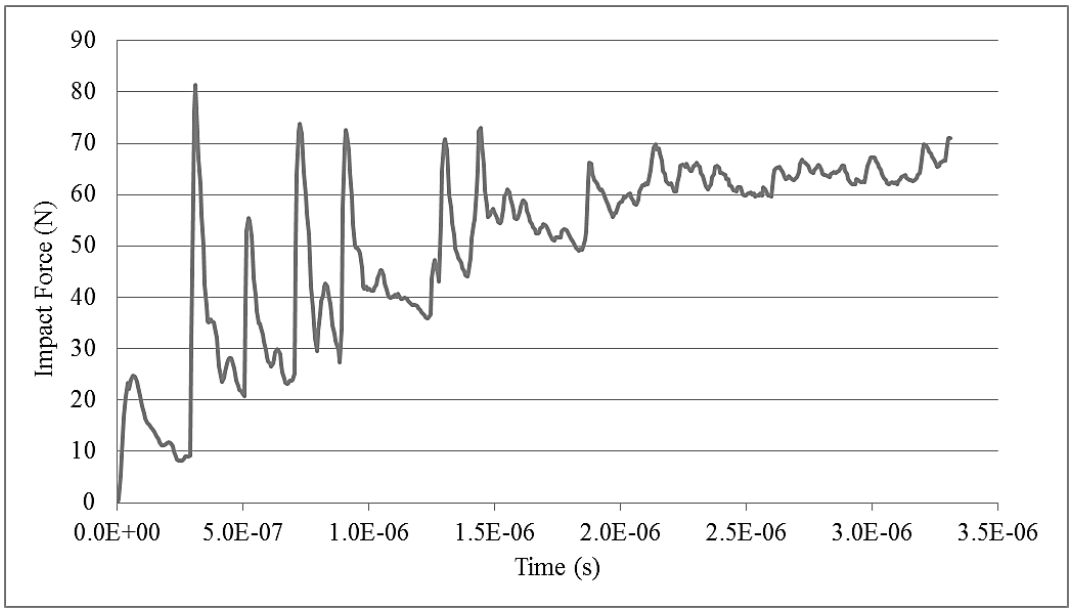

Figure 5-7. Impact force time history for a 3mm diameter droplet impacting at 100m·s^{-1}.

There is some variance in the force recorded; however there is a clear trend and a clear maximum of approximately 65N. Examining these force history plots for each impact velocity and ascertaining a maximum value of impact force makes it possible to plot the modelled relationship between impact velocity and maximum impact force. Figure 5-8 shows the modelled relationship between impact velocity and impact force obtained through the Eulerian modelling approach and compares the values of force obtained to those given by the theoretical impact force equation; described by Equation 3.6.

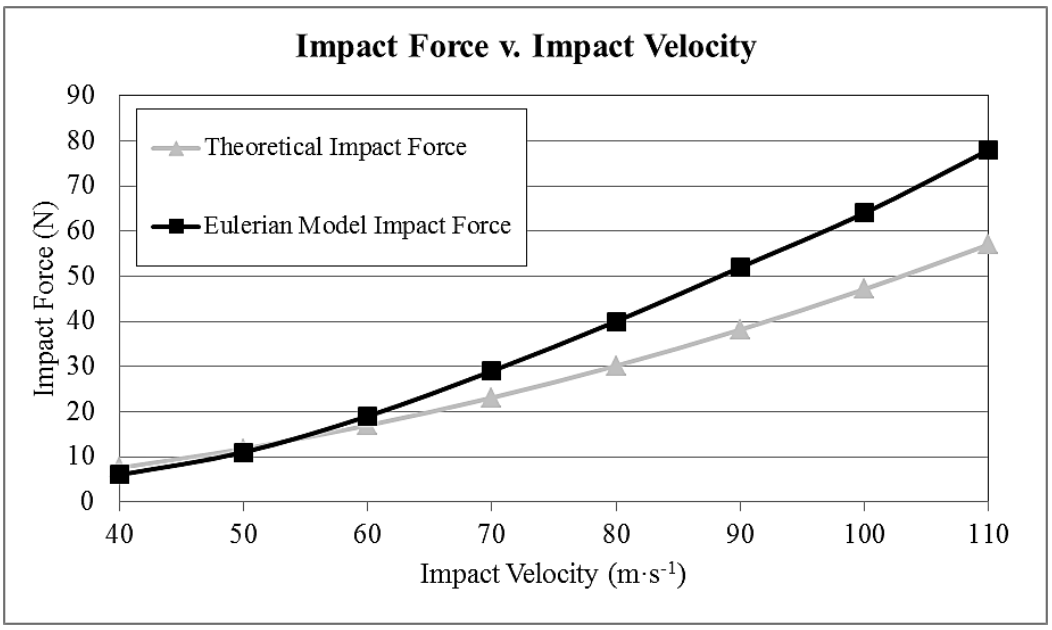

Figure 5-8. Comparison of water droplet impact force obtained through the theoretical impact force equation (Equation 3.6) and the Eulerian modelling approach, across a range of impact velocities.

It can be seen that in terms of magnitude, the modelled impact forces using the Eulerian approach compare well with the theoretically derived values; however it is important to remember that the values given by Equation 3.6 can only act as an approximate. The shapes of both curve are also comparable, however the modelling results tend to predict higher values of impact force when compared to the theoretical values.

It was also possible to review the pressure generated in the droplet during the Eulerian based simulations, both through plotting contours of pressure in the droplet geometry during impact and through time history plots of the maximum value of pressure during impact. Figure 5-9 shows contours of pressure in the 3mm diameter droplet impacting the rigid plate at 100m·s^{-1}, visible through creating a section cut through the droplet centre. It shows the progression of pressure shockwaves created in the droplet during the impact sequence.

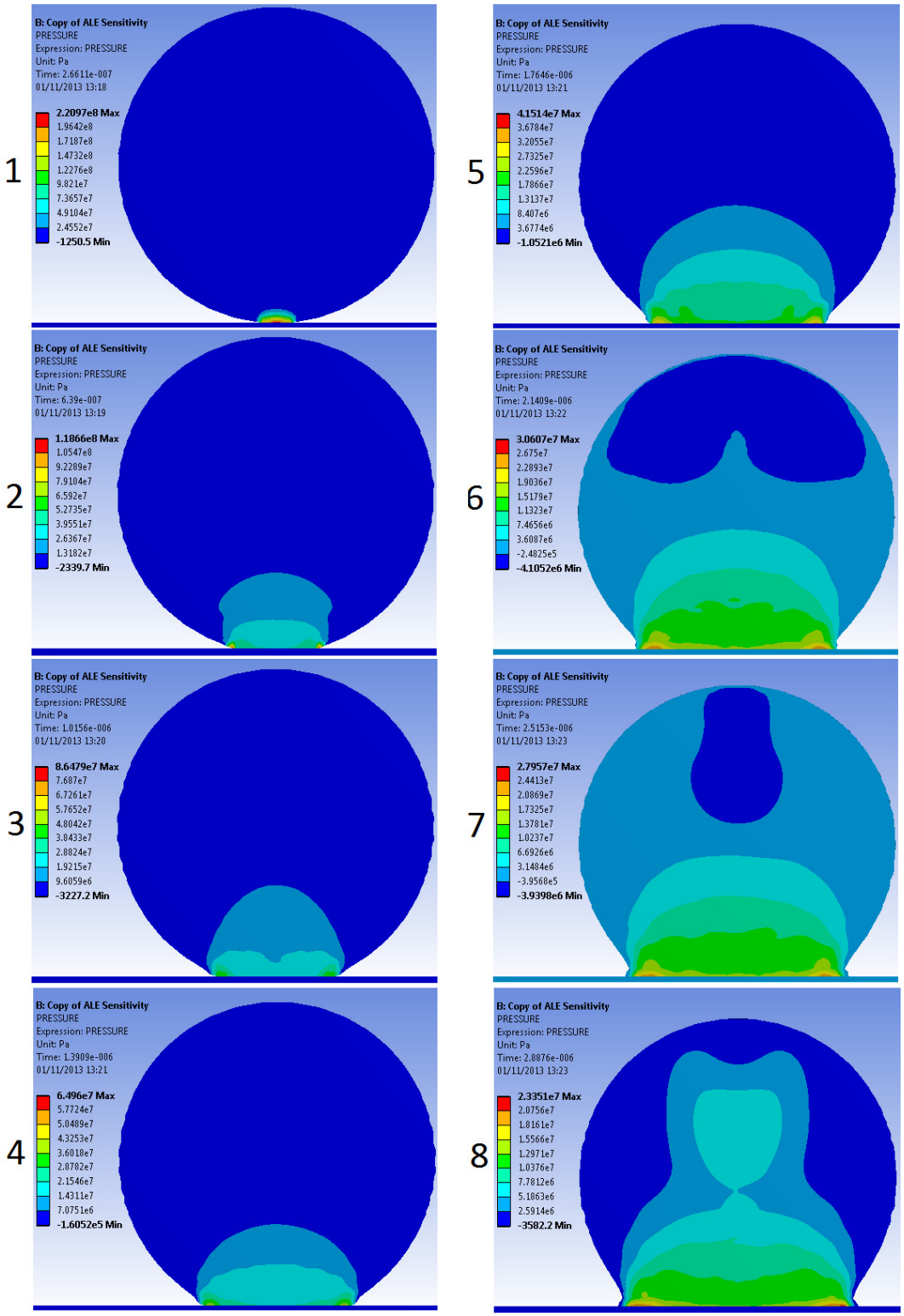

Figure 5-9. Time sequences showing the development and propagation of pressure (contoured) within a 3mm diameter water droplet during 100m·s^{-1} impact on a rigid surface. The droplet is sectioned through its centre to show internal effects. Note also that the range of contours changes at each time step.

As shown, the initial creation of the waterhammer pressure occurs almost instantaneously upon impact with the surface (frame 1). This value of pressure can be designated as the

waterhammer pressure as it occurs at the contact interface between the droplet and the target surface. A pressure wave is then propagated radially away from this initial contact zone upwards through the droplet, as illustrated in frames 2, 3 and 4. Between frame 4 and 5, the transition from the initial waterhammer creation phase to the lateral jetting phase can be observed, with the droplet exhibiting spreading behaviour at the periphery of the contact area. Although the maximum and average pressure in the droplet decreases following the creation of the initial waterhammer pressure, it can be observed that during the droplet spreading phase (frame 5-8) highly localised peak pressures are generated at the areas of lateral jetting; at the periphery of the contact area between the droplet and target surface. This phenomena highlights the necessity of not only considering the initial waterhammer pressure phase when investigation rain impact on materials, but of also considering the latter phases of droplet spreading and the added localised effects this may have.

The nature of pressure propagation as captured through the Eulerian modelling approach and illustrated in Figure 5-9 compares well with other examples in literature, such as Adler [161] (Figure 4-4), Li et al. [102] (Figure 4-3) and Gohardani [79] (Figure 3-17). Therefore, it would seem that these results act to further qualify the qualitative aspects of the pressure distribution results obtained through the Eulerian based approach.

In addition to examining the qualitative aspects of pressure creation and dissipation in the droplet during impact, it was also possible to quantitatively examine the results obtained through the Eulerian approach with regards to pressure generation. For example, Figure 5-10 shows the time history of the maximum value of pressure in the droplet during a $100m \cdot s^{-1}$ impact simulation.

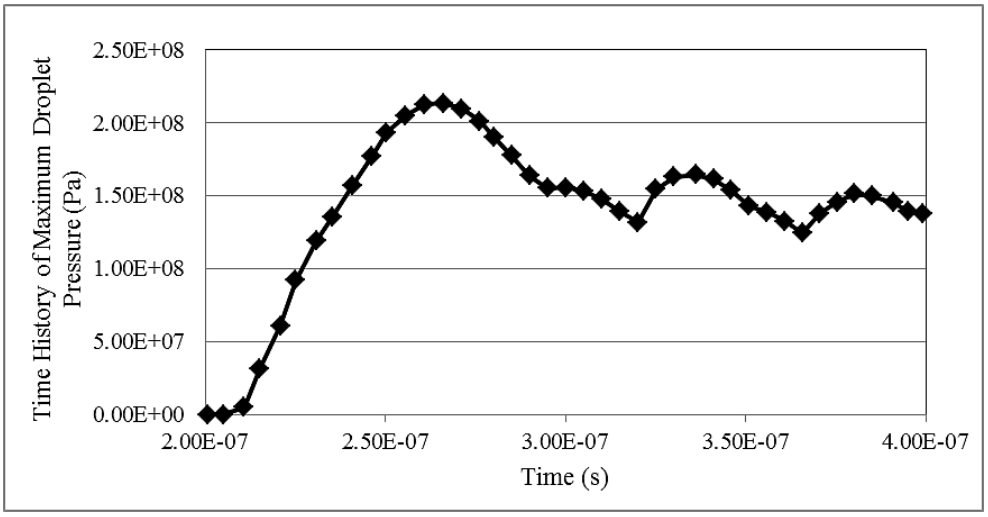

Figure 5-10. Time history of impact pressure created in 3mm diameter droplet geometry during $100m \cdot s^{-1}$ impact, modelled through Eulerian method.

A clear initial peak pressure value is created during the initial stages of contact between the droplet and the rigid surface, the maximum pressure value then begins to decrease, however subsequent peaks can also be observed. This maximum value represents the initial waterhammer pressure value.

Again, as with the method of reviewing impact force, it is possible to examine and identify such peak waterhammer pressure values across the range of impact velocities simulated with the Eulerian based approach. Doing so allows for comparison of these values to those predicted by the waterhammer equation (Equation 3.4). Figure 5-11 compares the maximum peak pressure values obtained across the range of impact velocities simulated through the Eulerian based approach, to the values predicted by the waterhammer equation (Equation 3.4), based on a speed of sound in water of 1500m·s^{-1} and a water density of 1000kg/m^3.

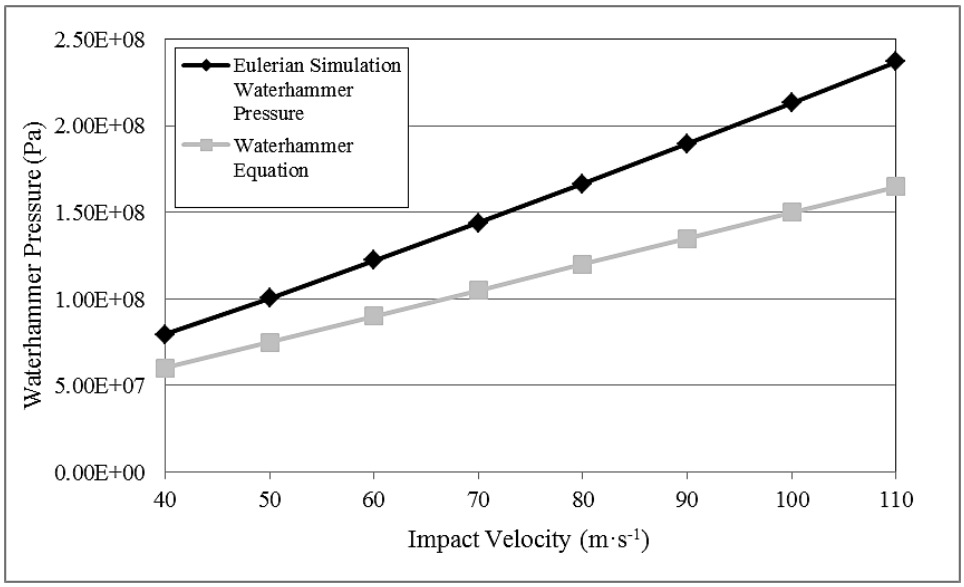

Figure 5-11. Comparison between predicted values of maximum pressure generated in a 3mm diameter water droplet during direct impact on a rigid surface (across a various impact velocities), using both the Eulerian based modelling approach and the theoretical waterhammer equation (Equation 3.4).

It is observed that there is reasonableagreement between the waterhammer pressure values predicted by both the Eulerian modelling approach and the waterhammer equation (Equation 3.4). The orders of magnitude of pressure are comparable as are the slopes of the lines – or the trend in increasing pressure – between the two value sets.

From reviewing the modelling outputs and data obtained, it is clear that with respect to modelling water droplet impact on a flat rigid target surface, the Eulerian modelling approach provided satisfactory results both qualitatively and quantitatively, when compared to theoretical approximations and observed and documented phenomena in the literature.

However, although there are indications of the modelling approach capturing aspects of the high pressure generation phenomenon at the onset of droplet spreading, they are not as prominent as suggested in the literature [161] [98] [102].

5.1.4.2 Smooth Particle Hydrodynamics

SPH Node Total Sensitivity Study

As with the Eulerian modelling process, a sensitivity study was conducted for the SPH approach to evaluate the effects of the total SPH node count on the outputs of the analyses. In order to evaluate this, the total SPH node count was varied between: 14k, 33k, 65k and 113k, for a 100m·s^{-1} impact velocity. Again, the key outputs of interest from the simulation were both the force and pressure time histories. Figure 5-12 shows the impact force imparted by the rain drop during the simulation, using the various node totals previously detailed.

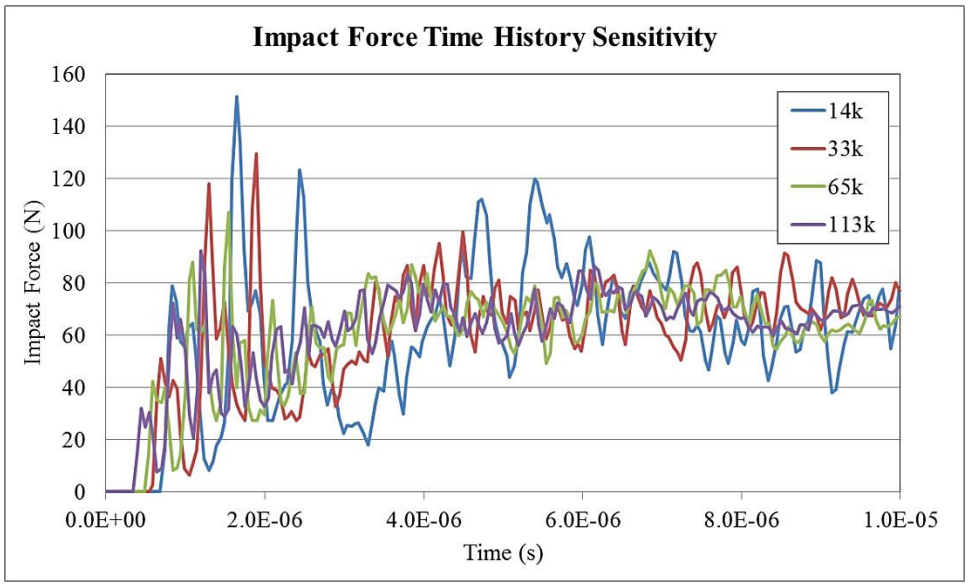

Figure 5-12. Impact force time history for SPH impact simulation using varying amounts of SPH nodes to represent the rain droplet (100m·s^{-1} impact velocity).

From the impact force time history results for the numerous simulations, it can be seen that increasing the total amount of SPH nodes representing the droplet body resulted in a smoother force history plot. However the smoothing effect was only slight, for a considerable increase in node total, therefore it may be suitable to opt for an intermediate value for total SPH nodes instead of setting a high and more computationally expensive value. To provide further insight it was possible to also review the effects of increasing SPH node count on the pressures created in the droplet during impact. Figure 5-13 shows the maximum pressure exhibited within the droplet body during impact with varying SPH node totals.

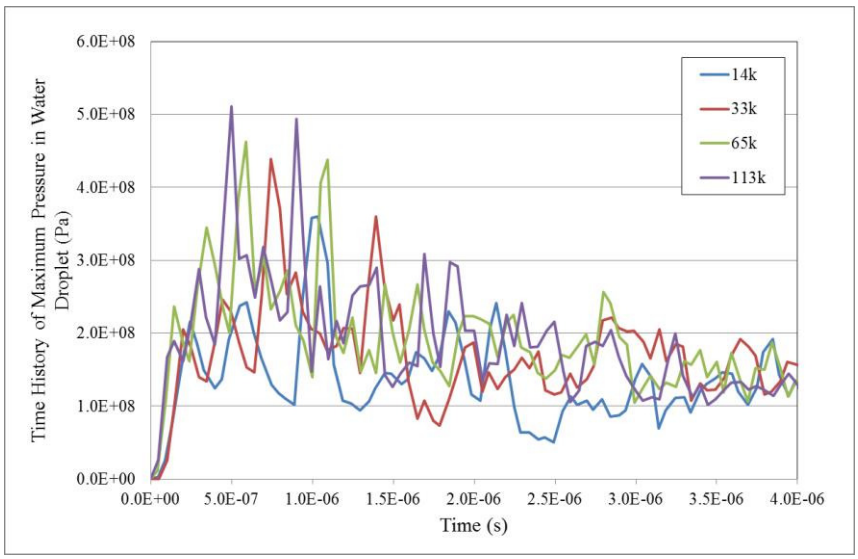

Figure 5-13. Maximum pressure in water droplet during impact, modelled using varying SPH node totals.

It is clear that the maximum value of pressure within the droplet during impact is highly oscillatory and erratic when modelled with a SPH approach. However these trends show the maximum pressure exhibited in any node anywhere in the droplet geometry during impact, and therefore these highly variable effects are averaged out across whole geometry (as will be discussed and illustrated later). With respect to the node total used to represent the droplet, it appears that with respect to the pressures created, the node total has no significant impact on the results.

From reviewing the force and pressure time history plots, it was decided that a node count total of 65k nodes would provide satisfactory results at relatively low computational costs; therefore this value was used in all subsequent SPH rain droplet analyses; except where stated otherwise.

Contact Damping Sensitivity Study

Due to the nature of SPH simulations, contact between an SPH body and a flat meshed surface can result in high frequency oscillation in model output (as illustrated in previously in Figure 5-12 and Figure 5-13). This can be attributed to the way in which contact is model, whereby each individual SPH node has a contact relationship with the target surface as well as interacting with surrounding SPH nodes. As such, large spikes in contact force can be created, subsequently leading to spikes in the pressure exerted on the target surface and the stresses created within the target. To combat the oscillations and spikes associated with SPH contact, it was decided that the effects of introducing damping to the contact definition would explored and assessed. Using the same SPH validation model set up as described

previously (i.e. direct impact on a rigid flat surface target), varying levels of viscous damping were introduced to the contact algorithm through assigning a percentage value to the damping coefficient 'VDC' parameter within the *CONTACT_AUTOMATIC_NODES_TO_SURFACE contact algorithm. Viscous damping coefficient values of 40%, 60%, 80% and 100% were implemented in order to assess the effects of increasing damping in the contact algorithm. In the interest of time and computational resources, the contact damping sensitivity analysis work was conducted using 33k SPH nodes to represent the droplet (as opposed to 65k, as used in later validation modelling); additionally a single impact velocity of 100m·s^{-1} was set for each simulation in the study.

Figure 5-14 shows the droplet spreading behaviour exhibited in the latter stages of the SPH impact simulations both in the absence of contact damping and with increasing values of damping.

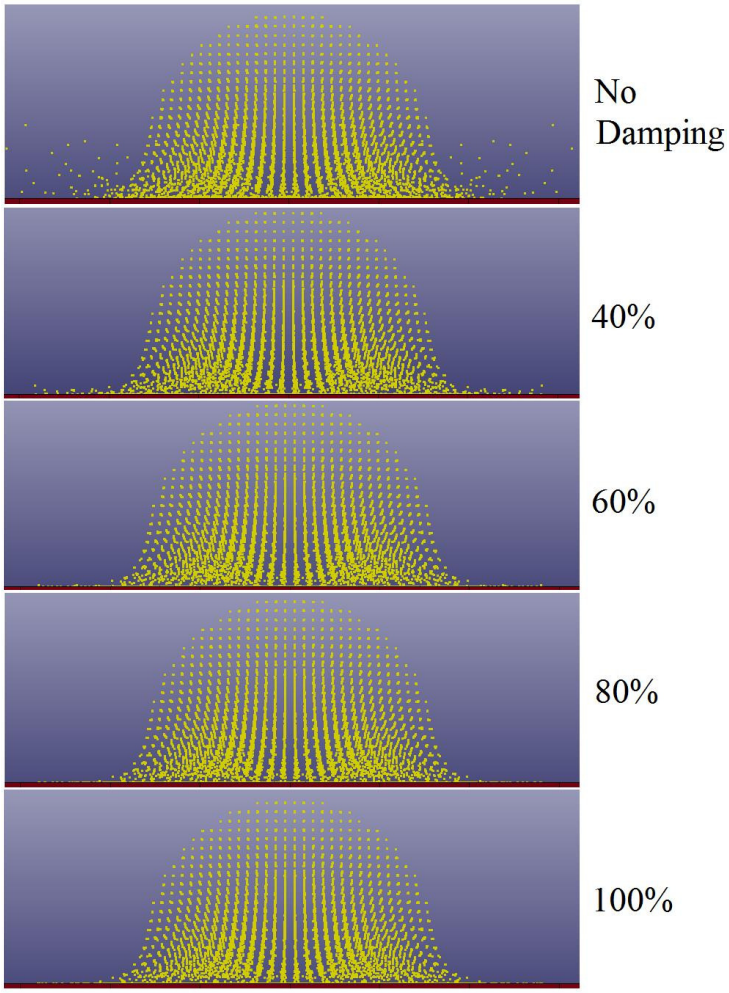

Figure 5-14. Spreading behaviour of a 3mm diameter droplet with impact velocity of 100m·s^{-1} modelled using and SPH approach, both without contact damping and with increasing values of contact damping.

Qualitatively, introducing viscous damping to the contact algorithm between the nodes and the surface results in a decrease in the occurrence of stray nodes and results in a more fluid-like impact spreading behaviour. However it is also clear that for values of damping of around 60% and upwards there is very little difference or change in the spreading behaviour; at least visually.

It was also possible to examine the effects of increasing contact damping on the impact force and water droplet pressure time histories. Figure 5-15 shows the effects of increasing contact damping on the impact force created between the droplet and the target surface during simulation.

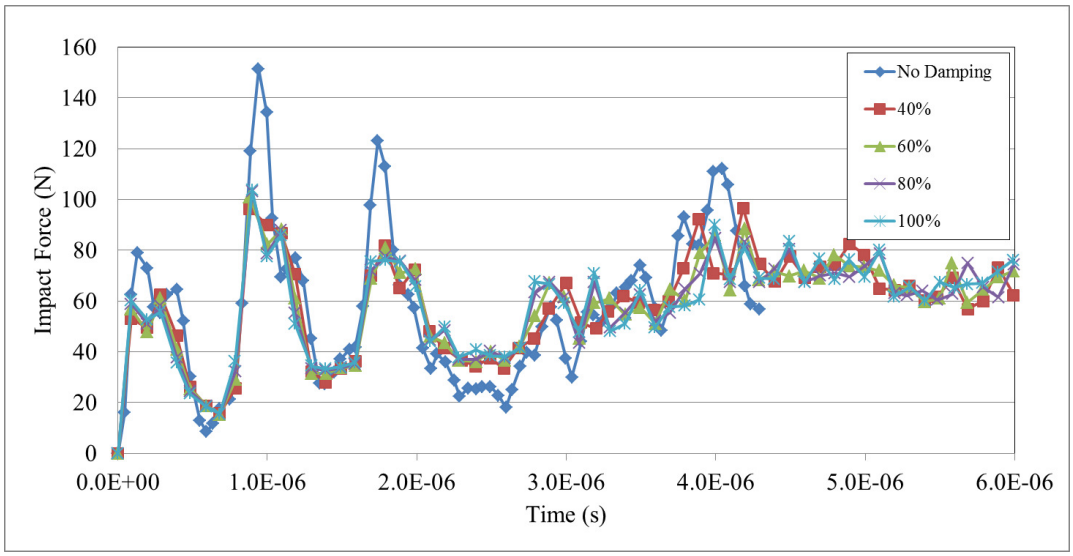

Figure 5-15. Impact Force Time history for a 3mm diameter water droplet impacting a rigid flat surface at 100m·s^{-1}, showing the effects of introducing varying levels of viscous damping to the contact algorithm.

From Figure 5-15 it can be seen that introducing damping effects to the contact algorithm acts to decrease peaks in the impact force history output and smooth out the overall output. However, as with the effects on the droplet spreading behaviour discussed previously, increasing the value of percentage damping above around 40-60% does not appear to significantly further smooth out the force output.

Similarly, it is also possible to examine the effects of increased damping effects on the pressure generated within the droplet during impact. Figure 5-16 shows a time history of the maximum value of pressure generated within the droplet during a simulated 100m·s^{-1} impact; with varying levels of applied damping.

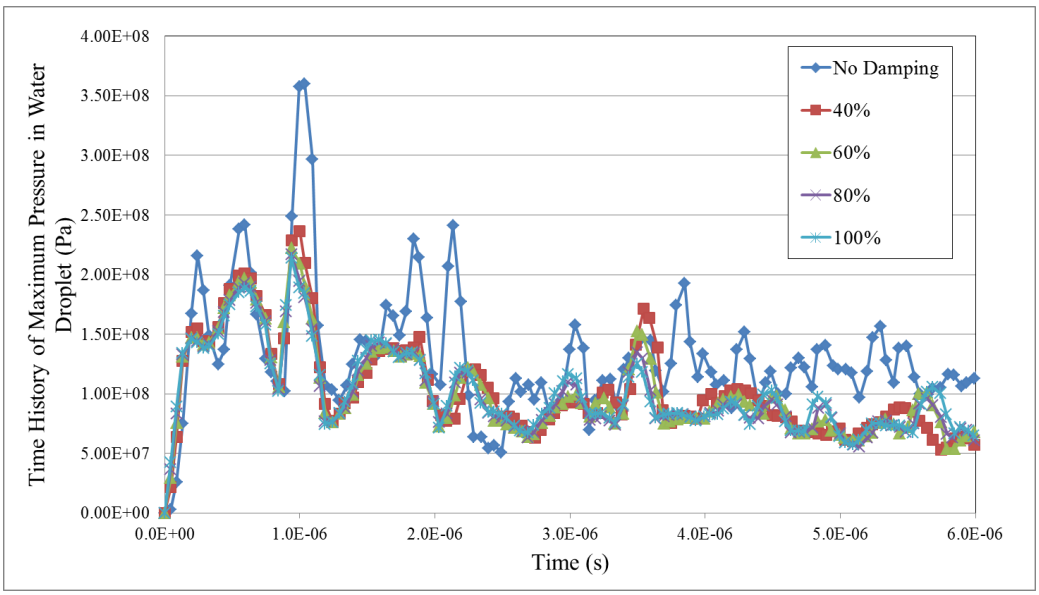

Figure 5-16. Maximum droplet pressure history for a 3mm diameter water droplet impacting a rigid flat surface at 100m·s^{-1}, showing the effects of introducing varying levels of viscous damping to the contact algorithm.

Introducing damping effects to the contact algorithm also reduces the occurrence of sharp peaks and drops in the value of maximum pressure generated within the water droplet during impact simulation. However, as with the droplet spreading behaviour (Figure 5-14) and impact force (Figure 5-15), increasing the percentage value of viscous damping in the contact algorithm above values of 60% appears to have little effect on the output.

From the results discussed from the damping sensitivity study, a viscous damping coefficient of around 40-60% provides adequate damping and improved model outputs. Increasing the level of damping to values greater than this appears to have a reduced effect on the model outputs. For this reason, the rest of the SPH approach validation modelling work was conducted using a viscous damping coefficient value of 60%.

Impact Results

All SPH based models created, ran successfully until the specified simulation end time. The total run time for the individual impact simulations ranged from around 10-15 minutes.

Before the quantitative aspects of the results from the SPH analyses could be reviewed, it was helpful to first review the spatial and temporal developments of the impact analyses. Figure 5-17 shows the droplet spreading behaviour as captured by the SPH modelling approach for a 3mm diameter water droplet impacting the rigid flat surface at 100m·s^{-1} (in profile).

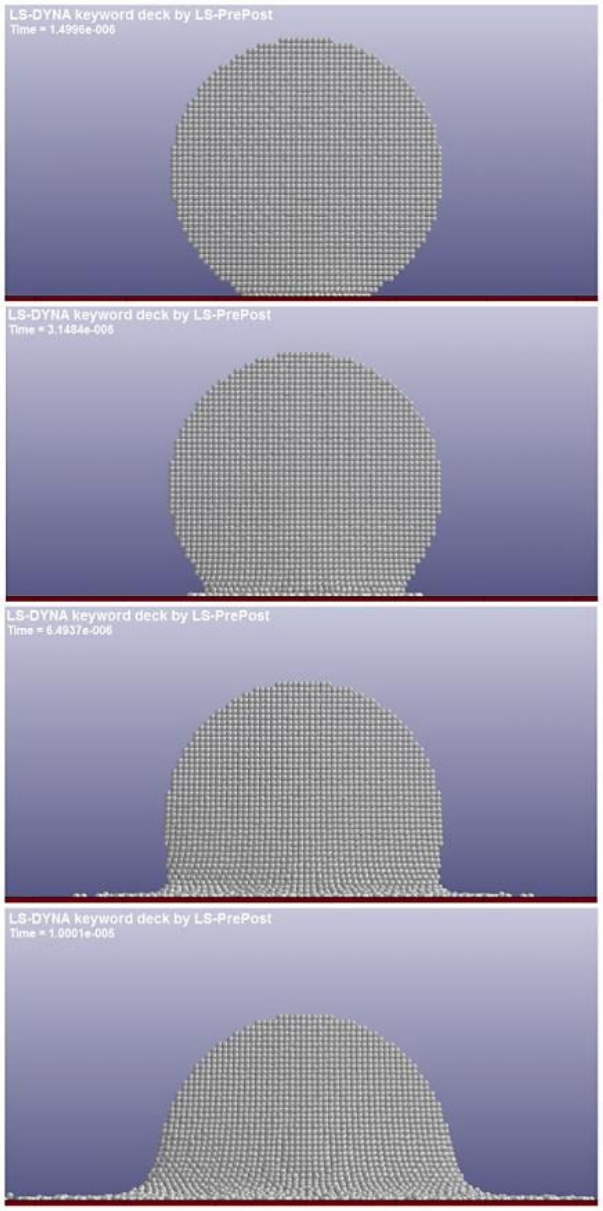

Figure 5-17. Droplet spreading behaviour of a 3mm diameter water droplet impacting a flat rigid target at 100m·s^{-1} (3D – shown in profile) modelled using the SPH method.

In Figure 5-17, the SPH modelling approach creates droplet spreading behaviour synonymous to that as described in the literature [161] [79] [98] and also modelled with the Eulerian based approach; discussed and shown previously in Figure 5-6 and Figure 5-9. Therefore, despite the node-based nature of the SPH based water droplet, the impact behaviour can still be described as fluid-like and representative of typical water droplet spreading as described in literature and observed in nature [79] [102] [161].

It is possible also to plot the velocity magnitude for each SPH node, to better understand the flow behaviour of the spreading droplet. Figure 5-18 plots the resultant velocity associated

with each SPH node shortly after the onset of lateral spreading at the droplet contact periphery.

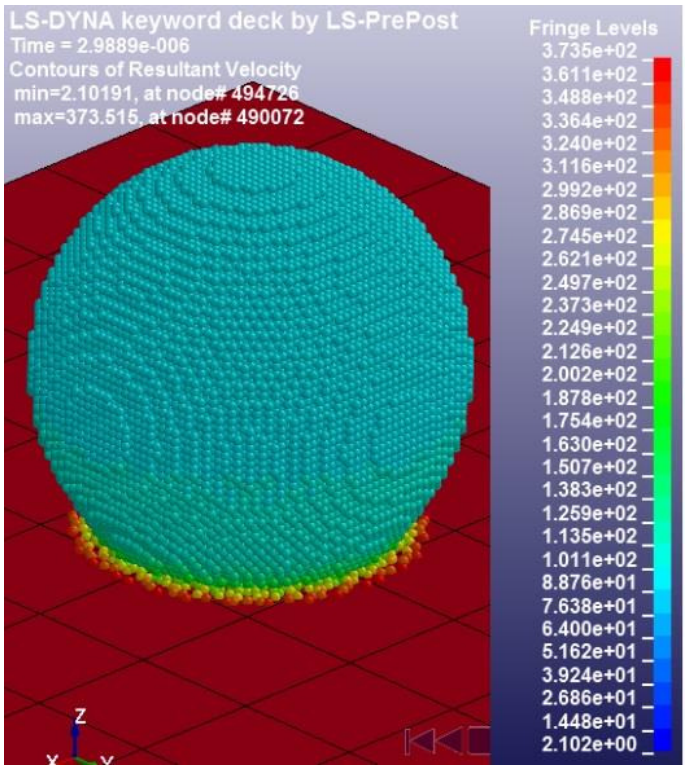

Figure 5-18. A plot showing contours of resultant velocity of the SPH nodes representing a 3mm diameter droplet, during an impact event with an initial velocity of 100m·s^{-1}; shortly after the onset of lateral spreading.

At this point of the impact event, the main body of water (as a whole) has decelerated from 100m·s^{-1} to around 70-80 m·s^{-1}. However, it is clear that at the wave front of the lateral spreading area of the droplet, the velocity of the water has more than doubled in some areas; and in the outermost regions almost quadrupled in magnitude. This phenomenon of rapid acceleration at the wave front of the laterally spreading areas of the droplet appears to agrees with the observations in the literature [102] [100].

In the Eulerian analysis discussed previously, to validate the quantitative aspects of the SPH based modelling approach, the impact forces imparted and pressure generated within the droplet during simulation were reviewed across the range of impact velocities previously specified.

Figure 5-19 shows the time history of contact force between the 3mm water droplet and target surface during a 100m·s^{-1} impact event, as modelled through the SPH approach. The raw contact force data is shown in blue and shows a degree of variance; however it is

possible to apply point averaging techniques to the data to provide a smoother output and provide a clearer indication of the overall trend, as shown in purple.

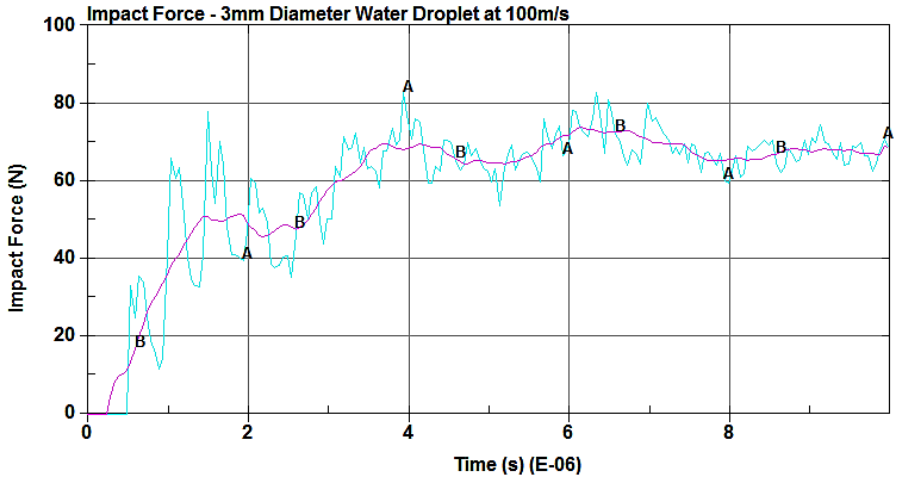

Figure 5-19. Impact force time history for a 3mm diameter water droplet impacting flat rigid surface at 100m·s^{-1}. Showing unfiltered (blue) and filtered (purple) data.

The impact force imparted by the water droplet rises sharply upon contact and then steadily flattens out to a maximum value of approximately 70N. From reviewing such impact force time histories across the range of impact velocities simulated, it is possible to examine the maximum impact force imparted by the 3mm diameter droplet across the range of velocities as simulated through the SPH based approach. Figure 5-20 plots these maximum force values against the associated impact velocities and compares them to the theoretical impact force values as predicted by Equation 3.6.

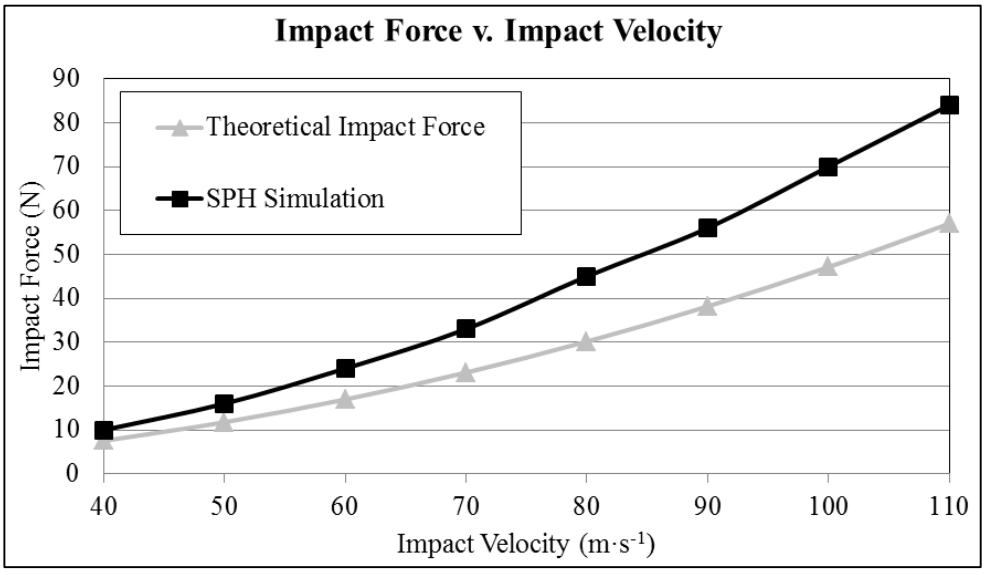

Figure 5-20. Comparison of water droplet impact force obtained through the theoretical impact force equation (Equation 3.6) and the SPH modelling approach, across a range of impact velocities.

There is good overall agreement between the impact forces predicted by the theoretical impact force equation (Equation 3.6) and the forces simulated in the SPH based modelling work. Quantitatively, there is strong agreement between the two data sets at lower impact velocities; however there is a divergence in the trend with increasing impact velocity as similarly observed in the Eulerian modelling results (Figure 5-7).

As with the Eulerian analyses, it is also possible within LS-PrePost to plot contours of pressure in the droplet during impact, and through creating a section cut through the centre of the body it is possible to view the pressure wave propagation within the droplet during impact. Figure 5-21 shows contours of pressure within the 3mm diameter water droplet during a $100 m \cdot s^{-1}$ impact simulation; visible through creating a section through the droplet.

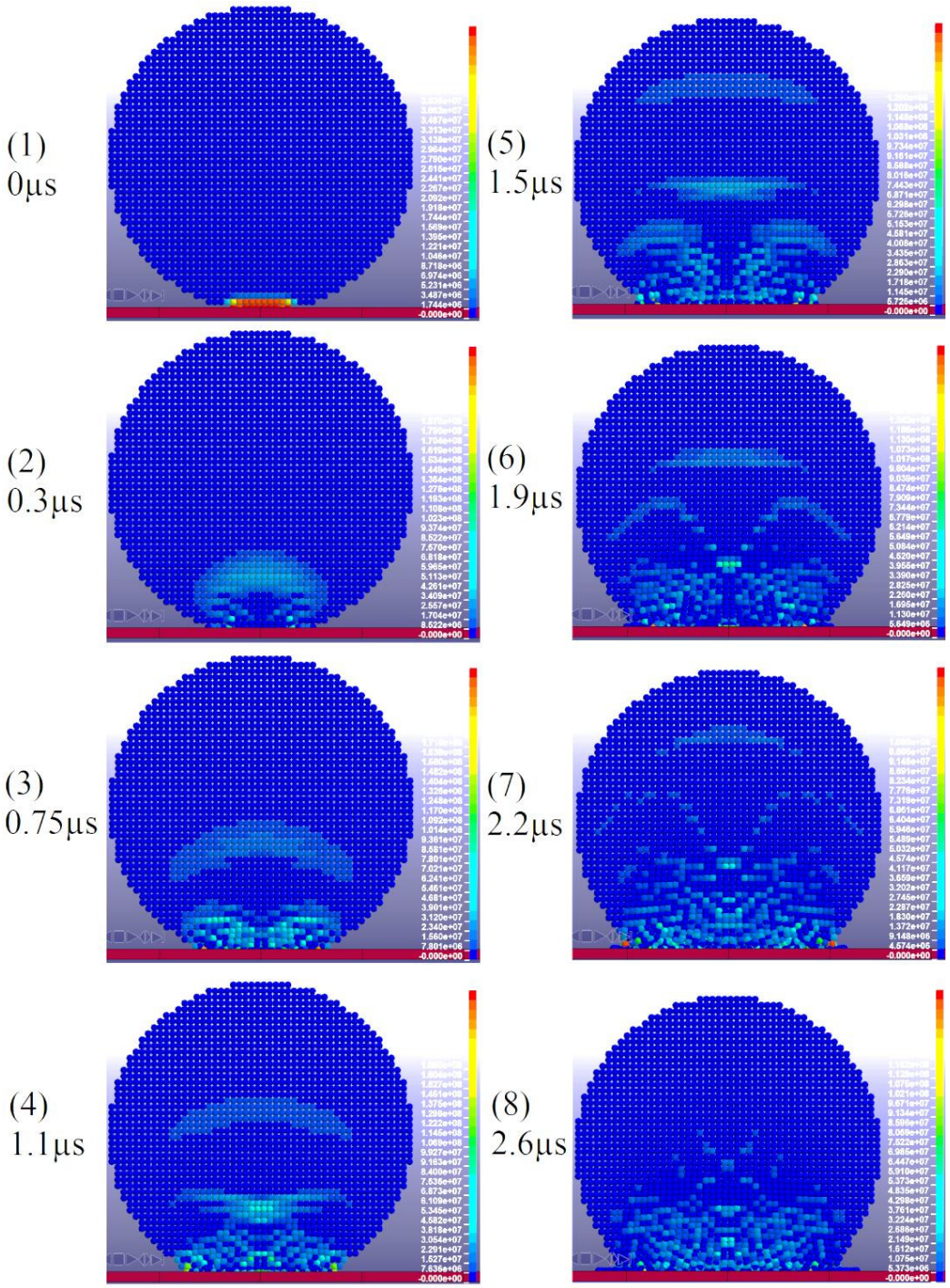

Figure 5-21. Contours of pressure in water droplet during 100m·s^{-1} impact. Showing a section view through the centre of the droplet profile. Units in Pascals.

Upon impact the peak waterhammer pressure is generated almost instantaneously. A pressure wave is then propagated upwards through the droplet, spreading radially away from the impact location, showing good agreement with findings in the literature [161] [79] [102] and the Eulerian modelling work described previously (and illustrated in Figure 5-9). After this initial propagation, and beginning in frame (3), it is possible to observe the creation of

areas of high pressure at the periphery of the contact area between the droplet and the surface. Subsequently, pressure waves can then be observed to propagate away from these areas through the droplet and interact with one another in the central region of the droplet.

Figure 5-22 shows the time histories of the maximum value of pressure exhibited within the water droplet during impact for each of the impact velocities simulated.

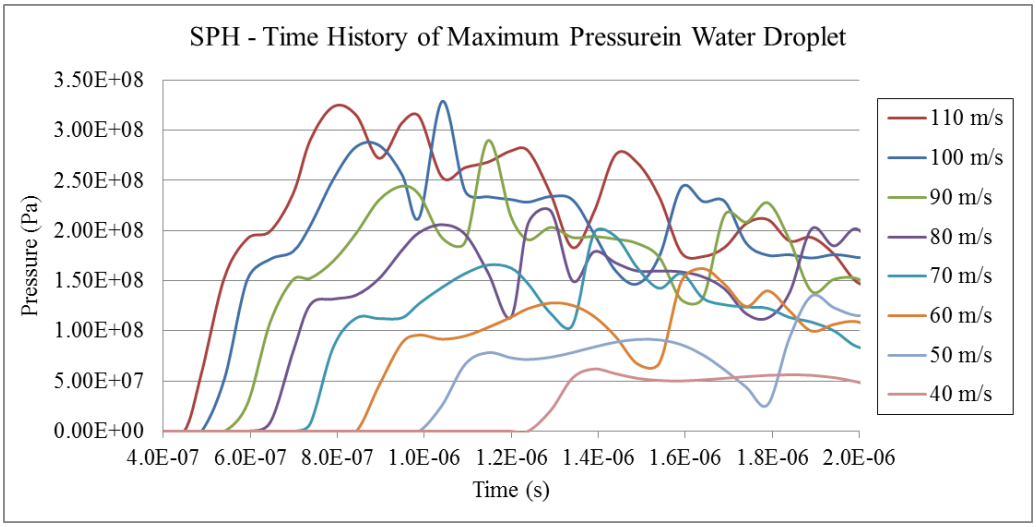

Figure 5-22. Time history of maximum pressure created within 3mm diameter droplet impacting a flat rigid surface at various impact velocities, utilising SPH based modelling approach.

It is noted, across the range of impact velocities simulated, an initial peak impact pressure is created within the droplet followed by a higher secondary peak. The initial peak may be designated as the waterhammer pressure as it occurs almost instantaneously upon impact and is generated at the droplet-surface interface. The secondary peak pressure is created at the periphery of the contact area between the droplet and the surface at the onset of spreading and outward jetting; forming a ring of high pressure at the contact edge. This phenomenon agrees with the findings of Heymann [98] and others [161] [102]; as discussed previously in Section 3.2.3. In most cases, the pressure created in these regions are double that of the initial waterhammer pressure peak.

Figure 5-23 plots the values of waterhammer pressure from Figure 5-22 against their associated impact velocities and compares them to values predicted by the waterhammer equation (Equation 3.4); assuming a water density of 1000kg.m^{-3} and a speed of sound in water of 1500m·s^{-1}.

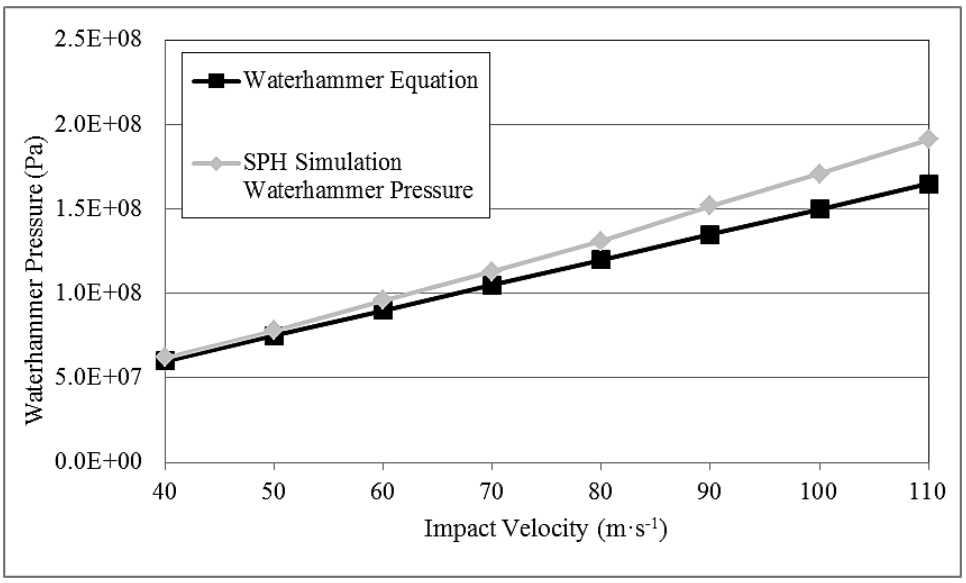

Figure 5-23. Comparison between predicted values of maximum pressure generated in a 3mm diameter water droplet during direct impact on a rigid surface (across a various impact velocities), using both the SPH based modelling approach and the theoretical waterhammer equation (Equation 3.4).

From Figure 5-23, there is good agreement between the values of waterhammer pressure obtained through the SPH based simulations and the values predicted by the waterhammer equation, both with respect to the actual values and the overall trend in the relationship between the waterhammer pressure and the impact velocity.

From reviewing both the qualitative and quantitative aspects of the result data obtained through the SPH based water droplet impact modelling approach described, it is clear that the method effectively captures the nature of water droplet impact on a solid surface; as described in the literature [161] [79] [98] and predicted by the analytical approximations discussed. Both the forces and pressure created during impact compare well to analytical predictions, and the spatial and temporal aspects of droplet impact and spreading are well represented. Additionally, the SPH approach appears to capture the phenomenon of high pressure generation in the droplet at contact periphery during the onset of lateral jetting.

5.1.5 Evaluation of Methods

Both the Eulerian and SPH approaches provided satisfactory outcomes with respect to modelling the phenomena of water droplet impact on a solid surface. Both methods gave impact force and pressure results comparable to that of the values derived through analytical means. The spatial and temporal aspects of the impact events were also successfully capture with regard to the impact and spreading behaviour upon impact.

In the interest of evaluating and comparing the suitability of each modelling approach, it is possible, furthermore, to compare the results obtained through each method. Figure 5-24 shows the impact force time histories for a 3mm diameter water droplet impacting at 100m·s^{-1} obtained through both the Eulerian and SPH approaches.

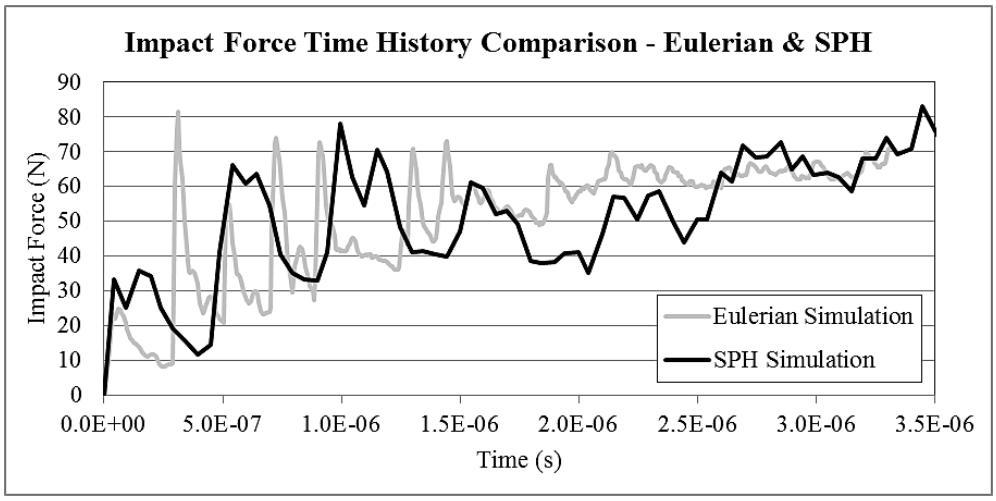

Figure 5-24. Impact force time histories for a 3mm diameter water droplet impacting at 100m·s^{-1} as obtained through both Eulerian and SPH based analyses.

Although both methods show some level of noise and variance in the force history results create (shown in Figure 5-24), both have an observable comparable overall trend and maximum value of around 60-70N.

To compare the results provided by both methods in a wider sense, it is possible to compare the relationships between impact velocity and impact force obtained through each method; as shown and discussed previously in Figure 5-8 and Figure 5-20. Figure 5-25 plots the relationship obtained between impact velocity and impact force obtained through both modelling approaches (for a 3mm diameter water droplet) as well as the values predicted by the theoretical impact force equation (Equation 3.6); allowing for comparison between the three data sets.

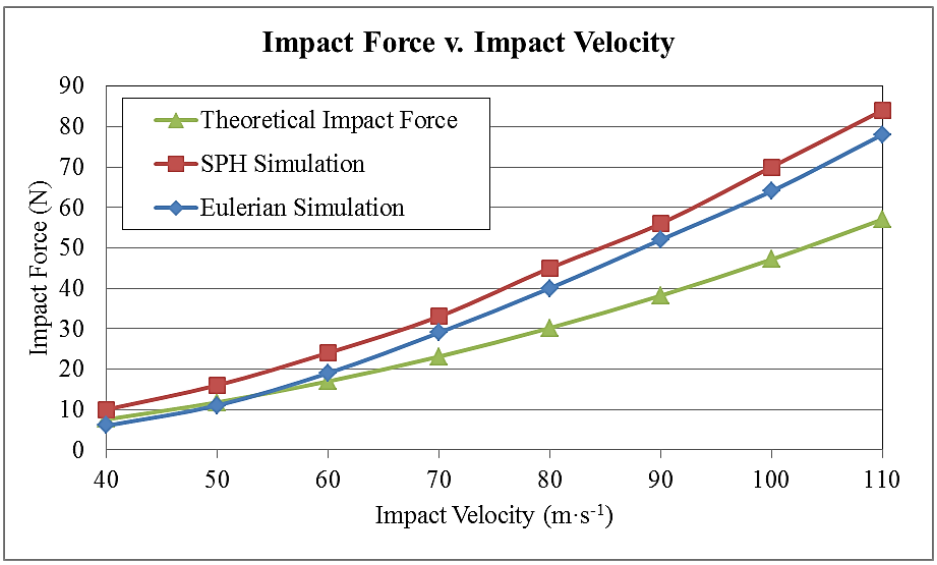

Figure 5-25. Relationship between impact velocity and impact force imparted by a 3mm diameter water droplet as modelled by both an Eulerian and SPH based approach and as predicted by the theoretical impact force equation (Equation 3.6).

The values of impact force obtained across the full range of impact velocities simulated for both modelling approaches compare very closely. Both trends predict higher values of impact force at higher velocities than Equation 3.6, and there is close agreement both in terms of magnitude and overall trend between the results of both modelling approaches. It is clear however, that although the results obtained from both modelling approaches are closely comparable, they are higher in value than those predicted by Equation 3.6. However, it must be remembered that Equation 3.6 is a simplified instantaneous approximation of the impact force imparted by a water droplet on a surface, whereas the modelling results are obtained from a much more dynamic and transient prediction method. Therefore, it is merely of interest to compare the order of magnitude of force predicted by the analytical and numerical approaches; which are agreeable.

Figure 5-24 plots the time history of maximum pressure generated within the 3mm diameter droplet during a 100m·s^{-1} impact event, as modelled by both the Eulerian and SPH based approaches.

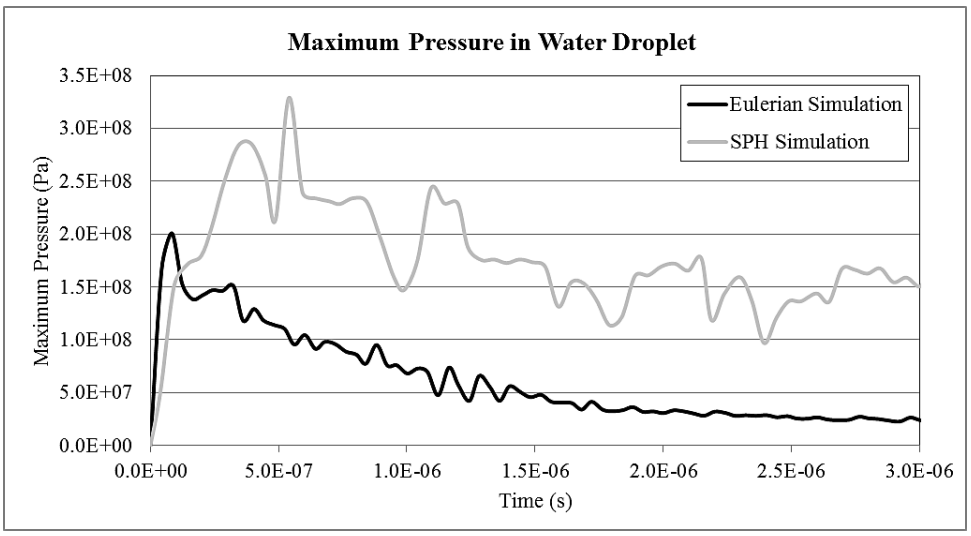

Figure 5-26. Time history of maximum pressure generated in a 3mm diameter water droplet during a 100m·s^{-1} impact event as simulated by Eulerian and SPH based approaches.

It is clear from Figure 5-26 that there are significant differences between the two time histories obtained for each method. The Eulerian method creates a distinct initial peak in pressure representative of the waterhammer pressure, followed by a steady decline to a nominal pressure value. However the SPH method creates an initial point of inflection representative of the waterhammer pressure value – comparable to the value predicted by the Eulerian approach - which is then immediately followed by a further increase in pressure brought on through the process of droplet spreading. Plotting these values of initial waterhammer pressure across the range of impact velocities simulated gives the plot shown in Figure 5-27. The plot also displays the values of waterhammer pressure as predicted by the waterhammer equation (Equation 3.4); assuming a water density of 1000kg.m^{-3} and a speed of sound in water of 1500m·s^{-1}.

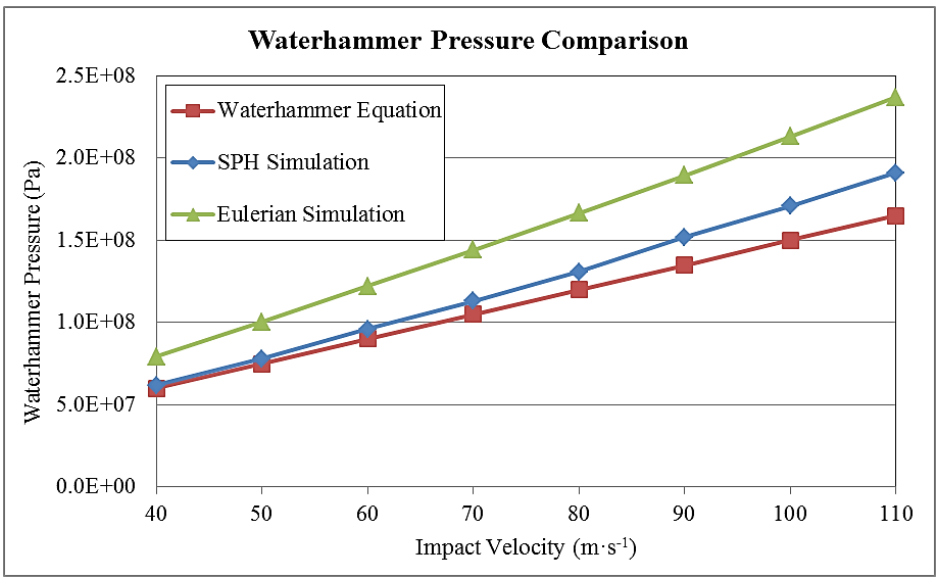

Figure 5-27. Waterhammer pressure for a 3mm diameter water droplet impacting a flat surface, across a range of impact velocities, as predicted by an Eulerian and an SPH based approach, as well as the waterhammer equation (Equation 3.4).

From Figure 5-27, in respect to the creation of the initial waterhammer pressure, both the Eulerian and SPH approach show a good level of agreement with one another, as well as the values predicted by the waterhammer equation. It seems then that there is only disagreement between the two modelling approaches with respect to the value of maximum pressure generated within the droplet during the post-waterhammer stages of impact. As discussed previously, the SPH seem to better capture the high pressure generating aspects associated with the droplet spreading phase, as highlighted and discussed in the literature [161] [98] [102]. However it is not clear with respect to the transfer of load to the target surface (for a non-rigid target) if the creation of these high internal pressures will alter the loads imparted on the target or the stress states induced within it. Indeed it is evident from the previous comparison of impact force time histories and peak impact forces (Figure 5-24 & Figure 5-25) that there is little observable difference in the force exerted by the droplet for each modelling approach; even with the presence of these high level secondary pressure creation events.

The SPH approach to modelling droplet impact and spreading is more representative of the natural phenomena; with respect to the creation of a high pressure ring at the contact periphery after the passing of the peak waterhammer pressure; as described in the literature [98] [101] [102].

As part of the process for selecting the most suitable approach to modelling water droplet impact, the advantages and disadvantages for both the Eulerian and SPH modelling approaches are summarised as follows.

5.1.5.1 Eulerian

Some of the main advantages and disadvantages of the Eulerian approach, utilised in the ANSYS software package are as follows:

- Advantages:
    - Through use of the ANSYS workbench environment geometry creation and model setup was easy to implement.
    - ANSYS workspace offers flexibility with respect to the import and export of results and model features between analyses.
    - The ANSYS software made it fairly straightforward to implement the Eulerian domain and it characteristics.
    - The results obtained through the Eulerian approach were agreeable with the theoretical values and observations in literature; both quantitatively and qualitatively. Except for the absence of significant post-waterhammer pressure creation.
    - The approach captured the fluid like behaviour of the droplet during impact.
- Disadvantages:
    - Setting up the Euler domain and its parameters took longer than creating and SPH body.
    - The author found limited flexibility and usability in the post-processing process when using ANSYS.
    - When using the ANSYS software, it was not readily apparent how certain aspects of the model were being set up and what tools the model created would utilise. Certain tools and processes possessed a ‘black box’ feel.
    - The Eulerian approach required greater computational resources and time – approximately an hour, depending on impact velocity - in comparison the SPH approach.

Some of the disadvantages described relate to the use and transparency of the ANSYS software package; however it may be the case that with prolonged use of the software some of these issues may be resolved and a greater proficiency gained.

5.1.5.2 SPH

Again the most apparent and significant advantages and disadvantages of the SPH approach employed are as follows:

- Advantages:
    - The process of creating an LS-DYNA analysis through compiling a keyword provided excellent transparency with respect to understanding the exact make-up of the model and all the inputs.
    - The creation of the SPH droplet in LS-PrePost was quick and straightforward to implement.
    - The SPH analyses were solved quickly in approximately 10-15 minutes
    - The results obtained through the SPH approach were agreeable with the theoretical values and observations in literature; both quantitatively and qualitatively. The approach also effectively captured the phenomenon of high pressure creation at the onset of droplet lateral jetting.
    - The LS-PrePost software tool provided extensive pre and post processing possibilities
- Disadvantages:
    - The fluid like response of the droplet upon impact was not quite as well captured by the SPH approach, in comparison to that of the Eulerian approach.
    - Care had to be taken to prevent the occurrence of contact irregularities by maintaining a low time step
    - Although the LS-PrePost software was found to be very powerful, transparent and flexible, the software is still in its relative infancy and some bugs were apparent.

5.1.5.3 Selection

From the results shown and discussed both the Eulerian and SPH approaches, using either the ANSYS or LS-DYNA software package, can provide satisfactory performance with regards to modelling rain droplet impact on a solid surface. However, from the results observed the SPH modelling approach proved the most effective with respect to capturing the post-waterhammer pressure spikes at the droplet/surface contact periphery. It may be the case that through further work and modelling alterations the Eulerian method could also capture these effects; however this was outside the scope and aims of the present work.

Additionally, the author found that the SPH approach used in LS-DYNA provided additional model transparency and flexibility. This, coupled with the reduced solve time associated with the SPH approach (in comparison to the Eulerian method), was key to the decision to proceed with the SPH approach described for future analyses.

5.2 Hailstone

The Carney model represents the most developed and validated material model for ice impact. It was for this reason that this model was adopted for the purposes of studying hailstone impact on the leading edge of wind turbine blades. However, due to the benefits highlighted by Anghileri et al. [156], it was decided that the SPH approach to meshing/modelling the hailstone geometry would be taken. Although the Carney model was initially implemented for use with an Eulerian modelling approach, a further paper by Anghileri et al. [167] suggested that the Carney model could be implemented with an SPH approach in LS-DYNA; however very limited information regarding the results obtained was detailed.

Therefore, before fully implementing the Carney model in analyses of hailstone impact in the context of impact on the leading edge of a wind turbine, it was prudent to first confirm the compatibility of the model with the SPH approach. To study this, it was decided that the analyses conducted in the paper by Carney et al. [128] would be replicated using their suggested ice model but through utilising an SPH approach, the results obtained could then be compared to both the numerical and experimental results detailed in the paper. This would then help evaluate the SPH approach and additionally provide confidence in the practical process of implementing the model in the LS-DYNA environment. It was decided that the normal impact setup at the three varying velocities would be simulated as describe in by Carney et al. [128].

5.2.1 Carney Model-SPH Validation Model Setup

For the task of setting up the required models the LS-PrePost software package [195] was again used. Due to the established nature of the Carney model it forms part of a test case method for ice impact analyses as established by the 'LS-DYNA Aerospace Working Group' (AWG) [193], which is a collaborative "partnership of federal agencies, corporations and universities working together to develop and publish aerospace test cases and modelling guidelines for finite element analyses with LS-DYNA®". As such, through their website it is possible to access an example '.k' input keyword file for LS-DYNA that sets up an analysis looking at ice ingestion and impact on a gas turbine blade [196]; using the ALE method. Through examining this keyword file it was possible to determine their method of implementing the Carney material model in an LS-DYNA analysis, therefore providing a valuable reference tool for implementation in the current work.

5.2.1.1 Geometry and Mesh/SPH

Due to the stiff nature and low predicted deformation of the target plate, (as in Carney et al. [128]) it was deemed suitable to model it through a classic FE Lagrangian mesh approach. Therefore the 63.5mm diameter, 19.05mm thick cylindrical plate geometry (as shown in Figure 4-20) was created in LS-PrePost and was given a hexahedral mesh with a total of 5332, 8-noded solid hexahedral elements (Figure 5-28). A greater level of mesh refinement was not required as the plate would be assumed rigid (as will be discussed) and therefore a simple mesh to represent the plate shape was adequate.

In setting up the modal characteristics of the target plate (shown in Figure 4-20), three 'discrete' elements [181] were incorporated to the underside of the plate to represent the load cell, bolt and backup structure which were then fixed to the 'ground', as shown in Figure 5-28.

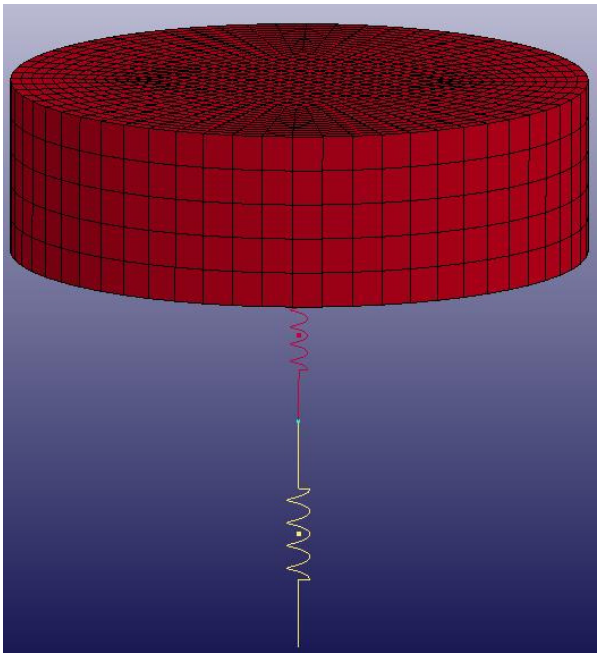

Figure 5-28. Target plate mesh, spring elements and mass

From Figure 5-28, it appears that there are only two discrete elements (springs in red and yellow), this is because the load cell and bolt elements share the same two nodes and therefore only one is visible. The blue dot between the two visible discrete elements is a mass element, representing the 0.3538kg mass in the modal characterisation as shown in Figure 4-20. The incorporation of this mass-spring system meant that the plate was only permitted to move in the plane of the spring elements during impact (the z-axis in the model) and all other degrees of freedom were constrained. As the connections between the top spring elements and the underside of the plate were rigid, the constraints of the spring

elements were transferred to the target plate, therefore allowing it to only translate in the vertical direction; these were the only boundary conditions applied to the model.

The ice cylinder projectile was modelled using an SPH approach and was represented by approximately 50k SPH nodes, as shown in Figure 5-29.

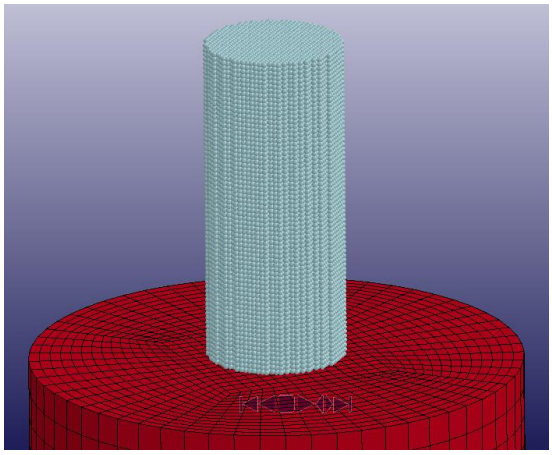

Figure 5-29. SPH representation of ice sphere (light blue)

This number of nodes was found to be refined enough to provide the results and behaviour required, whilst not being computationally expensive.

5.2.1.2 Material Models

As stated previously, the steel target plate was to be considered as a rigid component and as such *MAT_20 or *MAT_RIGID was used to represent the target plate material using the material properties of Type 304 Stainless Steel [197], shown in Table 5-2.

Table 5-2. Material properties of Type 304 Stainless Steel, source: **[197]**

Property	Value
Density (kg/m^3)	8000
Young's Modulus (GPa)	193
Poissons Ratio	0.29

The particular elastic properties of the material used were not of any great importance as a result of modelling the plate as a rigid body; however the density would play a factor in adding a particular mass to the target apparatus.

The discrete spring elements were simply represented by *MAT_S01 or *MAT_SPRING_ELASTIC which needed only the spring constants as detailed in Figure 4-20 as an input.

The Carney model is implementable in LS-DYNA through its purpose made material model, *MAT_155 or *MAT_PLASTICITY_COMPRESSION_TENSION_EOS. The material properties for single crystal ice, as shown previously in

Table 4-5 were input as the base material properties.

Two tabular inputs for the strain rate scaling effect on the yield stress for both compression and tension (LCSRC and LCSRT respectively) were required. The data in Table 4-6 was used to define the relationship in compression and in the absence of appropriate data the scaling effect in tension was assumed constant at a value of 1. To define the two curves 'LCIDC' and 'LCIDT' which describe the relationship between yield stress and plastic strain in compression and tension respectively, the two values of initial flow stress for compression and tension were used with the plastic tangent modulus (the slope of the line) – detailed in

Table 4-5 – to create a simple straight-line function for yield flow stress against plastic strain in both compression and tension.

The equation of state for the material model also required definition. This was implemented using the *EOS_TABULATED_COMPACTION feature. The inputs for the equation of state were taken directly from the values detailed by Carney et al. [128], as listed in Table 4-7.

5.2.1.3 Contact

In order to effectively model the impact between the ice projectile and the steel plate, an effective contact algorithm required chosen to model their interaction. For this purpose, the contact algorithm *CONTACT_AUTOMATIC_NODES_TO_SURFACE was implemented with the 'SOFT 1' constraint formulation activated, which enables better contact modelling between bodies with vastly varying stiffness (in our case ice and steel). The algorithm was set to check for contact partners once every computational cycle, this represents a high frequency of checking for most impact conditions but due to the high number and density of SPH nodes representing the ice, this level of checking was necessary to prevent unwanted artificial penetration between bodies.

5.2.1.4 Simulation Control

Each simulation was set to run for 900μs in accordance with the cases presented in Carney et al. [128]. The time step was determined automatically by the software package for each simulation however a time step reduction factor of 0.5 was input in order to keep the time

step small and therefore maintain an acceptable level of model stability/accuracy during the stages of high shape deformation of the ice projectile.

The model was set to record the contact force between the projectile and the plate and also the deformation force of the spring elements during impact.

5.2.1.5 Results

Each simulation was successfully run for the specified total simulation time, each taking approximately 1 hour to complete.

Figure 5-30 shows the development of the simulated ice impact at a velocity of 152.4m·s^{-1} obtained from the SPH simulation.

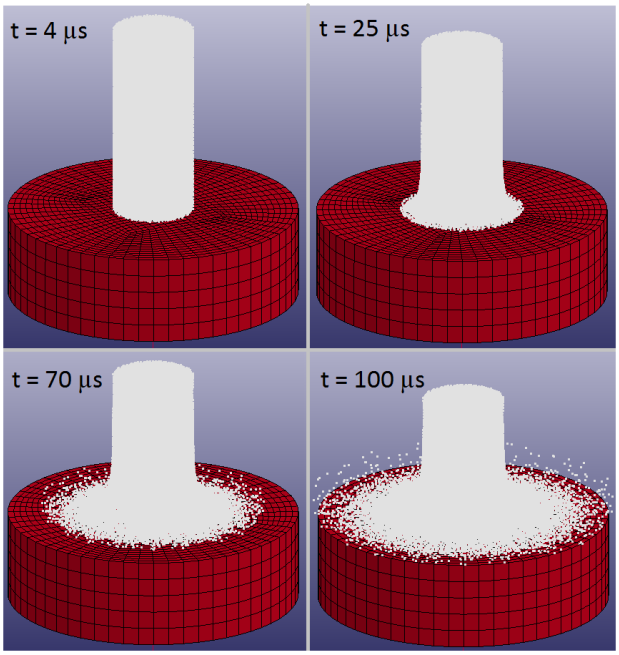

Figure 5-30. Simulated 152.4m·s^{-1} ice projectile impact

Comparing this to the images from the paper by Carney et al. [128], shown in Figure 5-31, the attempts to replicate the modelling work have produced qualitatively comparable results. Both Figure 5-30 and Figure 5-31 show the ice structure breaking down from a solid to a fluid/powder-like consistency as the impact event develops.

Figure 5-31. Solid to fluid transition using Eulerian formulation. Source: **[128]**

The three plots shown in Figure 5-32 show the deformation force time history plots of the discrete spring element representing the load cell during the SPH analysis (shown in red) and compares them to the analytical and experimental results detailed by Carney et al. [128].

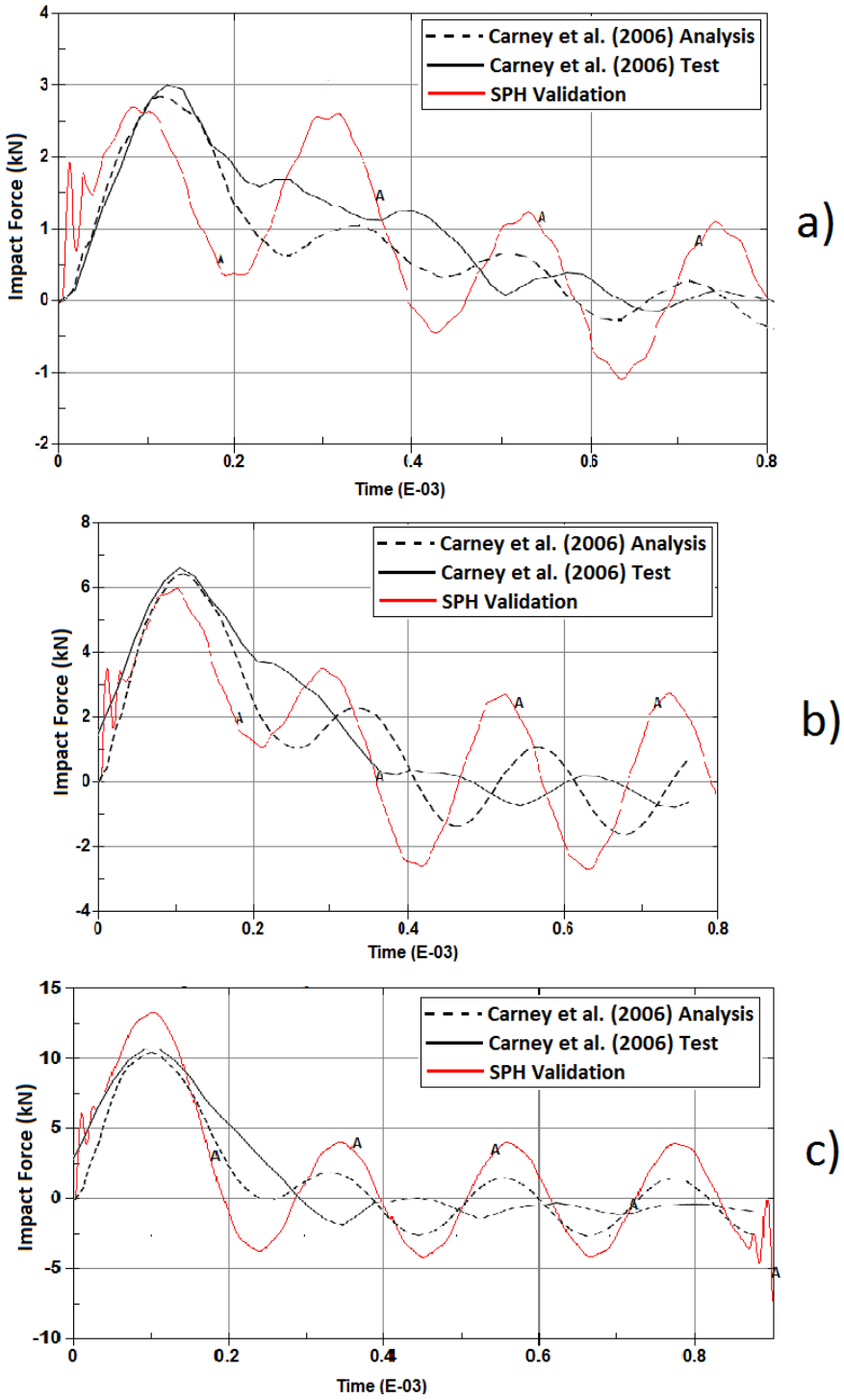

Figure 5-32. Deformation force time history results of load cell element in SPH implementation of Carney model, with comparison to results in Carney et al **[128]**, for impact at: a) 91.44m·s^{-1}, b)152.2m·s^{-1} and c) 231.36m·s^{-1}.

From these plots, it can be seen that the deformation force time histories for the load cell element obtained through the SPH method (at the three impact velocities simulated) compare well with the results detailed by Carney et al. [128]. Point averaging filtering techniques was to be applied to the force histories to smooth out regular sinusoidal wave characteristics to achieve a simpler trace of the impact force; similar filtering techniques were implemented by Carney et al. [128].

A comparison between the computed contact force in Carney et al. [128] (Figure 4-22) and that achieved through the SPH approach, was also made, the contact force history at an impact velocity 152.4m·s^{-1}, obtained through the SPH method is shown in Figure 5-33.

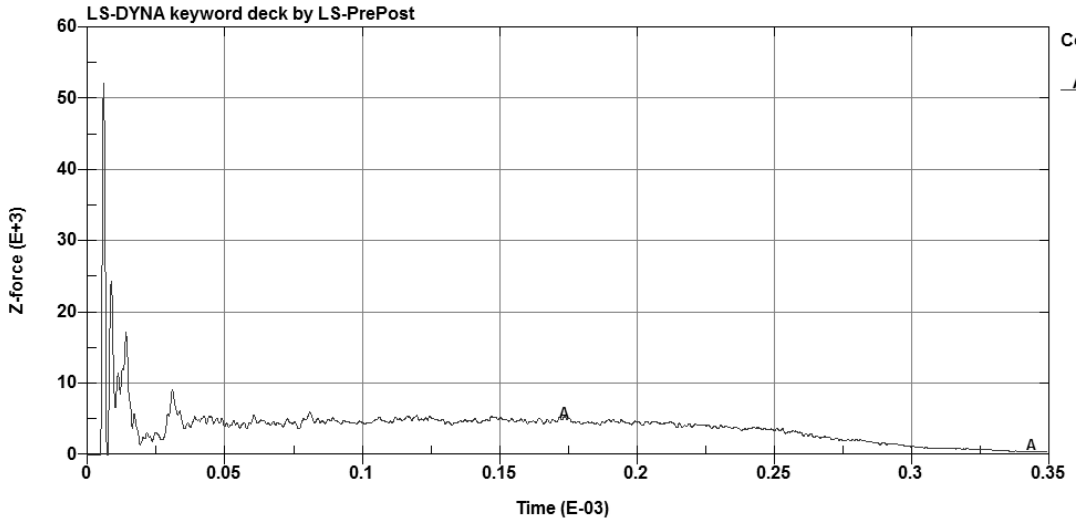

Figure 5-33. Simulated contact force (in N) during a 152.4m·s^{-1} ice impact using SPH approach.

Comparing the peak force of approximately 52kN shown in Figure 5-33 to the value of approximately 53kN (12,000 lbf) as found by Carney et al. [128] (Figure 4-22) shows that good agreement between the approaches is also displayed with regards to contact force.

From the results obtained and shown in Figure 5-30, Figure 5-32 and Figure 5-33 the SPH approach to implementing the Carney ice model provided both qualitatively and quantitatively comparable results to both experimental data and the results obtained through the initial Eulerian implementation of the model as both detailed by Carney et al. [128].

Using the SPH approach also makes it possible to examine the progression of failure in the ice projectile itself and compare this to experimental findings. Pereira et al. [198] conducted ice projectile impact tests and utilised high speed photography to monitor and record the impact sequence as shown in Figure 5-34.

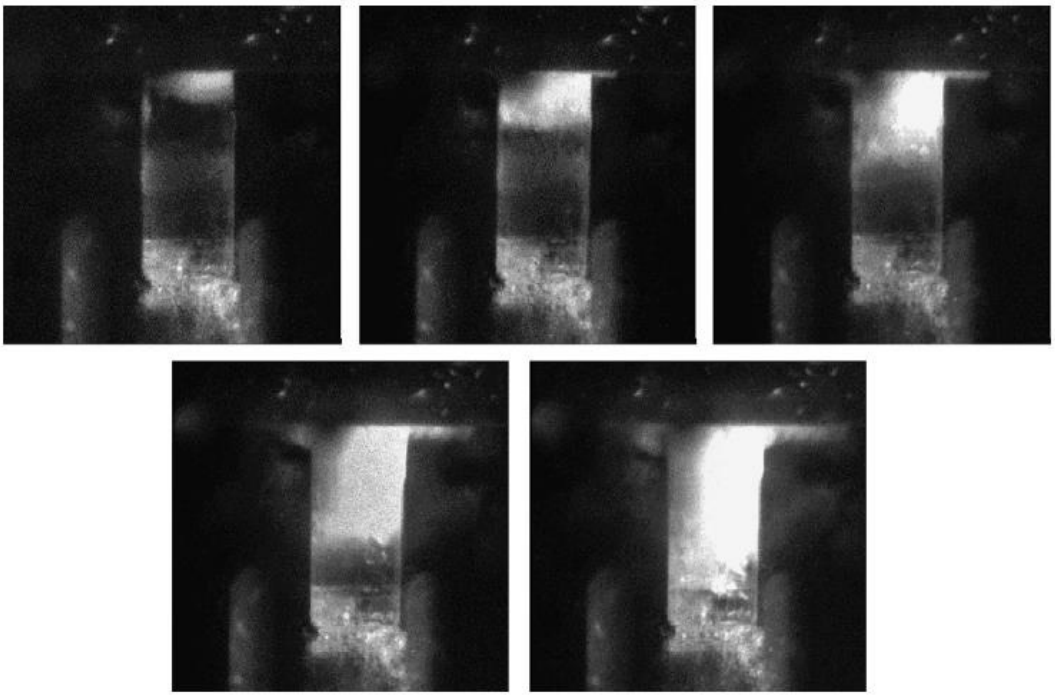

Figure 5-34. Ice projectile impact at 207.3m·s^{-1}, loss in transparency indicates damage in the ice. Source: **[198]**

The images show the impact of a 31.75mm diameter 76.3mm long cylindrical ice projectile impacting a plate at 207.3m·s^{-1}. It is possible to observe the spread of damage through the ice as a loss in the ice transparency. The images were taken at a rate of 260,010 frames per second and the velocity of the fracture wave was calculated to be approximately 10,000 ft·s^{-1} or 3048m·s^{-1}. Using the same SPH and Carney model approach as before, this experimental setup was replicated in LS-DYNA to evaluate the effectiveness of the SPH approach to modelling the Carney model in capturing the fracture behaviour of the ice. Time steps from the results of this analysis are shown in Figure 5-35, which uses contours of von-Mises Stress to illustrate the fracture shockwave through the ice projectile upon impact.

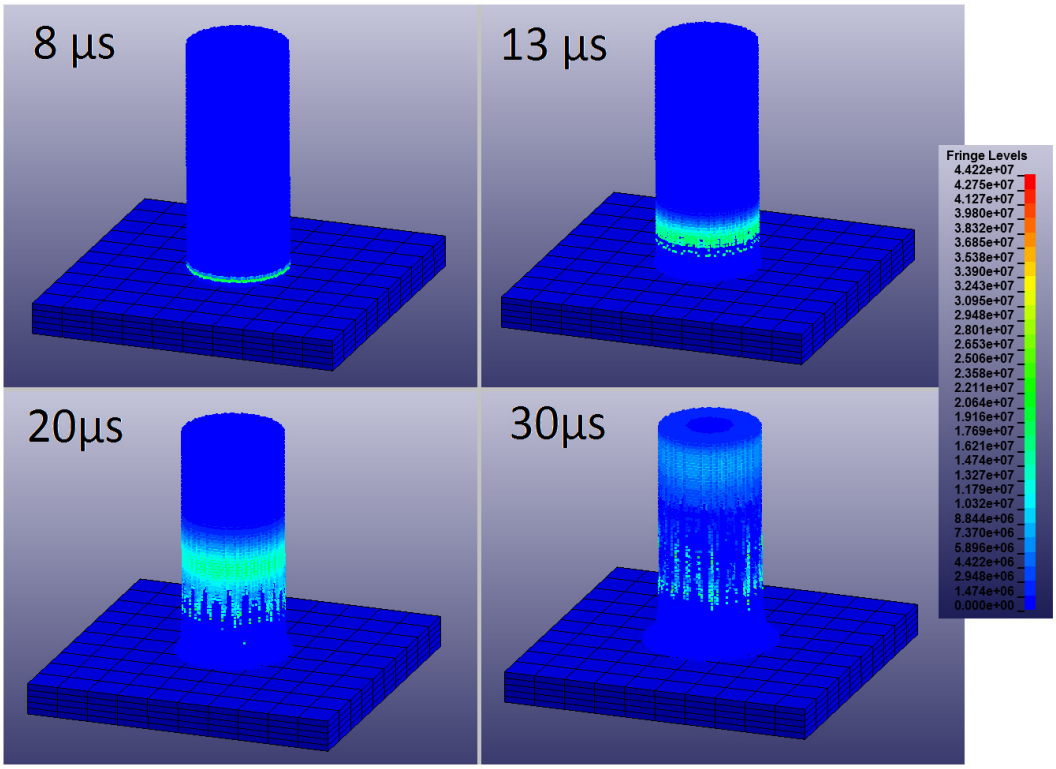

Figure 5-35. Ice Projectile impact at 207.3m·s^{-1}, contours of von-Mises stress (Pa)

From this, it is possible to observe the high speed spread of the shockwave up through the ice in the opposite direction to the impact. Through the results obtained it was possible to calculate a shockwave propagation speed of approximately 3400m·s^{-1} which compares quite well with the value of approximately 3000m·s^{-1} as stated by Pereira et al. [198].

5.2.1.6 Compatibility of Carney Model with SPH Approach

From the results described and their comparison with results from other studies, it was found that the Carney ice material model was compatible with an SPH approach to implementation. The impact force time histories obtained through the SPH implementation compare well to those found numerically and experimentally by Carney et al. [128], as shown previously in Figure 5-32. Additionally, the approach suitably models the ice failure mechanism as shown in Figure 5-35.

Through establishing the suitability of this approach, it was decided that this method of modelling ice impact would be further implemented in impact analyses concerning leading edge impact on wind turbine blades, as discussed later in Section 7.

5.2.2 SPH Sensitivity Study for Ice

As was the case with rain impact modelling, before the appropriate ice modelling methodology established could be further implemented, the sensitivity of such modelling work to the SPH node total representing the ice body required investigation.

The model created for the purpose of this investigation was similar to that employed for the rain droplet sensitivity study, featuring instead a 10mm diameter spherical hailstone body with a varying SPH node count of 552, 33552, 113104 and 523987 (523987 only employed for 100m·s^{-1} impact sensitivity analysis), impacting a flat rigid target body across an impact velocity range of 40-100m·s^{-1}. The impact force time history for each analysis was plotted for the purposes of investigating the sensitivity of the force imparted to the SPH total node count. The full data set obtained is detailed in Appendix I.

It was found that a low SPH node total of 552 did not provide consistent or satisfactory outputs with regards to the impact force created; across the range of impact velocities. Figure 5-36 shows the impact force time histories created for a 100m·s^{-1} impact event for SPH node totals of 33552, 113104 and 523984.

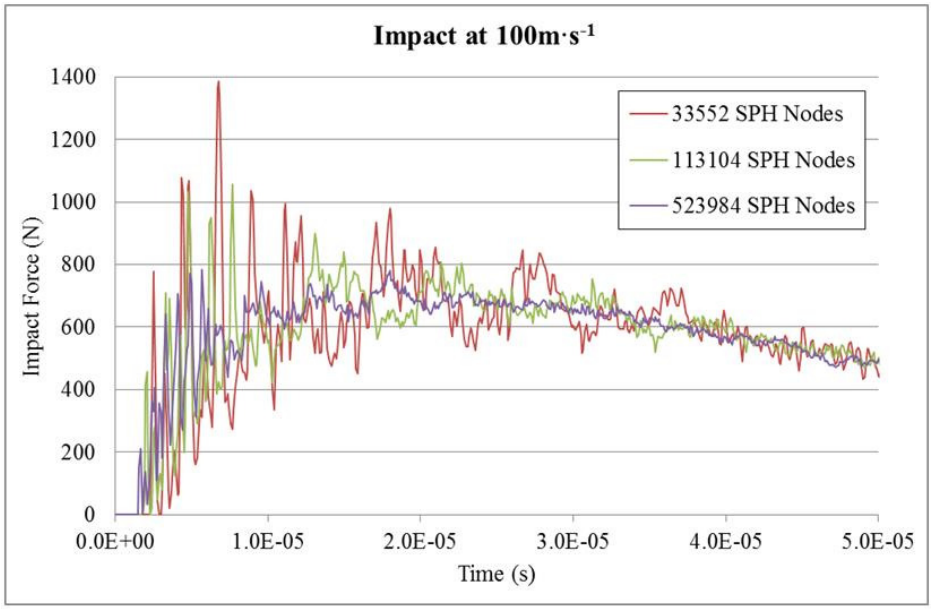

Figure 5-36. Impact force time history for 10mm diameter hailstone impact at 100m·s^{-1} using varying SPH node totals for the hailstone body.

The impact force time histories display a degree of sensitivity with respect to the total SPH node count applied for the hailstone body within the model. An SPH node count of 33552 for the hailstone body created a force output with considerably more variation (or noise) than outputs from the 113104 and 523984 analyses. However, as noted in the rain drop SPH

sensitivity study, these peaks in variance from the trend may be exacerbated by the rigid nature of the target body and may be smoothed out when considering impact on a deformable target body. Furthermore, the overall trend created from the simulation featuring 33552 SPH nodes for the hailstone, still shows strong agreement with overall impact force trend. There is little appreciable difference between the outputs from the 113104 and 523984 analyses; however the 523984 analysis took significantly longer to solve. It may be considered therefore, that simulations which require a significant amount of detail and definition in the impact and shatter response of the ice projectile, a node total in excess of approximately 100k will provide the best results; at a computational cost. However, if the response of the target body during impact is of more interest, a lower node count in the region of 33k may provide satisfactory performance at much reduced computational cost.

5.3 Characterisation of Wind Turbine Blade Properties for Numerical Analysis

It was apparent that the impact energies associated with each projectile type (rain and hailstone) differs significantly; as a result of the increased mass and (in most cases) terminal velocities of hailstone projectiles. For this reason, the aims, objectives and desired outputs from blade impact analyses differs between the two forms of impact. For instance, it was decided that rain impact analyses should mostly focus on the nature of erosion mechanisms, impact absorption and debonding of the protective coating systems; due to the limited impact energies involved. Whereas, as a result of the associated increased impact energy, hailstone analyses should investigate these issues as well as examining substrate damage and delamination.

In order to conduct appropriate modelling work, it was first necessary to define and establish the topology, layup and materials properties of an appropriate wind turbine blade leading edge; which would act as a reference blade for subsequent impact analyses.

5.3.1 Blade Target Configuration

The specific material layup and configuration of a wind turbine leading edge (near the tip) is considered by many manufacturers as commercially sensitive information. Therefore, there is very little detailed information on such typical properties available in the public domain; with respect to commercial designs.

There are however a number of reference or baseline blade designs, established by research organisations and bodies; which have comparatively well documented properties and characteristics. For instance Griffith and Ashwill [199] of SANDIA National Laboratories [200] detailed the conceptual development, design and specification of a 100 meter length all glass fibre research blade, proposed for use on a 13MW conceptual turbine. Although this is considerably larger than most current technologies, they detail some of the key blade material properties, still applicable to smaller designs. Similarly, there are a number of studies from the National Renewable Energy Laboratory (or NREL – US based) [201], which discuss reference/concept blade designs and their material configurations [202] [203] [204]. The independent DNV foundation [205] has also published a standard for the 'Design and Manufacture of Wind Turbine Blades, Offshore and Onshore Wind Turbines' (DNV-DS-J102) [206], which gives indications of the typical material employed and their required characteristics. Nijssen [207] detailed the laminate layup configuration of a large 5MW

reference blade for the UpWind project [208], giving detail on the individual laminate materials and thicknesses.

Drawing on these sources, and through consultation with a leading blade manufacturer, the following section discusses the establishment of an appropriate blade leading edge layup and associated material properties.

5.3.1.1 Blade Layup

Before the material properties of the candidate blade can be established, a suitable material layup configuration must be selected. Most leading edge sections at the blade tip will incorporate a number of fibre reinforced (unidirectional or fabric/multi-directional) composite layers which form the structural composite 'skin' of the blade. On top of this composite substrate, additional protective layers and coating technologies are applied.

Through discussions with a prominent blade manufacturer, a blade layup configuration as shown in Figure 5-37 was suggested as being typical or very close to the actual cross sectional layup of a blade leading edge (at the tip).

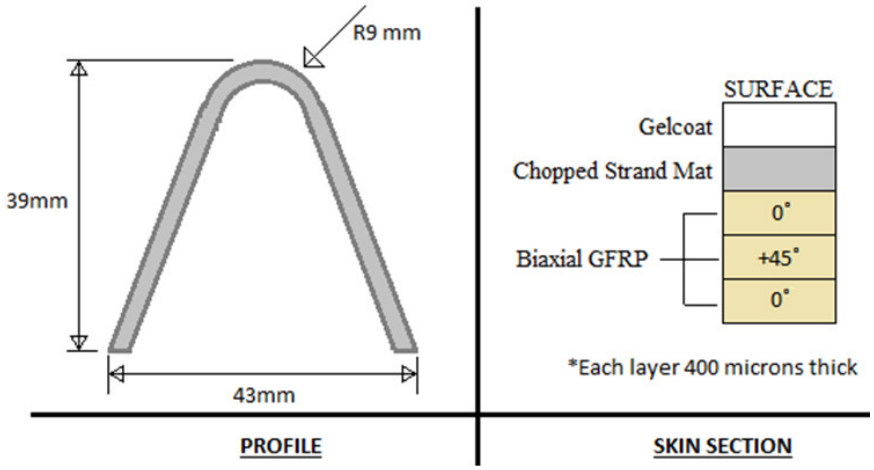

Figure 5-37. Typical blade leading edge profile at the tip and a cross section of the blade skin detailing the layup and material types used.

The cross section features three layers of biaxial glass fibre reinforced plastic, with a layer of chopped strand mat and a gelcoat acting as protective coatings. The exact fibre orientations and configurations (weave, stitched etc.) were not possible to fully establish and can vary with blade position. The approximate thickness of each material layer is approximately 400 microns, creating a skin section roughly 2mm thick.

This layup configuration compares closely to those identified and detailed in the literature. For instance, the blade detailed by Bir and Migliore [202] features a leading edge skin which

includes: a 0.53mm thick layer of biaxial FRP, a 0.51mm thick layer of 'Nexus' and a 0.381mm thick layer of gelcoat. Nexus is described as a soft-material mat which protects the rough composite substrate surface and provides an absorbent and smooth surface for the application of the gelcoat; performing a similar role to the chopped strand mat layer as shown in Figure 5-37. Additionally, although the standard describe by DNV [206] does not specify recommended laminate thicknesses, it does suggest a gelcoat thickness of between 0.3-0.6mm. The 5MW reference blade detailed by Nijssen [207] features a considerably larger skin thickness of about 11mm, consisting of a sandwich structure featuring a 6mm thick foam layer sandwiched between two 2.82mm thick triaxial laminate skins; no coating specification are given. This large skin thickness may be associated to the large size of the reference blade (>60m), and highlights the fact that laminate layup configurations may alter significantly between designs.

It is clear then that although layup configurations can vary vastly between designs and manufacturers, the layup shown in Figure 5-37, as suggested by manufacturing contacts, serves as an appropriate approximation of a typical wind turbine leading edge layup. As such, this layup configuration will be assigned to the blade modelled in the analyses of this study, which from now on will be simply referred to as the 'reference blade'.

5.3.1.2 Blade Material Selection

With a basic leading edge profile and cross sectional layup defined (Figure 5-37), the specific material properties of the individual layers of the reference blade laminate can now subsequently be defined. As with layup configurations, the exact nature and properties of typical blade materials are not openly publicised, however some material manufacturers do published some key material properties for their products.

Due to the prominence of glass/epoxy based composite systems in wind turbine blades, coupled with the higher availability of material properties of these materials, it was decided that the reference blade would be based upon glass fibre reinforced epoxy composites. This specification was also important when considering the gelcoat and other coatings materials; as such systems must be compatible with the composite substrate with regards to manufacturing considerations.

As the rain drop impact modelling would be wholly numerically based, the material properties used in the simulations will be based on values taken from the literature; discussed later in Section 6.1.1. To allow for comparison between the blade impact response from rain

droplet and hailstone impact, these materials would also be used in hailstone impact analyses.

However as experimental hailstone impact analyses were also to be performed, simulations using material properties as possessed by the subsequently manufactured composite samples would also be performed. The material properties of the samples created were ascertained through a combination of material testing and product literature quoted properties; and subsequently rule-of-mixtures calculations.

The approach to selecting and assigning material properties for both the rain and hailstone impact simulations is discussed in the following relevant chapters. However, the basic layup configuration outlined earlier (Section 5.3.1) was adopted (except where stated otherwise) in most simulations (and experimental work).

5.3.2 Structural Stress States

When investigating the phenomenon of single rain droplet or hailstone impact on the blade materials, certain assumptions and boundary condition simplifications are required, as it is not computationally feasible to model the impact response of large sections of the blade (or constitutive materials) whilst obtaining information on the finer details of the impact interactions. As such, in much of the modelling work discussed in the sections to follow, only a limited proportion of the target materials are included in the simulations, usually such that the target dimensions are large enough to encapsulate the meaningful aspects of the impact event within the material (with respect to energy dissipation) but small enough to be simulated in a reasonable time. It is from these limitations in feasible target dimensions that assumptions with respect to the boundary conditions have to be made. The conditions applied for each simulation are detailed in the relevant model setup discussions.

Wind turbine blades are subject constantly changing and highly complex loading conditions, such as gravity, wind and centrifugal forces [11], and as such whilst operating at maximum tip speed the materials in the blade will be subject to significant material loading through the skin thickness. However, given the variability in blade design, materials and turbine operating strategies it is difficult to characterise or fully establish the resulting stress states within the materials of the blade. Furthermore, given the anisotropic material behaviour of much of the typical blade composite materials used, the stress state characteristic become even more complex to characterise. For fully representative blade impact analyses the pre-stress in the blade materials should ideally be incorporated into the model setup as pre-stressed materials will behave differently under impact compared to stress-free materials.

However given the challenges discussed in relation to characterising these stress states, and the limited data available in relation to typical blade skin loading and stress states, it was not possible to confidently predict and apply such stress states to the simulated blade materials. As such, the materials were modelled in an initial relaxed elastic state, which can still provide useful results as the samples tested experimentally in industry are tested under such conditions also.

An alternative to applying pre-stress conditions to the individual blade materials in the model would be to apply strain conditions to the target model as a whole, along the principle axes of the model. If strain data were available for a given blade configuration, for the blade surface, this strain could then be applied to the blade section created in the model, before the subsequent impact event is then modelled. This approach would eliminate the need to understand the individual stress states in each material layer, through instead applying a measured strain level and allowing the solver to model/predict the stress levels in the material.

6. Rain Impact Modelling

Surface erosion and degradation are the primary form on damage observed and catalogued with respect to rain droplet impact on the leading edge of wind turbine blades. The limited impact energies associated with rain droplet impact (compared to hailstone) mean that other forms of substrate damage such as composite matrix cracking or fibre breakage are not considered likely.

However, when considering the application of flexible surface coatings and tape products on the blade surface, the occurrence of debonding between such material layers has been observed in a previous study by Haag [51] (as shown previously in Figure 3-3) and on operational wind turbines.

In light of this, rain impact modelling in LS-DYNA, again using LS-PrePost for pre and post processing, would be undertaken to investigate the following phenomena:-

1. **Rain impact induced damage of a standalone gelcoat:** The phenomenon of surface damage on a gelcoat material induced through rain impact would be thoroughly investigated through modelling. The analyses would look at the effects of increasing impact velocities and energies and the nature of the damage modes induced. Through altering the droplet diameter the Damage Threshold Velocity for the material considered would also be established. The effects of differing impact angles would also be investigated.
2. **Impact induced erosion of a gelcoat material:** The effects of repeated rain droplet impact on the surface and subsequent induced erosion would be modelled to gain greater insight of the phenomena.
3. **Rain impact induced damage of gelcoat on a composite substrate:**
   Primarily this modelling work would be performed to compare the results with those previously obtained for the standalone coating analyses. Furthermore it was expected that such modelling would also provide additional detail with respect to the nature of rain droplet impact absorption in a composite layup.
4. **Rain impact performance of flexible coatings:** It was decided that modelling work would be conducted to examine the performance of flexible polyurethane based coatings (compared to standard gelcoat technology). As with the gelcoat analyses, these simulations would also look to establish the primary damage modes associated with such materials; and the parameters which influence these.

5. **Protection provided by flexible tape and the risk of debonding:** The protection provided by the addition of flexible tape technologies would be evaluated, with respect to their energy absorption characteristics and the protection provided to a gelcoat substrate. The threat posed in relation to debonding of the tape from the gelcoat surface would also be investigated.

These studies are presented in detail along with the setup of the models and review the results obtained.

6.1 Rain droplet impact induced damage of a gelcoat

Before conducting extensive parameter studies and investigating the different impact and damage phenomena associated with rain impact on wind turbine blade leading edge materials, it was important to first fully investigate the simple mechanisms associated with the rain impact induced damage of a typical gelcoat material. The modelling work aimed to establish the fundamental aspects of the interaction between the two bodies during impact and the subsequent energy dissipation behaviour of the gelcoat, and the nature of any damage created. Subsequent parametric analyses would examine the effects of varying impact velocity, droplet diameter and impact angle. Therefore, the key desired outputs from the modelling work were identified as:

1. **Typical Gelcoat Impact Response -** Ascertain the typical impact response behaviour of the gelcoat material, with respect to stress propagation and any subsequent damage creation.
2. **Influence of droplet diameter on the Damage Threshold Velocity -** Evaluate the effects of increased droplet diameter and the influence this has on the required velocity for induced damage.
3. **Influence of impact angle on the gelcoat impact response -** Examine the influence that impact angle has on the impact response of the gelcoat

6.1.1 Gelcoat material properties

There is little publicly available data in relation to the typical material properties of blade materials. However, it is widely known that most blades utilises either epoxy or polyester based material technologies, and consequently many blades feature an epoxy or polyester based gelcoat material (if not a polyurethane based system). For modelling phase of this analysis an epoxy based blade system will be represented; however given the availability of relevant polyester material properties, a polyester based design could also be modelled.

There exists a wide range of material property data in the literature for epoxy resin systems (Table 6-1), however given the wide ranging ways in which an epoxy resin system can be created (i.e. mixing ratio with system hardener) and cured (different temperatures and times), the material property values quoted can vary widely. For example, Table 6-1 details the basic material properties of numerous epoxy based coating systems, gelcoats and matrix resins, sourced mostly from either manufacturer data or technical literature.

Table 6-1. Material properties of epoxy resin systems from numerous sources.

Material Description ([Source])	Density (kg/m^3)	Young's Modulus (GPa)	Poisson's Ratio	Tensile Strength (MPa)	Compressive Strength (MPa)	Failure Strain (%)
Resoltech Epoxy Matrix [209]	1100	3.6	-	65	-	17
Gurit PRIME 20LV [210]	1153	3.2	-	75	-	4.1
Gurit Prime 27 [211]	1133	3.146	-	69.6	-	5
Momentive Epikote 135 [212]	1100	3	-	80	-	8
Epoxy Resin [20]	1120	4	-	50	-	4
3501-6 epoxy [213]	-	4.2	0.34	69	250	1.7
BSL914C epoxy [213]	-	4	0.35	75	150	4
LY556/HT907/DY063 epoxy [213]	-	3.35	0.35	80	120	5
GelCoat [199]	1235	3.44	0.3	-	-	-

There is a certain degree of scatter in the values quoted in the literature for the various types of epoxy based material systems; as would be expected. However, it is apparent for many of the referenced materials that there is real lack of fullness with respect the number of material properties quoted. This is especially evident with respect to a lack of compressive strength values, which in many cases are far greater than tensile strength values. When considering the oblique impact of such materials - where a significant proportion of the stresses created are compressive – it is important to effectively represent the compressive behaviour of such materials through sourcing the relevant material properties.

Littel et al. [214] acknowledged the absence of detailed material property data for epoxy resin systems, also drawing attention to the potential usefulness of such data in relation to then numerically representing epoxies and epoxy based composites in finite element analyses. As such, Littel et al. [214] conducted a programme of numerous tests on Epon E862 epoxy resin samples - a commercially available material utilised in aerospace composites - to ascertain the compressive, tensile and shear properties of the material at varying strain rates. The samples for testing were created in accordance with ATMS D638 ‘Standard test method for tensile properties of plastics’ [215] and optical methods of recording strain rate were used [214]. Through the experimental approach implemented by Little et al. [214] they claim to have developed a reliable method of ascertaining the tensile,

compressive and shear properties of such epoxy polymers, across a range of temperatures and strain rates. Figure 6-1 shows the tensile stress-strain data obtained for the E862 epoxy resin material at varying strain rates and Figure 6-2 shows the compressive test results.

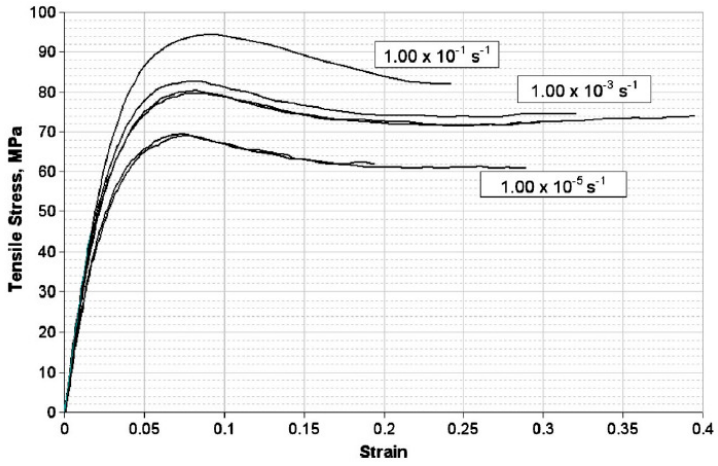

Figure 6-1. Room temperature tensile stress-strain data for Epon E862 epoxy resin. Source: **[214]**

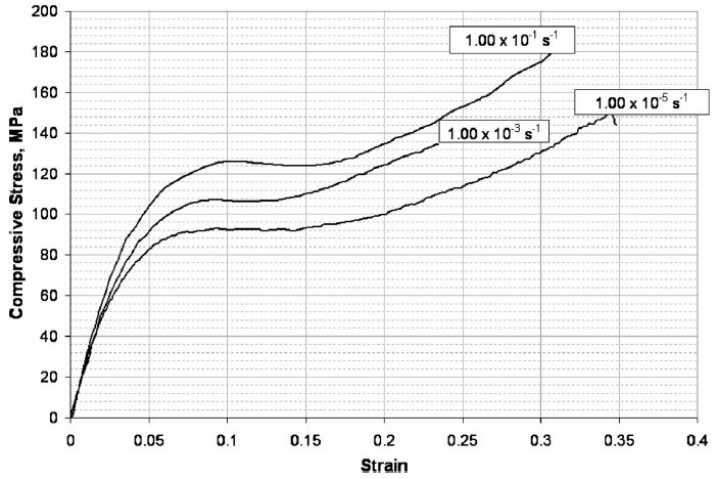

Figure 6-2. Room temperature compressive stress-strain data for Epon E862 epoxy resin. Source: **[214]**

Both figures highlight the effects of strain rate on the material strength exhibited, showing an ultimate tensile strength of approximately 70MPa for a strain rate of $1x10^{-5}s^{-1}$, increasing to approximately 95MPa at a strain rate of $1x10^{-1}s^{-1}$. It is also possible to observe that the material tested exhibits greater strength in compression than tension, which (as previously discussed) is prudent to the effective numerical representation of the material behaviour in impact simulations.

Although the Epon E862 epoxy tested and detailed by Littell et al. [214] is a product used in aerospace composites, given the fullness of the data presented with respect to both tension and compression testing, it was decided that the material properties presented by Littell et al.

[214] for the Epon E862 epoxy would be adopted for the gelcoat material in the rain impact simulations.

6.1.2 Model set up

The steps taken to set up the rain droplet/gelcoat impact simulation are presented, specifically describing the process of setting up a direct impact simulation. However, for the parametric analyses, several of the input parameters described required alteration to vary velocity, droplet size, impact angle etc. The relevant steps within the setup process where these alterations can be made will be identified, however for the purpose of explaining the set up process a simple direct impact simulation is shown in detail; specifically in this case, a 3mm diameter droplet impacting directly at $100 m \cdot s^{-1}$.

The gelcoat impact model featured a single gelcoat target layer 400 microns thick and a length (in both directions) of 6mm, as shown schematically in Figure 6-3. Figure 6-3 also shows the reference coordinate system adhered to in the modelling work, whereby the direction for perpendicular impact is along the z axis.

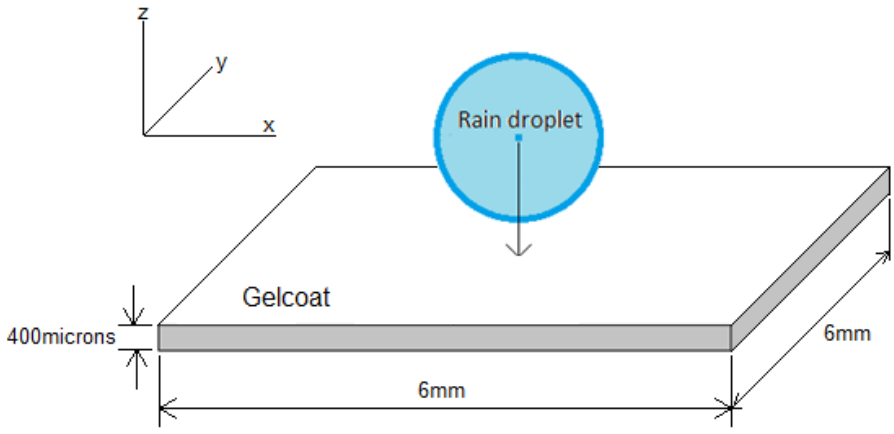

Figure 6-3. Illustration of basic model setup.

A target width of 6mm was found to enable the capture of the key impact dynamics in the simulations conducted; larger sizes provided negligible added insight. As with the rain drop impact modelling evaluation and validation work described previously, the pre and post processing software package LS-PrePost was used to set up the models and evaluate the results.

The 'Shape Mesher' tool was used to first create the gelcoat target body by selecting the 'Box_Solid' option and then specifying the characteristic dimensions shown in Figure 6-3. The characteristics of the desired mesh also require specification in this step, through inputting the desired number of elements along each axis. To establish a suitable mesh

density which would provide satisfactory results at an acceptable computational cost, a sensitivity study was conducted to determine a suitable element total for the gelcoat target, as detailed in Appendix II. From this study it was found that an element total of 337,500 with an element count of 150 along the x and y direction and 15 in the z direction provided satisfactory performance.

The droplet geometry was create using the 'SPH Generation' tool, through selecting a sphere geometry from the drop down menu, setting the sphere centre point origin, the radius, the desired node total (along the x, y and z axes) and finally setting the material density to $1000kg \cdot m^{-3}$. A node total of approximately 65k was set for the droplet geometry (irrespective of droplet diameter). For the simulation set up described here, a droplet diameter of 3mm was set, however for subsequent parametric analyses this input value was altered as necessary. Figure 6-4 shows the resulting model parts created, with the (3mm diameter) droplet positioned closely above the upper surface of the gelcoat layer. The mesh applied to the gelcoat can also be seen, as well as the nodes representing the droplet.

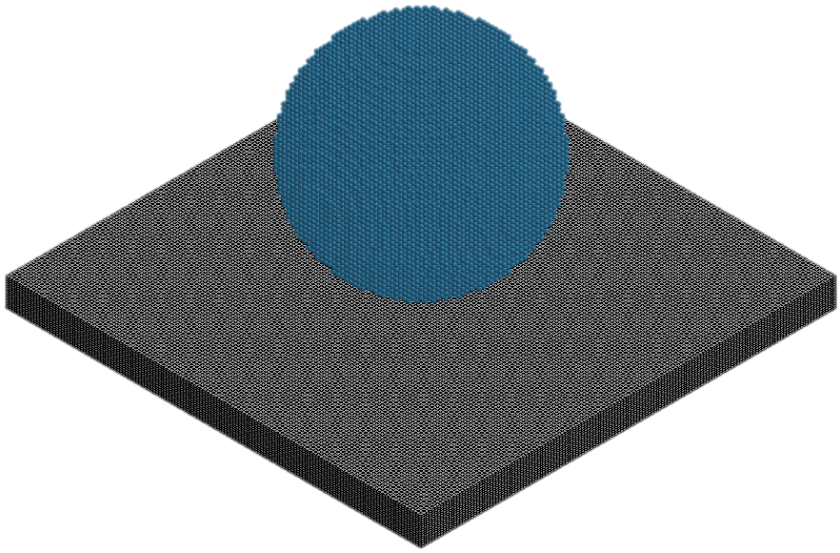

Figure 6-4. Droplet and gelcoat target bodies created within LS-PrePost, showing the SPH Nodes and mesh density applied to each body respectively.

With the relevant finite element and SPH parts created, the material properties and section type of each body had to then be input and created before being assigned to the relevant parts.

The water droplet part was assigned the section card *SECTION_SPH and assigned material properties through the material option *MAT_NULL and the equation of state *EOS_GRUNESIEN, using the values previously quoted in Table 5-1.

There are numerous suitable material models within LS-DYNA for modelling the behaviour of plastics. Given the availability of both compressive and tensile stress-strain data from the data given by Littell et al. [214] for Epon E862 epoxy, the material model *MAT_PLASTICITY_COMPRESSION_TENSION was assigned to the gelcoat part; as well as the section card *SECTION_SOLID. Reading from the data as shown in Figure 6-1 and Figure 6-2, the material properties assigned were represented by the values shown in Table 6-2.

Table 6-2. Material properties assigned to gelcoat material

Property	Value
Density	1150 $kg \cdot m^{-3}$
Young's modulus	2.5 GPa
Poisson's Ratio	0.4
Tensile Yield Stress	90 MPa
Tensile Strain @ break	0.25
Compressive Yield Stress	120 MPa
Compressive Stress @ break	180 MPa
Compressive Strain @ break	0.3

The material was assumed to behave in an elastic-perfectly-plastic manner in tension, based on the horizontal post yield stress-strain behaviour shown in Figure 6-1, whereas in compression it would behave as described by the values in the Table 6-2 (taken from the stress-strain data in Figure 6-2). This behaviour was characterised by definition of a curve to describe the yield stress v. plastic strain behaviour of the model (using *DEFINE_CURVE) which was then referenced by the material model *MAT_PLASTICITY_COMPRESSION_TENSION. The values assigned are based on those quoted by Littell et al. [214].

Utilising this material model meant that the material behaviour, when loaded elastically (in compression or tension), would be dictated by the Young's modulus value specified in Table 6-2. If the specified tensile yield stress of the material was exceeded, the material would then behave in a perfectly plastic behaviour, until unloading, upon which linear unloading with a slope equivalent to the Young's modulus would occur. This linear post-yield unloading behaviour would therefore result in permanent plastic deformation (and residual stress) of the area of material concerned; once fully unloaded. If the compressive yield stress was exceeded, the stress-strain behaviour would be dictated by the post yield tangent modulus defined by the stress and strain values at yield and at break in Table 6-2. As with the tensile

behaviour, unloading from compressive stresses would also occur linearly, again resulting in permanent plastic deformation when completely unloaded. This ratcheting strain behaviour characterised by the material model adopted, was deemed representative of epoxy resin behaviour, based on the experimental work carried out by Shen et al. [216]. In their study, they conducted a range of cyclic loading experiments on an epoxy polymer, to investigate the materials loading-unloading behaviour. The results from the testing of the epoxy polymer, exhibited the effects of strain ratcheting upon loading and then unloading; resulting in damage initiation; as shown in Figure 6-5.

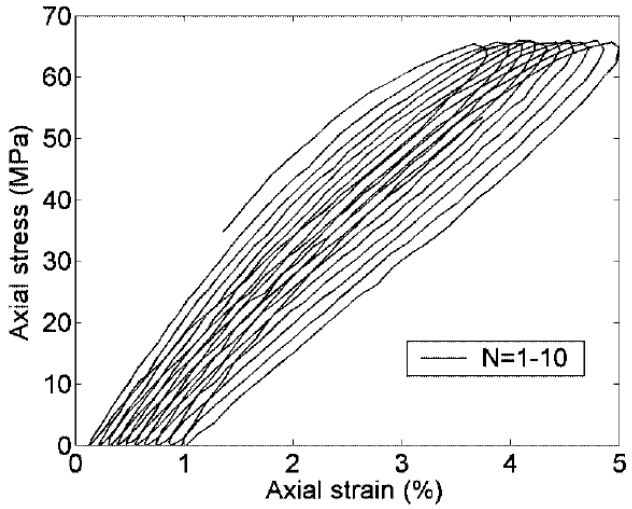

Figure 6-5. Results from study by Shen et al **[216]**, showing the stress strain loops for an Epon 826 epoxy polymer, loaded with a stress range of 66MPa and a mean stress of 33MPa. Source: **[216]**

The boundary conditions applied to the gelcoat consisted of fully fixed conditions (in all degrees of freedom) on the under surface of the gelcoat layer. However, it should be noted that applying fully constrained fixed boundary conditions to the under-surface makes the assumption that the (absent) composite substrate is substantially stiffer than the gelcoat material. It may be the case that in some thin-skinned section blade designs there is a degree of flexibility in the composite substrate and therefore these effects would have to be considered in respective modelling. The additional effects of substrate flexibility on the impact response of the coating system are investigated and detailed later in Section 6.3. The edges of the target plate were left unconstrained, as it was found that doing so did not appreciably alter the results obtained from modelling.

The velocity of the droplet was set using the 'Create Entity' function and applying an initial velocity to the nodes of the droplet with the 'Initial>Velocity' option; which in turn creates a *INITIAL_VELOCITY_NODES card. This process also allows for the input of different velocity vectors in order to alter the direction of the velocity, which was utilised for the

purpose of the parameter studies aimed at investigating the effects of changing impact angles; as discussed later in the results section.

Although the contact card *CONTACT_AUTOMATIC_NODES_TO_SURFACE worked well for the validation modelling discussed previously (i.e. contact with a rigid surface), it performed poorly in gelcoat impact analyses; resulting in missed contacts and therefore artificial SPH node penetration of the gelcoat. It was found for the gelcoat analyses that the contact definition *CONTACT_NODES_TO_SURFACE_SMOOTH result in better contact modelling between the two bodies.

The termination time for the analyses were altered depending on the setup of the model (impact velocity, angle, droplet size etc.), however for all simulations a time step reduction factor of 0.4 was applied through the 'TSSFAC' input in the *CONTROL_TIMESTEP card. This tool simply applies a scaling factor to the every computed time step throughout the simulation [181]. It was found that this value kept the timestep adequately low, so as to provide accuracy of results, without resulting in prohibitively long computational times.

The setup process detailed above, described the reasoning and methodology associated with the setup of the base rain-on-gelcoat impact analysis. This setup process was then altered depending on the aims of subsequent analyses; i.e. through varying impact velocity or angle. However, initially, the description given adequately describes the fundamental aspects behind all other subsequent analyses.

6.1.3 Results & Discussion

The following results discussion is split into three distinct sections covering each of the three desired key modelling outputs, previously identified as:

1. Typical Gelcoat Impact Response
2. Influence of droplet diameter on the Damage Threshold Velocity
3. Influence of impact angle on the gelcoat impact response

The simulations discussed took approximately 1 hour to complete, with only slight variations in this time brought about through the alterations made for the parameter studies.

6.1.3.1 Typical Gelcoat Impact Response

Through considering a single impact event in isolation, it is possible to review the simulated impact event step by step and evaluate the results provided in order to compare them with what would be expected with respect to the droplet impact behaviour and target material response (as suggested and reviewed in earlier chapters). If the results obtained compare well

with the analytical predictions (in relation to shockwave propagation etc.), higher confidence can then be associated with the accuracy of the results and therefore the subsequent results obtained from the parametric analyses.

For the purposes of this process, the results from the simulation of a 3mm diameter droplet impacting the gelcoat directly (at right angles) at 100m·s^{-1} will be examined. Firstly, the general droplet spreading behaviour of the droplet can be examined as shown in Figure 6-6.

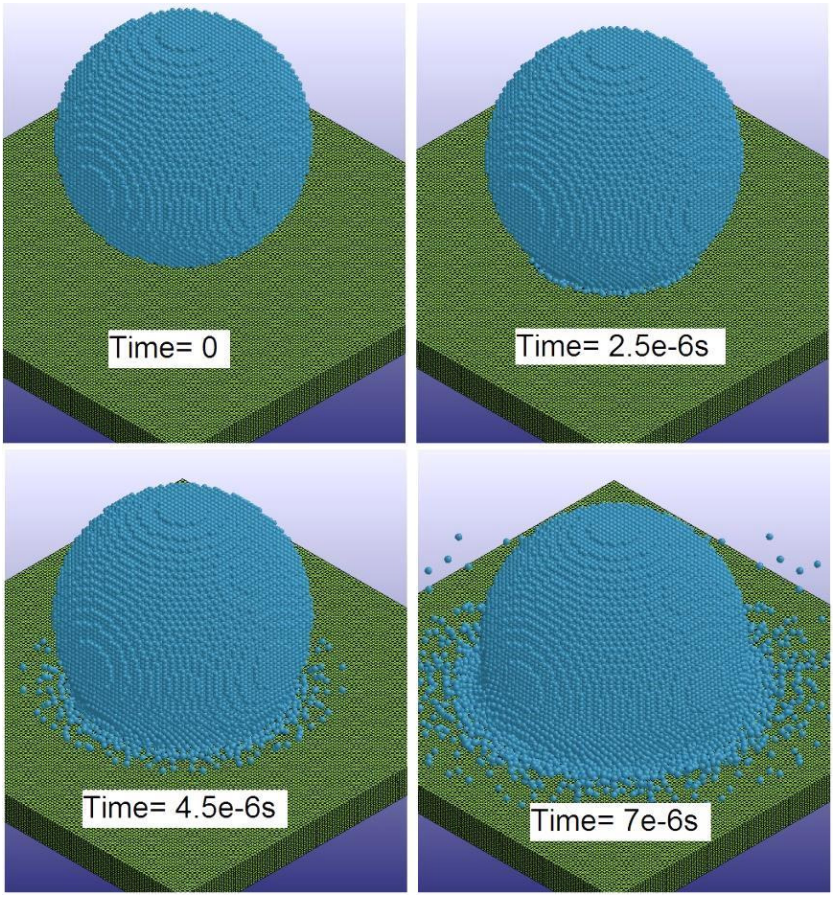

Figure 6-6. 3mm diameter water droplet impacting at 100m·s^{-1}, showing the droplet spreading behaviour

As with the SPH validation modelling work, the droplet spreading behaviour as modelled in LS-DYNA appears representative of the phenomena as observed in nature.

Through creating a section cut through the centre of the gelcoat layer and plotting contours of von-Mises stress during the impact event, it is possible to see the stress wave propagation through the gelcoat throughout the simulated impact. Figure 6-7 shows the section cut as well as the corresponding view of the surface during a 3mm diameter droplet, 100m·s^{-1}, impact event.

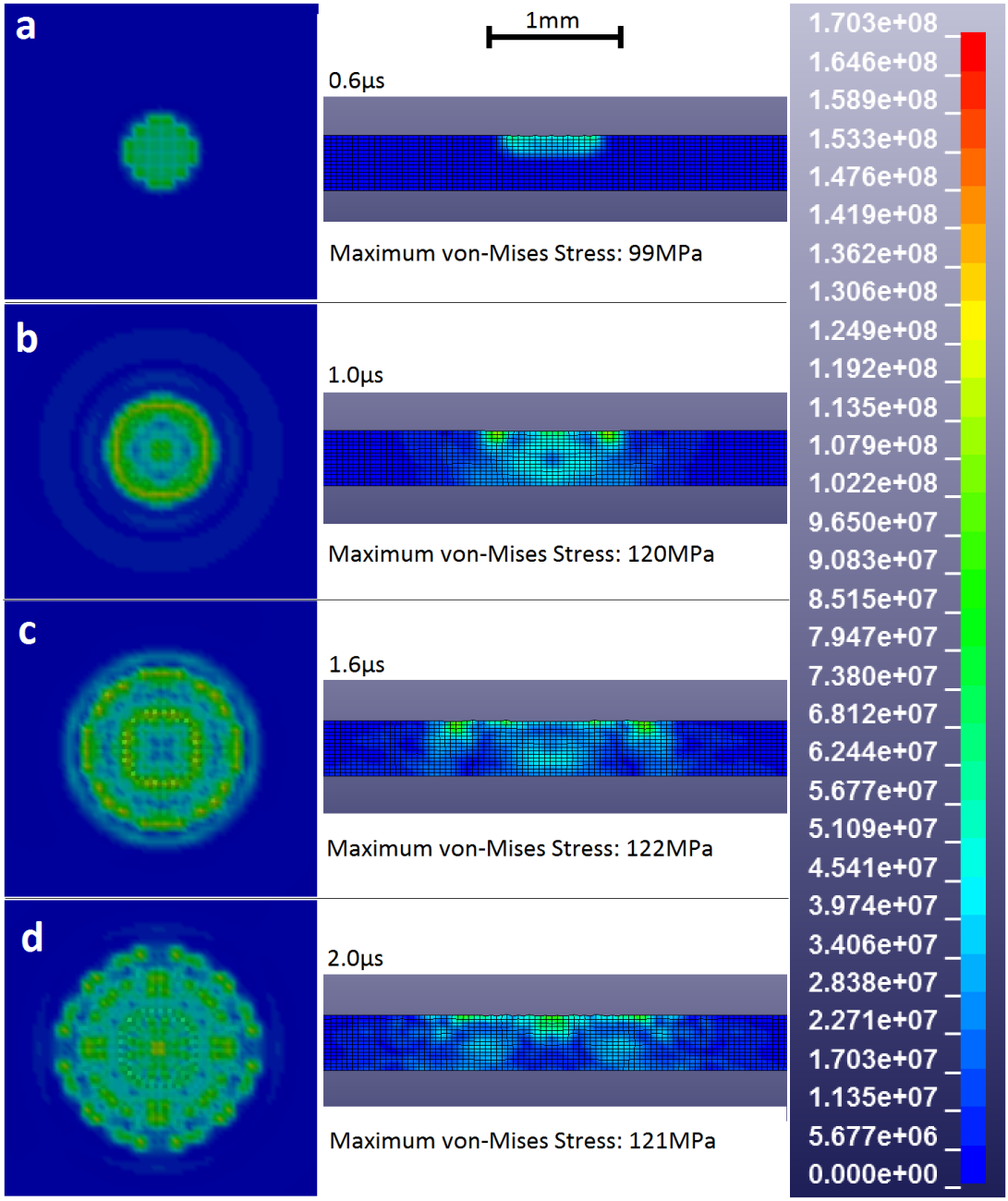

Figure 6-7. Contours of von-Mises stress (Pa) in the gelcoat during a 3mm diameter water droplet impact at 100m·s^{-1}. The upper surface of the gelcoat is show on the left and the corresponding sectional view (through the gelcoat thickness) on the right.

Figure 6-7 gives a thorough insight into the nature of stress creation within the gelcoat layer during impact. Upon impact (frame 'a') there is a clear high stress state created at the central area of contact between the droplet and the gelcoat upper surface. This shock front is then dissipated downwards through the thickness of the gelcoat in a manner similar to that characterised by Gohardani [79] and shown in Figure 3-17. After the dissipation of this initial impact energy, the droplet transitions from the waterhammer phase to the droplet

spreading phase of impact, whereupon the nature of stress distribution in the gelcoat changes. At 1µs into the impact (frame 'b'), the spreading behaviour has commenced and the creation of a high stress ring feature around the central axis of impact can be observed. At 1.6µs (frame 'c') the peak value of von-Mises stress can be observed as part of the growing ring feature first shown at 1µs, there are also secondary stress ring features observable (frames 'c' & 'd'); within the initial stress ring features. In the last image in the sequence, 2µs into the impact event (frame 'd'), it can be observed that although there are still high levels of stress state within the material, it is now predominantly located near the surface of the gelcoat. This behaviour is most probably linked to the fact that the initial peak in waterhammer pressure has been absorbed and dissipated throughout the material, and the main form of loading on the material is acting across its surface through the droplet lateral spreading behaviour.

It is possible to further examine the stress states within the gelcoat within the gelcoat during impact by plotting the time history of some of the key stress variables. For instance, Figure 6-8 plots the maximum values of von-Mises stress and maximum values (magnitudes) of stress in the z and x/y (x and y are equivalent due to axisymmetric impact conditions) directions in the gelcoat material (maximum value of all the nodes in the mesh) for a 3mm diameter droplet impact at 100m·s^{-1}.

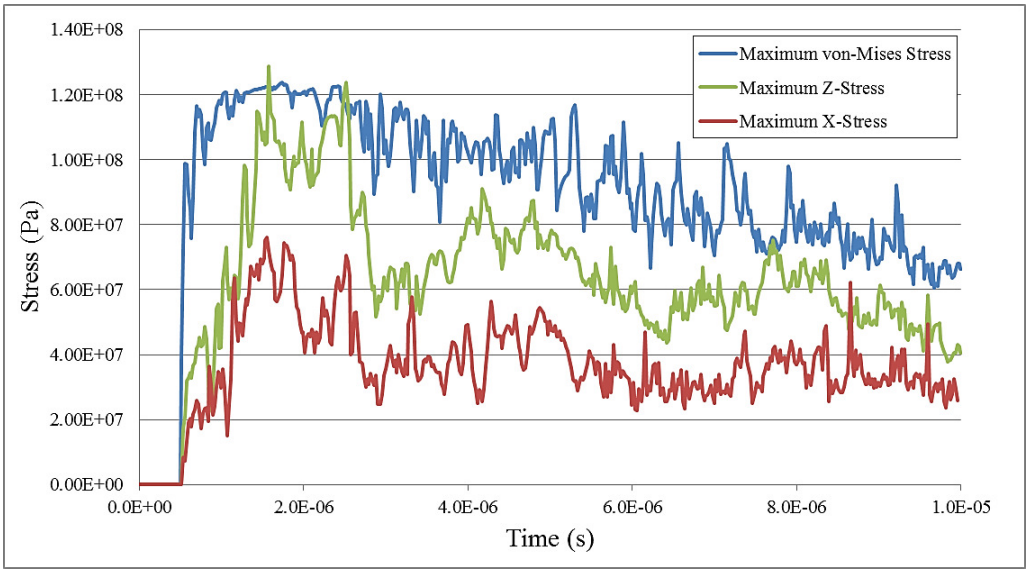

Figure 6-8. Time history of the maximum value of von-Mises stress and stress in the z-direction and x/y-directions in the gelcoat material during a 3mm diameter water droplet impact with initial impact velocity of 100m·s^{-1}. Due to axisymmetric impact conditions, stress in the x and y directions are equivalent.

As shown, with respect to the directional components of stress, stresses in the z direction are the most prominent with respect to the maximum values within the gelcoat at any one time.

However there are still significant stresses created in the in-plane direction and these too will have an important influence on the impact performance of the gelcoat, combining with the z stresses to create complex shear stresses.

Figure 6-9 shows the time history of the contact force between the impacting water droplet and the target surface during the simulated impact event, in the direction of impact (z-direction).

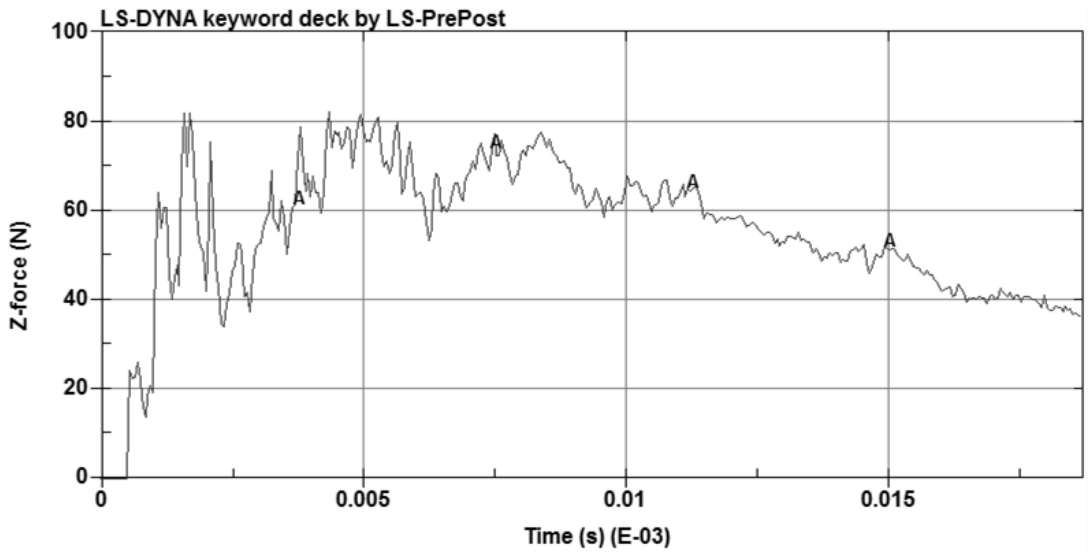

Figure 6-9. Time history of the contact reaction force between the droplet and the gelcoat surface in the impact direction (z-axis), for a 3mm diameter water droplet impact at $100m \cdot s^{-1}$.

As shown in Figure 6-9, upon impact the contact force rapidly rises to a peak value of around 80N after approximately 2µs, it then briefly decreases before again rising to a similar value after 5µs; after which it then gradually (and smoothly) declines. From this, it would appear that the initial peak (2µs) is imparted by the initial contact waterhammer pressure phase and the secondary peak (5µs) is imparted at the onset of the lateral jetting.

Looking specifically at the surface, it is possible to see the nature of displacement of the surface during impact by again creating a section cut through the centre of the gelcoat layer and scaling the z-direction displacements by a factor of 10. Figure 6-10 shows the scaled surface deformation behaviour of the gelcoat when impacted by a 3mm diameter droplet at $100m \cdot s^{-1}$ (at three points throughout the impact duration); displacements in the z-direction (vertical) are scaled by a factor of 10.

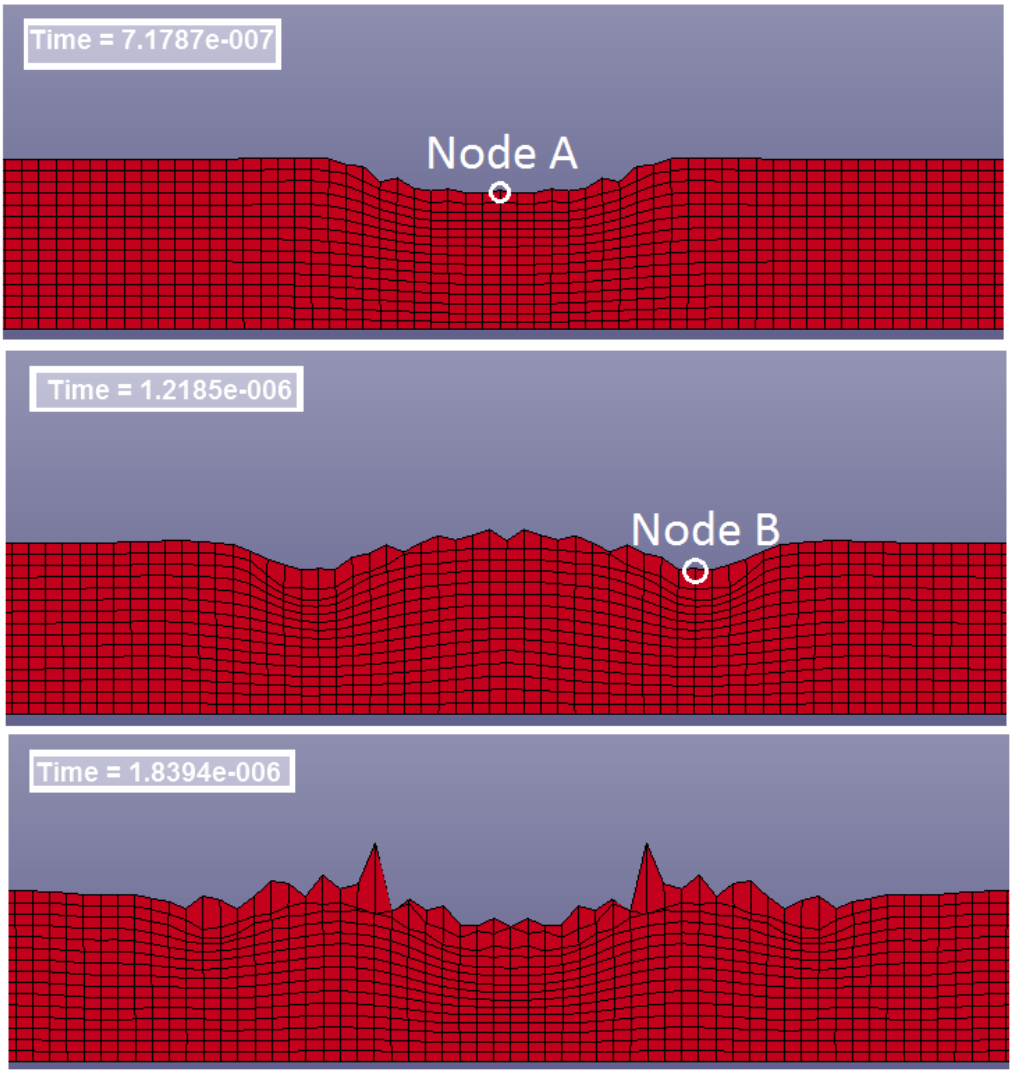

Figure 6-10. Sectional view through the centre of the gelcoat during impact from a 3mm diameter droplet; with initial impact velocity of 100m·s^{-1}. Deformation in the z-direction (vertical) is scaled by a factor of 10 to show the nature of surface displacement.

It can be seen that there is an obvious central depression during the initial phases of impact (as a result of the waterhammer pressure) which quickly rebounds upwards. This rebounding behaviour, coupled with the onset of droplet spreading creates a new depression some distance from the centre (forming a ring), which then appears to spread outwards as the centre is again depressed. This wave propagation behaviour agrees with the typical suggested Rayleigh wave behaviour as detailed by Gohardani [79], and shown schematically previously in Figure 3-17. Such wave formations result in the creation of significant shear stresses within the gelcoat as the material at the surface twists and bends. The sharp peaks in the surface are a result of the scaling of the displacements in the z direction by a factor of 10; therefore exacerbating the extreme displacements in these regions.

Figure 6-11 plots the time history of the z-displacement values for both Nodes A & B, as highlighted in Figure 6-10.

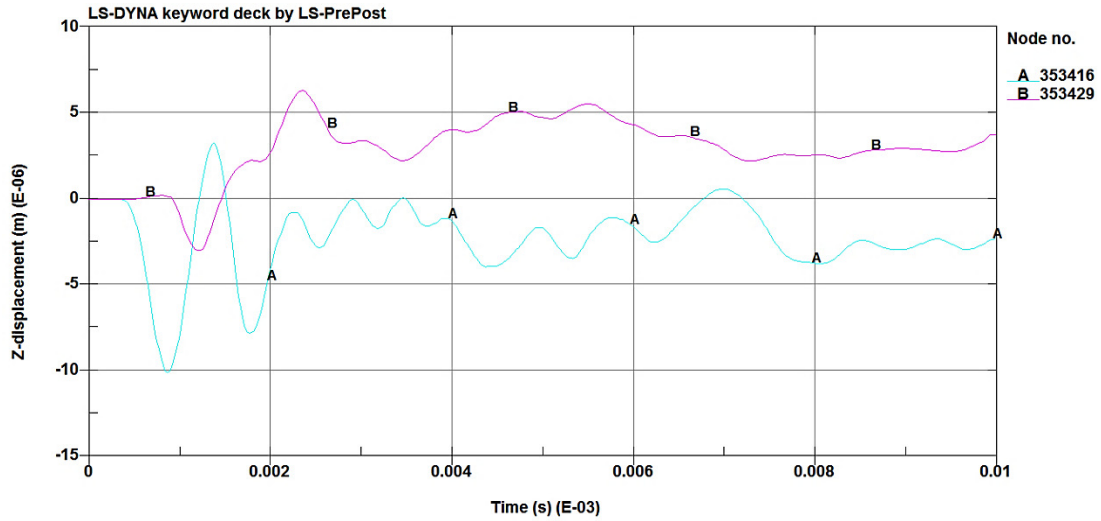

Figure 6-11. Time history of Z-displacement of Nodes A and B as identified in **Figure 6-10** during impact from a 3mm diameter water droplet with initial impact velocity of 100m·s^{-1}.

It can be seen that the central node (A) is depressed by around 10microns before rebounding above its initial position by about 3microns. The node position then oscillates for some time, before smoothing out at a depressed level of around 3microns, indicating permanent deformation of the surface; as will be discussed later. Node B displays similar oscillating behaviour but appears to settle at an elevated final position. Looking at both displacement curves, it is possible to again observe the Rayleigh wave behaviour of the gelcoat surface, whereby the displacement of Node A can be seen to propagate and influence the displacement of Node B.

Of obvious interest to this work is not only how the impact energy is absorbed by the gelcoat layer but also the way in which any damage is manifested. It is possible within LS-PrePost to plot contours of the effective plastic strain within the material, allowing for the identification of areas of damage (or plasticity) in the material. For instance, Figure 6-12 shows a plot of the contours of effective plastic strain on the surface of the gelcoat and through its thickness (again, from taking a sectional cut), at the end of a simulated 3mm diameter water droplet, 100m·s^{-1} impact event.

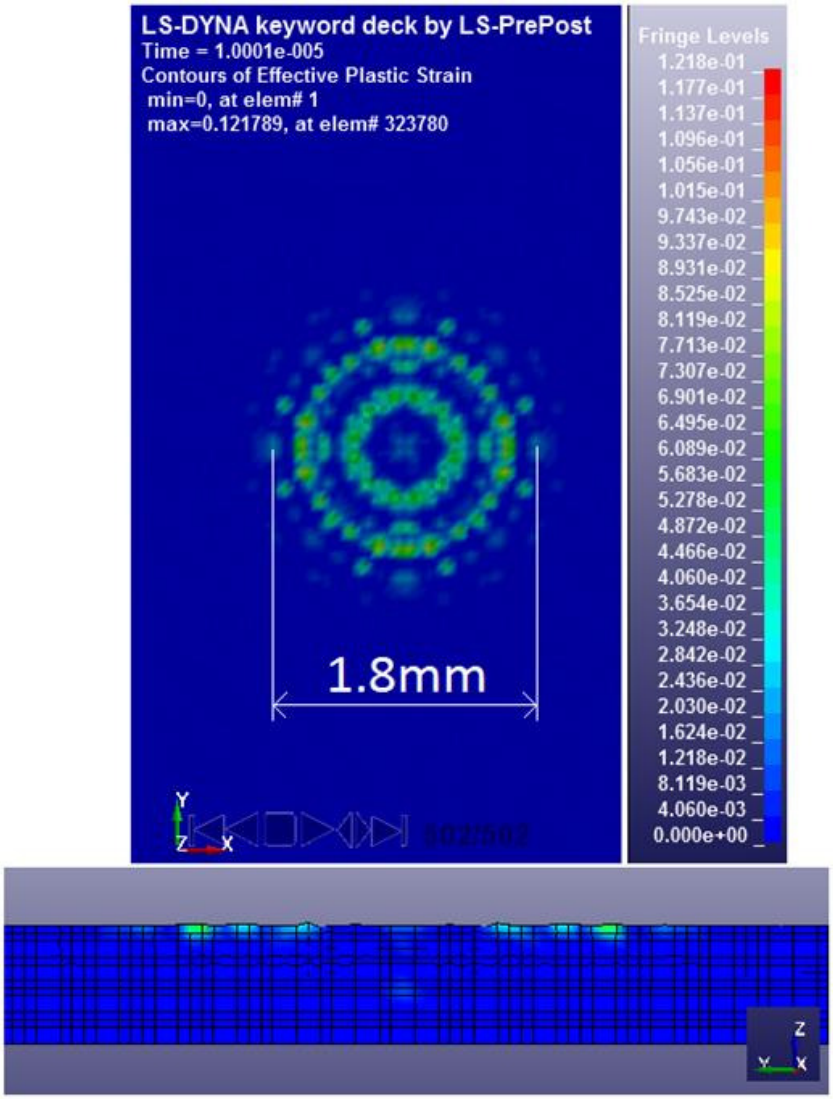

Figure 6-12. Contours of Effective Plastic Strain on the surface of the gelcoat layer (left) and through the thickness of the gelcoat layer (right), following a 3mm diameter water droplet impact event with initial impact velocity of 100m·s^{-1}.

Figure 6-12 shows that the simulation predicts that a 3mm diameter droplet impacting at 100m·s^{-1} will result in permanent plastic damage to the gelcoat material target. Plasticity in the material has been induced through the water droplet impact and has formed in multiple concentric ring structures, encircling the central impact location with a maximum ring diameter of approximately 1.8mm. A maximum level of effective plastic strain of around 0.12 has been induced in the material, most notably at the inner ring feature. However it is also observable that the areas of plasticity are almost exclusively limited to the surface of the material; as illustrated by the sectional view in lower portion of Figure 6-12.

Given that the damage created is formed both around and away from the central impact axis and only on the impact surface, it would seem that for the impact conditions given, the most

likely cause or mechanism of damage inducement arises from the rapid droplet lateral jetting phenomenon. However, it would seem that the application of the initial waterhammer pressure contributes significantly towards creating damage in the material in the two following ways:

1. By raising the stress values within the material to an initial peak value, as shown between 1-2μs in the von-Mises stress value in Figure 6-8 (and later in Figure 6-13).
2. Through creating the initial Rayleigh wave forms across the surface of the target.

These water hammer induced conditions consequently form the platform on which the droplet spreading phase can then create subsequent damage. The droplet wave front interacts and worsens the Rayleigh wave induced surface deformation causing the already highly stressed material to fail in these ring like structure.

In support of this proposed damage mechanism process, it is possible to examine, the time histories of the maximum values of both von-Mises stress and Effective Plastic Strain within the gelcoat throughout the impact simulation as shown in Figure 6-13.

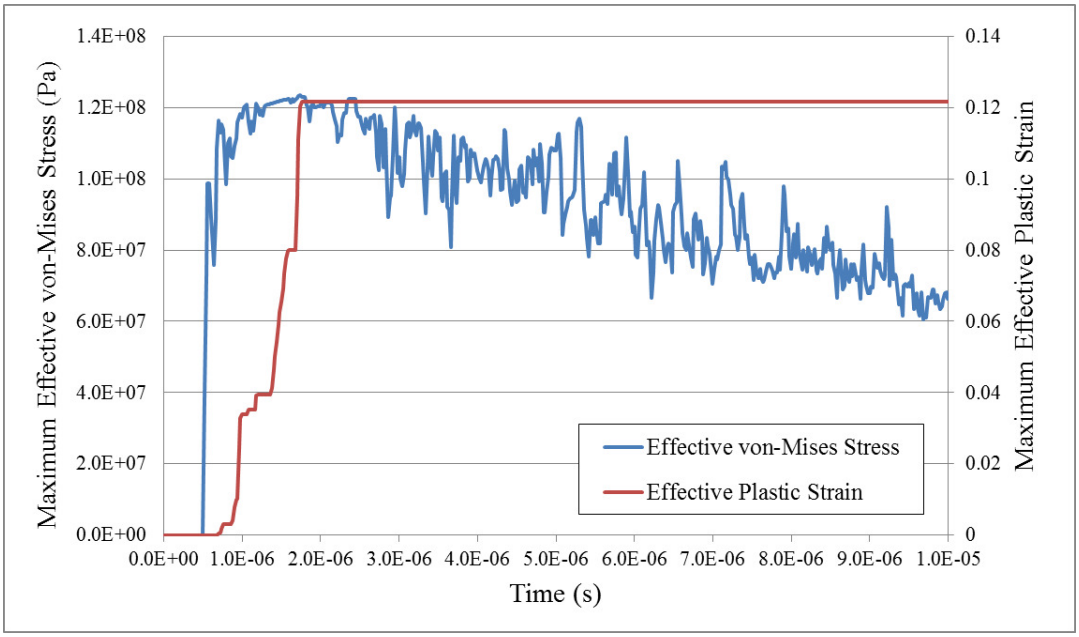

Figure 6-13. Time history of the maximum effective plastic strain within the gelcoat layer during a 3mm diameter droplet, 100m·s^{-1} impact event.

From this, it is clear that the most significant creation of plasticity within the target commenced during the onset of lateral jetting; after approximately 1μs. As suggested previously, the initial waterhammer pressure acts to raise the stress levels within the target to

an initial peak value. Subsequently, the lateral jetting process then commences, interacting with the high stress Rayleigh waves and inducing plasticity on the gelcoat surface.

On reflection of the previous results discussion, the following observations and findings were established:

1. Firstly, as with the previous SPH validation modelling work, the gelcoat impact modelling provides results which have been deemed to agree with the description of the phenomenon in literature [161] [107] [79] [98]; with respect to both the nature of the droplet spreading behaviour and the energy/stress dissipation within the target. The modelling captures the shockwave propagation down through the target and the Rayleigh wave creation on the surface, as observed in the natural phenomenon, as well as effectively modelling the creation of high pressure ring structures at the onset of lateral jetting.
2. From the previous literature review and through reviewing the modelling results shown, both quantitatively and qualitatively, the apparent primary mode of damage creation (at the impact velocities considered) has been identified. It appears that the waterhammer pressure created during the initial phase of impact, acts to heighten the general stress state within the material. During this phase, given sufficient impact energy, yielding of the material may occur. If this is not the case, then the high velocity lateral jetting of the droplet may create additional spikes in applied pressure, and cause the already stressed material to yield (or yield further if plasticity was already induced in the initial phase of impact).
3. It also appears that as a result of this impact and spreading process, the most likely mode of induced damage in the gelcoat from direct rain drop impact will occur in the form of ring like features of plasticity on the gelcoat surface; surrounding the initial point of contact.

With these established, there was then greater confidence gained in the accuracy and applicability of the modelling work; therefore allowing for the progression of further and varied analyses.

6.1.3.2 Influence of droplet diameter on the Damage Threshold Velocity

From the initial modelling work and results described in the previous sections, it became clear that the droplet spreading process of liquid droplet impact plays a dominant role in the damage mechanisms induced in the gelcoat. However, the previous section only reviewed the results from a single analysis of a 3mm diameter droplet, impacting at $100 m \cdot s^{-1}$.

Therefore it was hoped that a fuller set of analyses could firstly affirm and back up these initial findings, and secondly provide added insight into the nature of rain droplet impact induced damage in the gelcoat.

In this section, a parametric analysis aimed at investigating the effects of varying droplet diameter on the required impact velocity for damage creation (or DTV as previously described) is discussed. From both Equation 3.8 and subsequently the plot shown in Figure 3-23 it was previously shown that with increasing droplet diameter, the Damage Threshold Velocity decreases. In order to both add confidence to the modelling work conducted (through comparison to the analytical trend shown previously in Figure 3-23) and gain further insight into rain impact induced damage, a full parametric analysis was conducted to establish the DTV value for a range of droplet diameters.

However, before such modelling could be conducted, a decision on the definition of damage had to be established. As discussed previously in the literature review (Section 3.2), different authors have classified damage in different ways [79]. Some define it as the onset of fracture, the loss of optical transparency, weight loss and other diagnosable identifiers. For the purposes of the analyses proposed, it was decided that the onset of plastic strain (plasticity/yielding of material) would be the best indicator of damage occurring, as it is instantly identifiable and can occur through a single impact (loss of weight or instance, would require repetitive impact). Therefore, an effective plastic strain of 1% would signify the onset of damage; this value was large enough to ensure that the plasticity induced had not resulted from any computational errors etc.

The process of the parametric study involved creating a basic model following the same process as describe in the previous section; then altering the input droplet diameter to the required value. An iterative process of altering the initial impact velocity and reviewing the results was then followed to ascertain the minimum impact velocity at which a minimum of 1% effective plastic strain was induced in the gelcoat for each droplet diameter concerned.

Through this process it was possible to establish the DTV for 1, 2 and 3mm diameter water droplet impact events; at a 90˚ impact angle. The values obtained are plotted in Figure 6-14, which also shows the theoretical values of DTV calculated using Equation 3.8 and Equation 3.9 (as previously discussed) and the material property values quoted in Table 6-2 (the properties of water are as previously used for the plot shown in Figure 3-23). Given that the specific fracture toughness values is not known (as can vary for a given material), the plot

shows the theoretical DTV values for a range of fracture toughness values; detailed in the legend.

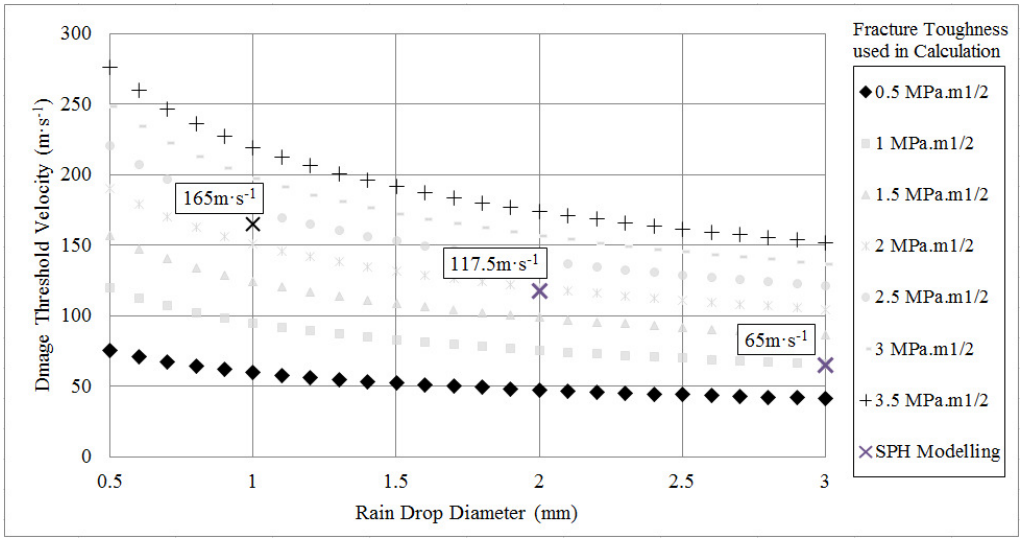

Figure 6-14. Plot showing the Damage Threshold Velocity of an epoxy target material, calculated using both Equation 3.8 and Equation 3.9 (with varying fracture toughness values) and as predicted by the LS-DYNA based impact simulation work.

As shown, when defining 'damage' as the creation of at least 1% plastic strain within the material during impact, the SPH based LS-DYNA modelling approach predicts DTV values within the range of expected values as predicted by Equation 3.8; however there is of course a degree of subjectivity with regards to the definition of damage. Indeed, for each droplet diameter simulated, the onset of plasticity below 1% within the target material was found to occur in many cases at velocities below those shown in Figure 6-14, and it may be the case that given repeated impact, these impact velocities may be significant enough to induce more definitive damage in the material (over time). It is clear however that the droplet diameter does have a significant influence on the likelihood of damage creation in the target. At smaller diameters more significant impact velocities are required to create lasting damage, whereas a larger diameter requires a much lower impact velocity to create damage; as shown in Figure 6-14. For a 3mm diameter droplet, damage was simulated with an impact velocity of only $65 m \cdot s^{-1}$, well below the tip speeds of many modern utility scale wind turbines. Reviewing the probability density of rain droplet size as shown previously in Figure 3-14, it is clear that 3mm diameter rain drops are most likely to occur during more extreme rain events (e.g. higher rain rates). As such, it would seem that the threat posed to the leading edge of the blade with respect to heavy rainfall events is significant.

Furthermore, as previously noted, plasticity was created at impact velocities below this value (at sub-1% levels), therefore significant damage could be created at lower velocities over a sufficient time period.

Again, it was possible to plot contours of effective plastic strain in the material at the end of the simulated impact event (as illustrated previously in Figure 6-12). Figure 6-15 shows the distribution of induced plasticity on the surface of the gelcoat target for each of the 3 droplet diameters simulated, at the 3 DTV values shown in Figure 6-14.

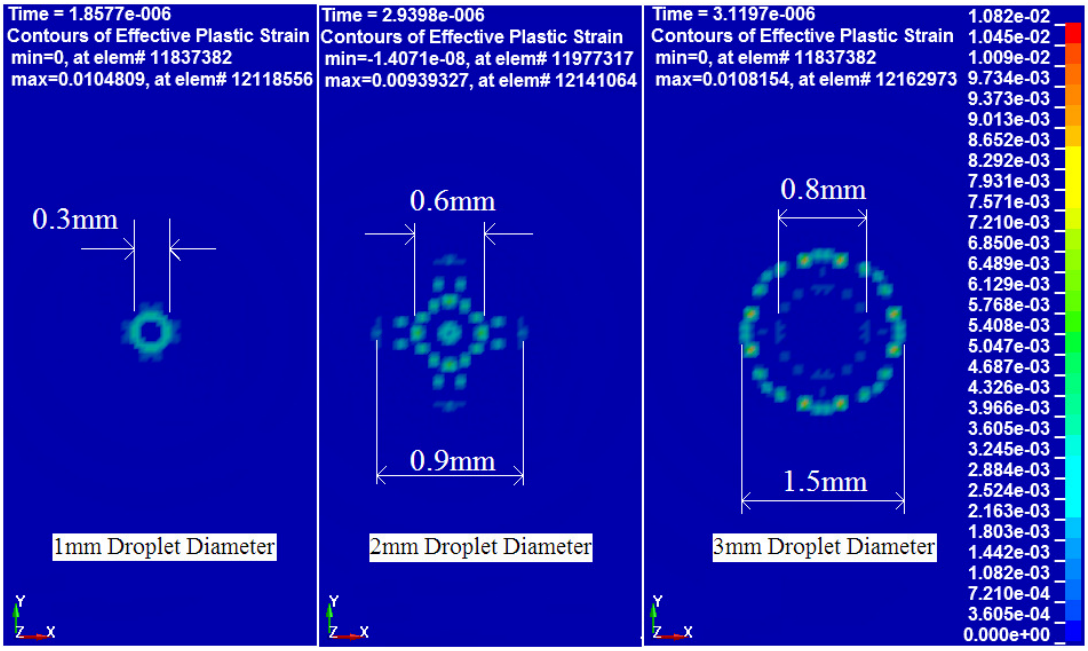

Figure 6-15. Contours of effective plastic strain on the surface of the gelcoat following 1, 2 and 3mm diameter water droplet impact events at the respective DTV impact velocities of 165, 117.5 and 65m·s^{-1}. The diameters of the plasticity rings created (both inner and outer where applicable) are also detailed.

As was illustrated previously in Figure 6-12, the damage created at the simulated DTV for each droplet diameter is formed in ring shaped patterns around central impact axis. In some cases, multiple concentric rings are formed at varying diameters from the impact centre.

Although there were consistencies obtained in the types of damage created in the different simulations (with respect to the ring-like topology), there were many complexities and some issues encountered when performing such modelling work. It was found firstly, that the level and extent of damage created was sensitive to the element size used to represent the gelcoat mesh. It was found that a larger element size (or coarse mesh) resulted in reduced damage creation or in some cases no damage creation. It was thought that this was a result of the larger elements not fully capturing the complex wave propagation behaviour on the gelcoat surface; conversely smoothing out the effect and limiting strain. However, it was also found

that too fine a mesh would result in, what was judged to be unrealistic, excessive damage and erosion.

6.1.3.3 Influence of impact angle on the gelcoat impact response

Given the curved and twisted nature of most wind turbine blades, the relative impact angle between the incoming rain droplets and the blade surface will vary widely across the blade surface. As such, it was necessary to investigate the effects of impact angle on the nature of the gelcoat impact response and any damage created.

For the purposes of such an investigation, it was decided that simulations featuring a 3mm diameter water droplet, impacting the flat gelcoat target and 30˚, 60˚ and 90˚ relative to the flat impact surface, over a range of velocities, would be conducted. The simulations were set up exactly as described in the previous sections, but with the alteration of the angle of the velocity vector applied to the rain droplet SPH nodes to the respective values of 30˚, 60˚ and 90˚.

To understand the effects of impact angle on the nature of the droplet impact phenomenon, it was possible to examine the droplet spreading behaviour exhibited for the three impact angles simulated. Figure 6-16 shows the droplet spreading behaviour of a 3mm diameter water droplet impacting the gelcoat surface at $100 m \cdot s^{-1,}$ at the three simulated impact angles of 30˚, 60˚ and 90˚.

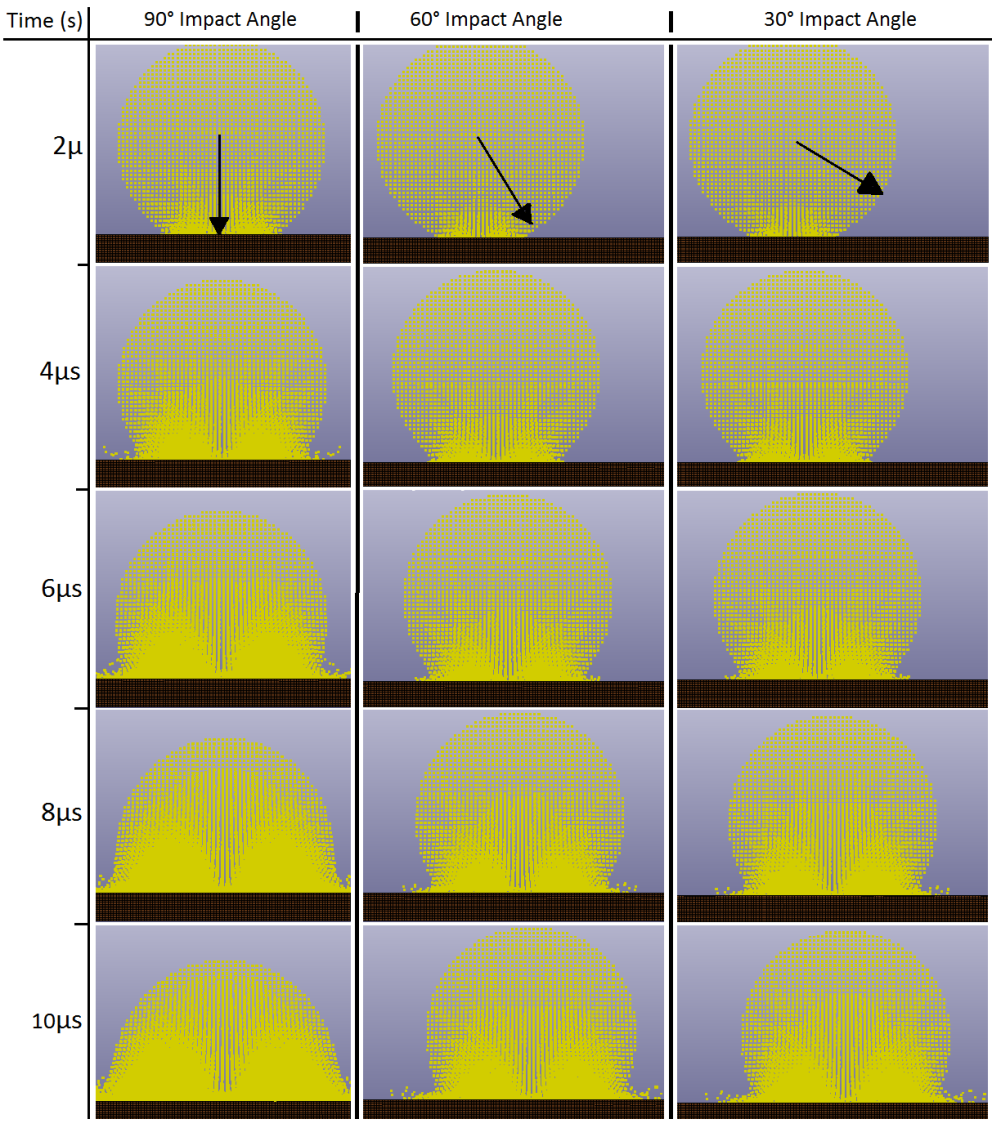

Figure 6-16. Sequences showing droplet impact spreading behaviour for a 3mm diameter water droplet impacting a gelcoat target at 100m·s^{-1} at 30˚, 60˚ and 90˚.

The impact angle appears to have limited effect on the initial droplet spreading behaviour. Indeed, at the two inclined impact angles, the droplet still appears to spread in a near symmetric way. However, as a consequence of the decrease vertical velocity component the duration of the impact event is prolonged, which will have an effect on the nature of the gelcoat impact response. As stated previously, given the high velocity nature of the simulations considered, the effects of surface tension and friction were considered negligible (as suggested by Adler [161]). However it may be that for inclined impact events, these effects could have a more significant role in the impact phenomenon, but such effects were outside the scope of the research conducted.

To gain an insight into the effects of varying impact angle on the impact response of the gelcoat target, it is useful to review stress created within the gelcoat during impact. Figure 6-17 shows the time history plots for the maximum value of effective von-Mises stress in the gelcoat when impacted (by a 3mm diameter water droplet) at 70, 80, 90 and 100m·s^{-1} at the varying impact angles of 30°, 60°, and 90° simulated.

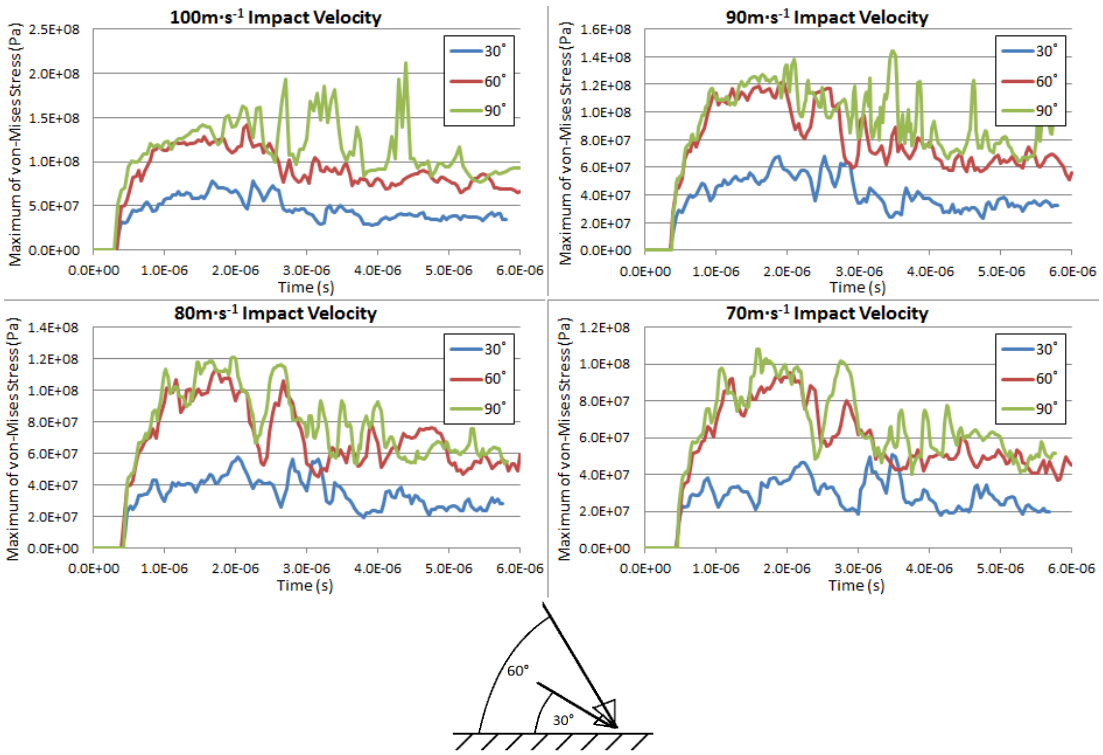

Figure 6-17. Time history plots of the maximum value of effective von-Mises stress within the gelcoat when subjected to a 3mm diameter water droplet impact event at varying velocities and impact angles. A key to the definition of impact angle is also shown.

It is clear from reviewing the plots at the four impact velocities tested that there is little significant difference between the stresses created in the gelcoat for impact events at 60˚ and 90˚. The only real discernable difference (other than a slight overall reduction in stress magnitudes) is that for the 60˚ impact events, there is a reduction in the stress spikes which occur after the initial peak; observed for 90˚ impact events as a result of the high velocity droplet spreading mechanism. It is clear however that at the shallower impact angle of 30˚, the stressed created in the gelcoat during impact are much reduced in comparison to that at 60˚ and 90˚. However, it is also observable that the peak stress levels created at 30˚ are sustained for a longer period (due to the slower rate of descent) and do not steadily decline in the same manner as observed for the more direct impact angles.

To gain further insight into the effect of impact angle on the gelcoat material response, it was possible to investigate nature of stress creation and distribution within the gelcoat during

impact. Figure 6-18 plots contours of effective (von-Mises) stress within the gelcoat when subjected to the 30˚ impact event described; at 100m·s^{-1}. The plot shows the stress contours on both the upper surface of the coating and through the thickness of the coating (through a sectional view) at various stages of the impact event; and also shows the droplet spreading behaviour (travelling left to right).

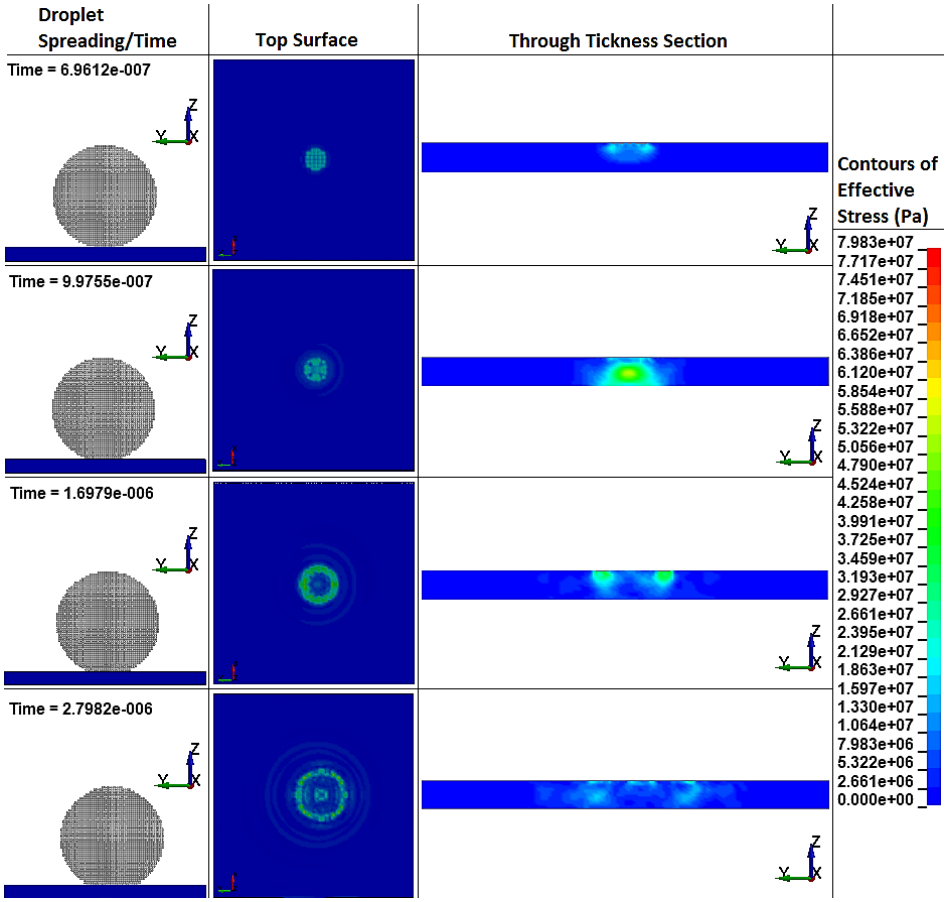

Figure 6-18. Plot showing the droplet spreading behaviour of a 3mm diameter water droplet impacting a gelcoat with a velocity of 100m·s-1 at a30˚ impact angle. Contours of effective von-Mises stress on both the top (impact) surface of the coating and through its thickness are shown, for various points during the impact event.

As shown, although the overall levels of stress created are reduced in comparison to a direct impact event, the nature of stress shockwave propagation is largely similar. The initial stage of impact features a waterhammer pressure induced compressional stress wave travelling downwards through the thickness (0.69-0.99µs). These stages are then subsequently followed by the onset of droplet spreading and the creation of associated ring like regions of high stress on the gelcoat surface.

It is apparent then from both the maximum effective stress time histories shown previously in Figure 6-17 and the stress distributions illustrated in Figure 6-18, that the only effects of a much decreased impact angle of 30˚ is to lower the overall stress values. As a result of the

relatively stiff characteristics of the gelcoat simulated, there are little observable effects of impact angle on the surface deformation; or at least enough to create any bow-wave like behaviour. Consequently, the stress distribution behaviour is very similar to that of direct impact events (Figure 6-7), other than the occurrence of a slight lateral shift in the overall distribution of stress in the direction of impact (left to right in Figure 6-18).

Considering also the 60˚ impact angle simulation, it is again possible to further explore the material response through a similar plot as shown previously in Figure 6-18 for the 30˚ impact angle simulation. Figure 6-19 shows the same plot, but for the simulated 60˚ impact angle event.

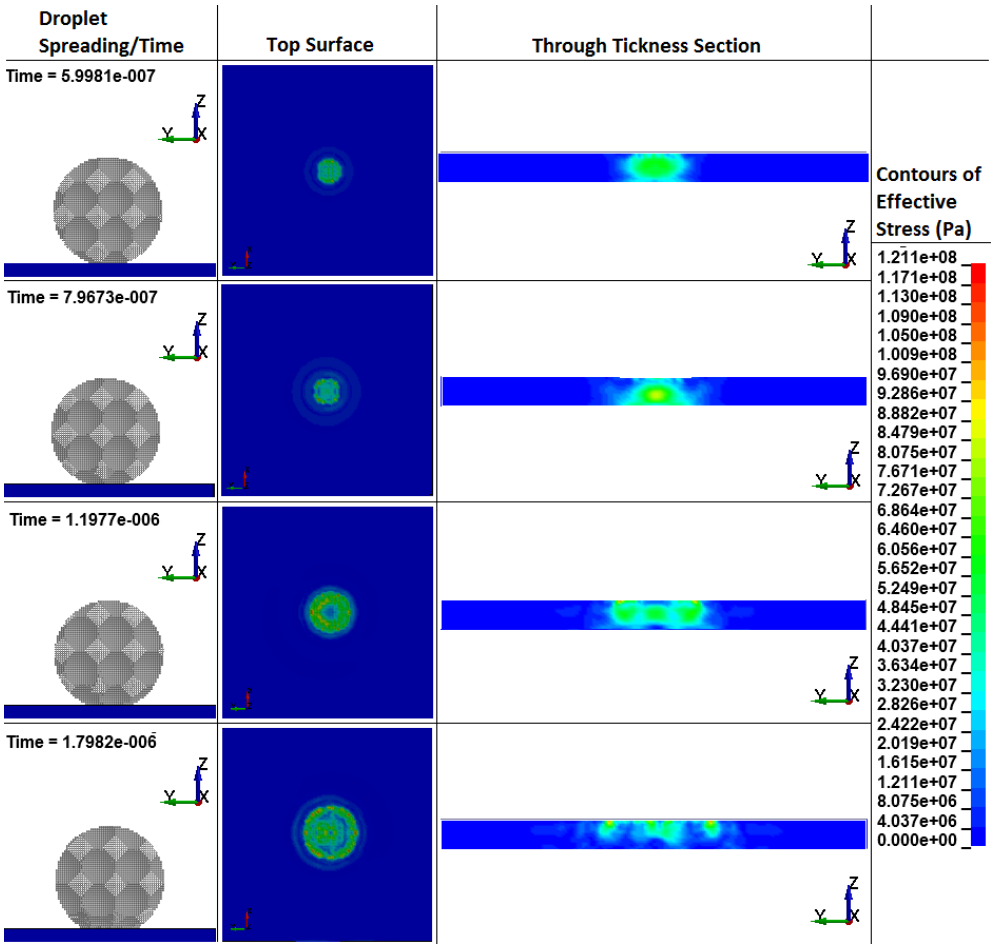

Figure 6-19 Plot showing the droplet spreading behaviour of a 3mm diameter water droplet impacting a gelcoat with a velocity of 100m·s-1 at a 60˚ impact angle. Contours of effective von-Mises stress on both the top (impact) surface of the coating and through its thickness are shown, for various points during the impact event.

As with the 30˚ impact angle simulation, with respect to the nature of stress/shockwave propagation, there is very little observable difference between the simulated 60˚ and 90˚ impact angle simulations. Again, the only real difference is observed in the overall maximum stress values which are reduced in comparison to those in the 90˚ simulation.

Figure 6-20 shows a plot of the induced plasticity on the gelcoat surface following the simulate 60˚, 100m·s^{-1} impact event.

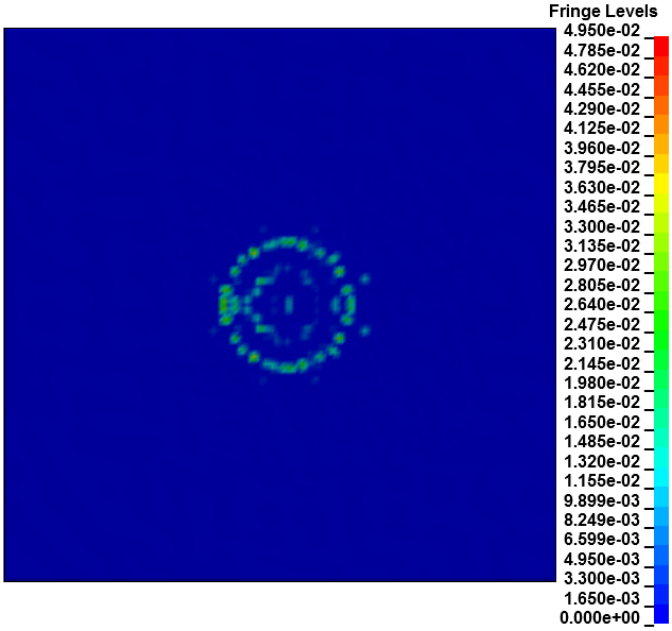

Figure 6-20. Induced plastic strain on the surface of the gelcoat material from a 3mm diameter simulated water droplet impact at 60˚ impact angle and 100m·s^{-1} impact velocity (travelling left to right).

A slightly decreased angle of 60˚ had little noticeable effect on the nature of damage creation of the gelcoat surface. As with the direct impact simulations, plasticity was created in concentric ring formations on the gelcoat surface, with a slight skew in distribution in the direction of impact (left-to-right). More noticeably, the magnitude of the induced plastic strain is comparably lower to those created through direct impact; and shown in Figure 6-12.

It would seem then that for the gelcoat material simulated, the effect of decreasing the impact angle is to reduce the stresses created within the material. Given the relative stiffness of the gelcoat material, decreased impact angles have little observable effect on the surface deformation of the coating during impact. However this may not be the case for all materials, for instance, if the target material were more flexible the inclination may bring about the creation of a leading bow wave on the surface and consequently create a gouging effect. Further modelling would be required to investigate the possibility of such effect, as discussed later in Section 6.4.

6.2 Rain droplet impact induced erosion of a gelcoat material

The previous section examined and established some of the key processes and damage mechanisms in relation to water droplet impact on a gelcoat material; through impact simulation methods. However, the issues associated with rain droplet impact on the leading edge of wind turbine relate more commonly to the occurrence of erosion (i.e. progressive long term damage). As such, the phenomenon of repetitive water droplet impact on a gelcoat surface was explored, based on the modelling methods developed.

As a typical case study, the simulations would feature a 3mm diameter droplet, impacting the same location 6 times at 90˚, at a velocity of $100 m \cdot s^{-1}$; using the same basic model setup as described in the previous section. These conditions represent a close-to-worst case scenario for a wind turbine blade, and were chosen as it was known (from the modelling described previously) that they would induce damage. Consequently, this would then make it possible to assess the capability of the LS-DYNA modelling approach with respect to simulating progressive damage, as well as predict the manner in which erosion may take place.

6.2.1 Model Setup

There were three apparent approaches to modelling the repetitive rain droplet impact of the gelcoat:

1. A simple direct impact simulation could be carried out as discussed previously in Section 6.1, featuring a 3mm diameter droplet impacting the surface at right angles at $100 m \cdot s^{-1}$. Following completion of the simulation, through utilising the 'Output' option in the post processing tools of LS-PrePost, the stress and strain values in the gelcoat for a given state (or time) in the simulation could then be exported into a new simulation. The simulation could then be repeated and the subsequent stress and strain values exported into another new simulation. Through repeating this simulate/export/import/simulate process it would be possible to investigate the effects of repetitive impact.
2. Similar to this first approach, a simple single impact simulation could be performed and a 'restart' file written at the end of the impact event. This restart file could then be used to reset the impact conditions for the next impact event, whilst keeping the same stress-strain state within the target from the previous simulation.
3. Alternatively, a simpler approach was to incorporate multiple impact events into one single simulation, through placing multiple droplets stacked vertically in the simulation and applying the impact velocity to each. The setup of such an approach

would be much simpler than the one discussed previously, however the computational time required would be increased dramatically.

All approaches were explored and although the export/import and restart processes reduced the simulations into smaller more manageable portions and allowed for alterations to the model between impacts, there were a number keyword formatting issues encountered with respect to importing the stress-strain values into new simulations. As such, it was not possible to fully utilise this approach for more than 2 impact events. Therefore, a multiple impact simulation approach would be employed.

The setup of this model was relatively straightforward and almost identical to the simple single 90°, 100m·s^{-1} impact simulations (gelcoat) described previously, requiring only the creation of the additional 5 water droplet bodies at positions above the first droplet (Figure 6-21) and the addition of extra contact definitions. For illustrative purposes, Figure 6-21 shows 3 rain droplets, however the actual analyses consisted of 6 rain droplet bodies.

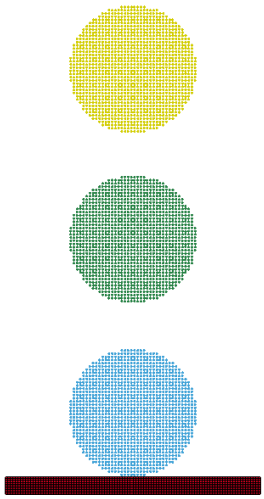

Figure 6-21. Multiple rain droplet impact simulation configuration, shown schematically with distance between droplets reduced.

To reduce the large computational solve time required for such a simulation, the target mesh element total was coarsened to a value of 100k and the individual droplet SPH node count to 33.5k. This was done in the interest of time and exploring the proposed repetitive impact modelling methodology. However, if a more comprehensive and through examination was required, the values could be increased. Additionally, the times at which contact between each of the droplets and the gelcoat surface was active were adapted so that once each droplet had imparted the significant portion of their load (i.e. shortly after the initial peak in impact stress and plasticity), the contact definition between the droplet and the surface would

be ignored. This meant that the droplet would then pass through the target, clearing the way for the subsequent impact event.

To incorporate the process of erosion in the simulations, the card *MAT_ADD_EROSION was created and associated with the gelcoat material model. This option allows for the addition of an element deletion (or erosion) criteria to the associated material model, through defining certain threshold values for states such as effective plastic strain, effective stress, pressure and many more. For the analyses considered, it was decided that the criteria for erosion would be based on the effective deviatoric strain in the material, any value greater than 0.3 would result in element deletion; as indicated in the stress-strain data for the epoxy resin considered (Figure 6-1).

6.2.2 Results and Discussion

Owing to the high node total and complexity of the model described a lengthy run time of approximately 6 hours was required to complete the simulation discussed.

To investigate the progressive damage creation brought about through repeated impact, it is possible to examine the plasticity created on the surface of the gelcoat after each impact event. Figure 6-22 shows contours of effective plastic strain on the gelcoat surface after 6 consecutive impact events; featuring 3mm diameter droplets impacting the surface directly, at 100m·s^{-1}.

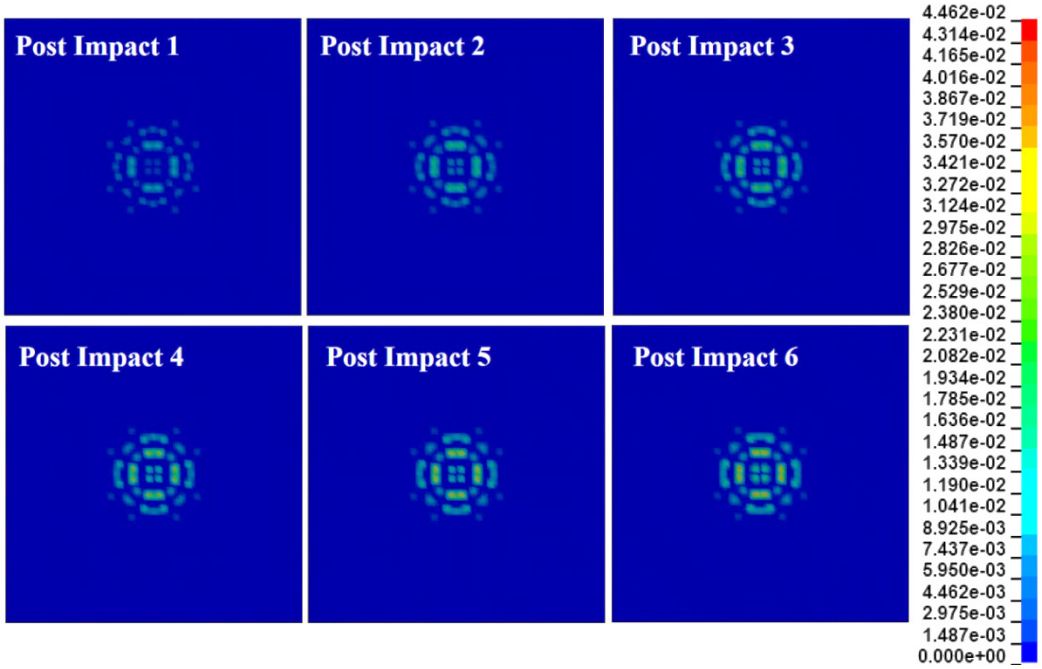

Figure 6-22. Contours of effective plastic strain on the surface of a gelcoat subject to 3 consecutive impacts from a 3mm diameter water droplet at 100m·s^{-1}.

It can be seen that repetitive impact at the same impact location acts to gradually increase the maximum effective plastic strain on the gelcoat surface, as well as spreading the overall area of plasticity. It can be observed that as a result of the droplet impacting the surface at the same location for each impact event, the subsequent ring-like damage mechanism is further emphasized and the occurrence of plasticity on the surface is concentrated mostly in these ring-like formations.

To better understand the magnitudes of the stresses and induced levels of plastic strain, it is possible to plot a time history of the maximum values of both effective (von-Mises) stress and effective plastic strain in the gelcoat body throughout the multiple impact simulation, as shown in Figure 6-23 shows a time history of the maximum values of von-Mises stress within the epoxy gelcoat during the simulation; incorporating all three impact events.

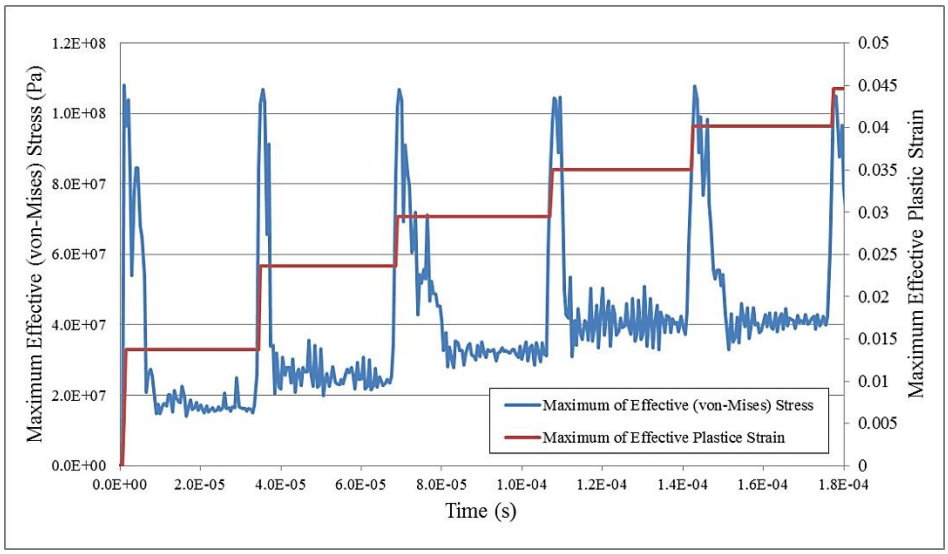

Figure 6-23. Time history plot of the maximum value of von-Mises stress and effective plastic strain within the gelcoat during an impact sequence of six 3mm diameter water droplets impacting at 100m·s^{-1}.

The time history shows that each droplet impact acts to first raise the stress in the target to a peak value of around 100MPa, after which (for each impact) the contact definition is then ignored, the droplet passes through the target, and the stress decreases to a relaxation stress level. It can be seen that this stress relaxation value is heightened in comparison to the initial stress state of the material (i.e. zero), and is further increased after each impact sequence. Similarly, it can be seen that the levels of effective plastic strain within the material are increased following each impact event (the source of the subsequent increase in residual stresses).

It is evident that for the nature and number of impacts considered in the analyses discussed, the levels of plastic strain created were insufficient for the onset of erosion on the gelcoat

surface. However, it is apparent that for the impact conditions simulated, erosion levels strains would eventually be created and the onset of erosion would begin. Indeed, examining Figure 6-23 further, it can be observed that from impact number 2 onwards, the induced effective plastic stain within the material appears to increase almost linearly with each impact event. Figure 6-24 plots the maximum effective plastic strain magnitudes in the gelcoat from impact 2 onwards.

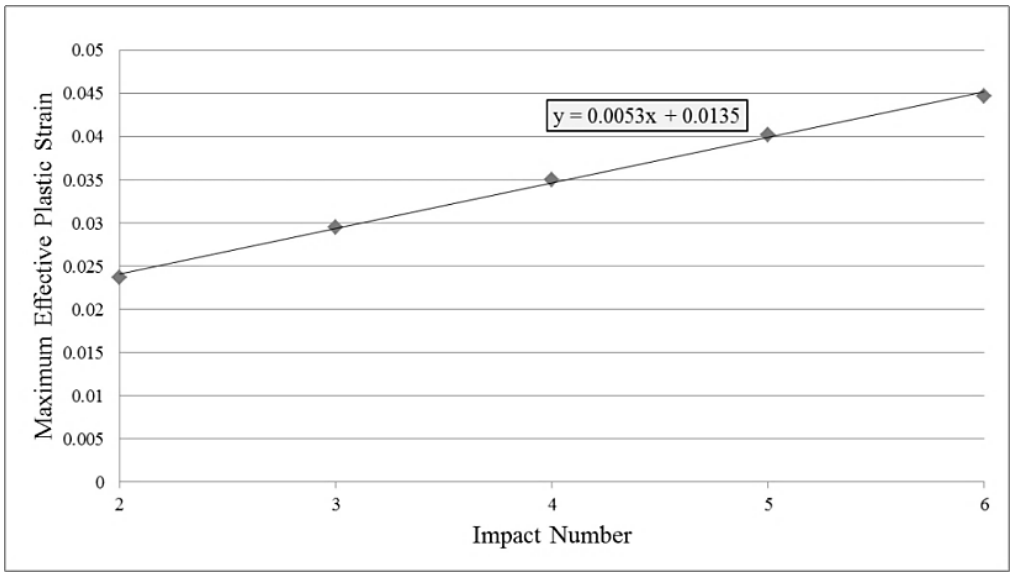

Figure 6-24. Plot showing the increasing value of maximum effective plastic strain within the gelcoat material (from impact number 2 onwards); following repetitive simulated impact.

From this plot, it can be seen that there is a degree of linearity in the increasing value of maximum effective plastic strain within the material through repetitive impact. Through extrapolating this trend line, it is possible to propose the number of impact events required for the plastic strains to reach the required erosion value of 0.3. From the equation shown in Figure 6-24, it could be predicted that approximately 54 impact events (given the same impact conditions) would be required for the plastic strains created to reach erosion levels. However this approach obviously makes many assumptions and would require extensive further investigation to establish whether this linear trend would apply beyond the number impact events simulated. It may be the case that the plastic strain increase per impact event actually increases or conversely begins to level out as a result of material work hardening. Further simulations would be required to further explore this issue.

However, it is clear from the results shown that LS-DYNA can capably model the phenomenon of progressive impact damage; given adequate computational resources and modelling time. The repetitive impact scenario considered in the analysis discussed

obviously represents a very specific (and in nature very unlikely) sequence of impact events. However the results of the analysis highlight the role of the creation of plasticity, and consequent residual stress, in creating the conditions for further progressive damage through repeated impact. Given enough time, the simulation could be extended to include many times more impact events and subsequently model the phenomenon of erosion or provide further confidence to the predictive trends produced (as shown in Figure 6-24). Additionally, although repetitive impact at an identical impact location cannot be described as representative of the likely impact conditions on a real blade, it could represent a conservative worst case scenario for the evaluation of material impact response. As it is clear that for the given material simulated, progressive damage could be a significant issue and prolonged repetitive impact at any impact velocity above the DTV value could result in eventual (or perhaps imminent) surface erosion damage.

6.3 Rain droplet impact induced damage of a gelcoat on a composite substrate

Although extensive parametric analyses were conducted to investigate the rain droplet impact induced damage of the simulated gelcoat in isolation (as discussed previously in Section 6.1), it was considered important to also model the impact response of the same coating when combined/attached to a relevant composite substrate. The aim of the modelling was to evaluate the difference in impact response between a simulated coating modelled in isolation and as part of a composite layup. Any significant differences in the impact response (and subsequent damage) would prove important in further understanding the likely impact response of gelcoat materials. Furthermore, any identified differences could also be of importance to the developing field of rain impact erosion testing standards, where the importance/influence of the chosen test substrate is not yet fully understood or documented.

Given the limited impact energies associated with rain droplet impact, the detailed impact response of the composite substrate was not of significant interest to the simulation work; as the occurrence of damage to the substrate was deemed highly unlikely. The role of the composite substrate was concerned mostly with providing representatively flexible boundary conditions for the gelcoat material. In light of this, the composite material bodies in the simulations could be kept relatively simple, therefore reducing computational requirements. Such simplifications also negated the requirement to fully consider the effects of scale with respect to the composite materials, as through modelling such materials at millimetre and sub-millimetre scale, challenges with respect to accurately modelling the material can arise; as recognised by Gohardani [79]. At such scales, the localised differences in material properties of the composite constituent materials can require consideration; i.e. the fibre and matrix constituents may be required to be simulated as separate finite element bodies. However for the modelling work described here, the reduced interest in the detailed impact response of the composite substrate materials meant that the individual composite layers could be modelled with simple orthotropic (or other) material properties; negating constituent material behaviour concerns.

6.3.1 Model Setup

To allow for direct comparison of the modelled impact response of the gelcoat material as attached to a composite substrate, to that of the previously modelled full fixed gelcoat (Section 6.1), instead of creating a completely new model, the fully fixed gelcoat model was altered to incorporate a composite substrate. Consequently, except where noted, all model

variables and parameters were kept identical to those previously implemented and discussed, such as the gelcoat material properties, geometry and mesh density.

Considering the main objective of the simulations, it was decided that a droplet diameter of 3mm would be used (following the same procedure as detailed in the fully fixed gelcoat analyses). The droplet impact velocity would then be altered accordingly to establish any differences in the results obtained between the full fixed and composite applied gelcoat analyses.

It was decided that the composite material layup configuration of the reference blade discussed previously in Section 5.3.1 would be implemented to form the composite substrate. As discussed, the layup consists - from surface downwards – of a gelcoat, a layer of randomly orientated chopped strand mat and three layers of biaxial composite, all composed of glass reinforcing fibre and an epoxy based matrix and all 400µm thick.

In the absence of reliable and verified blade material properties, suitable material properties had to be sourced from literature. Given the now wide spread use of glass fibre reinforce epoxy matrix composites, a range of material property sources were available. However for the biaxial weave composite, the material properties cited by Menna et al. [183] for a prepreg composite based on an E-glass plain weave with 295g·m^{-2} areal weight and Cycom 7701 epoxy resin matrix were implemented. Menna et al. [183] utilised these material properties, shown in Table 6-3, to conduct numerical impact tests on a multiple ply composite using LS-DYNA, and derived the material properties through both manufacturer literature and model calibration.

Table 6-3. Material properties used for biaxial reinforced glass/epoxy composite layers, as cited by Menna et al. **[183]**

Orientation	Young's Modulus (GPa)	Tensile Strength (MPa)	Compressive Strength (MPa)
1	26	414	458
2	26	414	458
3	8	120	500
	Shear Modulus (GPa)	Shear Strength (MPa)	Poissons Ratio
12	3.8	105	0.1
23	2.8	65	0.25
13	2.8	65	0.25

Although a high level of agreement between the composite material properties of actual blade materials and those used in the simulations was not required (an approximate flexible interface was all that was required), based on industrial consultation, the composite material system described by the properties in Table 6-3 was deemed to actually represent at least a good approximate of such actual material properties. The strength properties were of little importance to these simulations, but would be in later simulations.

Due to the quasi-isotropic material behaviour of chopped strand mat composite materials, accurate material properties are difficult to obtain experimentally, and as such, sparsely documented in the literature. For the purposes of this research it was decided that the material would be modelled as a standard isotropic material, as again the general flexible behaviour was the only key requirement of the simulated composite substrate. The material properties utilised for the chopped strand mat were based on numerous sources in the literature [217] [218] [219] [220] and are detailed in Table 6-4. In essence, these properties represent a slightly enhanced (stiffer/stronger) epoxy resin material.

Table 6-4. Material properties for chopped strand mat. Source: Various

Property	Value
Density (kg·m^{-3})	1452.8
Young's Modulus (GPa)	8
Poisson's Ratio	0.3
Yield Stress (MPa)	190

Again, the exact material properties of typical CSM materials as used in wind turbine blades were not required, as the CSM layer in the simulations was require only for the purpose of creating flexible boundary conditions for the gelcoat layer.

As with the creation of the gelcoat geometry, the substrate composite layers were created through using the 'Shape Mesher' tool, and subsequently specifying the main dimensions and the mesh density required. As the impact response of the actual composite substrate was of reduced interest in the simulations, the individual layers of the composite were represented by a single layer of solid elements. The target geometry – and associated mesh – are illustrated in Figure 6-25; as well as the droplet geometry.

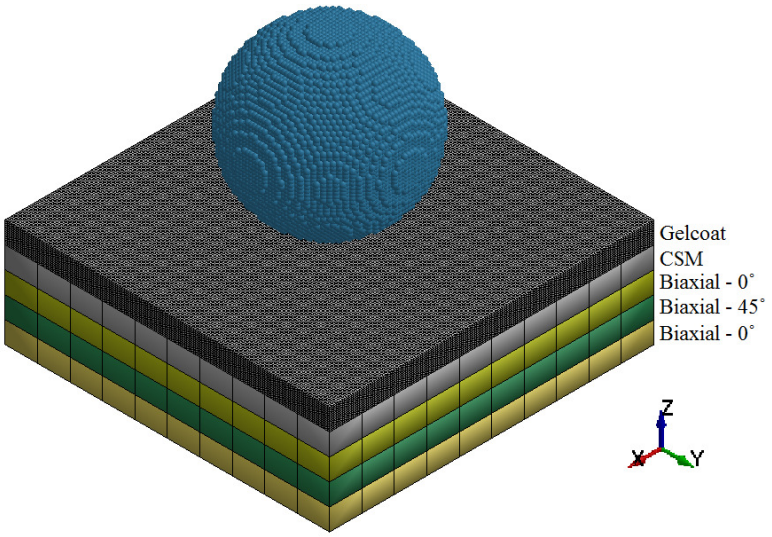

Figure 6-25. Layup geometry and mesh. Overall Dimensions: 6x6x2mm; 400µm thick constituent layers.

The CSM material properties were assigned using the material model *MAT_PLASTIC_KINEMATIC, which requires only the density, Young's modulus, Poisson's ratio, yield stress and post-yield tangent modulus. The values cited previously in Table 6-4 were entered and the material was assumed to behave in an elastic-perfectly-plastic way, therefore the post-yield tangent modulus was kept at zero.

For the biaxial reinforced composite layers, the material model *SOLID_COMPOSITE_FAILURE_SOLID_MODEL was used, with the properties cited by Menna et al. [183], and quoted previously in Table 6-3. As discussed previously in Section 4.5.3, this material model is quite sophisticated and incorporates a number of failure mechanisms, and as such would normally be excess to requirements in such simulations where failure is deemed unlikely. However, as subsequent hailstone impact analyses would look at composite failure, it was necessary to become familiar with the model in these early composite modelling analyses, which could then be built upon in the hailstone impact work.

Using such a composite material model automatically assigns principle material axes to the respective elements of the body. These axes can be checked visually in LS-PrePost using the 'Identify' tool and the material axis directions can also be altered using the element editing tools. These tools were used to establish the [0˚/45˚/0˚] layup configuration of the biaxial composite layers, as illustrated previously in Figure 6-25. This was done by fixing the A and B material axes (fibre orientations in weave) of all the elements in the 3 composite layers to align with the X and Y axes respectively (shown in Figure 6-25). The elements in the 45˚ orientated middle composite layer were then rotated 45˚ around their local material axis C (global-z). Again, the layup configuration was partly arbitrary and was assumed not to drastically alter the deflection characteristics of the resulting laminate; for the limited impact energies considered.

The contact definitions between the individual layers of the target body were defined using the *CONTACT_AUTOMATIC_SURFACE_TO_SURFACE_TIEBREAK contact card. The contact between the respective layers was set to fully fixed, through setting OPTION=1 in the contact definition. To account for the greatly differing levels of stiffness between the adjoining composite layers, the SOFT=1 option was also applied to each of the contact definitions.

To allow for full distribution of the contact energy throughout the composite layup and to approximate real wind turbine blade behaviour, symmetry boundary conditions were applied to the side surface faces of the composite layup. Such conditions allow for in plane

translation and rotation but restrict out of plane translation and rotation; in the respective surface plane. It was though that these boundary conditions would permit the composite layup to freely flex under impact loading. To restrict rigid body motion in the impact direction, the lower edges of the composite were restrained in in the z-direction.

All other model parameters were kept identical to those previous utilised in the fully fixed gelcoat analyses discussed previously. To more fully evaluate the effects of the added substrate flexibility on the gelcoat impact response, a range of impact velocities were simulates; as discussed in the following section.

6.3.2 Results & Discussion

The simulation describes was completed successfully, requiring a run time of approximately 3 hours.

As with the previous gelcoat analyses, the impact response of the gelcoat can be illustrated well through plotting the contours of effective von-Mises stress in the material through a given impact event. Figure 6-26 shows such a plot for the gelcoat during impact form the 3mm diameter water droplet, striking the surface at $100 m \cdot s^{-1}$. The plot shows both the stress distributions formed on the surface of the gelcoat (on the right) and through its thickness (through a sectional view on the left); the impinging droplet is also superimposed onto the sectional view to indicate the stages of the impact progression.

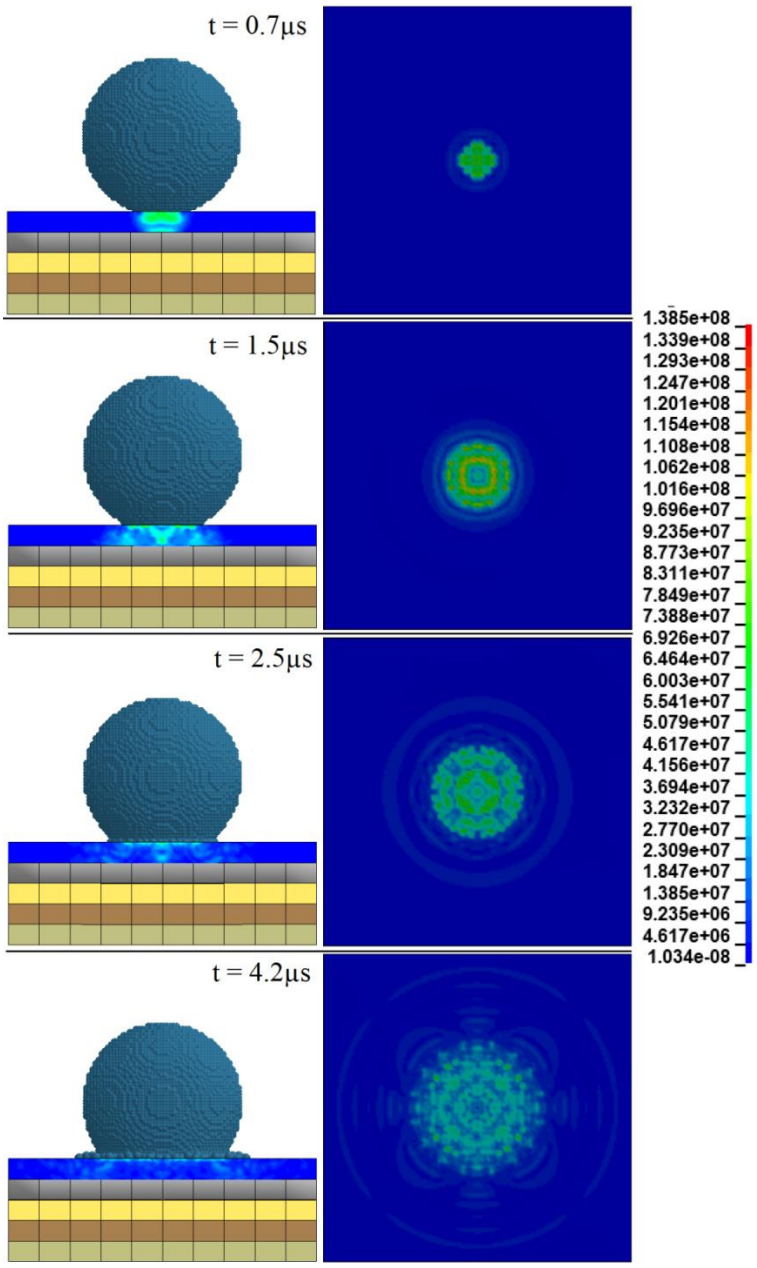

Figure 6-26. Plot showing the contours of effective von-Mises stress (Pa) in the simulated gelcoat during a 3mm diameter water droplet impact even at 100m·s^{-1}; at various stages. The images on the left show a sectional view of the stresses generated through the gelcoat thickness (at the centre of impact), with the water droplet spreading behaviour superimposed into the images to illustrate the impact development; the composite substrate is shown without contours. The images on the right show the stress distributions created on the gelcoat surface at the corresponding impact stages.

From Figure 6-26 it can be seen that the nature of stress propagation in the gelcoat when fixed to a composite substrate does not differ greatly to that exhibited when assumed fully fixed. The initial stages of impact feature a compressional stress wave at first point of contact, which then propagates outwards radially through the thickness. This phase is promptly followed by the creation of high stress ring features on the gelcoat surface as the droplet spreading process evolves.

For direct comparison between the stresses created in the gelcoat for the previously modelled fully fixed gelcoat in isolation to the gelcoat as modelled attached to a composite substrate, it is possible to plot and compare time histories of the maximum value of effective von-Mises stress in the gelcoat for both types of simulation, as shown in Figure 6-27.

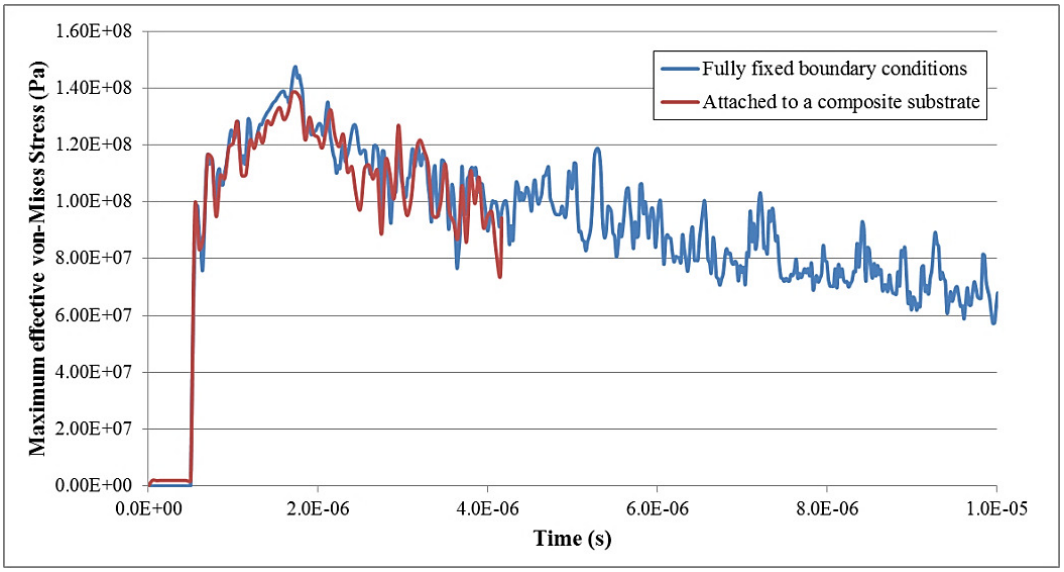

Figure 6-27. A plot of time histories of the maximum value of effective von-Mises stress in the simulated gelcoat, when both simulated alone with fully fixed boundary conditions on the lower surface and when simulated attached to a representative wind turbine blade composite substrate.

It is clear from Figure 6-27 that very little difference in the stresses created within the gelcoat for the two boundary conditions simulated was exhibited; indeed the curves show a high level of agreement. It would appear therefore that for composite substrate configuration modelled, the presence of said substrate had little appreciable effect on the stresses generated, compared to the results obtained from modelling the gelcoat in isolation; with fully fixed boundary conditions at the under surface.

The negligible effects of the inclusion of a composite substrate is most likely as a result of the relatively low impact energies associated with rain droplet impact, which are not sufficient enough to significantly deform the composite substrate. Given sufficient impact energy, for say hailstone impact, it may be the case that the whole blade section exhibits significant deformation and deflection under impact and under these conditions the flexibility of the substrate may have a more substantial effect on impact response of the coating system; when compared to fully fixed conditions. These issues are explored later in the hailstone impact modelling work and subsequent discussions.

6.4 Rain droplet impact performance of flexible coatings

The previous sections have looked at examining (through numerical modelling) the impact response of typical gelcoat material systems; in particular epoxy resin based coatings. Historically such systems (in combination with paints) were considered robust enough to provide protection to the blade and withstand erosion effects. However, it has been more recently recognised that more flexible coatings, such a polyurethane based materials, can provide enhanced impact and erosion performance.

Given the growing popularity of such protective material systems, it was decided that the impact response of such coatings would also be explored, through use of the rain impact modelling methods established and described. As such, the following objectives for the modelling work were identified as:

1. **Typical impact response of flexible coating –** As with the studies relating to the gelcoat (discussed previously), it was decided to first examine the typical material impact response behaviour of a typical flexible coating, when subject to rain impact; featuring a 3mm diameter droplet impacting directly at $100 m \cdot s^{-1}$. It was hoped that this would provide insight into the energy absorbing behaviour of the flexible coating as well as the damage mechanisms induced. It would also subsequently allow for direct comparison of the typical impact material response of both classical gelcoat materials (discussed in the previous section) and these newer and emerging flexible coatings.
2. **Effect of impact angle on flexible coating impact response** – Due to the more flexible nature of the coating considered, the effects of varying impact angle and the nature in which this alters the material impact response would be investigated.

There are numerous polyurethane based coatings and paint systems available to the wind energy market. However, due to the availability of published material properties, the impact response behaviour of the W4600 protective coating system [52] – manufactured by 3M [53] – would be investigated through modelling in LS-DYNA. Claus [77] detailed the stress strain behaviour of the 3M W4600 coating system, as shown in Figure 6-28.

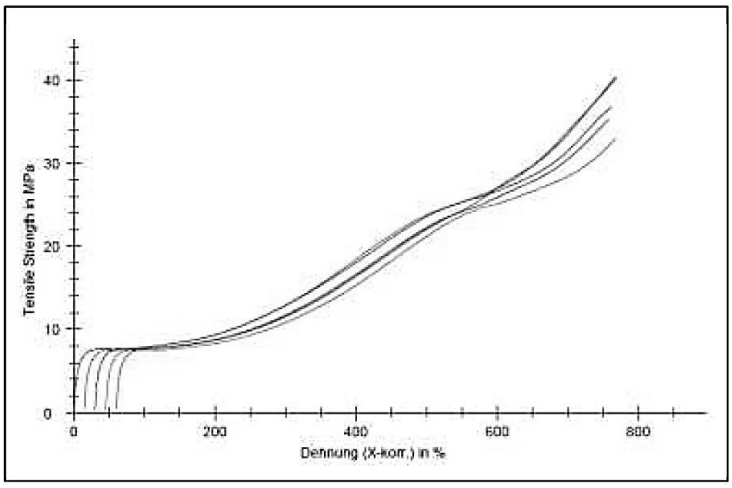

Figure 6-28. Tensile stress-strain behaviour of the W4600 coating system **[52]**; manufactured by 3M **[53]**. Image source: **[77]**.

As shown, in comparison to the stress-strain properties of the previously discussed and modelled epoxy resin gelcoat material (Figure 6-1 and Figure 6-2), the W4600 system is considerably more flexible with respect to the maximum strain to failure; failing at a value of around 700%, compared to around 30%. However, it is also possible to observe that the initial yielding of the material occurs at much lower strain value (~50%) and also at a comparatively low stress value of around 8MPa (compared to 90MPa for the epoxy system). Consequently, it would seem that the benefits offered by such a material system, in relation to the prevention of leading edge erosion, come from the extreme strains required to break or erode the material; rather than any high strength/stiffness characteristics.

Although the stress-strain behaviour of the W4600 coating system shown in Figure 6-28 gives a good insight into the tensile loading behaviour of the material, it does not inform on the unloading behaviour of the material or any hysteresis (or strain ratcheting effects). The absence of such data made it difficult to predict the unloading behaviour of the material, for instance, if it simply unloads linearly or exhibits hyperelasticity, and if residual stresses are created following yield level loading. As discussed in the following section, the absence of such data presented challenges with respect to selecting and setting up appropriate material models for the W4600 coating within LS-DYNA

6.4.1 Model Setup

As with the previous simulations, the LS-PrePost software tool was used to create the W4600 simulation models; as noted in the following.

The recommend applied thickness of the W4600 product is given as 250-350µm, however in order to subsequently compare the impact response of the material to that of the epoxy Epon

E862 previously simulated, it was decided that the simulations would also feature a 400µm thick layer of W4600. Further to this, the length and width were also set to a value 6mm; as was also the case in the epoxy resin simulations. As before, this geometry was create using the 'Shape Mesher' tool and specifying the length, width and height of the coating target. Issues were encountered however, with respect to the mesh density applied to the coating body, as a result of the highly flexible nature of the W4600 material implemented (as discussed later in Section 6.4.2). It was found that a finer mesh would result in large amounts of skewing and spiking in displacement of the mesh, resulting in deformation considered uncharacteristic of expected behaviour; which would subsequently lead to energy errors and premature solver termination. To investigate this issue further, a sensitivity study was conducted to examine the effects of varying mesh resolution on the outputs of the model; the results of which are detailed in Appendix III. From this process it was decided that a mesh with a cell total 125k would be implemented, as it provided a fine enough mesh to capture the details of the target impact response without resulting in the occurrence of excessive skewing or deformation.

As discussed in the previous section, the available material mechanical property data for the W4600 coating system was limited to a tensile stress-strain curve, and no information was available with respect to the unloading behaviour of the material. LS-DYNA has number of available material models for the purposes of modelling hyperelastic or viscoelastic materials [168], however without the availability or means to attain the relevant material properties for required for these models, it was not possible to utilise them. However, given that the simulations considered, predominantly involve the loading of the coating materials (material unloading during impact is limited), it was decided that an elastic-plastic material modelling approach could be adopted for the W4600 material; based on the stress-strain data in Figure 6-28. Banerjee [221] adopted such an approach to model the erosive performance of thin polyurethane films under solid particle impact and erosion in LS-DYNA. Banerjee [221] utilised the material model *MAT_PLASTIC_KINEMATIC [168], which requires only a Young's modulus value and post-yield tangent modulus to describe the stress-strain behaviour. Banerjee [221] accepted the limitations of this approach to modelling the material, with respect to the accuracy of the modelled unloading behaviour, but also recognised that for impact modelling studies the loading behaviour of the material is of primary importance; which could be well represented with the elastic-plastic modelling approach. Banerjee [221] obtained good agreement between the modelling results obtained through this approach, and the results obtained through an experimental approach. For these reasons, and the issues of data availability discussed previously, it was decided that the

modelling conducted in this research, involving the flexible coating materials, would also utilise elastic-plastic based material models.

As such, for the modelling discussed here it was decided that the material model *MAT_PIECEWISE_LINEAR_PLASTICITY would be used to represent the W4600 material. From the curve shown in Figure 6-28, the material properties detailed in Table 6-5 were derived; resulting in a piecewise approximation of the post yield stress-strain material behaviour.

Table 6-5. Material model inputs for W4600 material.

Property [Source]	Value
Density	1100 kg·m^{-3}
Young's modulus	32 MPa
Poisson's Ratio	0.3
Tensile Yield Stress	8 MPa
Failure Strain	700%
Plastic Strain	Yield Stress
0	8 MPa
2.25	9 MPa
7.25	35 MPa

Again, these values serve as an approximation of the real material properties and with the availability of more comprehensive data, a better representation could be obtained.

The other model parameters, such as droplet node total, contact definitions and boundary conditions were applied identically to that as applied to the previous gelcoat analyses discussed. Consequently, the same assumptions about the rigid substrate connection apply, as discussed previously in Section 6.1.2.

The only difference between the gelcoat and W4600 model set up was in the target mesh density and the constitutive material model (and associated property values). The assigned droplet diameter and impact velocity/angle were input and altered as described previously, depending on the desired model configuration.

6.4.2 Results & Discussion

The following results and discussion are split into two sections to consider the two modelling objectives, as previously established.

Owing to the low mesh density employed in the simulations, a run time of only 10-15 minutes was required to complete the simulations.

6.4.2.1 The typical impact response of a flexible coating

As with the gelcoat analyses discussed previously, it was useful to first inspect the nature in which stress were created within the simulated W4600 coating during impact. Figure 6-29 displays contours of effective von-Mises stress in the W4600 material during a 3mm diameter water droplet impact event at 100m·s^{-1}, showing the distribution both on the surface of the target (left) and through the thickness of the coating (right); at progressive stages throughout the impact simulation. The cross sectional views of the plate are zoomed into the impact regions to provide clearer illustrations of the stress shockwave behaviour; therefore the full width of the plate is not shown.

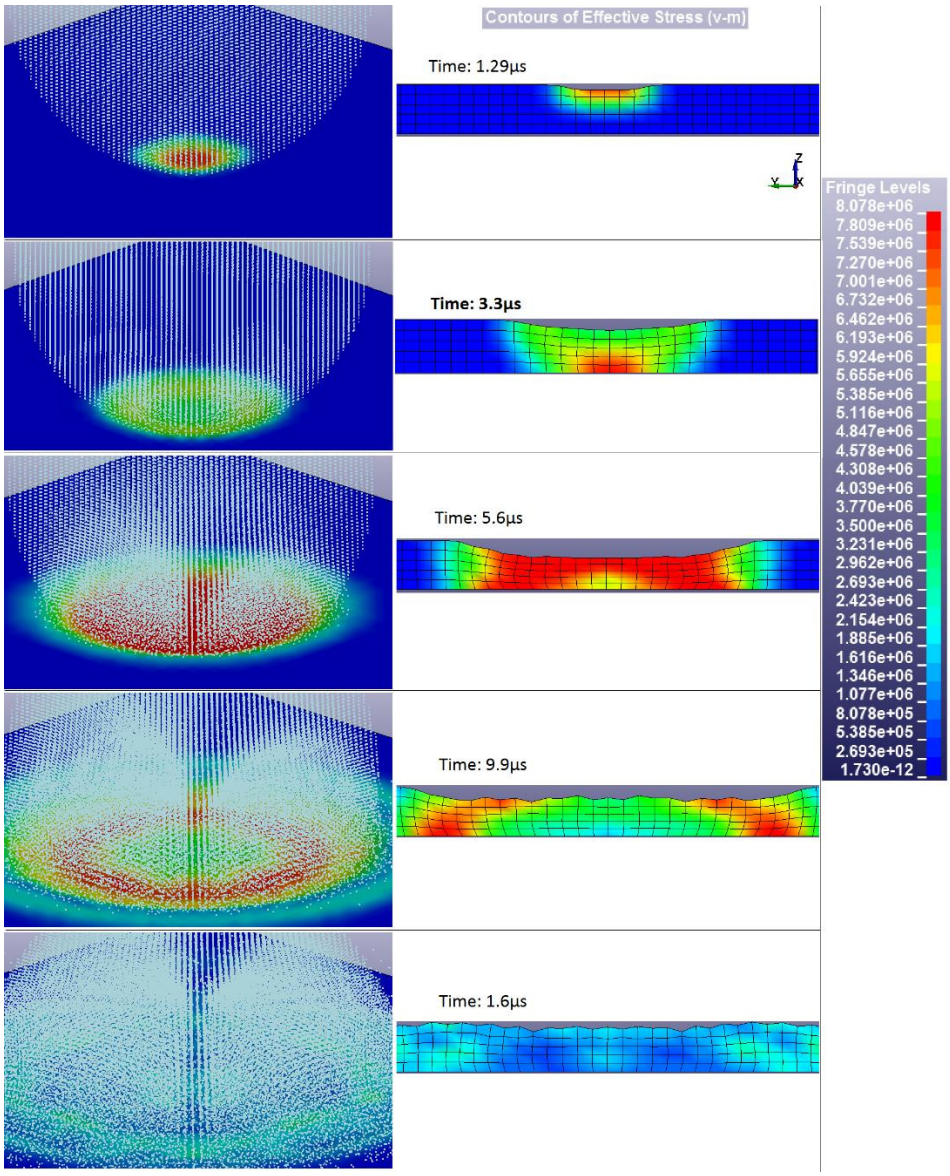

Figure 6-29. Contours of von-Mises stress (Pa) in the simulated W4600 coating during a 3mm diameter water droplet impact at 100m·s^{-1}. The upper surface of the gelcoat is show on the left and the corresponding sectional view (through the gelcoat thickness) on the right; the trough-thickness view has been scaled up, therefore the full target width is not shown.

As shown, and as expected, the W4600 coating responds to impact in a much more flexible manner in comparison to the previously simulated gelcoat (Figure 6-7). The displacements in the images shown are in true scale, thus it is clear to see that the coating responds to impact with significant deformation. As a result of this large deformation, the stresses are generally more widely distributed throughout the material; which is especially evident in the through thickness direction. There still exist some ring-like stress distribution features in the latter stages of the impact event; however they are less prominent than exhibited by the gelcoat simulations. In the final impact sequence step, it can be seen that the material promptly springs back to almost its original shape, resulting in a near flat target surface.

It is apparent then that the more flexible material characteristics of the simulated W4600 coating technology result in a more uniform and evenly-distributed stress/shock propagation behaviour during impact. A further consequence of the enhanced flexibility of the material is exhibited in the rate and manner in which the impact force load is imposed on the material. Figure 6-30 shows the time history of the contact force between the droplet and the target surface in the direction of the impact (z) and also shows the same output from the previous gelcoat analysis (Figure 6-9).

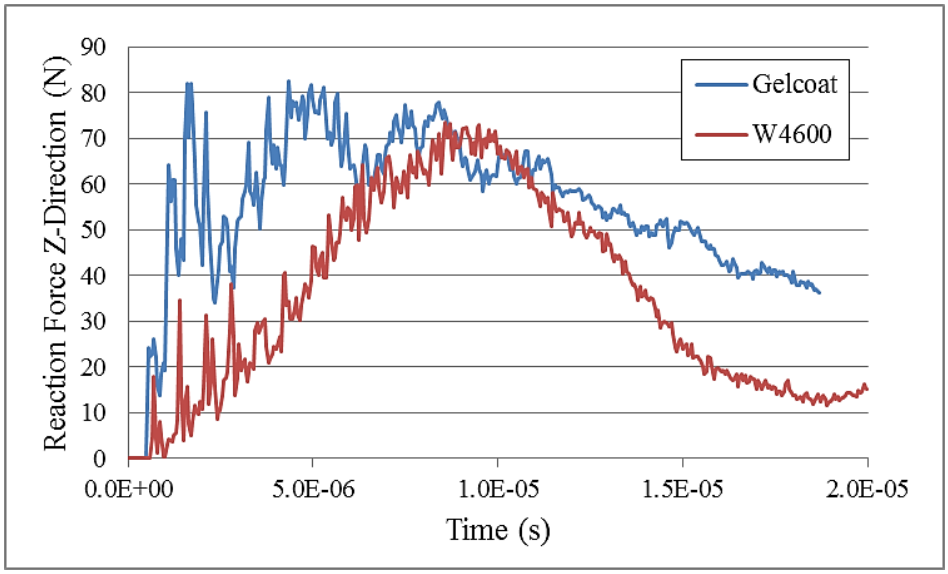

Figure 6-30. Time history of the reaction force in the z direction, between a 3mm diameter droplet impacting both a simulated gelcoat and W4600 coating target at right angles at 100m·s^{-1}.

From this time history, the difference in the nature of impact response between both coating technologies is evident. Whilst the gelcoat responds in a stiffer manner, resulting in a rapid increase in reaction force, the impact load is absorbed more gradually by the W4600 to a peak value; approximately half way through the impact event. This more gradual impact

absorption can be attributed to the more flexible nature of the material, which results in large deformations of the coating.

Further insight into the energy absorbing characteristics can be gained from examining the time history of the maximum value of von-Mises stress within the coating during impact, as shown in Figure 6-31.

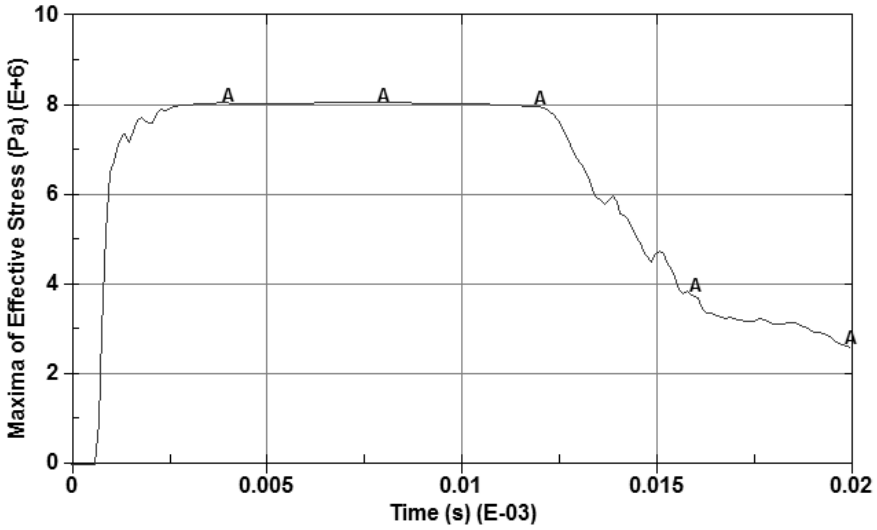

Figure 6-31. Time history of the maximum value of effect stress (von-Mises) within the simulated W4600 coating during a 3mm diameter water droplet, 100m·s^{-1} impact event.

It can be seen that upon impact an initial peak in stress within the coating is generated at around 2.5μs, with a value of approximately 8MPa. Examining the cross sectional distribution of stress through the thickness of the coating in Figure 6-29, it is clear that this rise in stress to the yield value is generated mostly at the under surface of the coating, in the region of the applied fully fixed boundary condition on the under-surface. It would seem therefore that the rise in stress (to yield) is brought about through the boundary conditions at the bottom surface restricting the free and continued distribution of the propagated stress wave. This phenomenon is of important consideration given that the simulated coating was assigned a thickness of 400μm, but the recommended thickness (according to the product literature [52]) is stated as 250-350microns. Therefore, this issue of stress propagation restriction at the fixed under-surface of the coating may be further exacerbated by a further reduction in the coating thickness.

To evaluate the material damage caused in the simulation, the contours of effective plastic strain created in the coating following the simulated impact event were examined. Figure 6-32 shows such contours on both the top surface of the coating and through the thickness (sectional) of the coating.

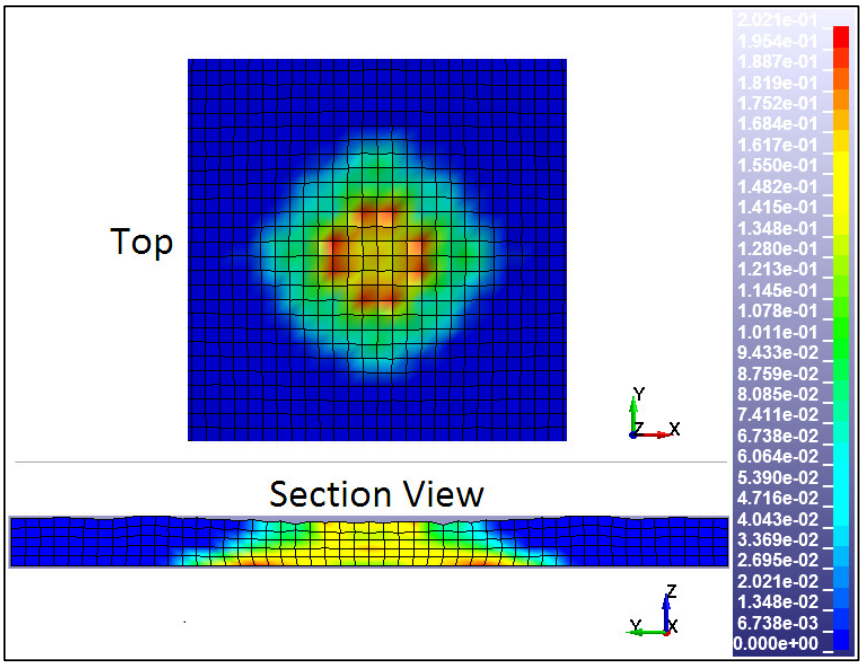

Figure 6-32. Contours of effective plastic strain in the simulated W4600 coating material following a 3mm diameter water droplet impact event at 100m·s^{-1}, showing both the top surface and a through thickness sectional view

From Figure 6-32 it is clear that the manner in which plasticity is induced through the droplet impact event simulated differs greatly to that exhibited by the simulated gelcoat previously (Figure 6-12). Whereas the gelcoat exhibited plasticity almost exclusively limited to the surface of the target, the simulate W4600 coating exhibits plasticity throughout the material thickness, growing more widespread down through the thickness; forming a cone shaped distribution. It can be seen that significant widespread plasticity is created at the under-surface regions, at the area of the applied fully fixed boundary conditions. Reviewing the plastic strain created on the surface, it is apparent that the maximum value is around 20%; following a 100m·s^{-1} impact event. This is considerably less than the required plastic strain to failure value of 725% as suggested by the relevant material stress-strain data, therefore it would seem that the onset on surface erosion would be highly unlikely in the short term, as a high number of impact events would be require to elevate the damage created to a value close to this.

As discussed previously in Section 6.4.1, due to the absence of material data in relation to unloading of the material, and the limitations this imposed on the material model selection, care must be considered when reviewing the damage created in the model. It may be the case that in the actual material, more limited plasticity would be induced, or that the material would rebound in a different manner. These considerations should also be carried over into the results discussed in the following section relating to the effects of impact angle.

However, the impact loading behaviour can still be studied to give an indication of the general material loading behaviour and the stress hot spots; as discussed.

Therefore, the results would appear to suggest that failure at the coating-substrate interface is more likely to occur before the onset of erosion; due to the restrictions imposed on the material at this interface during impact. This issue will be further explored in later sections, which will discuss the interlaminate behaviour of the coating material and the relevant substrate material.

6.4.2.2 Effect of impact angle on flexible coating impact response

In previous sections (Section 6.1.3.3) it was shown that for a gelcoat material target, introducing an incline to the impact angle resulted in a decrease in the stress and subsequent damage created in the material. However as discussed, given the highly flexible nature of polyurethane coating systems such as W4600, it was of interest to also explore the effects of impact angle on the impact response of such a material system.

As with the gelcoat analyses, in addition to the direct impact scenario, the effects of an impact angle of 30˚ and 60˚ would be examined (following the approach discussed previously). However, given that the effects of impact angle in the previous gelcoat analyses were only slightly altered by the effects of varying impact velocity, it was decided that for the W4600 analyses the impact velocity would be set constant as $100 m \cdot s^{-1}$; and the diameter at 3mm.

Before examining the resulting impact simulation for each of the impact angles tested individually, it is useful first to review the effect of impact angle on the stress creation within the target across the three impact angles. Figure 6-33 displays the time history of the maximum value of von-Mises effective stress created in the simulated W4600 coating during impact events for the three impact angles detailed; for a droplet diameter of 3mm and impact velocity of $100 m \cdot s^{-1}$.

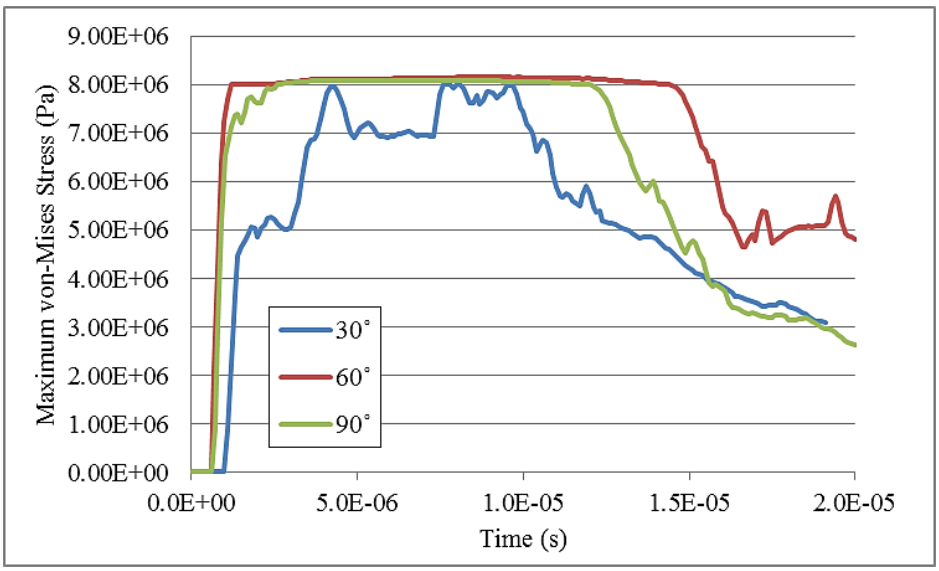

Figure 6-33. Time history plots of the maximum value of effective von-Mises stress within the simulated W4600 coating when subjected to a 3mm diameter water droplet impact event at varying impact angles. The angle reference system is as used previously for gelcoat analyses and as shown in **Figure 6-17**.

As was the case with the gelcoat analyses, it can be seen that with respect to the maximum value of von-Mises stress created in the coating during impact, there is very little difference between the results from impact at 60˚ and 90˚. Indeed the results from the simulations would suggest that the peak stress is reached more quickly at an impact angle of 60˚. For an impact angle of 30˚, the overall stress creation throughout the impact is lower than at 60˚ and 90˚; however the yield stress is also reached at various time points where the maximum stress value spikes upwards.

To get a better insight into the cause of these spikes in maximum stress, it is possible to examine the nature of stress creation in the target during impact, through plotting contours of effective von-Mises stress in the coating. Figure 6-34 shows the contours of effective von-Mises stress in the coating during a 30˚ impact angle event (at four separate time points), showing the distribution both on the top (impact) surface and through the thickness of the coating; the droplet spreading behaviour is also shown.

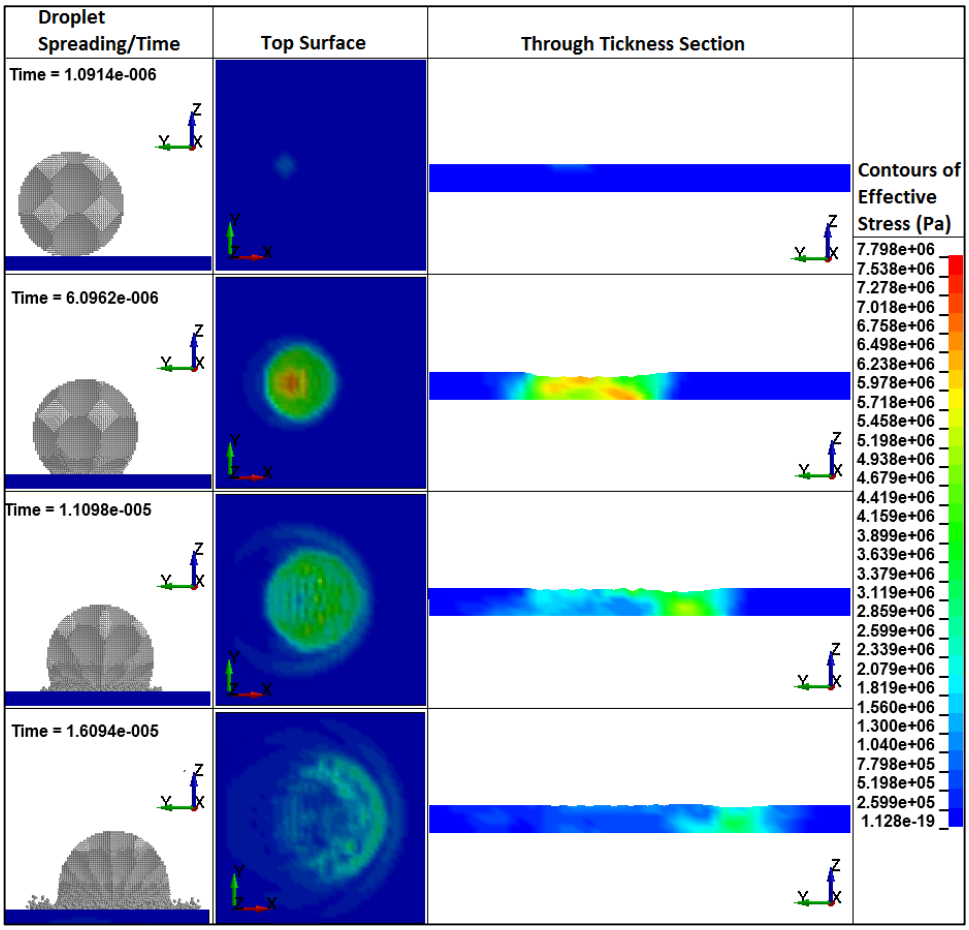

Figure 6-34. Plot showing the droplet spreading behaviour of a 3mm diameter water droplet impacting a simulated W4600 coating with a velocity of 100m·s^{-1} at 30˚ impact angle. Contours of effective von-Mises stress on both the top (impact) surface of the coating and through its thickness are shown, for various points during the impact event.

In comparison to the previously simulated gelcoat target, the incident impact angle has a far more significant effect on the nature of the coating impact response. It is evident that this shallow impact angle results firstly in stress creation throughout the thickness, subsequently followed by the creation of a bow wave in stress which travels (left to right in the view shown) laterally through the coating; at the leading edge of the droplet. However when compared to the stresses simulated previously in the direct impact analysis (90˚), it is clear that although some of the significant stresses are created in the lower subsurface regions of the coating (at the area of applied fixed boundary conditions), they are not as extreme. Consequently, the only (limited) plasticity created in the coating when subject to droplet impact under these condition is evident near the surface, as shown in Figure 6-35; which plots the contours of effective plastic strain in the coating through the thickness (via a sectional view).

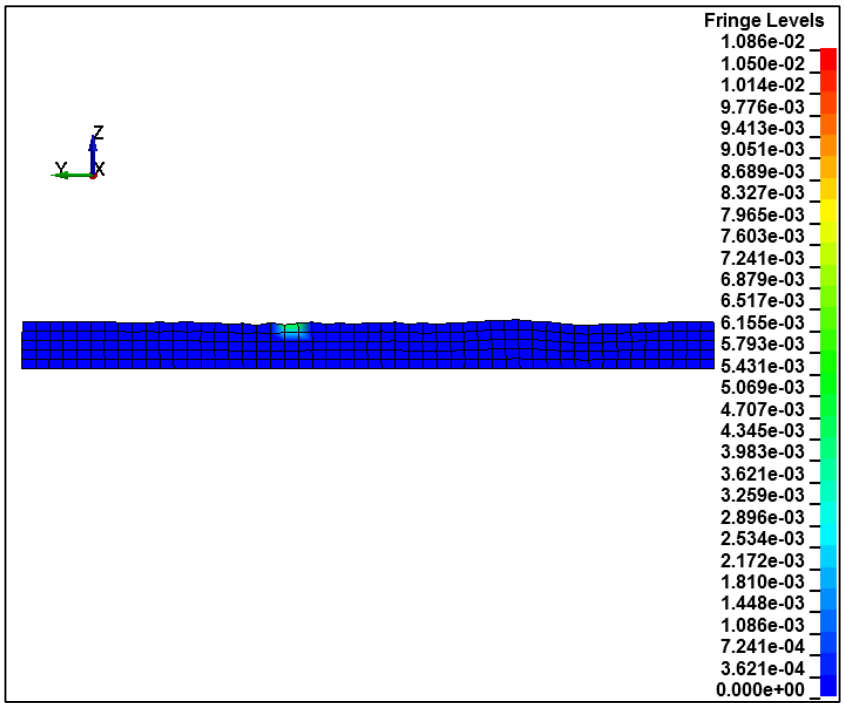

Figure 6-35. Contours of effective plastic strain through the thickness of the simulated W4600 coating following a 3mm diameter water droplet impact at an impact angle of 30˚ and velocity of 100m·s^{-1}.

Figure 6-36 features the same plot configuration as Figure 6-34, but instead shows the results from the simulation featuring an impact angle of 60˚.

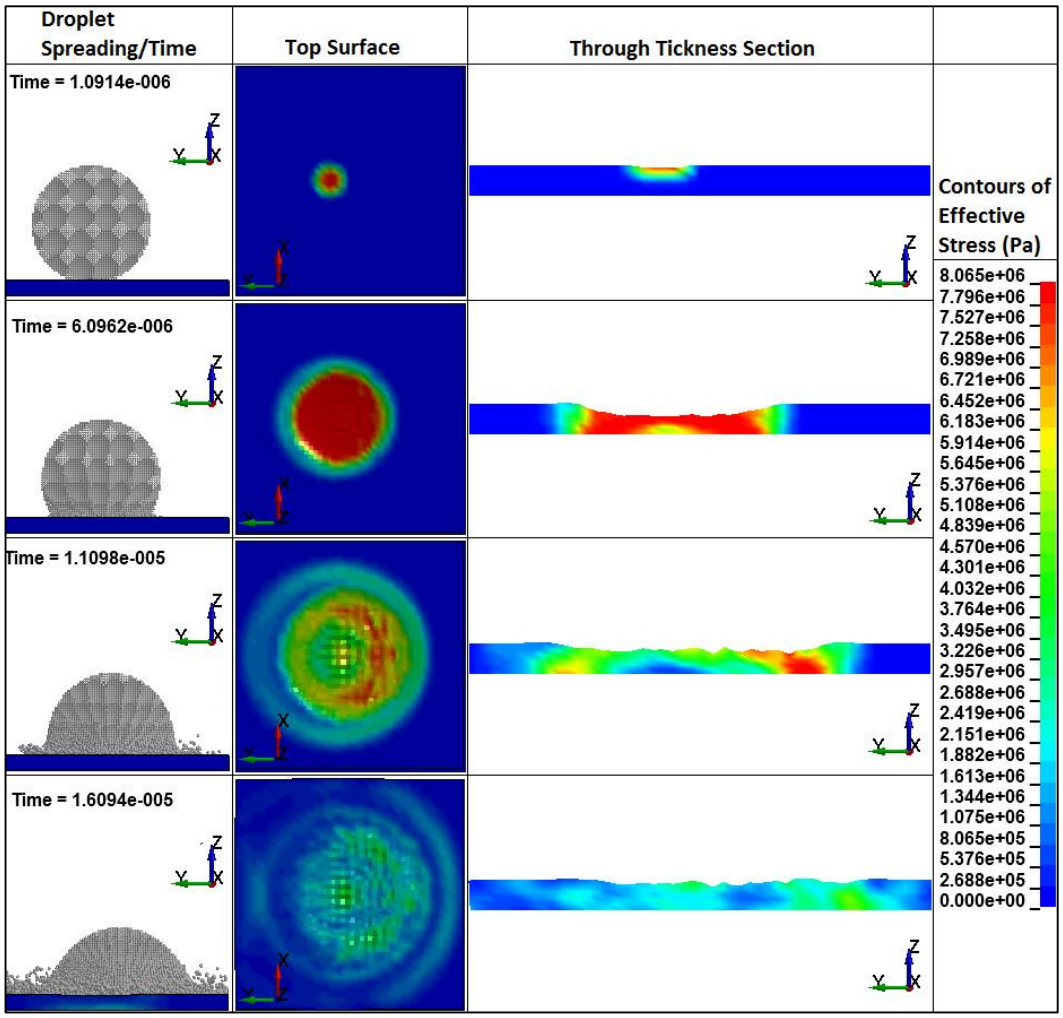

Figure 6-36. Plot showing the droplet spreading behaviour of a 3mm diameter water droplet impacting a simulated W4600 coating with a velocity of 100m·s^{-1} at 60˚. Contours of effective von-Mises stress on both the top (impact) surface of the coating and through its thickness are shown, for various points during the impact event.

The stress distribution behaviour exhibited in Figure 6-36 can be observed as a mixture of the behaviours exhibited in both the 30˚ and 60˚ impact angle simulations (Figure 6-29 and Figure 6-34 respectively). Similarly to the 90˚ impact simulation, high levels of compressive stress are created throughout the coating thickness in the early stage of impact as a result of the initial waterhammer pressure; as exhibited in the frame taken 6µs into the impact event shown in Figure 6-36. Subsequently, as the droplet spreads across the surface (left to right in Figure 6-36) a bow wave of high level stress is created at the leading edge of the advancing droplet and down through the coating thickness.

Figure 6-37 shows contours of effective plastic strain created through the thickness of the simulated W4600 coating during the 60˚, 100m·s^{-1} impact event; showing a sectional view through the central axis (where the droplet travelled left to right).

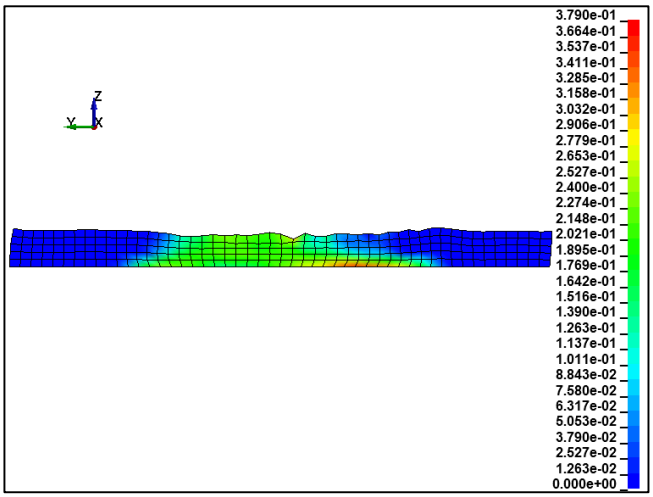

Figure 6-37. Contours of effective plastic strain through the thickness of the simulated W4600 coating following a 3mm diameter water droplet impact at an impact angle of 30˚ and velocity of 100m·s^{-1}.

It can be seen that as a consequence of both the initial waterhammer pressure induced stresses and the subsequent later bow wave stress distribution, asymmetrical plasticity has been created in the simulated W4600 coating. There are similarities between this distribution and those displayed previously for the simulated 90˚ impact event (Figure 6-32) with respect to the overall cone shaped distribution of plasticity; growing wider from the upper surface down to the lower surface. However there is also an additional asymmetric component of plasticity in the region right of the initial impact point, brought about through the lateral spreading (or bow-wave behaviour) of the stresses within the coating. It is also interesting to note that the maximum value of effective plastic strain created in the simulated 60˚ impact event is greater than that generated in the 90˚ simulation (0.379 compared to 0.202), suggesting that for certain conditions and coating thicknesses, direct impact may not be the most damaging and inclined impact may increase the risk of debonding and material failure.

The results from both the 30˚ and 60˚ impact simulations further support the suggestion (made previously) that when considering the impact response and associated damage mechanisms of flexible coating technologies, surface erosion and degradation may be of reduced concern (in comparison to more classical gelcoat material choices). However, the results also suggest that a critical risk to the performance of such coatings may lie in the bond characteristics between the coating and substrate; therefore it is of great importance that these characteristics are well understood. In the absence of relevant bond strength properties, it was not possible to fully explore these issues; however the following section looks at a very similar issue associated with the bond strength and threat of delamination associated with flexible tape technologies. These technologies are made from similar materials and therefore parallels may be drawn the results.

6.5 Protection provided by flexible tapes and the risk of debonding

The impact response and primary damage modes of both typical gelcoat and flexible coating materials have been investigated and discussed. However, due to the laminate nature of wind turbine blade constructions, the interlaminate response of the blade materials to rain droplet impact is also of importance.

For blades with purely a gelcoat surface coating, the occurrence of delamination is considered unlikely due to the inherent bonded nature between the gelcoat layer and the resin matrix of the composite substrate. The primary damage modes associated with gelcoat technologies are likely to be surface erosion and degradation, as shown previously in Figure 3-2.

Conversely, as shown previously in Figure 3-3 and Figure 3-6, and determined from the modelling work discussed previously, flexible coating technologies, specifically polyurethane tape products, are less likely to exhibit damage through pure erosion and more likely to fail as a result of debonding from the substrate (gelcoat or otherwise). The occurrence of debonding for such technologies may arise from the large difference in flexibility between the coating and the substrate to which it is bonded, as proposed previously.

To develop a fuller understanding of the debonding/blistering behaviour of flexible tape protection, it was decided that simulations within LS-DYNA would be conducted to explore the phenomenon further. These simulations would feature a layer of gelcoat material with an additional layer of flexible tape material applied to the surface, which would then be subjected to rain droplet impact; under various conditions.

It was hoped that such simulations would firstly provide additional insight into the energy absorbing characteristics of a typical polyurethane based tape product as well as the impact protection it provides to a gelcoat substrate. Crucially also, it was hoped that the simulation would help to evaluate the interlaminate stresses and forces and any debonding induced through impact. This layup configuration was chosen as tape products are most commonly applied to the surfaces of blades which feature a more traditional gelcoat surface coating (which may have proven susceptible to surface degradation); as opposed to the relatively newer polyurethane coating technologies (such as the W4600 technology).

6.5.1 Model Setup

In order to make comparisons to previous gelcoat modelling results, the same gelcoat configuration as described previously in section 6.1 would be used; featuring the same dimensions and material properties. Fully fixed boundary conditions were again applied to the under surface of the gelcoat, on top of which a layer of polyurethane tape would be created. A rain droplet size of 3mm (again represented by 65k SPH nodes) was once more implemented, using the same material properties and equation of state parameters as detailed previously. For the initial investigations into the impact protection provided by the tape, an impact velocity of 100m·s^{-1} at right angles to the surface was applied, to create the most damaging conditions for the gelcoat; as shown in the results discussed previously (Section 6.1.3). For the subsequent interlaminate response analyses, the applied velocity was altered accordingly (as discussed later in the results section).

As well as making OEM stage coatings, 3M [53] are also one of the most prominent suppliers of leading edge tape products for implementation on installed blades. These tape products are also polyurethane based and are applied to the surface of the blade with an attached layer of adhesive. Tensile stress-strain data for the 3M W8607 Wind Blade Protection Tape product is shown in Figure 6-38; key data points are also labelled.

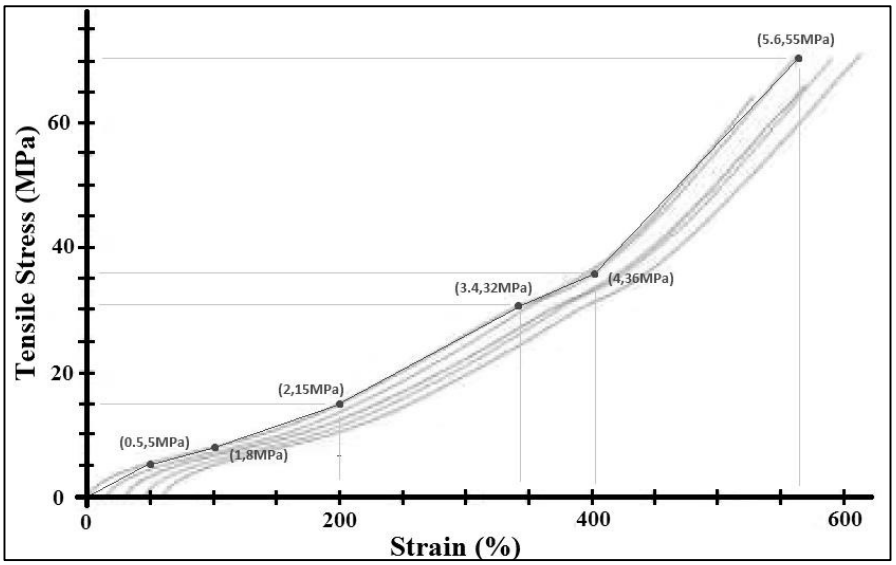

Figure 6-38. Tensile stress-strain behaviour of the W8607 Wind Blade Protection Tape product **[222]**; manufactured by 3M [46]. Points in red show the values taken from the data for the modelling material property inputs. Original image source: [68].

As shown, the tensile stress behaviour of the tape has similarities to the W4600 coating technology previously discussed Figure 6-28, exhibiting extreme deformation before break.

Given the availability of this material data and the widespread use of the product within the wind industry, it was decided that this material would be used to represent the tape product in the simulations conducted.

Given the similarities to the W4600 material featured in previous analyses, the material model *MAT_PIECEWISE_LINEAR_PLASTICITY was also used to represent the W8607 material, using the material properties shown in Table 6-6; taking post yield data from the stress-strain data shown in Figure 6-38.

Table 6-6. Material properties assigned to tape (based on data for 3M W8607 leading edge tape)

Property	Value
Density	1100 $kg \cdot m^{-3}$
Young's modulus	10 MPa
Poisson's Ratio	0.3
Tensile Yield Stress	5 MPa
Failure Strain	560%
Plastic Strain	Yield Stress
0	5 MPa
0.5	8 MPa
1.5	15 MPa
2.9	32 MPa
3.5	36 MPa
5.1	55 MPa

Again, the same limitations that applied to this material model in relation to the W4600 material, with respect to unloading behaviour (discussed in Section 6.4.1), also apply once more.

The W8607 tape product is stated in the product literature to have a thickness of 0.3mm and a 0.06mm layer of pressure sensitive acrylic adhesive. For the purposes of the simulations, it was decided that the tape would be modelled as a homogenous 0.36mm thick layer of the constitutive material (as characterised in Figure 6-38). Figure 6-39 shows the model configuration, with the 0.4mm thick gelcoat layer covered by a 0.36mm layer of the tape material (6x6mm).

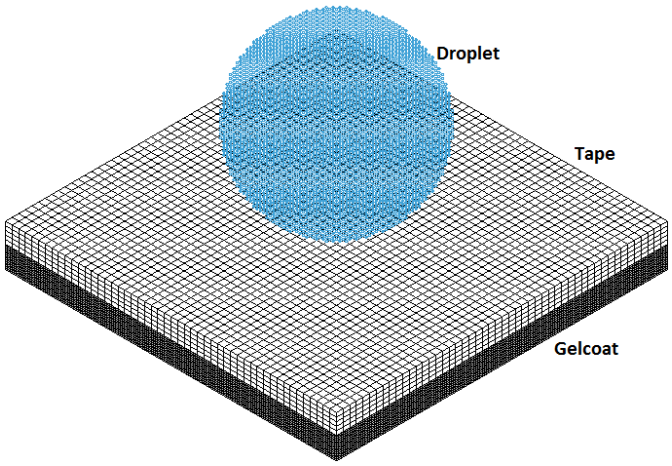

Figure 6-39. Configuration of tape analyses model, showing the (3mm diameter) water droplet, a 0.36m thick layer of tape and a 0.4mm thick layer of gelcoat (6x6mm).

As with the W4600 analyses discussed previously, the mesh applied to the flexible tape component of the assembly was relatively course (in comparison to the mesh applied to the gelcoat), with a total element count of 12,500 (50x50x5) in order to minimise excessive skewing of the flexible W8607 material. An identical mesh density was also applied to the gelcoat component of the assembly, this coarsened mesh (in comparison to previous analyses) was deemed acceptable as the detailed droplet/surface interaction modelled in previous analyses would not take place in these analyses; as the tape product would such interactions. Applying an identical mesh density also ensured more straightforward contact modelling between the tape lower surface and gelcoat upper surface, resulting in 1on 1 node contact pairings.

Again, the only boundary conditions implemented were fully fixed conditions applied to the underside of the gelcoat. Two different contact definitions between the gelcoat and tape product were implemented for the two different modelling objectives discussed. For the analyses concerned with the level of impact absorption protection provided to the gelcoat from the tape coating, the *AUTOMATIC_SURFACE_TO_SURFACE_TIEBREAK contact card was utilised, with OPTION 1 invoked. This contact definition results in a fully fixed bond between the nodes of the two interacting body surfaces and prohibits tangential motion; effectively creating a fully fixed unbreakable bond between the two surfaces. This contact definition was considered adequate for the initial analyses, wherein the primary result of interest was the reduction in loading of the gelcoat surface (in comparison to a fully exposed surface) and therefore the protection provided by the tape.

However, with respect to the analyses concerned with the bond interface loading and the potential onset of debonding, such a contact definition would obviously not suffice. For these analyses the same contact card (*AUTOMATIC_SURFACE_TO_SURFACE_TIEBREAK) was utilised, using OPTION 6. As discussed previously (Section 4.5.3.2) this option models failure based on a specified normal or shear stress. This can serve as a crude approximation for delamination, in the absence of the required fracture toughness data [193]. For this option, the interface failure criterion is given by,

$$\left(\frac{|\sigma_n|}{NFLS}\right)^2 + \left(\frac{|\sigma_s|}{SFLS}\right)^2 \geq 1 \qquad (6.1)$$

where σ_n and σ_s are the normal and shear stresses acting on the interface respectively, and NFLS and SFLS are the normal and shear interlaminate strength values respectively [181]. Upon fulfilling this creation, the stress between the respective nodes (initially in contact) is linearly reduced to zero as a function of the distance between the two [183]. Upon reaching a defined critical separation distance (CCRIT), tied contact modelling between the respective nodes is stopped, and subsequently automatically switched to surface to surface contact; which allows for sliding contact and prevents post-tie failure interpenetration of the surfaces.

Regrettably, there is limited publicly available data on the strength and characteristics of the typical bond between the W8607 tape and the substrate; other than peel adhesion strength [74]. There is however data on the typical tensile shear strength of typical 3M pressure sensitive acrylic adhesive products [223], quoted to range between 12-20MPa. Therefore, in the absence of actual bond strength data, it was decided that a typical value for both the normal and shear stress would be approximated as 20MPa. The critical distance between two contacting nodes at which the bond would break was input as 30µm (around 10% of the tape thickness). Although the actual values were unattainable, for the purposes of exploring the basic mechanisms of interlaminate impact energy dissipation, it was though these approximations would provide adequate. Given the relatively sizeable difference in the stiffness of the gelcoat substrate and the polyurethane tape, the SOFT=1 option in the contact definition was implemented to ensure satisfactory contact performance.

With respect to modelling the impact behaviour between the droplet and the target (tape) surface, the same *NODES_TO_SURFACE contact algorithm as used in previous analyses was utilised; with the same SOFT 1 parameters.

The configuration detailed formed the basic components of the subsequent modelling work, and as with previous analyses, for the purposes of parametric studies, other variables such as impact velocity were altered depending on requirements; as discussed in the results section.

However, in order to review the interlaminate forces, pressures and possible debonding, additional model parameters had to be incorporated. Additional interface outputs were included through adding the *EXTENT_INTFOR and *BINARY_INTFOR database cards. *EXTENT_INTFOR (INTerface FORce) allows for the specification of required interface (interlaminate) modelling outputs; such as forces, velocities, pressures and contact gap (failure). *BINARY_INTFOR dictates the desired output frequency of these modelling results throughout the simulation. Additionally, in order for the LS-DYNA solver to output such variables the command S=intfor was added to the solver input command.

6.5.2 Results and Discussion

The results of the flexible tape simulations are discussed in the following sections. Due to the low mesh density employed in the target materials, a short run time of approximately 30 minutes for each of the simulations detailed was required.

6.5.2.1 Impact Protection

The initial LS-DYNA simulations conducted featured a fully fixed surface to surface contact between the gelcoat substrate and the attached layer of tape, in order to purely evaluate the impact absorption characteristics of the tape component. For this modelling, severe impact conditions were established, featuring a 3mm diameter droplet impacting the tape surface at right angles, with an initial velocity of $100 m \cdot s^{-1}$. As used in the analyses of previous simulations discussed, plotting contours of effective stress throughout the target thickness (through a sectional view) at various stages of the impact provides insight into the impact response of the materials simulated. Figure 6-40 shows the contours of effective stress generated in both the tape and gelcoat (top and bottom) during the simulated 3mm diameter, $100 m \cdot s^{-1}$ impact event.

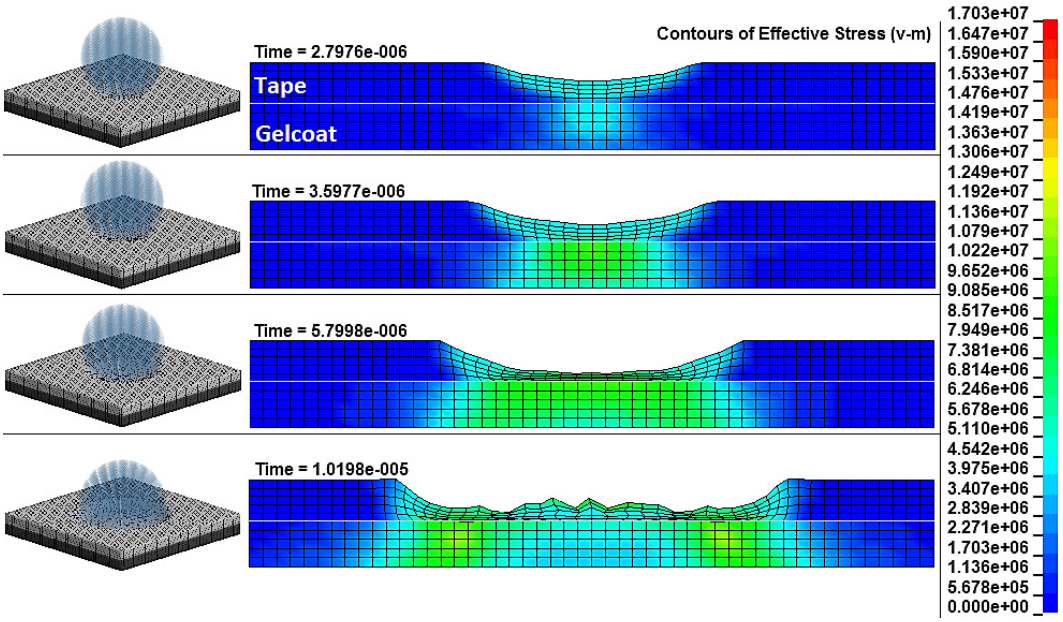

Figure 6-40. A plot showing contours of effective (von-Mises) stress (Pa) through the thickness of a simulated gelcoat/tape assembly (sectional view), at various stages throughout a simulated 3mm diameter water droplet impact event, at 100m·s^{-1}. An isometric view of the droplet impacting the surface is also shown.

It is immediately apparent that the tape component exhibits levels of deformation that far exceed those exhibited by the gelcoat (by multiple orders of magnitude) throughout the entire simulated impact event. The tape responds to the initial droplet impact in a comparatively flexible manner, compressing heavily in the direction of impact. This compression in the material at the locus of impact subsequently spreads laterally as the droplet does also. In the latter stages of the simulation, the occurrence of element skewing in the tape mesh can be observed, resulting from the extreme deformations imposed. This skewing presented problems in modelling work, resulting in some cases in the premature ending of solver runs as a result of energy errors. The challenges faced by this issue and possible solutions are discussed later.

In the gelcoat substrate, in spite of the presence of the layer of tape on the surface, the stress distributions bear a strong resemblance to those exhibited previously in the bare gelcoat impact analyses; as shown previously in Figure 6-7. Where the initial compressional stress wave down through the gelcoat thickness is subsequently followed by the outwards lateral propagation of a ring shapes stress distribution.

However, although there are similarities in the stress distributions created in the gelcoat for the simulations with and without the protective tape, the magnitudes of the stresses created differ significantly. Figure 6-41 plots the time history of the maximum effective stress in an

unprotected gelcoat (simulated and discussed previously), a tape protected gelcoat (discussed here) and the attached tape material; for a 3mm diameter, 100m·s^{-1} impact event.

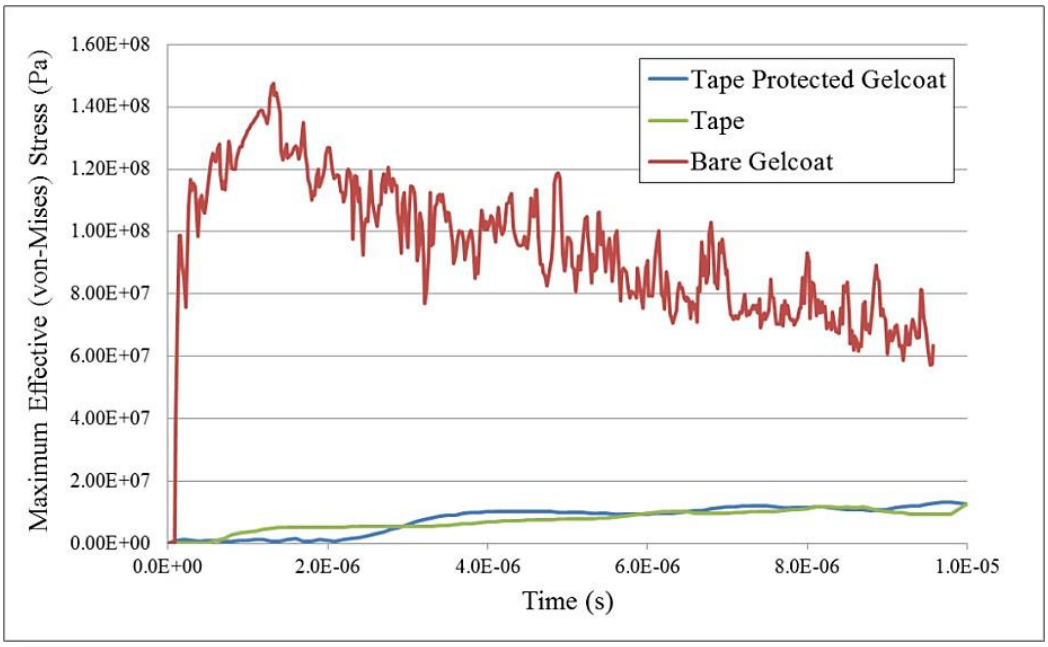

Figure 6-41. Time history of the maximum effective stress in an unprotected gelcoat and a tape protected gelcoat and attached tape material, for a 3mm diameter water droplet impact event, with 100m·s^{-1} impact velocity.

As shown, the stresses created in the gelcoat when protected by the tape component are drastically reduced in comparison to those exhibited in a bare gelcoat target. The nature of stress creation is also noticeably smoother and less erratic in the protected gelcoat.

Figure 6-42 looks specifically at the time histories of the maximum stress created in the protected gelcoat and the attached tape, providing a better illustration of the impact response characteristics of both.

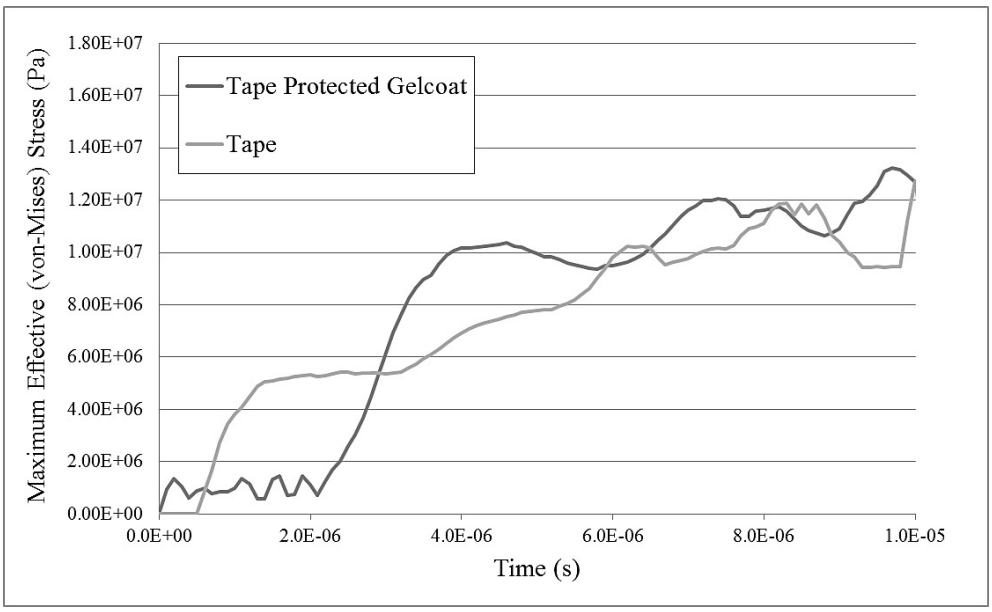

Figure 6-42. Time history of the maximum effective stress in the tape protected gelcoat and attached tape material, for a 3mm diameter water droplet impact event, with 100m·s^{-1} impact velocity.

Reviewing both Figure 6-41 and Figure 6-42, it is clear that the presence of the flexible protective tape acts to eradicate the creation of the sharp and significant increase in stress within the gelcoat during the initial phases of impact; as exhibited in the unprotected gelcoat material.

It would seem then, that with respect to protecting the erosion-susceptible gelcoat substrate, the simulated protective tape was extremely effective. The presence of the tape acts to drastically reduce the stress created in the gelcoat substrate, through absorbing the impact energy by deforming flexibly during the simulated impact event. However, it is clear that the deformations experienced by the protective tape could have damaging consequences. Figure 6-43 plots the contours of effective plastic strain in the tape/gelcoat assembly, 8.8µs into the impact simulation.

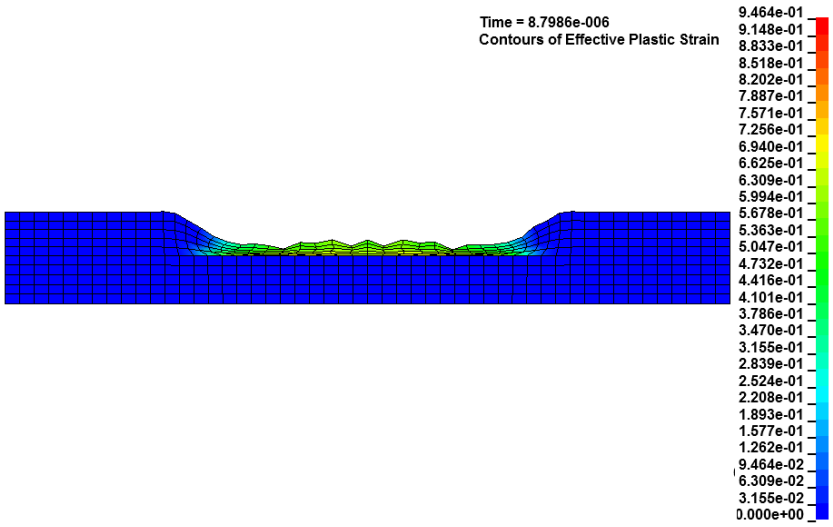

Figure 6-43. Contours of effective plastic strain through the thickness of the simulated tape/gelcoat assembly, 8.8µs into a 3mm diameter droplet impact event with initial impact velocity of 100m·s^{-1}.

As shown, and as expected, no plasticity was created in the gelcoat substrate, however significant plastic strain was exhibited in the protective tape layer; at values up to 90%. It is clear that the primary mode of damage creation was brought about through the compression of the tape in the direction of impact, as the plasticity is wholly limited to the regions subjected to such loading. Importantly also, the plasticity is induced throughout the thickness of the tape material, right down to the gelcoat interface, reinforcing the importance of a strong bond between the two materials. However, following this maximum level of compression of the tape material, the shape of the tape material exhibited rebounding behaviour, back to near original pre-impact conditions; i.e. a flat surface profile.

A plastic strain of around 90% is by no means negligible; however it is important to remember that the strain to failure value of the material simulated is around 510%. This would indicate that material failure of the tape through erosion would take a large number of repeat impact events and that perhaps failure of the interface is a more likely damage mechanism.

However, the geometric response of the tape surface during impact and the final resting state subsequently after are also of important consideration. Ideally, the tape surface should return to a flat even form, with a tape thickness similar to that at the beginning of the simulation (0.36mm). To investigate the geometric response, another simulation was conducted with the same setup, but a lower impact velocity of 80m·s^{-1}; to reduce energy errors and skewing. The simulation was allowed to run for a prolonged period and the contact definition between the droplet and the surface was deactivated after 10µs, to allow for the investigation of the post

impact (contact) response. Figure 6-44 shows the post impact material response of the simulated protective tape (and gelcoat) when subjected to an 80m·s^{-1} impact event; with the first image (at 10μs) showing the last point at which contact between the droplet and the tape surface is active.

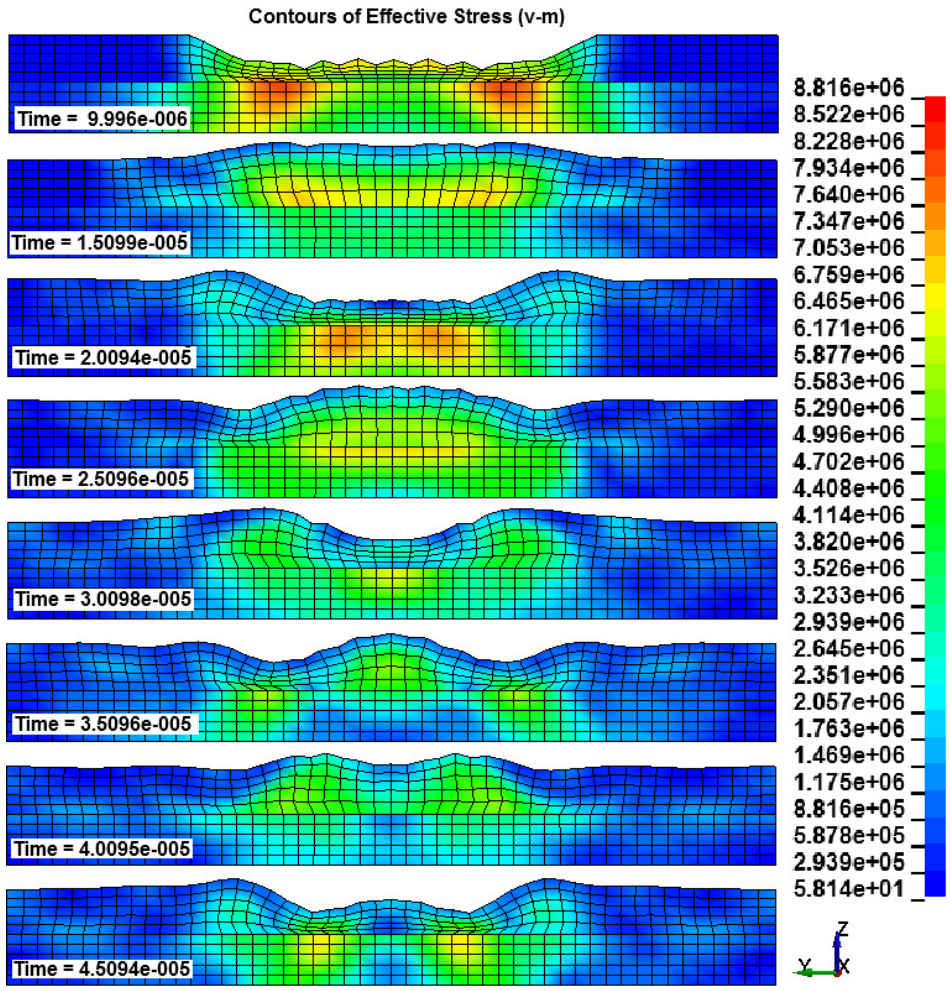

Figure 6-44. Post impact response of protective tape/gelcoat assembly, showing the deformation of the target surface, through a sectional view, and contours of effective (von-Mises) stress (Pa) in both materials, at various time points after contact death. Initial impact conditions: 3mm diameter droplet, 80m·s^{-1} initial impact velocity at right angles.

The post impact response of the protective tape material is highly oscillatory and exhibits wave like motion on its surface. The surface at the area of initial contact cycles through numerous rebounding motions, creating further stress oscillations in the tape material, which are subsequently transferred through to the gelcoat. These stresses are no larger in magnitude than those created during the initial stages of impact; however they do indicate a highly dynamic material response. It would appear then, that following the water droplet impact and a period of material rebound/relaxation, the surface of the tape will likely return to close to its original shape/form; however permanent damage will be induced in the material.

6.5.2.2 Interlaminate Impact Response & Threat of Debonding

Through requesting the output of interface variables (as detailed previously), it was possible to examine the pressures and forces acting on the bond between the tape and the gelcoat. This can be visualised by plotting contours of a given variable on the surface of the contact region. Figure 6-45 plots the pressures exerted on the bond between the tape and gelcoat at various stages throughout both a simulated 90˚ and 60˚impact angle event; featuring a 3mm diameter water droplet impacting at 100m·s^{-1}. The plot shows a view orientated at right angles to the contact surface (looking directly at it), as indicated by the reference system shown in the first image for the 90˚ impact angle results.

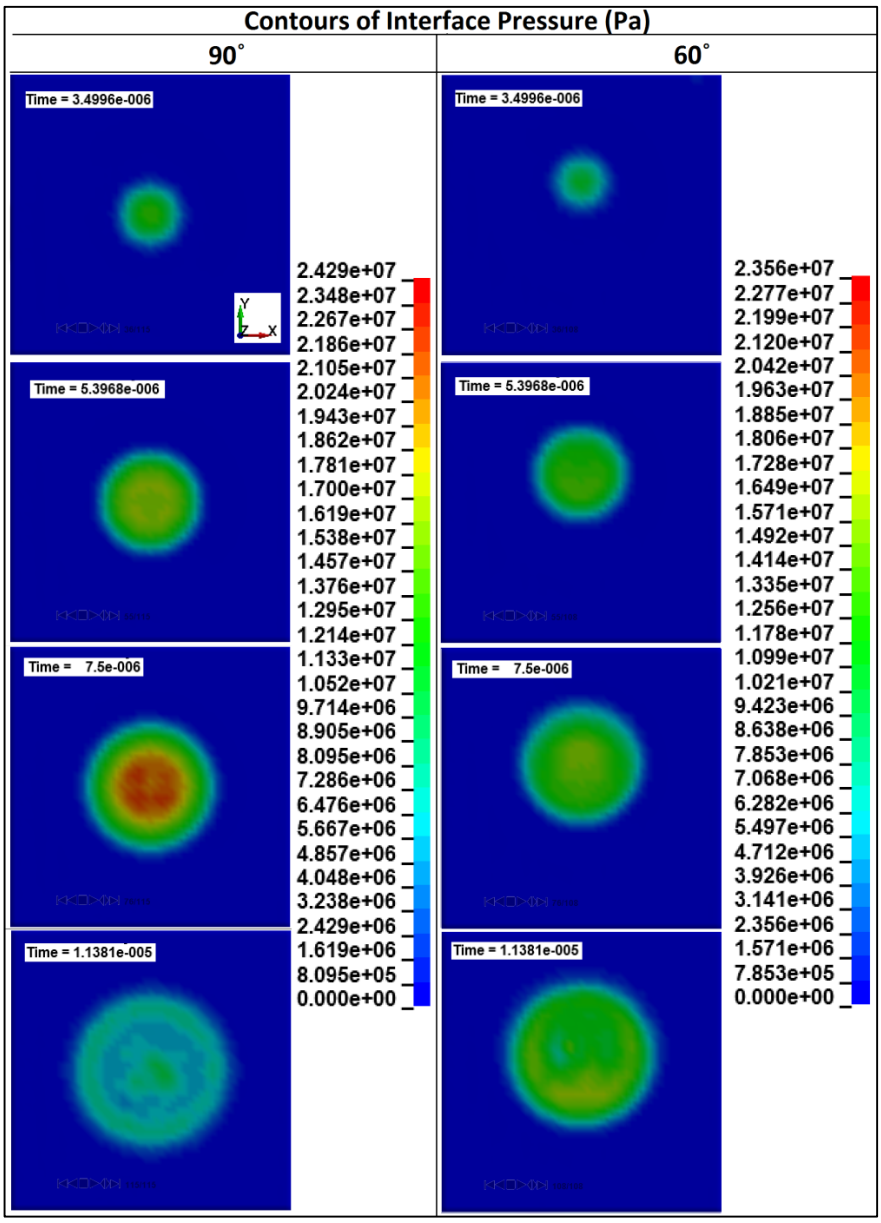

Figure 6-45. Contours of interface pressure (Pa) active between the gelcoat substrate and protective tape layer; viewed top down. Contours resulting from a 3mm diameter water droplet impact event with an initial impact velocity of 100m·s^{-1}, at an impact angle of both 90˚ and 60˚ are shown.

It can be seen that for both impact angles, there are similarities between the pressure created at the gelcoat/tape interface and the pressure exerted on the target surface by the droplet (shown previously). Both sets of images show the creation of an initial 'spot' of high pressure, this then grows larger and evolves into a ring like shape, which subsequently propagates outwards. The magnitudes of the pressures created are also significant, exceeding 20MPa in some regions of the contact area; the failure limit specified. However, for these impact conditions, and the normal and shear strength values used, the failure criterion detailed in Equation 6.1 was not met, and therefore no lasting damage was created in the interface. However, it is apparent from the pressures created that the conditions for damage are present. Improper application of such a tape product, or the gradual environmental degradation of the bond (through humidity, moisture etc.) could result in the gradual debonding of the protective layer.

6.6 Discussion

Through the modelling work conducted and discussed, and the results obtained and analysed, it was possible to evaluate the capabilities of LS-DYNA with respect to modelling rain droplet impact for a range of impact conditions and material configurations. The results shown highlight the flexibility and adaptability of LS-DYNA solver and associated LS-PrePost software tool, as well as giving an insight into the further possibilities of utilising the software. There were, of course, many issues and hurdles experienced with respect to successfully implementing the simulations discussed, however these will be discussed in context later, after the inclusion and discussion of the hailstone impact modelling.

As well as proving the merits of the modelling approach and software used, the results obtained also provided additional insight into the many impact rain droplet impact phenomena simulated. These points will be put into further context later in the closing chapters, with respect to their implications for current and future leading edge material technologies.

6.6.1 Rain droplet impact induced damage of the gelcoat

From the modelling conducted, the results obtained and their analysis, the following key points of insight and information with respect to the rain impact induced damage of typical gelcoat materials were established or identified:

1. Upon initial contact between the droplet and the gelcoat surface, as expected (and discussed at length previously), a waterhammer pressure is imparted on the gelcoat surface. This in turn results in the creation of strong compressional stresses in the

gelcoat material in the region of immediate contact, which is then subsequently propagated downwards through the gelcoat thickness (0.4mm in the simulations considered). Only under extreme impact conditions, are these initial stress values likely to create immediate damage (plasticity) in the gelcoat material.

2. The most damaging water droplet impact mechanism was identified as the droplet lateral jetting process, whereby following the initial (waterhammer) impact phase, the droplet begins to spread laterally across the gelcoat surface at extremely high velocity. In agreement with the observations made in the literature [161] [107] [98], this spreading phase resulted in the creation of high pressure rings around the initial contact locus, subsequently resulting in the creation of high stress levels in these highly localised regions and consequently the onset of plasticity; in concentric ring formations (as shown previously in Figure 6-12). In the simulations conducted, plasticity was induced almost exclusively on or near the gelcoat surface, very little significant subsurface damage was observed.
3. It is suggested then, both from the literature [161] [107] [98] and the modelling results discussed, rain droplet impact induced damage of the gelcoat will primarily be limited to the degradation of the surface or near-surface of the gelcoat. This also agrees with both the experimental and in-field observed damage of classic gelcoat technologies [51] [77] [75], which almost exclusively relates to surface erosion.
4. A general level of agreement was observed between the predicted Damage Threshold Velocities through both the analytical expressions and the LS-DYNA simulations; across a range of droplet diameters.
5. The effect of decreasing impact angle was to reduce the stress levels created in the gelcoat over impact duration. However little significant difference was exhibited between results from the 60˚ and 90˚ impact angle simulations; both with respect to stress levels and the ring shaped damage creation. Therefore, with respect to rain droplet-on-gelcoat impact, it is likely that more direct impact angles pose the biggest threat with respect to the creation of damage.

These are just some of the key points taken from the modelling results, however it must be noted that these simulations were based on a typical gelcoat material with best guess material properties, and the properties and characteristics of different gelcoat technologies will likely vary significantly between manufacturers. The impact response of polyester based gelcoat technologies may fundamentally differ to the simulated impact response of the epoxy based gelcoat discussed here. However the results and analysis point to the likely impact response

of typical stiff (thermosetting resin) gelcoat material technologies, indicating surface erosion as the most likely form of damage.

6.6.2 Rain droplet impact induced erosion of the gelcoat material

The key points of interest taken from the repetitive impact simulations discussed previously are:

1. Repetitive impact on the same surface area resulted in the further worsening of the ring shaped plasticity features created after the first impact event, heightening the effective plastic strain in the gelcoat after each subsequent impact event.
2. Although no erosive processes were modelled for the given impact conditions and limited number of impact events simulated, through inclusion of erosion conditions in the base model described, erosion could be modelled given appropriately extreme impact conditions or a sufficient number of impact events. Alternatively, the modelling processes described could be utilised to predict damage progression rates, and consequently the number of impacts required to erode the surface.

6.6.3 Rain droplet impact induced damage of a gelcoat on a composite substrate

Through modelling the rain droplet impact response of an epoxy based gelcoat as part of a larger glass/epoxy based composite laminate it was found that the results obtained from this method, with respect to the stresses created in the gelcoat, compared almost identically to the result obtained previously from modelling the gelcoat in isolation and with fully fixed boundary conditions on the under surface. Therefore it was found that as a result of the limited impact energies associated with rain droplet impact, such gelcoat materials can be modelled in a standalone capacity if the impact response of the gelcoat is the only point of interest in the modelling work.

6.6.4 Rain droplet impact performance of flexible coatings

The following key points in relation to the rain droplet impact performance of flexible coating technologies were identified and established:

1. The characteristic impact response of the flexible coating technology modelled was fundamentally different to that of the modelled gelcoat material. As expected, the coating exhibited significant geometric deformation and a smoother impact response when subject to a range of droplet impact conditions.
2. As a result of this vast difference in impact response behaviour, the likely damage mechanisms associated with such coatings also differ to those identified in relation to the gelcoat simulated. Surface damage in the form of induced plasticity in the

material was only observed in the flexible coating for the most extreme impact conditions simulated. Instead, the most significant damage was observed to occur in the subsurface regions of the coating at the interface with the coating and the respective substrate (or fixed boundary conditions), resulting in conical distribution of material plasticity.

3. It was proposed therefore that the most likely and threatening damage mechanisms associated with such flexible coating technologies relates to subsurface material degradation and weakening of the bond between the coating and respective substrate. Erosion, given sufficient time and the inclusion of other environmental exposure (such as UV), may still pose a threat to the material integrity of such a flexible coating, but the threat is much reduced in comparison to that associated with the modelled gelcoat

6.6.5 Protection provided by protective tapes and the risk of debonding

The key points identified from the protective tape modelling work were as follows:

1. The typical impact response of the protective tape modelled was very similar to that exhibited by the previously modelled flexible coating; as would be expected, given their comparative material properties.
2. As with the flexible coating, the probability of the surface erosion and degradation was predicted to be significantly less likely than that of a typical gelcoat material, indicating that such tape technologies should theoretically deliver enhanced erosion performance to such coatings.
3. However, again as observed for the modelled flexible coating, subsurface plasticity and material degradation at the tape/substrate interface was identified as the key likely damage mechanism associated with tape technology.
4. Further interlaminate analysis highlighted the threat posed by interlaminate pressures and forces with respect to damaging the bond between the tape and the substrate surface. The values of interlaminate pressure generated were found to be significant in the context of the overall estimated strength of the bond.
5. This threat takes on extra significance given that tapes are often applied to operational blades surfaces which have exhibited damage. Therefore the strength of the bond between the tape and the blade surface is critical to the performance of such technologies.

7. Hailstone Impact Modelling

It is known that the damage mechanisms associated with rain droplet impact are thought to relate primarily to surface degradation and erosion. However, with respect to hailstone impact on blade surfaces, although surface degradation and erosion may also be the primary damage mechanism, given enough impact energy (hailstone mass or impact velocity), composite substrate damage may also be an issue. As such, it was considered appropriate that in addition to surface degradation analyses, hailstone impact analyses should also be conducted to investigate the possibility of substrate damage.

Two different modelling approaches were adopted with respect to the material characteristics of the blade target in the simulations. Firstly, as with the rain analyses, a range of impact analyses aimed at investigating numerous and varied impact parameters were conducted, using the blade layup previously defined in Section 5.3.1.1 and material properties taken from the literature (detailed in Section 7.1.1). Such analyses should provide insight and information on a range of hailstone impact phenomena and characteristics, as well as allowing for the evaluation of the capabilities of the LS-DYNA based hailstone impact modelling approach; established previously in Section 5.2.

Secondly, modelling work featuring a laminate layup configuration and material properties similar to those of experimental samples - subsequently manufactured and tested in hailstone impact experiments - would also be conducted. These analyses would again initially provide insight into the hailstone on blade impact phenomenon, but also additionally allow for the comparison of the numerical results obtained to those later established experimentally. Such comparisons would subsequently allow for further evaluation of the effectiveness and accuracy of the numerical approaches adopted and discussed; and the results obtained.

Therefore, the following three hailstone impact simulation campaigns were established and conducted:

1. **Theoretical Wind Turbine Blade Coating Hailstone Impact Response**
   Similar in setup to much of the rain droplet impact simulation work, initial hailstone impact simulations would be conducted to investigate the hailstone impact response of typical blade coating materials. Identical coating types (gelcoat and flexible) and associated material properties as implemented in the previous rain droplet impact modelling work would be utilised in the hailstone investigations. Such simulations would make it possible to identify the primary potential damage mechanisms associated with such coating materials through hailstone impact. It would also make

it possible to compare the typical impact response behaviour of the coatings between rain droplet and hailstone impact.

2. **Theoretical Blade Cross Section Hailstone Impact Response**
   The impact response of a typical wind turbine blade skin section (at the leading edge) would be investigated, also utilising the same coating material types and properties and using material properties taken from the literature (detailed in Section 7.1.1) for the composite substrate. Such modelling would allow for the investigation of the substrate stresses and strains, any potential composite damage, and interlaminate forces, pressures and damage.
3. **Experimental Blade Sample Impact Simulation**
   Hailstone impact simulations would be conducted to replicate impact conditions later employed in experimental hailstone impact work. The relevant material properties used would be based on both experimental and analytically derived values (as discussed later in Section 7.3.1). Replicating experimental impact conditions within a finite element environment would then subsequently make it possible to validate the numerical results obtained; against the experimental results.

The modelling setup procedure and subsequent results obtained for each of these simulation regimes are discussed in the following relevant sections.

7.1 Theoretical Wind Turbine Blade Coating Hailstone Impact Response

As with the previous rain droplet impact modelling, the first real point of interest with respect to modelling hailstone impact on typical coating materials was to establish the associated damage mechanism through such impact phenomena. Primarily such modelling would focus on the typical stress distributions in the coating material during impact and the subsequent damage created. However, further to this, other parametric analyses to investigate the effects of hailstone impact velocity and diameter would also be conducted. Therefore, in summary, the following modelling aims were established and targeted:

- Characterisation of the typical hailstone impact response of the wind turbine blade coatings considered
- Establish the primary coating damage modes associated with hailstone impact
- Investigate the effects of increasing hailstone diameter
- Investigate the effects of increasing impact velocity

There are evidently many more parameter studies which could be performed to provide further insight into hailstone impact phenomena, however for the fundamental purpose of establishing the basic impact characteristics, these aims were established.

Once more, the two most commonly employed classes of surface coating would be featured in the analyses, specifically, both a classical thermosetting resin based gelcoat and polyurethane based flexible coating (as both featured in previous rain droplet impact simulations).

Given the extensive rain droplet-on-coating simulation work previously conducted and discussed, many of the lessons learned and techniques/approached employed in the rain droplet impact analyses were transferable to the subsequent hailstone-on-coating impact analyses. Additionally, to allow for more direct comparisons between the impact response of the simulated coating materials for both rain droplet and hailstone impact, many of the model parameters (where possible) were kept identical; discussed in the following sections.

7.1.1 Model Setup

LS-PrePost was again utilised for all pre and post processing for the LS-DYNA based hailstone impact simulations.

To examine the coating damaging effects of hailstone impact, it was decided that two hailstone diameters of 10mm and 20mm diameter (0.47 and 3.8 grams respectively) would be modelled, and the impact response of both an epoxy based gelcoat technology and a flexible polyurethane based coating would be modelled. The same coating thickness of 400µm (for both types) as used in the rain impact modelling work was again implemented, with a length and breadth of 20mm and 40mm for the 10mm and 20mm hailstone diameter simulations respectively. These target dimensions were found to provide adequate size to capture the important impact response mechanisms with the material. Sizes larger than these resulted in increased computational time whilst delivering little increased insight or significant differences in the modelled impact response.

Multiple simulations, covering a range of impact velocities would be simulated for each hailstone size, to examine the effects of increasing impact violence.

There follows a description of the general basic setup of the models created, which were then subsequently altered accordingly for parametric analyses.

To create the gelcoat target body the ‘Shape Mesher’ tool in LS-PrePost was utilised (with the ‘Box_Solid’ option) to create the 400µm thick coating layer; with length and breadth

dependant on respective hailstone size. As with the rain impact modelling work described previously, the modelling results obtained exhibited a high degree of sensitivity to the element size applied to the mesh representing the coating bodies (for both the gelcoat and flexible coating). It was found that too fine a mesh would result in excessive element deletion and subsequent energy error based solver termination, however too coarse a mesh delivered substandard detail with respect to stress distributions within the coating during impact. To prevent these issues, it was deemed necessary to conduct separate sensitivity studies in relation to element size for both the analyses featuring differing hailstone diameters and differing coating material properties. The results from these sensitivity studies are detailed in Appendix IV, and the decisions made based upon them, with respect to a suitable element size to use, are discussed later in the results section.

To create the SPH based hailstone geometry, the 'SPH Generation' tool was used with the 'Sphere' option. This tool was used to specify the sphere (hailstone) diameter, density (detailed later) and SPH node density. As discussed in Section 5.2.2, the SPH node density implemented for the hailstone geometry can have a significant effect on the modelling results obtained; with respect to the detail captured in the hailstone material behaviour. If finer hailstone detail and behaviour are required, a SPH node total in excess of 100k should provide satisfactory results. However, in analyses such as the ones considered here, where the impact response of the target is of more interest, an SPH node total of approximately 30k should provide adequate hailstone representation at a more reasonable computational cost. As such, an SPH node total of approximately 33k was established for the hailstone body.

The section and material properties assigned to the hailstone geometry were identical to those as described at length previously in Section 5.2.1.2 (based on the Carney model [128]). Similarly the section and material properties for both the epoxy gelcoat and polyurethane flexible coating were applied in the same manner as described in the rain modelling work previously in Sections 6.1.1 and 6.4.1 respectively.

As with the rain droplet impact analyses, the coating was again restrained through fully fixed conditions on the underside surface. As discussed, these boundary conditions assume a fully rigid substrate structure, which would not be observed in real conditions. However with respect to the creation of damage in the coating, these conditions represent the worst possible conditions and furthermore, greatly reduce the model complexity. Later modelling work would look at the impact response of the coatings as attached to a composite substrate, subsequently allowing for comparison with the result obtain from the fully fixed boundary conditions approach.

To model the contact between the hailstone and the respective coating, the contact card *CONTACT_NODES_TO_SURFACE_SMOOTH was again implemented, with the SOFT=1 option selected, to account for the significant variation in stiffness between the two contact bodies. The relevant impact velocity was established through assigning the nodes of the hailstone an initial velocity with the *INITIAL_VELOCITY_NODE card.

Due to the considerable difference is size between the hailstone geometries (across the range of simulated diameters) and the coating target in the simulations, a low solver time step had to be implemented to prevent contact misses between the SPH nodes and the coating surface. This was achieved by applying values ranging from 0.05 to 0.1 - decreasing with increased simulated impact velocity – for the reduction factor to initial calculated timestep, DTMIN, and the subsequent values of computed time step, TSSFAC.

The model setup described, formed the basic fundamental model base, which was then altered accordingly for the purposes of the parametric analyses detailed in the previous section.

7.1.2 Results and Discussion

The following sections review and discuss the results from the series of analyses conducted to evaluate the coating hailstone impact response of both the simulated epoxy based gelcoat and the polyurethane based flexible coating. However, the impact behaviour of the hailstone itself is first examined.

Both the epoxy and polyurethane based coating simulations required a run time of only approximately 10-15 minutes; owing to their low target material mesh density.

7.1.2.1 Hailstone Impact Behaviour

Figure 7-1 shows the stress distributions created within the 10 mm diameter hailstone body during direct impact with a simulated gelcoat material at $100 m \cdot s^{-1}$.

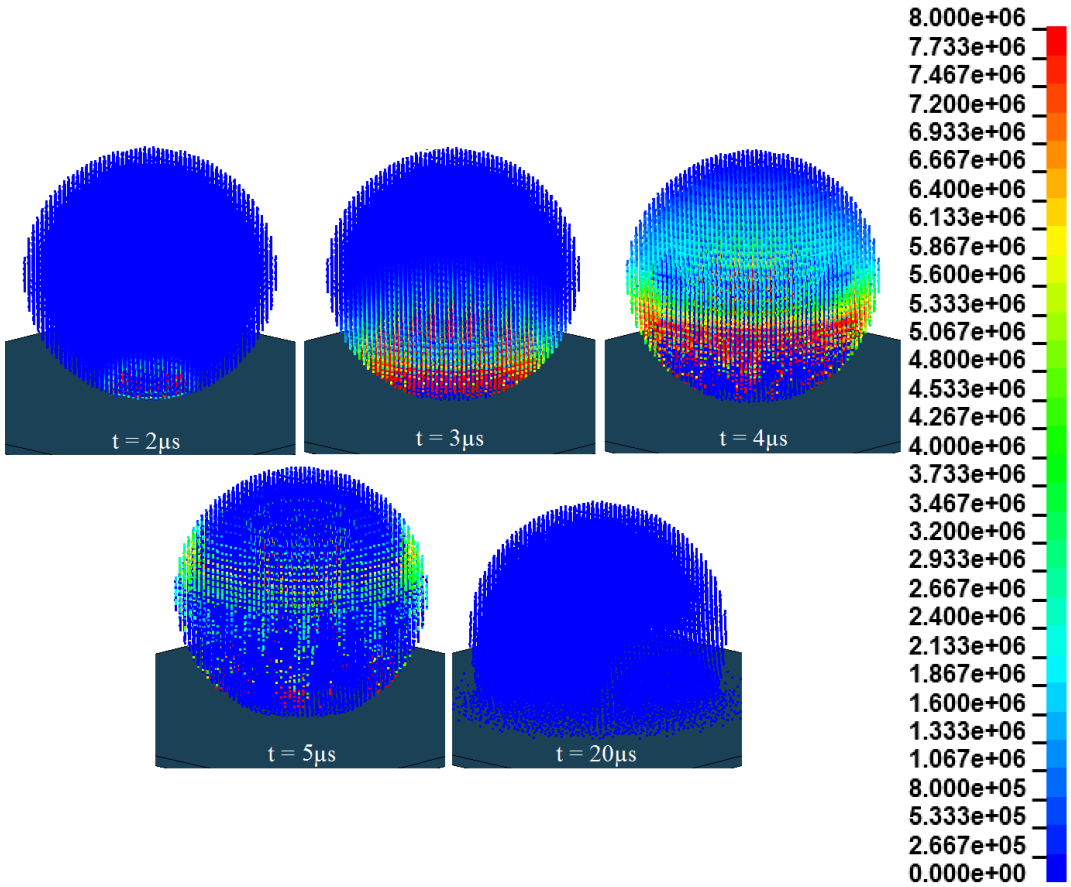

Figure 7-1. Contours of effective von-Mises stress (Pa) in a simulated hailstone; impacting a gelcoat target at 100m·s^{-1}.

As shown, the stress shockwave distribution modelled in the impact described shows good agreement with the examples shown in other modelling and experimental work in the literature; discussed and illustrated in detail in Section 4.3.1. Upon the point of initial contact, a stress shockwave is propagated radially away from the region of contact, and upwards through the hailstone body. This shockwave acts to create failure in the ice material as it passes through the body, resulting in relaxation of the material from a brittle ice state to a more fluid like behaviour; as shown at a time of 20µs. As with the modelling results shown by Tippmann [176] and Juntikka & Olssen [180] (also an SPH based approach), claw shaped failure patterns can also be observed to propagate across the hailstone surface throughout the impact event; most noticeably at times of 4µs & 5µs in Figure 7-1. Therefore it would appear that with respect to the modelled failure mechanism within the hailstone material, the modelling approach described and carried out, delivered satisfactory results.

7.1.2.2 Gelcoat

10mm Diameter Hailstone

For the simulations featuring a hailstone diameter of 10mm impacting a 400µm thick gelcoat layer, an element size of approximately 120µm in the length and bread directions was applied to the coating geometry; automatically adjusted to 133µm in the depth direction. These element dimensions were found to provide adequate through thickness stress distribution detail at significantly reduced computational cost compared to smaller sizes. Additionally, these sizes did not result in element skewing or energy errors during solving; often encountered with a finer mesh. It should of course be noted that the selection of an appropriate mesh size is partly arbitrary without the availability of experimental results for comparison and calibration. However, for the purposes of examining the fundamental aspects of hailstone impact on wind turbine blade coatings, and in the absence of experimental data for the modelled materials, the sizes selected were deemed a best guess for the most appropriate values. This of course also applies to the element sizes selected for the subsequent hailstone impact analyses discussed in the later sections. The issues associated with applying an appropriate mesh density are also further discussed later in Section 9.2.

Assuming a near worst case scenario, it is first useful to examine the potential damage created in the gelcoat through a 10mm diameter hailstone impacting at $100 m \cdot s^{-1}$. Figure 7-2 shows the stress propagation behaviour in the gelcoat under such impact conditions, through displaying contours of effective von-Mises stress as exhibited on the gelcoat surface and through the coating thickness (through the central impact axis); throughout the impact event.

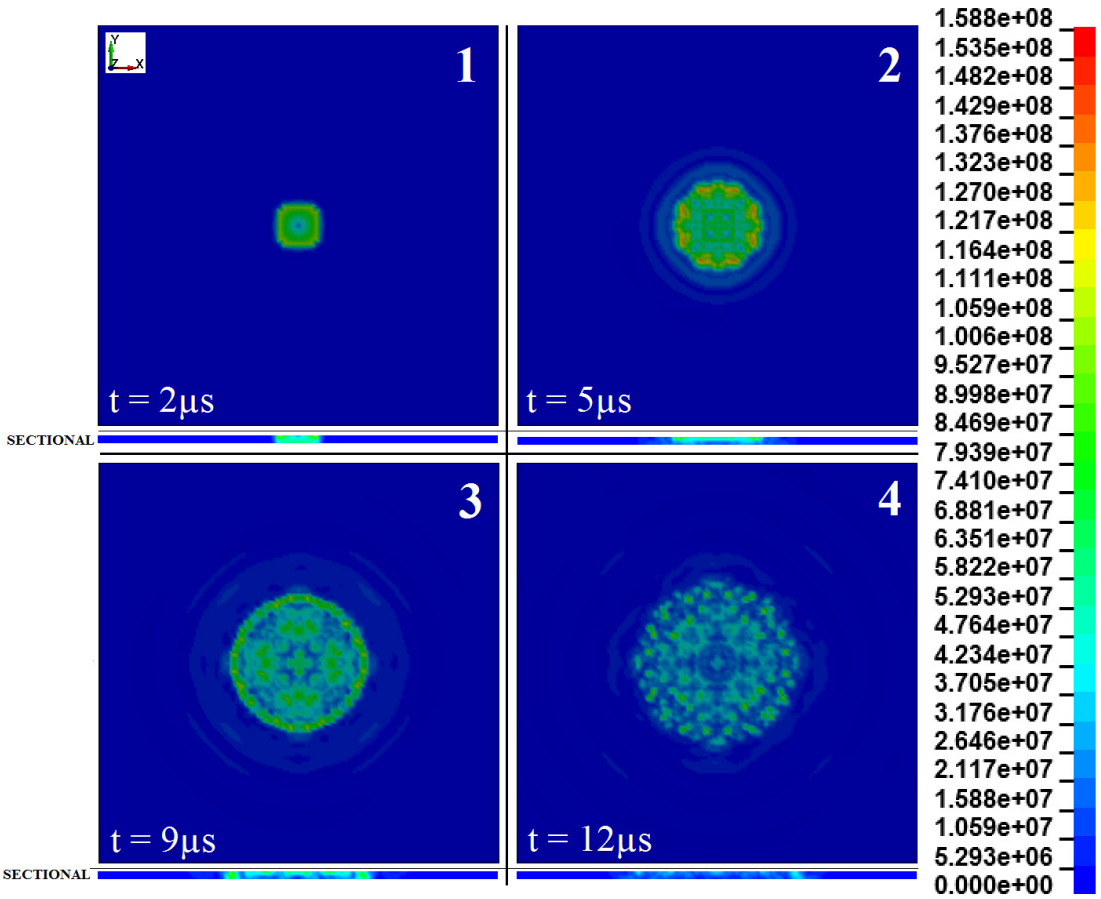

Figure 7-2. Contours of effective von-Mises stress (Pa) in the gelcoat during a 10mm diameter hailstone impact event at 100m·s^{-1}; at progressive stages throughout the impact. The upper surface of the gelcoat is shown with the corresponding sectional view below (through the gelcoat thickness). Gelcoat dimensions: 20x20x0.4mm.

From these contour plots, it is clear that there are many similarities in the nature of stress propagation in the gelcoat material when compared to those exhibited during rain droplet impact, specifically in relation to the creation of high stress rings. This is most likely attributable to the leading regions of the hailstone undergoing material failure (crushing) and subsequently jetting outwards laterally across the coating surface (as also associated with rain droplet impact), as illustrated in Figure 7-3 which plots contours of velocity magnitude for the SPH nodes.

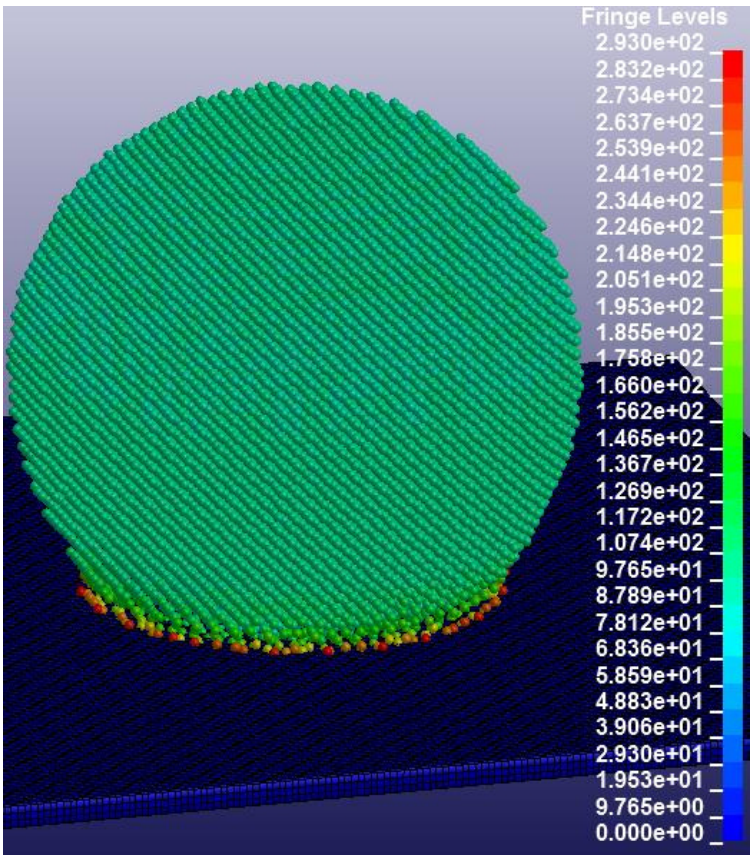

Figure 7-3. Contours of velocity magnitude ($m \cdot s^{-1}$) of the SPH nodes representing the hailstone body, following the onset of material crushing and lateral jetting.

The velocity of the ice material at the lateral jetting front is almost double that of the initial impact velocity.

However, it is also clear from stress distributions in Figure 7-2 that although there are significant peak stresses created in ring like structures, the intermediate stress between these stress bands are also considerable. Therefore, it is evident that the basic compressional impact behaviour in the direction of impact plays a significant role with respect to the creation of stresses in the coating.

Figure 7-4 plots the contours of effective plastic strain in the gelcoat created throughout the same 10mm diameter hailstone impact event (at $100m \cdot s^{-1}$).

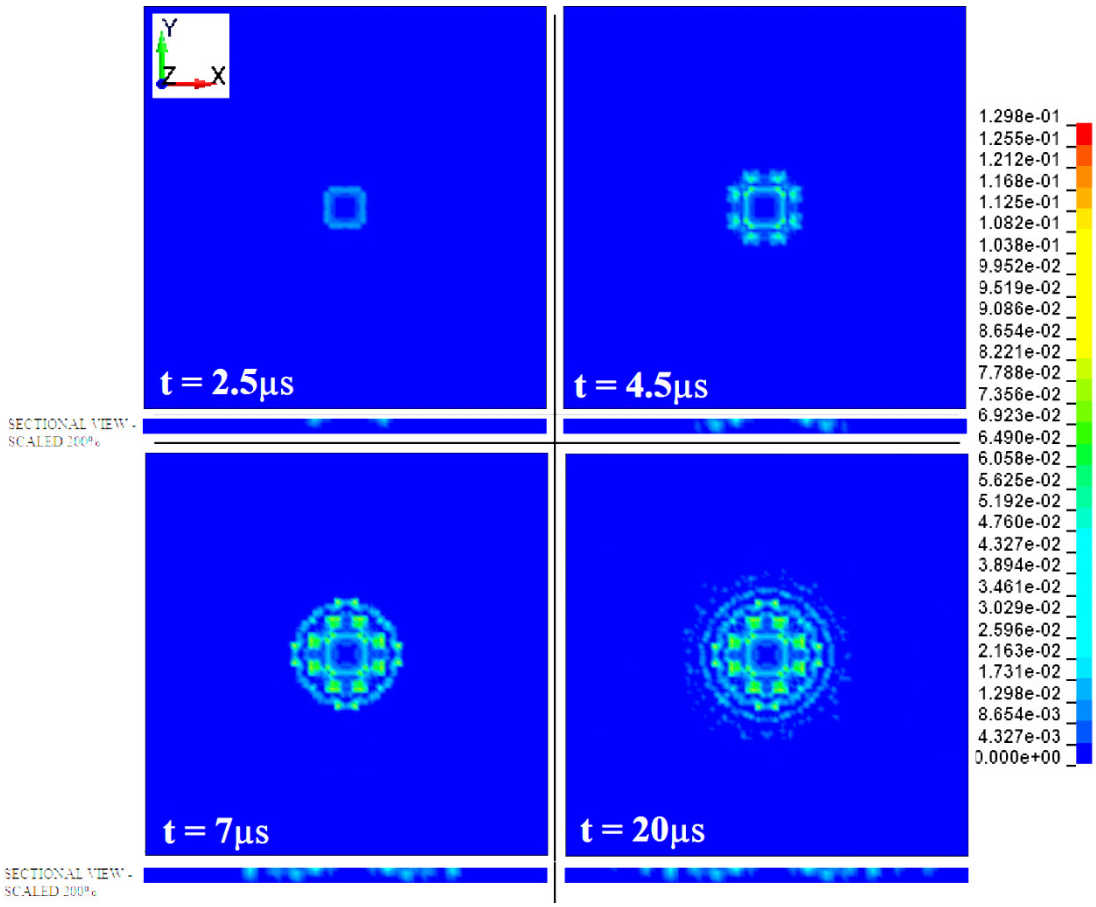

Figure 7-4. Contours of effective plastic strain in the gelcoat during a 10mm diameter hailstone impact at 100m·s^{-1}; at progressive stages throughout the impact. The upper surface of the gelcoat is shown with the corresponding sectional view below (through the gelcoat thickness). The sectional view has been scale by a factor of 2, for greater through thickness clarity; therefore full width of target is not shown in sectional view

As shown, through the lateral jetting phenomenon numerous concentric ring distributions of effective plastic strain were simulated in the gelcoat through hailstone impact; in formations similar to those observed in rain droplet impact simulations previously. However, between the ring shaped distributions, plasticity has also been induced, suggesting that the blunt impact force from hailstone impact is also a significant contributor to the occurrence of damage in the gelcoat.

The magnitudes of the plastic strains created are also significantly larger than those exhibited through rain droplet impact in the previous modelling work. A maximum effective plastic strain value of around 0.13 is exhibited, nearly half the assumed value required for erosion (0.3). It would seem therefore that for the material simulated (and the modelling conditions implemented), surface degradation and erosion could quickly develop given repetitive impact conditions.

As with the rain droplet impact modelling, a parametric analysis was conducted, varying the impact velocity, in order to establish the damage threshold velocity for the simulated gelcoat and a 10mm diameter hailstone size. Again, the threshold for damage was defined as the creation of effective plastic strain in the material in excess of 1%. It was found that an impact velocity as low as 45m·s^{-1} was require to create damage in the gelcoat material simulated. Although this value can be considered low, in the context of wind turbine blade tip speeds, it is prudent to note that many wind turbine sites will rarely witness hailstorms. However, on sites where such weather events are more frequent, the issue of hailstone induced damage of the wind turbine blade leading edge may be significant, even for a relatively small hailstone diameter and impact velocity. It is clear therefore, that a larger hailstone diameter (although rarer) could pose a serious threat to blade coatings; as discussed in the following section.

20mm Diameter Hailstone

For the 20mm diameter hailstone impact simulations, it was found (through the sensitivity study previously discussed and detailed in Appendix IV) that an element size of 224µm provided suitable material response behaviour. However, as detailed previously the applied element size is largely subjective and difficult in the absence of experimental data to verify or calibrate.

At elevated impact velocities for the 20mm diameter hailstone, element failure and subsequent erosion was exhibited in the model. As such, the original contact definition, *CONTACT_NODES_TO_SURFACE_SMOOTH was consequently altered to *CONTACT_ERODING_NODES_TO_SURFACE, to provide more effective contact modelling upon the onset of erosion (for the subsequently exposed subsurface elements).

Figure 7-5 shows the contours of effective stress on the surface of the gelcoat material during a 100m·s^{-1} impact event, with eroded elements highlighted in orange.

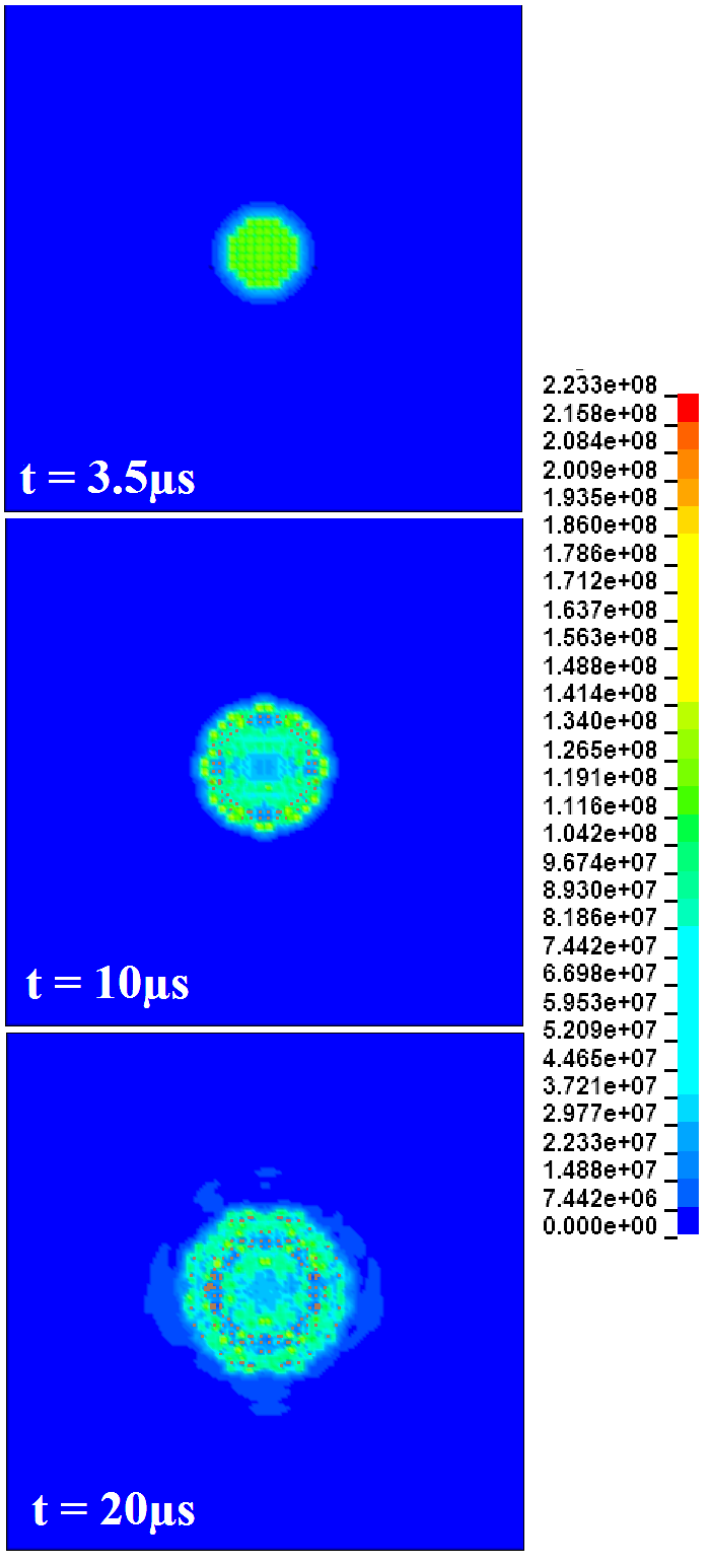

Figure 7-5. Contours of effective von-Mises stress (Pa) on the surface of the simulated gelcoat (40x40x0.4mm) during a 20mm diameter hailstone impact at 100m·s^{-1}. Eroded elements are highlighted in orange.

The stress distributions created for the 20mm diameter hailstone impact are very similar to those exhibited previously in the 10mm diameter hailstone simulation results. However, it

also apparent that the added violence associated with this larger hailstone results in the occurrence of surface erosion (or element deletion in the model). As detailed previously, element erosion in the simulated gelcoat material was set to occur upon the creation of deviatoric strain levels of 0.3 and higher (through the card *MAT_ADD_EROSION). As shown, erosion of the surface occurred mostly in the regions of the material where the high stress ring shape formations reached their peak, resulting in two concentric ring shaped erosion formations.

To gain further insight into the damage created, it is also possible to plot the contours of effective plastic strain on the surface of the gelcoat following the simulated hailstone impact event, as shown in Figure 7-6 which omits the eroded elements (highlighted by black outlines).

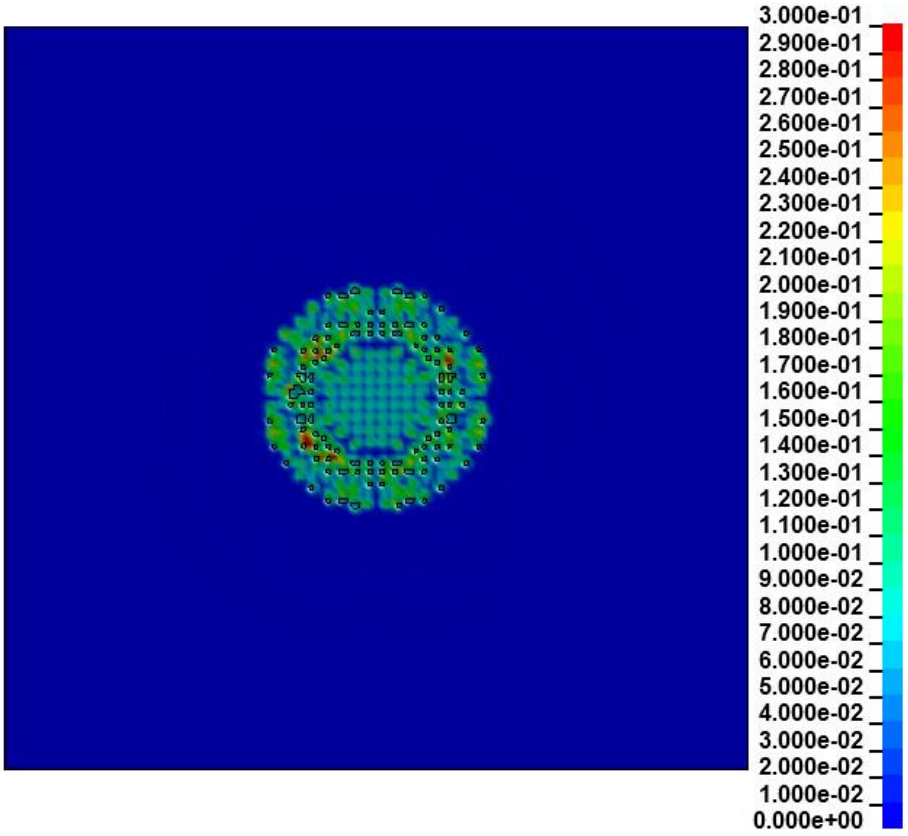

Figure 7-6. Contours of effective plastic strain on the simulated gelcoat surface following impact from a 20mm diameter hailstone at 100m·s^{-1}. Eroded elements are omitted from view however their locations are highlighted by the presence of black outlines.

It can be seen that, as well as the occurrence of significant surface erosion, the simulated impact of a 20mm diameter hailstone at 100m·s^{-1} also resulted in the creation of significant plastic strain levels in the regions not instantaneously eroded. It is therefore apparent that

such an extreme impact event could result in significant degradation of the gelcoat surface coating for only a limited number of impact events.

Again, a parametric analysis was conducted to establish the damage threshold velocity for the simulated gelcoat under impact from a 20mm diameter hailstone. From this study it was found that a velocity of only approximately $35 m \cdot s^{-1}$ was require to induce effective plastic strain levels of at least 1% in the simulated gelcoat.

Damage Creation and Boundary Condition Considerations

It is clear from the results shown, that through modelling the impact of 10mm and 20mm diameter hailstones on a standalone gelcoat, significant damage creation was simulated and exhibited. In the previous discussions on rain droplet impact, it was found that there was little appreciable difference in the impact response of a gelcoat layer when either fully fixed by its under-surface or when attached to a blade representative composite substrate. It was found that the limited energies associated with rain droplet impact meant that most of the significant material loading was induced near the coating surface and therefore the different stiffness levels in boundary conditions had little effect.

However, it is clear in the context of 10mm and 20mm diameter hailstone impact (as modelled in LS-DYNA) that given both the increased projectile size and impact energy, the material loading of the gelcoat is more widespread and distributed throughout the coating thickness; as shown in the cross sectional view in Figure 7-2 Therefore, it may be the case that the nature of the boundary conditions applied to the coating have a greater effect on its impact response and damage modes. This may therefore mean that applying fully fixed boundary conditions to the gelcoat under-surface results in an unrealistically stiff setup, which restricts through thickness energy dissipation, leading to heightened but overstated damage. These factors will be addressed more fully later, where the impact of a hailstone on a full composite layup (i.e. gelcoat on substrate) is modelled and discussed; allowing for subsequent impact response comparisons, as performed for rain impact previously and discussed in Section 6.6.3.

7.1.2.3 Flexible Coating

10mm Diameter Hailstone

The highly flexible nature of the simulated flexible coating presented challenges with respect to assigning a suitable mesh element size; as also encountered previously in the rain droplet impact modelling work. A fine mesh typically resulted in excessive skewing of the elements, contact misses (between the SPH nodes and the surface) and premature solver termination

due to energy errors. A coarse mesh presented a more limited insight into the impact response of the coating (particularly through its thickness), but encountered less issues with element skewing and the other problems detailed. However, as discussed in relation to the rain droplet impact modelling, the occurrence of surface material erosion was considered less likely in the flexible coating technologies; therefore a coarser mesh was permissible as the overall impact shape response is of more interest.

As with the gelcoat analyses, a sensitivity study was conducted to establish a suitable element size. For a hailstone diameter of 10mm a mesh size of approximately 360µm was implemented in the coating mesh. This relatively large element size resulted in the coating being represented by a single layer of elements in the thickness direction; therefore in essence the element dimensions were 360x360x400µm.

Figure 7-7 shows contours of effective von-Mises stress created in the flexible coating during an impact event featuring the 10mm diameter hailstone with an initial impact velocity of 100m·s^{-1}. The stresses on the surface of the flexible coating and through its thickness at the centre are both shown.

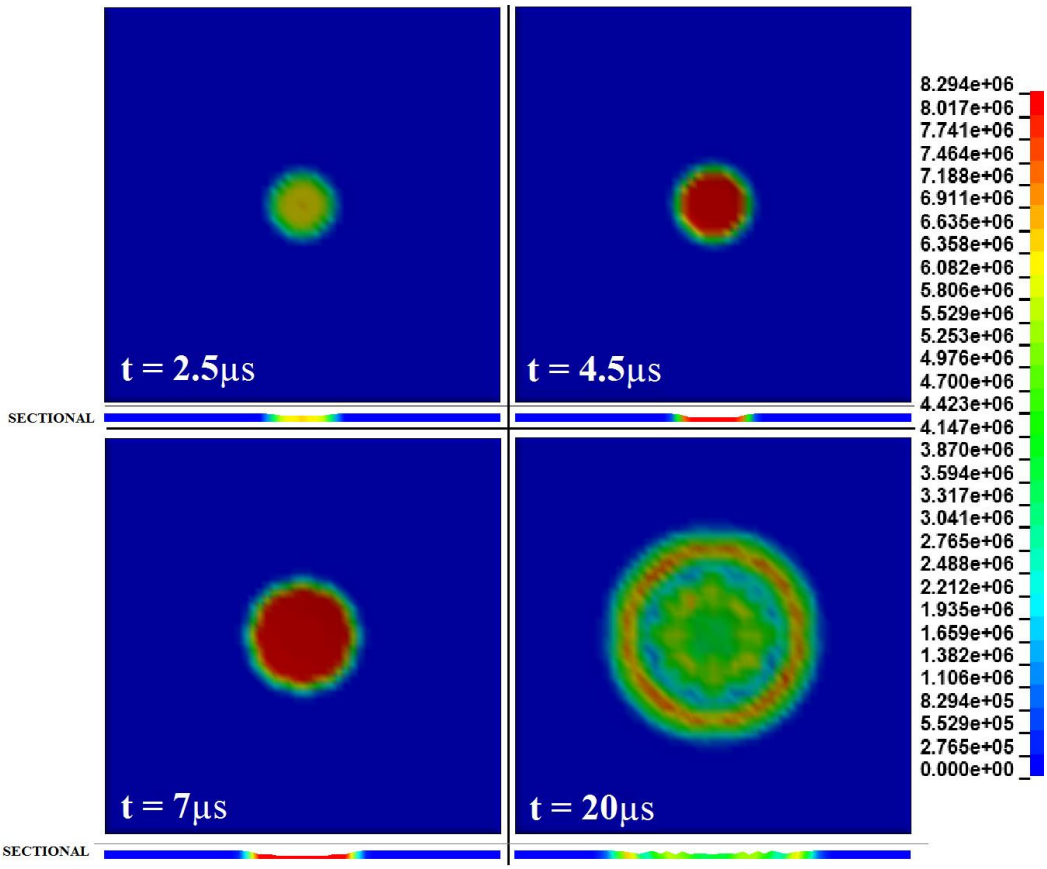

Figure 7-7. Contours of effective von-Mises stress (Pa) in the flexible coating during a 10mm diameter hailstone impact at 100m·s^{-1}; at progressive stages throughout the impact. The upper surface of the gelcoat is shown with

the corresponding sectional view below (through the coating thickness). Coating dimensions: 2x2cm, 400µm thick.

The modelled loading behaviour of the flexible coating material under hailstone exhibits many similar characteristic to those previously shown in relation to rain droplet impact. The thin and highly flexible nature of the coating results in high levels of deformation in a manner more even and widespread than exhibited by the gelcoat. These large deformations result in the creation of stresses throughout the coating thickness and a significant depression on the surface coating.

Figure 7-8 looks more specifically at the four cross sectional views displayed in Figure 7-7 (with the mesh also visible) in order to illustrate the impact response in greater detail.

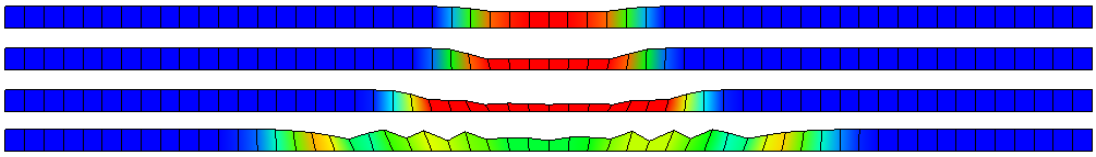

Figure 7-8. Enlarged view of the cross sectional views, through the coating thickness, shown previously in Figure 7-7; at the same time steps and plotting the same stress contours.

As shown, significant surface deformation is created through the compressional forces imparted, effectively squeezing the material downwards. As a result of the coarse mesh used (and only 1 integration point through the thickness), limited through thickness distribution details are available. For instance, in the previous rain droplet-on-flexible-coating analyses discussed, it was shown that a conical stress distribution was created throughout the coating thickness, resulting in high stresses at the boundary condition interface. Such definitions are not possible to observe in the results discussed here, however it is clear that significant through-thickness stresses are created. It is also observable that after the significant early periods of the impact event, the surface profile of the coating returns to near pre-impact conditions, resulting in a flat coating surface once more.

From the plots shown, it is also apparent that (expectantly) the stresses created in the flexible coating material during a 10mm diameter hailstone impact at 100m·s^{-1}, meet the yield stress value of the material (8MPa). As such, plastic strain is created in the flexible coating material, which is illustrated through the contour plot shown in Figure 7-9.

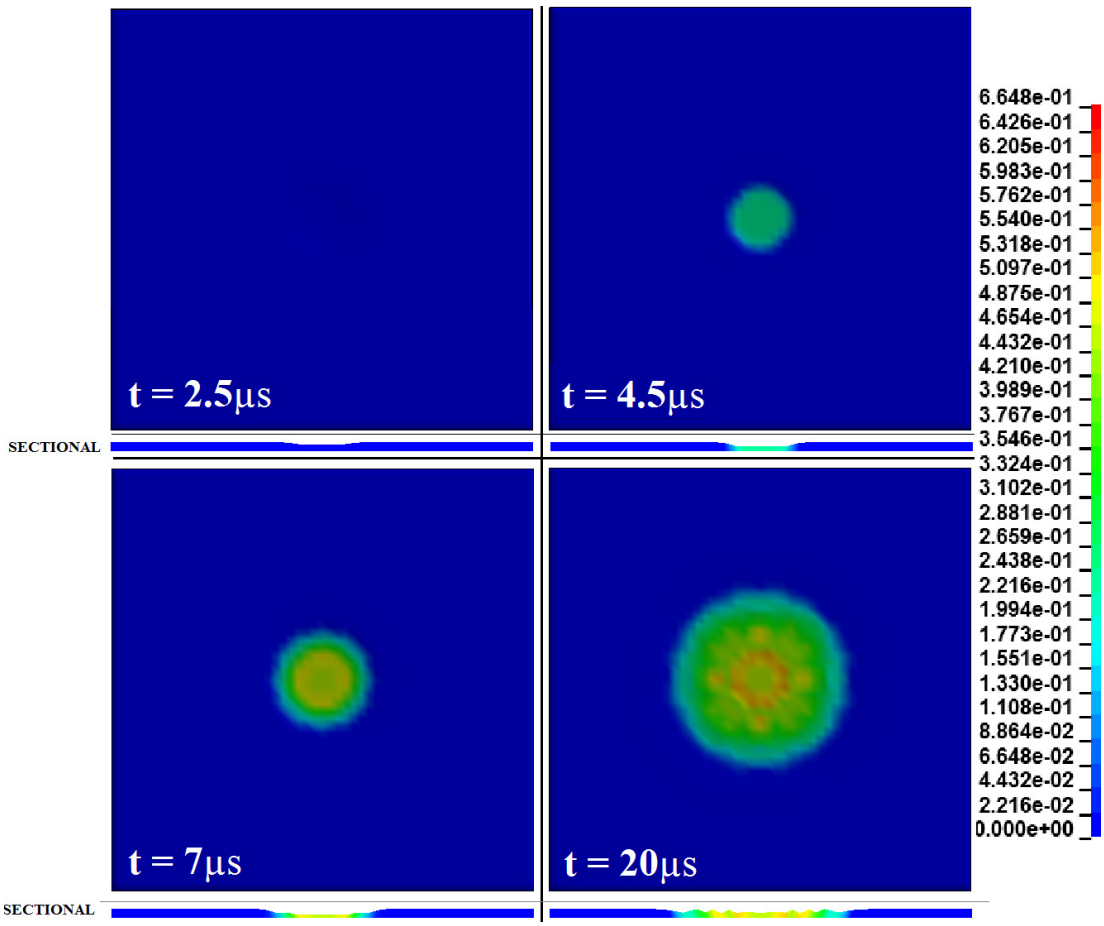

Figure 7-9. Contours of effective plastic strain in the flexible coating material during a 10mm diameter hailstone impact at 100m·s^{-1}; at progressive stages throughout the impact. The upper surface of the coating is shown with the corresponding sectional view below (through the coating thickness).

As shown, following a simulated 10mm diameter hailstone impact at 100m·s^{-1}, plastic strain values of up to 0.66 were created in the flexible coating material. The distribution of plastic strain on the surface appears evenly distributed across a growing circular area; however there are also peak value ring distributions visible on the surface, specifically towards the end of the impact sequence. The plasticity is also observable throughout the coating thickness (from the sectional views), however limited through thickness details are available as a result of the coarse mesh applied. It may be the case that given a finer mesh, the plasticity distribution through the thickness would vary with depth.

With respect to the magnitude of the plastic strains created in the material, a value of 0.66 is significant and although as illustrated in Figure 7-8 the surface does return to near pre-impact conditions, there is lasting damage deformation. The predicted value of strain required for the onset of erosion is however over 700%, therefore short term erosion of the flexible coating material may be unlikely (as with rain droplet impact). However, the through

thickness damage exhibited once more emphasises the importance of an effective and robust bonding method with any proposed substrate materials.

20mm Diameter Hailstone

Modelling the impact of a 20mm diameter hailstone on the flexible coating presented further issues with respect to the occurrence of mesh skewing and premature solver termination due to energy errors. In order to successfully solve the simulations, the element size in the target mesh had to be large in length and width (in depth it was restricted by the coating thickness dimension), therefore the results obtained were of little use and provided no real insight.

As such, it was not possible to fully investigate the impact of a 20mm diameter hailstone on the flexible coating.

7.1.2.4 Hailstone-on-Coating simulation challenges

It is clear from the results shown and discussed that there are many issues with respect to successfully and accurately modelling the impact response of coating materials subject to large hailstone impact. The great difference in size between the coatings and the impact projectile, make it difficult to effectively capture the coating impact response in any great detail without the requirement for excessive computational resources and time (through implementing a high number of SPH nodes or a very fine mesh for the coating). Although some success was achieved with respect to modelling the impact response of the stiffer gelcoat material, the modelling approach provided limited insight into the impact response of the flexible coating material. However, it should be noted that the characteristically stiff boundary conditions applied to both coatings may also have aggravated the energy errors and element skewing issues. This issue will be further explored through comparison with the results obtained for the impact response of the coating when attached to a composite substrate; discussed in the sections that follow.

The issues identified and described are further elaborated upon and discussed in the greater detail later in Section 9.2; along with all other major modelling issues and challenges encountered. However it is clear that although some useful results were obtainable with respect to modelling hailstone impact induced surface degradation, the modelling methods developed within the LS-DYNA environment may be both more suited and useful for larger scale simulations, investigating composite laminate impact response and related damage.

7.2 Theoretical Blade Skin Hailstone Impact Response

All modelling work discussed previously has primarily been concerned with establishing the detailed impact response of the different surface coating technologies, when subjected to both rain droplet and hailstone impact. However, LS-DYNA can also be utilised to study the impact response of composite material technologies, allowing for the investigation of impact induced damage and delamination. As such, it was decided that the hailstone impact response of the blade layup configuration described previously in Section 5.3.1 would be modelled, to provide insight into the characteristic response.

For this modelling work no experimental data was available for comparison and validation, and therefore only a certain level of confidence could be held in the accuracy of the result provided. However the objectives and aims of the modelling work conducted were firstly to give an indication of the possible range of impact response behaviours of typical blade materials, and secondly help to evaluate the modelling methods and approaches employed and their further potential use.

Two blade geometry configurations were be modelled and investigated. Firstly a simple flat material layup (similar to that described previously in Section 6.3) would be modelled to gain insight into the characteristic impact response of such a material layup to direct hailstone impact. Secondly, a curved leading edge profile geometry would be modelled (with the same material layup), to investigate the effects of the blade curvature on the material impact response. Both modelling approaches would adopt the material layup and material types as first identified in Section 5.3.1, and later implemented in Section 6.3. In the absence of both experimental data and corresponding material property data, the material properties cited by Menna et al. [183] (Table 6-3) were again implemented, owing to their fullness and experimental verification/calibration. Given the difficulties and limitations encountered with respect to effectively modelling the impact response of the flexible coating materials, it was decided that in these larger scale models only (epoxy) gelcoat coatings would be modelled.

Each target configuration would then be subjected to simulated impact from 10mm, 20mm and 40mm diameter hailstones at a velocity of $100 m \cdot s^{-1}$; in separate simulations. Such a velocity represents most likely the worst case possible for most current generation blades and would allow the evaluation of the effects of increasing hailstone size. For the flat target simulations, it was decided that direct impact at right angles to the target surface would be simulated, and in the curved target simulations the hailstone would be modelled to strike the target directly on the leading edge (shown later).

7.2.1 Model Setup

7.2.1.1 Flat Target

For the analysis featuring a flat composite target, the layup configuration specified first in Section 5.3.1 and later in more detail in Section 6.3, was again adopted with respect to the individual layer thicknesses and fibre orientations. In order to eliminate or minimise differences in the modelling setup between the respective varying hailstone diameter simulations, it was decided that the blade target body would be kept identical between simulations, with respect to principle dimensions, mesh sizes, boundary conditions and material properties. As such, accounting for the large 40mm diameter hailstone simulations, a relatively large target size was created, 120x120mm and 2mm thick (5, 400µm thick layers), which would be utilised for each varying hailstone diameter simulation. As before, the layup consisted of a layer of gelcoat, CSM and a substrate consisting of 3 layers of bi-axially reinforced composite with orientations [0˚/45˚/0˚]. The three layers of bi-axially reinforced composite are referenced hereafter as the Top, Middle and Bottom biaxial layers; where top refers to the layer nearest to the blade surface. As before in the rain impact analyses (Section 6.3.1), the fibre orientation axes of the Top and Bottom biaxial layers, A and B, were aligned with the global model reference system x and y axes; resulting the C axis aligning with the z axis. For the Middle biaxial layer, the A and B axes were then rotated by 45˚ around the local C material axis to give the desired fibre orientation.

The gelcoat layer was assigned a hexahedral mesh with an element size of 400µm, resulting in a single layer of elements in the thickness direction. The remaining substrate layers were each assigned and element size of 2mm in-plane and 400µm in the thickness direction. As before, the hailstone geometry was created using the SPH tools and assigning a node total of 33k. The resulting model geometries and associated meshes/SPH nodes are illustrated in Figure 7-10; viewed front on and featuring a 10mm diameter hailstone.

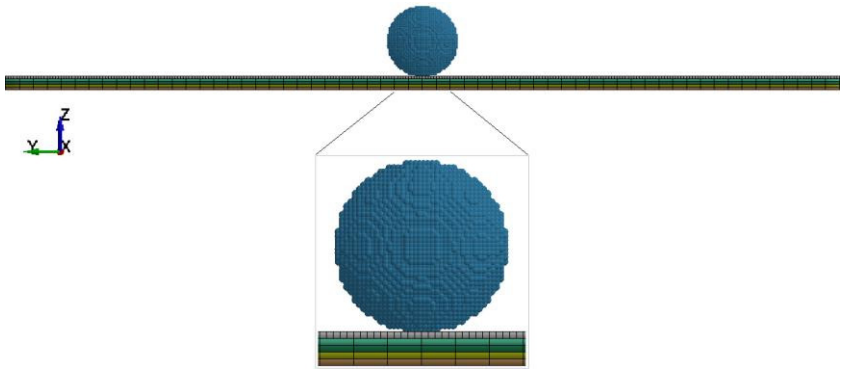

Figure 7-10. Flat blade layup and a 10mm diameter hailstone. Layup materials top-to-bottom: gelcoat, CSM, 3xBiaxial FRP. Layup dimensions: 120x120x0.4mm.

The relative coarseness of the mesh applied to the gelcoat layer in comparison to the previous coating impact studies was required in order to allow for effective impact modelling of the larger hailstone diameters. It was recognised that such a coarse mesh at the hailstone/target interface would deliver reduced detail with respect to the impact response of the coating material. However, as the impact response of the whole layup assembly was of most interest, this compromise was deemed acceptable.

The material and section properties of each material layer were applied identically as previously described in Section 6.3. Care had also to again be taken to ensure that the correct fibre orientations were modelled, through altering the material axis orientation of the composite material elements, through the same approach as described previously in Section 6.3.1.

The contact between the layers in the layup was defined using the contact card *CONTACT_AUTOMATIC_SURFACE_TO_SURFACE_TIEBREAK, however unlike the previous rain droplet impact analyses discussed in Section 6.3, the contact definition was not set to fully fixed. Instead, OPTION=6 (described previously in Section 4.5.3.2) was invoked in the contact card definition, to allow for the added option of modelling delamination; given sufficient impact violence. The interface normal failure stress (NFLS) and shear failure stress (SFLS) were set to 35MPa and 65MPa respectively, taken from the values implemented and cited by Menna et al. [183]. The critical distance required for complete interface failure (PARAM in the contact card) was set to 0.14mm. These interlaminate contact conditions were set between all interfaces in the laminate, not just between the composite plies, as it was though that as the matrix material was consistent throughout the layup (i.e. epoxy resin), this material would form the bond between layers and would therefore be identical for each interface. This of course assumes that fibre orientation, content and other parameters have no effect on the interlaminate normal and shear strength, which is most likely not the case. However for the purpose of the work conducted it was deemed an appropriate assumption in the absence of actual interlaminate strength data. As before, to account for the differing levels of stiffness between the adjoining composite layers, the SOFT=1 option was also applied to each contact definition. As with all other previous simulations, the contact option *CONTACT_NODES_TO_SURFACE_SMOOTH was implemented to model the hailstone-on-coating contact.

With respect to appropriate boundary conditions, many configurations were explored and trialled, such as symmetry and sliding plane conditions, however rigid body motion was often an issue with such approaches. As such, it was decided that for the purpose of

investigating the basic impact response characteristics of the simulated blade skin section, simple fully fixed boundary conditions should be applied at the edges of the target body. This would allow the laminate target to freely deflect under impact, whilst restricting complex rigid body motion.

As with previous analyses, the parameter investigated through the simulations was the effect of increasing hailstone diameter, at a fixed impact velocity of 100m·s^{-1}. Each simulation was to include only 1 impact event, in order to assess the magnitude of the loads and deformation imparted through the hailstone impact and any potential damage mechanisms simulated; discussed later in the results section.

7.2.1.2 Curved Target

The curved blade target geometry used was based upon the dimensions provided through industrial interaction [224], as shown in Figure 7-11 and discussed previously in Section 5.3.1, which were described by the source as a good representation of the geometry at the blade tip leading edge.

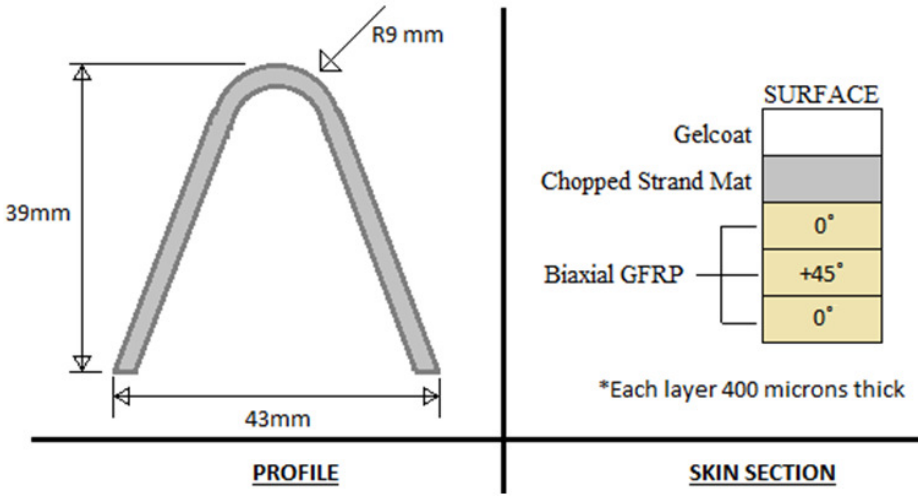

Figure 7-11. Typical blade leading edge profile at the tip and a cross section of the blade skin detailing the layup and material types used.

This cross sectional geometry was used to create a blade section with a width of 5cm. The material layup configuration (order, orientations etc.) described in the previous section for the flat target (and also shown in Figure 7-11) was again adopted for the curved target simulations.

Given the added complexity of the target shape and the resulting mesh, the geometry and mesh for the target body was initially created in the ANSYS Workbench Design Modeller tool [194]. This process could also have been performed using LS-PrePost, however a

greater level of familiarity was possessed within the Design Modeller software; with respect to geometry creation and meshing. The flat topside and underside regions of the blade material layers were assigned hexahedral element dimensions of approximately 1.0x0.7x0.2mm, whilst the material layers in the curved leading edge regions were assigned slightly smaller element dimensions of 1.0x0.4x0.2mm; resulting in 2 layers of elements through the thickness of each material layer. Following the creation of the geometry and the application of a mesh within Design Modeller, the resulting target body was then imported into the LS-PrePost environment for the rest of the model setup process. The resulting geometry and associated mesh are illustrated in Figure 7-12 (in the LS-PrePost environment), which shows both the whole geometry and the finer details of the applied mesh. The material axes reference system (A, B, C) adopted for the composite materials is also shown in detail.

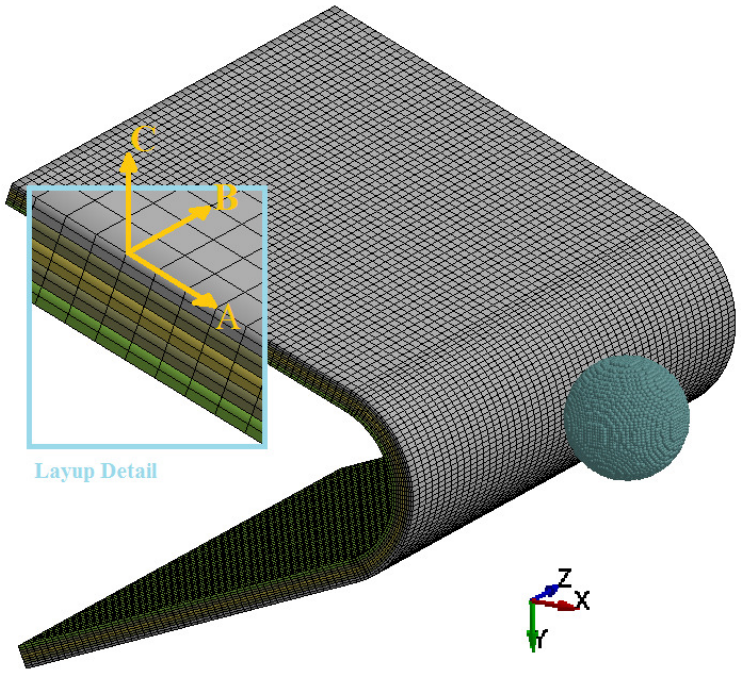

Figure 7-12. Curved blade target geometry and mesh, and 10mm diameter SPH hailstone. Zoom detail of layup mesh also shown in blue box, with composite material axes reference system shown.

The hailstone body was again created using the SPH tools previously described, and was once more assigned 33k SPH nodes; irrespective of hailstone diameter. The resulting model geometries and associated meshes are illustrated in Figure 7-12.

The material and section properties for each material layer and the hailstone were implemented as described in the previous section for the flat target configuration. However due to the curved profile of the target, additional complexity was introduced to the setup

process with respect to ensuring the correct material fibre orientations were applied to the composite material elements. Using the element editing tools, the material axis orientations were altered, such that the principle material axis A, of the top and bottom layers of biaxial GFRP, traced the profile of the blade curve and the other fibre axis B (the other weave direction), ran along the length of the target (Z-direction) as shown in Figure 7-12. The middle biaxial GFRP layer was altered such that these principle axes were rotated 45˚ about their local c-axis. The alterations resulted in the creation of the desired [0˚/45˚/0˚] layup configuration, following the material path around the blade profile.

The contact definitions both between the composite laminate layers and hailstone and gelcoat were applied identically as described the previous section for the flat target setup.

Applying representative boundary conditions for modelling the leading edge in isolation presented difficulties, as it is difficult to ignore or represent the influence of the rest of the blade as a whole. The two side faces in the x-y plane (corresponding to the coordinate reference system shown in Figure 7-12) were restrained with sliding plane conditions, whereby translation was restricted in the z-direction and rotation restricted about the x and y axes. The trailing faces at the root of the blade were fully fixed in all degrees of freedom. These boundary conditions were adjudged to allow for free energy dissipation from impact whilst restricting rigid body motion.

Finally, the hailstones of varying diameter (10, 20 and 40mm) were set to impact the blade leading edge directly at $100 m \cdot s^{-1}$ in the x-direction.

7.2.2 Results & Discussion

7.2.2.1 Flat Target

The 10mm and 20mm diameter hailstone simulations detailed, took approximately 30-40 minutes to fully run. However as discussed later in this section, run problems were encounter with the 40mm diameter hailstone simulation, resulting in an increased run time (for the simulation time shown) of around 2 hours.

Firstly, it is useful to review the fundamental physical aspects of the three simulated impact events through plotting the deformation of both the hailstone and the composite target during impact. Figure 7-13 shows the hailstone and target geometries (in profile) at approximately 150µs after initial contact, for the three simulations featuring varying hailstone sizes; impacting at 100m·s^{-1} with increasing impact energies of 2.3J, 18.8J and 150J.

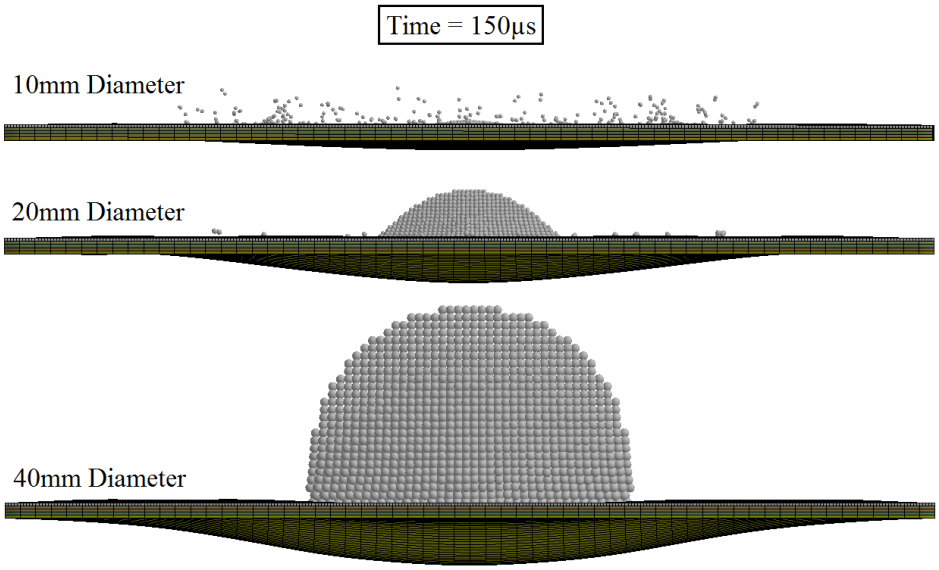

Figure 7-13. Target deformation and hailstone impact shattering behaviour at 150µs into the respective impact events, for the three hailstone diameters modelled in LS-DYNA; each impacting at 100m·s^{-1}.

From these three frames, taken from the three different respective simulations, it is apparent that the increase in hailstone diameter greatly alters the impact response of the composite target. There is observable deformation of the composite laminate target for all three simulations, increasing in severity with increasing hailstone diameter. Figure 7-14 details the displacement of the node at the centre of the target on the underside of the layup (i.e. the underside of the bottom biaxial composite layer) throughout each of the simulated impact events; illustrating the magnitudes of maximum target deformation/displacement.

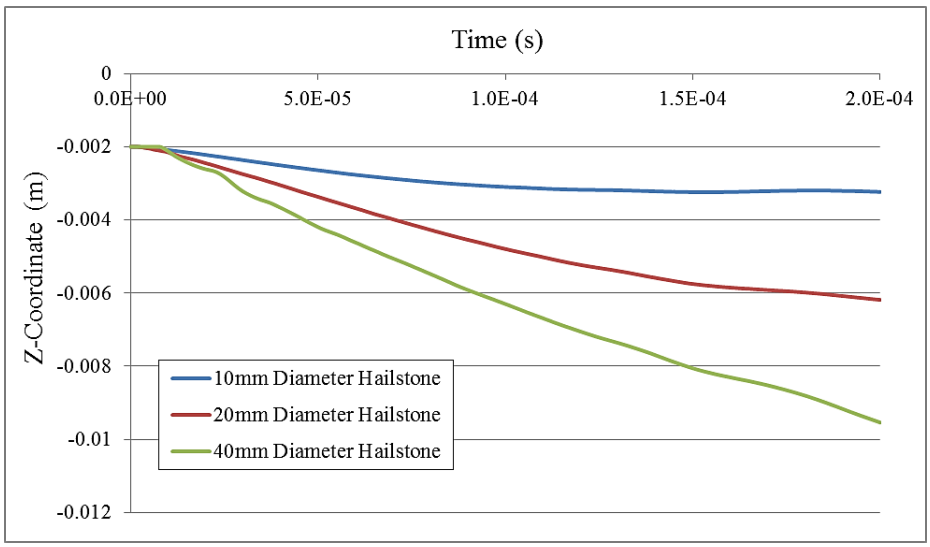

Figure 7-14. Time history of the z-coordinate of the central node on the lower face of the composite target for the three hailstone impact simulations, featuring hailstone diameters of 10, 20 and 40mm; impacting at 100m·s^{-1}.

From Figure 7-14 it can be seen that a maximum target deformation of approximately 1mm (in the direction of impact, z) was simulated when subjected to a 10mm diameter hailstone impact event (2.3J). It can also be seen that for the 10mm diameter hailstone impact, the maximum deflection of the target is reached after approximately 150µs from initial contact. However, for the two larger hailstone diameters of 20mm and 40mm (18.8J and 150J respectively) the displacement of the target is still increasing at and beyond the end of the simulated impact event; at which point the maximum deflection is around 4mm and 8mm respectively. There are indications however, that for the 20mm diameter hailstone simulation, the rate of target displacement begins to level off at around the 200µs point. The simulations featuring the two larger diameters were not run for longer, as due to the large deformations of the plate during these simulations, the computational time required to continue beyond 200µs rose significantly, making it unfeasible.

Further insight into the hailstone-target interaction for the three different simulations can be gained from reviewing the contact force between the two bodies throughout the respective impact events - in the direction of impact (z-direction) – as shown in Figure 7-15.

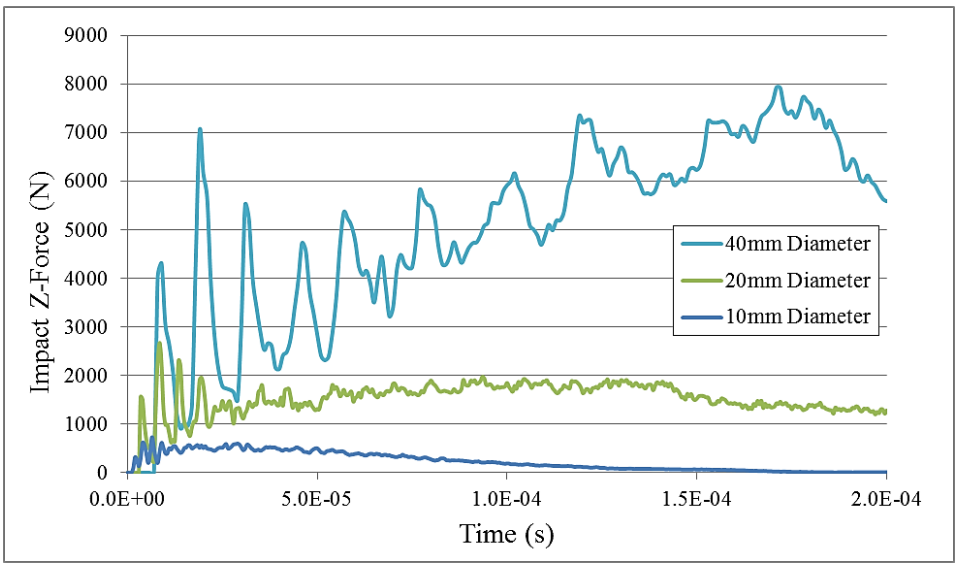

Figure 7-15. Impact contact force histories (in the z-direction) between the impacting hailstone bodies and the composite target, for the three simulated hailstone diameters; impacting at 100m·s^{-1}.

Figure 7-15 shows that for a simulated hailstone diameter of 10mm, the impact energy was quickly absorbed and dissipated by the composite target through the deformation exhibited previously both in Figure 7-13 and Figure 7-14. This impact interaction therefore produced a clear contact force peak shortly after initial contact, followed by a gradual decline to zero, indicating that at around 200µs after initial contact, the significant portion of the impact event in the context of target material loading was complete. For the 20mm diameter hailstone simulation, the contact impact force is observably larger than that of the 10mm diameter hailstone impact simulation. A more gradual peak impact force is reached after around 100µs, after which the beginning of the steady decline in impact force can be seen. The impact force history obtained from the 40mm diameter hailstone simulation differs significantly from those obtained from the other simulations, most notably with respect to the magnitude of the forces created.

From the plots shown, it is clear then that the hailstone size had a significant effect on the impact forces created in the simulations. It is therefore prudent to also investigate the effects of these increased loads in the context of material loading and potential damage creation.

Looking first at the impact loading of the epoxy based gelcoat, it is possible to review the stresses generated in the gelcoat during impact; for the three simulated hailstone diameters. Figure 7-16 plots the time history of maximum effective von-Mises stress within the gelcoat material throughout the three separate simulations.

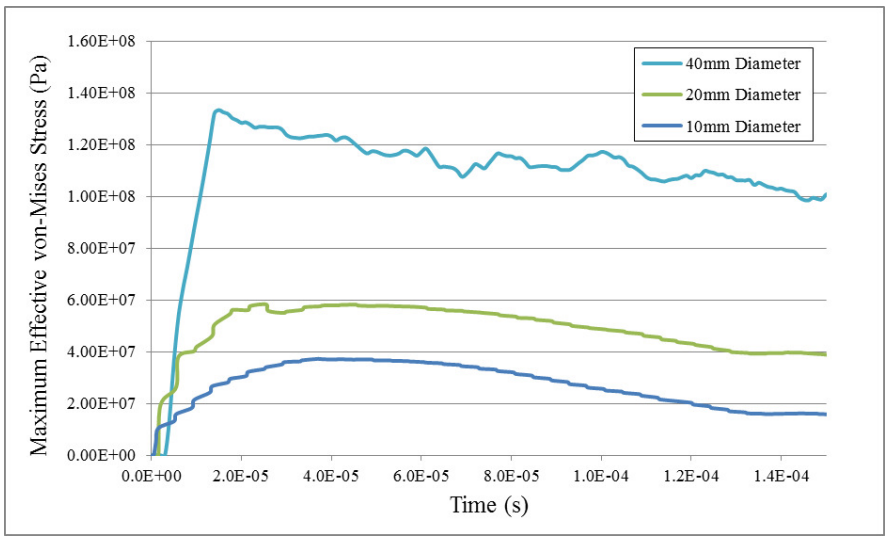

Figure 7-16. Time history of the maximum effective von-Mises stress within the gelcoat material layer during impact from the three simulated hailstone diameters of 10, 20 and 40mm; impacting at 100m·s^{-1}.

From the stress histories shown it is clear that the increased impact energies associated with the larger hailstone diameters results in significantly larger stress creation in the coating material. As shown, the simulated 40mm diameter hailstone had sufficient impact energy to induced yield level stresses within the epoxy material (based on the specified yield stress of 90MPa, detailed in Table 6-2), resulting in the creation of damage in the material in the form of plastic strain, as shown in Figure 7-17.

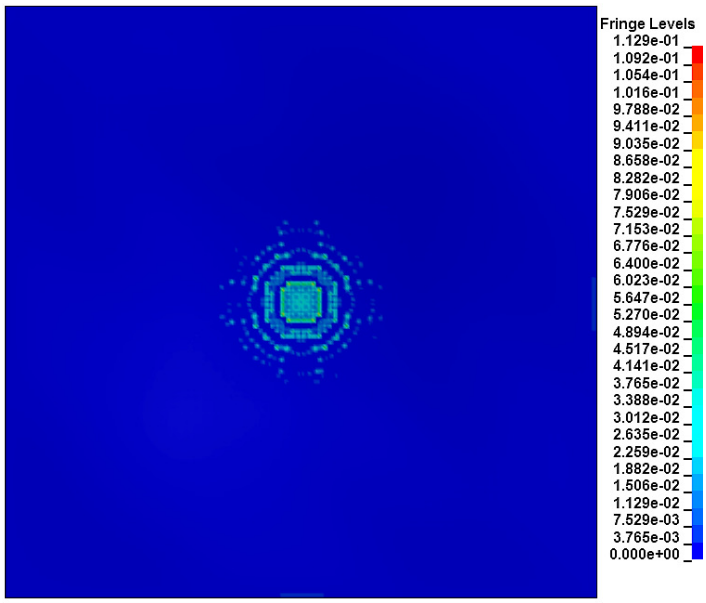

Figure 7-17. Contours of plastic strain on the gelcoat surface following impact from a simulated 40mm diameter hailstone impact at 100m·s^{-1}.

As illustrated, the damage distribution on the surface of the gelcoat compares closely with those observed in previous sections, forming in concentric ring patters around the initial zone

of contact. A maximum effective plastic strain value of around 12% is shown in the results, which is significant in the context of any potential repetitive impact and subsequent erosion.

Examining Figure 7-16 it can be seen that the two smaller diameter hailstones had insufficient impact energy to create such damaging stresses. However, it important to note that the loading behaviour in the gelcoat material captured by these simulations was relatively simplistic due to the coarse mesh applied to the coating; compared to the finer meshes applied in the previous standalone coating simulations. As such, the stress created in the gelcoat arose primarily from simple compressional loading from the hailstone in the impact direction, as the mesh was too coarse to capture any great detail in stress distribution within the coating. This is also partly why the stress levels observed in the gelcoat in the simulations discussed here are notably lower than those discussed previously, although the more flexible boundary conditions may also be a significant factor. However as detailed previously, the coating failure mechanisms were not the primary concern of the simulations discussed in this section, rather the overall composite loading mechanisms through hailstone impact were of interest.

Given the orthotropic material properties of the composite materials created within the LS-DYNA model, and the inherent directionality of their material properties and behaviour, the von-Mises stresses calculated for these materials by LS-DYNA were not as useful an indicator for the composite material behaviour. Instead, it was found more appropriate to review the directional stress created in these composite materials along their A, B and C material axes; as defined during the setup and described previously. However, as with gelcoat layer, given that only one layer of elements were used to represent each material layer, limited detail of the stresses in the C direction were available

Furthermore, as the model created was mostly symmetrical, the stresses generated in the A and B material axes compared almost identically for the given composite layer. As such, they can both be considered simply as in-plane, fibre orientated stress, referred to in the following as X/Y stresses (A/B with respect to local element material axes). Figure 7-18 plots the time histories of the maximum tensile stresses created in these orientations in the three biaxial composite layers for each of the three varying hailstone diameter simulations.

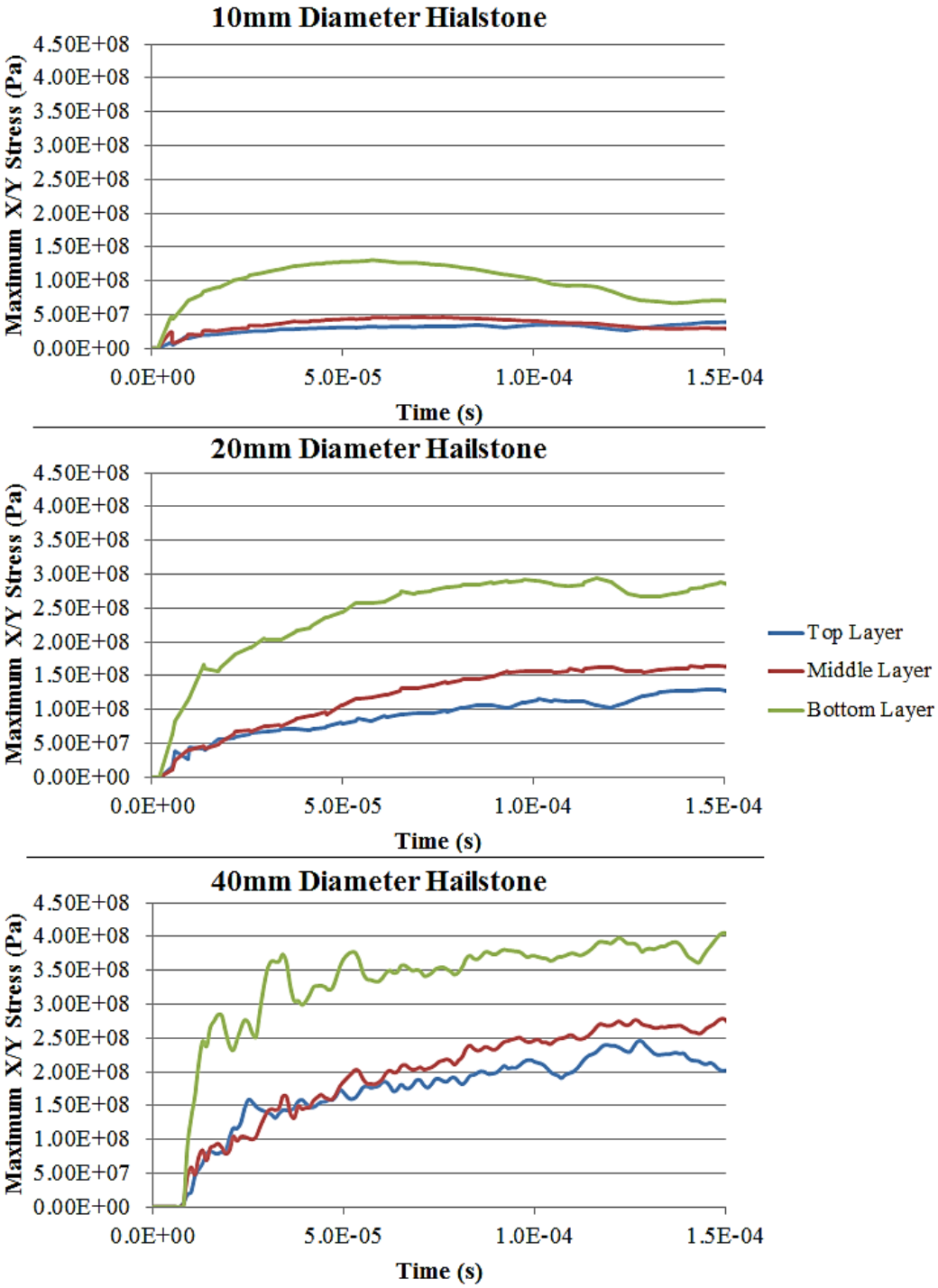

Figure 7-18. Time histories of the maximum X/Y stress (stresses in fibre dominated directions) in the three biaxial composite layers, for the three hailstone diameter simulations; 10, 20 and 40mm diameter hailstones impacting directly at 100m·s^{-1}.

From the plots, it is clear that the increasing impact energies associated with increasing hailstone diameter have a significant effect on the loading of the composite target. For a (comparatively) small hailstone diameter of 10mm, the stresses in the fibre direction within the composite layers are limited to a maximum of approximately 140MPa, which although

not insignificant is well below the yield limits (414MPa in tension, in-plane) of the defined material properties (Table 6-3). It is apparent that these maximum stress values occur in the Bottom biaxial layer, as is the case for the other two simulations; resulting from this layer being stretch and flexed under impact (as shown previously in Figure 7-13). For the largest simulated hailstone diameter of 40mm, the stresses in the composite material layers are considerably more significant in the context of approaching yield values. A maximum stress of approximately 400MPa is induced in the Bottom biaxial layer, a magnitude in the region of yield value for the material. However, it is prudent to remember that the failure mechanisms modelled by the composite material model utilised for the biaxial layers, *MAT_COMPOSITE_FAILURE_SOLID_MODEL, are based on a combination of given material state conditions (as described previously in Section 4.5.3.1), and exceeding the yield strength is not the sole criteria for material failure.

Significant compressional stresses were also created in the principle material axis directions within the biaxial layers in the three separate simulations. For brevity these are not reviewed in great depth here, as in addition to the complex tensile loading observed and discussed, they do not add significant clarity to the loading behaviour within the composite layers; and such further details are outside the requirements and aims of the modelling work discussed here. However contours of the stresses created along the principle material axes for the respective layers can be plotted to highlight such complexity in the loading distributions within the biaxial layers. For instance, Figure 7-19 shows plots of contours of x stress at various stages throughout the simulated 40mm diameter hailstone impact event (in the three biaxial layers), whereby positive and negative stress values indicate loading in tension and compression respectively.

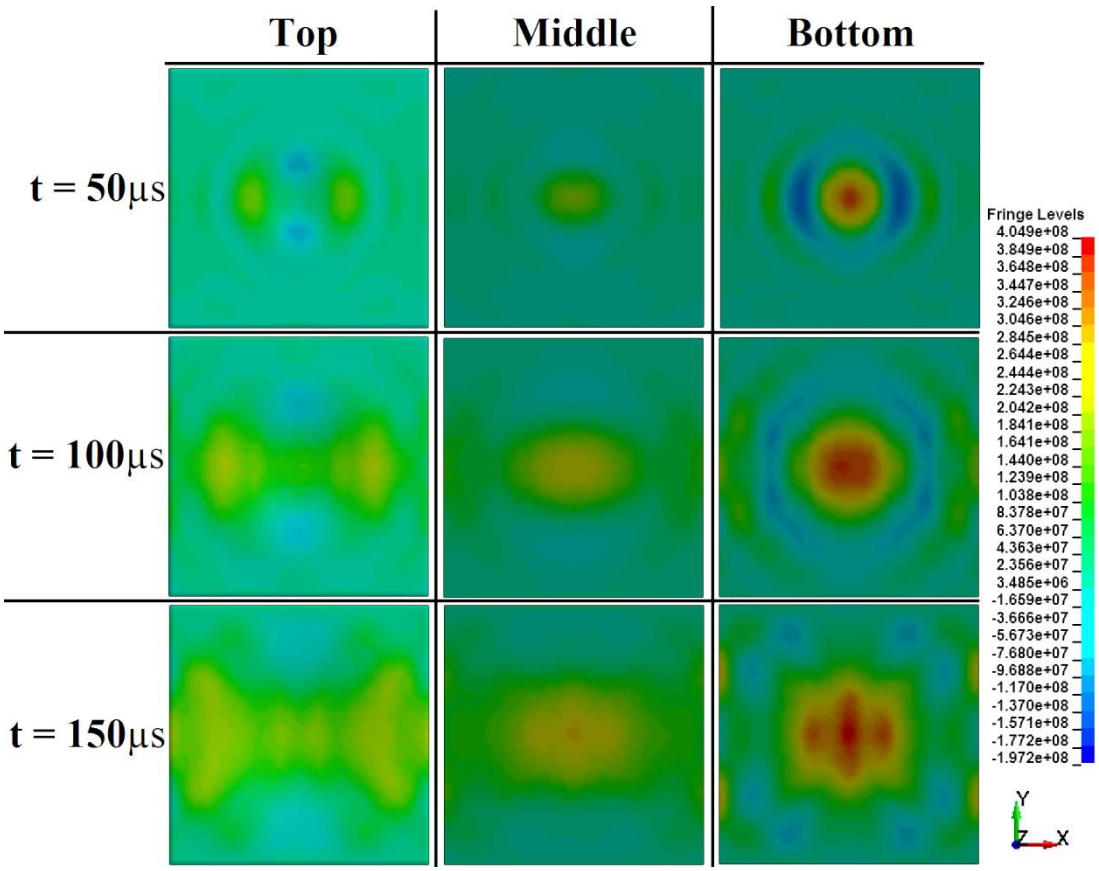

Figure 7-19. Contour plot of stresses (Pa) in the X-direction (fibre orientation for top and bottom layer) in the top, middle and bottom biaxial layers of the composite laminate when subjected to a simulated 40mm diameter hailstone impact at 100m·s^{-1}; at three time points in the simulation.

As shown, as a result of the complex fibre orientations in the composite materials, the loading behaviour of these materials is also highly complex, specifically in this example in the bottom biaxial layer where significant tensile and compressive loads in the x direction are exhibited at the same time. The consequences of such loads and their influence of blade impact response are out with the objectives of the simulations discussed. However, these plots illustrate the capabilities of the modelling approach adopted, with respect to modelling complex loading behaviour of anisotropic materials and obtaining meaningful outputs.

Material loading induced failure of the individual material layers in the laminate is of course not the only concern with respect to hailstone impact. The interface stresses and forces between the different material layers are also of interest. To investigate these issues with respect to the impact modelling results obtained, the stresses generated across each of the modelled interfaces were examined further.

The pressures created in the interface between each respective layer in the target layup (except the Middle-Bottom interface which exhibited low pressure levels), at varying stages

throughout the simulated 40mm diameter hailstone impact event (at 100m·s^{-1}) are shown in Figure 7-20.

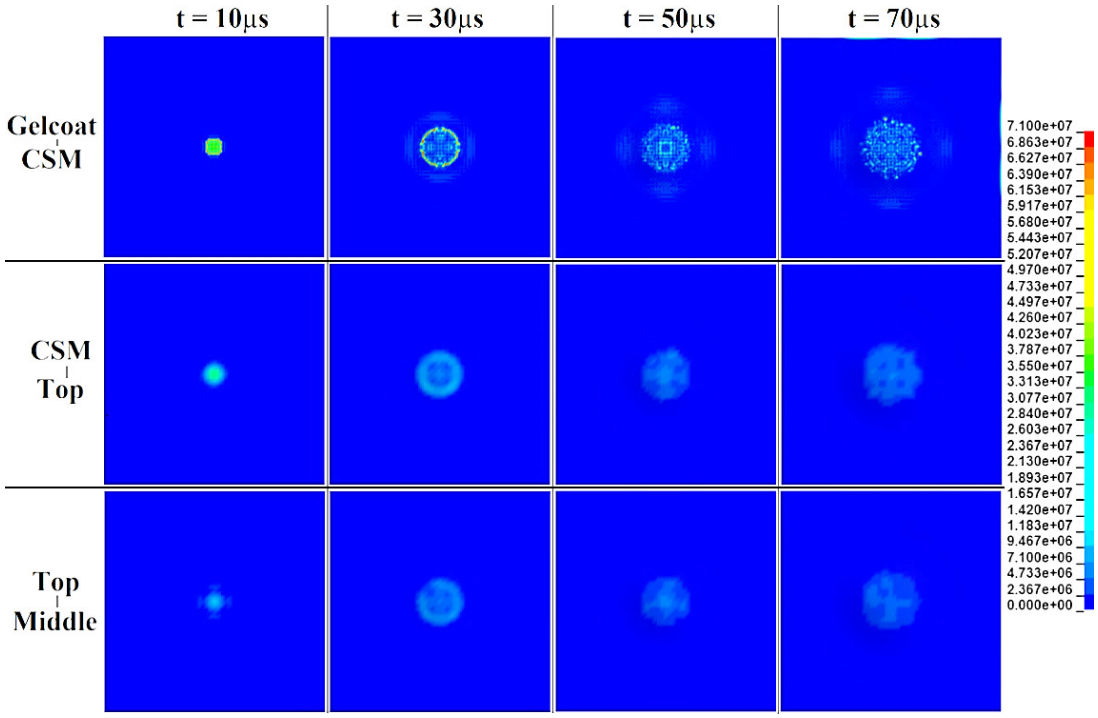

Figure 7-20. Contours of interface pressure between the individual laminate layers of the target at various stages throughout the simulated 40mm diameter hailstone impact; with an impact velocity of 100m·s^{-1}.

It can be seen that there are significant interlaminate pressures created throughout much of the target thickness during the 40mm diameter hailstone impact simulation. The highest pressure levels are exhibited in the bond between the gelcoat and CSM layer, the bond closest to the region of impact, reaching a maximum localised value of 71MPa. However the pressures created between the other bonds in the laminate are also significant, reaching peak levels of approximately 30MPa. The ring shaped formations in the pressure created between the bonds indicates that the loading characteristics observed on the surface during impact (i.e. the creation of ring shaped stress distributions) are transferred in similar distributions through the interlaminate bonds. The pressures and shear stresses generated in the interface between the gelcoat and CSM layer were significant enough to satisfy the damage criteria implemented (OPTION=6, discussed previously in Section 4.5.3.2), therefore creating permanent damage in the bond; but not creating absolute failure. Interface bond damage can be visualise in LS-PrePost by plotting contours of a variable named ‘Contact Gap’ , this variable is a simple damage indicator based on the specified interface failure criteria (OPTION=6 in these simulations), whereby a value of nought indicates no permanent damage to the interface and a value of 1 indicates total failure of the interface bond. Figure

7-21 plots the contours of Contact Gap in the gelcoat-CSM interface following the simulated impact of the 40mm diameter hailstone at 100m·s^{-1}.

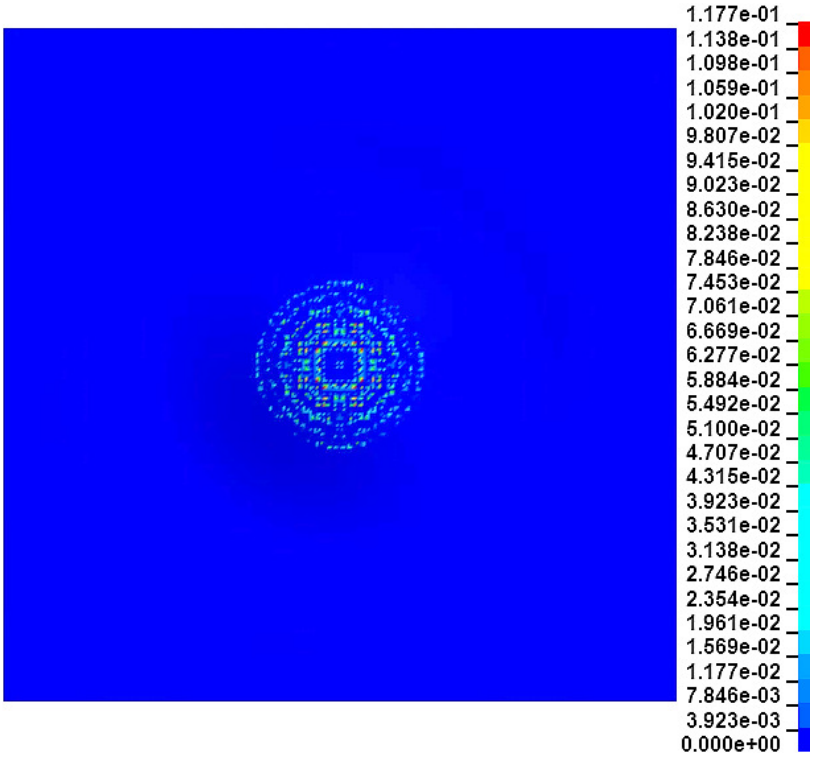

Figure 7-21. Contours of Contact Gap in the gelcoat-CSM interface following simulated impact from a 40mm diameter hailstone at 100m·s^{-1}.

It is noted that in some areas of the interface between the gelcoat and the CSM layers, the interface was damaged by up to 12% of its total strength. Again, significant ring shape distributions in the damage are observable, comparable to the plasticity formations created on the gelcoat surface.

The distributions obtained for the 10mm and 20mm diameter hailstone simulations were comparable to those shown for the 40mm diameter hailstone in Figure 7-20, however the maximum pressures generated were lower, at about 23MPa and 64MPa respectively.

From the results discussed, it is clear then that the effects of increasing hailstone diameter are significant in relation to the resulting impact response of the simulated flat wind turbine skin section. Increased diameters result not only in the creation of higher stresses in the surface coating, but also higher loads in the composite substrate materials. For a large hailstone diameter of 40mm, both these forms of loading are significant in the context of the overall strength of the respective material. For this size, significant plasticity was created in the gelcoat material and the loads within the composite substrate approach near yield levels. Significant interlaminate normal and shear stress were also created, resulting in the damage

of the bond between the gelcoat and CSM layer. However, it is also clear from reviewing the deformation of the composite target for each of the differing hailstone size simulations that the simple fully fixed boundary conditions at the target edges allow for a relatively free impact response of the target; resulting in rebounding behaviour. It may be that alternative boundary conditions would result in a change in the loads created and that the creation or structural loading related pre-stress in the material would result in heighten impact loading and subsequent damage. Also, a different surface profile (i.e. curved) may also result in greater loads being created as a result of natural body restrictions, as explored and discussed in the following section.

7.2.2.2 Curved Target

The three simulations conducted ran effectively and without error, however, the simulation featuring the larger hailstone diameter of 40mm took significantly longer to solve (approximately 12 hours until the point of premature termination at the simulation time stated); as a result of damage creation and the subsequent requirement for reductions in the time step. As such this simulation was terminate at an earlier model time of approximately 50μs, by which point the significant proportion of the load imparted had been transferred to the target. The 10mm diameter hailstone simulation took approximately 30-35 minutes to run, and the 20mm diameter simulation took around 40-50 minutes.

As applied in previous results analysis, in order to obtain a clearer understanding of the basic impact phenomenon, as simulated for the three hailstone diameters, it was first useful to review the visual aspects of the respective impact events. Figure 7-22 illustrates the impact progression of the three simulated hailstone diameters of 10, 20 and 40mm on the curved target, plotting contours of effective von-Mises stress within the hailstone material to show the ice material failure progression.

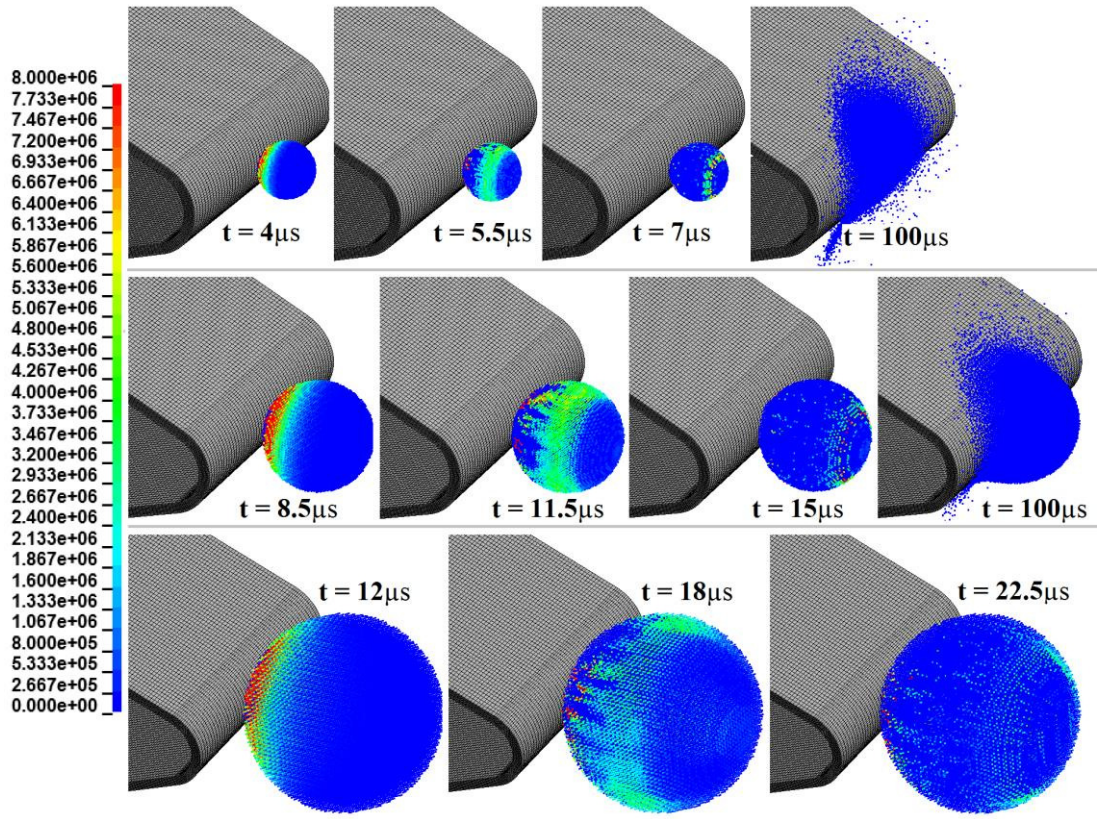

Figure 7-22. Visualisation of the impact progression of the three simulated impact events, featuring increasing hailstone diameters of 10, 20 and 40mm (shown top to bottom respectively), striking a leading edge blade profile. Contours of von-Mises stress (Pa) are plotted in the hailstone body to detail the material failure progression in the ice material during impact.

From Figure 7-22 there are clear similarities in the nature of material failure propagation in the different hailstone sizes, characterised by a clear stress shockwave in the material propagated away from the initial point of contact, result in sweeping damage of the ice material and subsequent relaxation to a near fluid state. The only appreciable difference in the hailstone damage progression behaviour relates to the time required for complete failure of the ice material. The shockwave propagation speed was recorded at approximately 2000m·s^{-1} for each simulation, therefore resulting in a longer time requirement for complete failure of the larger hailstone sizes.

Figure 7-23 plots the resultant contact impact force between the impacting hailstones (of varying diameter) and blade surface.

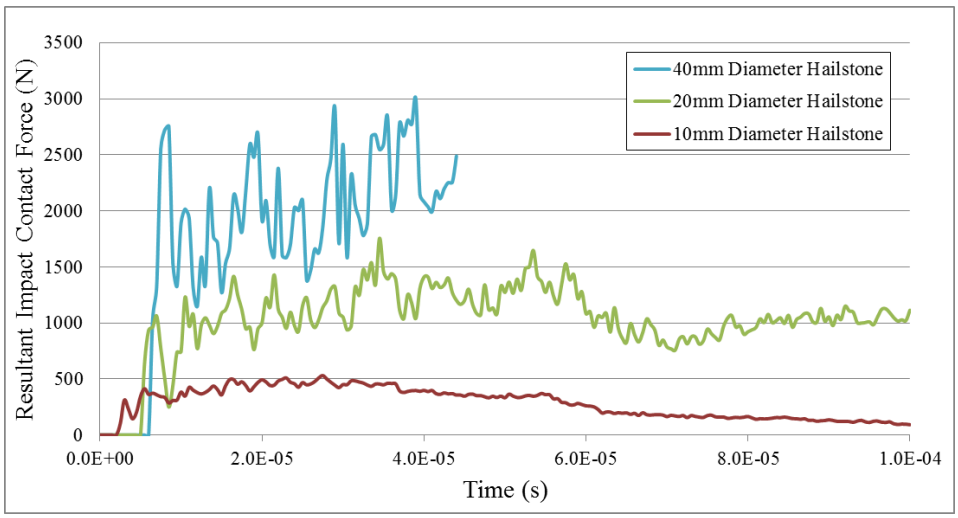

Figure 7-23. Time histories of the resultant contact impact force between the varying sized hailstones (10, 20 and 40mm in diameter; impact energies of 2.3J, 18.8J and 150J respectively) and the simulated blade leading edge, during a 100m·s^{-1} impact events.

As expected, the increased hailstone diameters result in increased impact force values. However, in comparison to the results obtained previously for the flat target simulations (Figure 7-15), the difference between the forces imparted by the 20mm and 40mm diameter hailstones (impact energies of 18.8J and 150J respectively) are not as significant. This may be as a result of the curved leading edge reducing the available immediate blunt impact contact area for the incoming hailstone, as illustrated in Figure 7-24, therefore limiting or smoothing the impact force created (in comparison to the flat target values).

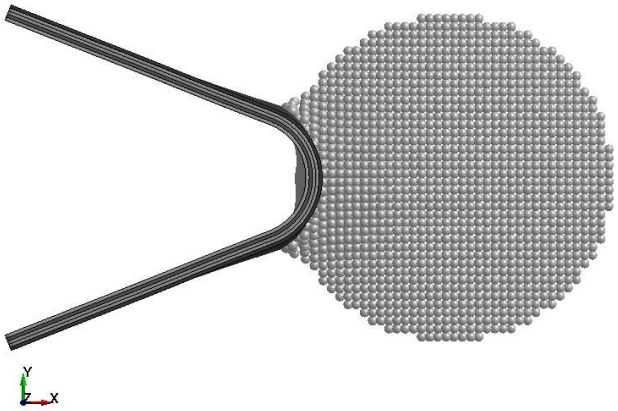

Figure 7-24. Visualisation of the simulated 40mm diameter hailstone impacting the blade leading edge at 100m·s^{-1}.

From Figure 7-24 it can be seen that the curvature on the blade leading edge acts to spread out the load around the surface, therefore the load is imparted more dynamically around the blade curvature, rather than in a more concentrated area which absorbs the load bluntly; the case with the flat target.

Figure 7-25 plots the impact force time histories obtained for both the flat and curved target as a means of comparison (for the three hailstone diameters).

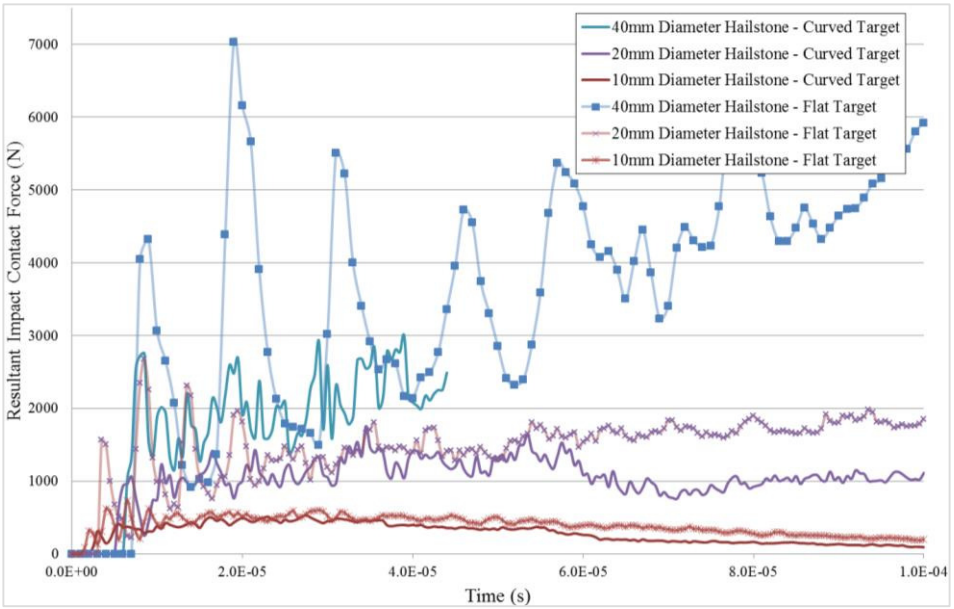

Figure 7-25. Time histories of the resultant contact impact force between the varying sized hailstones (10, 20 and 40mm in diameter) and the simulated blade leading edge (flat and curved), during 100m·s^{-1} impact events.

From Figure 7-25, it is clear that there is little observable difference in the impact force time histories obtained from the 10mm diameter hailstone impact simulations between the flat and curved target configurations. This is most likely because in the curved simulation this hailstone diameter is small enough in comparison to the curvature of the leading edge such that it is effectively akin to impacting a flat surface. However for the larger hailstone diameters more noticeable differences are observed, most notably for the 40mm diameter time histories. For this diameter it appears that the overall increasing trends in contact force for both flat and curved target simulations are comparable (with respect to their slope), however the curved leading edge results in a smoother contact force, levelling out the large spikes in contact force exhibited in the flat target simulation results.

With respect to the stresses and loads created within the blade material for each of the simulations, although significant stresses were created in the materials of the leading edge in each of the three simulations with varying hailstone size, only the loads created through the 40mm diameter hailstone impact were significant enough to create permanent damage. However, as a result of the creation of damage in the simulation and the added complexity this brings to solving the model, it was feasible only to model the impact event until an impact time of 46µs. After this point the CPU time required to solve each time step increased dramatically, as a direct result of the added complexity introduced both by the material

failure and interlaminate debonding (as will be shown). Given enough time and computational power, the simulation could be completed; however it is unclear whether such an endeavour would provide any additional useful insight, as the onset and nature of damage creation are the primary concerns.

Figure 7-26 shows the contours of effective plastic strain induced on the surface of the gelcoat at 45µs into the simulated 40mm diameter hailstone impact at 100m·s^{-1}, as well as the surface displacement of the gelcoat in the direction of impact at this same time point.

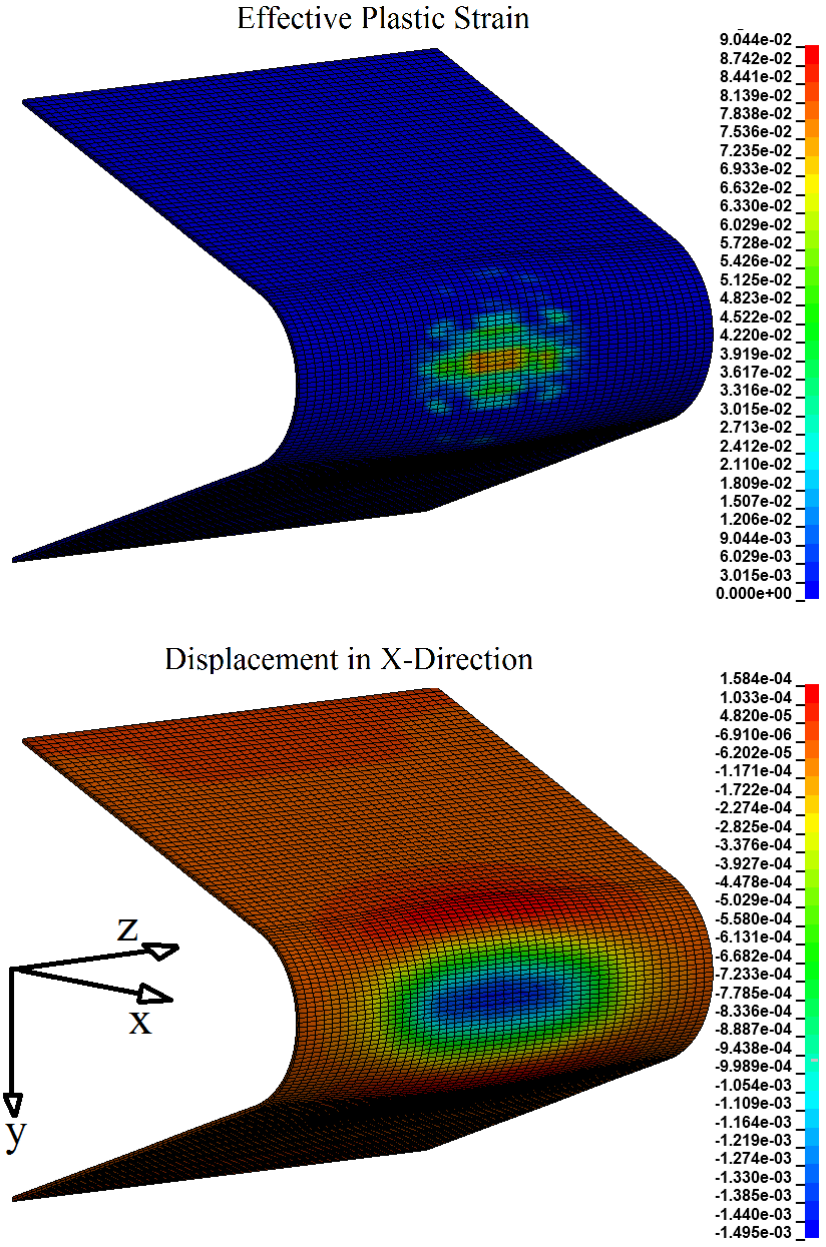

Figure 7-26. Contours of effective plastic strain and x-direction displacement (m) of the gelcoat at 45µs into the simulated 40mm diameter hailstone impact on the leading edge at 100m·s^{-1}.

There are significant areas of material plasticity induced from the 40mm diameter hailstone impact, reaching a maximum value of approximately 10% at the centre of the impact location. This would indicate that only a small number of repeat impacts of the kind modelled would be required to increase these plasticity levels to the erosion inducing values.

Significant geometric deformation of the blade profile is also evident through the impact simulation results, exhibiting a maximum depression at the point of impact and across the leading edge face of approximately 1.5mm.

Such large deformations and loads also resulted in the creation of damage in the composite materials of the substrate. The material model used to represent the composite materials (*MAT_59) can model a variety of different failure modes in the respective material. Two of the most fundamental failure modes are calculate in terms of longitudinal tension and through thickness shear (based on the longitudinal directions). Contours of these two failure modes as exhibited in the three bi-axial weave reinforced composite substrate materials (TOP, MIDDLE & BOTTOM) are plotted in Figure 7-27, where by a value of 1 (red) indicates no damage and a value of 0 indicates total failure of the material (with respect to the plotted failure criterion).

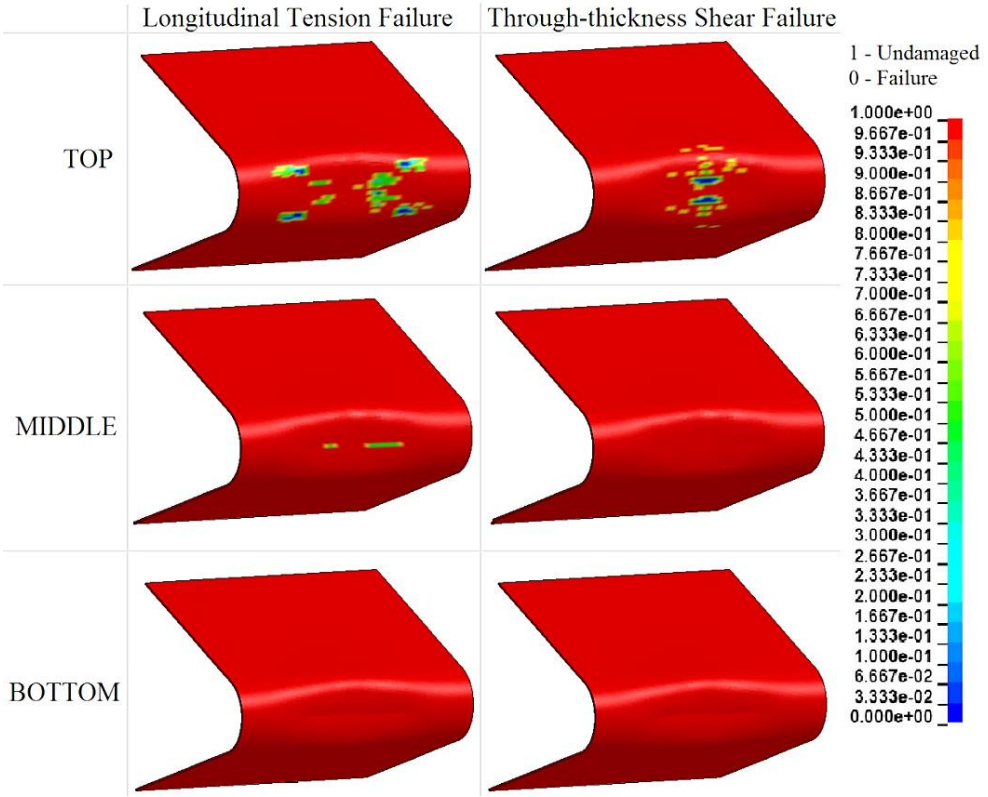

Figure 7-27. Contours of Longitudinal Tension and Through-thickness Shear failure (1=no damage, 0=total failure) in the three bi-axial weave reinforced composite materials of the blade leading edge substrate, at 45µs into the 40mm diameter hailstone impact simulation (at 100m·s^{-1}).

There is significant damage of the TOP composite layer created in the hailstone impact simulation, both with respect to longitudinal tension and through thickness-shear failure. The blue contoured areas indicate areas of the material which underwent complete material failure with respect to the given failure criteria. Limited damage creations is visible in the other two composite layers, however significant geometric deformation is still observable, therefore further damage may have been created had the simulation been allowed to run for a longer time. Such material damage as exhibited in the TOP layer would obviously have significant implications with respect to the ongoing material performance and integrity of the blade in this given region, resulting in a weakening of the static load bearing strength and most likely dramatically altering the fatigue life of the material; as observed in other composites in the literature [143] [144] [145] and illustrated previously in Figure 3-37.

As well as significant loading of the laminate layers, considerable interlaminate forces and stresses were also generated during the simulation. Figure 7-28 plots the contours of interlaminate interface pressure between the respective material layers at a time of 10μs into the impact event.

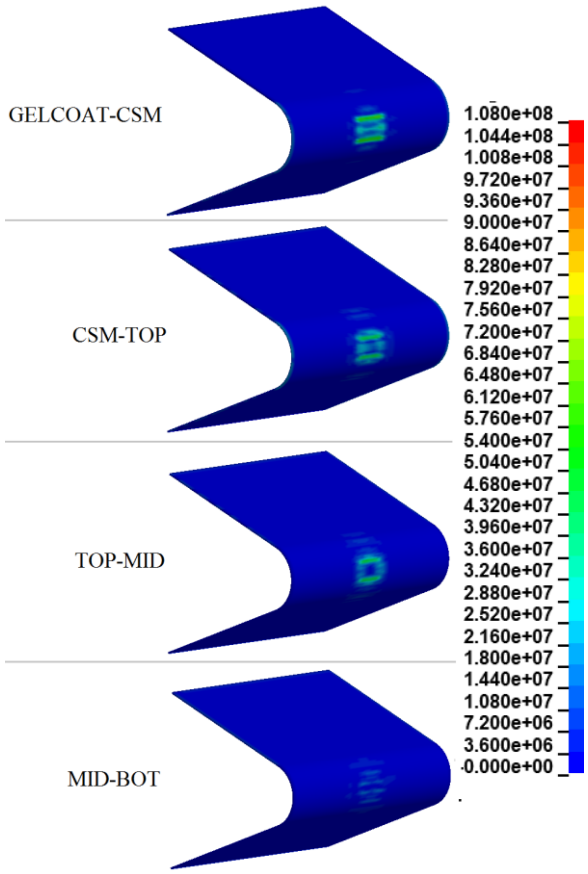

Figure 7-28. Contour plots of the interface pressure (Pa) in the bonds between the layers of the laminate, at a time of 10μs.

In addition, significant interface pressures were created in the impact simulation to values exceeding the normal and shear limits, resulting in localises contact failure (delamination) in regions between the material layers.

7.3 Experimental Blade Sample Impact Simulation

In an effort to validate the numerical findings it was proposed that simulations which replicated the experimental work conducted (Section 8) should be performed, in order to provide a means of comparison between the results obtained for both.

As discussed in more detail later (in Section 8.3.5.1), for the hailstone diameters utilised in the experimental work (10mm diameter), insufficient observable damage was created in the manufactured composite material samples for the impact conditions applied in testing. As a result, it was subsequently decided that a projectile with the same diameter (to enable the use of the same barrel) but significantly higher mass would be fired at the samples, in order to evaluate the effects of heightened impact energies on the impact response of the material samples created. The projectiles sourced for this objective were small ceramic beads, which were not only significantly greater in mass but were often also reusable in multiple impact tests; as a result of not shattering during impact. It was therefore decided that these test conditions should be replicated within the LS-DYNA simulation environment.

The setup of this modelling work is described in the following sections, which also gives a brief indication of the experimental setup, which is subsequently fully detailed in Section 8.

7.3.1 Model Setup

In the experimental work conducted, two sample configurations were manufactured in-house for the purposes of impact testing and subsequent damage evaluations. The two layups are shown schematically in Figure 7-29, which shows the individual laminate layer configurations and fibre orientations.

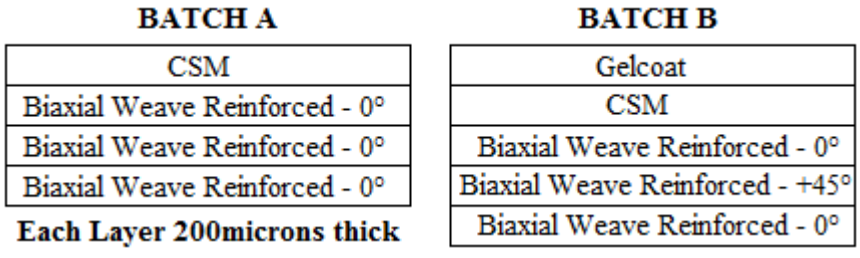

Figure 7-29. Layup configurations of two experimental sample batches, shown schematically in cross section, with individual layer materials and fibre orientations.

Each sample was manufactured using individually sourced glass fibre and epoxy resin constituents, as fully detailed later in the experimental discussion. For the epoxy resin matrix and gelcoat component, the commercially available multi-purpose SP106 epoxy resin [225], manufactured by Gurit [30], was sourced and used. For the chopped strand mat reinforcement, MAT92 reinforcement [226] with a mat density of $300g \cdot m^{-2}$ was used; sourced from PPG Fibre Glass [227]. Biaxial weave reinforcement named EWR300-1000, with a glass density of $300g \cdot m^{-2}$, was sourced from Taishan Fibreglass Inc. [228].

Each sample created was subsequently sized to square dimensions of approximately 55x55mm, attached to the load cell in the experimental rig (by clamps) and impacted with the ceramic beads at a velocity of $87.5m \cdot s^{-1}$; ice impact testing was also conducted, as discussed later in Section 8.3.4.1.

These conditions were therefore the ones replicated within the modelling work, which would look at the simulated impact response of both the Batch A & B samples under impact from the 10mm diameter ceramic bead at $87.5m \cdot s^{-1}$.

Again, LS-PrePost [195] was utilised for both pre and post processing of the simulation work. The experimental setup was replicated in the LS-PrePost environment as shown in Figure 7-30, which shows the created finite element bodies.

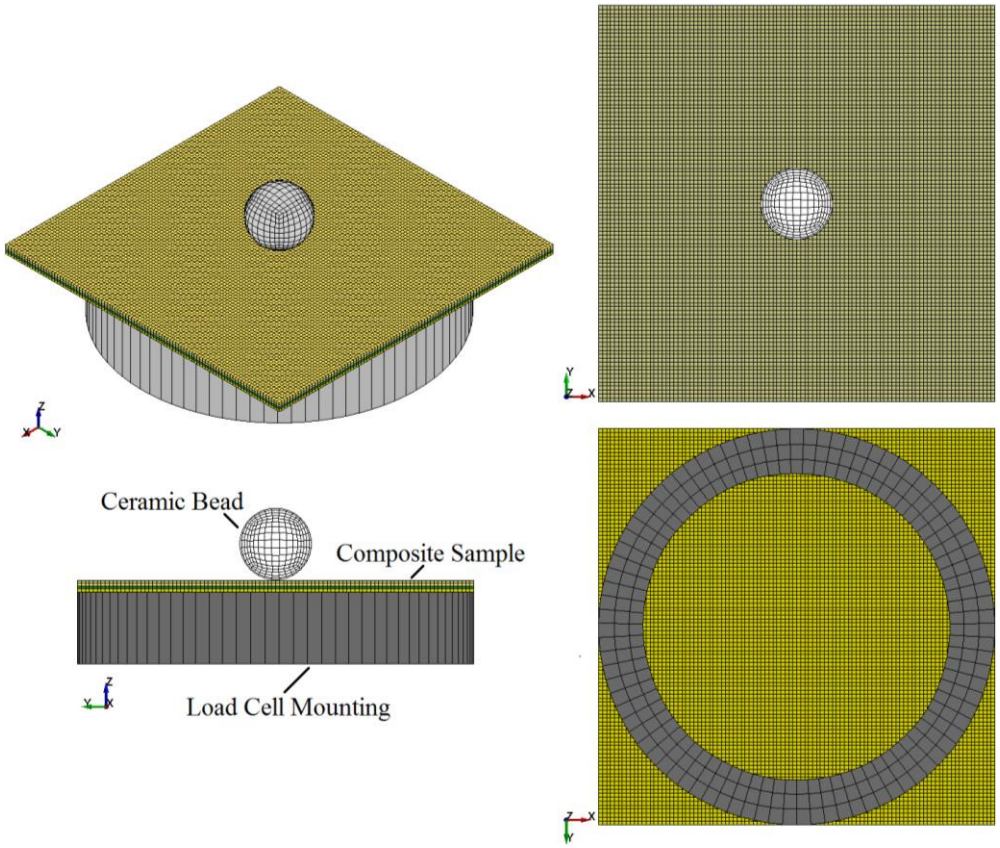

Figure 7-30. Model set up to replicate experimental impact test conditions. Showing the position of the 55x55mm composite sample (Batch A in this image), the ceramic bead projectile and the aluminium load cell mount (55 and 45mm inner and outer diameters respectively

Figure 7-30 shows the composite laminate sample, mounted upon the ring shaped load cell mounting platform, as well as the ceramic bead in the centre of the sample. Each of these finite element bodies were created using the 'Shape Mesher' tool within Pre-Post and inputting the appropriate dimensions and desired element totals.

Owing to the heightened strength and stiffness of the ceramic bead projectile, in comparison to ice, it was possible to model the ceramic projectile using a standard Lagrangian meshing technique. Each layer of the composite laminate was represented by a single layer of solid elements, with an element count of 100 in each direction. The only adjustments made to the model between the two sample configurations was to include the additional epoxy resin layer in the Batch B sample and alter the fibre orientations (following composite material card assignment); as described in previous sections. The load cell mounting (with inner and outer diameters of 55 and 45mm respectively) was assigned a comparatively coarse mesh, as it was to be represented as a rigid body; as the boundary conditions presented by the presence of the mount were the key consideration.

Each finite element body was assigned the section *SECTION_SOLID and the load cell mount body was assigned wholly arbitrary material properties with the material card *MAT_RIGID. Detailed material properties of the ceramic beads used in testing were not obtainable and therefore the simple *MAT_ELASTIC material card was used to represent the beads with a (measured) density of 2673kg·m^{-3}, a Young's modulus of 70GPa and a Poisson's ratio of 0.2. It was found through initial modelling work that differing material properties (with the exception of density) had little noticeable effect on the impact response of the sample; as long as the properties were sufficiently stiff/brittle.

Assigning the appropriate material properties for the composite layers presented a larger challenge, as the samples were not made from prepreg material and therefore very little manufacturer material property data was available. As such, the material properties had to be calculated based upon the constituent materials and their properties using the rule of mixtures [20] where possible. To establish the basic material properties of the SP106 epoxy resin [225] which formed both the gelcoat layer (in the Batch B configuration) and the matrix material of the composite substrate, simple tensile tests were performed. The stress strain curves obtained from these test are shown in Figure 7-31.

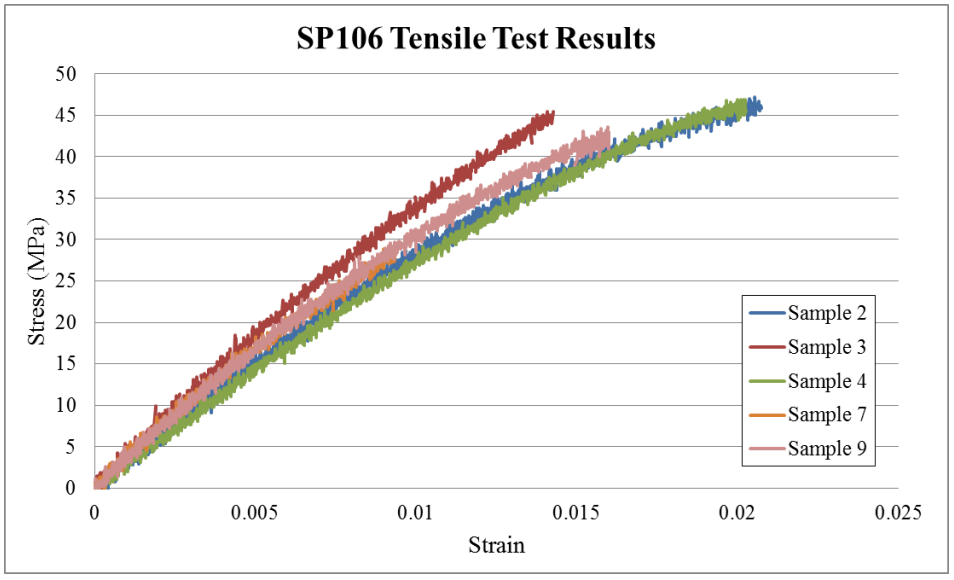

Figure 7-31. Stress-strain relationship obtained for the SP106 epoxy resin through tensile testing.

From reviewing the stress-strain curved obtained, it is apparent that abrupt and total failure occurred in all samples test, most probably as a result or combination of an excessive loading rate and imperfections in the tensile samples created. Consequently, limited post-yield behaviour was capture through the testing.

However, from these test results, an approximate value of 2.5GPa can be assumed for the Young's modulus with a yield stress value of 45MPa. From the limited samples tests and the abrupt failure recorded, these values were assumed at best as an approximation of the true material properties, which would suffice for general modelling purpose. As the gelcoat employed in the Batch B configuration was purely a layer of neat resin, these material properties, along with an assumed Poisson's ratio of 0.4 were applied to the gelcoat layer by the *MAT_PLASTIC_KINEMATIC material card. Although little post yield behaviour was captured in the tensile testing, it was assumed that the material would behave in an elastic-perfectly-plastic way, and that eventual failure would occur at a strain of 0.4.

Using the previous approach, the layer of chopped strand mat was assumed to behave in an isotropic manner, which was a necessary assumption given the difficulty is ascertaining accurate orthotropic material properties for such a material. As such, the material properties defined for the CSM layers represented the properties of a much enhanced layer of neat resin; calculated through use of the rule of mixtures. *MAT_PLASTIC_KINEMATIC was again used to represent the CSM layer, with a density of 1453kg·m^{-3}, a Young's modulus and yield stress of 4.83GPa and 200MPa respectively, a Poisson's ratio of 0.2 and a failure strain of 0.3. The CSM material was also assumed to behave in an elastic-perfectly-plastic way.

For the biaxial reinforced composite layers, the rule of mixtures was used – with the limited constituent material property data available – to predict the primary material properties of the composite formed. Through this approach it was possible to approximate most of the important material properties of the composite; however for the properties for which no reliable predictions method was available, the properties cited by Menna et al. [183] were substituted. Although this was not an ideal assumption, given the comparative nature of the material constituents and layup configuration used in this research and that of Menna et al. [183], it was deemed the best possible assumption. Table 7-1 shows the calculated material properties of the manufactured biaxial woven glass reinforced epoxy composite, marking the substituted values from those cited by Menna et al. [183] with an asterisk; where 1 and 2 are the fibre dominated orientations, and 3 is the normal direction.

Table 7-1. Material properties of the manufactured biaxial weave glass reinforced epoxy composites, as calculated by the rule of mixtures and (where marked with an asterisk) approximated to the values cited by Menna et al. **[183]**.

Orientation	Young's Modulus (GPa)	Tensile Strength (MPa)	Compressive Strength (MPa)
1	22.5	535	535
2	22.5	535	535
3	8*	120*	500*
	Shear Modulus (GPa)	Shear Strength (MPa)	Poissons Ratio
12	3.8*	105*	0.1*
23	1.74	88	0.25*
13	1.74	88	0.25*

These material properties were assigned to the composite layers using the material card *MAT_COMPOSITE_FAILURE_SOLID_MODEL; as used in all other previous modelling work.

The contact between the individual composite layers was again modelled by the contact algorithm *CONTACT_AUTOMATIC_SURFACE_TO_SURFACE_TIEBREAK. Once more, OPTION=6 was invoked in the contact card definition, to allow for the added option of modelling delamination; given sufficient impact violence. The interface normal failure stress (NFLS) and shear failure stress (SFLS) were set to 35MPa and 65MPa respectively, taken from the values implemented and cited by Menna et al. [183]. The critical distance required for complete interface failure (PARAM in the contact card) was set to 0.14mm.

The contact between the ceramic bead and the composite target was defined using the *CONTACT_SURFACE_TO_SURFACE_SMOOTH contact card. This contact card was applied between not only the ceramic bead and the surface of the target but also the ceramic bead and each layer of the substrate, to allow for effective contact modelling in the result of surface penetration. The contact between the under surface of the composite sample and the upper surface of the load cell mount was defined by the contact card *CONTACT_AUTOMATIC_SINGLE_SURFACE_SMOOTH, with the SOFT=1 option invoked, to ensure effective contact modelling between the two bodies with greatly differing stiffness.

In the experimental work (Section 8) the samples are fixed in place on the load cell mount by the attachment of two clamps at either side of the sample. In an effort to recreate these conditions within the model, fully-fixed boundary conditions were applied to the upper surface of the sample in the regions where the clamps were placed in the experimental procedure, as shown by the black marked nodes in Figure 7-32.

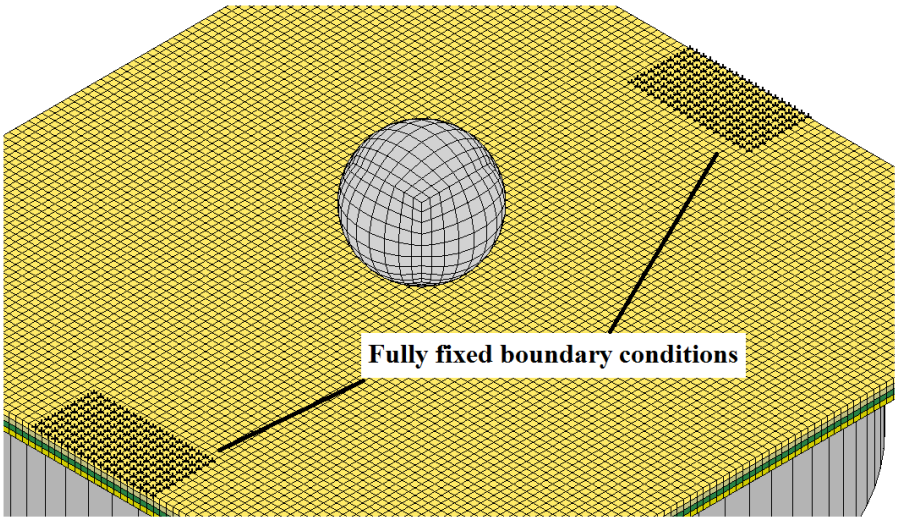

Figure 7-32. Fully fixed boundary conditions applied to the sample surface.

In reality, the conditions in these clamped regions would not be fully represented through these simple boundary conditions; however it was hoped that these conditions would serve as a good approximate and reduce model complexity/solve time.

The experimental test impact velocity of 87.5m·s^{-1} was applied to the ceramic bead using the *INITIAL_VELOCITY_NODE option. A time step reduction factor of 0.3 was implemented to prevent energy errors and premature solver termination, and the *DATABASE_EXTENT_INTFOR option was applied in order to make interlaminate behaviour examination possible in post-processing.

Given that the aim of the modelling work discussed in this section was to provide a means of comparison with experimental results, the results of the subsequent modelling work are discussed later in Section 8.4; in the possession of experimental results.

7.4 Hailstone Impact Modelling Discussion

It was found that the loads and deflections created through hailstone impact far exceeded those imposed by rain droplet impact; as modelled previously. Resultantly, the impact velocities required to induce damage in a standalone gelcoat material target were far reduced in comparison to rain droplet impact. However, although the violence exhibited by hailstone impact far exceeded that of the rain droplets, many of the observed characteristics and traits of the modelled hailstone impacts exhibited strong similarities to the modelled water droplet impact behaviour. Most notably, upon initial fracturing of the ice material at the point of impact, the material was then observed to turn to a fluid/powder-like state, subsequently exhibiting the same high velocity spreading behaviour of the water droplets. As a result of this, the damage induced in the coating materials through hailstone impact also displayed

strong similarities to the rain droplet impact induced damage, creating concentric ring shaped regions of plasticity around the impact zone (albeit on a greater scale).

It was also found that given a hailstone with sufficient mass, both laminate and interlaminate damage were exhibited in the leading edge materials, both in a flat and curved configuration, indicating the potential added threats of hailstone impact in comparison to rain.

From the result shown and discussed in relation to the simulation of direct hailstone impact on characteristic wind turbine blade composite targets, the capabilities and flexibility of the LS-DYNA based modelling approach are apparent. The constitutive composite material models made it possible to model the anisotropic material properties of the composite material layers and the surface to surface contact definitions allowed for interlaminate loading and damage behaviour. These useful model inputs coupled with the range of extensive post-processing capabilities make it possible to thoroughly and extensively investigate the blade material impact response.

The insight and value provided by the modelling work discussed in the greater context of hailstone impact on actual wind turbine blades are discussed in more depth in the closing sections. However, it is clear from the selective range of modelling work conducted that the modelling methods developed and employed provide a potentially very valuable analysis and design tool. Gaining a greater understanding of the impact response of the blade materials through such modelling should then make it possible to subsequently address any design issues and test and evaluate alternative solutions. For instance, although not modelled here, the added benefits or potential drawbacks of flexible coating technologies in the context of the impact response of the whole blade section could also be explored and evaluated through appropriate method. However, it must also be noted that for full confidence in the results provided by the modelling methods to be gained, supporting experimental validation would also be required.

8. Experimental Hailstone Impact Analysis

To assist in validating the hailstone impact simulations, as well as compliment and add to the findings made, experimental hailstone impact investigations were identified as key requirement of the research work. As such, a suitable hailstone impact experimental apparatus was proposed, designed and manufactured.

It was decided that the rig performance should focus on delivering a better understanding of the fundamental impact characteristics of hailstone impact, therefore the design would be centred more on individual impact event tests (similar to the gas-fired apparatus detailed previously in Section 3.3.4) rather than high frequency impact erosion based testing. Such a rig would therefore focus more on the ice impact progression mechanisms, the target response and the failure modes induced.

Initially, the fundamental performance requirements for the proposed experimental rig were identified as:

1. **Variable Speed** – The apparatus should be capable of firing projectiles at variable velocities, which should be easily and reliably adjusted to meet the requirements of the given investigation.
2. **Variable Projectile Size** – The apparatus should be capable of firing a range of different projectile size, through either the initial fundamental rig design or subsequent additions and alterations to the apparatus.
3. **Monitorable –** The apparatus should include the capability to closely monitor the impact events created, and useful experimental outputs should be delivered
4. **Useable & Safe –** The apparatus should be as user friendly as possible to maximise experimental productivity and make obtaining relevant results straightforward. Safety was also of course critical to the success of the proposed rig design.
5. **Alterable & Flexible** – The design should allow for the possibility of future adaptations and performance enhancements.

These fundamental design principles helped to shape and inform the design and manufacture process described in the following section.

8.1 Rig Design & Build

The experimental rig developed for the research would be based on similar designs already in use at other institutions (as reported in Section 3.3.4), based on a compressed gas-fired gun configuration.

Based on this decision and the desired performance characteristics described in the previous section, it was apparent that the key fundamental components required for the rig were:

1. **Compressed Gas Reservoir & Valve Trigger Mechanism** – In order to provide the power for projectile propulsion a compressed gas reservoir was required to supply compressed gas to the chamber when required. Further to this a trigger mechanism to release the gas would also be required.
2. **Breach** – A breach component would be required to allow for the loading of the ice (or other) projectiles at the base of the barrel.
3. **A gun barrel** – A barrel would be required to guide and direct the projectile from the initial gas propulsion point to desired target body.
4. **Data Acquisition Apparatus** – Data acquisition apparatus (DAQ) would be required to obtain useful experimental indicators, results and other output.
5. **Control Mechanisms** – The operation of the apparatus had to be easily controlled and manipulated by suitable control mechanisms, allowing for gas reservoir loading/unloading, gun firing and DAQ control.

Based on the desired rig performance requirements and the associated key fundamental components requirements discussed, the rig design illustrated in Figure 8-1 was devised and constructed.

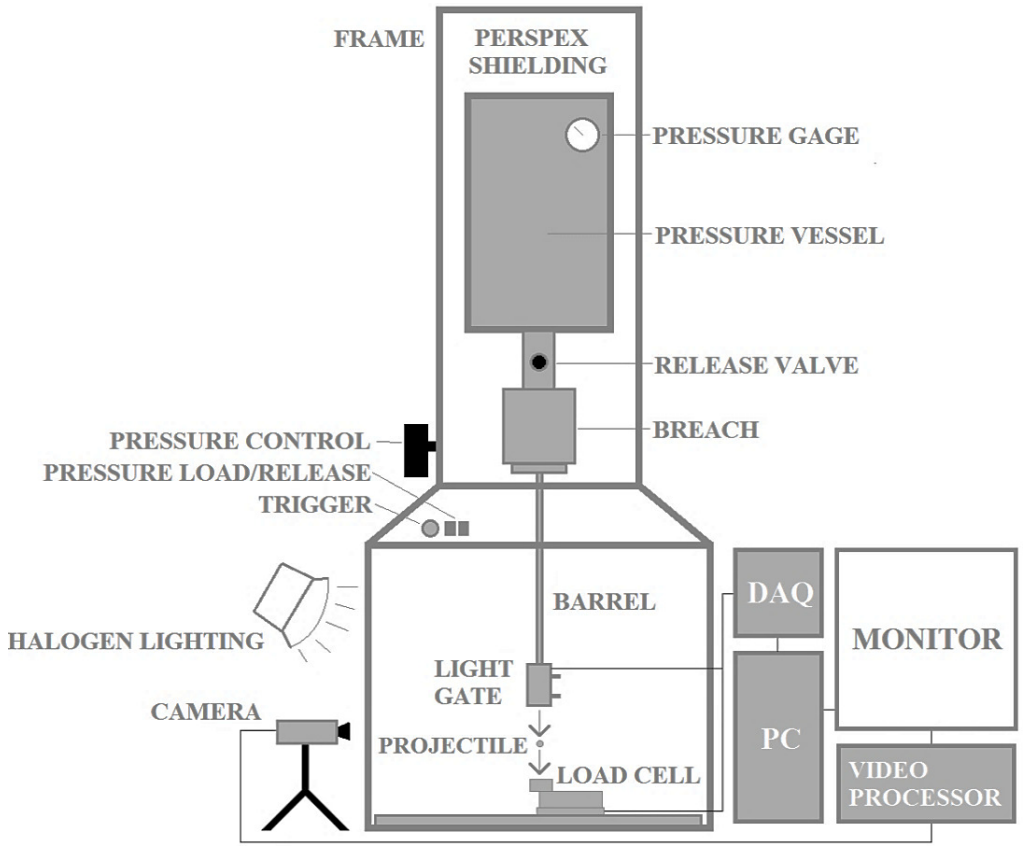

Figure 8-1. Schematic of the finalised hailstone impact experimental rig, detailing the individual components and their basic layout.

For space and safety considerations it was decided that the apparatus firing direction would be orientated vertically, firing downwards. The gun apparatus would be fully enclosed by steel frame, cladded in clear plastic shielding to allow for full visual access to the rig apparatus. The gas reservoir would be mounted onto this steel frame work at the top of the apparatus, with an attached pressure gauge, allowing for visual identification of the set pressure. Between the pressure vessel and the breach component, a poppet valve trigger mechanism was included. The barrel would attach to the breach component through a rotate and lock feature, allowing for quick release and attachment in a secure manner. The relevant projectiles would be loaded by insertion into a small plastic sabot, which was then placed in the top of the barrel and rotated and locked into the breach. For the initial design ,a barrel diameter capable of accommodating projectiles up to 10mm in diameter was manufactured, however if required in future this could be altered to include larger diameters.

Three control mechanisms were incorporated into the gun design: a load pressure switch, an unload pressure switch and a firing trigger. The controls could be manipulated to increase or decrease the gas reservoir pressure to the desired value and then subsequently fire the projectile. Upon firing, the projectile would travel downward through the barrel and (in the

absence of any DAQ equipment) strike a large steel base plate on the rig floor. In addition to these controls, the maximum reservoir pressure could also be set by altering a pressure control vale.

These components formed the basic gun apparatus; however a wide range of DAQ and monitoring equipment was also included in the design (shown schematically in Figure 8-1). In order to ascertain the projectile barrel velocity a light gate based velocity sensor was created and attached to the end of the barrel. The signals from the light gate were fed into a National Instruments CompactDAQ 9178 chassis [229] (with relevant modules), and processed in the National Instruments LabVIEW software package [230] to output the measured barrel velocity. On the floor of the rig, a 7kg rated TEDEA 1042 Model load cell [231] was placed, upon which the relevant target bodies could then be mounted. The TEDEA 1042 load cell uses a combined cantilever/strain gauge configuration to determine the load applied at a single point. The subsequent impact load measurement could then be fed into the same DAQ system and software as the light gate signals, and (following signal/data manipulation) the impact load could be displayed on screen as a time history plot. To visualise the impact events created, a FASTCAM Super10KC high speed video camera [232], with a maximum frame rate of 10,000fps was used. Following impact, the recorded impact video could then be transferred in to the PC environment for analysis and export. Extensive lighting was required to sufficiently illuminate the impact event in order for the camera to capture clear frames at the high frame rates used, to provide such illumination four high power halogen lights were used.

The complete manufactured apparatus is shown in Figure 8-2 with the main components detailed and labelled (the camera/lighting is omitted for clarity).

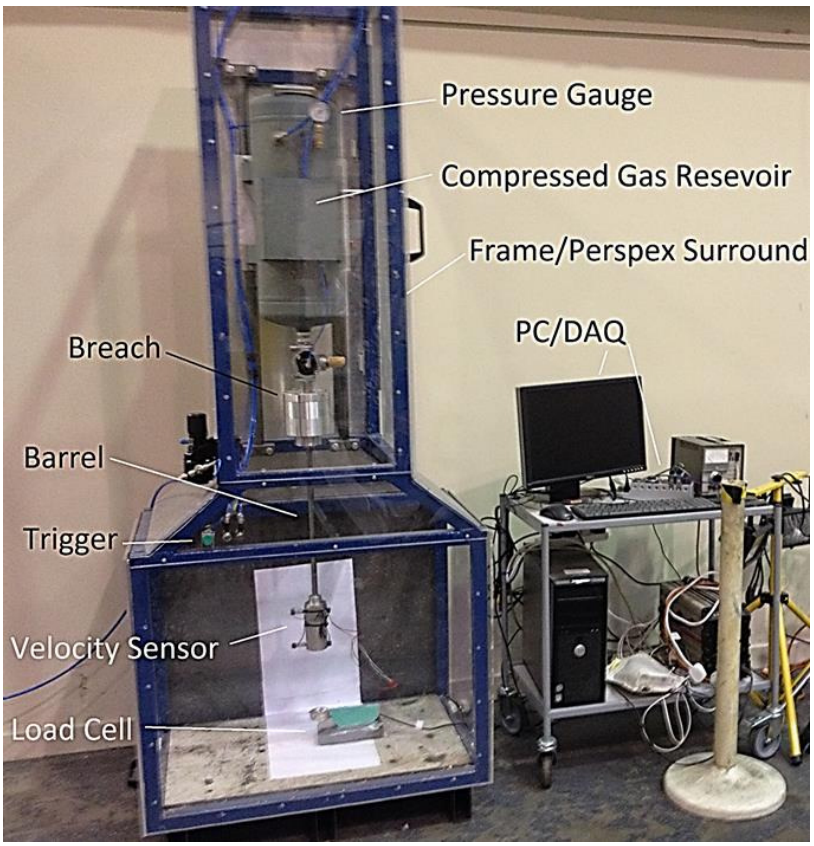

Figure 8-2. Manufactured Hailstone Impact Rig with major components and features labelled.

In addition to the manufacture of the rig, a means of reliably manufacturing ice spheres was also required. For this purpose a small ice mould apparatus was created, as shown in Figure 8-3.

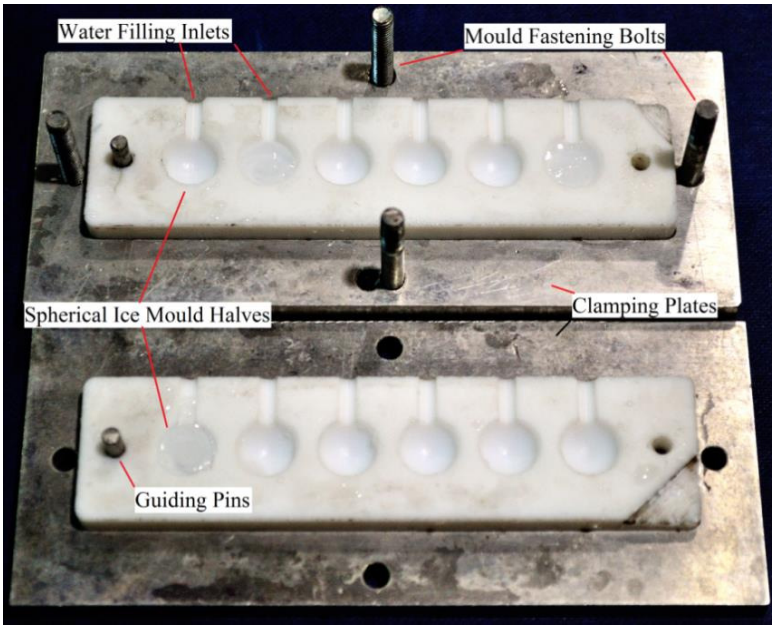

Figure 8-3. Hailstone mould apparatus

The mould consists of two polymer based half-moulds, which when joined together form 6 individual spherical moulds, 10mm in diameter. These two halves were joined together and clamped in place by an aluminium assembly of two clamping plates and 4 fixing bolts. The most efficient method by which to manufacture the hailstones is discussed in the next section.

8.2 Hailstone Impact Rig Commissioning & Calibration

Before relevant and targeted experimental investigations could be conducted, the hailstone impact gun apparatus had to be extensively trialled, tested and eventually commissioned as ready for research work.

This commissioning process would incorporate all the major components of the rig to ensure that they each operated reliably, effectively and met the desired requirements. This process involved many trial and error processes and ongoing alterations to the different experimental setups.

The first challenge with respect to conducting experimental hailstone impact analyses is establishing a reliable and effect method by which to manufacture hailstone projectiles. The mould created for the hailstone manufacturing process was shown previously in Figure 8-3. However, there were several methodologies and processes developed in relation to its use, in order to improve the manufacturing process. It was found early on that merely positioning the mould inlets under a flowing water source would not guarantee proper filling of the mould, as this approach would often result in the inclusion of air bubbles in the mould; which would not be found until removing from the mould. To combat this, the water was instead injected into the mould with the use of a hypodermic needle, with the needle tip inserted through the inlet and into spherical mould compartment, allowing for direct filling of the mould. The closed and filled mould would then be place in a chest freezer for a minimum of approximately 40 minutes to allow for complete freezing. Upon removing the mould from the freezer, the mould assembly was then allowed to thaw for a few minutes (accelerate if required by heating with hands), as it was found that if the mould was opened too soon after removing from the freezer the ice inside would fracture into two halves. The thawing process allowed the bond between the ice spheres and the mould to weaken therefore reducing tear force when the two mould halves were separated. Upon opening the mould, plastic tweezers were then used to free the manufactured hailstones from the mould and place them in a plastic container for freezer storage. When subsequently using the ice in impact studies, a cool box and freezer packs were used to create a cool environment to store

the ice in for transit between the freezer and the impact rig; and for temporary cool storage whilst performing experimental setup tasks.

The next important calibration task was to establish the relationship between the set gun pressure and the resulting barrel velocity of ice projectile. Although the impact velocity for a given impact study could be read from the DAQ system (described previously) it was useful in the setting up process to know the required reservoir pressure for a specific desired impact velocity. To obtain these relationships, numerous impact tests were conducted at various reservoir pressures and the resulting barrel velocities were noted. However, issues were encountered when using the light gate velocity sensor for the ice projectiles. As a consequence of the near transparent properties of the ice projectiles, when passing through the light beams in the velocity sensor, rather than completely blocking out the light reaching the sensor, some of the light was scattered or passed through the ice. This resulted in unclear data signals, and resultantly, uncertain velocity measurements for the ice. To combat this issue, hailstones were manufactured with the inclusion of a small amount of black dye to reduce the transparency of the ice. This solution partly resolved the issue for some recorded impact events; however complete confidence could still not be taken in all the results provided. Therefore, as an alternative to using the light gate velocity sensor, the high speed video camera was used in conjunction with a ruler to visually determine the impact velocity for the given gun pressure. This was done simply by recording the impact event, replaying the video captured and taking a note of two positions of the hailstone along the ruler length (as shown in Figure 8-4) and the related frame time stamp and then calculating the velocity from these values.

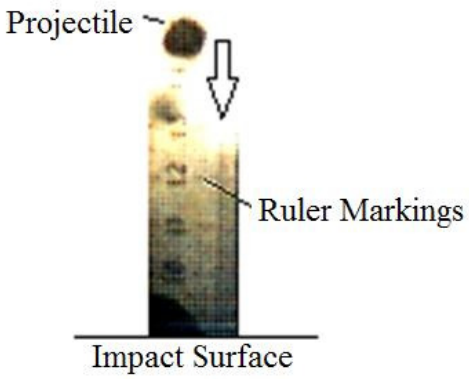

Figure 8-4. Frame from high speed video recording of ceramic projectile travelling in front of ruler before impact.

From this process the pressure-velocity relationship shown in Figure 8-5 was obtained for the manufactured 10mm diameter hailstones; through averaging the results from multiple impact tests (minimum of 4) at each set pressure.

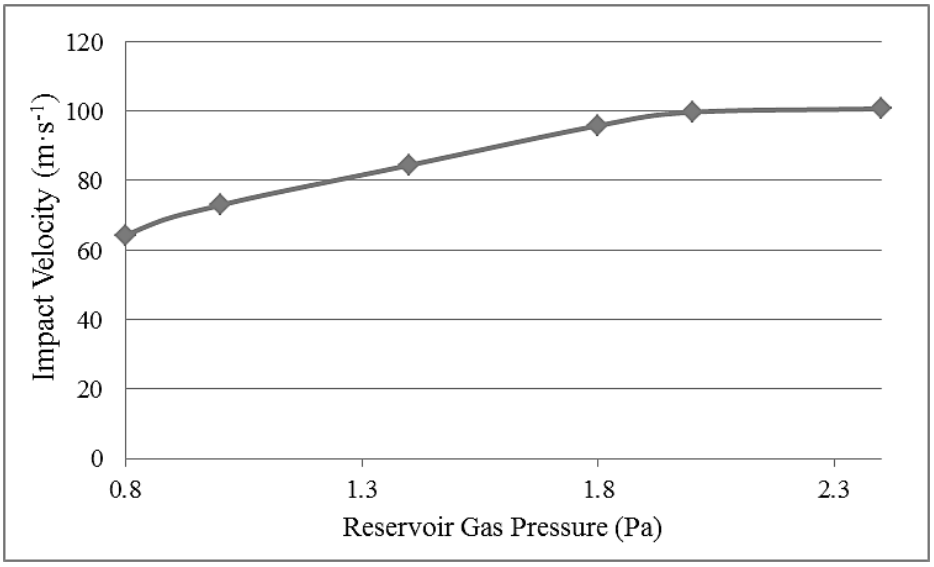

Figure 8-5. Relationship between gas reservoir pressure and impact velocity for a 10mm diameter hailstone.

The load cell also required calibration through simply obtaining the relationship between the load applied to the load cell by dead weights and the voltages output for each of these weight increments.

The issues discussed were the main commissioning tasks; however there were several other tasks relating to establishing proper testing protocol (detailed later), ensuring effective and accurate data handling through the DAQ system and associated software and other device and apparatus issues. However, most issues encountered during the commissioning process were overcome and dealt with, and therefore research related impact studies could be performed with confidence in the apparatus performance.

8.3 Wind Turbine Blade Composite Impact Verification Experiments

8.3.1 Aims & Objectives

The hailstone impact rig manufactured and commissioned provided a valuable additional tool with respect to further investigating the impact phenomenon associated with hailstones on the blade leading edge. The flexibility and capabilities of the rig presented the opportunity to study and explore a wide range of issues with respect to hailstone impact on the leading edge. However, pragmatic decisions were required in order to establish the best possible use of the apparatus in the limited time available. As such, two experimental impact testing campaigns would be conducted, to investigate both:

1. **Hailstone Impact Testing** - The effects of high speed impact of manufactured 10mm diameter hailstones on wind turbine blade representative composite material laminates.
2. **Ceramic Bead Impact Testing** - The effects of increased impact energies, through impacting the same type of composite targets with ceramic beads, also 10mm in diameter but significantly greater in mass.

It was expected that the first objective would shed light on any potential hailstone impact induced damage mechanisms within the composite materials. However, from the hailstone impact simulations previously conducted it was considered unlikely that a 10mm diameter hailstone would create any significant instantaneous impact damage, other than potential surface roughening. It was for these reasons that the second objective was established, in order to allow for the evaluation of the effects of increased impact energies. Using ceramic bead projectiles allowed for such increased impact energies, through their increased mass, without the requirements of increasing the barrel diameter or creating another mould for larger hailstone diameters.

The impact velocity used would be held constant within each experimental campaign, in order to evaluate the repeatability of the results provided by the experimental approach. For the hailstone impact experiments an impact velocity of $100 m \cdot s^{-1}$ was selected to establish the likely worst case impact conditions for a wind turbine blade. For the increased impact energy experiments (ceramic beads) an impact velocity of $87.5 m \cdot s^{-1}$ was selected. Although the impact velocities for the respective experimental campaigns were kept constant, the target material layup and configuration used in each were altered between two separate designs.

8.3.2 Target Sample Configuration &Manufacturing

In order to make subsequent comparisons with numerical work conducted, the material samples created for experimental testing were based on the reference blade configuration described previously in Section 5.3 and implemented in a selection of the modelling campaigns discussed. As such, two different blade layup configurations were established for manufacture and subsequent testing, referred to as Batch A and B, as shown schematically in Figure 8-6 which shows the layup configurations in cross section.

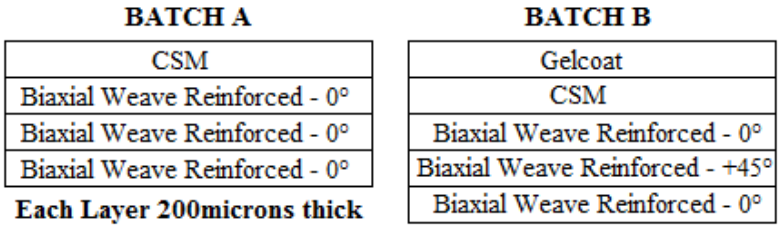

Figure 8-6. Layup configurations of two experimental sample batches, shown schematically in cross section, with individual layer materials and fibre orientations.

Batch A was to be a simple four ply layup consisting of a top layer of CSM and three substrate layers of biaxial weave reinforced composite; with identical fibre orientations. Batch B was to incorporate an additional gelcoat layer on the surface and introduced a variation in fibre orientation to +45° for the middle biaxial weave reinforced composite layer.

For consistency the layup was based wholly on an epoxy based resin and glass fibre based reinforcement; ass detailed previously in Section 7.3.1.

The samples batches were manufactured as large sheets approximately 20x30cm in a bench-top hand layup manufacturing process, using base plate apparatus shown in Figure 8-7, which shows the whole base plate with a raised working platform (approximately 20x40cm) in the centre; upon which the samples are created.

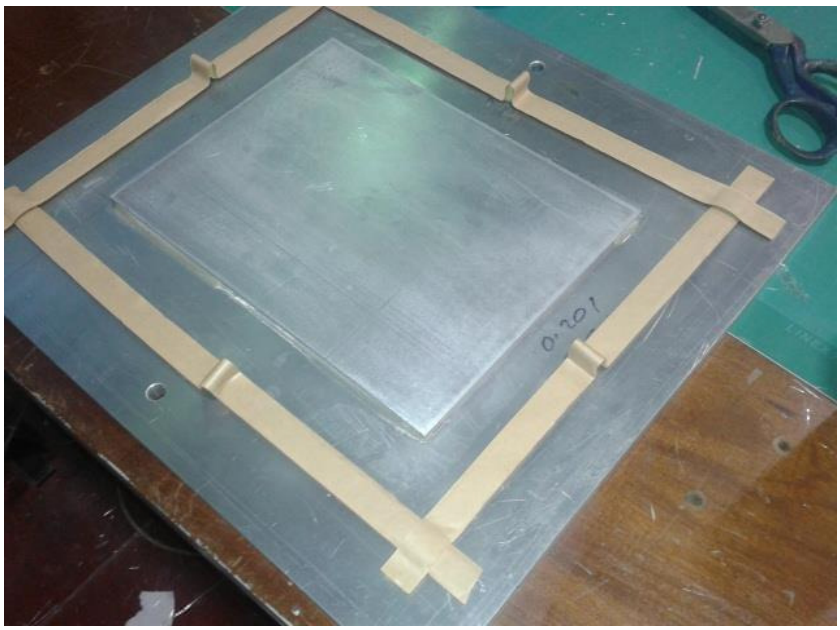

Figure 8-7. Composite manufacturing layup baseplate.

The manufacturing process for both sample batches is described in the following steps:

1. The (CSM and biaxial weave) fibre reinforcements required for the sample were measured and cut to dimensions of approximately 20x30cm, for later placement on top of the raised base plate plinth during the hand layup process.
2. Sealing plastic film layers required for the vacuuming process and non-stick plastic film layers required for placement under and over the layup during the vacuum and curing process were also pre-cut for quick application. A layer of absorbent cloth required in the layup to absorb resin leakage was also cut to size.
3. The first non-stick plastic film sheet was then positioned over the raised base plate plinth and the first layer of fibre reinforcement positioned on top, ready for the application of the resin.
4. The epoxy resin system was then mixed and created, using a mixing ratio of 5:1 for the resin and hardener components respectively. Once mixed, the resin had to be applied to the layup quickly before hardening began to occur.
5. Using a brush, the resin was then applied to the first layer of reinforcement pre-positioned in the mould (in step 3), using a dabbing motion as not to disturbed the fibres in the reinforcement.
6. Once the first reinforcement layer was fully wetted by the resin, the next layer of reinforcement was then added, and further resin was then added to the layup to wet-out the next layer of fibres. This process was then repeated for all subsequent

reinforcement additions, until all fibres were in position and fully wetted by the resin.

7. To seal in the resin another layer of the non-stick plastic film was placed on top of the created (wet) layup and a steel plat positioned on top of this to weight the layup down and keep the components in place.
8. A layer of the pre-cut absorbent cloth was then draped over the top of this layup, and an additional steel plate and vacuum nozzle were rested upon this, before the whole assembly was covered and sealed in the vacuum film, held in place by strong tape
9. The top of the vacuum nozzle was then pierced through the top of the vacuum sealing film therefore allowing for attachment of the vacuum pipe.
10. The vacuum was then switched on and the air inside the vacuum bag evacuated. Any gaps in the vacuum seal were then diagnosable from hissing noises, which were then resealed until a total seal was established.

The resulting layup configuration created through this process is shown in Figure 8-8.

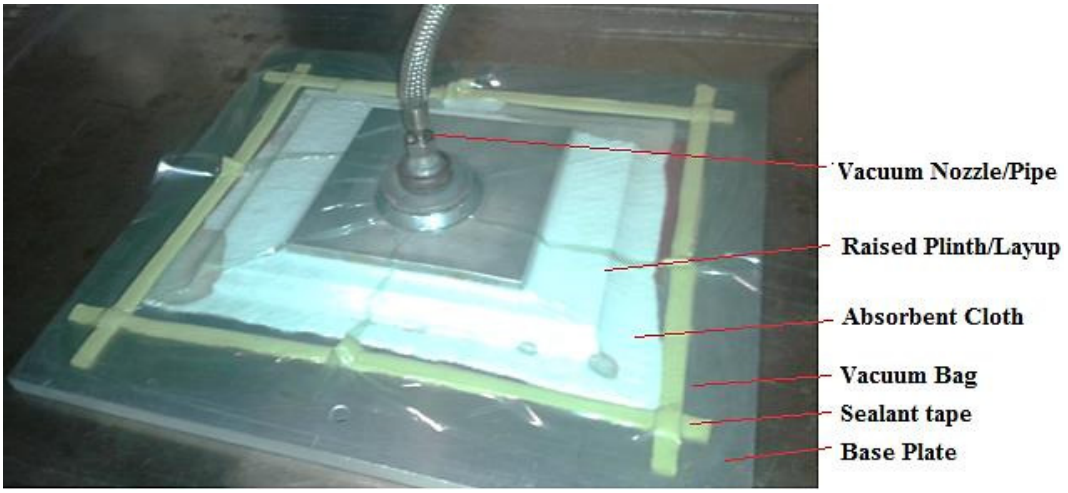

Figure 8-8. Finished composite manufacturing layup configuration.

This finished layup was then left to cure at room temperature for approximately one week, before the finished composite ply was subsequently removed from the layup assembly. For Batch B, upon removal from the mould, a further resin layer was applied to the surface to act as a gelcoat layer. This method of gelcoat application most likely differs from that used in blade manufacturing, where the coating is created in mould, however given the restraints of the manufacturing setup this was the only reliable method of created a gelcoat layer.

The finished composite sheets were then cut by guillotine into smaller 55x55mm samples, ready for subsequent testing.

8.3.3 Projectile Manufacturing and Sourcing

The manufacturing process for the hailstone was described in detail previously in Section 8.2. The process resulted in the creation of hailstones with a diameter off approximately 10mm and a mass ranging from 0.4-0.5g, indicating a density range of 764-955kg·m^{-3}, although there were obvious challenges with respect to measuring these variables.

For the increased impact energy testing, small ceramic baking beads were sourced, made from a simple homogenous ceramic material. These projectiles were initially sourced for the trialling and commissioning of the rig, owing to their ease of handling and reusability in comparison to ice. However, it was soon realised that given the fixed barrel diameter the ceramic beads could also be used to investigate the effects of much increased impact energies; for the same projectile diameter. The weight and size of the beads varied slightly, however and average diameter of 10mm was recorded for most, with an average weight of approximately 1.4g, indicating a material density of approximately 2674kg·m^{-3}; significantly higher than the manufactured hail.

Figure 8-9 plots the theoretically calculated impact energies associated with ceramic beads for increasing impact velocity, comparing the values to those predicted for the varying hailstone diameters.

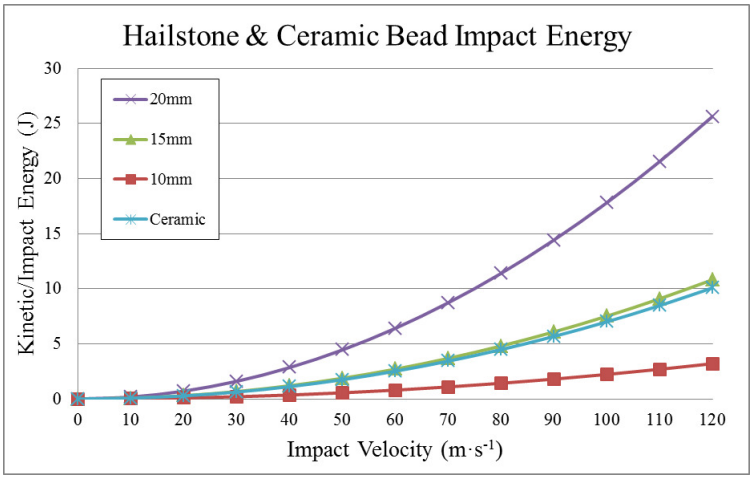

Figure 8-9. Theoretical impact energies associated with impact from hailstones with varying diameters and the ceramic beads used in testing; across a range of impact velocities. Assuming an ice density of 850kg·m^{-3} and a ceramic bead weight of 1.4g.

As shown Figure 8-9, as a result of the comparative masses of a 15mm diameter hailstone and the ceramic beads, the impact energies across the range of possible impact velocities compare almost identically. Impact energy however is obviously not the only important parameter with respect to the impact mechanisms between a given projectile and target, as

other factors such as hardness will play an important role. However, given their relative comparative impact energies and diameters, the impact conditions created through use of the ceramic bead were though to at least give a good approximation of those associated with the larger hailstone diameters.

8.3.4 Experimental Procedure

8.3.4.1 Hailstone Impact Testing

The general impact testing procedure for the ice impact experimental work was based on the following key steps and methods:

1. The sample was placed on top of the load cell and clamped to the load cell by two clamps, as shown in Figure 8-10.

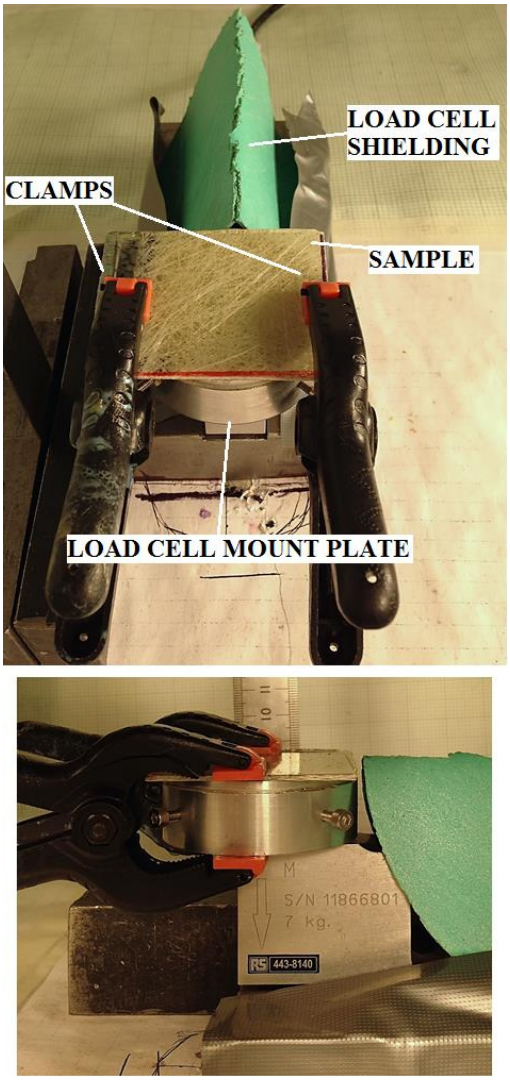

Figure 8-10. Sample mounting configuration on load cell.

2. The pressure controller was then adjusted to allow a maximum reservoir pressure of 2.4 bar, correlating to an impact velocity of 100m·s^{-1} for the hailstones. Setting the maximum reservoir pressure allowed for subsequent quick and accurate pressure loading.
3. Approximately 4-6 hailstones were removed from freezer storage (depending on the amount currently available) and placed in a portable cool box with two freezer packs to allow for cool transportation to the impact rig and subsequently greatly increase the time required for the ice to melt whilst kept on hold before use in the rig.
4. A hailstone was then taken from the cool box with plastic tweezers and place in the plastic sabot and loaded into the breach securely.
5. The reservoir was then loaded to the pre-set pressure.
6. Simultaneously, the gun trigger, DAQ processor and (if required) the high speed camera were triggered.
7. The logged DAQ data was then quickly reviewed (impact velocity and load outputs) and saved to file.
8. The target was then checked for any indications of material damage.
9. If required another hailstone was then loaded and steps 5-8 repeated.

For the experimental campaign conducted, single samples from batches A and B were subjected to 20 repeated impacts at 100m·s^{-1} targeted at the centre of the respective sample.

8.3.4.2 Ceramic Bead Impact Testing

The experimental impact procedure for the ceramic bead testing was based closely on the ice procedure described in the previous section, apart from the difference in projectile handling as a large stock of beads were available for use as and when required. Furthermore, if a given ceramic bead did not shatter or break during impact it was then re-used in subsequent impact tests for the same sample.

As with the hailstone impact testing, samples from both batches A and B were subjected to repetitive impact testing.

Given the significantly greater mass of the ceramic beads, the reservoir pressure used was also 2.4 bar, resulting in a lower impact velocity (than the hailstone tests) of 87.5m·s^{-1}. However, due to the increased mass/hardness of the ceramic beads, damage was created in most cases after a single impact (as will be discussed) and as such the number of repeated impact tests were typically much lower.

8.3.5 Results & Discussion

8.3.5.1 Hailstone Impact Testing

One of the first steps taken to ensure that good impact conditions were created for the hailstone impact tests was to observe the actual impact event through the high speed video recording apparatus. Typically at an impact velocity of 100m·s^{-1} only one or two frames of the incoming hailstone were capture before impacting the target, limited by the available maximum frame rate of the camera (10,000fps). However, even only capturing a single frame of the incoming hailstone allowed for verification that the hailstone projectile was indeed coming out of the barrel intact and without breaking up; through the extreme pressure force or from striking the barrel interior. The sequence of images shown in Figure 8-11 display a 40m·s^{-1} impact event as recorded at 10,000fps, with this lowered impact velocity allowing for the capture of more impact detail. As a result of image data corruption when transferring the images from the camera to the computer, a small vertical slice of the images was lost, replaced in Figure 8-11 by a grey line.

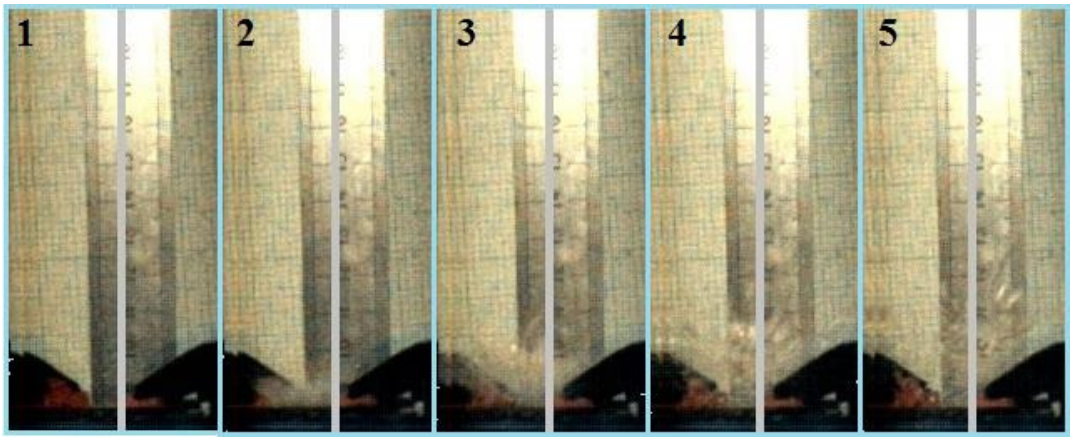

Figure 8-11. High speed camera imaging of a 40m·s^{-1} hailstone impact test at progressive stages throughout the impact.

Frame 1 in Figure 8-11 shows the impact apparatus just before the hailstone impacts the target, however due to the image data corruption the hailstone is almost entirely obscured from view. The subsequent frames show the ice fracturing, spreading outwards and then rebounding off the target surface in a fluid/ice particle cloud. From reviewing such images it was found that in the vast majority of the impact tests conducted with the manufactured hailstones, the hailstone reached the target surface intact and whole. In the cases where the ice had already fractured it was typically indicated by an uncharacteristic force history output, discernibly different in either magnitude of trend when compared to other tests.

Figure 8-12 plots the load cell outputs taken from the 20 different repeated hailstone impacts on the Batch A sample; at 100m·s^{-1}.

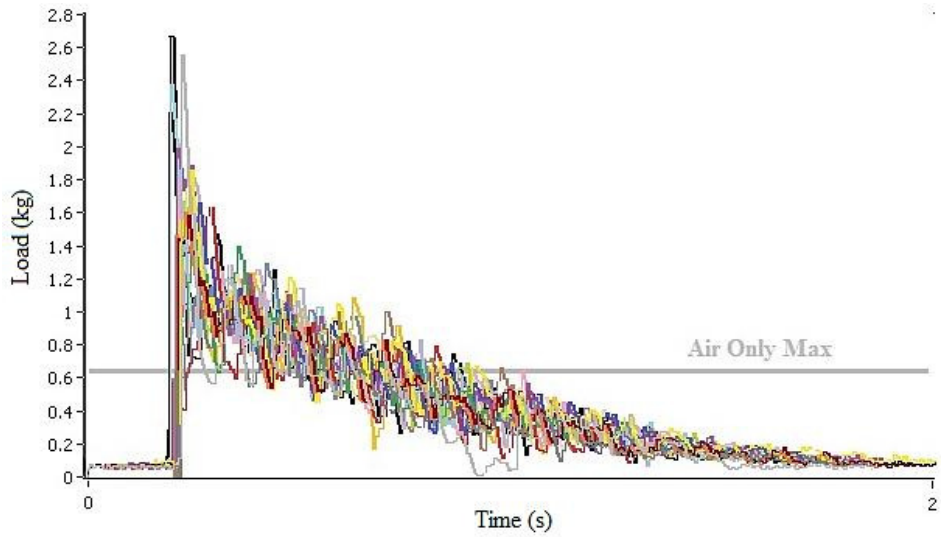

Figure 8-12. Load cell outputs from (20) hailstone impact tests on the Batch A sample, with an impact velocity of 100m·s^{-1}. The maximum load recorded when dry firing the gun (i.e. no projectile) with the same reservoir pressure (2.4 bar) is shown by the flat grey line.

From reviewing the many impact load outputs obtained, there is a clear overall trend to the outputs obtained. The trend is characterised by a sharp initial peak value followed by a more gradual decrease in load back to pre-impact levels, typically lasting just under two seconds in all.

At first inspection, the data and resulting trend obtained seemed to indicate both good repeatability in the results obtained and a good indication of the typical impact forces imparted on the load cell by the hailstones when impacting at 100m·s^{-1}. However, closer scrutiny revealed some underlying issues with the load measuring apparatus and consequently the results obtained. Figure 8-12 also shows the maximum load output value (peak) obtained when firing the pressurised gas alone through the apparatus at the target and load cell apparatus. As shown, through firing only the compressed gas at the target a maximum load of just over 0.6kg was recorded (from repeated testing) by the load cell. The time history of this load also compared closely to that obtained for the actual hailstone impacts as shown in Figure 8-12. Therefore it is evident that care has to be taken to differentiate between the ice impact components and the pressure wave components of the load cell outputs obtained. The first challenge with respect to accurately determining the ice impact component lies with ensuring that the sampling rate and sensitivity of the load cell apparatus used are suitable for the requirements of the tests. It became apparent following testing that the load cell employed did not fully satisfy these requirements. Firstly, the load

cell consists fundamentally of an aluminium cantilever beam with attached strain gauges along its length, the outputs of which were then calibrated against dead weights, to determine the relationship between the outputs and the load. This configuration is therefore characteristically stiff and therefore did not have the required impact sensitivity for a lightweight impact projectile such as ice. Further exacerbating this issue, the maximum sampling rate of the apparatus proved ineffective in capturing the actual ice impact event in great detail. The outputs shown in Figure 8-12 show a total load cell response time of just less than two seconds, however it is apparent that the actual duration of the hailstone impact is significantly shorter than this, lasting typically only a fraction of a second. Looking in more detail at the hailstone impact load output which exhibited the highest peak value, shown in Figure 8-13, it is more apparent at which point the ice impact event occurred.

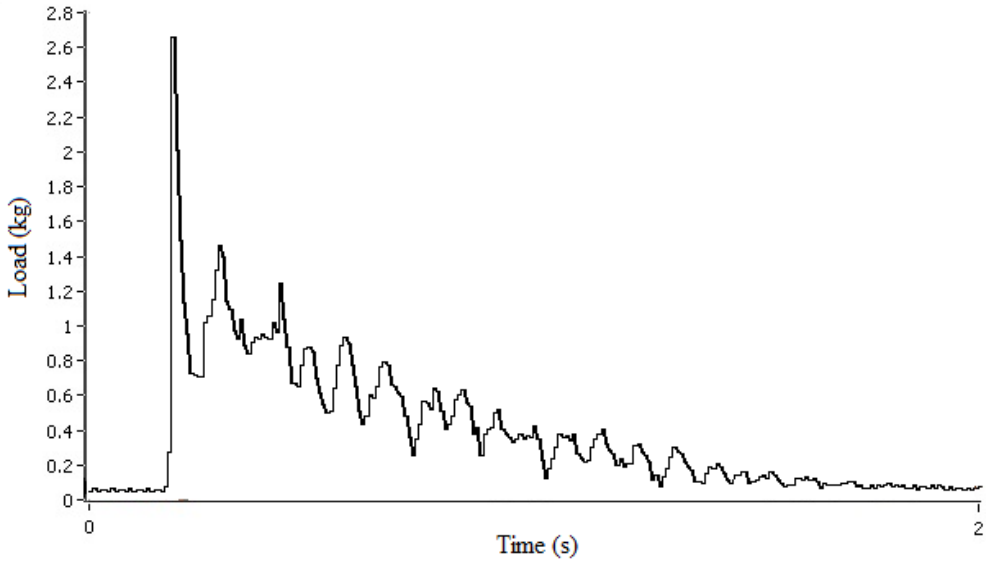

Figure 8-13. Maximum recorded load output from 10mm diameter hailstone impact at 100m·s^{-1}.

With the added context of the aforementioned detail on the performance of the load cell apparatus, it is clear from revisiting this load curve that the entire ice impact event likely occurs entirely within the first peak and decrease of the curve. After this point the majority of the load exhibited is as a result of the pressure wave loading and some component of leftover post-ice impact resonance; although the exact make up is impossible to determine from the curve alone. From looking closer at the initial ice impact peak, it is apparent that within this period only a limited number of data points were actually recorded, therefore reducing the detail/clarity of the ice impact sequence. Important further still, it may be the case that given the low data point resolution at the time of the peak load, the true peak load value was created between the data points obtained and therefore the peak value obtained is not a true reflection of the peak load.

Irrespective of the given load cell performance, as set out and described previously, single samples from both Batch A and B were subjected to 20 repeated hailstone impacts at $100m \cdot s^{-1}$; at the same target location. However neither sample displayed any visual damage or change in state of conditions following the impact testing. From other previous testing and calibration work any damage of target material was typically identifiable from a whitening of loss of relative transparency of the resin material. Neither samples displayed any such obvious damage indicators, however it may be possible that some form of damage was created that could be diagnosable by microscopy methods or other approaches. It may also be the case that continued repetitive impact testing may have eventually led to some form of material damage.

However, for the testing conducted it can be stated that for a hailstone diameter of 10mm, the samples created exhibited a damage threshold velocity at an undetermined value in excess of $100m \cdot s^{-1}$. The precise value of the damage threshold velocity is not possible to predict from the work conducted, however the impact velocity required may far exceed $100m \cdot s^{-1}$.

8.3.5.2 Ceramic Bead Impact Testing

As with the hailstone impact testing, the first method of reviewing impact events created through firing the ceramic beads was to review the high speed video camera footage. Figure 8-14 shows a selection of frames taken from high speed video footage of a ceramic bead impacting a target at $40m \cdot s^{-1}$; at a reduced speed to enable the capture of more frames.

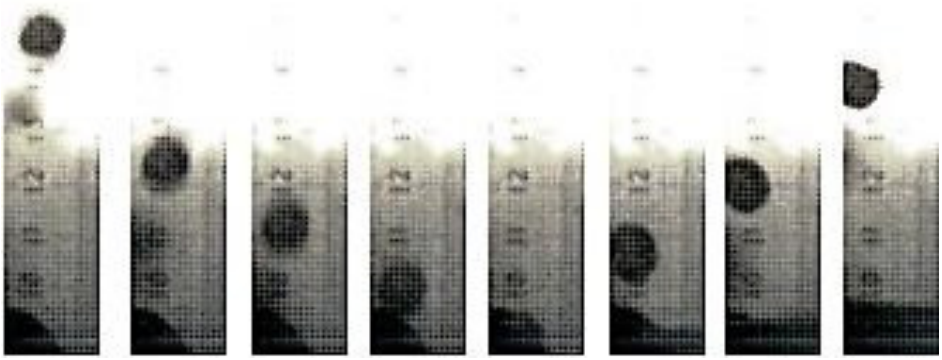

Figure 8-14. High speed camera imaging of a $40m \cdot s^{-1}$ ceramic bead impact test at progressive stages throughout the impact.

As shown, the impact progression of the ceramic bead differs significantly to that as exhibited in the hailstone impact (shown previously Figure 8-11), whereby the ceramic bead does not shatter, but instead rebounds off the target surface. However, it should be noted that

in many subsequent impact tests the ceramic ball shattered upon impact; either instantaneously or after repetitive use, due to material failure.

Given the issues encountered with load cell apparatus for the hailstone impact testing it was not deemed necessary or useful to record the ceramic bead impact loads for analysis purposes.

Unlike the hailstone impact testing, the ceramic bead impact tests created significant observable damage in both the samples from Batch A & B; as discussed in the following sections.

Batch A Samples

Figure 8-15 shows the top (impact) and bottom surface of a Batch A sample following a single ceramic bead impact at 87.5m·s^{-1}.

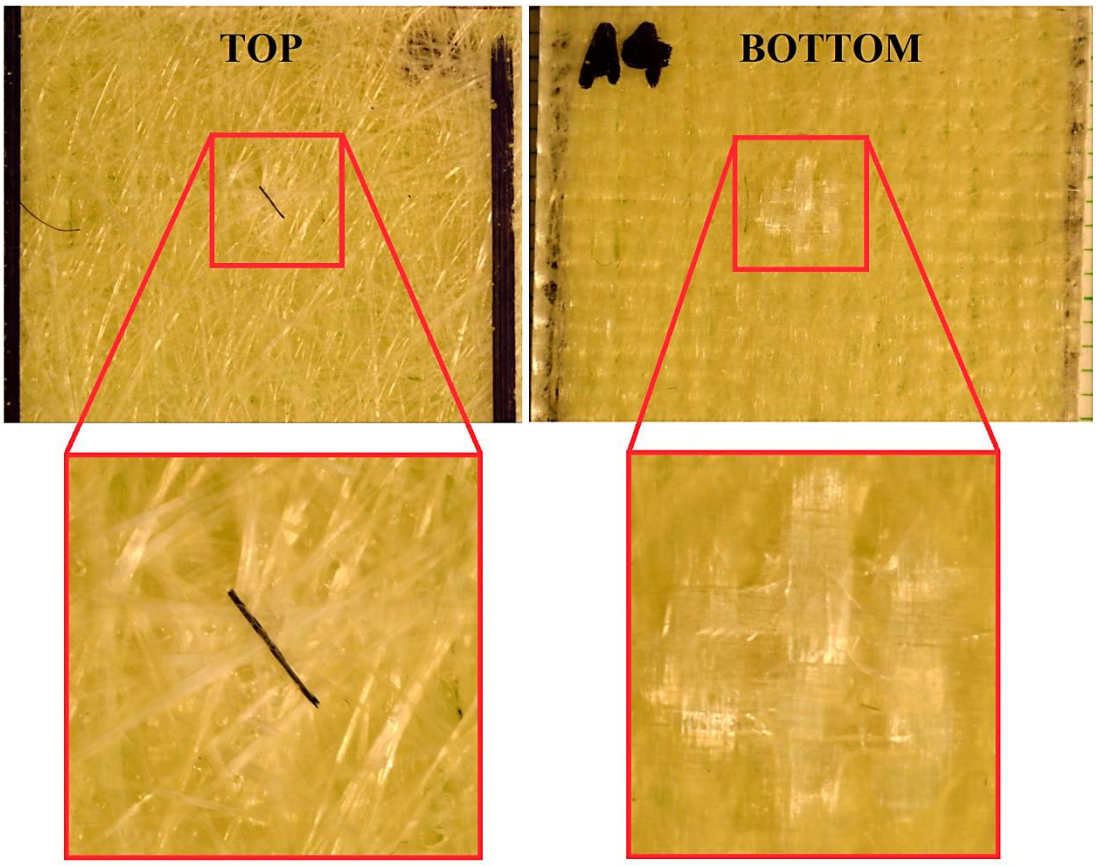

Figure 8-15. Photographs of the top (impact-side) and bottom surface of a Batch A sample following a single ceramic bead impact at 87.5m·s^{-1}. Red boxes show the damaged areas in enhanced detail.

It can be seen that only a single impact from a ceramic bead at 87.5m·s^{-1} was required to create visible damage in the Batch A composite sample, equating to an impact energy of approximately 5.3J. From reviewing the impact energies associated with varying hailstone

diameters shown previously in Figure 8-9, such an impact energy is theoretically equivalent to a hailstone with a diameter of 20mm impacting at 50m·s^{-1} or a diameter of 15mm at 80m·s^{-1}.

From Figure 8-15 there is clear damage of the fibres in the chopped strand mat material, indicated by a whitening of the fibres. Additionally, the surface in this region was considerably roughened, established through simply touching the surface. However, the damage is not limited only to the immediate contact surface, as considerable damage is observable on the underside of the sample also; again indicated by the whitening of fibres. On the underside, the fibres can be observed to have failed along the fibre orientations bi-axially, resulting in a damage area greater than that created on the surface. Additionally, the whitening between the fibre orientations, visible through the transparent resin indicates the occurrence of delaminations and damage between the fibre layers.

Figure 8-16 shows the damage created in another Batch A sample following 6 repetitive ceramic bead impacts (again at 87.5m·s^{-1}) on approximately the same sample surface location.

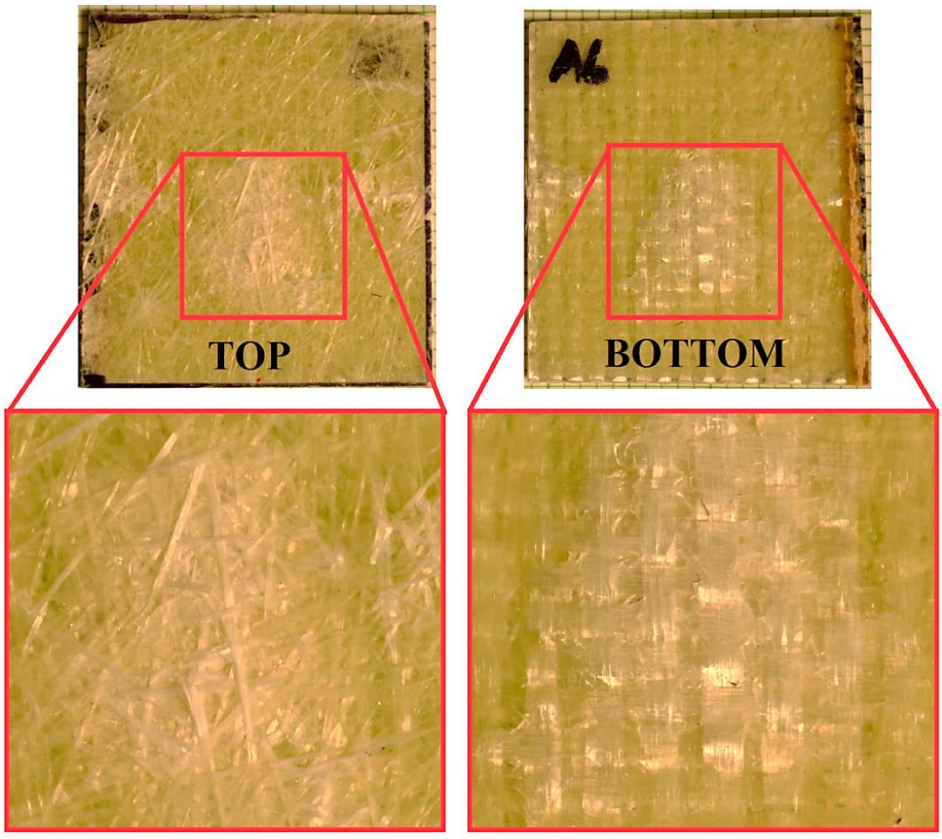

Figure 8-16. Photographs of the top (impact-side) and bottom surface of a Batch A sample following 6 repeated ceramic bead impacts at 87.5m·s^{-1}. Red boxes show the damaged areas in enhanced detail.

Figure 8-16 shows the effect of repetitive impact was to create a worsening and deepening of the damage created, causing widespread and significant damage in this case after 6 impact events. Again, the surface of the CSM shows considerable fibre damage and also clear debonding between the fibres and the matrix material. On the underside, similar but more extreme and widespread damage as observed for the single impact is exhibited, characterised primarily by the bi-axial distribution of fibre damage. As with the top surface there are also clear indications of debonding between the fibres and the resin matrix, with a broad vertical section of fibres visibly debonded from the surrounding matrix material.

Batch B Samples

Figure 8-17 shows the damage created in a Batch B sample following a single impact from a ceramic bead at 87.5m·s^{-1}, as visible on the top and bottom surface of the sample.

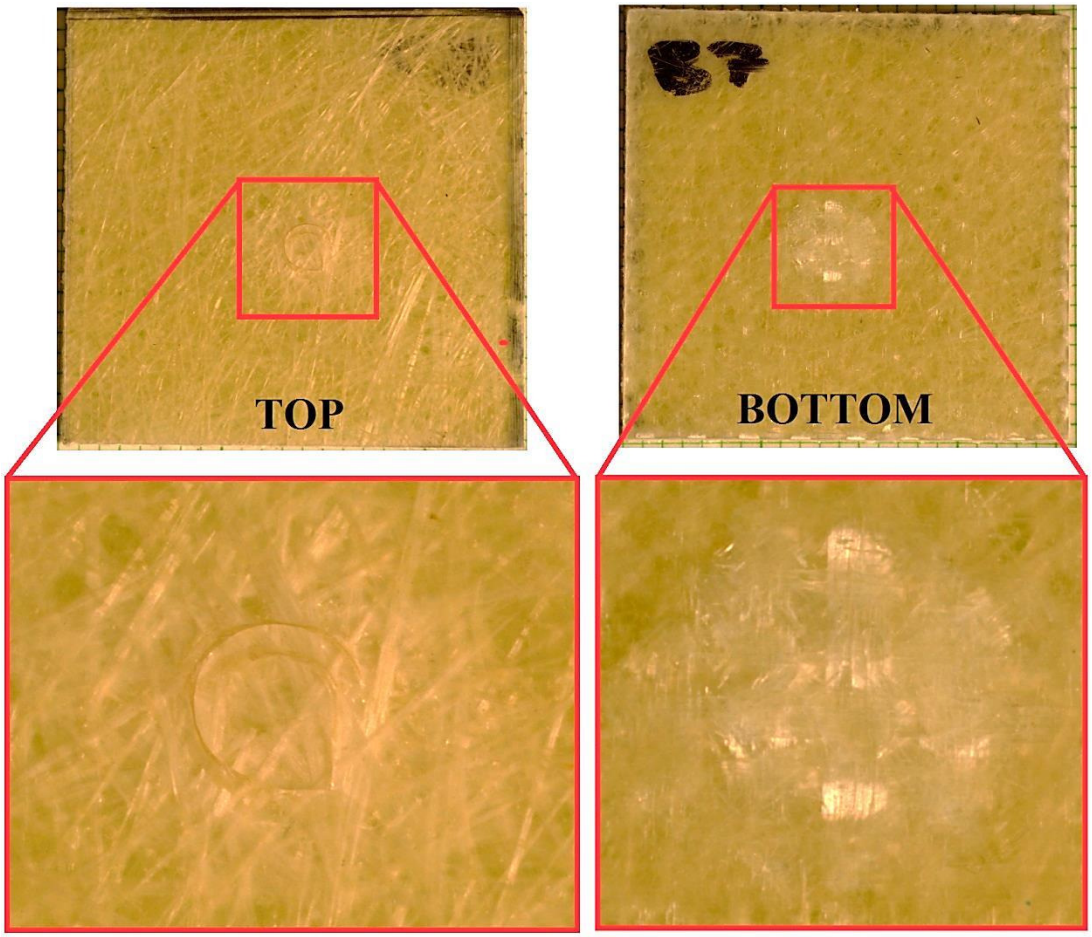

Figure 8-17. Photographs of the top (impact-side) and bottom surface of a Batch B sample following a single ceramic bead impact at 87.5m·s^{-1}. Red boxes show the damaged areas in enhanced detail.

Figure 8-17 shows that following a single impact clear damage of the sample gelcoat was induced, resulting in the creation of ring like cracking distributions on the material surface.

On the underside of the sample, extensive damage is also observable along the fibre orientations of the composite materials of the substrate. However, whereas in the Batch A sample such distributions were biaxial (horizontal and vertical in the image), in the Batch B sample the distribution is also observed along the fibres of the laminate orientated at 45°. The creation of such visible damage on the bottom surface indicates that through thickness damage was created in the sample through the impact test. Furthermore, as observed in the Batch A test results, there is significant whitening of the matrix material, observed throughout the semi-transparent sample, indicating matrix cracking and interlaminate damage.

Figure 8-18 shows the damage created in a Batch B sample following 5 repetitive ceramic bead impacts at 87.5m·s^{-1}; impacting approximately the same target location.

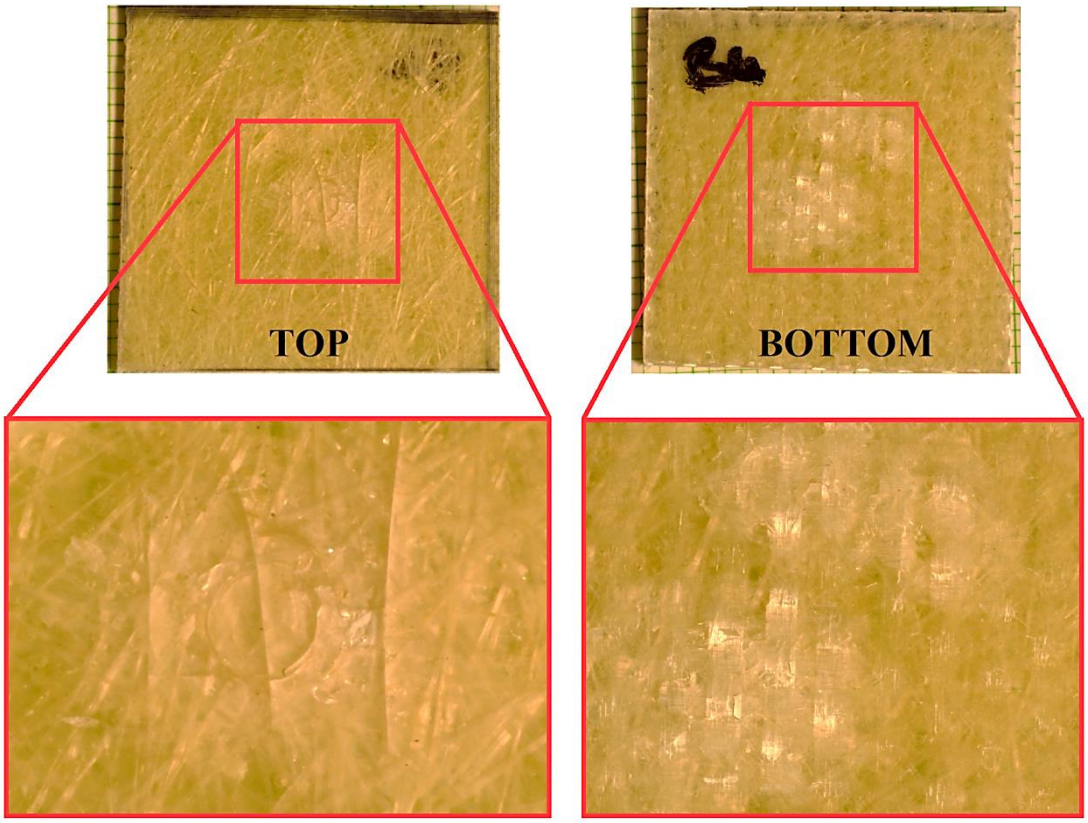

Figure 8-18 Photographs of the top (impact-side) and bottom surface of a Batch B sample following 5 repeated ceramic bead impacts at 87.5m·s^{-1}. Red boxes show the damaged areas in enhanced detail.

In Figure 8-18, it can be seen that on the top surface similar ring shaped cracking damage as exhibited previously in the single impact results (Figure 8-17) is visible, as well as additional surrounding gelcoat cracking. There is also evidence of material erosion of the gelcoat material, with several segments of the material removed from the surface. On the bottom

surface, there is widespread damage visible; again forming in distributions aligned with the fibres of the composite substrate layers.

8.3.5.3 Apparatus Effectiveness

From the testing procedure developed and discussed and the results shown and analysed, it is clear that the experimental apparatus developed worked effectively for the purposes of the research considered. Some of the key strengths of the apparatus developed were found as the following:

- The modular construction of the apparatus and associated DAQ system resulted in the creation of a highly flexible and adaptable piece of equipment.
- The reservoir pressure controls and switching features allowed for fine control of the impact conditions and ensured consistent ballistic pressures were created in testing.
- The barrel velocities generated for both the ice and ceramic projectiles displayed a high level of repeatability and predictability (in relation to reservoir pressure).
- The breach component of the apparatus allowed for easy and quick loading of the respective projectiles; vital when handling and firing ice projectiles.
- The DAQ systems implemented provided some useful outputs, such as the barrel velocity. However, issues were encountered with the load cell apparatus utilised; as discussed previously.
- The high speed camera apparatus allowed for the visual examination of the impact conditions created, however an improved lighting and camera system could provide enhanced and clearer visualisations.

However, although the rig performed to meet the requirements of the validation programme, the following issues and areas for improvement were also established and identified:

- The load cell apparatus did not possess the impact sensitivity and sample rate required to fully and accurately measure the impact events created. Alternative types of load cell such as piezoelectric based equipment, used in other impact studies [133] [128] may provide higher impact resolution and sensitivity. In addition to this, a more robust and secure method by which to attach the sample to the respective load cell would also greatly improve the testing method.
- Although the camera apparatus provided reasonable clarity in visualising the impact events at lower impact velocities, at high impact velocities the maximum frame rate of 10,000fps provided limited insight. A higher frame rate camera would also provide clearer visualisations of the ice fracturing behaviour during impact. In the

experimental work conducted, the camera was mounted of a small standalone tripod, however a more fixed and permanent method of positioning the camera would improve the ability to properly positions and focus the camera, as well as established appropriate lighting conditions.

- An ice mould apparatus with significantly more mould holes would greatly increase the manufacture rate of the hailstone projectiles whilst also reducing the labour requirements associated with their creation.

Although these issues were encountered and identified, as described, the flexibility and adaptability of the apparatus designed and develop would make it possible to address these issues as well as make further improvements and alterations.

8.4 Experimental-Numerical Ceramic Validation

With the availability of the experimental results shown and discussed, it was then possible to compare these to the results obtained through the coupled simulation work; described previously in Section 7.3. The following sections compare the results obtained through both approaches for both sample types (Batch A & B) used, in order to evaluate and validate the numerical approach employed.

8.4.1 Batch A Results Comparison

The Batch A simulation was successfully run to completion, taking approximately 1 hour to finish.

In order to gain a better insight into the modelled impact response of the Batch A sample, it is useful to first review the geometric impact response of the material. Figure 8-19 shows a cross sectional view of the model, cut through its centre (at the applied clamp boundary conditions) during the simulated ceramic bead impact event at 87.5m·s^{-1}.

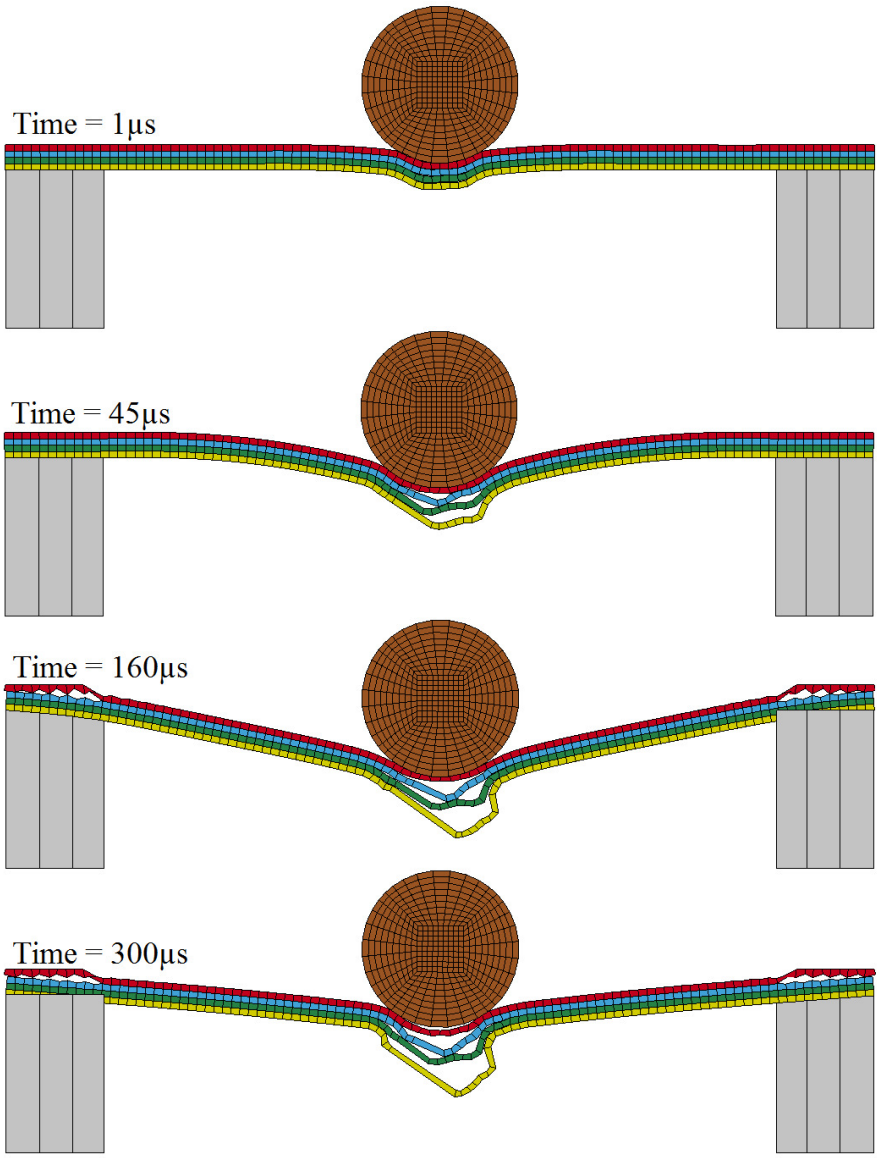

Figure 8-19. Cross sectional view through the model centre (through the clamped boundary conditions) showing the simulated impact progression of the ceramic bead impacting the Batch A sample at 87.5m·s^{-1}.

Figure 8-19 reveals much about the modelling method strengths and drawbacks. Firstly, as observed in the experimental work, the model captures the rebounding nature of the ceramic bead projectile as it first depresses the composite target and is then repelled back upwards away from the target. The approach clearly predicts a significant amount of deformation in the target during impact, and substantial permanent damage thereafter in the form of composite damage and delaminations. However, it is also observable that large levels of skewing were modelled in the meshes associated with the lower substrate layers. This is brought about through the modelled damage and subsequent weakening of the material throughout impact. Additionally, there is also significant damage exhibited in the regions of the applied boundary conditions, resulting from the overly stiff boundary conditions applied

in these regions. In some of the testing work, similar damage was observed around the clamped regions following impact, but not with such severity. However, given that these areas are well out-with the impact zone of interest, they were thought not to greatly affect the modelling results or their validity.

Figure 8-20 shows both the upper surface of a Batch A sample following a single impact test and the upper surface of the simulated Batch A target at the end the corresponding simulated impact, with contours of effective plastic strain in the CSM (surface) layer shown. Both images are presented in the same scale, showing the whole target geometry.

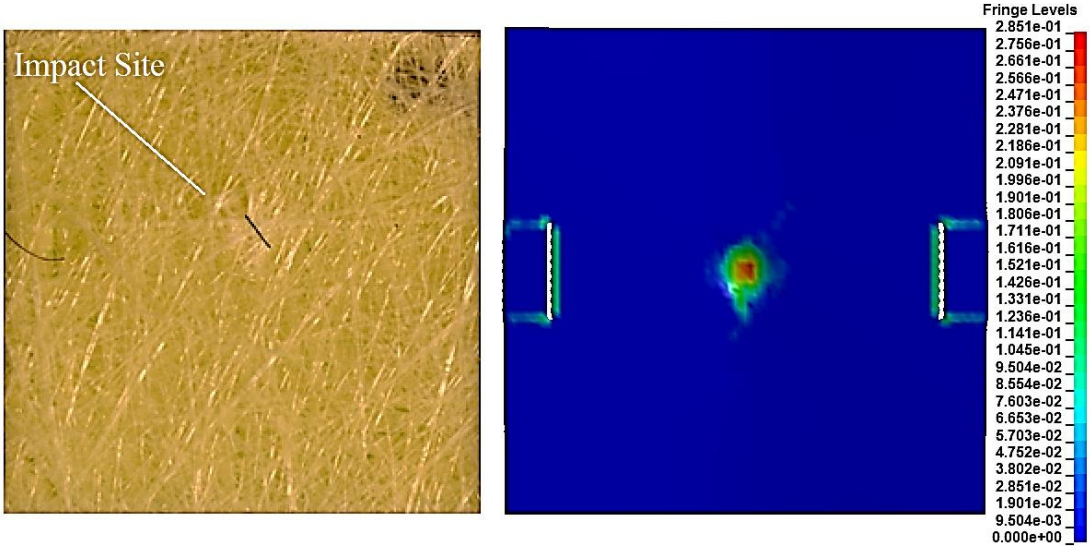

Figure 8-20. Surface of the CSM layer following both experimental and simulated impact from a ceramic bead at 87.5m·s^{-1}, with contours of effective plastic strain plotted in the simulated CSM layer. Both images are presented in the same scale, showing the whole target geometry.

From comparing the two surfaces, it is clear that the area of surface damage created, indicated by the (faint) whitening of the physical sample and creation of plastic strains in the simulated material, are comparable in size and shape (approximately circular). However, it also clear that at such scales of interest that the homogenisation of the assumed CSM material properties may not be fully suitable, as there exists a strong degree of fibre directionality at the impact site of the physical sample.

Examining at the biaxial composite substrate layers in the modelling results, the material model used to represent these layers made it possible to evaluate a wide number of failure criteria in the material. Figure 8-21 plots contours of the damage conditions in the three biaxial composite layers with respect to tensile failure in the dominant fibre directions (horizontal/longitudinal and vertical/transverse in the image shown); where a value of 1 (red)

represents no failure and 0 (blue) represents complete material failure (of the specified failure criteria).

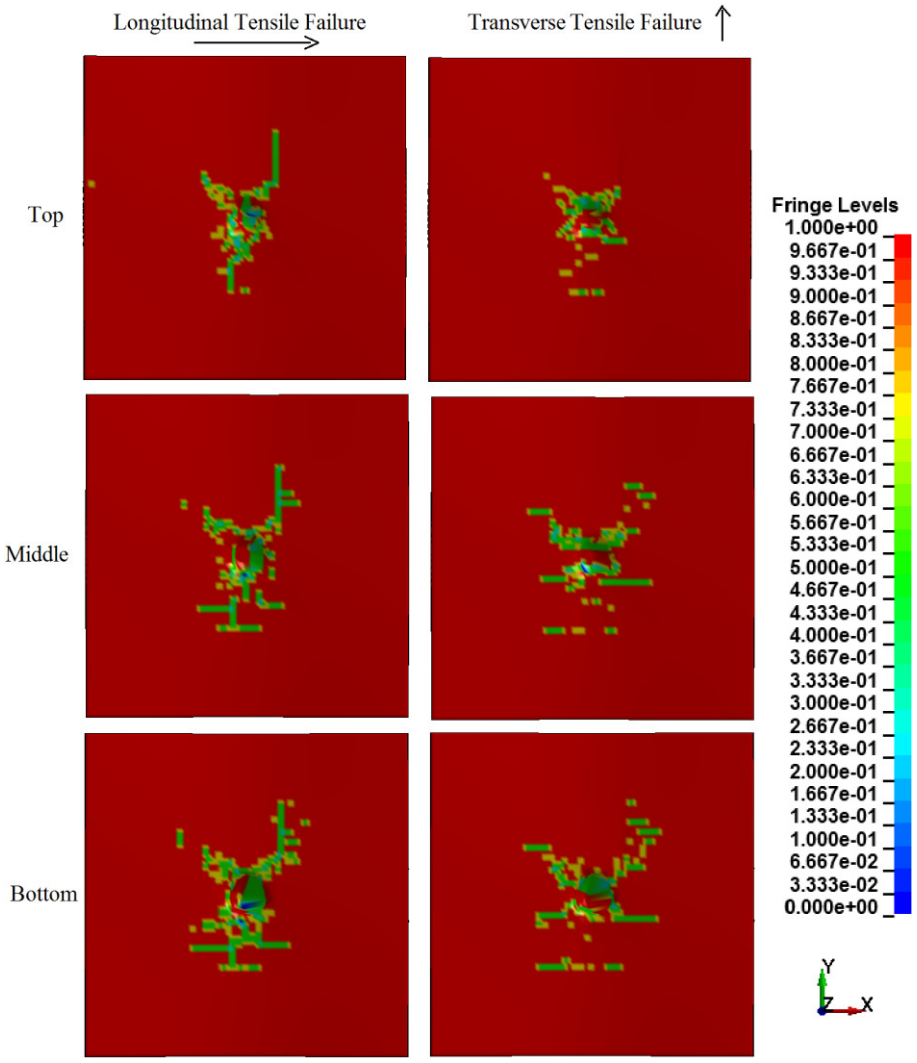

Figure 8-21. Longitudinal and Transvers damage in the three biaxial composite layers of the simulated Batch A sample, following simulated impact from a ceramic bead at 87.5m·s^{-1}. A value of 1 (red) represents no damage and a value of 0 (blue) represents complete failure for the respective failure criterion (i.e. longitudinal/transverse tension.

From these images, it is clear that the modelling work predicted significant tensile damage in the fibre dominated directions; indicated by the strong presence of vertical and horizontal damage distributions. Such strong orthogonal damage distributions were also observed in the experimental results shown previously in Figure 8-15, however the distributions in the modelling results show a much wider spread in comparison to the highly localised distribution created in the physical sample.

Figure 8-22 plots the modelled delaminations between the respective layers of the simulated Batch A sample following impact from the ceramic bead at 87.5m·s^{-1}; where a value of zero indicates undamaged tied contact and a value of 1 indicates complete bond failure.

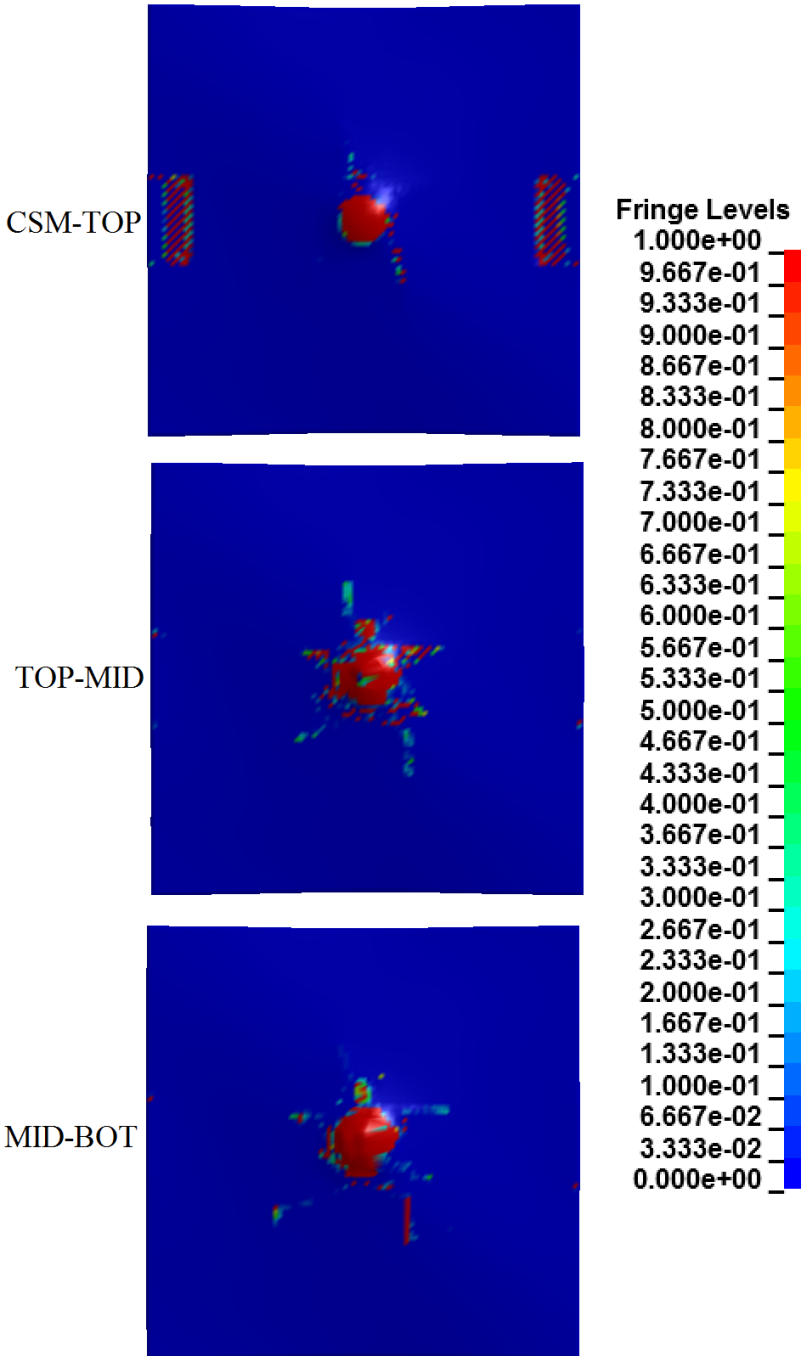

Figure 8-22. Contour plots of contact gap between the respective layers of the simulate Batch A sample. Where a value of 1 (red) indicates complete failure of the bond and a value of zero (blue) indicates an undamaged bond.

From the contour plots above, it is shown that the modelling results predict significant delaminations in the composite layup throughout the thickness. The delaminations created are mostly localised to a small area around the impact zone, which would appear to compare

well with the experimental findings shown previously in Figure 8-15. However as it was not possible to fully evaluate the nature of delaminations in the experimentally tested sample, this comparison can only be declared qualitatively valid.

Indeed, although it was not possible within the time constraints of the research to fully quantify the damage created in the experimentally tested samples, for the Batch A sample it can be said that there is good agreement at least in a qualitative sense between the numerically and experimentally obtained results.

8.4.2 Batch B Results Comparison

The Batch B simulation was successfully run to completion, also taking approximately 1 hour to finish.

Figure 8-23 shows the simulated impact progression of the ceramic bead impacting the Batch B sample at 87.5m·s^{-1}, showing the deformation of the target through a cross sectional view through the target centre.

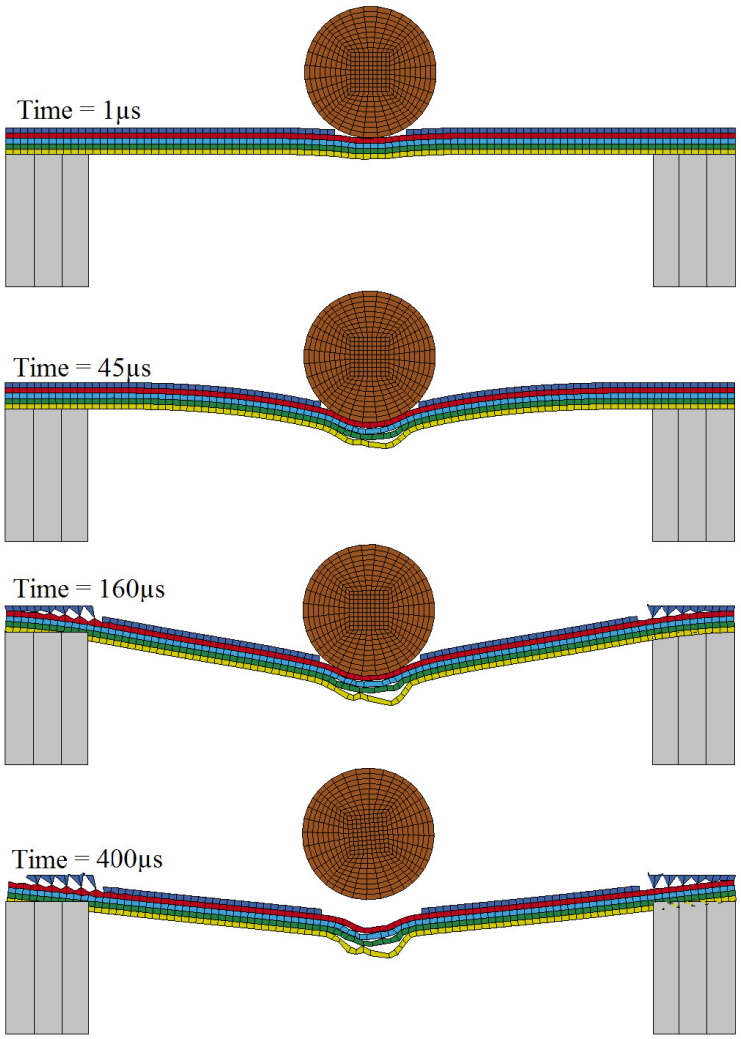

Figure 8-23. Cross sectional view through the model centre (through the clamped boundary conditions) showing the simulated impact progression of the ceramic bead impacting the Batch A sample at 87.5m·s^{-1}.

From Figure 8-23, it can be seen that as observed in the experimental work, the ceramic bead is rebounded upwards shortly after impacting the surface; as also simulated for the Batch A sample. It is also apparent that almost immediately upon impact; the top gelcoat layer undergoes material failure and is eroded/removed from the simulations. The levels of deformation and the apparent delaminations exhibited in the results are reduced in comparison to those exhibited in the Batch A sample numerical results, however significant levels of both the failure modes are still exhibited in the lower layers of the substrate.

Looking specifically at damage in the gelcoat layer, Figure 8-24 shows the gelcoat surface following both the experimental and simulated impact of a ceramic bead at 87.5m·s^{-1}, with contours of effective plastic strain plotted on the simulated surface. Both images are presented in the same scale, showing the whole target geometry.

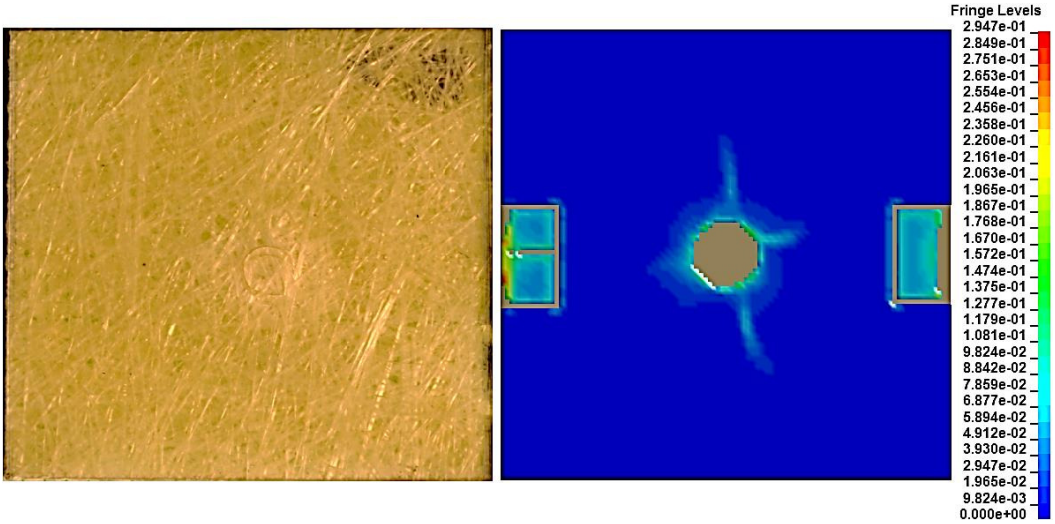

Figure 8-24. Surface of the gelcoat layer following both experimental and simulated impact from a ceramic bead at 87.5m·s^{-1}, with contours of effective plastic strain plotted in the simulated gelcoat layer and deleted elements represented in grey. Both images are presented in the same scale, showing the whole target geometry.

The areas of damage exhibited in the gelcoat from both the experimental and numerical results are comparable in size in distribution shape. However, whereas significant erosion of the gelcoat is exhibited in the numerical results (indicated by the greyed out regions), only cracking and fracturing of the gelcoat material is exhibited in the experimentally tested sample; shown in greater detail previously in Figure 8-17. This heightened level of damage exhibited in the simulated gelcoat may arise from the low predicted values of yield stress in the material (as discussed previously in Section 7.3) and the assumption that the material behaves in an elastic-perfectly-plastic way (i.e. no plastic hardening occurs). Nevertheless, the comparative size and distribution of the damage created – as well as the occurrence of damage exhibited in both methods – is encouraging with respect to the validity of the modelling approach in simulating and capturing the formation of damage in the gelcoat.

Figure 8-25 plots contours of the damage created with respect to tensile failure in the biaxial composite layers in the longitudinal and transverse directions in the Batch B simulated target; following the simulated bead impact at 87.5m·s^{-1}.

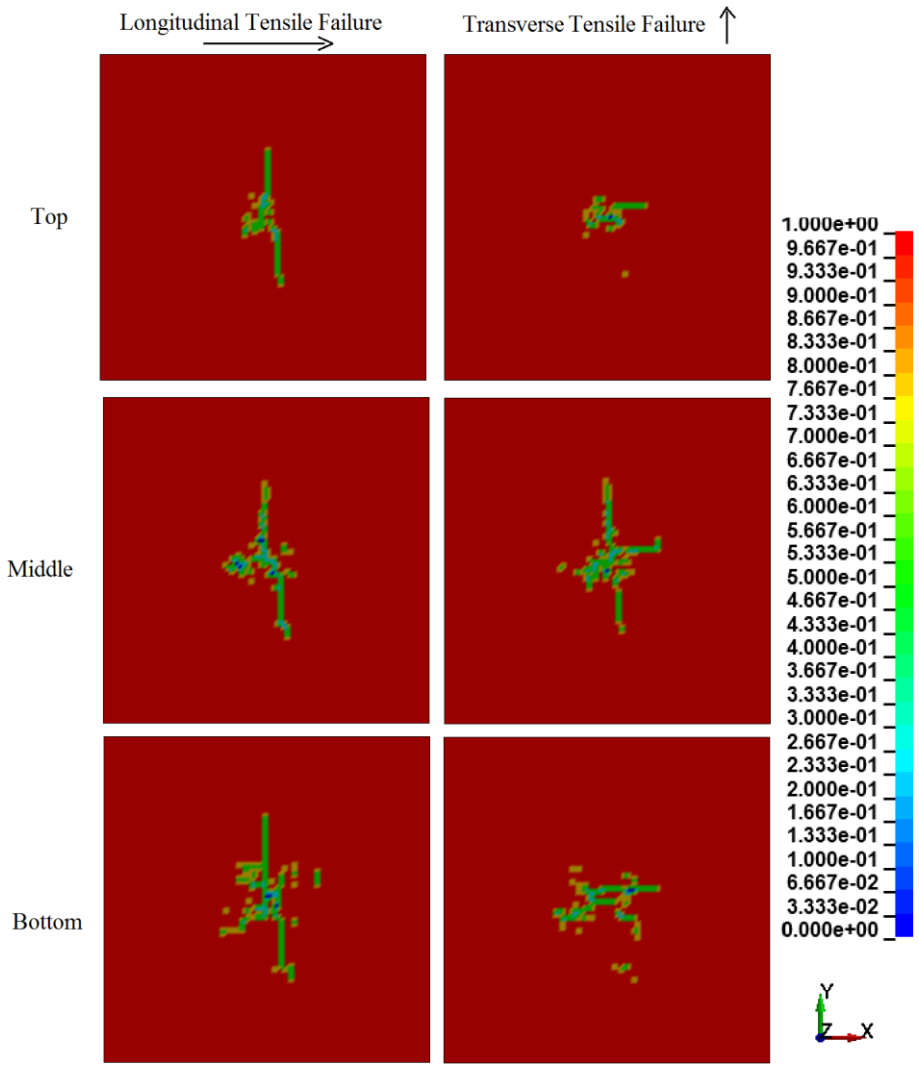

Figure 8-25. Longitudinal and Transvers damage in the three biaxial composite layers of the simulated Batch B sample, following simulated impact from a ceramic bead at 87.5m·s^{-1}. A value of 1 (red) represents no damage and a value of 0 (blue) represents complete failure for the respective failure criterion (i.e. longitudinal/transverse tension.

The damage distributions created in the biaxial composite layers of the simulate Batch B sample target are slightly less fibre direction dominated than those exhibited in the Batch A sample. This is most likely due to the +45° orientation of the fibre reinforcement in the middle composite layer, which results in a slightly more complex loading state. However it is clear that significant composite material damage is predicted in the simulation results, centred mostly in the impact regions, but also spreading outwards away from this centre. Furthermore, there is still a strong bias in the distribution of the damage along the fibre dominated directions, as exhibited in the damage created in the physical samples tested experimentally.

Figure 8-26 plots the contours of interlaminate damage between the composite layers of the Batch B target following the simulated impact; where a value of 1 (red) signifies complete bond failure and a value of zero (blue) indicates an undamaged bond.

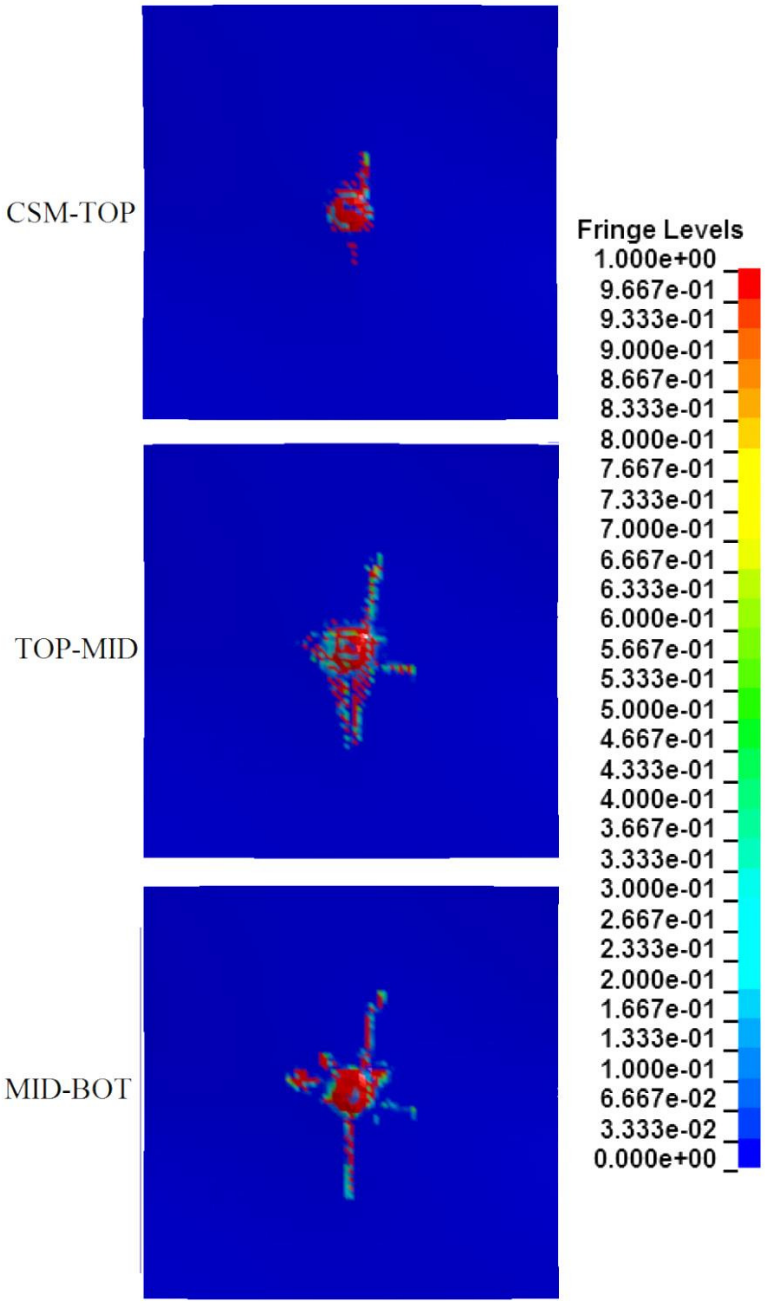

Figure 8-26. Contour plots of contact gap between the respective layers of the simulate Batch B sample. Where a value of 1 (red) indicates complete failure of the bond and a value of zero (blue) indicates an undamaged bond.

It can be seen that there is significant interlaminate damage and delamination in the numerical results, between each of the respective layers throughout the sample thickness. Again, most of the damage is exhibited in the region of initial impact contact, however there are also delamination distributions spreading outwards from this initial region. From looking

closer at the bond failure modelled between the middle and bottom composite layer, there are indications of the effect of the +45° orientated fibres of the middle layer influencing the damage created in the bond; with failure spreading outwards not only orthogonally but at diagonally also.

Figure 8-27 looks specifically at the failure distributions in the bond between the middle and bottom layer and compares them with the observable damage on the under surface of the experimentally tested sample. Both images are presented in the same scale, showing the whole target geometry.

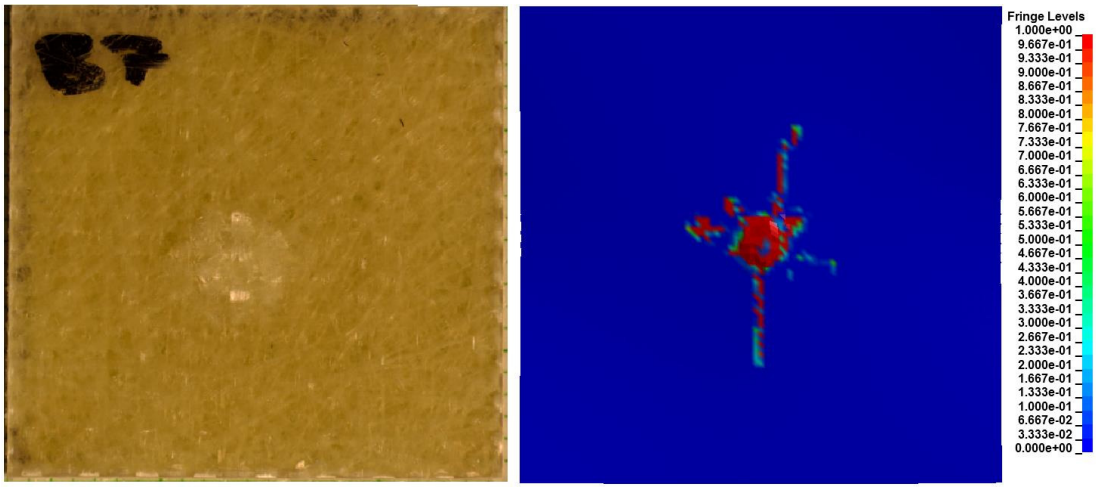

Figure 8-27. The image on the left shows the observable damage on the underside of the experimentally tested Batch B sample following impact from ta ceramic bead at 87.5m·s^{-1}. The image on the right shows the distribution of interface damage between the middle and bottom layer composites following the same impact event as simulated in LS-DYNA. Both images are presented in the same scale, showing the whole target geometry.

From comparing the two images, it is clear that the shape and size of the distribution of damage observable on the under surface of the test sample compares closely with the interlaminate damage created between the middle and bottom composite layers in the numerical work. In both there is a strong but small circular region of concentrated damage in the composite layup at in region of impact contact, as well as both orthogonal and diagonal damage distributions spreading away from this region.

It would appear from the comparisons of the results obtained from both the experimental and numerical approaches, that there is a good degree of qualitative agreement in the both the size and shape of the distributions of damage created in the Batch B sample; through the impact event considered.

8.4.3 Numerical Validation Discussion

From the results shown and compared for both the Batch A & B samples and the subsequent discussion on each, it is clear that many aspects of results obtained through the modelling approach employed compare well with the experimentally obtained results. Strong qualitative agreement with the experimental results obtained was achieved with regards to many aspects of the numerically derived impact test results. Most notably, the general size and shape of the different forms of damage creation in the numerical work compared closely with those observed in the experimental work.

However there were also some observed differences in the results obtained, which could be as a result of any number of influences. Central to the modelled impact response of any target body in a finite element environment are the material properties and constitutive material model applied to the respective body. In the sample study considered, the vast majority of the material properties of the modelled components were derived through both theoretical expressions and justified assumptions. Gaining a more in-depth knowledge of the relevant material properties of the systems concerned would greatly improve the accuracy of any results obtained. This also applies to the projectile body implemented in the model, which in the modelling work discussed was approximated by a simple elastic material model and approximate material properties. It was clear also form the numerical results obtained that the boundary conditions applied were not the most suitable for the impact event concerned. Therefore, a good understanding of the actual boundary conditions, or better control over those applied in experimentation, would also greatly improve model accuracy.

It is apparent therefore, that although strong similarities were observed between the numerical and experimental results, further improvements to the numerical modelling process (with respect to key model inputs) could further increase the accuracy and relevancy of the approach. A stronger understanding of key variables such as the target and projectile material properties and interlaminate strengths and the relevant boundary conditions would help to improve the modelling process and its usefulness.

9. Discussion

9.1 Impact and Research Findings

The following sections examine the wider impact and consequences of the findings made from both numerical and experimental work, in the context of wind turbine blade leading erosion as an ongoing and developing concern.

9.1.1 Rain Impact

Rain droplet induced leading erosion is a significant, growing and developing concern for many stakeholders within the wind industry. Consequently, in the last few years there has been a wide range of different material technology development efforts within the wind industry, aimed at mitigating or eradicating the issue; to improve blade performance. Additionally, there are also now ongoing efforts to develop and establish suitable testing standards to aid in the evaluation and grading of proposed leading edge erosion protection materials.

The key focus of the work discussed in this thesis was to first review the literature and engage with industry to collate the limited information available on rain. Following on from this, the physics of liquid droplet impingement on solid surfaces were reviewed, and then through numerical modelling the consequences of such impact phenomena in the context of blade leading edge were investigated.

Currently, the two most commonly employed blade coating materials within the wind industry are based on either the more classical thermosetting based gelcoat materials or the more recently developed flexible coating materials and paints (typically polyurethane based). The modelling work of the research investigated the phenomenon of rain droplet impact on both such coating technologies. From the modelling work conducted it was found that with respect to classical thermosetting polymer resin based gelcoat material technologies, the dominant and most likely form of damage is surface degradation and erosion; supported by experimental investigations detailed in the literature. The highly dynamic nature of water droplet impact was also made evident through the modelling work, capturing the initial waterhammer behaviour and subsequent high velocity lateral jetting. It was found that this spreading behaviour played a central role in the creation of potential damage and further erosive mechanisms; as also suggested in the literature. From these numerical findings and supporting evidence in the literature and manufacturer test results, it is clear that in regions which encounter at least moderate rainfall rates, classical gelcoat material technologies will likely exhibit rain induced erosion damage over the lifetime of the blade.

Given the limitations and susceptibility of classical gelcoats to such erosion, alternative flexible coating technologies have grown in prominence with many manufacturers developing and proposing their own solutions. Some technologies are utilised by blade manufacturers as an integrated surface coating or applied post-installation as a tape product. The manufacturer performed testing of such technologies [77] [51] [75] highlights much improved rain erosion performance in comparison to the classical gelcoat materials. The modelling work conducted and discussed previously highlighted the characteristic differences in the impact response of a simulated flexible coating in comparison to a classical gelcoat material, exhibiting high levels of deformation under impact. The damage creation mechanisms through rain droplet impact also differed to those exhibited in the modelled gelcoat material, and although surface damage was created for extreme impact conditions, the typically high strain to failure value of the flexible coatings indicated that surface erosion through rain droplet impact alone was unlikely. However, the high levels of deformation associated with the impact response of such coatings in the simulation work indicated the potential for high stresses and subsequent damage at the coating-substrate interface. Consequently, although the risk of rain impact induced erosion of flexible coating technologies appear far reduced, care is still necessary to ensure a robust and long-lasting bond between the coating and substrate is formed. This is particularly prudent when considering flexible leading edge tape technologies which are often applied on blades in situ, presenting numerous challenges with respect to ensuring appropriate surface and environmental conditions for application.

The modelling results indicated that short term substrate damage through rain droplet impact is highly unlikely as a result of the low impact energies associated with such impact (<1J). However from the test results shown in the literature review, is it clear that following the complete erosion of a given surface coating, the composite substrate is then also extremely susceptible to rain induced erosive effects.

In the context of testing and standards development, the modelling work presented indicates that for a flat target surface the impact response of the simulated gelcoat material was almost identical whether modelled as attached to a composite substrate or fully fixed at its underside (i.e. a more rigid substrate). However, the effects of test coupon curvature were not fully investigated and therefore this may have a significant effect on the impact response (and subsequent damage) of the gelcoat when considering attachment to a flexible or rigid substrate.

9.1.2 Hailstone Impact

One of the greatest challenges with respect to developing a fuller understanding of the threat posed by hailstone impact on the leading edge of wind turbine blades was the almost complete absence of any discussion or research of the topic in the available literature. As a result, information and context on the issue of hailstone impact on composite materials had to be drawn and source from other spheres of research, relating primarily to work in the aerospace sector.

Although rain erosion is currently an area of growing concern and subsequent investigation (as a result of its frequent occurrence), the issue of hailstone induced erosion and damage of wind turbine blades sited in hail-susceptible regions should not be discounted. From the meteorological data detailed it was made clear that in some regions of the UK significant hailstorm events can occur on more than 20 days over the period of a year. In such regions the additional threat posed by exposure to hailstorms cannot be ignored and a greater understanding of the issue is still required. However, there are also obvious challenges with respect to understanding and separating the damaging influences of both rain and hailstone impact on the blade leading edge; as the damage created by both will likely be almost indistinguishable.

Indeed, the hailstone impact modelling results shown and discussed suggest that although the scale of surface damage created through hailstone impact is greater than that of rain (due to the increased diameter of hailstones), the distribution of the damage created compares closely; forming in concentric rings on the surface. However, as a result of the increased diameters of hailstones in comparison to rain droplets and consequently the increased impact energies, the impact velocities required to create damage in the simulations conducted were considerably lower. Consequently, it was suggested from the damage exhibited in the modelling that exposure to hailstone impact at a frequency similar to rain droplet impact would result a far greater erosion rate. However unlike rain droplet impact on the blade, which is considered to pose only a threat to the coating surface integrity, the modelling results obtained suggest that in extreme hailstorm conditions with hailstones in excess of 20mm in diameter, considerable composite substrate damage could also be created. Such damage may take the form of direct composite laminate damage or damage to the interlaminate bonds of the system. Although such events may be rare for a given site, given the lengthy service life of most utility scale turbines, the possibility of such impact events occurring may not be safely disregarded. Furthermore, the occurrence of substrate damage

will also be extremely difficult to diagnose, and impossible to identify through visual inspection alone.

The influence of blade curvature with respect to the forces imparted by hailstones during impact were also highlighted by the modelling work, indicating the complex impact dynamics associated with impact on such surfaces.

Although no observable damage was created through experimental impact testing on the composite samples created with the limited hailstone diameter of 10mm, only a limited number of repeat impacts were conducted (20 for each sample). Given enough time and resources the longer term erosive effects of 10mm diameter hailstone impact could be investigated (as discussed later in Section 10). Impact testing with heightened impact energy through use of ceramic beads as a projectile resulted in significant damage creation in the composites samples tested, in the form of substrate material damage and surface wear. Although the material properties of the ceramic projectiles differ significantly from those of the manufactured hailstones (specifically with respect to stiffness/strength), the impact energy associated with their impact is within the same order of magnitude of those associated with 15-20mm diameter hailstones, at similar velocities. Resultantly, damage created through the ceramic bead impact testing may be indicative of the damage created through impact of hailstones with such diameters; however further investigation would be required to validate this.

9.2 Modelling Challenges and Barriers

A major challenge with respect to modelling the various types of impact stemmed from implementing an effective method of contact modelling between the projectiles and target surface. Issues with such contact modelling arose from a range of influencing factors and challenges. Most fundamentally, the greatly differing characteristic stiffness of the two contacting bodies meant that appropriate adjustments to the contact definition were required, to scale the stiffness values of each during contact. The high velocities associated with the impact also meant that a suitably low computational time step was enforced when solving the models, as too large a time step often results in missed contacts and consequently artificial penetrations between the two bodies. The effects of material erosion also greatly influenced the approach to modelling contact between the two bodies, as upon removal of the target surface layers, an appropriate contact definition between the projectile and the newly exposed subsurface layers was then required. Fortunately, as a result of the widespread use of LS-DYNA across a range of research activities, significant development

of the contact algorithms within the software had historically been performed. As such, suitable contact algorithms for most impact simulation studies were identified; however the vast range of available contact methods did initially make it difficult to ascertain the most applicable.

It was found in most impact studies that the element size employed in the target mesh had a significant effect on the levels of damage created in the material during impact. For instance, in rain impact simulations, a coarse mesh would not fully capture the Rayleigh wave dissipation on the target surface and would therefore not capture the associated loading of this phenomenon. However, for a much refined mesh the opposite issue was encountered and what was considered to be unrealistic and excessive damage was created. Without appropriate experimental data and calibration, the most appropriate mesh density was impossible to ascertain and, as such, engineering judgement had to be used.

Similarly, issues were also encountered in relation to the most suitable number of SPH nodes to be implemented to represent the projectile bodies. A high SPH node count would result in a much smoother contact front for the projectile but at a much increased computational cost. Again, judgement was required to establish the most suitable number, which was aided through sensitivity studies and reviewing the results obtained. Establishing the most appropriate boundary conditions to apply in each simulation was also a challenge, as little was known of the typical blade conditions at the tip during operation. Consequently, there was difficulty in determining the likely boundary response during impact and as such fully fixed conditions had to be applied.

The LS-PrePost working environment proved a powerful and adaptable tool for the creation of modelling input files for LS-DYNA. However, the software is still in its relative infancy and many of the functions within it are under constant revision and update, consequently care had to be taken when referencing supporting literature to ensure the correct version was being referenced. Additionally, many of the newer and developing features suffered from a lack of supporting literature. However, a strong online support and development community for the software does exist [233], which proved a valuable resource throughout the development of the various impact models.

Despite the challenges discussed, it is apparent that the modelling methodologies developed for both the rain droplet and hailstone impact modelling proved robust and successful, delivering results comparable to those predicted by analytical and experimental means. Such an approach, could readily be adapted and applied to a whole range of other impact and wear

research activities, to further still enhance the understanding of the leading edge erosion phenomenon.

10. Further Work and Future Developments

From the work discussed it is apparent that there is still a great deal to be investigated and understood on the issue both in an academic and industrial sense. Given the inherent multifaceted nature of the issue, there are numerous strands of potential further research.

10.1 Rain

Research into the occurrence of rain induced leading edge erosion suffers greatly from a lack of widespread industrial understanding and collaboration, partly as a direct consequence of the new and emerging/developing nature of the issue. As a consequence, there is very limited field based operational blade erosion data available in the literature, and any data that is held in industry in often regarded as proprietary and confidential. However, given the widespread nature and growing seriousness of the issue, there is now a developing consensus within the industry that a more collaborative and focussed approach to solving the issue is required; signalled by large buy-in to conferences on the topic [234] and the development of appropriate future standards [118]. If such collaborations were to result in the publication of wind turbine blade erosion data – even if anonymised/normalised – then a wide range of future research activities could be conducted. Such data could be used to conduct widespread and holistic reviews of the occurrence of wind turbine blade leading edge erosion, to identify the key influencing parameters such as: site topography and meteorological conditions, blade sizes and tip speeds, active service life and maintenance, blade materials and coating technologies used. Such research activities would then better set the scene for future research and act as a solid foundation for further research. The findings of such studies would undoubtedly lead to the identification of the key influencing parameters and subsequent focussing and further investigation of these issues. It is clear therefore that given the appropriate openness from industry and the availability of relevant data, that a more thorough and robust understanding of the issue could be developed and therefore greater improvements could be made within the industry to tackle the issue. However, it is recognised that the wind turbine industry is a competitive industry and open collaboration is therefore difficult to fully establish. Therefore it is hoped that through future conferences and more critically the input from the key stakeholders into the development of appropriate standards, that greater levels of cooperation and openness can be developed.

With respect to further developing an understanding the of the dynamics and damage mechanisms associated with rain droplet impact on wind turbine blade materials, there are numerous potential areas of future research. It is apparent that from previous discussion that the availability of either rain erosion test data or access to a rain erosion test facility would

both: provide additional insight into the rain erosion damage mechanisms and aid in validating the results obtained from the numerical simulation work conducted.

Experimental rain erosion investigation could be performed in many ways, utilising a variety of different experimental apparatus. As most commonly employed, a rotating arm apparatus could be utilised to establish erosion rates and the relevant material damage threshold velocity; which could then be used to validate numerical proposals. However a more targeted single droplet impact approach could also be utilised to better understand the basic impact mechanisms associated with rain droplet impact, in relation to factors such as: impact forces and pressures, impact durations, individual impact induced damage modes and droplet spreading behaviour. Such work would assist greatly in validating the numerical findings obtained and discussed previously.

Experimental validation of the numerical results obtained (in additional to the analytical validations discussed) would provide heightened confidence in the accuracy and flexibility of the rain impact modelling method developed and described. Such confidence would subsequently make possible to further investigate the damage mechanisms associated with rain droplet impact and propose methods by which to mitigate or eradicate the issue. Such methods may include: proposing alternative material thicknesses and layup configurations, utilising new or alternative material technologies, or developing new blade technologies to protect vulnerable areas of the blade.

10.2 Hailstone

The availability of leading edge erosion data would also allow for the investigation of the erosion aggravating effects of hailstone impact on the blade. Evaluation of erosion damage in locations more susceptible to hailstorms could potentially help to evaluate such effects, therefore helping to quantify the additional risks posed by such exposure. Currently, it is extremely difficult to surmise the influence of hailstorms on the wear of the blade leading edge, therefore such studies would help to evaluate the risk and focus future research.

Through use of the combined numerical-experimental approach developed and employed in the research presented, there are many possible further areas of research in relation to hailstone impact on wind turbine blades. First and foremost the most prudent area of research would be to evaluate the more long term erosive effects of hailstone impact on the blade leading edge. With the current experimental apparatus (as described) such testing would require a significant amount of labour hours to repeat the impact test a sufficient number of times in order to induced clear and identifiable damage. Although this approach could be

implemented given the appropriate resources, appropriate alterations to the hail impact gun rig could also be made to streamline the process, such as making it possible to load multiple hailstones at once and fire them in quick succession. There would of course be many challenges with respect to successfully implementing such changes, but they would add a great deal of additional function and value to the rig. If such testing were conducted, the findings could then be compared to those obtained through the modelling approaches described to both compliment and validate the numerical results.

In addition to investigating the erosive effects, the instantaneous impact damage threat posed by larger hailstone impact events could also be explored. Again, alterations would be required to be made to the rig to accommodate the larger hailstone sizes, but such changes would be simple to implement. Impact simulations could again compliment and inform on the testing work, in order to develop a fuller understanding of the damage mechanisms induced. Again, validation of the simulation results through comparison with such experimental results would also imbue greater confidence in accuracy of the modelling approaches.

10.3 Further Flexible Coating Impact Analyses

Significant insight was gained from the modelling work conducted investigating the impact response of flexible coatings under rain droplet impact. However, as discussed in Seciton 6.4.1 there were limitations and simplifications associated with the elastic-plastic based material modelling approach developed. Future work could look to improve on this approach by exploring alternative material models within LS-DYNA which are capable of modelling hyperelasticity and viscoelasticity. However, additional material property data would most likely be required to successfully carry out such work.

Additionally, at the larger scales associated with hailstone impact, the classical FE approach utilised was less suitable. Therefore, further research and exploration into alternative methods of modelling such thin flexible coatings at these scales could provide a more suitable approach. For example, it may be feasible to explore alternate meshing approaches for the flexible coating, representing the coating with mesh free methods such as the SPH approach utilised for the hailstone and rain droplet projectiles.

Given the growing prominence of such flexible coating technologies within the wind industry, such research would be well placed to provide valuable insight into their typical impact response and dominant damage modes under different forms of impact.

10.4 Other Damage Influencing Factors

There are a wide range of other potentially influential factors with respect to the degradation and wear of the leading edge. From the rain erosion test results from industry shown in the literature review, it is clear that the effects of UV exposure cannot be ignored in the context of the long term erosion resistance performance of blade materials. In almost all cases found in the literature, exposure to UV light markedly degraded the long term wear performance of the respective blade materials. In an experimental context it would be feasible to examine the effects of UV exposure on erosion/impact performance through pre-test exposure of the relevant samples to a UV light source; as performed in other studies. In the context of including the material property degrading effects of UV exposure in future modelling work, this would also be feasible given the availability or determination of the relationship between the length of exposure and the degradation of the key material properties. These degraded material properties could be implemented in the modelling work to determine their influence on the impact response of the materials to the different forms of impact.

Similarly, the effects of salinity, humidity and temperature could also be investigated through the similar approaches. However, there is obviously a strong need to first understand the typical conditions of the environment within which the blade is situated upon which the experimental and numerical work would be based upon.

Also, in some regions the presence of high concentrations of dust, dirt or insects in the operational environment may pose a significant threat to the material integrity of the blade leading edge. Many of the modelling approaches developed herein could quite easily be adapted to investigate the effects of impingement from these forms of airborne particulates on the leading edge.

10.5 Probability Analyses

A clearer understanding of both the impact dynamics and related damage mechanisms associated rain droplet and hailstone impact have been developed. However, in order to fully understand the consequences of these findings in the context of damage to the blade over its lifetime, it would also be helpful to better understand the probability and frequency with which such forms of impact occur. Combining such predictions with the predicted accumulated damage associated with such impact events, would make it possible to better predict erosion rate and probable blade service life; before repair is required.

10.6 Related Studies

As alluded to previously, given the appropriate blade erosion field data, a great number of different research activities could be conducted to better understand the phenomenon of blade erosion. However, such data would also make a wide range of other, less technical but broader, tangential studies possible too. Of most interest to the key stakeholders within the wind industry, would be research aimed at better understanding the economic and cost aspects related to the phenomenon of blade leading edge erosion; wind turbines are most commonly intended to be profit making devices. Given enough appropriate data, in depth analyses could be conducted to estimate the costs associated with the occurrence of blade erosion as a result of power losses and corrective maintenance. Further to this, cost benefit analyses could also be conducted to evaluate the effectiveness of strategies such as: additional leading edge protection, preventative maintenance and tip speed curtailment during extreme weather events. Additionally, given the sheer number of operational wind turbines now commissioned globally, in many regions the issue of blade erosion will be a significant factor in the operation and maintenance strategies (O&M) of owners and operators; made more complex owing to the currently developing and evolving understanding of the issue.

11. Conclusion

At the start of the current research programme, the issues of wind turbine blade leading edge erosion was sparsely cited or elaborated upon in the public domain. What detail was available was restricted to: first-hand accounts through industrial interaction, anecdotal evidence in the form photographs of erosion in industry periodicals, and footnotes and brief citations in research papers discussing related but separate issues.

Currently, there is now a more widespread and open recognition of the issue within the wind industry, resulting primarily from the recorded prevalence of leading edge erosion across many large wind turbine fleets; threatening turbine profitability, structural integrity and effecting the longer term O&M strategies of many stakeholders.

However, the original lack of information and publications on the issues presented a challenge in effectively identifying and targeting the most appropriate area of research to target. As a result, it was decided that the most suitable area of research lay within investigating and better understanding the core behaviour in a study of the impact dynamics and damage mechanisms associated with both rain droplet and hailstone impact; identified as two of the most potentially erosive environmental influences.

Despite the absence of experimental verification, significant insight into the phenomenon of liquid droplet impact on solid surface was gained through numerical simulation within LS-DYNA; validated against analytical models and experimental findings, both found in in the literature. The methods developed to simulate such water droplet impact phenomena were then used to investigate the associated impact response of typical wind turbine blade materials. From this, the key rain impact induced damage mechanisms associated with both classical gelcoat materials and newer flexible coating systems were identified and discussed. Namely, surface degradation and erosion was found to be the key issue for classical gelcoat materials, and bonding and substrate interface issues were identified for the newer flexible coating materials.

A combined numerical-investigation of the phenomenon of hailstone impact on the leading edge of a wind turbine was conducted to assess both the associated erosive and substrate damaging effects of such exposure. The numerical results obtained for hailstone impact on the modelled blade could not be validated experimentally as a result of insufficient damage creation in the experimentally tested sample; for the limited hailstone diameter of 10mm. However, through utilising ceramic beads with identical diameters but significantly increased mass it was possible to experimentally assess the effects of significantly increased

impact energies (equal to a 15mm diameter hailstone) on the impact response of the manufactured blade sample. The results of this experimental work were then used to qualitatively validate many aspects of the modelling methods employed.

The findings of the hailstone impact investigations were that the forces and stress imparted to the blade materials through such impact events were significantly larger than those associated with rain droplet impact. Subsequently, it was predicted that the erosive influence of hailstone impact will be significantly greater than that of rain droplet impact. However, the impact frequency associated with such impacts is obviously highly variable between regions and almost exclusively considerably lower than that of rain droplet impact. Therefore, there are real challenges with respect to fully separating the erosive threat posed by each form of impact in regions where both are common.

The hailstone impact modelling and experimental work also indicated that given a sufficient diameter, hailstone impact may also pose a real threat with respect to the instantaneous creation of damage in wind turbine blade leading edge materials. Significant substrate laminate and interlaminate damage were observed both experimentally and in modelling results obtained for hailstones of significant size.

In addition, significant insight into the impact mechanics and damage mechanisms associated with both rain droplet and hailstone impact on the leading edge of wind turbine blades has been developed. However, it is recognised that there are still a wide range of potential future research activities which could further elucidate the issue of wind turbine blade leading edge erosion for the industry at large. Indeed, central to making much of the proposed further research possible is the requirement for heightened collaboration and data availability within the wind industry.

It is clear then that wind turbine blade leading edge erosion is an ever growing concern within the industry, and that the current understanding of the problem is still in the formative stages of development. Encouragingly, many leading material solution specialist companies now provide a range of leading edge protection solutions; spurred on by the recognition of a strong technological need. However, it is clear from the test results detailed and discussed previously in the literature review for the various leading edge protection products, that as of yet there is no full proof material technology which can guarantee against leading edge erosion over the lengthy lifetime of most blades. Further related research on the issue, coupled with improved industrial test standards, may assist in moving towards creating such a material solution. However, it may be the case that given the extreme operational

requirements of modern blades, coupled with a hostile operating environment, that a cost effective and technically sound full proof solution is not possible. Provided with such an eventuality, the industry will therefore need to move towards developing/employing the best available material solutions, whilst altering and improving the applied O&M strategies.

The modelling methodologies developed in the current work provide a valuable tool and pathway, to gaining an essential understanding of the impact response of any proposed blade leading edge design. The methodology possesses great flexibility, making it possible to adapt the inputs to consider the impact response of a wide range of material choices, laminate layup configurations and blade profile topologies.

12. References

[1] European Commission, “Europe 2020,” 2014. [Online]. Available: http://ec.europa.eu/europe2020/index_en.htm.

[2] Global Wind Energy Council, “Global wind statistics 2012,” 2013.

[3] The European Wind Energy Association, “Wind in power - 2012 European statistics,” 2013.

[4] The European Wind Energy Assoiation, “EWEA,” 2012. [Online]. Available: www.ewea.org. [Accessed February 2013].

[5] European Environment Agency, “North Sea physiography (depth and main currents),” 2005. [Online]. Available: http://www.eea.europa.eu/data-and-maps/figures/north-sea-physiography-depth-distribution-and-main-currents. [Accessed 2013].

[6] Garrad Hassan and Partners Ltd, “Measurement Offshore,” [Online]. Available: http://www.wind-energy-the-facts.org/en/part-i-technology/chapter-5-offshore/wind-resource-assessment-offshore/measurement-offshore.html. [Accessed 2013].

[7] The Crown Estate, “The Crown Estate,” 2013. [Online]. Available: www.thecrownestate.co.uk.

[8] H. d. Rooijen, “UK offshore wind report 2012,” The Crown Estate, 201.

[9] BiGGAR Economics, “Onshore wind - direc & wider economic impacts,” Department of Energy and Climate Change & RenewableUK, 2012.

[10] N. Dalili, A. Edrisy and R. Carriveau, “A review of surface engineering issues critical to wind turbine performance,” Renewable and Sustainable Energy Reviews, vol. 13, pp. 428-438, 2009.

[11] T. Burton, D. Sharpe, N. Jenkins and E. Bossanyi, Wind Energy Handbook, Chichester: John Wiley & Sons, 2001.

[12] G. C. Putnam, Power from the wind, New York: Van Nostrand Rheinhold, 1948.

[13] J. Paska, M. Salek and T. Surma, “Current status and perspectives of renewable energy sources in Poland,” Renewable and Sustainable Energy Reviews, vol. 13, no. 1, pp. 142-154, 2009.

[14] D. Quarton, Wind energy technology and the research challenge, Glasgow: Wind Energy Centre for Doctoral Training Inaugural Seminar: FutureWind, 2013.

[15] G. L. Johnson, Wind Energy Systems, Kansas State University, 2006.

[16] R. Gasch and J. Twele, Wind Power Plants: Fundamentals, Design, Construction and Operation, Springer, 2012.

[17] Gurit, “Wind Energy Hand Book,” 2013. [Online]. Available: http://www.gurit.com/wind-energy-handbook-1.aspx. [Accessed 2013].

[18] “Specific Stiffness - Specific Strength,” [Online]. Available: http://www-materials.eng.cam.ac.uk/mpsite/interactive_charts/spec-spec/NS6Chart.html. [Accessed August 2011].

[19] Gurit, “Guide to Composites,” 2011. [Online]. Available: http://www.gurit.com/guide-to-composites.aspx. [Accessed August 2011].

[20] F. L. Matthews and R. R. D, Composite Materials: Engineering and Science, Woodhead Publishing, 1999.

[21] J. L. Mishnaevsky, P. Brøndsted, R. Mijssen, D. J. Lekou and T. P. Philippidis, “Materials of large wind turbine blades: recent results in testing and modelling,” Wind Energy, vol. 15, no. 1, pp. 83-97, 2011.

[22] K. J. Jackson, M. D. Zuteck, C. P. van Dam, K. J. Standish and D. Berry, “Innovative design approaches for large wind turbine blades,” Wind Energy, vol. 8, no. 2, pp. 141-171, 2004.

[23] NAFEMS, Composites in FEA, Sect.1 ed., vol. 1.1, 2011.

[24] Solid Works, “Ply Angle,” 1195-2011. [Online]. Available: http://help.solidworks.com/2011/English/SolidWorks/cworks/LegacyHelp/Simulation/CompositeShells/Ply_Angle.htm. [Accessed August 2011].

[25] P. Hogg, Wind Turbine Blade Materials, Loughborough, 2010.

[26] O. T. Thomsen, “Sanwich Materials for Wind Turbine Blades - Present and Future,” Journal of Sandwich Structures and Materials , vol. 11, no. 7, pp. 7-25, January 2009.

[27] The Fibre Reinforced Plastic & Composite Technology Resource Centre, December 2010. [Online]. Available: http://www.blogger-index.com/feed182957.html.

[28] O. T. Thomsen, “Sandwich materials for wind turbine blades - present and future,” Journal of Sandwich Structures and Materials, vol. 11, 2009.

[29] K. v. Rijswijk and B. Harald, “Thermoplastic Composite Wind Turbine,” in Dutch Wind Workshops,

Delft, 2006.

[30] Gurit, “Gurit,” [Online]. Available: www.gurit.com. [Accessed March 2013].

[31] Siemens, “Wind Turbine with Record-Breaking Rotors,” 2013. [Online]. Available: http://www.siemens.com/innovation/en/news/2012/e_inno_1223_2.htm. [Accessed 2013].

[32] Enercon, “E48 Ideal machine for any site,” 2013. [Online]. Available: http://www.enercon.de/en-en/492.htm. [Accessed 2013].

[33] Gamesa, “Wind Turbines,” 2010. [Online]. Available: http://www.gamesacorp.com/en/products-and-services/wind-turbines/gamesa-g97-20-mw-iiia-en.html. [Accessed 2013].

[34] LM Wind Power, “We Understand How Our Blades Perrform,” [Online]. Available: www.lmwindpower.com/Rotor-Blades/Technology/Materials. [Accessed 2013].

[35] SandwichPanels.org, 2007. [Online]. Available: http://www.sandwichpanels.org/articles/article_thermoplasticresin.html.

[36] K. Azouaoui, Z. Azari and G. Pluvinage, “Evaluation of impact fatigue damage in glass/epoxy composite laminate,” International Journal of Fatigue, vol. 32, pp. 443-452, 2010.

[37] S. J. Pickering, “Recycling technologies for thermoset composite materials—current status,” Composites Part A: Applied Science and Manufacturing, vol. 37, pp. 1206-1215, 2006.

[38] M. Favaloro, 2011. [Online]. Available: http://www.ticona.com/home/beta_homepage/beta_composites/composites_paper_contreinaircraft.pdf.

[39] Eire Composites, 2011. [Online]. Available: http://www.eirecomposites.com/Thermoplastic_Composites_Explained.asp.

[40] Fiber Forge, 2011. [Online]. Available: http://www.fiberforge.com/thermoplastic-composites/thermoplastic-composite-materials.php.

[41] J. L. Thomason and G. E. Schoolenberg, “An investigation of glass fibre/polypropylene interface strength and its effect on composite properties,” Composites, vol. 25, no. 3, p. 197, 1994.

[42] Sustainable Energy Authority of Ireland, “GreenBlade Project,” [Online]. Available: http://www.seai.ie/Grants/Renewable_Energy_RD_D/Projects_funded_to_date/Wind/Greenblade_Project/. [Accessed 2014].

[43] O. Gunneskov, V120-4.5MW Leadership in Offshore, 2004.

[44] Gamesa, “Manufacturing and Assembly Process,” 2010. [Online]. Available: http://www.gamesacorp.com/en/products-and-services/wind-turbines/design-and-manufacture/manufacturing-and-assembly-process.html. [Accessed 2013].

[45] Department of Mechanical Engineering, Wichita State University, UV Degradation Prevention on Fibre-Reinforced Composite Blades, 2009.

[46] B. G. Kumar, R. P. Singh and T. Nakamura, “Degradation of Carbon Fibre-reinforced Epoxy Composites byUltraviolet Radiation and Condensation,” Journal of Composite Materials, vol. 36, no. 24, pp. 2713-21, 2002.

[47] Z. Barnes, “Offshore Wind - Opportunities for the composites industry,” May 2011. [Online]. Available: http://www.bvgassociates.co.uk/LinkClick.aspx?fileticket=ATY-pZn0xqQ%3D&tabid=102.

[48] Engineers Hand Book, 2004-2006. [Online]. Available: http://www.engineershandbook.com/MfgMethods/polyurethanecoatings.htm.

[49] Gallagher Corporation, 2011. [Online]. Available: http://www.gallaghercorp.com/urethane/benefits-of-castable-urethane.shtml.

[50] Enercon, July 2010. [Online]. Available: http://www.enercon.de/p/downloads/EN_Eng_TandS_0710.pdf.

[51] M. D. Haag, “Advances in leading edge protection of wind turbine blades,” in European Wind Energy Conference, Vienna, 2013.

[52] 3M, “3M™ Wind Blade Protection Coating W4600,” 2013. [Online]. Available: http://solutions.3m.com/wps/portal/3M/en_US/Wind/Energy/Products/Coatings/.

[53] 3M, “3M.com,” 2012. [Online]. Available: http://multimedia.3m.com/mws/mediawebserver?mwsId=66666UF6EVsSyXTtoXT6l8T2EVtQEVs6EVs6EVs6E666666--&fn=WindErosionControlBrochure_DMR_9. [Accessed March 2013].

[54] 3M, 2010. [Online]. Available: http://multimedia.3m.com/mws/mediawebserver?mwsId=SSSSSu7zK1fslxtUOxmS5x_Zev7qe17zHvTSevTSeSSSSSS--&fn=WindTapesBroch_DMR.pdf.

[55] University of Dayton Research Institute, 2011. [Online]. Available: http://www.udri.udayton.edu/NONSTRUCTURALMATERIALS/COATINGS/Pages/RainErosionTestFacility.aspx.

[56] P. Brøndsted, H. Lilholt and A. Lystrup, “Composite materials for wind power blades,” Annu. Rev. Mater. Res., vol. 35, pp. 505-38, 2005.

[57] Siemens, “Wind Turbines - Blades,” 2002-2011. [Online]. Available: http://www.energy.siemens.com/mx/en/power-generation/renewables/wind-power/wind-turbines/#content=Technology. [Accessed 2013].

[58] D. S. Cairns, T. Riddle and J. Nelson, “Wind turbine composite blade manufacturing: the need for understanding defect origins, prevalence, implicactions and reliability,” Sandia National Laboratories, Albuquerque, 2011.

[59] M. H. Keegan, D. H. Nash and M. M. Stack, “Modelling Rain Drop Impact of Offshore Wind Turbine Blades,” in TURBO EXPO 2012, Copenhagen, 2012.

[60] M. H. Keegan, D. Nash and M. Stack, “Numerical modelling of hailstone impact on the leading edge of a wind turbine blade,” in EWEA, Vienna, 2013.

[61] M. H. Keegan, D. H. Nash and M. M. Stack, “On erosion issues associated with the leading edge of wind turbine blades,” Jounral of Physics D: Applied Physics, vol. 46, 2013.

[62] K. Wood, “Blade repair: Closing the maintenance gap,” Composites Technology, April 2011.

[63] L. Rempel, “Rotor blade leading edge erosion - real life experiences,” Wind Systems Magazine, October 2012.

[64] TGM Services, 2011. [Online]. Available: http://tgmwind.com/bladeerosion.html#bladeerosion.

[65] Henkel, “Henkel,” 2013. [Online]. Available: http://www.henkelna.com/industrial/blade-maintenance-19836.htm. [Accessed March 2013].

[66] R. Karmouch and G. G. Ross, “Superhydrophobic wind turbine blade surfaces obtained by a simple deposition of silica nanoparticles embedded in epoxy,” Applied Surface Engineering, vol. 257, pp. 665-669, 2010.

[67] F. Sayer, F. Bürkner, B. Buchholz, M. Stobel, A. M. van Wingerde, H.-G. Busmann and H. Seifert, “Influence of a wind turbine service life on the mechanical properties of the material and the blade,” Wind Energy, vol. 16, pp. 163-174, 2013.

[68] Wind Turbine Models, “DFVLR DERBA-25,” 2013. [Online]. Available: http://en.wind-turbine-models.com/turbine/429/dfvlr/debra-25. [Accessed 2013].

[69] Climatic Research Unit, “Climatic Research Unit - University of East Anglia,” 2013. [Online].

[70] Global Energy Services, “GES - Global Energy Services,” [Online]. Available: http://www.services-ges.com/. [Accessed 2013].

[71] T. Zander, “Benefits of a long-term blade service strategy,” in Wind Power Monthly - Blade Inspection, Damage and Repair, Hamburg, 2013.

[72] M. D. Haag, Interviewee, Private Communication. [Interview]. October 2013.

[73] Polytech, “Polytech Rain Erosion,” 2012. [Online]. Available: www.rainerosion.com. [Accessed April 2013].

[74] 3M, 2011. [Online]. Available: http://catalogue.3m.eu/en_EU/eu-wind/Tapes/3M%E2%84%A2_Wind_Protection_Tapes_and_Accessories.

[75] S. Powell, “3M wind blade protection coating W4600,” in Industrial Presentation, 2011.

[76] University of Dayton Research Institute, 2011. [Online]. Available: http://www.udri.udayton.edu/NONSTRUCTURALMATERIALS/COATINGS/Pages/RainErosionTestFacility.aspx.

[77] C. E. Claus, “Effects of leading edge erosion on wind turbine efficiency & innovative erosion protection solutions,” in Wind Power Monthly - Blade Inspection, Damage and Repair, Hamburg, 2013.

[78] W. D. Weigel, “Advanced rotor blade erosion protection system,” Kaman Aerospace Corporation, Bloomfield, 1996.

[79] O. Gohardani, “Impact of erosion testing aspects on current and futute flight conditions,” Progress in Aerospace Sciences, vol. 47, pp. 280-303, 2011.

[80] C. W. Huang, K. Yang, Q. LIU, L. Zhang, J. Y. Bai and J. Z. Xu, “A study on performance influences of airfoil aerodynamic parameters and evaluation indicators for the roughness sensitivity on wind turbine blade,” Technological Sciences, vol. 54, no. 11, pp. 2993-2998, 2011.

[81] A. Sareen, S. A. Chinmay and M. S. Selig, “Effect of leading edge erosion on wind turbine blade performance,” Wind Energy, vol. Online, 2013.

[82] S. Chinmay, “Turbine blade erosion and the use of wind protection tape,” University of Illinois, Champaign, 2012.

[83] 3M, “A 3M study is the first to show the effects of erosion on wind turbine efficiency,” 5 September

2011. [Online]. Available: http://www.pressebox.com/pressrelease/3m-deutschland-gmbh/A-3M-Study-Is-the-First-to-Show-the-Effects-of-Erosion-on-Wind-Turbine-Efficiency/boxid/445007.

[84] V. Karkkolainen, "Extending the lifetime of a blade through preventative maintenance," in Blade Inspection, Damage and Repair Forum, Hamburg, 2013.

[85] M. E. Calvert, T. C. Wong and O. J. A, "Blade contour deformation and helicopter performance," in AIAA Applied Aerodynamics Conference 2, San Francsisco, 2006.

[86] M. M. Shokreih and A. Bayat, "Effects of ultraviolet radiation on mechanical properties of glass/polyester composites," Composite Materials, vol. 41, no. 20, pp. 2443-2455, 2007.

[87] B. G. Kumar, R. P. Singh and T. Nakamura, "Degradation of carbon fiber-reinforced epoxy composites by ultraviolet radiation and condensation," Composite Materials, vol. 36, no. 24, pp. 2713-2733, 2002.

[88] B. Faulkner, "Post warranty maintenance - evaluating the options," in Wind Power Monthly - Blade repair, inspection and maintenance, Hamburg, 2013.

[89] DNV GL, "DNV GL," [Online]. Available: www.dnvgl.com. [Accessed 2014].

[90] Germanischer Lloyd, "Rules for Classification and Construction - II Materials an Welding," Germanischer Lloyd Aktiengesellschaft, Hamburg, 2006.

[91] Bladefence, "Bladefence," [Online]. Available: www.bladefence.com. [Accessed 2014].

[92] Met Office, "Met Office - UK mapped climate averages," 2013. [Online]. Available: http://www.metoffice.gov.uk/climate/uk/averages/ukmapavge.html. [Accessed March 2013].

[93] G. Elert, 2001. [Online]. Available: http://hypertextbook.com/facts/2001/IgorVolynets.shtml.

[94] E. Villermaux and B. Bossa, "Single-drop fragmentation determines size of distribution of raindrops," Nature Physics, vol. 5, pp. 697-702, 2009.

[95] A. Kubilay, D. Derome, B. Blocken and J. Carmeliet, "CFD simulation and validation of wind driven rain on a building facade with an Eulerian multiphase model," Building and environment, vol. 61, pp. 69-81, 2013.

[96] A. C. Best, "The size distribution of raindrops," Q J R Meteorological Soc, vol. 76, pp. 16-36, 1950.

[97] R. Gunn and G. D. Kinzer, "The terminal velocity of fall for water droplets in stagnant air," Journal of Meteorology, vol. 6, pp. 243-248, 1949.

[98] F. J. Heymann, "High-speed impact between a liquid drop and a solid surface," Journal of Applied Physics, vol. 40, no. 13, pp. 5113-5122, December 1969.

[99] J. P. Dear and J. E. Field, "High-speed photography of surface geometry effects in liquid/solid impact," Journal of Applied Physics, vol. 63, no. 4, pp. 1015-1021, Februaru 1988.

[100] D. Bartolo, C. Josserand and D. Bonn, "Singular jets and bubbles in drop impact," Physical review letters, vol. 96, no. 124501, 2006.

[101] J. E. Field, J. P. Dear and J. E. Ogren, "The effects of target compliance on liquid drop impact," Physics and Chemistry of Solids, vol. 65, no. 533, pp. 533-40, 1989.

[102] R. Li, H. Ninokata and M. Mori, "A numerical study of impact force caused by liquid droplet impingment onto a rigid wall," Progress in Nuclear Energy, vol. 53, no. 7, pp. 1-5, 2011.

[103] A. C. Imeson, R. Vis and E. de Water, "The measurement of water-drop impact forces with a piezo-electric transducer," CATENA, vol. 8, no. 1, pp. 83-96, 1981.

[104] M. A. Nearing, J. M. Bradford and R. D. Holtz, "Measurement of Force vs. Time Relations for Waterdrop Impact," Soil Science Society of America Journal, vol. 50, no. 6, pp. 1532-1536, November-December 1986.

[105] N. Du and G. Elert, "hypertextbook," 2000. [Online]. Available: http://hypertextbook.com/facts/2000/NickyDu.shtml. [Accessed April 2013].

[106] J. P. Dear and J. E. Field, "High-speed photography of surface geometry effects in liquid/solid impact," Journal of Applied Physics, vol. 63, no. 4, pp. 1015-1021, February 1988.

[107] W. F. Adler and S. V. Hooker, "Rain erosion mechanisms in brittle materials," Wear, vol. 50, pp. 11-38, 1978.

[108] D. A. Gorham, M. J. Matthewson and J. E. Field, "Damage mechanisms in polymers and composites under high-velocity liquid impact," Mechanisms in polymers and composites under high-velocity liquid impact, pp. 320-342, 1979.

[109] A. G. Evans, G. M. E, E. G. E and R. M, "Impact damage in brittle materials in the plastic response regime," Rockwell International Science Center, 1976.

[110] A. J. D, Wave propagation in elastic solids, North Holland, 1973.

[111] M. F. Ashby, H. Shercliff and D. Cebon, Materials: Engineering, Science, Processing and Design, Butterworth-Heinemann, 2007.

[112] ASTM, “ASTM G73 - 10 "Standard Test Method for Liquid Impingement Erosion Usind Roatating Apparatus",” ASTM, 2013.

[113] J. Zahavi and S. Nadiv, “Indirect damage in composite materials due to raindrop impact,” Wear, vol. 72, pp. 305-313, 1981.

[114] E. Tobin, 2011. [Online]. Available: http://www2.ul.ie/pdf/305950313.pdf.

[115] E. F. Tobin, T. M. Young, R. D and O. Rohr, “Comparison of liquid impingement results from whirling arm and water-jet erosion test facilities,” Wear, vol. 271, pp. 2625-2631, 2011.

[116] E. F. Tobin, T. M. Young and D. Raps, “Evaluation and correlation of interlaboratory results from rain erosion test campaign,” in International Congress of the Aeronautical Sciences, Brisbane, 2012.

[117] EADS, “EADS,” [Online]. Available: www.eads.com. [Accessed 2013].

[118] ISO/DIN, “ISO/TC 35/SC 9/WG 32 Coating materials for wind-turbine rotor blades and tidal-stream-driven rotor blades,” [Online]. Available: http://www.nab.din.de/cmd?level=tpl-untergremium-home&languageid=en&subcommitteeid=179308215. [Accessed 2014].

[119] The Irish Meteorological Service , “met.ie,” 2013. [Online]. Available: http://www.met.ie/climate/30year-averages.asp. [Accessed April 2013].

[120] Met Office, “What is Precipitation?,” 2013. [Online]. Available: http://www.metoffice.gov.uk/learning/rain/what-is-precipitation.

[121] Allen Press, 2012. [Online]. Available: http://amsglossary.allenpress.com/glossary/search?id=hail1.

[122] Wikimedia Commons, November 2009. [Online]. Available: http://commons.wikimedia.org/wiki/File:Hagelkorn_mit_Anlagerungsschichten.jpg.

[123] TORRO, “H,” 2011. [Online]. Available: http://www.torro.org.uk/site/hscale.php.

[124] P. R. Field, W. Hand, G. Cappelluti and M. A, “Hail Threat Standardisation,” Met Office & Qinetiq, 2010.

[125] S. E. M, “Brittle failure of ice,” Engineering Fracture Mechanics, vol. 68, pp. 1839-1887, 2001.

[126] P. V. F and W. R. W, Physics of Ice, Oxford UP, 1999.

[127] E. M. Schulson, “Brittle failure of ice,” Engineering Fracture Mechanics, vol. 68, pp. 1839-1887, 2001.

[128] K. S. Carney, D. J. Benson, P. DuBois and R. Lee, “A phenomenological high strain rate model with failure for ice,” International Journal of Solids and Structures, vol. 43, pp. 7820-7839, 2006.

[129] M. Shazly, V. Prakash and B. Lerch, “High strain rate compression testing of ice,” NASA TM-2005-213966, 2005.

[130] H. Hertz, “Ueber die Beruhrung fester elastischer Korper (On the contact of rigid elastic solids),” J. reine und angewandte Mathematik, vol. 92, no. 1986.

[131] Georgia State University, Last accessed: 2012. [Online]. Available: http://hyperphysics.phy-astr.gsu.edu/hbase/airfri2.html.

[132] H. Kim, D. Welch and K. Kedward, “Experimental Investigation of High Velocity Ice Impacts on Woven Carbon/Epoxy Composite Panels,” Composites Part A: Applied Science and Manufacturing, vol. 34, no. 1, pp. 25-41, 2003.

[133] H. Kim and K. T. Kedward, “Modelling Hail Ice Impact and Predicting Impact Damage Initiation in Composite Structures,” AIAA Journal, vol. 38, no. 7, pp. 1278-1288, July 2000.

[134] BladeCleaning, “BladeCleaning,” [Online]. Available: http://www.bladecleaning.com/. [Accessed 2013].

[135] V. S. Kumar, N. J. Vasa and R. Sarathi, “Detecting salt deposition on a wind turbine blade using laser induced breakdown spectroscopy technique,” Applied Physics A, 2012.

[136] T. Naka, N. J. Vasa, S. Yokoyama, A. Wada and S. Arinaga, “Experimental studies of lightning protection design for wind turbine blades,” in European Wind Energy Conference, Athens, 2006.

[137] The Engineering Tool Box, “Salinity of Water,” 2013. [Online]. Available: http://www.engineeringtoolbox.com/water-salinity-d_1251.html. [Accessed 2013].

[138] M. Takaffoli and M. Papini, “Numerical simulation of solid particle impacts on Al6061-T6 Part II: Materials emoval mechanisms for impact of multiple angular particles,” Wear, vol. 296, no. 1-2, pp. 648-655, 2012.

[139] P.-T.-S. Phan and S.-C. Huang, “Analysis of material loss from brittle erosion,” Journal of Engineering Technology and Education, vol. 5, pp. 141-155, 2008.

[140] P. Balu, F. Kong, S. Hamid and R. Kovacevic, “Finite element modeling of solid particle erosion in AISI 4140 steel and nickel-tungsten carbide composite material produced by the laser-based powder deposition process,” Tribology International, vol. 62, pp. 18-28, 2013.

[141] D. Aquaro, “Erosion rate of stainless steel due to the impact of solid particles,” in International Conference on Tribology, Parma, 2006.

[142] M. S. ElTogby, E. Ng and M. A. Elbestawi, “Finite element modeling of erosive wear,” International Journal of Machine Tools & Manufacture, vol. 45, pp. 1337-1346, 2005.

[143] G. Prayogo, H. Homma, T. P. Soemardi and A. S. Danardono, “Impact fatigue damage of GFRP materials due to repeated raindrop collisions,” Transactions of the Indian Institute of Metals, vol. 64, pp. 501-506, 2011.

[144] G. Zhou, “Effect of impact damage on residual compressive strength of glass-fibre reinforce polyester (GFRP) laminates,” Composite Structures, vol. 35, pp. 171-181, 1996.

[145] T. Yuanjian and D. H. Isaac, “Combined impcact and fatigue of glass fiber reinforced composites,” Composites: Part B, vol. 39, pp. 505-512, 2008.

[146] K. W. Kang, J. K. Kim and H. S. Kim, “Fatigue behaviour of impacted plain-weave glass/epoxy composites under tensile fatigue loading,” Key Engineering Materials, Vols. 297-300, pp. 1291-1296, 2005.

[147] ANSYS Inc., “ANSYS,” [Online]. Available: www.ansys.com. [Accessed 2013].

[148] ANSYS Inc., “ANSYS Explicit STR,” [Online]. Available: http://www.ansys.com/Products/Simulation+Technology/Structural+Mechanics/Explicit+Dynamics/ANSYS+Explicit+STR. [Accessed 2013].

[149] ANSYS Inc, “ANSYS Workbench Platform,” [Online]. Available: http://www.ansys.com/Products/Workflow+Technology/ANSYS+Workbench+Platform. [Accessed 2013].

[150] ANSYS Inc., “ANSYS Autodyn,” [Online]. Available: http://www.ansys.com/Products/Simulation+Technology/Structural+Mechanics/Explicit+Dynamics/ANSYS+AUTODYN. [Accessed 2013].

[151] ANSYS Inc., “ANSYS LS-DYNA,” [Online]. Available: http://www.ansys.com/Products/Simulation+Technology/Structural+Mechanics/Explicit+Dynamics/ANSYS+LS-DYNA. [Accessed 2013].

[152] Livermore Software Technology Corporation, “LS-DYNA - About,” 2011. [Online]. Available: http://www.lstc.com/products/ls-dyna. [Accessed 2013].

[153] Livermore Software Technology Corporation, “About LS-PrePost,” [Online]. Available: http://www.lstc.com/lspp/. [Accessed 2013].

[154] M. R. Jensen, Introduction to LS-DYNA Implicit, LS-DYNA.

[155] LS-DYNA, “Elements,” [Online]. Available: http://www.dynasupport.com/tutorial/ls-dyna-users-guide/elements. [Accessed 2013].

[156] M. Anghileri, L. M. L. Castelletti, F. Invernizzi and M. Mascheroni, “A survey of numerical models for hail impact analysis using explicit finite element codes,” International Journal of Impact Engineering, vol. 31, pp. 929-944, October 2005.

[157] J. L. Lacome, “Smooth Particle Hydrodynamics (SPH): A new feature in LS-DYNA,” in 6th International LS-DYNA Conference, Detroit, 2000.

[158] V. Năstăsescu, “SPH method in applied mechanics,” University Politehcnica of Bucahrest Scientific Bulletin, vol. 72, no. 4, 2010.

[159] J. O. Hallquist, LS-DYNA Theory Manual, California: Livermore Software Technology Corporation, 2006.

[160] T. Sanada, K. Ando and T. Colonius, “Numerical analysis of high speed droplet impact,” in 7th International Conference on Multiphase Flow, Tampa, 2010.

[161] W. F. Adler, “Waterdrop Impact Modelling,” Wear, Vols. 186-187, pp. 341-351, 1995.

[162] Livermore Software Technology Company, “Corporate Profile,” 2011. [Online]. Available: http://www.lstc.com/corporate/profile. [Accessed 2013].

[163] H. A. Salman and R. O. Yıldırım, “Investigation of rain erosion on a brittle material by means of numerical simulation,” Journal of Defense Modeling and Simulation Applications, vol. 9, no. 4, pp. 327-34, 2012.

[164] M. Anghileri, L. M.-L. Castelletti and E. Francesconi, “Water impact: experimental tests and numerical simulations using meshless methods,” in 6th European LS-DYNA Users' Conference, Gothenburg, 2007.

[165] K. E. Jackson and Y. T. Fuchs, “Comparison of ALE and SPH simulations of vertical drop tests of a composite fuselage section into water,” in 10th International LS-DYNA Users Conference, Detroit, 2008.

[166] E. Francesconi and M. Anghileri, “A numerical-experimental investigation on crash behaviour of skin panels during water impact comparing ALE and SPH approaches,” in 7th European LS-DYNA Conference, Salzburg, 2009.

[167] M. Anghileri, L.-M. L. Castelletti, A. Milanese and Semboloni, “Modelling hailstone impact onto

composite material panel under a multi-axial state of stress," in 6th European LS-DYNA Users' Conference, 2007.

[168] Livermore Software Technology Corporation, LS-DYNA Keyword User's Manual - Volume II Material Models, 2012.

[169] R. A. Batto and E. M. Schulson, "On the Ductile-to-Brittle Transition in Ice Under Compression," Act Metallurgica et Materialia, vol. 41, no. 7, pp. 2219-2225, 1993.

[170] E. M. Schulson, "The Brittle Compressive Fracture of Ice," Acta Metallurgica et Materialia, vol. 38, no. 10, pp. 1963-1976, 1990.

[171] M. Mellor, "Mechanical Properties of Polycrystalline Ice," Physics and Mechanics of Ice, pp. 217-245, 1980.

[172] R. G. Thomson and R. J. Hayduk, "An improved analytical treatment of the denting of thin sheets by hail," Washington, 1971.

[173] R. G. Thomson and R. J. Hayduk, "An analytical evaluation of the denting of airplane surfaces by hail," Washington, 1969.

[174] R. A. Brockman and T. W. Held, "Explicit finite element method for transparency impact analysis," Dayton, 1991.

[175] I. I. McNaughton and S. W. Chisman, "A Study of Hail Impact at High Speed on Light Alloy Plates," Farnborough, Hampshire, 1940.

[176] J. D. Tippmann, "Development of a Strain Rate Sensitive Ice Material Model for Hail Ice Impact Simulation," University of California, Thesis, 2011.

[177] J. N. Kuene, "Development of a Hail Ice Impact Model and the Dynamic Compressive Strength Properties of Ice," 2004.

[178] H. Park, "Resistance of Adhesively Bonded Composite Lap Joints to Damage by Transverse Ice Impact," 2006.

[179] V. F. Petrenko and R. W. Whitworth, Physics of Ice, Oxford: Oxford University Press, 1999.

[180] R. Juntikka and R. Olsson, "Experimental and modelling study of hail impact on composite plates," in ICCM 17, Edinburgh, 2009.

[181] Livermore Software Technology Company, "LS-DYNA Keyword User's Manual," 2012.

[182] BASF, "Elastollan®. Shaping the world around you," 2013. [Online]. Available: http://www2.basf.us/urethanechemicals/tpu/img/pdf/Elastollan_Material_PropertiesR1.pdf. [Accessed 2013].

[183] C. Menna, D. Asprone, G. Caprino, V. Lopresto and A. Prota, "Numerical simulation of impact tests on GFRP composite laminates," International Journal of Impact Engineering, vol. 38, no. 8-9, pp. 667-685, August-September 2011.

[184] A. Deb, P. Lakshmanan, D. K. Kharat and S. C. Lakkad, "Composite versus steel rails for vehicle front impact safety," in IMPLAST , Providence, 2010.

[185] F.-K. Chang and K.-Y. Chang, "A progressive damage model for laminated composites containing stress concentrations," Journal of composite materials, vol. 21, pp. 834-855, 1987.

[186] P. Griškevičius, D. Zeleniakienė, V. Leišis and M. Ostrowski, "Experimental and numerical study of impact energy absorption of saftey important honeycomb cor sandwich structures," Material Science, vol. 16, no. 2, pp. 119-123, 2010.

[187] P. Kumrungsie, K. Maneeratana and N. Chollacoop, "Effects of fiber orientation on ballistic impact upon polymer composite plate," in 21st Conference of Mechanical Engineering Network of Thailand, Chonburi, 2007.

[188] W. Cheng and J. Hallquist, "Implementation of three-dimensional composite failure model into DYNA3D," [Online]. Available: http://ftp.lstc.com/anonymous/outgoing/jday/composites/mat_059_Hallquist_Cheng.pdf. [Accessed 2013].

[189] K.-H. Nguyen, J.-H. Ahn, J.-H. Kweon and J.-H. Choi, "Optimization of composite laminates subjected to high velocity impact using a genetic algorithm," International Journal of Aeronautical and Space Science, vol. 11, no. 3, pp. 227-33, 2010.

[190] Livermore Software Technology Corporation, "LS-OPT," [Online]. Available: www.lstc.com/products/ls-opt. [Accessed 2013].

[191] L. L. Peng, X. J. Gong and L. Guillaumat, "Numerical simulation of damage propagation in CFRP laminates repaired by external bonded patched under tensile loading," in 18th International Conference on Composite Materials, Jeju Island, 2011.

[192] J. LeBlanc and A. Shukla, "Dynamic response and damage evolution in composite materials subjected to

underwater explosive loading: An experimental and computational study," Composite Structures, vol. 92, no. 10, pp. 2421-30, 2010.

[193] LS-DYNA Aerospace Working Group, "Modeling Guidelines Document," 2012. [Online]. Available: http://awg.lstc.com/tiki/tiki-index.php. [Accessed 2013].

[194] ANSYS Inc., "ANSYS DesignModeler," 2013. [Online]. Available: http://www.ansys.com/Products/Workflow+Technology/ANSYS+Workbench+Platform/ANSYS+Design Modeler. [Accessed 2013].

[195] LSTC, 2012. [Online]. Available: http://www.lstc.com/lspp/.

[196] LS-DYNA Aerospace Working Group, Sept 2012. [Online]. Available: http://awg.lstc.com/tiki/tiki-index.php?page=QA+test+example+6.

[197] ASM Aerospace Specification Metals Inc., Last accessed Sept 2012. [Online]. Available: http://asm.matweb.com/search/SpecificMaterial.asp?bassnum=MQ304A.

[198] J. Pereira, D. Revilock and M. Melis, "Force measurements in ballistic impact tests with ice projectiles," 2006.

[199] D. T. Griffith and T. D. Ashwill, "The sandia 100-meter all-glass baseline wind turbine blade: SNL100-00," Sandia National Laboratories, Albuquerque, 2011.

[200] Sandia National Laboratories, "Wind Energy," 2013. [Online]. Available: http://energy.sandia.gov/?page_id=344. [Accessed 201].

[201] National Renewable Energy Laboratory, "NREL," 2013. [Online]. Available: www.nrel.gov. [Accessed 2013].

[202] G. Bir and P. Migliore, "Preliminary structural design of composite blades for two and three blade rotors," National Renewable Energy Laboratory, Golden, 2004.

[203] J. Jonkman, S. Butterfield, W. Musial and G. Scott, "Definition of a 5-MW reference wind turbine for offshore system development," National Renewable Energy Laboratory, Golden, 2009.

[204] J. L. Tangler, "The evolution of rotor and blade design," in American Wind Energy Association WindPower, Palm Springs, 2000.

[205] Det Norske Veritas, "DNV," 2013. [Online]. Available: www.dnv.com. [Accessed 2013].

[206] Det Norske Veritas, "Design and manufacture of wind turbine blades, offshore and onshore wind turbines," Det Norske Veritas, 2010.

[207] R. Nijssen, "WMC5MW laminate lay-out of reference blade for WP 3," Project UpWind, Wieringerwerf, 2007.

[208] UpWind, "Welcome UpWind," 2013. [Online]. Available: www.upwind.eu. [Accessed 2013].

[209] V. Çeçen, M. Sarikanat, H. Yildiz and H. T. Ismail, "Comparison of mechanical properties of epoxy composites reinforced with stitched glass and carbon fabrics: characterization of mechanical anisotropy in composites and investigation on the interaction vetween fiber and epoxy matrix," Polymer Composites, vol. 29, no. 8, pp. 840-853, 2008.

[210] Gurit, "PRIME™ 20LV EPOXY INFUSION SYSTEM," 2013. [Online]. Available: http://www.gurit.com/prime-20lv-1.aspx. [Accessed 2013].

[211] Gurit, "PRIME™ 27 PREMIUM EPOXY INFUSION SYSTEM," 2013. [Online]. Available: http://www.gurit.com/prime-27-1.aspx. [Accessed 2013].

[212] Momentive, "EPIKOTE™ Resin MGS® LR 135 and EPIKURE™ Cruing Agent MGS® LH 133-138," 2013. [Online]. Available: http://www.momentive.com/Products/TechnicalDataSheet.aspx?id=8119. [Accessed 2013].

[213] P. D. Soden, M. J. Hinton and A. S. Kaddour, "Laminate properties, lay-up configurations and loading conditions for a range of fibre-reinforced composite laminates," Composite Science and Technology, vol. 58, no. 7, pp. 1011-22, 1998.

[214] J. D. Littel, C. R. Ruggen, R. K. Goldberg, G. D. Robert, W. A. Arnold and W. Binienda, "Measurement of epoxy resin tension, compression and shear-strain curves over a wide range of strain rates using small test specimens," Journal of Aerospace Engineering, vol. 21, no. 3, pp. 162-73, 2006.

[215] ASTM, "Standard test method for tensile properties of plastics," ASTM D638, 2004.

[216] X. Shen, Z. Xia and F. Ellyin, "Cyclic deformation behaviour of an epoxy polymer. Part I: Experimental Investigation," Polymer Engineering and Science, vol. 44, no. 12, 2004.

[217] DNV GL, "Chopped Strand Mat; EMC300, EMC450,," 2014. [Online]. Available: https://exchange.dnv.com/taridocs/TA-CERT/32/eljjaxxx.htm.

[218] Pecolit, "Products - Information - Giella Design," 2014. [Online]. Available: http://gielladesign.com/calvillocomm/images/_notes/3.pdf.

[219] Youngs Corp, “Youngs Corp - Chopped Strand Matt,” 2014. [Online]. Available: http://www.youngscorp.com/bbs/download.php?bo_table=export&wr_id=98&no=0..

[220] Hongkong Elite Industrial Group Limited, “Hongkong Elite Industrial Group Limited - Chopped Strand Mat,” [Online]. Available: http://www.ibuonline.com/productdetail/Chopped-Strand-Mat-CSM/4cb415628906a88337f95402.

[221] S. Banerjee, “Modeling and simulation of solid particle erosion of protective films,” Texas A&M University, Thesis, 2010.

[222] £M, “3M Wind Protection Tapes,” 2013. [Online]. Available: http://solutions.3m.com/wps/portal/3M/en_US/Wind/Energy/Products/Wind_Protection_Tapes/. [Accessed 2013].

[223] 3M, “Scotch-Weld Acrylic Adhesive SA30,” 2013. [Online]. Available: http://catalogue.3m.eu/en_EU/EU-Industrial/3M_Adhesives/Scotch-Weld_Structural_Adhesives/Scotch-Weld%E2%84%A2~Acrylic_Adhesive~SA30/Acrylic_Adhesive.

[224] M. D. Haag, Interviewee, Private Communication. [Interview]. September 2012.

[225] Gurit, “SP 106 Multi-purpose epoxy system,” 2014. [Online]. Available: http://www.gurit.com/sp-106.aspx. [Accessed 2014].

[226] PPG Fiber Glass, “Chopped Strand Mat 92,” 2014. [Online]. Available: http://www.ppg.com/glass/fiberglass/products/Documents/Chopped_Strand_Data_Sheets/CS%20Mat%2092.pdf.

[227] PPG Fiber Glass, “PPG Fiber Glass,” [Online]. Available: http://www.ppg.com/glass/fiberglass/. [Accessed 2014].

[228] Sinoma, “Taishan Fiberglass Inc.,” [Online]. Available: http://en.sinoma.cn/about/200907/211.html. [Accessed 2014].

[229] National Instruments, “NI cDAQ-9178,” 2014. [Online]. Available: http://sine.ni.com/nips/cds/view/p/lang/en/nid/207534.

[230] National Instruments, “LabVIEW System Design Software,” 2014. [Online]. Available: http://www.ni.com/labview/.

[231] RS, “75kg Compression Load Cell,” [Online]. Available: http://uk.rs-online.com/web/p/load-cells/4438213/. [Accessed 2014].

[232] Photron High Spee Cameras, “Legacy Products,” 2014. [Online]. Available: http://www.photron.com/?cmd=products&type=legacy.

[233] LSTC, “LS-PrePost User's Group,” [Online]. Available: http://groups.google.com/group/ls-prepost. [Accessed 2014].

[234] Wind Power Monthly Events, “Blade Inspection, Damage and Repair,” [Online]. Available: http://www.windpowermonthlyevents.com/events/blade-inspection-damage-repair/. [Accessed 2014].

[235] Broadwind Energy, “Broadwind Energy,” 2012. [Online]. Available: http://www.bwen.com/WindTurbineBladeServices_7777.aspx. [Accessed March 2012].

[236] Ropeworks, 2011. [Online]. Available: http://www.ropeworks.com/service_wind_blade.htm.

Appendix I – Sensitivity study: Hailstone SPH node total

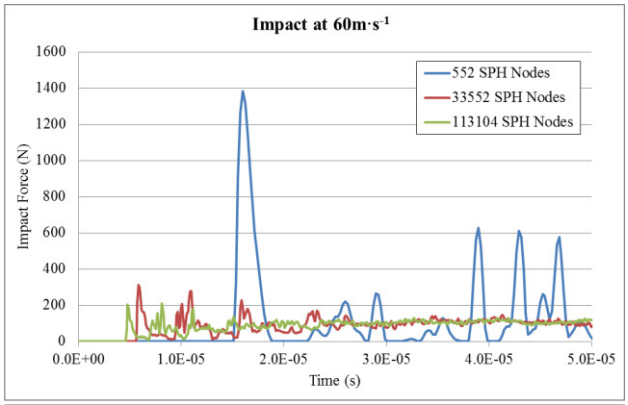

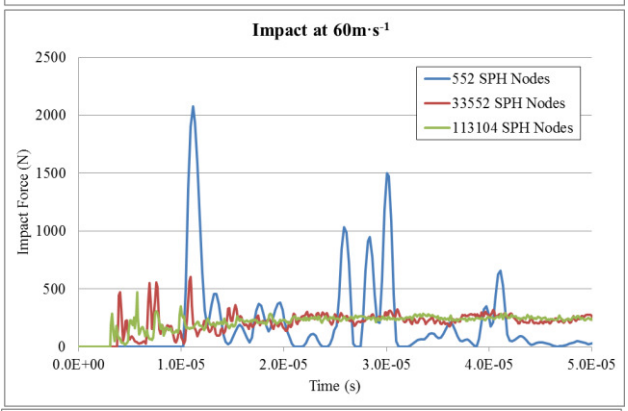

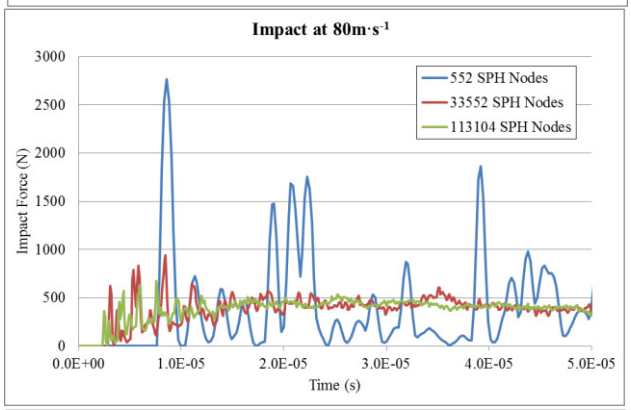

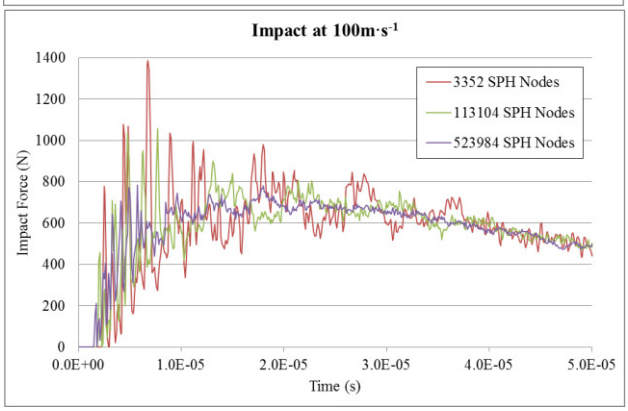

Appendix II – Sensitivity study: Gelcoat target mesh sensitivity

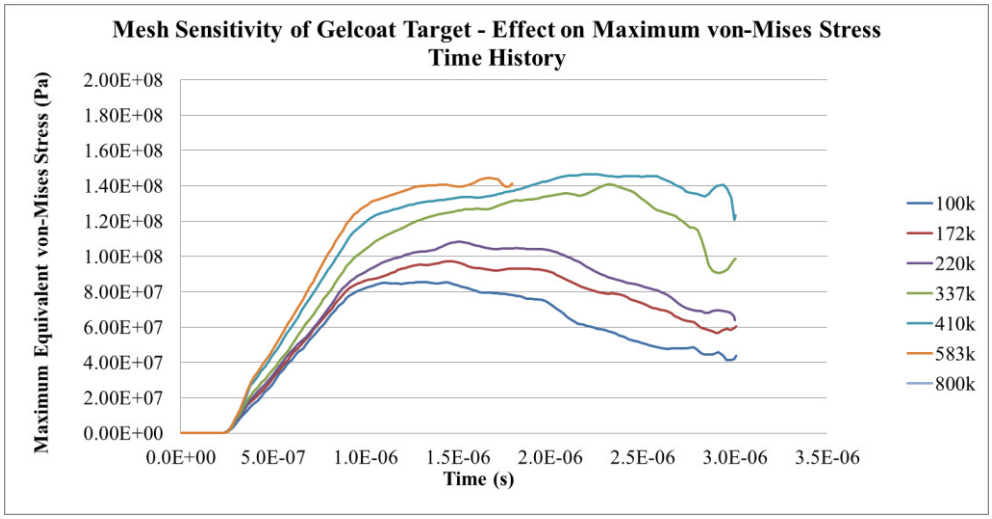

Appendix III – Sensitivity Study: W4600 target mesh sensitivity

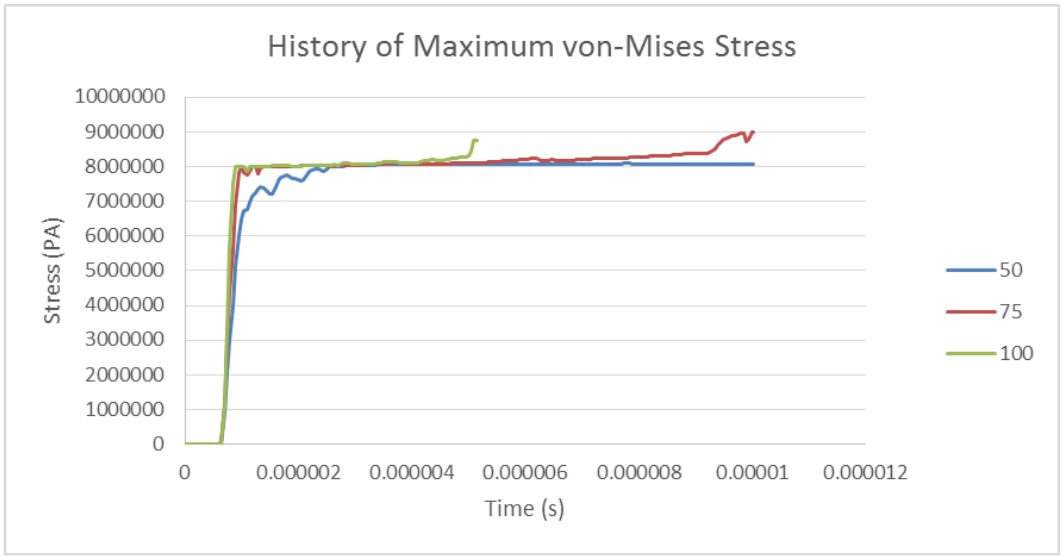

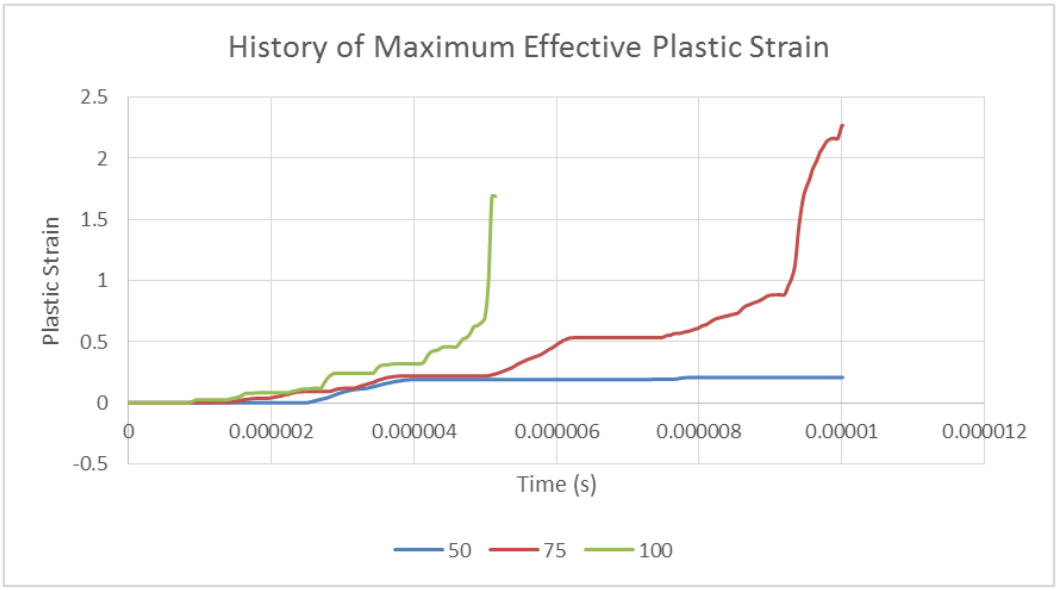

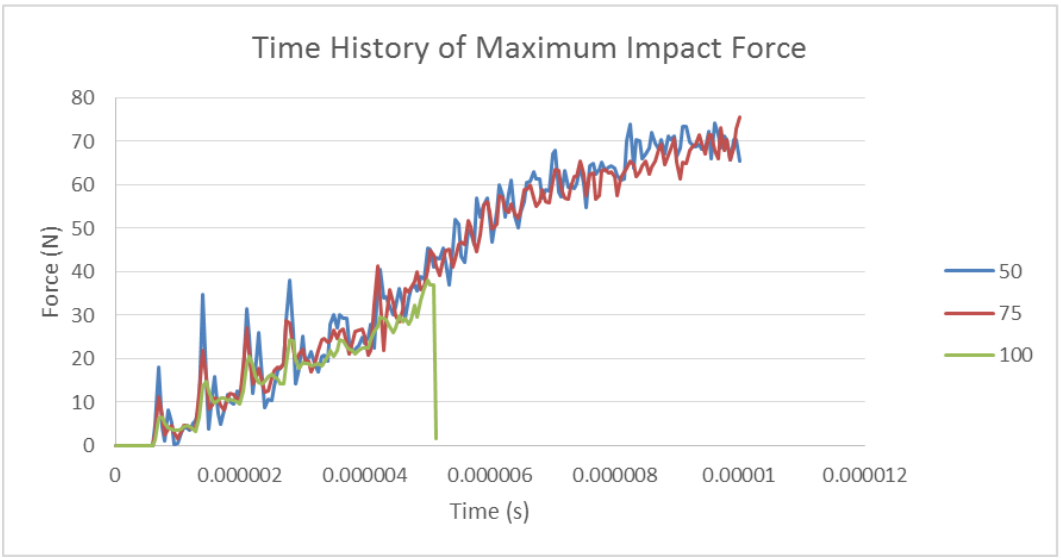

Appendix IV – Sensitivity Study: Hailstone Impact, Gelcoat Target Mesh Sensitivity

5mm Diameter

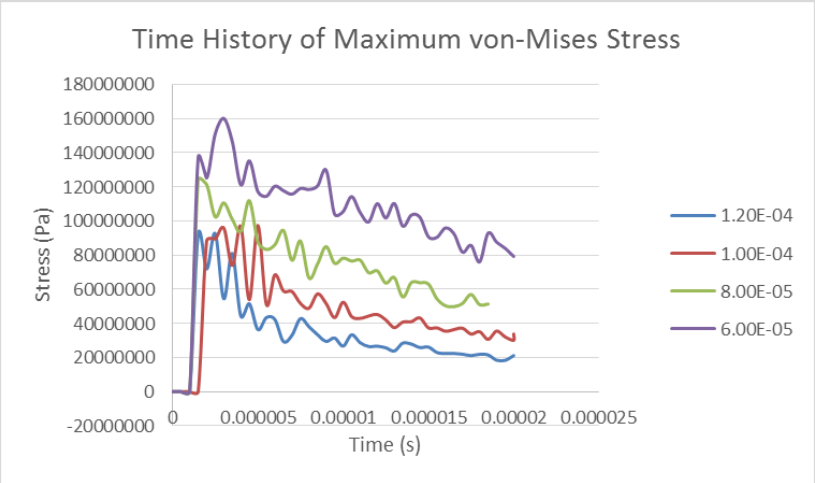

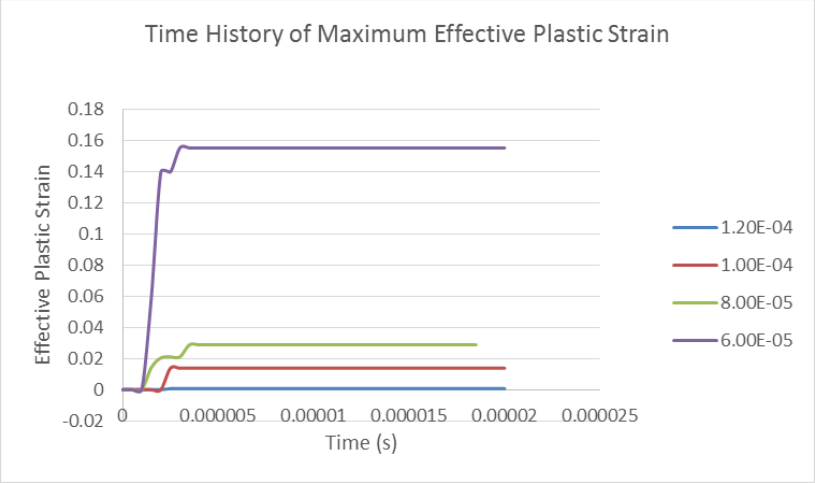

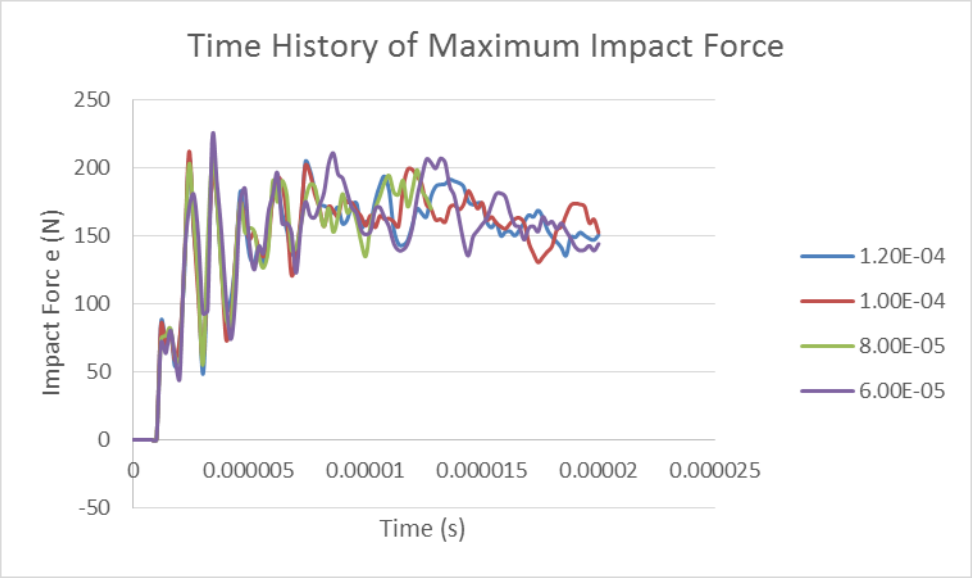

10mm Diameter

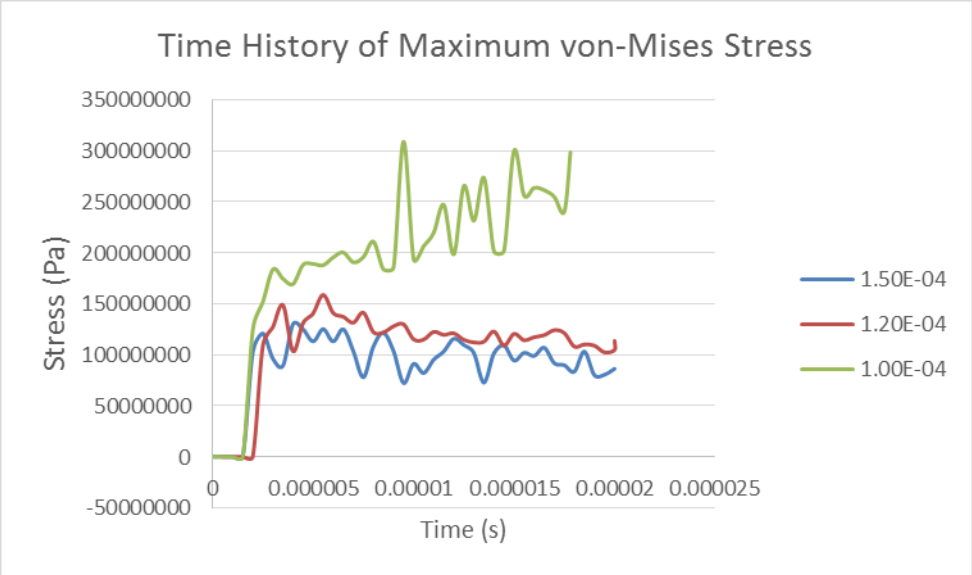

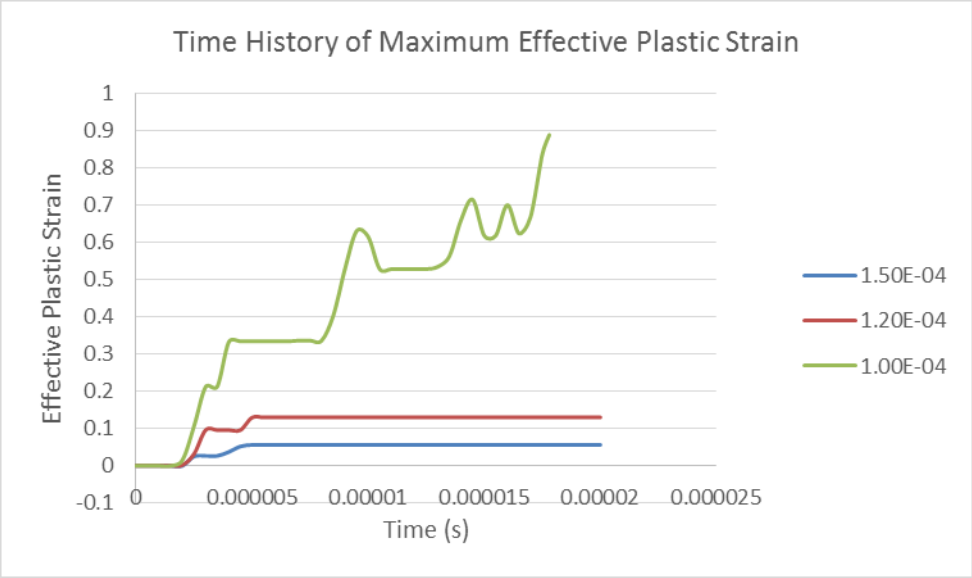

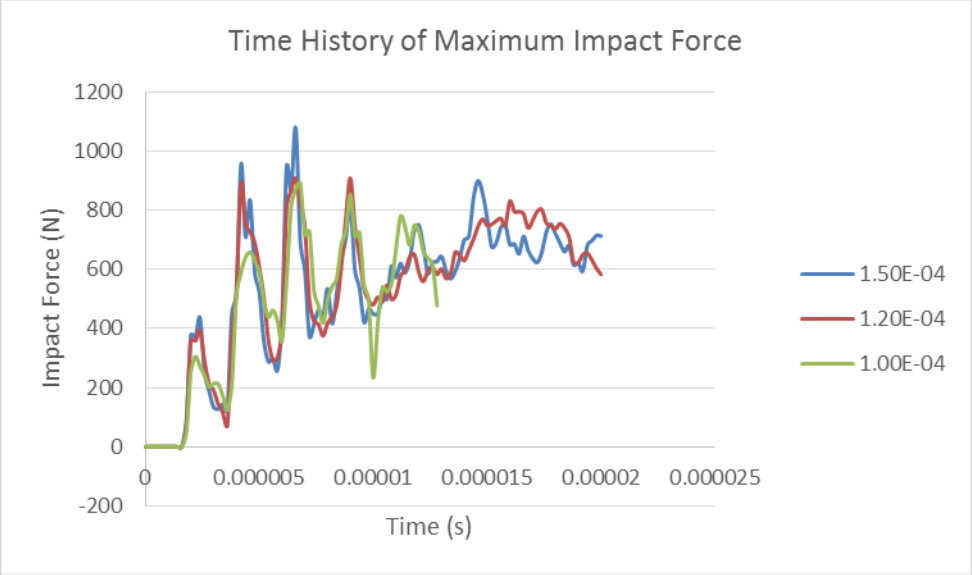

15mm Diameter

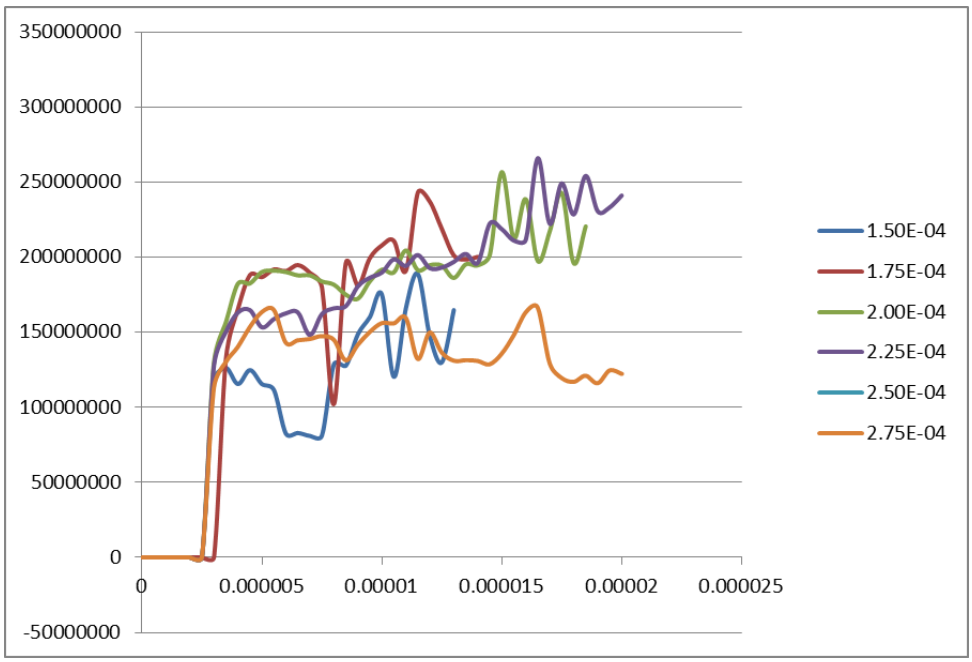
350000000
300000000
250000000
200000000
150000000
100000000
50000000
0
-50000000
0
0.000005
0.00001
0.000015
0.00002
0.000025
1.50E-04
1.75E-04
2.00E-04
2.25E-04
2.50E-04
2.75E-04

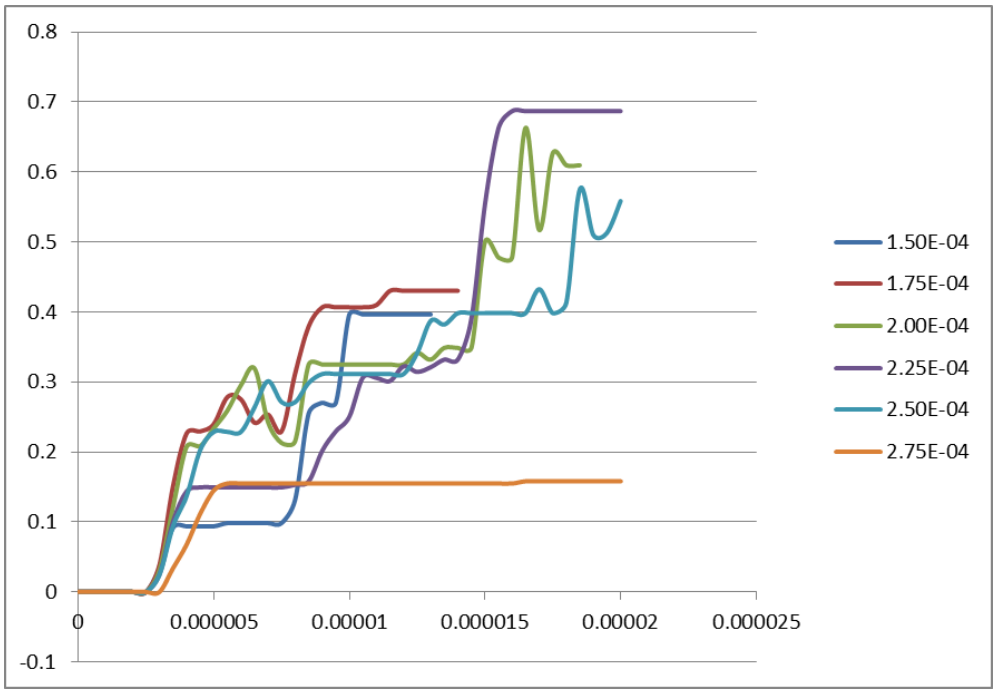
0.8
0.7
0.6
0.5
0.4
0.3
0.2
0.1
0
-0.1
0
0.000005
0.00001
0.000015
0.00002
0.000025
1.50E-04
1.75E-04
2.00E-04
2.25E-04
2.50E-04
2.75E-04

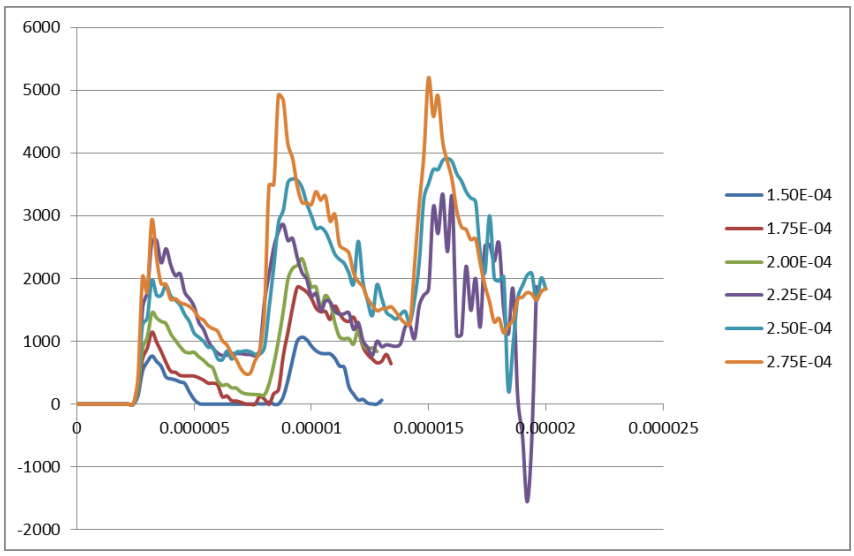
6000
5000
4000
3000
2000
1000
0
-1000
-2000
0
0.000005
0.00001
0.000015
0.00002
0.000025
1.50E-04
1.75E-04
2.00E-04
2.25E-04
2.50E-04
2.75E-04